Vol. 64 ▪ No. 10 ▪ October 2023

JNM

The Journal of Nuclear Medicine

FEATURED ARTICLE

^{68}Ga-SSO-120 PET for Initial Staging of Small Cell Lung Cancer Patients: A Single-Center Retrospective Study. David Kersting. See page 1540.

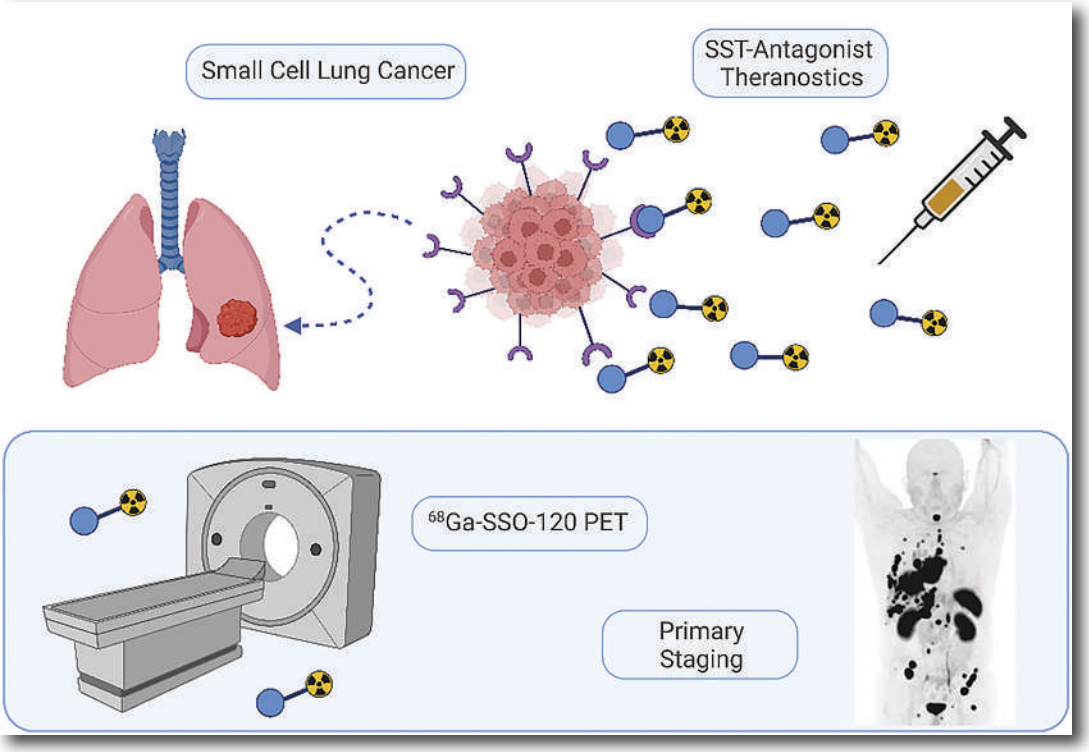

Enhancing antibody–drug conjugate efficacy: HER2-targeted immuno-PET demonstrates tumor response and highlights unexpected advantages of statin coadministration. Emma Brown et al. See page 1638.

SNMMI SOCIETY OF NUCLEAR MEDICINE & MOLECULAR IMAGING


2023 SNMMI Annual Grants & Awards Winners Brochure
download
SNMMI Annual Grants & Awards Recognition
2023 RECIPIENTS
SNMMI
SOCIETY OF NUCLEAR MEDICINE & MOLECULAR IMAGING
www.snmmi.org/2023AwardsBrochure

NEUROLITE®

KIT FOR THE PREPARATION OF TECHNETIUM Tc99m BICISATE FOR INJECTION

Critical information when you need it

High Contrast Perfusion Images

- Rapid brain uptake[1]
- Rapid blood clearance[1,2,3]
- Rapid washout from facial muscles[2,4]
- Negligible intracerebral redistribution[1,3,5]

Extended *In Vitro* stability in syringe or vial

- Greater patient scheduling flexibility[1,5,6]
- Facilitates use in multiple settings[1,5,6]
- May result in fewer doses[6]

INDICATIONS:

NEUROLITE® single photon emission computerized tomography (SPECT) is indicated as an adjunct to conventional CT or MRI imaging in the localization of stroke in patients in whom stroke has already been diagnosed. NEUROLITE® is not indicated for assessment of functional viability of brain tissue or for distinguishing between stroke and other brain lesions.

CONTRAINDICATIONS:

None known.

IMPORTANT SAFETY INFORMATION:

In clinical trials, NEUROLITE® has been administered to 1063 subjects (255 normals, 808 patients). In the 808 patients with neurologic events, there were 11 (1.4%) deaths, none of which were clearly attributed to NEUROLITE®. The following adverse effects were observed in ≤ 1% of the subjects: headache, dizziness, seizure, agitation/anxiety, malaise/somnolence, parosmia, hallucinations, rash, nausea, syncope, cardiac failure, hypertension, angina, and apnea/cyanosis.

WARNINGS:

None known.

PRECAUTIONS:

General

USE WITH CAUTION IN PATIENTS WITH RENAL OR HEPATIC IMPAIRMENT. TECHNETIUM Tc99m BICISATE IS ELIMINATED PRIMARILY BY RENAL EXCRETION. WHETHER TECHNETIUM Tc99m BICISATE IS DIALYZABLE IS NOT KNOWN. DOSE ADJUSTMENTS IN PATIENTS WITH RENAL OR HEPATIC IMPAIRMENT HAVE NOT BEEN STUDIED.

Patients should be encouraged to drink fluids and to void frequently during the 2-6 hours immediately after injection to minimize radiation dose to the bladder and other target organs. As with any other radioactive material, appropriate shielding should be used to avoid unnecessary radiation exposure to the patient, occupational workers, and other people. Radiopharmaceuticals should be used only by physicians who are qualified by specific training in the safe use and handling of radionuclides.

Please see following page(s) for brief Prescribing Information. Full Prescribing Information may be accessed at https://www.lantheus.com/assets/NEUROLITE_513073-0719mktg.pdf

References:

1. NEUROLITE® [package insert]. N. Billerica, MA: Lantheus Medical Imaging, Inc. 2. Leveille, J, Demonceau, G, Walovitch, R, Intrasubject Comparison Between Technetium-99m-ECD and Technetium-99m-HMPAO in Healthy Human Subjects, *JNM,* 1992;33(4):480-484 3. Vallabhajosula, S, Zimmerman, R, Picard, M, et al, Technetium-99m ECD: A New Brain Imaging Agent: In Vivo Kinetics and Biodistribution Studies in Normal Human Subjects, *JNM,* 1989; 30(5):599-604 4. Castagnoli, A, Borsato, N, Brung, A, et al, Cerebral *Ischemia and Dementia.* Springer-Verlag;1991: Chapter 39: SPECT Brain Imaging in Chronic Stroke and Dementia: A Comparison of ^{99m}Tc-ECD and ^{99m}Tc-HMPAO; 327-333 5. Siennicki-Lantz, A, Lilja, B, Elmstahl, S, How to interpret differing cerebral blood flow patterns estimated with ^{99}Tc^{m}-HMPAO and ^{99}Tc^{m}-ECD SPET in a healthy population, *Nuclear Medicine Communications,* 1999;20:219-226 6. Koslowsky, I, Brake, S, Bitner, S, Evaluation of the Stability of 99mTc-ECD and Stabilized 99mTc-HMPAO Stored in Syringes, *J Nucl Med Technol,* 2001;29(4):197-200

LANTHEUS™

NEUROLITE®
KIT FOR THE PREPARATION OF TECHNETIUM Tc99m BICISATE FOR INJECTION

FOR DIAGNOSTIC USE

BRIEF SUMMARY
Please see Full Prescribing Information available at https://www.lantheus.com/assets/NEUROLITE_513073-0719mktg.pdf for complete information.

INDICATIONS
Neurolite single photon emission computerized tomography (SPECT) is indicated as an adjunct to conventional CT or MRI imaging in the localization of stroke in patients in whom stroke has already been diagnosed.

Neurolite is not indicated for assessment of functional viability of brain tissue. Also, Neurolite is not indicated for distinguishing between stroke and other brain lesions.

CONTRAINDICATIONS
None known

WARNINGS
None known

PRECAUTIONS

General

USE WITH CAUTION IN PATIENTS WITH RENAL OR HEPATIC IMPAIRMENT. TECHNETIUM Tc99m BICISATE IS ELIMINATED PRIMARILY BY RENAL EXCRETION. WHETHER TECHNETIUM Tc99m BICISATE IS DIALYZABLE IS NOT KNOWN. DOSE ADJUSTMENTS IN PATIENTS WITH RENAL OR HEPATIC IMPAIRMENT HAVE NOT BEEN STUDIED.

Patients should be encouraged to drink fluids and to void frequently during the 2-6 hours immediately after injection to minimize radiation dose to the bladder and other target organs.

Contents of the vials are intended only for use in the preparation of Technetium Tc99m Bicisate and are not to be administered directly to the patient without first undergoing the preparation procedure.

The contents of each vial are sterile and non-pyrogenic. To maintain sterility, aseptic technique must be used during all operations in the manipulations and administration of Neurolite.

Technetium Tc99m Bicisate should be used within six hours of the time of preparation.

As with any other radioactive material, appropriate shielding should be used to avoid unnecessary radiation exposure to the patient, occupational workers, and other people.

Radiopharmaceuticals should be used only by physicians who are qualified by specific training in the safe use and handling of radionuclides.

ADVERSE REACTIONS
In clinical trials, Neurolite has been administered to 1063 subjects (255 normals, 808 patients). Of these, 566 (53%) were men and 494 (47%) were women. The mean age was 58 years (range 17 to 92 years). In the 808 patients, who had experienced neurologic events, there were 11 (1.4%) deaths, none of which were clearly attributed to Neurolite.

A total of 60 subjects experienced adverse reactions; the adverse reaction rates were comparable in the <65 year, and the <65 year age groups.

The following adverse effects were observed in ≤ 1% of the subjects: headache, dizziness, seizure, agitation/anxiety, malaise/somnolence, parosmia, hallucinations, rash, nausea, syncope, cardiac failure, hypertension, angina, and apnea/cyanosis.

In clinical trials of 197 patients, there were inconsistent changes in the serum calcium and phosphate levels. The cause of the changes has not been identified and their frequency and magnitude have not been clearly characterized. None of the changes required medical intervention.

To report SUSPECTED ADVERSE REACTIONS, contact Lantheus Medical Imaging, Inc. at 1-800-362-2668 or FDA at 1-800-FDA-1088 or www.fda.gov/medwatch.

Distributed by:

Lantheus Medical Imaging®

331 Treble Cove Road

N. Billerica, Massachusetts 01862 USA

For Ordering Tel: Toll Free: 800-299-3431

All Other Business: 800-362-2668

LANTHEUS™

513073-0318

PM-US-NE-0004

JNM

Volume 64 • Number 10 • October 2023

JNM The Journal of NUCLEAR MEDICINE

The Official Publication of **SNMMI**

MISSION STATEMENT: *The Journal of Nuclear Medicine* advances the knowledge and practice of molecular imaging and therapy and nuclear medicine to improve patient care through publication of original basic science and clinical research.

JNM (ISSN 0161-5505 [print]; ISSN 2159-662X [online]) is published monthly by SNMMI, 1850 Samuel Morse Drive, Reston, VA 20190-5316. Periodicals postage is paid at Herndon, VA, and additional mailing offices. Postmaster, send address changes to *The Journal of Nuclear Medicine,* 1850 Samuel Morse Drive, Reston, VA 20190-5316. The costs of publication of all nonsolicited articles in *JNM* were defrayed in part by the payment of page charges. Therefore, and solely to indicate this fact, these articles are hereby designated "advertisements" in accordance with 18 USC section 1734.

DISCLOSURE OF COMMERCIAL INTEREST: Johannes Czernin, MD, editor-in-chief of *The Journal of Nuclear Medicine,* has indicated that he is a founder of Sofie Biosciences and holds equity in the company and in intellectual property invented by him, patented by the University of California, and licensed to Sofie Biosciences. He is also a founder and board member of Trethera Therapeutics and holds equity in the company and in intellectual property invented by him, patented by the University of California, and licensed to Triangle. He also serves on the medical advisory board of Actinium Pharmaceuticals and on the scientific advisory boards of POINT Biopharma, RayzeBio, and Jubilant Pharma and is a consultant for Amgen. No other potential conflicts of interest were reported. Manuscripts submitted to *JNM* with potential conflicts are handled by a guest editor.

EDITORIAL COMMUNICATIONS should be sent to: Editor-in-Chief, Johannes Czernin, MD, *JNM* Office, SNMMI, 1850 Samuel Morse Drive, Reston, VA 20190-5316. Phone: (703) 326-1185; Fax: (703) 708-9018. To submit a manuscript, go to https://submit-jnm.snmjournals.org.

BUSINESS COMMUNICATIONS concerning permission requests should be sent to the publisher, SNMMI, 1850 Samuel Morse Drive, Reston, VA 20190-5316; (703) 708-9000; home page address: jnm.snmjournals.org. Subscription requests and address changes should be sent to Membership Department, SNMMI at the address above. Notify the Society of change of address and telephone number at least 30 days before date of issue by sending both the old and new addresses. Claims for copies lost in the mail are allowed within 90 days of the date of issue. Claims are not allowed for issues lost as a result of insufficient notice of change of address. For information on advertising, contact Team SNMMI (Kevin Dunn, Rich Devanna, and Charlie Meitner; (201) 767-4170; fax: (201) 767-8065; TeamSNMMI@cunnasso.com). Advertisements are subject to editorial approval and are restricted to products or services pertinent to nuclear medicine. Closing date is the first of the month preceding the date of issue.

INDIVIDUAL SUBSCRIPTION RATES for the 2023 calendar year are $633 within the United States and Canada; $680 elsewhere. Make checks payable to the SNMMI. CPC IPM Sales Agreement No. 1415158. Sales of individual back copies from 1999 through the current issue are available for $60 at http://www.snmmi.org/subscribe (subscriptions@snmmi.org; fax: (703) 667-5134). Individual articles are available for sale online at http://jnm.snmjournals.org.

WHAT IS AN SNMMI RPT CENTER OF EXCELLENCE?

To learn more and apply, visit
www.snmmi.org/RPTCOE

SNMMI SOCIETY OF NUCLEAR MEDICINE & MOLECULAR IMAGING

SNMMI created the Radiopharmaceutical Therapy (RPT) Center of Excellence (COE) Program to allow centers with expertise in RPT to showcase their capabilities and services, including research. A designation means that your site has the personnel, expertise, and equipment to manage the care of patients requiring RPT. The designations levels are Comprehensive, Clinical, or Basic Therapy Center.

Targeted RPTs are changing the way patients with cancer are treated. These advances have allowed providers to treat and manage a multitude of other cancers and diseases. Not all sites have the expertise to use these agents clinically or in clinical trials.

If your site has experience with one or more radiopharmaceutical therapies, we encourage you to apply for the SNMMI RPTCOE designation.

COMPREHENSIVE RPT CENTER

An application fee of $1,500 for members and $2,500 for non-members is required for a 2-year designation.

SCAN QR CODE TO APPLY

CLINICAL RPT CENTER

An application fee of $900 for members and $1,500 for non-members is required for a 2-year designation.

SCAN QR CODE TO APPLY

BASIC RPT CENTER

The designation does not require any application fee and is valid for a 2-year designation.

SCAN QR CODE TO APPLY

SNMMI SOCIETY OF NUCLEAR MEDICINE & MOLECULAR IMAGING
MID-WINTER MEETING

ACNM
ANNUAL MEETING

REGISTRATION OPENS IN MID-OCTOBER

WWW.SNMMI.ORG/MWM

Feb. 1-3 2024 SNMMI Mid-Winter and ACNM Annual Meeting

Hilton Orlando Lake Buena Vista

ORLANDO, FLORIDA

Discussions with leaders: Czernin speaks with Patricia A. Ganz, an internationally recognized medical oncologist, about her pioneering work in quality-of-life outcomes and cancer survivorship. *Page 1506*

AI deployment and governance ethics: Herington and members of the SNMMI Artificial Intelligence Task Force identify 4 major ethical risks in deployment of AI medical devices and offer preliminary recommendations for managing these risks. *Page 1509*

Looking ahead to actinium: Zimmermann summarizes 5 different technologies for production of ^{225}Ac and reviews remaining issues to be resolved before widespread clinical application of ^{225}Ac-labeled agents. *Page 1516*

TSPO PET in glioblastoma: Albert and colleagues investigate the association of 18-kDa translocator protein PET imaging results with survival outcomes in a cohort of patients with histologically proven isocitrate dehydrogenase–wild-type glioblastoma. *Page 1519*

PSMA imaging and expression in GBM: van Lith and colleagues quantify uptake of various PSMA-targeting tracers in glioblastoma multiforme and correlate the results with PSMA expression in tumor biopsy samples from the same patients. *Page 1526*

^{68}Ga-FAPI PET and uHCC response: Wu and colleagues compare baseline ^{68}Ga-labeled fibroblast activation protein inhibitor PET/CT and ^{18}F-FDG PET/CT in response and survival prediction in unresectable hepatocellular carcinoma treated with the programmed cell death 1 inhibitor and lenvatinib. *Page 1532*

^{68}Ga-SSO-120 PET in SCLC: Kersting and colleagues report on tumor uptake and detection rates of PET using the ^{68}Ga-labeled somatostatin receptor 2 antagonist satoreotide trizoxetan in comparison to ^{18}F-FDG PET in initial staging of small cell lung cancer. *Page 1540*

[^{68}Ga]PSMA PET and bPFS prediction: Chen and colleagues explore the association between changes on [^{68}Ga]PSMA PET/CT and biochemical progression-free survival in high-risk patients who underwent neoadjuvant therapy before radical prostatectomy. *Page 1550*

^{68}Ga-PSMA PET during ^{223}Ra therapy: de Jong and colleagues determine the utility of ^{68}Ga-PSMA PET/CT for response evaluation of ^{223}Ra treatment in patients with metastatic castration-resistant prostate cancer. *Page 1556*

SN procedure in MiN0 PSMA PET: Duin and colleagues assess the diagnostic value of the sentinel node procedure for lymph node staging in primary intermediate- and high-risk prostate cancer patients with node-negative results on PSMA PET/CT. *Page 1563*

[^{177}Lu]Lu-PSMA-617 patient waste: Graves evaluates the relative radiation safety merits of contaminated waste disposal in the normal household stream in comparison to other management strategies in patients with metastatic castration-resistant prostate cancer undergoing radiopharmaceutical treatment. *Page 1567*

Radioligand therapy in CKD: Mercolli and colleagues describe dosimetric evaluation of PSMA-based radioligand treatment for metastatic prostate cancer in a patient with autosomal-dominant polycystic kidney disease. *Page 1570*

[^{225}Ac]Ac-PSMA in end-stage mCRPC: Alan-Selcuk and colleagues retrospectively analyze the outcomes of 23 patients with advanced-stage metastatic castration-resistant prostate cancer refractory to [^{177}Lu]Lu-PSMA and treated with [^{225}Ac]Ac-PSMA. *Page 1574*

mHTT PET in an NHP model of HD: Bertoglio and colleagues validate the novel radioligand ^{11}C-CHDI-180R using PET imaging for quantification of cerebral mutant huntingtin protein aggregates in a macaque model of Huntington disease. *Page 1581*

Biogen OGA PET: Cook and colleagues detail development of 2 ^{11}C-labeled PET tracers targeting *O*-GlcNAcase, a protein with a potential role in tau aggregation in Alzheimer disease, through studies in rodents, human brain tissue, and nonhuman primates. *Page 1588*

Automated ^{18}F-FET PET response assessment: Gutsche and colleagues report on a method for automated metabolic tumor volume segmentation in amino acid PET imaging and evaluate its performance for response assessment in patients with gliomas. *Page 1594*

Machine learning in DLBCL prognostication: Zhao and colleagues outline an analytic approach based on [^{18}F]FDG PET radiomics using stacking ensemble learning to improve outcome prediction in diffuse large B-cell lymphoma. *Page 1603*

Single-time-point dosimetry after PRRT: Chicheportiche and colleagues describe and validate a multiple-linear-regression model to predict absorbed doses in ^{177}Lu-DOTATATE peptide receptor radionuclide therapy from a single-time-point posttreatment study. *Page 1610*

Single- vs. multiple-time-point dosimetry: Scheuermann and Pryma offer perspective on the importance of dosimetry in radiopharmaceutical therapy and question the advantages of simplified approaches in a complex field with many unresolved questions. *Page 1617*

^{177}Lu or ^{161}Tb TRT: Larouze and colleagues compare uniform and nonuniform targeted radionuclide therapy with these agents within tumor cell clusters using the Monte Carlo code CELLDOSE and suggest that dual targeting may minimize heterogeneity in results. *Page 1619*

^{161}Tb-based radioligand therapy: Tschan and colleagues assess the dosimetry and therapeutic efficacy of ^{161}Tb and ^{177}Lu in tumor-bearing mice using SibuDAB and PSMA-I&T, which differ in blood residence time and tumor uptake. *Page 1625*

TCP and Monte Carlo dosimetry model: Mellhammar and colleagues calculate tumor control probability from dosimetry simulations of heterogeneous absorbed dose distributions within xenografts treated with PSMA-617–ligated radioactivity. *Page 1632*

Immuno-PET and ADC efficacy: Brown and colleagues use the ^{89}Zr- or ^{64}Cu-labeled anti-HER2 antibody trastuzumab to investigate different dosing regimens of antibody–drug conjugate therapy with and without coadministration of lovastatin in 2 xenografted models. *Page 1638*

Ambient light–resistant SWIRFI: Mc Larney and colleagues explore in preclinical studies the potential of pH low-insertion peptide conjugated to indocyanine green, currently in clinical trials, as a candidate for cancer-targeted shortwave infrared fluorescence imaging. *Page 1647*

^{64}Cu- and ^{68}Ga-labeled GRPR ligands: Koller and colleagues research theranostic applications of a novel gastrin-releasing peptide receptor ligand with improved metabolic stability and potential for enhancing diagnostic and therapeutic efficacy. *Page 1654*

Postinfarction renal fibrosis and PET: Unterrainer and colleagues provide a case report on the use of [^{68}Ga]Ga–fibroblast activation protein inhibitor–46 PET for visualization of postinfarction renal fibrosis. *Page 1660*

A Tribute to Our *JNM* Associate Editors

Johannes Czernin

David Geffen School of Medicine at UCLA, Los Angeles, California

As I enter my eighth year as editor-in-chief, *The Journal of Nuclear Medicine* (*JNM*) continues to mirror the best in our field, reflecting an expanding international focus on the integration of new techniques, agents, and instrumentation into the broadest range of diagnostics, therapeutics, and theranostics. Our success is the result of the efforts of a constellation of extraordinary editorial and production contributors, who manage more than 1,100 submissions from around the globe every year.

I owe a special debt of gratitude to our expert volunteers who serve as *JNM* associate editors (AEs), bringing their subject matter expertise and scientific insight to the evaluation of these submissions, identifying the most promising work and providing oversight throughout the rigorous editorial process. Together, the *JNM* AEs are a powerful force, not only in maintaining the highest standards but in working with me to determine the future direction of the journal in a rapidly changing nuclear medicine landscape. They are also effective in outreach to their respective practice communities, actively recruiting leading authors and scientists with new and exciting investigative work and perspectives.

This year, H. William Strauss ended his long and productive service as the continuing education section AE, a role he has shared for the past 8 y with Dr. Heiko Schöder. Dr. Strauss will continue to serve as a consultant to the editor-in-chief. Dr. Schöder also stepped down from his continuing education responsibilities but will continue as an AE with special responsibilities for oncology topics, among many other important themes. Lale Kostakoglu and Hossein Jadvar are the new AEs for the continuing education section. Dr. Kostakoglu previously served as an AE for oncology, and Dr. Jadvar joined the AE team in July 2022.

Also joining the AE group last year was Thomas A. Hope, who, among other responsibilities, is helping the journal navigate the growing number of practice procedure standards and guidelines. As a member of the Society of Nuclear Medicine and Molecular Imaging Committee on Procedure Standards, he is well prepared for this role.

Marcelo F. Di Carli has stepped down after long-time service as the AE for cardiology topics, which he managed jointly with Frank M. Bengel. All of us at *JNM* thank Dr. Di Carli for his remarkable contributions and congratulate him on his appointment as the new editor-in-chief of the *Journal of Nuclear Cardiology*. Drs. Di Carli and Bengel also are the editors of an upcoming *JNM* special supplement on cardiovascular imaging. Sharmila Dorbala will join Dr. Bengel as the new *JNM* AE team member for cardiology.

Editing a discipline-leading medical journal is a rewarding challenge, possible only through the contributions of many individuals. I want to thank all the *JNM* AEs—those in changing roles and others who continue their valuable work—for their excellent counsel, dedication, and unfailing collegiality.

DOI: 10.2967/jnumed.123.266620

Pioneering Research on Cancer Quality of Life and Outcomes

Johannes Czernin Discusses a Half-Century of Whole-Patient Focus with Patricia A. Ganz

Patricia A. Ganz[1] and Johannes Czernin[2]

[1]*UCLA Fielding School of Public Health, Los Angeles, California; and* [2]*David Geffen School of Medicine at UCLA, Los Angeles, California*

Johannes Czernin, MD, editor-in-chief of *The Journal of Nuclear Medicine,* spoke with Patricia A. Ganz, MD, a medical oncologist who is internationally recognized for pioneering work on quality-of-life outcomes in cancer patients and in cancer survivorship. She is a Distinguished Professor of Health Policy & Management at the Fielding School of Public Health (since 1992) and a professor of medicine at the David Geffen School of Medicine (since 1978), both at the University of California, Los Angeles (UCLA). She received her undergraduate degree from Harvard University (Radcliffe College, Boston, MA) and her medical degree from the UCLA School of Medicine. She completed her training in internal medicine and hematology/oncology at UCLA Medical Center. Since 1993 she has been the Associate Director for Population Science Research at the Jonsson Comprehensive Cancer Center at UCLA, where she also leads the Cancer Control and Survivorship Program. In 1999 she was awarded an American Cancer Society Clinical Research Professorship for "Enhancing Patient Outcomes Across the Cancer Control Continuum."

Dr. Ganz was elected to the Institute of Medicine (now the National Academy of Medicine) in 2006. She served on the National Cancer Institute Board of Scientific Advisors from 2002 to 2007 and on the American Society of Clinical Oncology Board of Directors from 2003 to 2006. She received the American Cancer Society Medal of Honor in 2010 and recently was the recipient of the American Association for Cancer Research–American Cancer Society Award for Research Excellence in Cancer Epidemiology and Prevention.

Dr. Czernin: *Patricia, you have made major contributions to cancer prevention and treatment and to our understanding of therapy consequences such as cognitive dysfunction after chemotherapy and cardiotoxicity. You were a pioneer in patient-centered outcomes, emphasizing the importance of quality of care and introducing survivorship programs. But as an undergraduate at Harvard you started out in a different direction, with a degree in biology and no hint of your future work.*

Dr. Ganz: My first publication was in the *American Journal of Physiology* (1970;219:604–612) describing my senior thesis research on an isolated rat heart preparation. This followed several previous summers during undergraduate years volunteering in a UCLA pediatric cardiology research laboratory (where I met my future husband, Tom Ganz). Encouraged by my physician father and these laboratory experiences, I decided to apply to medical school, returning to Los Angeles to attend UCLA Medical School. Tom was finishing his senior year of college, and we were married at the end of my first year of medical school. My first exposure to cancer patients occurred during my internship. Cisplatin was in phase II trials and being tested in testicular cancer patients. There were amazing responses, with young men who were on their death beds rising like Lazarus. Then we had doxorubicin and began to treat lymphomas and even breast cancer with chemotherapy. With these exciting therapeutic innovations, I decided to become an oncologist rather than pursue a career in cardiology. When I joined the UCLA faculty, hospice care was only beginning to be evaluated. At the Veterans Affairs hospital at Sepulveda, I was asked to lead a palliative care unit, providing multidisciplinary care for veterans with advanced cancers that were incurable. This proved to be a wonderful setting for research. We developed one of the first quality-of-life questionnaires. We created a cancer research team that included a psychiatrist, a psychologist, and a medical oncologist. You can really do a lot more together. And it was from that moment that we did team science.

Patricia A. Ganz, MD

Dr. Czernin: *What would you add to this group today?*

Dr. Ganz: Thinking about quality-of-life outcomes was important. But to understand the impact of cancer on patients, today imaging, biomarkers, and inflammatory markers should be included. We would add psychosocial research in terms of survey research and would get the help of statisticians for population science research.

Dr. Czernin: *The concept of survivorship did not actually exist at this time?*

Patricia Ganz: The concept of cancer survivors emerged in the mid-1980s, reflecting new cures in lymphoma and testicular cancer patients, as well as childhood cancer survivors. Although palliation of symptoms was being developed at that time for patients with advanced cancer, we now realize that palliation is important anywhere along the continuum, whether for newly diagnosed patients, those with advanced disease, or long-term survivors—especially noteworthy for young adults surviving childhood cancers.

Late effects from chemotherapy and radiation were causing damage to the brain and heart, leading to chronic disease and early mortality, as well as to second cancers. To better understand the late effects of cancer treatment it was important to capture

DOI: 10.2967/jnumed.123.266602

information directly from the patient. In 1990 I chaired a National Cancer Institute workshop on including quality-of-life assessment in clinical trials. The Food and Drug Administration was extremely resistant. They were at the meeting and said, "Well, how can you believe what the patient says?"

Dr. Czernin: *When did you start to focus on patients at high risk for cancer through inheritance?*

Dr. Ganz: Family studies in the early 1990s showed potential hereditary genetic abnormalities on chromosomes 17 and 13, which were named *BRCA1* and *BRCA2*. The genes were cloned in the mid-1990s, and commercial testing for mutations became available. Some ethicists were concerned about offering testing, with the argument that we did not have much to offer to these patients. However, many patients were interested in having information that could help their families understand their risk for cancer. With cancer center support, we were able to start a family registry that provided genetic counseling through a research protocol.

Dr. Czernin: *What did you offer the patients at that time?*

Dr. Ganz: In 1998, prophylactic mastectomies were not performed very often. Our research protocol assessments were done with a certificate of confidentiality, and we did not put the test results in the medical record. People were worried about insurance discrimination. We are so much farther ahead now, to the point where some are even arguing for universal testing in unaffected individuals. Eventually genetic testing became a clinical standard of care for cancer patients and their family members.

Dr. Czernin: *When and how did knowledge about high-risk patients transform early diagnostic approaches?*

Dr. Ganz: Initially, stigmas were attached, and it was difficult to get people tested. But once they began to be tested, around the early 2000s, we offered them either oophorectomy or bilateral mastectomies for prevention. However, it was not until the Genetic Information Nondiscrimination Act (GINA) of 2008 that most people felt safe getting tested. GINA protects individuals against health coverage or employment discrimination based on their genetic information. Screening with MRI began, for early identification of individuals with family histories who might just want to have surveillance.

Dr. Czernin: *Recently the mammography guidelines have changed, with the recommended screening age changing from 50 to 40 years old. Can you elaborate on what happened?*

Dr. Ganz: There are no new data at all on women in their 40s. All of the randomized mammography studies were done in the 1990s or even 1980s. As we know, mammography is not a perfect test; there are many false-positives. A few years ago, the U.S. Preventive Services Task Force (USPSTF) said, "Only start screening at 50, and it should be every other year. For women in their 40s, a discussion should take place." But the American Cancer Society recommended that women should start screening at 45, with screening annually through the 50s and then every other year after 60. So the new USPSTF guideline was actually not based on any new data. However, breast cancer is so much more common in younger African American women, so the USPSTF saw this as an opportunity for early detection, despite the risk of false-positives. Patients who are at high risk or a member of a group at high risk definitely needs to be screened at these younger ages.

Dr. Czernin: *There was still some controversy about this change, but you are clearly in favor.*

Dr. Ganz: I think so. The problem is that they recommend screening every other year, which doesn't make sense. We need better guidelines for who is at high risk and needs MRI.

Dr. Czernin: *What are some of the major advances in breast cancer care, and what are the next challenges?*

Dr. Ganz: We converted women with triple-negative or HER2-positive cancers who were not hormone receptor–positive into long-term survivors. That's an amazing story. For patients with estrogen receptor–positive cancers, we have the problem of lifelong continuous recurrence and very late relapses. So a lot of what we are looking at now is tumor dormancy. Why is it that 15 or 20 years later, those cells suddenly start to wake up? Can we figure out who those women are? Can we identify individuals who might be at risk for recurrence? And if we treat them early, will it make a difference? We have no idea. But that is the direction in which things are going with treatment of patients with hormone receptor–positive disease.

Dr. Czernin: *Many of your major research themes have come together in the concept of patient-reported outcomes, including cancer-related cognitive impairment or fatigue.*

Dr. Ganz: These persistent symptoms can actually happen with surgery or radiation alone but more often occur with chemotherapy or endocrine therapy. A lot of what we think is going on with fatigue or with cognitive changes is increased inflammation in the brain. The systemic inflammation associated with chemotherapy or radiation crosses through the blood–brain barrier, activates the microglia, and causes local inflammation. That is what we think slows down thinking and functioning. So we are testing oxaloacetate in a phase 2 trial to determine whether this glutamate scavenger can reduce some of that inflammation.

Dr. Czernin: *Is cognitive dysfunction after chemotherapy usually fairly stable?*

Dr. Ganz: As I began my interest in this 20 or more years ago, I would ask anyone to whom we gave chemotherapy, "Are you having any troubles?" And it was mostly women, 55 years old or younger, who were having problems. Patients in their 60 s who received the same recipe—no problem. Daniel Silverman, MD, PhD, and I used brain PET to study patients who had undergone chemotherapy, surgery, and radiation, and we picked up some subtle differences in patients who were getting endocrine therapy and those who were not. This was before ovarian suppression was widely used. Today we are about to launch a trial that includes 5 years of ovarian suppression with endocrine therapy, with or without chemo. I am really worried for those younger women, so I'm working very hard to do a parallel cohort study that can look at these women 10 or 15 years later. I won't be around to analyze it, but it's my legacy.

Dr. Czernin: *Another line of your research is centered around quality of care. What should be the key metrics for quality of care?*

Dr. Ganz: What does patient-centered care delivery mean? It means that patients and their families know from the beginning

---

" . . . .[Cancer patients] have psychologic, behavioral, and family settings that can either help promote their well-being and recovery or adversely affect it. If we think only about the tumor and not the whole person, we are not going to deliver the best care."

---

what their diagnoses are and what treatment options are available. Some patients will say "I want you to decide," and others will say "No, I want to be more involved." Psychosocial services must be included in these decisions, with screening for depression and anxiety and appropriate management with professional interventions and medications. Palliative care must be available from the very beginning; we cannot wait until the patient reaches the end-of-life stage. We also need to talk frankly about the cost of care. If a new targeted agent costs $20,000–$30,000 out-of-pocket, some patients with advanced disease may choose not to spend their life savings on that. These are decisions that require a team. From my own perspective, most oncology professionals focus on the tumor, its biologic characteristics, and the extent of disease; they do not think about the person in whom the tumor grows. That person has a life history—one that, in fact, may have affected the kind of cancer with which they have been diagnosed. But they also have psychologic, behavioral, and family settings that can either help promote their well-being and recovery or adversely affect it. If we think only about the tumor and not the whole person, we are not going to deliver the best care.

Dr. Czernin: *The final question I have is on the topic of aging and cancer, another focus of your current work. Does adaptation to disease become more and more difficult with age?*

Dr. Ganz: A lot of work has demonstrated epigenetic and inflammatory changes after chemotherapy or radiation, with accelerated aging in the tissues. This may be influenced by host factors predisposing some people to such age acceleration. We did a very nice study about 20 years ago that included a group of breast cancer survivors who were previously evaluated and persistently fatigued at 5–10 years after cancer treatment and a group who were not fatigued. We exposed them to a standardized stressful evaluation in which they did mental arithmetic and gave a speech before a panel of judges. We found that the cortisol response was blunted in persistently fatigued survivors and that without this elevation in cortisol there was more inflammation in the body. What we are seeing now in long COVID is that only certain individuals are experiencing "brain fog" or fatigue, just like after cancer treatment, with only some individuals predisposed. By the way, fatigue is one of the hallmark manifestations for age-related frailty. It is my view that the body has only a limited repertoire for response to these kinds of stresses. Very intensively treated breast cancer patients are more likely to see these problems. There is an interaction among the host factors, the person, their biology, their genetics, and the exposure, so that in that group we tend to see clinical and biologic evidence of acceleration of aging features.

Dr. Czernin: *We do not need to belabor the challenges of access to care, because they are so obvious and pervasive. But in your opinion, what is our responsibility to improve access, expand the availability of screening, and address health care disparities in cancer?*

Dr. Ganz: The cancer care system sometimes can give people an advantage in getting services, especially since it is more likely that patients will get emergency medical assistance. Think of what Mark Litwin, MD, MPH, has done with his prostate cancer program throughout California, supported by the state government. Those men getting access to the state program get a lot of attention and resources for neglected conditions. But I think all along the continuum, we need to be able to identify high-risk people from multiple perspectives: genetic, socioeconomic, or racial.

Dr. Czernin: *What is your advice for young people today as they enter the medical field? Who should enter it, and what should be their driving force?*

Dr. Ganz: I just came back from the American Society of Clinical Oncology meeting, and I was impressed with the number of young people there. People are being attracted now to focus on cancer in a different way from when you and I were in our early careers. We were attracted because we were interested in the whole person. We didn't always expect to cure someone, but we could care for them. The disease was interesting scientifically, and the research opportunities were there. Young physicians today are really focused on therapeutics and new targets; I think that is what attracts them. I have an oncology fellow who is getting a PhD in health policy with me, and at an upcoming research retreat she is presenting her work in psychosocial outcomes for young adults treated for cancer. Very few of the current fellows are interested in these topics; instead, they are focused on new drug targets.

Dr. Czernin: *What do you think should be driving them?*

Dr. Ganz: Part of the problem is that our health care system is so fragmented that it is difficult to deliver good care. Most community physicians don't have social workers, nurse practitioners, or other specialized individuals who can serve to extend the physicians' care. One minute the physician is seeing somebody with advanced lung cancer, the next minute someone with melanoma, and the next someone with advanced pancreatic cancer. It's really hard. Cancer care is not organized in a way that protects the physician from burnout or that encourages opportunities for team care experiences. We need to change the way cancer care is delivered.

Dr. Czernin: *Thank you, Patricia, for taking the time to talk with our readers and provide them with your unique insights into cancer care.*

Ethical Considerations for Artificial Intelligence in Medical Imaging: Deployment and Governance

Jonathan Herington[1], Melissa D. McCradden[2], Kathleen Creel[3], Ronald Boellaard[4], Elizabeth C. Jones[5], Abhinav K. Jha[6], Arman Rahmim[7], Peter J.H. Scott[8], John J. Sunderland[9], Richard L. Wahl[10], Sven Zuehlsdorff[11], and Babak Saboury[5]

[1]*Department of Health Humanities and Bioethics and Department of Philosophy, University of Rochester, Rochester, New York;* [2]*Department of Bioethics, Hospital for Sick Children, and Dana Lana School of Public Health, University of Toronto, Toronto, Ontario, Canada;* [3]*Department of Philosophy and Religion and Khoury College of Computer Sciences, Northeastern University, Boston, Massachusetts;* [4]*Department of Radiology and Nuclear Medicine, Cancer Centre Amsterdam, Amsterdam University Medical Centres, Amsterdam, The Netherlands;* [5]*Department of Radiology and Imaging Sciences, Clinical Center, National Institutes of Health, Bethesda, Maryland;* [6]*Department of Biomedical Engineering and Mallinckrodt Institute of Radiology, Washington University in St. Louis, St. Louis, Missouri;* [7]*Departments of Radiology and Physics, University of British Columbia, Vancouver, British Columbia, Canada;* [8]*Department of Radiology, University of Michigan Medical School, Ann Arbor, Michigan;* [9]*Departments of Radiology and Physics, University of Iowa, Iowa City, Iowa;* [10]*Mallinckrodt Institute of Radiology, Washington University in St. Louis, St. Louis, Missouri; and* [11]*Siemens Medical Solutions USA, Inc., Hoffman Estates, Illinois*

The deployment of artificial intelligence (AI) has the potential to make nuclear medicine and medical imaging faster, cheaper, and both more effective and more accessible. This is possible, however, only if clinicians and patients feel that these AI medical devices (AIMDs) are trustworthy. Highlighting the need to ensure health justice by fairly distributing benefits and burdens while respecting individual patients' rights, the AI Task Force of the Society of Nuclear Medicine and Molecular Imaging has identified 4 major ethical risks that arise during the deployment of AIMD: autonomy of patients and clinicians, transparency of clinical performance and limitations, fairness toward marginalized populations, and accountability of physicians and developers. We provide preliminary recommendations for governing these ethical risks to realize the promise of AIMD for patients and populations.

Key Words: AI ethics; software as medical device; fairness; explainability; justice

J Nucl Med 2023; 64:1509–1515
DOI: 10.2967/jnumed.123.266110

Artificial intelligence (AI) and machine learning systems will likely soon be incorporated into various aspects of patient care in nuclear medicine. These AI medical devices (AIMDs) fuse traditional medical devices with continuously learning software systems to improve patient care and health-care worker practices. AI in nuclear medicine offers a tremendous opportunity for faster and more reliable diagnoses (*1*), and over 340 medical imaging AIMDs have been approved by the U.S Food and Drug Administration at the time of writing this publication (*2*). The ethical benefits of AIMD may be particularly profound in nuclear medicine, where the use of radiation generates a strong imperative to use all feasible means to minimize exposure doses (e.g., the ALARA principle) and improve the accuracy of treatment. However, the deployment of AI without regard to potential ethical risks may result in unintended harm to patients and health-care systems (*3*). Many have raised concerns regarding patient privacy, the opacity of algorithms, deskilling of clinicians, and the robustness of systems in lower resource contexts (*4–7*). Moreover, there is mounting evidence that AIMDs may exacerbate existing health disparities based on race, ethnicity, sex, and socioeconomic status (*8–10*). Grappling with these ethical issues is essential before the widespread adoption of AIMDs in nuclear medicine.

The AI Task Force of the Society of Nuclear Medicine and Molecular Imaging has set out to make clear the assignments of responsibility between developers, physicians, and regulators by distinguishing between the development and deployment of AIMDs. In a companion paper (*11*), we will discuss the ethical duties of researchers in 3 phases of the AIMD production pipeline: during data collection, training and validation, and evaluation of the tool. In this paper, we focus on the obligations of clinicians and regulators during the deployment of AIMD.

The use of medical devices has historically been constrained by the traditional 4 principles of medical ethics—autonomy, nonmaleficence, beneficence, and justice—with the greatest emphasis placed on patient autonomy and nonmaleficence (*12*). AIMDs are sometimes thought to make compliance with these first 2 principles more challenging. By automating diagnostic and prognostic tasks within opaque AI models, they make informing patients and catching errors more difficult. Professional societies have thus sought to extend the core ethical principles of autonomy, beneficence, nonmaleficence, and justice to include further principles such as explicability and transparency to buttress patient autonomy and prevent harmful errors (*6*).

Although these extended frameworks are well suited to interactions between clinicians and individual patients, they are less well suited to the governance of AIMDs within complex health systems. Governance of AIMDs requires distributing benefits and burdens between multiple stakeholders. For instance, reasonable people may disagree about the appropriate tradeoff between false-positive and false-negative rates for the detection of malignancies, but an AIMD may be able to encode only a single tradeoff for all

Received Nov. 28, 2022; revision accepted Jul. 11, 2023.
For correspondence or reprints, contact Babak Saboury (babak.saboury@nih.gov).
Published online Aug. 24, 2023.

TABLE 1
Ethical Dimensions of AIMDs According to Primary Responsible Party: Clinicians During Deployment, Governance by Administrators and Professional Societies, and Governance by State and Federal Regulators

Ethical dimension	Clinicians during deployment	Governance by administrators and societies	Governance by regulators
Welfare	Ensure familiarity with performance and limitations of AIMDs before use	Ensure clinicians are trained in AIMD performance and limitations	Ensure that clinical utility, not just in silico performance, is evaluated and declared
	Avoid off-label or unevaluated use of AIMD	Avoid automation bias through technical and policy interventions	Ensure that legal liability for harm is clearly demarcated
Autonomy	Ensure consent to direct data collection and that risks, benefits, and limitations of AIMD are declared to patient	Ensure clear protocols for declaring risks and benefits of AIMD to patients	Ensure that performance and limitations are declared in ways that enable patient and clinician decision-making
	Consider notification for secondary reuse of data in learning AIMDs	Promote legitimacy by involving patients in policy priority setting for AIMD use	Promote techniques that explain salience of input features at population level
Justice	Carefully justify use of sensitive attributes (race, sex, etc.) as input features	Ensure regular auditing of performance disparities by race, sex, etc.	Require evaluation of performance disparities by race, sex, etc.
	Avoid conflicts of interest as clinician/researcher	Ensure clear mechanisms for managing clinician/researcher conflicts of interest	Promote broad access to AIMDs through subsidy and regulation

Use of term *ensure* or *required* denotes legally or ethically required conduct; use of term *promote* or *avoid* denotes ethically ideal conduct.

patients. The traditional principles of clinical ethics, which focus on the obligations of caregivers or researchers in direct contact with patients, cannot be straightforwardly applied to these multiagent decisions (*13,14*). In this respect, the governance of AIMDs ought to take seriously the problem of navigating the circumstances of justice, where multiple stakeholders must work together to produce a shared good (i.e., AIMDs) while respecting one another's rights and fairly distributing benefits and burdens (*14*). Although some of the traditional principles of clinical ethics may be useful as starting points, their application to AIMDs requires a greater emphasis on the principle of justice. Throughout this paper, we consider the deployment and governance of AIMDs in nuclear medicine through the lens of 3 domains of value: patient welfare, patient autonomy, and health justice (Table 1).

NOTEWORTHY

- Clinicians retain primary ethical responsibility for the appropriate use of AIMDs in nuclear medicine.
- Protecting patient and physician autonomy requires declaring the intended use, performance, and limitations of the AIMD for specific clinical tasks.
- Ensuring that AIMDs promote health equity requires attention to structural inequalities to ensure that the system is equally accurate and accessible for all demographic subgroups.
- Governance of AIMDs should foster warranted trust in AIMDs by defining legal responsibilities, incentivizing transparency, and providing appropriate funding, training, and infrastructure.

CLINICAL USE OF AIMD IN NUCLEAR MEDICINE

Clinicians possess the primary ethical responsibility for the use of AIMDs in patient care. This places burden on clinicians to understand the capacities and limits of algorithms but also reinforces the case for developers to clearly specify the performance of the algorithm and its intended-use cases. In this section, we review some ethical considerations for clinicians as they deploy AIMDs to improve patient well-being, respect patient autonomy, and promote health justice.

Patient Well-Being

One of a clinician's primary responsibilities is to act in the best interests of the patient, avoiding harm and benefitting well-being when possible. This requires that clinicians be attentive to automation bias, knowledgeable about the task-specific performance and limitations of an AIMD, and appropriately cautious about the implementation of AIMDs in their practices. Moreover, identifying whether the use of an AIMD is in a patient's best interest requires consideration of the specific values of individual patients.

Intended Use and Performance. Although AIMDs are emerging as incredibly powerful new tools in health care, increasingly able to make diagnostic or treatment recommendations, the nature of the physician–patient relationship requires that those at the bedside retain responsibility and accountability for potential errors in AI-based medical diagnosis or risk stratification. Although developers and regulators carry an ethical burden to ensure that AIMD performance claims are warranted (*15*), the clinician who is credentialed by the appropriate professional body is responsible for the clinical action. This suggests 3 considerations.

TABLE 2
U.S. Food and Drug Administration Grading System for Risk Evaluation of Software as Medical Device (*15*)

Patient condition	Significance of AIMD		
	Non-CADe (e.g., measure, denoise, annotate; no interpretation)	CADe (e.g., identify abnormalities; dosimetry calculation)	CADx (e.g., guide diagnosis or treatment)
Not serious	I	I	II
Serious	I	II	III
Critical	II	III	IV

I–IV represent lowest risk through highest risk.

First, clinicians should be knowledgeable about the intended use of an AIMD system. The Food and Drug Administration has done substantial work to define a typology of AIMD (what they call Software as a Medical Device), based on the level of computer-aided detection (CADe) or computer-aided diagnosis (CADx) that the AIMD is intended to provide (Table 2) (*16*). Non-CADe systems provide measurement or annotation of imagery without interpretation. CADe refers to an AI device that intends to identify abnormalities but does not attempt diagnosis or treatment recommendations. CADx systems attempt to directly diagnose the presence (and severity) of a disease (*4*).

Grading AIMDs on this scale allows clinicians to identify the level of risk associated with using a specific AIMD in a clinical workflow. Consider AIMD systems involved in PET workflows. Most systems at the non-CADe level, such as a PET quantification tool, may pose lower risks since they simply provide additional information that the physician incorporates into decision-making. Although even at this level, AIMDs may inadvertently eliminate or de-emphasize malignant features in imagery (*17*). At the CADe level, the risk increases since physicians may deviate from their judgment on the basis of overreliance on AI-based detection and segmentation of tumors on, for example, ^{18}F-FDG PET. The highest risk comes with CADx systems, since they provide binary (or categorical) diagnostic information and may obscure the underlying evidence or reasoning for the diagnosis from the clinician. In all cases, clinicians should not use an AIMD outside its intended use.

Second, responsible use of AIMDs requires that clinicians be familiar with the task-specific performance of an AIMD within the population that the clinician serves. In a previous paper (*15*), we noted that AIMDs should ultimately be evaluated by their performance on clinical tasks in representative clinical contexts and populations. To avoid inappropriate use, clinicians should familiarize themselves with these performance data, including differences in accuracy for race or sex subpopulations.

Finally, clinicians must consider the risks of automation bias (*18*). Automation bias occurs when users come to unquestioningly accept the output of AIMD, without appropriate regard for predictive errors or uncertainties. In general, clinicians should act with an appropriate level of skepticism with respect to the outputs of AIMDs, until such time as they are well integrated into routine clinical practice. Indeed, most Food and Drug Administration–approved AIMDs specifically include a statement that the software is not intended to diagnose or treat a disease and may only be applied as a measurement tool. Nonetheless, as CADx systems start to appear, and as AIMDs begin to demonstrate better accuracy than physicians at a specific task, automation bias may become difficult to resist (*19*). It is critical to remain attentive to the fact that ethical clinical decision-making requires sustaining the shared decision-making paradigm, where AI is but one source of information in a set of considerations that, together, contribute to a decision (*20*).

Patient Best Interest. The outputs of AIMDs will inform clinician decision-making about a host of tradeoffs in medical imaging: for example, between false-positive and false-negative diagnoses, or acceptable dosage of radioisotopes relative to investigational value. Two considerations are relevant.

First, minimizing harm and maximizing benefit require that we recognize imbalances in the harm of false positives and false negatives for a specific task. For example, in a cancer diagnosis task, false negatives will often have higher costs for patients than false positives (*21*). This suggests that common performance measures for AIMDs may not provide sufficient information to clinicians and patients involved in shared decision-making. For instance, the area under the receiver-operating-characteristic curve is a threshold agnostic performance metric that treats false positives and negatives as equivalently weighty (which is rarely true in the clinical context) (*22*). Nor does task-specific selection of simple metrics (e.g., minimizing false negatives) solve the problem, since for almost all tasks both false negatives and false positives harm patients (i.e., through under- and overtreatment). Instead, clear communication of confusion matrices may be a necessary component of clinical evaluation, to ensure that doctors and patients can navigate the complex assessment of costs and benefits themselves.

Second, minimizing harm and maximizing benefit require careful consideration of the different ways patients make tradeoffs between the risks and benefits of interventions. Many interventions in nuclear medicine carry grave tradeoffs between longevity and quality of life. In this respect, AIMDs—and especially CADx or CADe systems (*23*)—should avoid unnecessarily hard coding judgments about the appropriate risk and benefit tradeoffs (*24*). For instance, during radiation therapy planning, an AIMD that segments tumors in PET/CT could provide an estimate of how much diseased tissue is present in each voxel of the image (*25*), allowing caregivers and physicians to discuss risk tolerances with patients. Of course, not all value judgments can be avoided in the development of an AIMD. Tasks such as image denoising or instrument calibration (*26*)—although they affect the error rates of downstream diagnosis or intervention—are too abstracted from patient outcomes for meaningful dialogue with each individual patient to occur. In these cases, reasonable effort should be made to ensure

that embedded value judgments—that is, aggressiveness of denoising, or sensitivity to patient motion—reflect broadly held standards. If well-established standards do not exist to guide the selection of critical thresholds, developers should seek to involve stakeholders, including patients and providers, in the selection process (*27*).

Patient Autonomy

Clinicians must respect their patients' autonomy, and this requires that they provide patients with sufficient information to consent to interventions (*12*). At a minimum, patients must be notified of the use of an AIMD during diagnostic or therapeutic interventions, the safety and efficacy of the AIMD for patients such as them, and any known risks or limitations associated with the AIMD. Furthermore, whereas explainability techniques may facilitate patient autonomy in the future, physicians should be cautious in overly relying on them given current limitations.

Notification and Risk Declaration. Clinicians have an obligation to notify patients regarding the use of AIMDs in a clinical workflow when the clinicians have reason to believe that this information would be material to the patients' decision-making. First, performance information should be clinically relevant (e.g., false-positive and -negative rates in clinical contexts) and not simply abstract performance metrics (e.g., area under the receiver-operating-characteristic curve). This will enable informed discussions with patients about the relative risks and benefits of AIMD use and the relevance of an AIMD's findings to the overall prognosis or treatment plan. Second, performance limitations for racial or sex subpopulations should be declared to patients who are members of the disadvantaged class. This requires that the performance of the AIMD be evaluated in subpopulations that are likely to be encountered. Moreover, alternatives to the use of the AIMD, and the relative performance of these alternatives, should also be provided to patients.

Explainability. The black box nature of deep learning means that detailed information about the decision procedure of AIMDs is not always accessible or interpretable, arguably undermining clinician and patient understanding (*28,29*) (the standard practice for preparing informed consent forms is to use an eighth-grade reading level). Explainability refers to a cluster of techniques that aim to help physicians understand and explain the AI's internal decision-making process. Although explainability techniques may sometimes be useful, we argue that understanding the performance and limits of the AI system is likely more important. We do so for 2 reasons.

First, currently existing explainability techniques are not able to reliably explain predictions at the individual level (*30*). Calls for greater explainability often assume that these techniques can describe the precise computational pathway between individual inputs and outputs (*31*). One purported strategy is to create a parallel regression model that identifies the statistical association of particular input features to an AIMD's output. Another is to develop heat maps that purport to identify the areas of an image that were relevant to the prediction. It is unclear, however, whether these techniques deliver information about individual predictions or about the general parameters of the model (*6,19*). Moreover, emerging evidence indicates that explainability techniques may actually compromise clinicians' ability to identify incorrect outputs and thus worsen automation bias (*19*).

Second, calls for explainability often conflate the different forms of explanation that are desirable in different contexts (*32*). Ferretti et al. (*28*) distinguish among 3 forms of opacity in medical AI: lack of disclosure, epistemic opacity, and explanatory opacity. Lack of disclosure refers to instances in which patients are unaware that diagnostic or interventional decisions are being made with the aid of an AIMD. These can be dealt with through simple notifications on the use and performance of AIMD. Second, epistemic opacity refers to the inability to inspect the precise computational pathway (i.e., feature weights and parameters) between inputs and predictions. Although this information may be useful to developers, this level of transparency about decision pathways is rarely demanded of other medical interventions (*33*). Finally, explanatory opacity refers to the inability to explain why the input data are causally connected to the prediction—a problem of particular importance in machine learning, which relies on identifying statistical regularities that may not have well-characterized causal explanations. It is unclear, however, whether principles of informed consent require clinicians to explain to patients the precise causal pathway between diseases and diagnostic tests (*33,34*). Moreover, a detailed explanation of the causal mechanisms underlying imaging results and disease diagnosis would require a greater understanding of statistics and nuclear medicine than most patients possess. These considerations suggest that explainability techniques—although of technical interest to developers—may not be necessary to satisfy existing informed consent practices.

Justice and Algorithmic Fairness

Basic principles of procedural and distributive justice require that AIMDs treat subgroups within a population fairly. It is well established, however, that machine learning models in medicine can exhibit race, sex, or socioeconomic biases (*35,36*). Many of these biases may be encoded before deployment (*37*), but even carefully trained models can create unfairness when they are inappropriately deployed (i.e., in out-of-sample populations or by ignoring shifts in the deployment population). In this context, users and administrators are obligated to ensure that the deployment of AIMDs is procedurally fair and promotes distributive fairness.

Procedural Fairness. Procedural fairness requires that patients be treated with equal consideration, regardless of their race, sex, religion, or other protected characteristics (*12*). Unfortunately, there is some evidence that clinicians (both in nuclear medicine and in other specialties) have often failed to live up to this requirement with respect to the provision of medical imaging (*38*). Although structural barriers mean that equal access does not ensure equal opportunity to benefit from AIMD, procedural fairness requires that the medically indicated use of AIMDs be offered to patients regardless of their protected characteristics.

Procedural fairness also discourages the use of a patient's protected characteristics as an input feature. Historically, some medical decision-making tools have used features such as patient race or ethnicity as direct inputs (*39,40*), informed by ill-conceived genetic and biologic understandings of race (*41*). For instance, a common breast-cancer screening tool uses race alongside family history, age, and the Breast Imaging Reporting and Data System breast density score (*42*), with the result that it may underestimate risk in nonwhite patients (*40*). Although some now argue that race can act as a proxy for the influence of racist oppression on patient's health, naïve attempts to try to correct systemic bias may unintentionally introduce biases of their own (*43*). For instance, it can impose tradeoffs on marginalized groups: by using features such as race to improve the accuracy of risk predictions, we may reduce access to desired treatments or interventions for that

group (*39*). Moreover, the capture of demographic information (e.g., through self-identification or physician assessment) is imprecise and can contribute to the reification of stereotypes among clinicians about patient risk. As our understanding of the link between health, race, and other socially salient attributes improves, we believe that the use of these categories to make clinical decisions requires careful justification. These justifications should include robust knowledge of the data sources for demographic information, the causal structure of the association between the attribute and health, and the effect on marginalized people of using socially salient attributes to make clinical decisions.

Distributive Fairness. Another potential concern is the accuracy of AIMDs by ethnicity, socioeconomic status, or sex. Encouragingly, there has been much recent work on technical methods to remove bias from AIMDs (*37*). In a companion paper (*11*), we will note that a variety of techniques during the data collection and development phase can help ameliorate biases introduced during the training phase. Nonetheless, these techniques are not sufficient to ensure that AIMDs reduce health disparities, for at least 2 reasons.

First, the impact of an AIMD on disparities will be dependent on its precise pattern of accessibility. There are well-documented inequities in structural access to medical imaging for coronavirus disease 2019 diagnostics, mammography, and lung cancer screening (*8*). The cost of AI implementation is not only limited to the cost of developing or purchasing the AIMD but also includes supportive technology infrastructure, training staff, and patient education. Careful assessment of whether AIMDs should be adopted is especially critical for low-income or rural areas, where implementing expensive AI technology may divert resources from lower-tech interventions, with a greater impact on patient outcomes (*44*).

Second, even if an AIMD is equally accurate and accessible for all demographic subgroups, it may exacerbate existing structural inequalities (*45*). For instance, an AIMD designed to schedule future appointments based on a no-show predictor may schedule patients with a history of missed appointments to overbooked days. Of course, missed appointments are often related to a patient's structural determinants of health—an inability to cover transportation costs or childcare or to take time off from work—and hence the very patients who may need additional care must now experience longer wait times or overbooked clinics. Thus, even if the AIMD predicts absenteeism correctly regardless of race or socioeconomic status, its deployment may widen health disparities due to background structural injustice.

GOVERNANCE OF AIMD

Alongside awareness of the ethical considerations of clinical deployment, a sustainable governance framework for AIMD is necessary to ensure its potential is realized. In this section, we will discuss the need for clear and effective performance claims and the appropriate way to navigate the assignment of ethical responsibility for the use of AIMDs.

Ensuring Safety and Efficacy

To discharge their ethical duties, physicians must have reliable information about the task-specific performance, safety, and functional limits of AIMDs. In a prior paper, we note that AIMDs should be evaluated by robust trials on clinical tasks, not just retrospective datasets, before deployment (*15*). Three additional considerations arise for regulators seeking to evaluate the safety and efficacy of an AIMD.

First, the safety and efficacy of an AIMD may be relative to the deployment environment. Consider that an algorithm trained in a high-resource context with a predominately high-income population may not have the same accuracy in other patient populations or clinical contexts. If the AIMD is deployed in a lower-resource context, it may expose marginalized patients to harm through misdiagnosis, inappropriate treatment recommendations, or misdirected therapy. At minimum, the deployment of AIMDs to environments with more limited resources should be done with caution to avoid situations in which patients receive inaccurate diagnoses or treatment recommendations. More expansively, if health equity is of overriding importance, regulators might require demonstrations of efficacy in both low-resource and high-resource contexts before deployment anywhere.

Second, even after initial clinical evaluation, performance testing is an unfinished project. Postdeployment evaluation is essential for maintaining the trustworthiness of a system and for ensuring that the AI continues to perform as expected not only when changes are made to the software but also when populations, diseases, and clinical ecosystems change over time (*18*). Tools such as algorithmic audits can help support continuous monitoring of AIMD performance after deployment (*46*).

Finally, regulators should be attentive to the fact that, once certified as efficacious and safe, AIMD solutions may be deployed as a replacement for physician-directed care. AIMDs can potentially assist when there may otherwise be no available resources. For instance, in a region without an on-call trained nuclear medicine physician, an AI assistant could notify the primary care team and generate a preliminary report for unexpected urgent findings, such as pneumothorax in an oncologic PET/CT examination, while waiting for evaluation by a qualified physician. Although this ability appears to improve access to high-quality care, reliance on AIMD decisions by untrained clinicians may lead to inappropriate diagnosis or treatment that may be worse than delayed care.

Supportive Infrastructure

The performance of an AIMD may have less to do with the model itself and more to do with the ecosystem around the AIMD. The successful deployment of an AIMD in nuclear medicine thus requires 3 key supportive investments.

First, data and standards are needed to support the development, validation, and testing of AIMDs. Relevant and reliable training data, comprehensive test sets (*26*), standardized evaluation and validation methods (*47*), and comprehensive imaging archive repositories are crucial to fair, efficacious, and reliable development of AIMDs. Some of this can be achieved by professional self-governance. Cognate professional societies in nuclear medicine, radiology, and medical imaging should consider collaborative efforts to develop a central repository for developing standards and sharing reliable datasets for AIMD research and development.

Second, the deployment of AIMDs may require substantial investment in supportive infrastructure by hospitals and public agencies. The digital divide prevails in lower-resource contexts and results in uneven access to, or efficacious use of, medical imaging technologies due to a lack of basic information technology, bioinformatics, and database support (*48*). Efficacious AIMD deployment may require vastly increased access to remote and telemedicine services, as well as access to reliable power and Internet service in many parts of the globe (*49*).

Third, the deployment of AIMD requires appropriate training and policies. Too often, especially in lower-resource health

systems, new technologies are not used or are used inappropriately, thereby wasting scarce resources that could have been invested in simpler, proven interventions (*50*). Moreover, the use of AIMDs without up-to-date patient privacy or data protection policies (or appropriate regulators to enforce these policies) can compound, rather than remediate, the harm of the digital divide in medicine.

Legal and Regulatory Oversight

Establishing responsibility and accountability pathways is crucial to maintain trust, respect legal limits, and protect human rights (*49*). We identify 3 problems for regulators seeking to build community trust in the use of AIMDs within diagnostic radiology and nuclear medicine.

First, assigning legal liability for the harm generated by AIMD may be difficult because of the so-called responsibility gap generated by systems that automate some components of tasks previously supervised by humans. Clinicians are ethically responsible for the use of both CADe and CADx systems, but this does not absolve developers and administrators of responsibility. If a systematic error occurs because of inaccurate performance claims, obscured limitations, or failures of the system in intended-use cases, responsibility should be placed on those who trained, tested, and validated the AI device. The assignment of legal liability for harm is made more complex by the evolving legal status of AIMDs as regulated medical devices in the United States and Europe (*51,52*) and the unsettled requirements for premarket and postmarket disclosure. As we build a regulatory structure around AIMDs, the locus of liability for harm must be proactively addressed by lawmakers and regulators.

Second, AI software is usually proprietary, and external researchers typically have little or no access to training data or performance evaluations. Ensuring that developers meet their obligations with respect to performance transparency and fairness may thus require independent auditors, researchers, or government agencies to have access to underlying models and performance info (*53*). This may build trust by ensuring there is a public mechanism for holding AIMDs accountable, reliable, and consistent (*54*).

Third, the task of oversight and regulation of AI in health care may not be feasible through a single regulatory agency. The responsibilities of most current agencies in the Department of Health and Human Services are narrow. For instance, the Federal Trade Commission aims to prevent anticompetitive harm, the Food and Drug Administration ensures the safety and efficacy of devices, and the Centers for Medicare and Medicaid Services administer and regulate payment for health-care services (*55*). AIMD implementation within nuclear medicine involves all of these regulatory areas. As a result, there may be either a need to create a formal method for these agencies to collaborate or a need to form a new agency to regulate the safety, competition, and ethical aspects of AI-based devices.

CONCLUSION

There is undoubtedly enormous potential in the use of AI tools and software in medical imaging. Appropriate implementation of these technologies can not only increase efficiency and accuracy but also reduce the burden on clinicians and narrow health inequity gaps. This paper aimed to anticipate potential ethical considerations for widespread rapidly evolving AIMDs in medical imaging. Viewing these considerations through the lens of health disparities permits us to conceive of potential harm to certain groups in the population and protect against them.

DISCLOSURE

Melissa McCradden acknowledges funding from the SickKids Foundation pertaining to her role as the John and Melinda Thompson Director of AI in Medicine at the Hospital for Sick Children. Abhinav Jha acknowledges support from NIH R01EB031051-02S1. Peter Scott also acknowledges support from the National Institutes of Health (R01EB021155). Sven Zuehlsdorff is a full-time employee of Siemens Medical Solutions USA, Inc. No other potential conflict of interest relevant to this article was reported.

ACKNOWLEDGMENT

The members of the task force acknowledge Bonnie Clarke for her support.

REFERENCES

1. Saboury B, Bradshaw T, Boellaard R, et al. Artificial intelligence in nuclear medicine: opportunities, challenges, and responsibilities toward a trustworthy ecosystem. *J Nucl Med.* 2023;64:188–196.
2. Artificial intelligence and machine learning (AI/ML)-enabled medical devices. Federal Drug Administration website. https://www.fda.gov/medical-devices/software-medical-device-samd/artificial-intelligence-and-machine-learning-aiml-enabled-medical-devices. Updated October 5, 2022. Accessed July 17, 2023.
3. Brady AP, Neri E. Artificial intelligence in radiology: ethical considerations. *Diagnostics (Basel).* 2020;10:231.
4. Currie G, Hawk KE. Ethical and legal challenges of artificial intelligence in nuclear medicine. *Semin Nucl Med.* 2021;51:120–125.
5. Currie G, Hawk KE, Rohren EM. Ethical principles for the application of artificial intelligence (AI) in nuclear medicine. *Eur J Nucl Med Mol Imaging.* 2020; 47:748–752.
6. Geis JR, Brady A, Wu CC, et al. Ethics of artificial intelligence in radiology: summary of the joint European and North American multisociety statement. *Insights Imaging.* 2019;10:101.
7. Larson DB, Magnus DC, Lungren MP, Shah NH, Langlotz CP. Ethics of using and sharing clinical imaging data for artificial intelligence: a proposed framework. *Radiology.* 2020;295:675–682.
8. Mach JC, Omar A, Abujudeh H. Public health foundations for radiology resident education: healthcare disparities in radiology. *Curr Probl Diagn Radiol.* 2022;51: 403–407.
9. Cho JK, Zafar HM, Lalevic D, Cook TS. Patient factor disparities in imaging follow-up rates after incidental abdominal findings. *AJR.* 2019;212:589–595.
10. Bucknor MD, Lichtensztajn DY, Lin TK, Borno HT, Gomez SL, Hope TA. Disparities in PET imaging for prostate cancer at a tertiary academic medical center. *J Nucl Med.* 2021;62:695–699.
11. Herington J, McCradden MD, Creel K, et al. Ethical considerations for artificial intelligence in medical imaging: data collection, development, and evaluation. *J Nucl Med.* In press.
12. Beauchamp TL, Childress JF. *Principles of Biomedical Ethics.* 8th ed. Oxford University Press; 2019.
13. Faden RR, Kass NE, Goodman SN, Pronovost P, Tunis S, Beauchamp TL. An ethics framework for a learning health care system: a departure from traditional research ethics and clinical ethics. *Hastings Cent Rep.* 2013;spec no:S16–S27.
14. Herington J, Tanona S. The social risks of science. *Hastings Cent Rep.* 2020;50: 27–38.
15. Jha AK, Bradshaw TJ, Buvat I, et al. Nuclear medicine and artificial intelligence: best practices for evaluation (the RELAINCE guidelines). *J Nucl Med.* 2022;63: 1288–1299.
16. IMDRF Software as a Medical Device (SaMD) Working Group. *"Software as a Medical Device": Possible Framework for Risk Categorization and Corresponding Considerations.* International Medical Device Regulators Forum; 2014;14.
17. Yang J, Sohn JH, Behr SC, Gullberg GT, Seo Y. CT-less direct correction of attenuation and scatter in the image space using deep learning for whole-body FDG PET: potential benefits and pitfalls. *Radiol Artif Intell.* 2020;3:e200137.
18. Akinci D'Antonoli T. Ethical considerations for artificial intelligence: an overview of the current radiology landscape. *Diagn Interv Radiol.* 2020;26:504–511.

19. Shen J, Zhang CJP, Jiang B, et al. Artificial intelligence versus clinicians in disease diagnosis: systematic review. *JMIR Med Inform.* 2019;7:e10010.
20. McCradden MD, Kirsch RE. Patient wisdom should be incorporated into health AI to avoid algorithmic paternalism. *Nat Med.* 2023;29:765–766.
21. US Preventive Services Task Force, Grossman DC, Curry SJ, et al. Screening for prostate cancer: US Preventive Services Task Force recommendation statement. *JAMA.* 2018;319:1901–1913.
22. Halligan S, Altman DG, Mallett S. Disadvantages of using the area under the receiver operating characteristic curve to assess imaging tests: a discussion and proposal for an alternative approach. *Eur Radiol.* 2015;25:932–939.
23. Software as a medical device (SaMD). Food and Drug Administration website. https://www.fda.gov/medical-devices/digital-health-center-excellence/software-medical-device-samd. Updated December 4, 2018. Accessed July 17, 2023.
24. Birch J, Creel KA, Jha AK, Plutynski A. Clinical decisions using AI must consider patient values. *Nat Med.* 2022;28:229–232.
25. Liu Z, Mhlanga JC, Laforest R, Derenoncourt P-R, Siegel BA, Jha AK. A Bayesian approach to tissue-fraction estimation for oncological PET segmentation. *Phys Med Biol.* 2021;66:10.1088/1361-6560/ac01f4.
26. Bradshaw TJ, Boellaard R, Dutta J, et al. Nuclear medicine and artificial intelligence: best practices for algorithm development. *J Nucl Med.* 2022;63:500–510.
27. Wale JL, Thomas S, Hamerlijnck D, Hollander R. Patients and public are important stakeholders in health technology assessment but the level of involvement is low: a call to action. *Res Involv Engagem.* 2021;7:1.
28. Ferretti A, Schneider M, Blasimme A. Machine learning in medicine: opening the new data protection black box. *Eur Data Protection Law Rev.* 2018;4:320–332.
29. Amann J, Blasimme A, Vayena E, Frey D, Madai VI; Precise4Q consortium. Explainability for artificial intelligence in healthcare: a multidisciplinary perspective. *BMC Med Inform Decis Mak.* 2020;20:310.
30. Tonekaboni S, Joshi S, McCradden MD, Goldenberg A. What clinicians want: contextualizing explainable machine learning for clinical end use. In: *Proceedings of the 4th Machine Learning for Healthcare Conference.* PMLR; 2019: 359–380.
31. Ghassemi M, Naumann T, Schulam P, Beam AL, Chen IY, Ranganath R. A review of challenges and opportunities in machine learning for health. *AMIA Jt Summits Transl Sci Proc.* 2020;2020:191–200.
32. Lipton ZC. The mythos of model interpretability: in machine learning, the concept of interpretability is both important and slippery. *Queue.* 2018;16:31–57.
33. London AJ. Artificial intelligence and black-box medical decisions: accuracy versus explainability. *Hastings Cent Rep.* 2019;49:15–21.
34. Bromwich D, Millum J. Disclosure and consent to medical research participation. *J Moral Philos.* 2013;10:195–219.
35. Char DS, Shah NH, Magnus D. Implementing machine learning in health care: addressing ethical challenges. *N Engl J Med.* 2018;378:981–983.
36. Vayena E, Blasimme A, Glenn Cohen I. Machine learning in medicine: addressing ethical challenges. *PLoS Med.* 2018;15:e1002689.
37. Chen IY, Pierson E, Rose S, Joshi S, Ferryman K, Ghassemi M. Ethical machine learning in healthcare. *Annu Rev Biomed Data Sci.* 2021;4:123–144.
38. Schrager JD, Patzer RE, Kim JJ, et al. Racial and ethnic differences in diagnostic imaging utilization during adult emergency department visits in the United States, 2005 to 2014. *J Am Coll Radiol.* 2019;16:1036–1045.
39. Grobman WA, Sandoval G, Rice MM, et al. Prediction of vaginal birth after cesarean delivery in term gestations: a calculator without race and ethnicity. *Am J Obstet Gynecol.* 2021;225:664.e1–664.e7.
40. Vyas DA, Eisenstein LG, Jones DS. Hidden in plain sight: reconsidering the use of race correction in clinical algorithms. *N Engl J Med.* 2020;383:874–882.
41. Root M. The use of race in medicine as a proxy for genetic differences. *Philos Sci.* 2003;70:1173–1183.
42. Tice JA, Miglioretti DL, Li C-S, Vachon CM, Gard CC, Kerlikowske K. Breast density and benign breast disease: risk assessment to identify women at high risk of breast cancer. *J Clin Oncol.* 2015;33:3137–3143.
43. McCradden MD, Joshi S, Mazwi M, Anderson JA. Ethical limitations of algorithmic fairness solutions in health care machine learning. *Lancet Digit Health.* 2020; 2:e221–e223.
44. Joshi I, Morley J. Artificial intelligence: how to get it right. National Health Service; 2019;64–65.
45. Herington J. Measuring fairness in an unfair world. In: *Proceedings of the AAAI/ACM Conference on AI, Ethics, and Society.* Association for Computing Machinery; 2020:286–292.
46. Liu X, Glocker B, McCradden MM, Ghassemi M, Denniston AK, Oakden-Rayner L. The medical algorithmic audit. *Lancet Digit Health.* 2022;4:e384–e397.
47. Jha AK, Myers KJ, Obuchowski NA, et al. Objective task-based evaluation of artificial intelligence-based medical imaging methods: framework, strategies, and role of the physician. *PET Clin.* 2021;16:493–511.
48. Morris MA, Saboury B. Access to imaging technology in global health. In: Mollura DJ, Culp MP, Lungren MP, eds. *Radiology in Global Health: Strategies, Implementation, and Applications.* Springer International Publishing; 2019:15–33.
49. *Ethics and governance of artificial intelligence for health: WHO guidance*. World Health Organization; 2021.
50. Mollura DJ, Shah N, Mazal J. White paper report of the 2013 RAD-AID conference: improving radiology in resource-limited regions and developing countries. *J Am Coll Radiol.* 2014;11:913–919.
51. Minssen T, Mimler M, Mak V. When does stand-alone software qualify as a medical device in the European Union? The CJEU's decision in SNITEM and what it implies for the next generation of medical devices. *Med Law Rev.* 2020;28:615–624.
52. Price WN II. Artificial intelligence in health care: applications and legal implications. *The SciTech Lawyer.* 2017;14:10–13.
53. Asan O, Bayrak AE, Choudhury A. Artificial intelligence and human trust in healthcare: focus on clinicians. *J Med Internet Res.* 2020;22:e15154.
54. Yanisky-Ravid S, Hallisey SK. "Equality and privacy by design": a new model of artificial intelligence data transparency via auditing, certification, and safe harbor regimes. *Fordham Urban Law J.* 2019;46:428–486.
55. Department of Health and Human Services. Health and Human Services Agencies and Offices. https://www.hhs.gov/about/agencies/hhs-agencies-and-offices/index.html (2015). Accessed August 15, 2023.

Is Actinium Really Happening?

Richard Zimmermann

Chrysalium Consulting, Lalaye, France; MEDraysintell, Louvain-la-Neuve, Belgium; and Oncidium Foundation, Mont-Saint-Guibert, Belgium

The most recent survey (*1*) related to α-radiotherapy development showed that 27 molecules labeled with ^{225}Ac are presently under development, among which 13 have already reached human test level. The first ^{225}Ac-labeled molecule has entered the clinical phase III stage (*2*) and might reach the market by 2028. These molecules cover the most important indications that are studied with β-emitting radionuclides, but it is obvious that each single ^{177}Lu-labeled drug will be explored as a ^{225}Ac-labeled analog. Among the 35 ^{177}Lu-labeled molecules that have already reached the clinical stage, an estimated dozen have a high chance to reach the market before 2030, not even taking into account all the generics. Actinium-labeled drugs will follow the same trend, with a delay of about 5 y. A global target of half a million patients represents only 1% of the 5-y prevalence of cumulated cancers (Global Cancer Observatory; https://gco.iarc.fr), which remains realistic in terms of share of the market compared with surgery, external radiotherapy, or chemotherapy.

Evaluation of further needs is based on today's average patient dose of 100 kBq/kg. At least 10–12 MBq at end of bombardment must be produced per dose, taking into account losses during handling and transport and labeling yields. On the basis of an average of 3 doses for a full treatment, each patient will need a total of 30–36 MBq of ^{225}Ac at end of bombardment. In other words, 3,000 GBq at end of bombardment would be sufficient to treat 100,000 patients each year. Industry will have to guarantee capacity for 5–6 times this yearly amount by 2032.

Over the past few years, several large investments were made in 5 different technologies to develop large-scale production of ^{225}Ac. The different routes have been described in the literature (*3,4*). Already-operating sites and new-development units for technologies A–E are summarized in Table 1 with their production capacities.

THE 5 TECHNOLOGIES

Technology A

Carrier-free ^{225}Ac has been produced through the natural decay of ^{229}Th. The 3 sites that can presently produce high-quality ^{225}Ac (United States, Russia, and Germany) will not significantly increase their production capacity. Only Russia is planning such capacity improvement, but the additional amount will remain insignificant compared with the future demand. Fortunately, the war has not (yet) altered access of ^{225}Ac to U.S. patients in clinical trials from Russian sources. In the United States, the company TerraPower obtained access to larger amounts of ^{229}Th that still need to be purified and plans stepwise progress over the next 10 y, although the output will still be only a small fraction of the future need. If alternative routes become successful, this generator route will not remain competitive, but for the time being, it remains the largest source of very clean ^{225}Ac.

Technology B

The ^{232}Th activation programs (United States and Canada) have progressed well. A very high capacity can be reached, and the technology might allow production of several terabecquerels per year. Unfortunately, this product remains contaminated with ^{227}Ac (half-life, 21.8 y). The mixture can be used for development purpose up to clinical phase II without limitation, but cleaner forms of ^{225}Ac will be preferred in routine applications and as marketed forms. Specifications limit the ^{227}Ac threshold to 2%, a level that was demonstrated not to affect patients (*5,6*). Release of radioactive waste from patients in the waste tanks of hospitals is the real issue. Although European authorities will probably recommend, if not constrain, users to avoid ^{227}Ac, in the United States this radionuclide needs to be added to the radioactive waste and will directly affect the level of the decommissioning financial assurance that is supposed to be in place at the user's end. A similar situation was experienced in the past when the industry was given a choice between no-carrier-added ^{177}Lu and ^{177m}Lu-contaminated carrier-added ^{177}Lu. ^{225}Ac/^{227}Ac might find better applications in the development of ^{225}Ac/^{213}Bi generators, provided that the industry becomes interested in ^{213}Bi.

Technology C

In the thorium activation process B, ^{225}Ra as a by-product can easily be separated from the mixture, allowing indirect access to clean ^{225}Ac through its decay. Unfortunately, yields are limited to only 10% compared with the ^{225}Ac/^{227}Ac mix, generating high levels of waste and limiting financial attractiveness.

Technology D

Accelerator production is possible by irradiating ^{226}Ra targets using small cyclotrons. Several large-scale production sites are now under construction, supported by companies in the United States and Europe. Eventually, large amounts of ^{225}Ac might be produced per week, in theory more than 4 TBq a month (*7*), but realistically a tenth of this figure would allow us to stay on the safe side, with cooling of larger targets becoming the limiting factor.

Technology E

More recent developments have shown that photoconversion technology not only is a way to generate very clean ^{225}Ac but also

Received May 1, 2023; revision accepted Jul. 25, 2023.
For correspondence or reprints, contact Richard Zimmermann (richard.zimmermann@chrysalium.com).
Published online Aug. 17, 2023.

DOI: 10.2967/jnumed.123.265907

TABLE 1
Technologies Under Development and Operating Sites for ^{225}Ac Production, Including Estimated Present and 2032 Capacities

Technology	Source	Yearly production capacity (GBq/y/site) 2023	2032	Total (GBq/y) in 2032	Comment
A: [(^{233}U→) ^{229}Th→^{225}Ac] (generator)	ORNL, United States	26	26	Up to 3,000 [80]	Highest quality of *nca* ^{225}Ac; may enter price competitivity
	IPPE, Russia	37 (est.)	150 (est. 2025) to 300 (est. 2030)		
	JRC-ITU, Germany	11	11		
	TRIUMF, Canada	0.4	0.4		
	TerraPower, United States	>10	≤2,700		
	Pantera, Belgium	0	>70		TerraPower source
B: [^{232}Th(p,x)^{225}Ac+^{227}Ac] (high-energy accelerator)	BNL/ORNL LANL; Tri-Lab, United States	16.7	Potential, >3,700	>9,000 [>240]	Contaminated with ^{227}Ac (0.2% EOB - ~1.5% at calibration); not suitable for large scale routine use
	CNL/TRIUMF, Canada; BWXT/ITM, United States/Germany	>1	Idem >3,700		
	INR, Russia		≤1,000		
	SpectronRx, United States	>1	>200		
	Others: Arronax, France; IsoDar, Japan; CIAE, China	First GBq in 2024	Potential, >200 each		
C: [+ … +^{225}Ra→^{225}Ac] (as side product)	~10% of above; CNL/TRIUMF, Canada	0.3	>370 (theory)	>370 [>10]	High level of waste - expensive
D: [^{226}Ra(p,2n)^{225}Ac] (cyclotron)		First GBq		>4,500 [>120]	Additional sites under evaluation in other countries (Asia)
	SpectronRx, United States	2023	>500		
	Ionetix, United States	2023	1,900		
	Eckert&Ziegler, Germany	2024	550		
	Alfarim, Netherlands	2025	450–850		
	N-MediPhysics, Japan	>2023	>500		
	KIRAMS, South Korea	>2025	>500		
D: [^{226}Ra(d,3n)^{225}Ac] (linear accelerator)	Nusano, United States		≤160,000		Under evaluation
E: [^{226}Ra(γ,n)^{225}Ra→^{225}Ac] (photoconverter)	NorthStar, United States	2023	3,700–15,000	>37,000 [>1,000]	Rhodotron: *nca* ^{225}Ac
	Pantera, Belgium	2027	3,700–5,000		
	TerraPower, United States	2029	3,700–5,000		
	Niowave, United States	2023	≤18,000		Linac: *nca* ^{225}Ac
	Hitachi, Japan	>2024	>3,700		
F: [^{226}Ra(n,2n)^{225}Ra→^{225}Ac] (n from d on beryllium target)	Nusano, United States		≤44,000		Under evaluation

ORNL = Oak Ridge National Laboratory; *nca* = no carrier added; IPPE = I.I. Leypunsky Institute of Physics and Power Engineering, Obninsk; est. = estimated; JRC-ITE = Joint Research Centre–Institute for Transuranium Elements; TRIUMF = TRI University Meson Facility; BNL = Brookhaven National Laboratory; LANL = Los Alamos National Laboratory; EOB = end of bombardment; CNL = Canadian Nuclear Laboratories; BWXT = BWX Technologies Inc.; ITM = Isotope Technologies Munich SE; INR = Institute for Nuclear Research of the Russian Academy of Science; CIAE = China Institute of Atomic Energy; KIRAMS = Korea Institute of Radiological and Medical Sciences.

Data in brackets are curies.

should allow large-capacity production. Facilities are under construction in the United States and Europe.

ISSUES TO BE SOLVED

Even if high capacity and reliable access to ^{225}Ac is confirmed from 2025 on, production of actinium still raises a series of other issues, some of which are on their way to being solved.

Access to Larger Amounts of ^{226}Ra

Although access and handling of ^{232}Th does not seem to be an issue, access to larger amounts of ^{226}Ra remains questionable. Most of the companies are on their way to finding a solution, either by getting access to domestic (waste) stocks or by extracting radium from older devices (e.g., paintings, radiotherapy tools, and older brachytherapy material). In the worst case, this issue should also be solved by 2025.

Need for Additional Safety Investments

Handling of ^{226}Ra is a more complex issue because this radionuclide generates the gas ^{222}Rn, which is difficult to store and trap. The increase in patients will proportionally lead to a higher need for radium and higher production of radon, leading to the need for additional safety investments.

Risk of Explosion and Contamination

Cyclotron and photoconversion technologies may face the risk of explosion of the radioactive radium target as cooling will remain difficult and the limiting factor, leading to potential contamination with long-half-life radionuclides. The increase in capacity will therefore be performed stepwise, and the upper limit remains theoretic.

Potential Toxicity and Limited Therapeutic Efficacy

^{225}Ac is an α-emitter that decays through a 6-step cascade to stable ^{209}Bi, releasing consecutively 4 α- and 2 β-particles. Recoil effects and the restricted capacity of chelators to trap decay products limit therapeutic efficacy to the first emitted α-particle. The additional α- and β-particles released by the daughter radionuclides decay elsewhere in the body. ^{223}Ra shows a similar profile, and the associated drug (Xofigo) was approved by the authorities without a request for additional studies. Potential toxic effects simply define the level of the maximum tolerated dose.

Contamination Issues

It is still not clear whether patients eventually will be handled on an outpatient basis or will be required to stay in shielded rooms, but patients treated with ^{225}Ac (half-life, 9.92 d) cannot be kept sufficiently long at therapeutic centers to collect all their waste until full decay. Releasing this waste in nature is not a problem if the number of treated patients remains low. The situation becomes different if millions of doses are used yearly and a fraction is disseminated in nature. We yet have a few years for the authorities at the national level to think seriously about this issue, which is not specific to ^{225}Ac and will—over the long term—also affect other long-half-life radionuclides, including ^{131}I, ^{177}Lu, and ^{161}Tb (*8*). This issue creates an opening for a next generation of radiotherapeutic agents with shorter half-lives such as ^{67}Cu, ^{211}At, and ^{212}Pb, but this is another story.

CONCLUSION

Altogether, the worldwide ^{225}Ac production capacity by 2032, estimated largely above 25 TBq (670 Ci), should be sufficient to produce at least 2 million patient doses a year. With an additional investment remaining below $100 million (e.g., accelerator), another 300,000 doses could be produced per new site. The situation is much more comfortable than for ^{177}Lu and ^{161}Tb, for which access to reactors will soon become the bottleneck. In the meantime, ^{225}Ac-labeled radiopharmaceuticals are just the beginning of a success story spanning 15-plus years.

DISCLOSURE

No potential conflict of interest relevant to this article was reported.

REFERENCES

1. Goethals PE, Zimmermann R. *Nuclear Medicine Report and Directory*. 9th ed. MEDraysintell; 2022.
2. Study of RYZ101 compared with SOC in pts w inoperable SSTR+ well-differentiated GEP-NET that has progressed following 177Lu-SSA therapy (ACTION-1). ClinicalTrials.gov website. https://clinicaltrials.gov/ct2/show/NCT05477576. Published July 28, 2022. Updated July 12, 2023. Accessed August 2, 2023.
3. Morgenstern A, Apostolidis C, Bruchertseifer F. Supply and clinical application of actinium-225 and bismuth-213. *Semin Nucl Med.* 2020;50:119–123.
4. Radchenko V, Morgenstern A, Jalilian AJ, et al. Production and supply of α-particle-emitting radionuclides for targeted α-therapy. *J Nucl Med.* 2021;62:1495–1503.
5. Jiang Z, Revskaya E, Fisher DR, et al. In vivo evaluation of free and chelated accelerator-produced actinium-225: radiation dosimetry and toxicity results. *Curr Radiopharm.* 2018;11:215–222.
6. Sgouros G, He B, Ray N, et al. Dosimetric impact of Ac-227 in accelerator-produced Ac-225 for alpha-emitter radiopharmaceutical therapy of patients with hematological malignancies: a pharmacokinetic modeling analysis. *EJNMMI Phys.* 2021;8:60.
7. Robertson AK, Ramogida CF, Schaffer P, Radchenko V. Development of ^{225}Ac radiopharmaceuticals: TRIUMF perspectives and experiences. *Curr Radiopharm.* 2018;11:156–172.
8. Zimmermann R. Alpha-emitters from an industrial perspective: 2023–2032. Presented at: TAT12 Conference; March 1, 2023; Cape Town, South Africa.

Prognostic Value of TSPO PET Before Radiotherapy in Newly Diagnosed IDH–Wild-Type Glioblastoma

Nathalie L. Albert*[1–3], Debie V. Nelwan*[1], Daniel F. Fleischmann[4], Stefanie Quach[5], Katharina von Rohr[1], Lena Kaiser[1], Nico Teske[2,5], Lena M. Unterrainer[1], Laura M. Bartos[1], Viktoria C. Ruf[6], Matthias Brendel[1,7,8], Markus J. Riemenschneider[9], Christian Wetzel[10], Jochen Herms[6–8], Rainer Rupprecht[10], Niklas Thon[2,5], Joerg-Christian Tonn[2,5], Claus Belka[2–4], Peter Bartenstein[1,2,7], Louisa von Baumgarten[2,3,5], Maximilian Niyazi[2–4], Marcus Unterrainer[2,11], and Adrien Holzgreve[1]

[1]*Department of Nuclear Medicine, LMU University Hospital, LMU Munich, Munich, Germany;* [2]*German Cancer Consortium, Partner Site Munich, German Cancer Research Center, Munich, Germany;* [3]*Bavarian Cancer Research Center, Erlangen, Germany;* [4]*Department of Radiation Oncology, LMU University Hospital, LMU Munich, Munich, Germany;* [5]*Department of Neurosurgery, LMU University Hospital, LMU Munich, Munich, Germany;* [6]*Institute of Neuropathology, Faculty of Medicine, LMU Munich, Munich, Germany;* [7]*SyNergy, University of Munich, Munich, Germany;* [8]*German Center for Neurodegenerative Diseases, Munich, Germany;* [9]*Department of Neuropathology, Regensburg University Hospital, Regensburg, Germany;* [10]*Department of Psychiatry and Psychotherapy, University of Regensburg, Regensburg, Germany; and* [11]*Department of Radiology, LMU University Hospital, LMU Munich, Munich, Germany*

The 18-kDa translocator protein (TSPO) is gaining recognition as a relevant target in glioblastoma imaging. However, data on the potential prognostic value of TSPO PET imaging in glioblastoma are lacking. Therefore, we investigated the association of TSPO PET imaging results with survival outcome in a homogeneous cohort of glioblastoma patients. **Methods:** Patients were included who had newly diagnosed, histologically confirmed isocitrate dehydrogenase (IDH)–wild-type glioblastoma with available TSPO PET before either normofractionated radiotherapy combined with temozolomide or hypofractionated radiotherapy. SUV_{max} on TSPO PET, TSPO binding affinity status, tumor volumes on MRI, and further clinical data, such as O^6-alkylguanine DNA methyltransferase (*MGMT*) and telomerase reverse transcriptase (*TERT*) gene promoter mutation status, were correlated with patient survival. **Results:** Forty-five patients (median age, 63.3 y) were included. Median SUV_{max} was 2.2 (range, 1.0–4.7). A TSPO PET signal was associated with survival: High uptake intensity ($SUV_{max} > 2.2$) was related to significantly shorter overall survival (OS; 8.3 vs. 17.8 mo, $P = 0.037$). Besides SUV_{max}, prognostic factors for OS were age ($P = 0.046$), *MGMT* promoter methylation status ($P = 0.032$), and T2-weighted MRI volume ($P = 0.031$). In the multivariate survival analysis, SUV_{max} in TSPO PET remained an independent prognostic factor for OS ($P = 0.023$), with a hazard ratio of 2.212 (95% CI, 1.115–4.386) for death in cases with a high TSPO PET signal ($SUV_{max} > 2.2$). **Conclusion:** A high TSPO PET signal before radiotherapy is associated with significantly shorter survival in patients with newly diagnosed IDH–wild-type glioblastoma. TSPO PET seems to add prognostic insights beyond established clinical parameters and might serve as an informative tool as clinicians make survival predictions for patients with glioblastoma.

Key Words: prognostication; survival; glioma

Received Nov. 23, 2022; revision accepted May 31, 2023.

For correspondence or reprints, contact Adrien Holzgreve (adrien.holzgreve@med.uni-muenchen.de).

*Contributed equally to this work.

Published online Aug. 3, 2023.

J Nucl Med 2023; 64:1519–1525
DOI: 10.2967/jnumed.122.265247

Glioblastoma is the most frequent malignant primary brain tumor in adults, and diagnosis is associated with a short life expectancy (*1*). Although median overall survival (OS) can reach up to 4 y with a molecular profile favorable to adapted chemotherapy regimens, most glioblastoma patients have a shorter survival period (*1*). Overall, successful treatment options remain limited and there is a need to explore new targets for both diagnostics and therapy of glioblastoma.

The 18-kDa translocator protein (TSPO) is a ubiquitous mitochondrial protein that is gaining recognition as a relevant target in glioblastoma (*2*). TSPO has been widely studied in neuroinflammatory diseases because it is considered a marker for activated microglia. However, evidence is growing that TSPO also intervenes in multiple pathophysiologic processes in glioblastoma, including proliferation, invasiveness, and resistance to apoptosis (*2*). TSPO ligands can be radiolabeled and therefore are suitable for in vivo imaging by PET. As a result, TSPO PET has been used in several neurologic disease areas with an immune-mediated component well beyond primary neuroinflammatory disorders, such as neurodegeneration (*3*). The coincidence of genuine tumor cell–associated TSPO expression and neuroinflammation in glioblastoma underscores that TSPO PET could be a valuable imaging modality in glioblastoma patients as well.

Preliminary in vivo studies or case reports using TSPO imaging in glioma were promising, revealing high tumoral tracer uptake, especially in glioblastoma (*4–7*). However, studies investigating a clinical benefit of TSPO PET in neurooncology remain scarce, and data on its potential prognostic value are lacking. Therefore, we investigated the association of TSPO PET imaging results with survival outcome in a homogeneous cohort of histologically proven isocitrate dehydrogenase (IDH)–wild-type glioblastoma before radiotherapy.

MATERIALS AND METHODS

Patients

Patients were included who had newly diagnosed, neuropathologically confirmed glioblastoma and available TSPO PET before normofractionated (2-Gy dose per fraction and 60-Gy total dose) or hypofractionated (2.67-Gy dose per fraction and 40.05-Gy total dose) radiotherapy. In all cases of tumor resection, only postoperative PET images were used. Normofractionated radiotherapy was combined with temozolomide in all cases. Patients undergoing hypofractionated radiotherapy received concomitant temozolomide if recommended by the interdisciplinary tumor board, primarily based on the molecular tumor profile. The local ethics committee gave permission to perform the study (Institutional Review Board 601-16 and 17-457). All patients signed an informed consent form.

Histopathologic and Molecular Diagnostics

Patients received either stereotactic biopsy or microsurgical tumor resection according to clinical routine. Histologic and molecular genetic assessments were performed according to clinical routine, and all cases were classified on the 2021 World Health Organization's Classification of Tumours of the Central Nervous System (*8*).

Polymorphism Genotyping

The evaluation of patients' TSPO binding affinity status—low-affinity binding (LAB), medium-affinity binding (MAB), or high-affinity binding (HAB)—was conducted as previously described (*4*).

TSPO PET Acquisition and Assessment

TSPO PET was performed on a Biograph-64 PET/CT scanner (Siemens Healthineers). The TSPO radioligand [^{18}F]GE-180 was synthesized as previously described (*4*). [^{18}F]GE-180 was intravenously injected (181 ± 17 MBq). Low-dose CT was performed for attenuation correction. PET emission data were recorded 60–80 min after injection, and the summation images taken 60–80 min after injection were used for image analyses. Reconstruction parameters were applied as previously described (*4*). For evaluation of PET images, tumoral SUV_{max} was assessed.

MRI

As part of the clinical routine, all patients received MRI scans for radiation treatment planning (median time between PET and MRI, 12 d). In all cases of tumor resection, only postoperative images were used. Axial T1-weighted sequences before and after intravenous injection of 0.1 mmol/kg gadobenate dimeglumine contrast agent (MultiHance; BraccoImaging) were analyzed to measure the total contrast-enhancing tumor, and T2 or fluid-attenuated inversion recovery (FLAIR) sequences were used to measure non–contrast-enhancing tumors. Tumor volumes were manually delineated as defined by the Advisory Committee for Radiation Oncology Practice of the European Society for Radiotherapy and Oncology guidelines using the institutional imaging software (BrainLab Smartbrush; BrainLab) (*9*). In cases of multifocal disease, each focus was quantified separately and summed together. In patients undergoing microsurgical tumor resection before radiotherapy, we ensured that postoperative T2 or FLAIR abnormalities were not surgically induced edema or ischemia by reviewing diffusion-weighted imaging sequences.

Clinical Evaluation, Tumor Progression, and Clinical Endpoints

Regular clinical follow-up consisted of clinical evaluation and MRI evaluation every 3 mo, supplemented by *O*-(2-[^{18}F]-fluoroethyl)-L-tyrosine ([^{18}F]FET) PET if appropriate. Tumor progression was defined according to Response Assessment in Neuro-Oncology criteria (*10*): at least 25% diameter increase of the contrast-enhancing lesion; a significant increase in the T2 or FLAIR nonenhancing lesion; new lesions; clinical deterioration, probably caused by the tumor and no other causes apart from it; failure to show up; or death.

The clinical primary endpoint of this study was OS, defined as the time from first diagnosis until death of the patient. The secondary endpoint was progression-free survival (PFS), defined as the time from first diagnosis until tumor progression.

Statistics

SPSS version 26 (IBM) was used for the statistical analysis. The Shapiro–Wilk test was used to assess normal distribution. The Wilcoxon signed-rank test, the Mann–Whitney *U* test or Kruskal–Wallis H test, and finally the Dunn–Bonferroni post hoc test were used to investigate group differences. Linear bivariate association between variables was obtained using the Pearson correlation. For survival analysis, continuous parameters underwent median split dichotomization. Univariate survival analysis consisted of the Kaplan–Meier estimator and log-rank test. Parameters found to be prognostic in univariate analysis were

TABLE 1
Patient Characteristics

Characteristic	Data
Age (y)	63.3 (30.6–84.2)
Sex	
Male	27 (60.0%)
Female	18 (40.0%)
MGMT promoter methylation status	
Methylated	12 (26.7%)
Unmethylated	33 (73.3%)
TERT promoter mutation status	
Mutant	39 (86.7%)
C250T mutation	15 (53.3%)
C228T mutation	24 (33.3%)
Wild-type	6 (13.3%)
KPS	80% (60–100%)
Mode of radiotherapy	
Conventional	23 (51.1%)
Hypofractionated	22 (48.9%)
Mode of surgery	
Stereotactic biopsy	35 (77.8%)
Microsurgical resection	10 (22.2%)
Contrast enhancement	
Yes	40 (88.9%)
No	5 (11.1%)
CE-T1w MRI volume (mL)	11.1 (0.0–112.6)
T2w MRI volume (mL)	40.9 (0.0–272.0)
TSPO polymorphism genotype	
LAB	6 (13.3%)
MAB	15 (33.3%)
HAB	18 (40.0%)
Not specified	6 (13.3%)
SUV_{max}	2.2 (1.0–4.7)

MGMT = O^6-alkylguanine DNA methyltransferase gene; *TERT* = telomerase reverse transcriptase gene; KPS = Karnofsky performance status scale; CE-T1w = contrast-enhanced T1-weighted; T2w = T2-weighted.

Qualitative data are number and percentage; continuous data are median and range.

TABLE 2
Univariate Survival Analyses

Parameter	OS		PFS	
	Median OS	Significance*	Median PFS	Significance*
Age		**$P = 0.046$**		**$P = 0.014$**
Median < 63 y, $n = 22$	16.33 (9.39–23.27)		10.41 (7.07–13.76)	
Median ≥ 63 y, $n = 23$	9.69 (7.28–12.11)		5.88 (3.46–8.30)	
Sex		$P = 0.330$		$P = 0.259$
Male, $n = 27$	10.48 (2.90–18.06)		6.41 (3.12–9.70)	
Female, $n = 18$	10.84 (8.32–13.37)		9.69 (5.94–13.45)	
MGMT promoter methylation status		**$P = 0.032$**		**$P = 0.028$**
Methylated, $n = 12$	19.38 (3.16–35.61)		10.84 (4.60–17.09)	
Unmethylated, $n = 33$	10.42 (8.60–12.23)		7.26 (4.49–10.03)	
TERT promoter mutation status		$P = 0.939$		$P = 0.896$
Mutant, $n = 39$	10.42 (8.04–12.79)		7.69 (4.99–10.38)	
Wild-type, $n = 6$	11.30 (6.93–15.70)		8.35 (3.02–13.67)	
KPS		$P = 0.117$		$P = 0.104$
Median < 80, $n = 26$	8.61 (4.83–12.38)		6.21 (4.32–8.10)	
Median ≥ 80, $n = 19$	17.77 (13.15–22.40)		9.69 (7.54–11.84)	
Mode of radiotherapy		$P = 0.105$		$P = 0.175$
Conventional, $n = 23$	16.33 (11.48–21.18)		8.90 (7.41–10.40)	
Hypofractionated, $n = 22$	6.83 (0.72–12.95)		5.29 (2.61–7.97)	
Conventional radiochemotherapy		$P = 0.081$		**$P = 0.024$**
≥ 1 cycle adjuvant temozolomide, $n = 12$	19.29 (13.99–24.58)		10.42 (8.93–11.90)	
No adjuvant temozolomide, $n = 11$	9.86 (3.67–16.04)		6.21 (5.50–6.92)	
Hypofractionated radiotherapy		$P = 0.064$		$P = 0.100$
With concomitant temozolomide, $n = 13$	10.84 (0.0–26.94)		8.08 (1.21–14.96)	
Without concomitant temozolomide, $n = 9$	6.83 (1.16–12.51)		5.29 (3.98–6.60)	
Mode of surgery		$P = 0.118$		$P = 0.443$
Stereotactic biopsy, $n = 35$	9.86 (7.31–12.41)		6.83 (3.90–9.77)	
Microsurgical resection, $n = 10$	19.29 (16.77–21.80)		8.35 (2.61–7.97)	
Contrast enhancement		$P = 0.070$		$P = 0.419$
Yes, $n = 40$	9.86 (8.63–11.08)		6.83 (4.54–9.13)	
No, $n = 5$	21.22 (17.42–25.03)		10.61 (7.79–13.43)	
CE-T1w MRI volume		$P = 0.289$		$P = 0.372$
Median < 11.1 mL, $n = 23$	15.77 (7.90–23.64)		8.90 (7.52–10.29)	
Median ≥ 11.1 mL, $n = 22$	6.21 (0.70–11.72)		5.65 (3.65–7.65)	
T2w MRI volume		**$P = 0.031$**		$P = 0.118$
Median < 40.9 mL, $n = 23$	17.77 (6.20–29.34)		8.90 (6.47–11.33)	
Median ≥ 40.9 mL, $n = 22$	6.83 (1.32–12.35)		5.65 (2.90–8.41)	
TSPO polymorphism genotype		$P = 0.360$		$P = 0.333$
LAB	10.84 (8.91–12.77)		9.69 (5.91–13.48)	
MAB	17.77 (7.99–27.56)		8.90 (4.76–13.05)	
HAB	8.28 (0.78–15.79)		5.29 (3.72–6.86)	
SUV_{max}		**$P = 0.037$**		$P = 0.333$
Median < 2.2, $n = 23$	17.77 (4.40–31.14)		8.41 (7.56–9.23)	
Median ≥ 2.2, $n = 22$	8.28 (3.67–12.89)		6.83 (3.63–10.04)	

*Bold font highlights the statistically significant associations.

MGMT = O_6-alkylguanine DNA methyltransferase gene; *TERT* = telomerase reverse transcriptase gene; KPS = Karnofsky performance status scale; CE-T1w = contrast-enhanced T1-weighted; T2w = T2-weighted.

Data in parentheses are 95% CI.

subsequently included in multivariate survival analysis using the Cox proportional hazards model. Statistical significance was defined as a 2-tailed P value of less than 0.05.

RESULTS

Patient Characteristics

Forty-five patients were included. Patient characteristics are displayed in Table 1. Cycles of concomitant and adjuvant temozolomide are given in Table 2.

Median PFS and OS for the overall group were 8.1 mo (95% CI, 6.0–10.2 mo) and 10.8 mo (95% CI, 8.5–13.2 mo), respectively. At the last follow-up, 43 of 45 patients (95.6%) had experienced tumor progression and 40 of 45 patients (88.9%) had died. Of the remaining patients, 1 of 5 was lost to follow-up and 4 of 5 were alive at the last follow-up. Progression was attributable to the following criteria defined by the Response Assessment in Neuro-Oncology Working Group: increase of a contrast-enhancing lesion or a T2 or FLAIR nonenhancing lesion in 14 of 43 patients (32.6%), new contrast enhancement outside the radiation field in 5 of 43 patients (11.6%), failure to return for evaluation because of death or deteriorating condition in 24 of 43 patients (55.8%), and no patients lost to follow-up regarding tumor progression.

TSPO PET Findings in Correlation to TSPO Binding Affinity Status, MRI Findings, and Molecular and Clinical Parameters

Median SUV_{max} for the overall group was 2.2 (range, 1.0–4.7). TSPO polymorphism genotyping results are given in Table 1. Median SUV_{max} was highest in LAB, which was 2.6 (range, 2.4–3.3), followed by MAB of 2.2 (range, 1.0–3.8) and HAB of 2.0 (range, 1.5–4.7; $P = 0.026$).

Contrast enhancement in MRI was absent for 5 patients, all of whom showed a low tumoral TSPO PET signal with SUV_{max} of less than 2.2; the median uptake in those patients was SUV_{max} of 1.8 (range, 1.5–2.1). Otherwise, there were no significant differences between the groups with SUV_{max} greater or less than the median value in PET (all $P > 0.05$; Table 3). SUV_{max} did not correlate with contrast-enhanced T1-weighted MRI volume ($r = 0.092$, $P = 0.547$) or T2-weighted MRI volume ($r = 0.025$, $P = 0.872$).

TABLE 3
Comparison of Patients with Low Versus High Tumoral Uptake on TSPO PET

Characteristic	$SUV_{max} < 2.2$, $n = 23$	$SUV_{max} \geq 2.2$, $n = 22$	Significance*
Age (y)	62.6 (51.2–80.4)	63.9 (30.6–84.2)	$P = 0.910$
Sex			$P = 0.270$
Male	12 (52.2%)	15 (68.2%)	
Female	11 (47.8%)	7 (31.8%)	
MGMT promoter methylation status			$P = 0.563$
Methylated	7 (30.4%)	5 (22.7%)	
Unmethylated	16 (69.6%)	17 (77.3%)	
TERT promoter mutation status			$P = 0.954$
Mutant	20 (86.9%)	19 (86.4%)	
C250T mutation	9 (39.1%)	6 (27.3%)	
C228T mutation	11 (47.8%)	13 (59.1%)	
Wild-type	3 (13.0%)	3 (13.6%)	
KPS	80% (60–100%)	80% (60–90%)	$P = 0.161$
Mode of surgery			$P = 0.528$
Stereotactic biopsy	17 (73.9%)	18 (81.8%)	
Microsurgical resection	6 (26.1%)	4 (18.2%)	
Mode of radiotherapy			$P = 0.185$
Conventional	14 (60.9%)	9 (40.9%)	
Hypofractionated	9 (39.1%)	13 (59.1%)	
Concomitant temozolomide			$P = 0.266$
Yes	19 (82.6%)	15 (68.2%)	
No	4 (17.4%)	7 (31.8%)	
Contrast enhancement			**$P = 0.022$**
Yes	18 (78.3%)	22 (100.0%)	
No	5 (21.7%)	0 (0.0%)	
CE-T1w MRI volume (mL)	10.2 (0.0–112.6)	14.5 (0.4–78.6)	$P = 0.188$
T2w MRI volume (mL)	35.2 (0.0–272.0)	56.2 (0.4–168.5)	$P = 0.188$

*Bold font highlights the statistically significant associations.

MGMT = O_6-alkylguanine DNA methyltransferase gene; *TERT* = telomerase reverse transcriptase gene; KPS = Karnofsky performance status scale; CE-T1w = contrast-enhanced T1-weighted; T2w = T2-weighted.

Qualitative data are number and percentage; continuous data are median and range.

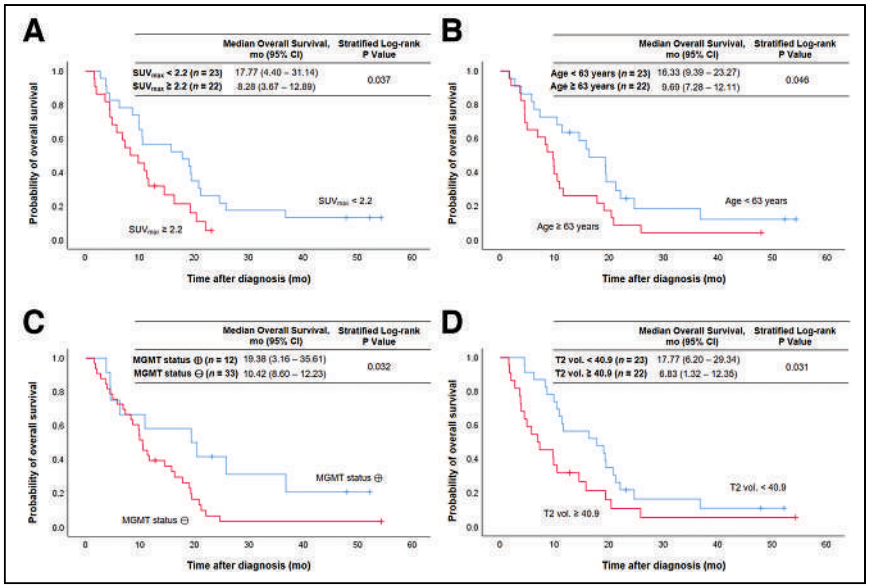

FIGURE 1. Kaplan–Meier curves of OS for entire patient group using median split of SUV_{max} (A), age (B), *MGMT* promoter methylation status (C), and median split of tumor volume on T2-weighted MRI (T2 vol.) (D). ⊕ = methylated; ⊖ = unmethylated.

Association of TSPO PET Findings and Clinical Parameters with Survival

Tumoral uptake on TSPO PET was associated with OS (Fig. 1). High SUV_{max} was related to significantly shorter OS (8.3 vs. 17.8 mo, $P = 0.037$) (Fig. 1A). Figure 2 illustrates a case with high tumoral TSPO radioligand uptake associated with short survival (Fig. 2A) and a case with low tumoral TSPO radioligand uptake associated with long survival (Fig. 2B).

Besides SUV_{max}, age ($P = 0.046$) (Fig. 1B), O^6-alkylguanine DNA methyltransferase (*MGMT*) promoter methylation status ($P = 0.032$) (Fig. 1C), and T2-weighted MRI volume ($P = 0.031$) (Fig. 1D) were prognostic for OS. All results of the univariate analyses for OS and PFS are shown in Table 2.

In the multivariate survival analysis, SUV_{max} in TSPO PET was significantly associated with OS ($P = 0.023$), with high SUV_{max} of more than 2.2 leading to a hazard ratio of 2.212 (95% CI, 1.115–4.386) for death. The results of the multivariate analyses are presented in Table 4.

DISCUSSION

In this study, we corroborate TSPO as a promising imaging target in glioblastoma because tumoral TSPO radioligand uptake in PET appears to be associated with prognosis of glioblastoma patients. In a homogeneous cohort of patients with newly diagnosed IDH–wild-type glioblastoma undergoing TSPO PET before radiotherapy, high tumoral uptake was associated with shorter OS, independent of known clinical risk factors for short survival.

A potential prognostic relevance of TSPO in glioma was proposed more than 25 y ago (*11*). Multiple efforts have been made to better understand the role of TSPO in glioblastoma at a pathophysiologic level, and now, the potential prognostic relevance of TSPO seems to integrate more coherently into the overall picture of TSPO as a relevant functional player in glioblastoma (*2*). Recently, we found a TSPO PET signal to be associated with survival in patients with recurrent glioma (*12*). However, data on the potential prognostic relevance of TSPO PET in newly diagnosed IDH–wild-type glioblastoma were missing until now.

In the current study, patients with high SUV_{max} greater than the median of 2.2 in TSPO PET survived for a significantly shorter period than patients with lower tumoral uptake (OS, 8.3 vs. 17.8 mo; $P = 0.037$). This association persisted when performing multivariate analysis that included prognostic clinical factors: compared with patients with low tumoral uptake on TPSO PET, patients with SUV_{max} of more than 2.2 had a significantly higher risk for death, with a hazard ratio of 2.2 in the multivariate analysis ($P = 0.023$).

Contrast enhancement on MRI was absent for 5 patients, all of whom showed relatively low tumoral uptake in PET and a tendency toward longer OS. Although lack of blood–brain barrier disruption may have been the mechanistic cause for the low uptake in terms of low tracer delivery in those patients, the altered blood–brain barrier passage instead might be merely an epiphenomenon of a diverging biology of the tumor microenvironment with inherently diverging TSPO expression (*13,14*). Because the relationship between specific TSPO radioligand uptake and blood–brain barrier disruption has already been the subject of vivid discussion (*15*), the latter hypothesis may provide an outlet for further research on the underlying pathophysiology, with the potential to better understand the temporal evolution of contrast enhancement and TSPO expression in the context of disease progression. Apart from this association, groups of patients with low and with high tumoral uptake on TSPO PET did not significantly differ with regard to known clinical prognosticators. All 6 LAB cases

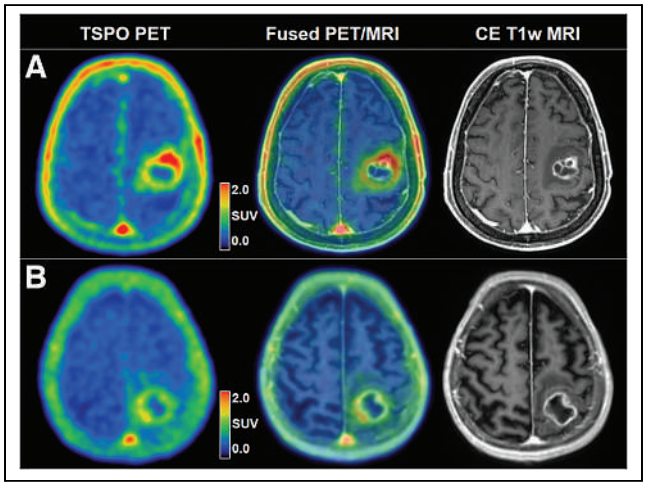

FIGURE 2. (A) 76-y-old male patient with left precentral IDH–wild-type glioblastoma (*MGMT* promoter-methylated, telomerase reverse transcriptase promoter C228T mutation; TSPO HAB) before hypofractionated radiotherapy and temozolomide chemotherapy. Tumoral TSPO radioligand uptake was high (SUV_{max}, 2.4), and survival was short (OS, 4.5 mo). (B) 71-y-old female patient with left postcentral–parietal IDH–wild-type glioblastoma (*MGMT* promoter-methylated, telomerase reverse transcriptase promoter C250T mutation; TSPO MAB) before hypofractionated radiotherapy and temozolomide chemotherapy. Tumoral TSPO radioligand uptake was low (SUV_{max}, 1.8), and survival was long (OS, 25.8 mo). CE-T1w = contrast-enhanced T1-weighted.

TABLE 4
Multivariate Survival Analyses

Parameter	OS		PFS	
	Hazard ratio	Significance*	Hazard ratio	Significance*
Age	2.573 (1.284–5.156)	***P* = 0.008**	2.604 (1.341–5.057)	***P* = 0.005**
MGMT promoter methylation status	3.174 (1.368–7.363)	***P* = 0.007**	2.695 (1.266–5.737)	***P* = 0.010**
T2w MRI volume	1.896 (0.993–3.619)	$P = 0.053$	—	—
SUV_{max}	2.212 (1.115–4.386)	***P* = 0.023**	—	—

*Bold font highlights the statistically significant associations.
T2w = T2-weighted.
Data in parentheses are 95% CI.

were among patients with high tumoral uptake in PET. In a previous study, it was reported that LAB status is associated with survival in male glioblastoma patients; in the current study, subgroups were too small to investigate the sex-specific impact of LAB status on survival (*16*). Yet TSPO binding affinity status, as assessed by genotyping, was not associated with survival in the overall group, either with PFS or with OS.

Apart from SUV_{max} on TSPO PET, parameters associated with survival were age, *MGMT* promoter methylation status, and T2-weighted MRI tumor volume. Patients with higher SUV_{max} did not exhibit significantly larger tumor volumes on MRI, rendering partial-volume effects or SUV_{max} as a confounding surrogate for tumor volume improbable (e.g., there was no correlation of SUV_{max} with T2-weighted MRI volume, $r = 0.025$, $P = 0.872$). As addressed earlier, lack of contrast enhancement on MRI showed a tendency toward longer OS ($P = 0.070$). Historically, contrast enhancement on MRI is an established sign of malignancy in gliomas, which would in principle fit this finding—although the association between contrast enhancement and clinical outcome is continuously critically revisited, embracing resurgence of the topic of the appropriate extent of surgical resection in glioma with regard to non–contrast-enhancing tumor parts (*17,18*). The statistical significance of this association in the present study might potentially have been missed because of the inherently small number of non–contrast-enhancing glioblastomas ($n = 5$ vs. 40). The mode of radiotherapy also showed a tendency toward an association with OS, with a better outcome in the group receiving combined normofractionated radiochemotherapy (16.3 vs. 6.8 mo, $P = 0.105$). This can be partly related to receipt of concomitant temozolomide by all patients under the normofractionated radiotherapy regimen but by only 13 of 22 patients in the course of hypofractionated radiotherapy. Still, in a subgroup analysis of the patients undergoing hypofractionated radiotherapy, a trend toward superior survival could be observed depending on the administration of temozolomide, but no significant survival difference was observed as would have been expected—for example, $P = 0.064$ for OS versus $P < 0.001$ in the randomized study of Perry et al. (*19*). The latter association reveals the limitation of a low case number for distinct subgroups. Instead, in line with the literature, the radiotherapy mode may be associated with clinical outcome because less frail patients were selected for the normofractionated regimen according to clinical routine (*9,19,20*). This is also valid for the patients included in this study, who were significantly younger (59.1 vs. 73.7 y, $P < 0.001$) and functionally less impaired (Karnofsky performance status scale group difference, $P = 0.003$). Within the group of patients with conventional chemoradiotherapy, longer PFS could be observed in those receiving adjuvant temozolomide. This may be attributable partly to undertreatment of patients in whom temozolomide could not be administered (e.g., because of thrombocytopenia) but also may relate to a certain selection bias, because patients with early progression during chemoradiotherapy did not receive adjuvant temozolomide. In the overall group, the percentage of patients with unmethylated *MGMT* promoter (73.3%) was higher than in most MGMT landmark trials and therefore might have contributed to the rather short OS of 10.8 mo in our study cohort (*20–22*). Patient age and *MGMT* status were significantly associated with both OS and PFS. In contrast, SUV_{max} was significantly associated only with OS, not with PFS. Although we used criteria defined by the Response Assessment in Neuro-Oncology Working Group for progression, this may be partly caused by progression constituting a continuum, rather than a definite point of time (*10*). The accurate capture of progression depends on imaging time points and is especially difficult in this case because most patients received only a biopsy, not a tumor resection. Conversely, OS is a well-defined, hard endpoint and therefore the more rigid and preferred parameter for survival analyses (*10*).

Beyond the limitation of the retrospective study design and a rather small sample size regarding distinct subgroups, as elucidated earlier, further points are worth discussing. A benefit of PET imaging for survival prediction in glioma has already been shown using the amino acid analog [^{18}F]FET, which is an established PET imaging tracer for gliomas (*23*). Therefore, inclusion of [^{18}F]FET PET data into the current study would have been interesting. Unfortunately, most patients received [^{18}F]FET PET later in the disease course, and dual-tracer PET before radiotherapy was not available in a large number of cases in this cohort. Intentionally, this study addressed the association of TSPO PET findings and survival in newly diagnosed glioblastoma before radiotherapy (not during or after radiotherapy, where radiation treatment–related alterations of tumoral tracer uptake may occur in TSPO PET) (*24*). However, serial TSPO PET imaging during radiotherapy will be of interest as a potential tool for treatment response assessment. In particular, dual-tracer approaches using amino acid and TSPO PET, as well as the monitoring of changes of TSPO radioligand uptake in glioblastoma patients undergoing radiotherapy, harbor a chance of allowing a better understanding of the role of TSPO in the frame of radiotherapy. Recently, we illustrated the potential value of such an approach in a case of an IDH–wild-type glioma with remarkably long survival in the context of chemoradiotherapy. The distinct uptake patterns in dual PET over the disease course in this case led us to speculate that serial TSPO PET, in conjunction

with [^{18}F]FET PET, might capture the treatment-induced immune response as a potential biomarker (*25*). In addition, some promising preclinical studies hint at the potential future clinical value of multitracer approaches for PET imaging of glioma. Pigeon et al. revealed TSPO to be an earlier marker for glioma infiltration (*26*). Foray et al. (*27*) and Zinnhardt et al. (*28*) substantiated that each imaging biomarker might identify distinct areas of the heterogeneous glioma tissue and tumor microenvironment; for example, TSPO indicated specific areas of myeloid cell infiltration. Foray et al. used a dual-tracer TSPO and FET approach to image glioma-associated microglia and macrophage dynamics under immunomodulating treatment (*29*). Further studies are warranted and will enhance the evaluation of TSPO PET for prognostication in glioma patients.

CONCLUSION

High tumoral uptake in TSPO PET before radiotherapy is associated with significantly shorter survival within the homogeneous group of molecularly defined, newly diagnosed IDH–wild-type glioblastoma. TSPO PET seems to add prognostic insights beyond established clinical parameters and might serve as an informative tool as clinicians make survival predictions for patients with glioblastoma.

DISCLOSURE

Funding was provided by the Deutsche Forschungsgemeinschaft (DFG), Research Unit FOR 2858, project numbers 421887978 and 422188432. Nathalie Albert was funded by Else Kröner-Fresenius-Stiftung. Matthias Brendel was funded by the DFG under Germany's Excellence Strategy within the framework of the Munich Cluster for Systems Neurology (EXC 2145 SyNergy 390857198). No other potential conflict of interest relevant to this article was reported.

ACKNOWLEDGMENTS

Nathalie Albert and Matthias Brendel are members of the EANM neuroimaging committee. Adrien Holzgreve, Nathalie Albert, and Joerg-Christian Tonn are members of the EORTC brain tumor group and the EORTC imaging committee. Adrien Holzgreve is a member of the DGN PET committee. Parts of this paper are related to the doctoral project of Debie Nelwan.

KEY POINTS

QUESTION: Is a TSPO PET signal associated with survival in glioblastoma patients?

PERTINENT FINDINGS: In a homogeneous cohort of patients with newly diagnosed IDH–wild-type glioblastoma before radiotherapy, a TSPO PET signal was associated with survival. High uptake intensity ($SUV_{max} > 2.2$) was related to significantly shorter OS. In the multivariate survival analysis, SUV_{max} in TSPO PET remained an independent prognostic factor for OS.

IMPLICATIONS FOR PATIENT CARE: TSPO PET seems to add prognostic insights beyond established clinical parameters and might serve as an informative tool as clinicians make survival predictions for patients with glioblastoma.

REFERENCES

1. Low JT, Ostrom QT, Cioffi G, et al. Primary brain and other central nervous system tumors in the United States (2014-2018): a summary of the CBTRUS statistical report for clinicians. *Neurooncol Pract.* 2022;9:165–182.
2. Ammer LM, Vollmann-Zwerenz A, Ruf V, et al. The role of translocator protein TSPO in hallmarks of glioblastoma. *Cancers (Basel).* 2020;12:2973.
3. Xiang X, Wind K, Wiedemann T, et al. Microglial activation states drive glucose uptake and FDG-PET alterations in neurodegenerative diseases. *Sci Transl Med.* 2021;13:eabe5640.
4. Albert NL, Unterrainer M, Fleischmann DF, et al. TSPO PET for glioma imaging using the novel ligand ^{18}F-GE-180: first results in patients with glioblastoma. *Eur J Nucl Med Mol Imaging.* 2017;44:2230–2238.
5. Jensen P, Feng L, Law I, et al. TSPO imaging in glioblastoma multiforme: a direct comparison between ^{123}I-CLINDE SPECT, ^{18}F-FET PET, and gadolinium-enhanced MR imaging. *J Nucl Med.* 2015;56:1386–1390.
6. Unterrainer M, Fleischmann DF, Diekmann C, et al. Comparison of ^{18}F-GE-180 and dynamic ^{18}F-FET PET in high grade glioma: a double-tracer pilot study. *Eur J Nucl Med Mol Imaging.* 2019;46:580–590.
7. Unterrainer M, Fleischmann DF, Vettermann F, et al. TSPO PET, tumour grading and molecular genetics in histologically verified glioma: a correlative ^{18}F-GE-180 PET study. *Eur J Nucl Med Mol Imaging.* 2020;47:1368–1380.
8. World Health Organization. *WHO Classification of Tumours of the Central Nervous System.* 5th ed, Vol 6. International Agency for Research on Cancer; 2021.
9. Niyazi M, Brada M, Chalmers AJ, et al. ESTRO-ACROP guideline "target delineation of glioblastomas." *Radiother Oncol.* 2016;118:35–42.
10. Wen PY, Chang SM, Van den Bent MJ, Vogelbaum MA, Macdonald DR, Lee EQ. Response assessment in neuro-oncology clinical trials. *J Clin Oncol.* 2017;35:2439–2449.
11. Miettinen H, Kononen J, Haapasalo H, et al. Expression of peripheral-type benzodiazepine receptor and diazepam binding inhibitor in human astrocytomas: relationship to cell proliferation. *Cancer Res.* 1995;55:2691–2695.
12. Quach S, Holzgreve A, Kaiser L, et al. TSPO PET signal using [^{18}F]GE180 is associated with survival in recurrent gliomas. *Eur J Nucl Med Mol Imaging.* 2023;50:859–869.
13. Varn FS, Johnson KC, Martinek J, et al. Glioma progression is shaped by genetic evolution and microenvironment interactions. *Cell.* 2022;185:2184–2199.e16.
14. Yeo AT, Rawal S, Delcuze B, et al. Single-cell RNA sequencing reveals evolution of immune landscape during glioblastoma progression. *Nat Immunol.* 2022;23:971–984.
15. Albert NL, Unterrainer M, Kaiser L, et al. In response to: anatomy of ^{18}F-GE180, a failed radioligand for the TSPO protein. *Eur J Nucl Med Mol Imaging.* 2020;47:2237–2241.
16. Troike KM, Acanda de la Rocha AM, Alban TJ, et al. The translocator protein (TSPO) genetic polymorphism A147T is associated with worse survival in male glioblastoma patients. *Cancers (Basel).* 2021;13:4525.
17. Karschnia P, Vogelbaum MA, van den Bent M, et al. Evidence-based recommendations on categories for extent of resection in diffuse glioma. *Eur J Cancer.* 2021;149:23–33.
18. Karschnia P, Young JS, Dono A, et al. Prognostic validation of a new classification system for extent of resection in glioblastoma: a report of the RANO resect group. *Neuro-oncol.* 2023;25:940–954.
19. Perry JR, Laperriere N, O'Callaghan CJ, et al. Short-course radiation plus temozolomide in elderly patients with glioblastoma. *N Engl J Med.* 2017;376:1027–1037.
20. Malmström A, Grønberg BH, Marosi C, et al. Temozolomide versus standard 6-week radiotherapy versus hypofractionated radiotherapy in patients older than 60 years with glioblastoma: the Nordic randomised, phase 3 trial. *Lancet Oncol.* 2012;13:916–926.
21. Hegi ME, Diserens AC, Gorlia T, et al. MGMT gene silencing and benefit from temozolomide in glioblastoma. *N Engl J Med.* 2005;352:997–1003.
22. Wick W, Platten M, Meisner C, et al. Temozolomide chemotherapy alone versus radiotherapy alone for malignant astrocytoma in the elderly: the NOA-08 randomised, phase 3 trial. *Lancet Oncol.* 2012;13:707–715.
23. Suchorska B, Giese A, Biczok A, et al. Identification of time-to-peak on dynamic ^{18}F-FET-PET as a prognostic marker specifically in IDH1/2 mutant diffuse astrocytoma. *Neuro-oncol.* 2018;20:279–288.
24. Tuominen S, Keller T, Petruk N, et al. Evaluation of [^{18}F]F-DPA as a target for TSPO in head and neck cancer under normal conditions and after radiotherapy. *Eur J Nucl Med Mol Imaging.* 2021;48:1312–1326.
25. Quach S, Holzgreve A, von Baumgarten L, et al. Increased TSPO PET signal after radiochemotherapy in IDH-wildtype glioma-indicator for treatment-induced immune activation? *Eur J Nucl Med Mol Imaging.* 2022;49:4282–4283.
26. Pigeon H, Pérès EA, Truillet C, et al. TSPO-PET and diffusion-weighted MRI for imaging a mouse model of infiltrative human glioma. *Neuro-oncol.* 2019;21:755–764.
27. Foray C, Valtorta S, Barca C, et al. Imaging temozolomide-induced changes in the myeloid glioma microenvironment. *Theranostics.* 2021;11:2020–2033.
28. Zinnhardt B, Pigeon H, Thézé B, et al. Combined PET imaging of the inflammatory tumor microenvironment identifies margins of unique radiotracer uptake. *Cancer Res.* 2017;77:1831–1841.
29. Foray C, Barca C, Winkeler A, et al. Interrogating glioma-associated microglia and macrophage dynamics under CSF-1R therapy with multitracer in vivo PET/MRI. *J Nucl Med.* 2022;63:1386–1393.

PET Imaging and Protein Expression of Prostate-Specific Membrane Antigen in Glioblastoma: A Multicenter Inventory Study

Sanne A.M. van Lith*[1], Ilanah J. Pruis*[2], Nelleke Tolboom[3], Tom J. Snijders[4], Dylan Henssen[1], Mark ter Laan[5], Maarten te Dorsthorst[5], William P.J. Leenders[6,7], Martin Gotthardt[1], James Nagarajah[1], Pierre A. Robe[4], Philip De Witt Hamer[8], Harry Hendrikse[9], Daniela E. Oprea-Lager[9], Maqsood Yaqub[9], Ronald Boellaard[9], Pieter Wesseling[10,11], Rutger K. Balvers[12], Frederik A. Verburg[2], Anita A. Harteveld[2], Marion Smits[2,13], Martin van den Bent[14], Sophie E.M. Veldhuijzen van Zanten*[2], and Elsmarieke van de Giessen*[9]

[1]Medical Imaging, Radboud University Medical Center, Nijmegen, The Netherlands; [2]Radiology and Nuclear Medicine, Erasmus MC, Rotterdam, The Netherlands; [3]Radiology and Nuclear Medicine, University Medical Center Utrecht, Utrecht, The Netherlands; [4]Neurology and Neurosurgery, UMC Utrecht Brain Center, University Medical Center Utrecht, Utrecht, The Netherlands; [5]Neurosurgery, Radboud University Medical Center, Nijmegen, The Netherlands; [6]Biochemistry, Radboud University Medical Center, Nijmegen, The Netherlands; [7]Predica Diagnostics, Nijmegen, The Netherlands; [8]Neurosurgery, Amsterdam UMC, VUmc, Amsterdam, The Netherlands; [9]Radiology and Nuclear Medicine, Amsterdam UMC, VUmc, Amsterdam, The Netherlands; [10]Pathology, Amsterdam UMC, VUmc, Amsterdam, The Netherlands; [11]Pathology, Princess Máxima Center for Pediatric Oncology, Utrecht, The Netherlands; [12]Neurosurgery, Erasmus MC, Rotterdam, The Netherlands; [13]Medical Delta, Delft, The Netherlands; and [14]Brain Tumor Center at Erasmus MC Cancer Institute, Erasmus MC, Rotterdam, The Netherlands

Upregulation of prostate-specific membrane antigen (PSMA) in neovasculature has been described in glioblastoma multiforme (GBM), whereas vasculature in nonaffected brain shows hardly any expression of PSMA. It is unclear whether PSMA-targeting tracer uptake on PET is based on PSMA-specific binding to neovasculature or aspecific uptake in tumor. Here, we quantified uptake of various PSMA-targeting tracers in GBM and correlated this with PSMA expression in tumor biopsy samples from the same patients. **Methods:** Fourteen patients diagnosed with de novo ($n = 8$) or recurrent ($n = 6$) GBM underwent a preoperative PET scan after injection of 1.5 MBq/kg [^{68}Ga]Ga-PSMA-11 ($n = 7$), 200 MBq of [^{18}F]DCFpyl ($n = 3$), or 200 MBq of [^{18}F]PSMA-1007 ($n = 4$). Uptake in tumor and tumor-to-background ratios, with contralateral nonaffected brain as background, were determined. In a subset of patients, PSMA expression levels from different regions in the tumor tissue samples ($n = 40$), determined using immunohistochemistry ($n = 35$) or RNA sequencing ($n = 13$), were correlated with tracer uptake on PET. **Results:** Moderate to high (SUV_{max}, 1.3–20.0) heterogeneous uptake was found in all tumors irrespective of the tracer type used. Uptake in nonaffected brain was low, resulting in high tumor-to-background ratios (6.1–359.0) calculated by dividing SUV_{max} of tumor by SUV_{max} of background. Immunohistochemistry showed variable PSMA expression on endothelial cells of tumor microvasculature, as well as on dispersed individual cells (of unknown origin), and granular staining of the neuropil. No correlation was found between in vivo uptake and PSMA expression levels (for immunohistochemistry, $r = -0.173$, $P = 0.320$; for RNA, $r = -0.033$, $P = 0.915$). **Conclusion:** Our results indicate the potential use of various PSMA-targeting tracers in GBM. However, we found no correlation between PSMA expression levels on immunohistochemistry and uptake intensity on PET. Whether this may be explained by methodologic reasons, such as the inability to measure functionally active PSMA with immunohistochemistry, tracer pharmacokinetics, or the contribution of a disturbed blood–brain barrier to tracer retention, should still be investigated.

Key Words: glioblastoma; prostate-specific membrane antigen (PSMA); PET; immunohistochemistry; RNA sequencing

J Nucl Med 2023; 64:1526–1531
DOI: 10.2967/jnumed.123.265738

Glioma is the most frequent type of primary brain tumor, of which glioblastoma multiforme (GBM) is the most malignant subtype. Newly diagnosed GBM patients face a dismal prognosis, with a median overall survival time of 15–18 mo. Treatment options are limited, especially at progression. Therefore, research into targeted therapies is highly desired.

A target that has gained increased attention is prostate-specific membrane antigen (PSMA), a type 2 transmembrane glycoprotein receptor that was found to be expressed on neovasculature of various solid tumors (*1*). Immunohistochemistry studies have shown that in GBM, PSMA is expressed on neovasculature in 31%–100% of cases (*2–12*) and absent from vasculature in nonaffected brain areas. High expression of PSMA on neovasculature in GBM correlates with increased angiogenesis (*9*) and poor prognosis (*3,5,8,9*). Besides expression on neovasculature, expression of PSMA has been observed on tumor cells, although to a lesser extent (*8,13*), and tumor cell expression levels did not correlate with survival (*5*).

Various PSMA-targeting radiotracers are used in clinical practice for detection, staging, recurrence evaluation, and radionuclide therapy in prostate cancer (*14*). Some of these tracers have been applied recently to molecular imaging of GBM. These studies showed enhanced uptake of all investigated PSMA-targeting tracers in both de novo and recurrent GBM (*7,15–21*). However, it is unknown whether the current tracers bind specifically to PSMA-expressing

Received Mar. 16, 2023; revision accepted May 31, 2023.
For correspondence or reprints, contact Sophie Veldhuijzen E.M. van Zanten (s.veldhuijzenvanzanten@erasmusmc.nl).
*Contributed equally to this work.
Published online Aug. 31, 2023.

microvasculature or tumor cells or the uptake visible on PET images simply reflects a disturbed blood–brain barrier, resulting in aspecific retention of the tracer. For the potential of PSMA-targeting radionuclide therapy, exact localization of the tracer in the tumor area is considered important, because lack of internalization in tumor cells could lead to rapid washout and short retention times (*22*). Furthermore, particularly for α-emitting radionuclides with high linear energy but short range, internalization into tumor cells—or at least sufficient retention time at the tumor site—would likely be needed to enable effective induction of cellular damage.

In this multicenter inventory study, we aimed to evaluate tumor uptake of several PSMA-targeting tracers ([^{18}F]PSMA-1007, [^{18}F]DCFPyl, and [^{68}Ga]Ga-PSMA-11) in patients with histopathologically confirmed de novo or recurrent GBM. In a subset of patients, we correlated tracer uptake visible on PET images with PSMA expression in image-guided multisector tumor biopsy samples obtained during resection of the tumor.

MATERIALS AND METHODS

Patients

Nine patients with high suspicion of a de novo or recurrent GBM based on MRI were included in separate prospective studies that were performed at Erasmus Medical Center Rotterdam (Erasmus MC, 5 patients; NCT05798273) and Radboud University Medical Center Nijmegen (Radboudumc, 4 patients; NCT04588454). Ethical approval was obtained separately by each of the local institutional review boards. At Amsterdam University Medical Center (Amsterdam UMC, 3 patients) and University Medical Center Utrecht (UMCU, 2 patients), patients with high suspicion of a recurrent GBM were scanned under compassionate use as part of regular clinical care. All patients gave written informed consent for use of their data. Available data were combined for the purpose of this article in a retrospective setting. More details on materials and methods are presented in the supplemental materials (supplemental materials are available at http://jnm.snmjournals.org).

Image Acquisition

All patients underwent PET scanning on injection of 1 of the 3 PSMA-targeting tracers ([^{68}Ga]Ga-PSMA-11, [^{18}F]DCFPyl, or [^{18}F]PSMA-1007) within a range of 1–17 d before surgery or 1–3 mo before surgery for 2 patients who were scanned at UMCU. The image acquisition details are described in Supplemental Table 1.

Image Analysis

SUVs were calculated to enable semiquantitative analysis of tracer uptake in tumor using in-house software. Volumes of interest were automatically drawn around the brain regions that showed high focal uptake. Tumor-to-background ratios were calculated by dividing SUV_{max} of tumor by SUV_{max} of background, as in Kunikowska et al. (*23*), and SUV_{mean} of tumor by SUV_{mean} of background. In addition, the overlaps between gadolinium-based contrast agents enhancing areas of tumor on MRI and tracer uptake on PET were visually assessed by nuclear physicians. SUV_{max} was also assessed for parotid tissue and liver.

Results of the dynamic (Amsterdam UMC, $n = 3$) and sequential (Erasmus MC, $n = 5$) PET scans were used to determine time–activity curves.

Navigation of Biopsy Samples

In 12 of 14 patients, multiple tissue biopsy samples were collected using per-operative neuronavigation (*24*) from tumor areas with low and high tracer uptake on PET to correlate with PSMA expression on immunohistochemistry or as determined with targeted RNA sequencing. Neuronavigation screenshots were used to visually match the corresponding PET frame and volume of interest to the exact biopsy location. In UMCU, only material from the resected tumor was analyzed according to standard clinical care, and no intraoperative biopsy samples were taken.

PSMA Immunohistochemistry

Tissues samples were either snap-frozen ($n = 8$ biopsy samples in 2 patients at Radboudumc) or formalin-fixed and paraffin-embedded ($n = 12$ biopsy samples in 5 patients at Erasmus MC and $n = 15$ biopsy samples in 3 patients at Amsterdam UMC). Tissue sections were immunostained with mouse anti-PSMA (M3620; Dako). The complete biopsy samples were evaluated by an experienced neuropathologist using a visual 5-point scale, which combined both intensity and extent of the staining (0 = none, 1 = limited, 2 = moderate, 3 = high, and 4 = very high) for 3 tissue components that were found to have the highest PSMA expression in all samples: tumor microvasculature (especially in luminal or endothelial cells, rather than abluminal cells or pericytes), individual cells (of unknown nature) in the periphery of the tumor, and neuropil (which showed granular-like staining). The identified individual cells were well organized and located in the transition zone of tumor tissue and preexistent brain tissue. They were therefore not deemed tumor cells, because these showed a disorganized arrangement and no or hardly any PSMA expression. Because of these low PSMA expression levels, tumor cells were not scored. For each biopsy sample, a total immunohistochemistry score was calculated from the sum of the 3 component scores.

Targeted RNA Sequencing

Tissue biopsy samples ($n = 13$ in 4 patients at Radboudumc) were snap-frozen. Targeted RNA sequencing (*25*) was performed to detect PSMA, angiogenesis-related vascular endothelial growth factor receptors 1 and 2, angiopoietin 1, and angiopoietin 2.

Statistical Analyses

Statistical analysis was performed with SPSS version 24.0.0.1 (IBM Corp.) or with GraphPad Prism version 5.0 (GraphPad Software Inc.). PSMA and angiopoietin 1, angiopoietin 2, and vascular endothelial growth factor expression levels in the biopsy samples obtained from immunohistochemistry or RNA expression were correlated with SUV_{max} obtained from 1-cm spheric volumes of interest on PET. Pearson ρ-correlation and Spearman ρ-correlation were used for normally and nonnormally distributed variables, respectively. A P value of less than 0.05 was considered a statistically significant difference.

RESULTS

Uptake of PSMA-Targeting Tracers in GBM

We included 14 patients with histopathologically confirmed de novo GBM ($n = 8$) or recurrent GBM ($n = 6$) (median age, 64 y; interquartile ratio, 54–74 y; $n = 10$ male, 71%; Supplemental Table 2). Tumor uptake values are summarized in Table 1 (all segmentation data are shown in Supplemental Table 3). Figure 1 shows a representative image from each of the centers. Heterogeneous, moderate to high uptake of all PSMA tracers was found in all tumors. SUV_{max} and tumor-to-background ratio (SUV_{max} of tumor divided by SUV_{max} of background) values ranged from 1.3 to 20.0 and 7.5 to 359.0 for [^{68}Ga]Ga-PSMA-11, from 4.5 to 13.1 and 13.6 to 36.5 for [^{18}F]DCFPyl, and from 3.4 to 14.6 and 6.1 to 39.6 for [^{18}F]PSMA-1007, respectively. Uptake in contralateral nonaffected brain was low (SUV_{max}, <0.1–1.6). Overall, the uptake distribution, as seen on PET, showed good visual overlap with the area of gadolinium-based contrast agent enhancement on T1-weighted MRI. However, an inhomogeneous pattern of PET uptake was seen in the areas enhanced by gadolinium-based contrast agents, which did not exactly follow the contrast agent pattern in all cases (Fig. 1).

TABLE 1
Tumor Uptake of Various PSMA-Targeting Tracers

No.	Radioligand	Time after injection (min)	SUV_{max}	SUV_{mean}	$TBR_{max/max}$
1	[^{68}Ga]Ga-PSMA-11	90 (WB)	15.3	4.4	32.6
		165	20.0	4.5	66.7
		240	17.0	4.0	38.6
2	[^{68}Ga]Ga-PSMA-11	90 (WB)	3.6	1.7	359.0
		165	5.9	2.9	295.0
		240	5.8	2.8	35.9
3	[^{68}Ga]Ga-PSMA-11	90 (WB)	7.4	2.5	185.3
		165	9.8	2.6	98.4
		240	10.0	2.8	26.3
4	[^{68}Ga]Ga-PSMA-11	90 (WB)	6.5	3.1	10.3
		165	9.0	3.5	17.3
		240	9.0	3.6	7.5
5	[^{68}Ga]Ga-PSMA-11	90 (WB)	7.3	1.9	66.6
		165	7.7	2.3	29.5
		240	9.0	2.6	64.6
6	[^{18}F]DCFPyl	80	4.5	2.1	21.9
		NA (WB)	NA	NA	NA
		140	6.8	2.9	25.7
7	[^{18}F]DCFPyl	80	5.3	2.1	23.5
		95 (WB)	4.5	2.3	13.6
		140	7.4	2.7	24.4
8	[^{18}F]DCFPyl	80	10.3	4.6	34.8
		95 (WB)	12.6	5.3	29.9
		140	13.1	6.0	36.5
9	[^{68}Ga]Ga-PSMA-11	60	2.2	1.0	72.3
10	[^{68}Ga]Ga-PSMA-11	60	1.3	0.6	10.3
11	[^{18}F]PSMA-1007	120	3.4	1.6	6.1
12	[^{18}F]PSMA-1007	120	8.1	3.4	10.1
13	[^{18}F]PSMA-1007	120	14.6	6.8	39.6
14	[^{18}F]PSMA-1007	120	12.4	4.7	7.8

$TBR_{max/max}$ = SUV_{max} tumor divided by SUV_{max} background; WB = whole body; NA = not available.

Because normal tissue biodistribution patterns are similar for [^{18}F]DCFPyl and [^{68}Ga]Ga-PSMA-11 (*26*), time–activity curves for tracer uptake in the tumors of patients 1–8, covering 0–240 min after injection, are combined in Figure 2A. These time–activity curves demonstrate that there is still an increase in [^{18}F]DCFPyl binding 120 min after injection and gradual flattening of the curve but still slightly increasing [^{68}Ga]Ga-PSMA-11 binding approaching 240 min after injection. A representative perfusion image of the tumor in the first 2 min after injection for [^{18}F]DCFPyl (Fig. 2B) demonstrates that tumor uptake of [^{18}F]DCFPyl at late time points does not follow the perfusion pattern; that is, tumor uptake primarily depends on factors other than perfusion. Time–activity curves normalized for SUV_{mean} of parotid tissue and SUV_{max} of liver are shown in Supplemental Figure 1.

Uptake of PSMA-Targeting Tracers in Nontarget Organs

Uptake in the parotid glands increased gradually on each of the successive scans within patients and showed high variability between patients, irrespective of the type of tracer (Supplemental Table 2; for the SUV_{max} range, [^{68}Ga]Ga-PSMA-11, 10.4–34.7; [^{18}F]DCFPyl, 9.1–45.6; [^{18}F]PSMA-1007, 22.9–43.8). Uptake in the liver was found with SUV_{max} ranging from 7.7 to 12.9 for [^{68}Ga]Ga-PSMA-11 and 6.6 to 6.7 for [^{18}F]DCFPyl (Supplemental Table 2).

Correlation of Tracer Uptake with PSMA Expression

Figures 3A–3D show representative images of PSMA immunohistochemistry of tumor biopsy samples demonstrating PSMA expression on the 3 tissue components. PSMA expression on microvasculature was mainly found within the boundaries of tumor tissue, whereas PSMA-expressing individual cells were generally located in the transition zone of tumor tissue and preexistent brain tissue. A negative correlation was found between tracer uptake visible on the PET images and immunohistochemistry scores for the individual cells ($r = -0.372$, $P = 0.028$), and no significant correlation was found between PET uptake and immunohistochemistry

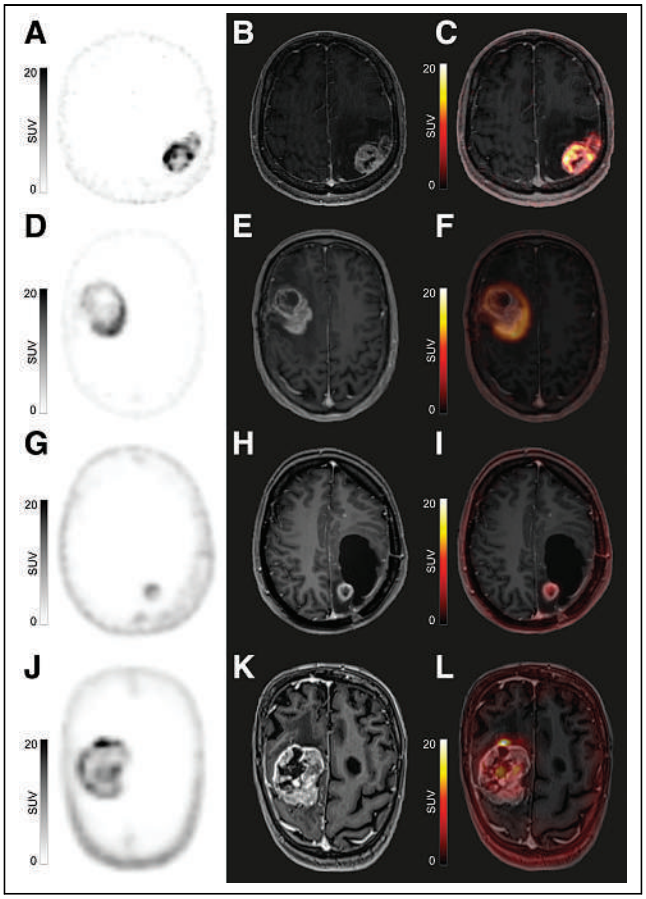

FIGURE 1. Selected examples of PET (A, D, G, and J), MRI (B, E, H, and K), hybrid PET/MRI (C), and fused PET/MRI (F, I, and L) of patients injected with [^{68}Ga]Ga-PSMA-11 (patient 1 from Erasmus MC [A–C], SUV_{max}, 20.0, and patient 10 from UMCU [G–I], SUV_{max}, 1.3), [^{18}F]DCFpyl (patient 8 from Amsterdam UMC [D–F], SUV_{max}, 13.1), and [^{18}F]PSMA-1007 (patient 14 from Radboudumc [J–L], SUV_{max}, 12.4). Note heterogeneity of tracer uptake within tumors.

scores for vasculature ($r = 0.211$, $P = 0.225$), neuropil ($r = -0.077$, $P = 0.660$; Supplemental Fig. 2A), or total immunohistochemistry scores ($r = -0.173$, $P = 0.320$; Fig. 3E). No correlations were found when separated for tracer type (Supplemental Table 4).

No correlation was found between tracer uptake of [^{18}F]PSMA-1007 on PET and PSMA RNA expression ($r = -0.033$, $P = 0.915$; Fig. 3F). PSMA immunohistochemistry and PSMA RNA expression analyses did correlate, confirming the validity of both techniques ($r = 0.773$, $P = 0.029$; Supplemental Fig. 2B). No correlations were found between tracer uptake on PET and RNA expression ratio of angiopoietin 2 to angiopoietin 1 ($r = -0.202$, $P = 0.509$) or vascular endothelial growth factor RNA expression ($r = -0.425$, $P = 0.148$; Supplemental Fig. 2C).

DISCUSSION

Here, we found moderate to high uptake on PSMA PET with heterogeneous distribution in tumor irrespective of tracer type in both de novo and recurrent GBM. No correlation was found between uptake on PSMA PET and PSMA expression, as determined with immunohistochemistry or RNA sequencing.

The reported SUV_{max} and values for SUV_{max} of tumor divided by SUV_{max} of background are comparable to those reported in previous literature (*20,27–29*) and show that variation between tumors is larger than variation between tracers. PSMA immunohistochemistry showed strong staining of microvasculature in the tumor tissue but not in nonaffected brain vasculature or cells, which is in accordance with multiple studies (*6,7,30,31*). The strong granular PSMA staining in neuropil, which is built up from glial cells and neurites or neuronal processes, remains to be unraveled. In addition, the nature of PSMA-positive individual cells, especially in the transition zone of tumor tissue and preexistent brain tissue, awaits further elucidation. On the basis of their morphologic and immunohistochemical characteristics, these cells do not qualify as neoplastic cells or macrophages. These cells possibly are peritumoral single cells related to astrocytosis because of glial fibrillary acidic protein positivity, as found by others (*6,8,32*).

Few earlier studies have shown that PSMA expression correlates with tracer uptake in high-grade glioma (*21*) and other tumor types (*33*). One found a nonsignificant trend ($P > 0.1$) in prostate cancer (*34*). We and others (*35*) did not find a correlation between PSMA expression and tracer uptake. Studies correlating expression levels of other targets, such as L-type amino acid transporters (*36,37*) and somatostatin receptor (*38,39*) with tracer uptake of *O*-(2-[^{18}F]fluoroethyl)-L-tyrosine and [^{68}Ga]Ga-DOTA peptides, respectively, in various types of glioma also found no correlation. This is not surprising given the complex and largely still unknown interplay of in vivo tracer kinetics, (heterogeneous) blood–brain barrier disruption, efflux rates, target localization, tracer–target complex kinetics, and downstream function or actions of the target. In addition, methodologic issues, such as the use of different tracers, protocols, or scanners and sample size, may have contributed to not finding a correlation in this study. Future studies to advance knowledge with regard to tracer-specific uptake versus retention could encompass

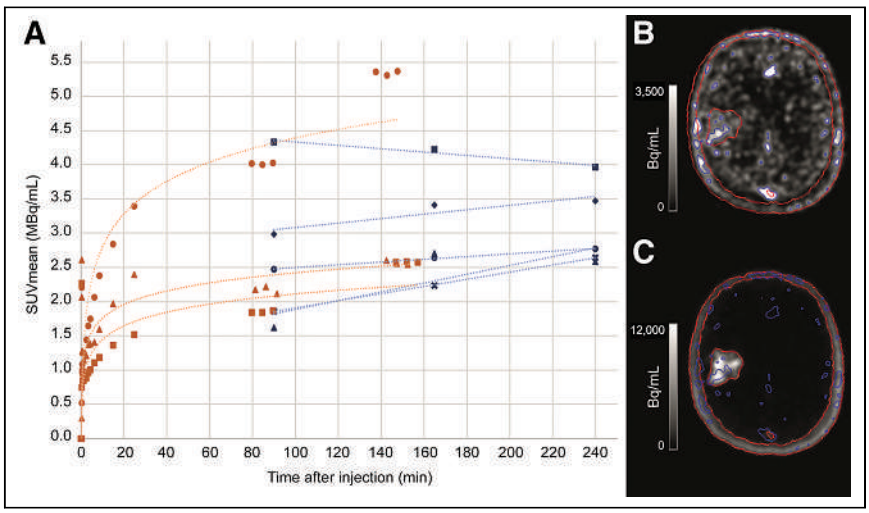

FIGURE 2. (A) Time–activity curves showing tumor uptake of [^{18}F]DCFpyl (orange) and [^{68}Ga]Ga-PSMA (blue) in MBq/mL from 0 to 240 min after injection for patients 1–8 (each marker icon represents one patient). Representative images of early (B, blue contour) and late (C, red contour) perfusion in first 2 min after injection of [^{18}F]DCFpyl in patient 6.

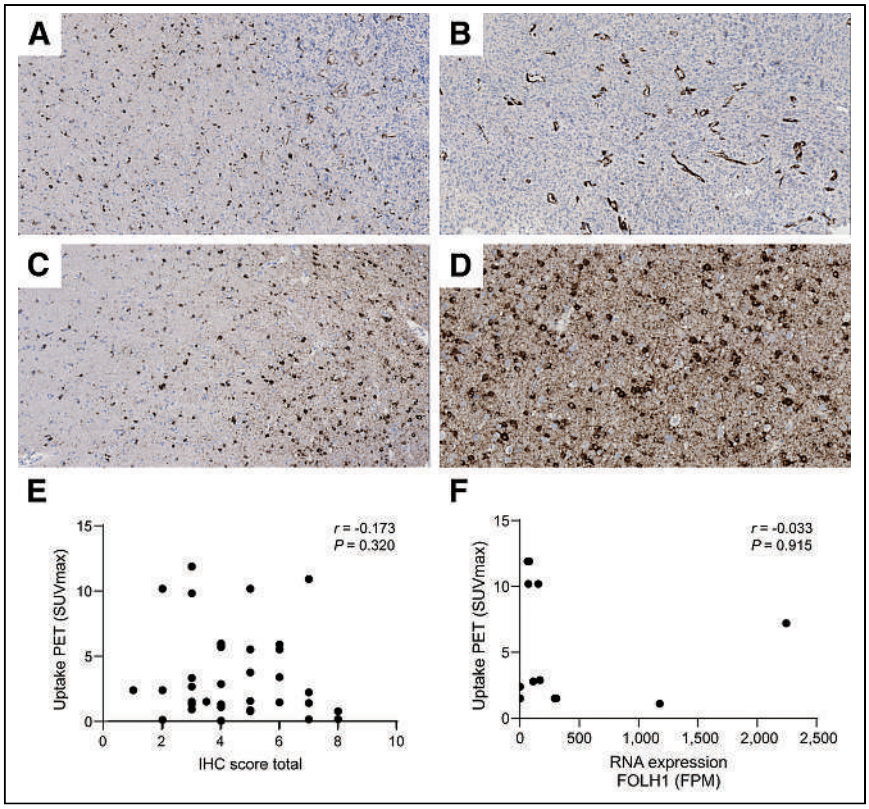

FIGURE 3. Representative images of PSMA immunohistochemistry in formalin-fixed and paraffin-embedded biopsy samples. (A) Positive, dispersed individual cells of unknown origin in periphery of tumor and positive vasculature in tumor cell–dense region. (B) Positive vasculature in tumor cell–dense region. (C) Positive, dispersed individual cells and granular staining in neuropil. (D) Positive individual cells and strong granular staining in neuropil. To exemplify method used for scoring IHC findings, following scores would have been given for these snapshot figures for microvasculature, individual cells, and granular staining in neuropil (sum score), respectively: 2, 3, and 1 (sum, 6) (A); 4, 0, and 0 (sum, 4) (B); 0, 3, and 3 (sum, 6) (C); and 0, 4, and 4 (sum, 8) (D). (E) Correlation between total IHC score and tracer uptake. (F) Correlation between normalized RNA expression of *FOLH1* (PSMA-encoding gene) and tracer uptake. Tracer uptake is expressed in SUV_{max} and measured on PET in 1-cm spheric volumes of interest in region on scan where biopsies were performed. IHC = immunohistochemistry; FOLH1 = folate hydrolase 1; FPM = fragments per million.

spatial transcriptomics or proteomics to study tracer heterogeneity within tumor or the tumor microenvironment at a cellular level. PET studies using radionuclides with long half-lives, such as ^{89}Zr, would enable in vivo quantitative uptake kinetics up to late time points. Animal models of GBM could be used to dynamically assess PSMA tracer uptake (by in vitro immunofluorescence) and combine this with ex vivo autoradiography, such as performed by Lindemann et al. (*30*). Competition experiments, such as with the PSMA inhibitor 2-phosphonomethyl pentanedioic acid, can be used to assess specific PSMA receptor binding on tumor neovasculature or cells (*32*).

In the clinical setting, for most studies on PSMA imaging in patients with GBM, PET scans have been acquired 60 min after injection of [^{68}Ga]Ga-PSMA-11 (*18,20,27,28*). Our composed time–activity curve implies that tumor-to-background ratios likely increase up to 240 min after injection for [^{68}Ga]Ga-PSMA-11. However, semiquantitative measures cannot be compared between scans acquired at different time points after injection of different tracers, because equilibrium kinetics vary and have not yet been reached within 240 min after injection.

In nonaffected brain tissue, we observed very low uptake of tracer, leading to high tumor-to-background ratios. In parotid tissue, expected high uptake of all PSMA tracers was observed, indicating this is the organ at risk for radionuclide therapy. Uptake in liver was comparable between patients, as previously reported (*26*), indicating that the liver is the most favorable organ to use as reference tissue for normalization of tracer uptake in tumor, although this does require whole-body scanning and thus more time.

This study has some limitations. The data originated from different centers that used different tracers, varying PET acquisition protocols, and reconstruction methods. We limited the influence of decay by choosing time points within the closest range from each of the centers for the SUV measurements at the biopsy locations (i.e., 120, 145, and 160 min after injection), and we chose those time points for which the time–activity curves showed a near-plateau phase of tracer uptake. Second, it is well known that the PET reconstruction method can influence the outcome of SUV measurements (*40,41*), and these differed across centers. Therefore, we also performed correlational analyses per tracer or center. The image analyses and immunohistochemistry scoring were uniformly performed to prevent additional variabilities because of data processing differences among the centers. Moreover, we think that the heterogeneity of the data represents the real-life clinical setting and gives important information on the comparability of the PSMA-targeting tracers for GBM imaging.

CONCLUSION

The observation in this study that various PSMA-targeting tracers show moderate to high uptake in GBM is hopeful and warrants further research into the exact mechanisms of PSMA accumulation or retention. Studies are needed to determine the actual potential of PSMA-targeted radionuclide therapy as an option for patients with GBM.

DISCLOSURE

Ilanah Pruis and Sophie Veldhuijzen van Zanten were financially supported by the Semmy Foundation. Marion Smits received speaker honoraria from Auntminnie and GE Healthcare and consultancy fees from Bracco. Daniela Oprea-Lager reports unrestricted grants from Janssen for consensus meeting attendance. Frederik Verburg received speaker honoraria from Sanofi, AstraZeneca, and Bayer and is a consultant to GE Healthcare. James Nagarajah received research support, consulting fees, and speaker fees from AAA/Novartis, POINT Biopharma, ABX, Curium, Bayer, Telix, and Sanofi. William Leenders is a shareholder and part-time employee at Radboudumc spin-off Predica Diagnostics. No other potential conflict of interest relevant to this article was reported.

ACKNOWLEDGMENTS

We thank Sandra Bossmann and Fleur Brienen for their help in patient inclusion, Benno Kusters for immunohistochemistry analyses,

and Marcel Segbers and Vera van Dis for their contribution to data acquisition and analysis.

KEY POINTS

QUESTION: What is the correlation between tumor uptake of PSMA-targeting tracers and PSMA expression in image-guided tumor biopsies in patients with de novo or recurrent GBM?

PERTINENT FINDINGS: In a multicenter inventory study in 14 GBM patients using [^{68}Ga]Ga-PSMA-11 ($n = 7$), [^{18}F]DCFPyl ($n = 3$), or [^{18}F]PSMA-1007 ($n = 4$) PET imaging, heterogeneous and significant uptake in tumor was found. PSMA expression was found on endothelial cells of tumor microvasculature, dispersed individual cells (of unknown origin), and granular staining of the neuropil, but no significant correlation was found between in vivo tracer uptake and PSMA expression levels.

IMPLICATIONS FOR PATIENT CARE: Various PSMA-targeting tracers show uptake in GBM, and further research into the exact mechanisms of PSMA accumulation or retention is warranted.

REFERENCES

1. Van de Wiele C, Sathekge M, de Spiegeleer B, et al. PSMA expression on neovasculature of solid tumors. *Histol Histopathol.* 2020;35:919–927.
2. Tanjore Ramanathan J, Lehtipuro S, Sihto H, et al. Prostate-specific membrane antigen expression in the vasculature of primary lung carcinomas associates with faster metastatic dissemination to the brain. *J Cell Mol Med.* 2020;24:6916–6927.
3. Traub-Weidinger T, Poetsch N, Woehrer A, et al. PSMA expression in 122 treatment naive glioma patients related to tumor metabolism in ^{11}C-methionine PET and survival. *J Pers Med.* 2021;11:624.
4. Wernicke AG, Edgar MA, Lavi E, et al. Prostate-specific membrane antigen as a potential novel vascular target for treatment of glioblastoma multiforme. *Arch Pathol Lab Med.* 2011;135:1486–1489.
5. Saffar H, Noohi M, Tavangar SM, Saffar H, Azimi S. Expression of prostate-specific membrane antigen (PSMA) in brain glioma and its correlation with tumor grade. *Iran J Pathol.* 2018;13:45–53.
6. Nomura N, Pastorino S, Jiang P, et al. Prostate specific membrane antigen (PSMA) expression in primary gliomas and breast cancer brain metastases. *Cancer Cell Int.* 2014;14:26.
7. Matsuda M, Ishikawa E, Yamamoto T, et al. Potential use of prostate specific membrane antigen (PSMA) for detecting the tumor neovasculature of brain tumors by PET imaging with ^{89}Zr-Df-IAB2M anti-PSMA minibody. *J Neurooncol.* 2018;138:581–589.
8. Holzgreve A, Biczok A, Ruf VC, et al. PSMA expression in glioblastoma as a basis for theranostic approaches: a retrospective, correlational panel study including immunohistochemistry, clinical parameters and PET imaging. *Front Oncol.* 2021;11:646387.
9. Gao Y, Zheng H, Li L, et al. Prostate-specific membrane antigen (PSMA) promotes angiogenesis of glioblastoma through interacting with ITGB4 and regulating NF-κB signaling pathway. *Front Cell Dev Biol.* 2021;9:598377.
10. Mahzouni P, Shavakhi M. Prostate-specific membrane antigen expression in neovasculature of glioblastoma multiforme. *Adv Biomed Res.* 2019;8:18.
11. Salas Fragomeni RA, Menke JR, Holdhoff M, et al. Prostate-specific membrane antigen-targeted imaging with [^{18}F]DCFPyL in high-grade gliomas. *Clin Nucl Med.* 2017;42:e433–e435.
12. Schwenck J, Tabatabai G, Skardelly M, et al. In vivo visualization of prostate-specific membrane antigen in glioblastoma. *Eur J Nucl Med Mol Imaging.* 2015;42:170–171.
13. Tanjore Ramanathan J, Lehtipuro S, Sihto H, et al. Prostate-specific membrane antigen expression in the vasculature of primary lung carcinomas associates with faster metastatic dissemination to the brain. *J Cell Mol Med.* 2020;24:6916–6927.
14. Haberkorn U, Eder M, Kopka K, Babich JW, Eisenhut M. New strategies in prostate cancer: prostate-specific membrane antigen (PSMA) ligands for diagnosis and therapy. *Clin Cancer Res.* 2016;22:9–15.
15. Bertagna F, Albano D, Cerudelli E, Gazzilli M, Giubbini R, Treglia G. Potential of radiolabeled PSMA PET/CT or PET/MRI diagnostic procedures in gliomas/glioblastomas. *Curr Radiopharm.* 2020;13:94–98.
16. Pilati E, Nicolotti DG, Ceci F, et al. ^{68}Ga-prostate-specific membrane antigen 11 PET/CT detects residual glioblastoma after radical surgery in a patient with synchronous recurrent prostate cancer: a case report. *Clin Nucl Med.* 2020;45:e151–e153.
17. Gupta M, Choudhury PS, Premsagar IC, Gairola M, Ahlawat P. Role of ^{68}Ga-prostate-specific membrane antigen PET/CT in disease assessment in glioblastoma within 48 hours of surgery. *Clin Nucl Med.* 2020;45:204–205.
18. Kumar A, ArunRaj ST, Bhullar K, et al. Ga-68 PSMA PET/CT in recurrent high-grade gliomas: evaluating PSMA expression in vivo. *Neuroradiology.* 2022;64:969–979.
19. Jiang JY, Kang C, Bui P, Mansberg R. Incidental prostate-specific membrane antigen-avid glioblastoma detected on ^{68}Ga-prostate-specific membrane antigen PET/CT. *Radiol Case Rep.* 2022;17:2023–2025.
20. Kunikowska J, Kulinski R, Muylle K, Koziara H, Krolicki L. ^{68}Ga-prostate-specific membrane antigen-11 PET/CT: a new imaging option for recurrent glioblastoma multiforme? *Clin Nucl Med.* 2020;45:11–18.
21. Truckenmueller P, Graef J, Scheel M, et al. [^{68}Ga]Ga-PSMA PET/MRI, histological PSMA expression and preliminary experience with [^{177}Lu]Lu-PSMA therapy in relapsing high-grade glioma. *Front Oncol.* 2022;12:980058.
22. Giraudet AL, Kryza D, Hofman M, et al. PSMA targeting in metastatic castration-resistant prostate cancer: where are we and where are we going? *Ther Adv Med Oncol.* 2021;13:17588359211053898.
23. Kunikowska J, Charzyńska I, Kuliński R, Pawlak D, Maurin M, Królicki L. Tumor uptake in glioblastoma multiforme after IV injection of [^{177}Lu]Lu-PSMA-617. *Eur J Nucl Med Mol Imaging.* 2020;47:1605–1606.
24. Cranial navigation application. Brainlab website. https://www.brainlab.com/surgery-products/overview-neurosurgery-products/cranial-navigation/. Published 2022. Accessed July 18, 2023.
25. de Bitter T, van de Water C, van den Heuvel C, et al. Profiling of the metabolic transcriptome via single molecule molecular inversion probes. *Sci Rep.* 2017;7:11402.
26. Ferreira G, Iravani A, Hofman MS, Hicks RJ. Intra-individual comparison of ^{68}Ga-PSMA-11 and ^{18}F-DCFPyL normal-organ biodistribution. *Cancer Imaging.* 2019;19:23.
27. Sasikumar A, Joy A, Pillai MR, et al. Diagnostic value of ^{68}Ga PSMA-11 PET/CT imaging of brain tumors: preliminary analysis. *Clin Nucl Med.* 2017;42:e41–e48.
28. Sasikumar A, Kashyap R, Joy A, et al. Utility of ^{68}Ga-PSMA-11 PET/CT in imaging of glioma: a pilot study. *Clin Nucl Med.* 2018;43:e304–e309.
29. Verma P, Malhotra G, Goel A, et al. Differential uptake of ^{68}Ga-PSMA-HBED-CC (PSMA-11) in low-grade versus high-grade gliomas in treatment-naive patients. *Clin Nucl Med.* 2019;44:e318–e322.
30. Lindemann M, Oteiza A, Martin-Armas M, et al. Glioblastoma PET/MRI: kinetic investigation of [^{18}F]rhPSMA-7.3, [^{18}F]FET and [^{18}F]fluciclovine in an orthotopic mouse model of cancer. *Eur J Nucl Med Mol Imaging.* 2023;50:1183–1194.
31. Sácha P, Zámecník J, Barinka C, et al. Expression of glutamate carboxypeptidase II in human brain. *Neuroscience.* 2007;144:1361–1372.
32. Oliveira D, Stegmayr C, Heinzel A, et al. High uptake of ^{68}Ga-PSMA and ^{18}F-DCFPyL in the peritumoral area of rat gliomas due to activated astrocytes. *EJNMMI Res.* 2020;10:55.
33. Thompson SM, Suman G, Torbenson MS, et al. PSMA as a theranostic target in hepatocellular carcinoma: immunohistochemistry and ^{68}Ga-PSMA-11 PET using cyclotron-produced ^{68}Ga. *Hepatol Commun.* 2022;6:1172–1185.
34. Rüschoff JH, Ferraro DA, Muehlematter UJ, et al. What's behind ^{68}Ga-PSMA-11 uptake in primary prostate cancer PET? Investigation of histopathological parameters and immunohistochemical PSMA expression patterns. *Eur J Nucl Med Mol Imaging.* 2021;48:4042–4053.
35. Ferraro DA, Rüschoff JH, Muehlematter UJ, et al. Immunohistochemical PSMA expression patterns of primary prostate cancer tissue are associated with the detection rate of biochemical recurrence with ^{68}Ga-PSMA-11-PET. *Theranostics.* 2020;10:6082–6094.
36. Stockhammer F, Plotkin M, Amthauer H, van Landeghem FK, Woiciechowsky C. Correlation of F-18-fluoro-ethyl-tyrosin uptake with vascular and cell density in non-contrast-enhancing gliomas. *J Neurooncol.* 2008;88:205–210.
37. Vettermann FJ, Diekmann C, Weidner L, et al. L-type amino acid transporter (LAT) 1 expression in ^{18}F-FET-negative gliomas. *EJNMMI Res.* 2021;11:124.
38. Lapa C, Linsenmann T, Lückerath K, et al. Tumor-associated macrophages in glioblastoma multiforme: a suitable target for somatostatin receptor-based imaging and therapy? *PLoS One.* 2015;10:e0122269.
39. Kiviniemi A, Gardberg M, Frantzén J, et al. Somatostatin receptor subtype 2 in high-grade gliomas: PET/CT with ^{68}Ga-DOTA-peptides, correlation to prognostic markers, and implications for targeted radiotherapy. *EJNMMI Res.* 2015;5:25.
40. Rogasch JMM, Hofheinz F, van Heek L, Voltin CA, Boellaard R, Kobe C. Influences on PET quantification and interpretation. *Diagnostics (Basel).* 2022;12:451.
41. Mansor S, Pfaehler E, Heijtel D, Lodge MA, Boellaard R, Yaqub M. Impact of PET/CT system, reconstruction protocol, data analysis method, and repositioning on PET/CT precision: an experimental evaluation using an oncology and brain phantom. *Med Phys.* 2017;44:6413–6424.

Comparison of Baseline ^{68}Ga-FAPI and ^{18}F-FDG PET/CT for Prediction of Response and Clinical Outcome in Patients with Unresectable Hepatocellular Carcinoma Treated with PD-1 Inhibitor and Lenvatinib

Meiqi Wu*[1], Yanyu Wang*[2], Qiao Yang[1], Xuezhu Wang[1], Xu Yang[2], Haiqun Xing[1], Xinting Sang[2], Xiang Li[3], Haitao Zhao[2], and Li Huo[1]

[1]*Department of Nuclear Medicine, State Key Laboratory of Complex Severe and Rare Diseases, Center for Rare Diseases Research Beijing Key Laboratory of Molecular Targeted Diagnosis and Therapy in Nuclear Medicine, Peking Union Medical College Hospital, Chinese Academy of Medical Science and Peking Union Medical College, Beijing, China;* [2]*Department of Hepatobiliary Surgery, Peking Union Medical College Hospital, Chinese Academy of Medical Sciences and Peking Union Medical College, Beijing, China; and* [3]*Division of Nuclear Medicine, Department of Biomedical Imaging and Image-Guided Therapy, Medical University of Vienna, Vienna, Austria*

Fibroblast activation protein contributes to immunosuppression and resistance to immunotherapies. This study aimed to compare baseline ^{68}Ga-labeled fibroblast activation protein inhibitor (^{68}Ga-FAPI) PET/CT and ^{18}F-FDG PET/CT in response and survival prediction in unresectable hepatocellular carcinoma (uHCC) patients treated with the combination of programmed cell death 1 (PD-1) inhibitor and lenvatinib. **Methods:** In this prospective cohort study, 22 patients with uHCC who underwent baseline ^{18}F-FDG and ^{68}Ga-FAPI PET/CT and soon began taking a combination of PD-1 inhibitor and lenvatinib were recruited. Semiquantitative indices of baseline PET/CT were measured as ^{18}F-FDG SUV_{max}, metabolic tumor volume, total lesion glycolysis, ^{68}Ga-FAPI SUV_{max}, ^{68}Ga-FAPI–avid tumor volume (FTV), and total lesion fibroblast activation protein expression (TLF). The primary endpoint was durable or nondurable clinical benefit after treatment, and the secondary endpoints were progression-free survival (PFS) and overall survival (OS). **Results:** The overall response rate of the combination therapy was 41% (9/22). Fifty percent of patients had durable clinical benefit. Median PFS and OS were 4.8 and 14.4 mo, respectively. Patients with nondurable clinical benefit showed a significantly higher FTV and TLF than those with durable clinical benefit, whereas ^{18}F-FDG parameters overlapped. A higher ^{68}Ga-FAPI–avid tumor burden (FTV $>$ 230.46 cm^3 or TLF $>$ 961.74 $SUV_{body\ weight}{\cdot}cm^3$) predicted both shorter PFS (4.0 vs. 13.5 mo, P = 0.016) and shorter OS (7.8 mo vs. not reached, P = 0.030). Patients with a higher metabolic tumor burden (metabolic tumor volume $>$ 206.80 cm^3 or total lesion glycolysis $>$ 693.53 $SUV_{body\ weight}{\cdot}cm^3$) showed a shorter OS although the difference did not reach statistical significance (P = 0.085). In multivariate analysis, a higher ^{68}Ga-FAPI–avid tumor burden (hazard ratio [HR], 3.88 [95% CI, 1.26–12.01]; P = 0.020) and macrovascular invasion (HR, 4.00 [95% CI, 1.06–15.14]; P = 0.039) independently predicted a shorter PFS, whereas a higher ^{68}Ga-FAPI–avid tumor burden (HR, 5.92 [95% CI, 1.19–29.42]; P = 0.035) and bone metastases (HR, 5.88 [95% CI, 1.33–25.93]; P = 0.022) independently predicted a shorter OS. **Conclusion:** Volumetric indices on baseline ^{68}Ga-FAPI PET/CT were potentially independent prognostic factors to predict durable clinical benefit, PFS, and OS in uHCC patients treated with a combination of PD-1 and lenvatinib. Baseline ^{68}Ga-FAPI PET/CT may facilitate uHCC patient selection before combination therapy.

Key Words: unresectable hepatocellular carcinoma; PD-1 inhibitor; prognosis; ^{68}Ga-FAPI; PET/CT

J Nucl Med 2023; 64:1532–1539
DOI: 10.2967/jnumed.123.265712

Pharmaceutical advances have changed the therapeutic landscape of unresectable hepatocellular carcinoma (uHCC) (*1*). In particular, the combination of immune checkpoint blockade (ICB) and multikinase inhibitors has gained remarkable successes in clinical settings (*2*).

However, only a subportion of patients with uHCC could benefit from ICB therapies (*3,4*). Reliable predictors for response and patient selection before such combination therapy remained a challenge because of the complexity of the cancer cell metabolism and tumor microenvironment components. Characterization of hepatocellular carcinoma (HCC) by ^{18}F-FDG PET was linked with glycolytic enzymatic activity and differentiation grade, with suboptimal sensitivity in intrahepatic HCC lesions (*5*). ^{18}F-FDG uptake in HCC and metastasis is significantly associated with recurrence and outcome after curative surgical resection or targeted therapies (*6–8*). Nevertheless, it is not a reliable marker to predict disease response to systemic therapy.

Tumor microenvironment plays an important role in tumor progression and influences therapeutic response to ICB. Cancer-associated fibroblasts represent the most prominent component of the tumor microenvironment and are composed of different subpopulations exerting distinct functions (*9*). Fibroblast activation protein (FAP)–positive cancer-associated fibroblasts contribute to immunosuppression in the tumor microenvironment by recruiting inhibitory immune populations such as regulatory T cells and subsets of myeloid cells and are found indicative of primary resistance to immunotherapies (*9*). In clinical practice, the utility of biomarkers based

Received Mar. 13, 2023; revision accepted May 31, 2023.
For correspondence or reprints, contact Li Huo (huoli@pumch.cn) or Xiang Li (xiang.li@meduniwien.ac.at).
*Contributed equally to this work.
Published online Jul. 27, 2023.

on tumor tissue is hindered by spatial heterogeneity. PET allows for noninvasive, quantitative, and sensitive whole-body detection of molecular targets. ^{68}Ga-labeled FAP inhibitor (^{68}Ga-FAPI) provided localization and quantification for FAP-positive HCC tumors in our previous studies (*10*). Particularly, ^{68}Ga-FAPI was superior to ^{18}F-FDG for the detection of primary HCC, allowing improved delineation of whole-body tumor burden (*11*).

In this prospective study, we aimed to evaluate and compare in vivo tumor metabolism and cancer-associated fibroblast activation using ^{68}Ga-FAPI and ^{18}F-FDG PET/CT for prediction of therapeutic response and survival in uHCC patients treated with a combination of programmed cell death 1 (PD-1) inhibitor and multikinase inhibitor lenvatinib.

MATERIALS AND METHODS

Study Design and Patient Recruitment

This was a prespecified subgroup analysis of a prospective cohort study evaluating the role of ^{68}Ga-FAPI PET/CT in liver and biliary cancer patients and was approved by the Institutional Review Board of Peking Union Medical College Hospital (protocol ZS-1050) and registered at ClinicalTrials.gov (NCT 05662488).

In total, 29 patients with suspected uHCC scheduled to begin receiving PD-1 inhibitor at Peking Union Medical College Hospital were consecutively recruited from July 2020 to April 2022. The diagnosis of uHCC was confirmed by 2 or more experienced hepatobiliary surgeons using the National Comprehensive Cancer Network guidelines. The flowchart of patient enrollment is shown in Figure 1. Clinical, laboratory, and imaging evaluations (contrast-enhanced CT or MRI of the abdomen) were done at enrollment. Previous treatment was recorded. The inclusion criteria were HCC pathologically confirmed or indicated by imaging criteria (*12,13*); lack of suitability for curative surgery or regional therapy alone, or disease progression after previous therapy; preserved liver function (Child–Pugh class A or B); an Eastern Cooperative Oncology Group performance status score of 0–2; no prior immunotherapy; and no regional therapy within 2 wk. After enrollment, written informed consent was obtained from each patient. Patients were referred for ^{18}F-FDG and ^{68}Ga-FAPI PET/CT performed no more than 3 d apart. Combination therapy with PD-1 inhibitor (camrelizumab, toripalimab, tislelizumab, or pembrolizumab) and lenvatinib was initiated within 2 wk later. We excluded 7 patients with baseline PET/CT who were later diagnosed with intrahepatic cholangiocarcinoma or combined hepatocellular-cholangiocarcinoma, showed resectability on PET/CT and underwent surgery, did not receive PD-1 inhibitor, or began taking PD-1 inhibitor more than 2 wk after PET/CT. The remaining 22 patients were included in the current study.

PET/CT

The ^{68}Ga-FAPI-04 was radiolabeled manually before injection according to previously published procedures (*14*). Briefly, ^{68}Ga was chelated after pH adjustment with sodium acetate. The reaction mixture was heated to 100°C for 10 min, and the completeness of the reaction was checked by thin-layer chromatography. ^{18}F-FDG was synthesized in house. All PET/CT scans were performed with a dedicated PET/CT scanner (Polestar m660; SinoUnion) from the tip of the skull to the middle of the thigh (2 min/bed position). Unenhanced low-dose CT scans were obtained for attenuation correction and anatomic positioning. For ^{18}F-FDG PET/CT, the patients fasted for at least 6 h, and blood glucose levels were monitored (<11.0 mmol/L) before injection of ^{18}F-FDG (5.55 MBq/kg). The PET/CT images were acquired with an uptake time of 57–105 min. ^{68}Ga-FAPI PET/CT was performed with an uptake time of 42–90 min after injection (2.22–2.96 MBq/kg). The acquired data were reconstructed using ordered-subset expectation maximization (2 iterations, 10 subsets, gaussian filter, image size of 192 × 192).

Image Analysis

Two nuclear medicine physicians (both with 4 y of experience in PET/CT reading) reviewed the PET/CT images and recorded focal accumulations not explained by physiologic uptake or inflammation. The physicians were in consensus for image interpretation. Semiquantitative analysis of the PET/CT data was performed on a MIM Workstation (version 6.6.11; MIM Software). The whole-body metabolic tumor burden was measured as metabolic tumor volume (MTV) and total lesion glycolysis (TLG). The whole-body ^{68}Ga-FAPI–avid tumor burden was measured in the same way as the ^{18}F-FDG parameters—as ^{68}Ga-FAPI–avid tumor volume (FTV) and total lesion FAP expression (TLF). A cuboid volume of interest was drawn including all focal lesions in each scan. The tumor contours were semiautomatically segmented with an SUV cutoff of 2.5. The contours were checked and adjusted manually to exclude physiologic or inflammatory uptake. If tracer uptake in the liver with a normal appearance on contrast-enhanced CT or MRI was diffusely elevated and above an SUV of 2.5, a manual contour was applied to enclose hepatic HCC lesions with uptake higher than background. ^{18}F-FDG SUV_{max}, MTV, TLG, ^{68}Ga-FAPI SUV_{max}, FTV, and TLF were automatically generated from the final volumetric extraction.

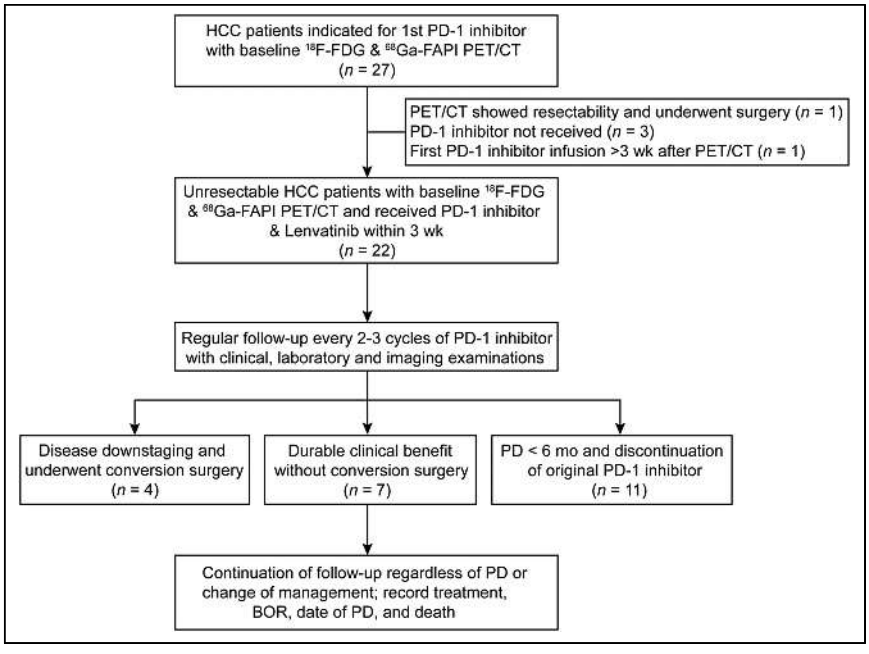

FIGURE 1. Flowchart of patients' enrollment, treatment, and follow-up. BOR = Best objective response.

Follow-up and Clinical Endpoint

All 22 patients were followed up regularly every 2–3 cycles of PD-1 inhibitors (median, 2.1 mo; range, 1.4–3.1 mo) with clinical, laboratory, and imaging examinations (contrast-enhanced CT or MRI). The treatment

response (complete response, partial response, stable disease, or progressive disease) and objective response were evaluated with modified RECIST (*15*). Durable clinical benefit (DCB) was defined as either the patient's being alive, without next-line systemic treatment and without progressive disease at 6 mo since the first infusion of PD-1 inhibitor, or the patient's experiencing prominent disease downstaging followed by conversion surgery within 6 mo. Nondurable benefit (NDB) was defined as progressive disease or death within 6 mo. Progression-free survival (PFS) and overall survival (OS) were measured from the first PD-1 inhibitor infusion. Treatment regimen, response to therapy, disease progression, and death were recorded. Patients without an event were censored at the time of the last clinical assessment, on December 29, 2022.

Statistical Analysis

The Wilcoxon signed-rank test was applied to test the difference between ^{18}F-FDG and ^{68}Ga-FAPI SUV_{max}, between MTV and FTV, and between TLG and TLF for each patient, whereas the Spearman correlation coefficient was applied to test correlation for each pair. Patients were divided into DCB and NDB groups. The characteristics of the 2 groups were compared using the Fisher exact test for discrete variables and the Student *t* test or Mann–Whiney *U* test for continuous variables. Receiver-operating-characteristic curves were analyzed to estimate the best cutoffs for ^{18}F-FDG SUV_{max}, MTV, TLG, ^{68}Ga-FAPI SUV_{max}, FTV, and TLF between the 2 groups with the maximum Youden index. The Kaplan–Meier method was used to estimate survival curves, which were compared by the log-rank test. Univariable and multivariable analyses using Cox proportional-hazards regression models were performed for PFS and OS. All statistical analyses were done with SPSS (version 25.0; IBM). *P* values of less than 0.05 denoted statistical significance.

RESULTS

Baseline Clinical Characteristics and Dual-Tracer PET Imaging

In total, 22 patients with uHCC who received combination therapy with a PD-1 inhibitor and lenvatinib (19 male and 3 female patients; median age, 62.0 y) were included. Nineteen patients were classified as Barcelona Clinic Liver Cancer stage C. Ten and 5 patients had prior regional or molecular targeted therapy, respectively. All patients had at least 1 lesion with an SUV_{max} above 2.5 on both PET/CT scans. FTV was significantly higher than MTV ($Z = -2.808$, $P = 0.005$), whereas differences between ^{68}Ga-FAPI and ^{18}F-FDG SUV_{max} or between TLG and TLF were not significant. The 3 paired indices all showed medium correlation. The baseline clinical characteristics and PET parameters are summarized in Table 1.

TABLE 1
Baseline Characteristics of uHCC Patients ($n = 22$)

Characteristic	Data
Median age (y)	62.0 (range, 35–76)
Age > 65 y	7 (32%)
Sex	
Female	3 (14%)
Male	19 (86%)
Hepatitis B surface antigen A–positive	18 (82%)
Ascites	6 (27%)
Cirrhosis	13 (59%)
ECOG PS	
0 or 1	19 (87%)
2	3 (14%)
Child–Pugh class	
A	15 (68%)
B	7 (32%)
α-fetoprotein > 200 ng/mL	9 (41%)
Macrovascular invasion	16 (73%)
Extrahepatic spread	12 (53%)
Metastases to distant organs	7 (32%)
Bone metastases	3 (14%)
Barcelona Clinic Liver Cancer stage for HCC	
B	3 (14%)
C	19 (86%)
Prior regional treatment	10 (45%)
Partial resection	3 (14%)
Transarterial chemoembolization/ radioembolization	8 (36%)
Radiofrequency ablation	2 (9%)
Radiotherapy for bone metastasis	1 (5%)
Prior targeted therapy	5 (23%)
Median ^{18}F-FDG SUV_{max}	6.7 (IQR, 4.5–10.9)
Median MTV (cm^3)	157.4 (IQR, 18.3–365.3)
Median TLG ($SUV_{bw}{\cdot}cm^3$)	534.8 (IQR, 58.9–1599.5)
Median ^{68}Ga-FAPI SUV_{max}	8.9 (IQR, 6.7–10.9)
Median FTV (cm^3)	312.6 (IQR, 106.4–525.4)
Median TLF ($SUV_{bw}{\cdot}cm^3$)	1,274.8 (IQR, 323.8–1,840.1)

ECOG PS = Eastern Cooperative Oncology Group performance status; IQR = interquartile range.
Data are number followed by percentage in parentheses, unless indicated otherwise.

Treatment Efficacy

After baseline assessment, combination therapy with PD-1 inhibitor and lenvatinib began (median interval between PET/CT and initiation of treatment, 4.0 d). Nine, 6, 5, and 2 patients received camrelizumab, toripalimab, tislelizumab, and pembrolizumab, respectively. The choice of PD-1 inhibitor was based on various factors, including the stage of the disease, the line of treatment, individual patient preferences, and the insurance coverage of the drug.

The median duration of follow-up was 16.5 mo (range, 8.0–28.2 mo). All 22 patients had complete radiologic evaluations. During the initial combination therapy, the overall response rate was 41% (9/22): a complete response was achieved in 1 patient, 8 patients had a partial response, 4 patients had stable disease, and 9 patients experienced progressive disease. Eleven (50%) patients had DCB; 4 of them with prominent disease downstaging underwent conversion surgeries. The other 11 (50%) patients had NDB.

At the time of the analysis, 19 patients discontinued the original combination therapy because of radiologically confirmed

TABLE 2
Comparison of Potential Predictors Between Patients with DCB and NDB

Characteristic	DCB (n = 11)	NDB (n = 11)	P
Age > 65 y	3 (27%)	4 (36%)	1.000
Male	8 (73%)	11 (100%)	0.214
Hepatitis B surface antigen A–positive	8 (73%)	10 (91%)	0.586
Ascites	1 (9%)	5 (45%)	0.149
Cirrhosis	4 (36%)	9 (82%)	0.080
ECOG PS			0.214
0	7 (64%)	4 (36%)	
1	4 (36%)	3 (27%)	
2	0 (0%)	3 (27%)	
Child–Pugh class B	1 (9%)	6 (55%)	0.063
α-fetoprotein > 200 ng/mL	5 (45%)	4 (36%)	1.000
Macrovascular invasion	7 (64%)	9 (82%)	0.635
Extrahepatic spread	6 (55%)	6 (55%)	1.000
Metastases to distant organs	3 (27%)	4 (36%)	1.000
Bone metastases	1 (9%)	2 (18%)	1.000
Barcelona Clinic Liver Cancer stage C	9 (82%)	10 (91%)	1.000
Prior regional treatment	7 (64%)	3 (27%)	0.198
Prior targeted therapy	4 (36%)	1 (9%)	0.311
Median ^{18}F-FDG SUV_{max}	5.7 (IQR, 5.0–10.2)	6.9 (IQR, 3.3–13.0)	1.000
Median MTV (cm^3)	154.2 (IQR, 16.1–200.7)	212.9 (IQR, 21.6–463.5)	0.438
Median TLG (SUV_{bw}·cm^3)	492.2 (IQR, 57.2–693.5)	693.5 (IQR, 62.3–3701.0)	0.365
Median ^{68}Ga-FAPI SUV_{max}	8.8 (IQR, 6.0–10.7)	8.9 (IQR, 8.3–11.5)	0.401
Median FTV (cm^3)	121.3 (IQR, 35.6–337.0)	436.1 (IQR, 289.1–838.9)	0.003
Median TLF (SUV_{bw}·cm^3)	359.2 (IQR, 120.0–1,344.5)	1,514.3 (IQR, 1,266.8–4,150.3)	0.004

ECOG PS = Eastern Cooperative Oncology Group performance status; IQR = interquartile range.
Data are number followed by percentage in parentheses, unless indicated otherwise.

progressive disease (n = 15), intolerable adverse events (n = 3), or complete response (n = 1). DCB patients tended to receive more cycles of PD-1 inhibitors than NDB patients (median, 12 [interquartile range, 9–14] vs. 3 [interquartile range, 2–5]; P = 0.13). Fewer DCB patients than NDB patients experienced progressive disease (7/11 vs. 11/11, P = 0.09), with a longer time to progression (13.1 mo [interquartile range, 7.5–15.6 mo] vs. 3.6 mo [interquartile range, 2.8–4.3 mo], P < 0.01). Two (18%) patients in the DCB group died after 13.4 and 14.4 mo, respectively. Nine (82%) patients in the NDB group died, with a median OS of 7.3 mo; the follow-up time of the 2 surviving patients was 9.0 and 12.6 mo, respectively. For the entire cohort, the median PFS was 4.8 mo (95% CI, 1.5–8.5 mo) and the median OS was 14.4 mo (95% CI, 12.2–16.6 mo).

Comparison of Imaging and Clinical Factors Between DCB and NDB Groups

Potential predictive factors were compared between patients with DCB and NDB, as shown in Table 2. Patients with DCB had a significantly lower FTV and TLF than patients with NDB (P < 0.01). The difference in ^{18}F-FDG SUV_{max}, MTV, TLG, and ^{68}Ga-FAPI SUV_{max} between the 2 groups was not significant. A comparison of the 6 PET indices is shown in Figure 2. Representative baseline ^{68}Ga-FAPI and ^{18}F-FDG PET/CT images of patients with DCB and NDB are shown in Figures 3–5.

More NDB patients than DCB patients had cirrhosis (P = 0.08) and Child–Pugh class B (P = 0.06), though statistical significance was not reached. No significant difference was found in other clinical factors between patients with DCB and NDB (P > 0.1).

To determine the best cutoff of ^{18}F-FDG SUV_{max}, MTV, TLG, ^{68}Ga-FAPI SUV_{max}, FTV, and TLF for survival analyses, receiver-operating-characteristic analysis was performed (Fig. 6). The thresholds selected as the optimal cutoffs for predicting NDB were a TLF of more than 961.74 $SUV_{body\ weight}$ (SUV_{bw})·cm^3 (area under the receiver-operating-characteristic curve [AUC], 0.85; sensitivity, 1.00; specificity, 0.73), an FTV of more than 230.46 cm^3 (AUC, 0.86; sensitivity, 1.00; specificity, 0.73), a ^{68}Ga-FAPI SUV_{max} of more than 7.04 (AUC, 0.61; sensitivity, 0.91; specificity, 0.45), a TLG of more than 693.53 SUV_{bw}·cm^3 (AUC, 0.62; sensitivity, 0.55; specificity, 0.82), an MTV of more than 206.80 cm^3 (AUC, 0.60; sensitivity, 0.55; specificity, 0.82), and an ^{18}F-FDG SUV_{max} of more than 6.69 (AUC, 0.50; sensitivity, 0.63; specificity, 0.64). To note, a TLF of

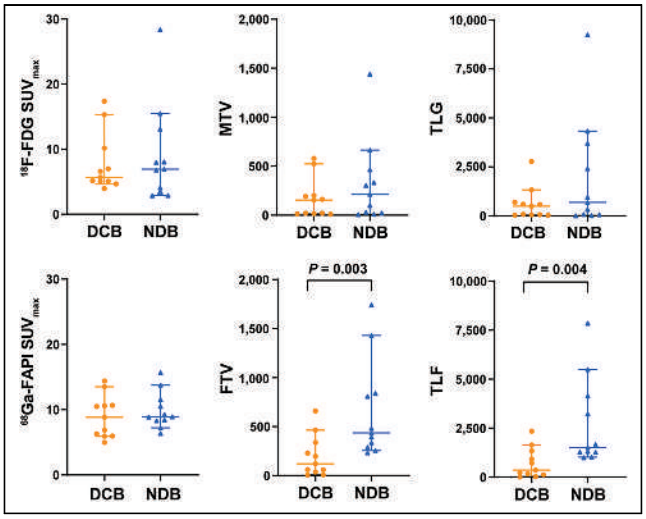

FIGURE 2. Comparison of ^{18}F-FDG SUV_{max}, MTV, and TLG and of ^{68}Ga-FAPI SUV_{max}, FTV, and TLF between DCB and NDB patients.

more than 961.74 $SUV_{bw}{\cdot}cm^3$ and an FTV of more than 230.46 cm^3 separated the same groups with 14 patients in the higher ^{68}Ga-FAPI–avid tumor burden group and 8 patients in the lower group; a TLG of more than 693.53 $SUV_{bw}{\cdot}cm^3$ and an MTV of more than 206.80 cm^3 also separated the same groups with 8 patients in the higher metabolic tumor burden group and 14 in the lower group.

Prognostic Factors for PFS and OS

As shown in Figure 7A, patients with a higher ^{68}Ga-FAPI–avid tumor burden demonstrated a significantly shorter PFS (median PFS, 4.0 mo [95% CI, 3.1–4.8 mo] vs. 13.5 mo [95% CI, 11.5–15.6 mo]; $P = 0.016$). Stratification by ^{18}F-FDG SUV_{max}, MTV/TLG, or ^{68}Ga-FAPI SUV_{max} did not exhibit a different PFS. In univariate analysis, cirrhosis, an Eastern Cooperative Oncology Group performance status of 2, macrovascular invasion, and a higher ^{68}Ga-FAPI–avid tumor burden were significantly associated with poor PFS ($P < 0.1$, Table 3). In multivariate analysis, a higher ^{68}Ga-FAPI–avid tumor burden (hazard ratio [HR], 3.88 [95% CI, 1.26–12.01]; $P = 0.020$) and macrovascular invasion (HR, 4.00 [95% CI, 1.06–15.14]; $P = 0.039$) were significant independent predictors for a shorter PFS.

As shown in Figure 7B, patients with a higher metabolic tumor burden showed a shorter OS, though significance was not reached (median OS, 7.8 mo [95% CI, 5.9–9.6 mo] vs. not reached; $P = 0.085$); patients with a higher ^{68}Ga-FAPI–avid tumor burden showed a significantly shorter OS (median OS, 7.8 mo [95% CI, 5.2–10.4 mo] vs. not reached; $P = 0.030$). In univariate analysis, Child–Pugh B, bone metastases, a higher metabolic tumor burden, and a higher ^{68}Ga-FAPI–avid tumor burden were associated with poor OS ($P < 0.1$, Table 3). In multivariate analysis, bone metastases (HR, 5.88 [95% CI, 1.33–25.93]; $P = 0.022$) and a higher ^{68}Ga-FAPI–avid tumor burden (HR, 5.92 [95% CI, 1.19–29.42]; $P = 0.035$) independently predicted a shorter OS.

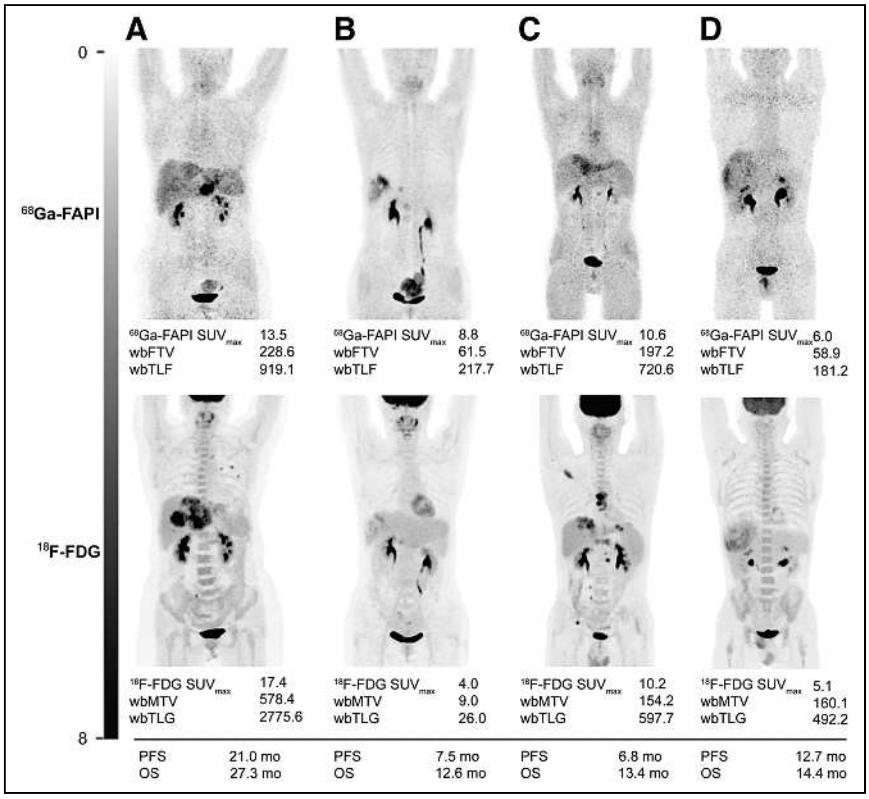

FIGURE 3. Representative baseline ^{68}Ga-FAPI and ^{18}F-FDG PET/CT images of patients with DCB. (A) A 63-y-old woman with multiple hepatic HCC, portal vein invasion, and lung metastases showing low ^{68}Ga-FAPI avidity and high metabolic tumor burden. (B) A 47-y-old woman with right-lobe HCC, portal vein invasion, and lymph node metastases showing low ^{68}Ga-FAPI avidity and metabolic tumor burden. Patients in A and B reached partial response and underwent conversion surgery. (C) A 40-y-old man with multiple intrahepatic lesions, portal vein invasion, lymph node metastases, and bone metastases. (D) A 50-y-old man with right-lobe HCC and portal vein invasion. Patients in C and D had low ^{68}Ga-FAPI avididy and metabolic tumor burden, with stable disease for >6 mo. All 4 patients had OS > 12 mo. wb = whole body.

DISCUSSION

The ever-growing novel ICB therapies in uHCC have shown distinct efficacies. Therefore, reliable noninvasive biomarkers for response prediction to ICBs are urgently needed to improve patient selection and management. Classic pathologic biomarkers have been evaluated to predict response to PD-1/programmed death ligand 1 inhibitors in HCC patients but have presented contradictory outcomes across studies (*1,4*). In the current study, we found that the molecular burden of ^{68}Ga-FAPI–avid tumor (FTV and TLF) determined by ^{68}Ga-FAPI PET/CT was strongly associated with a shortened PFS and OS and with NDB in uHCC patients treated with PD-1 inhibitor and lenvatinib. The combination of a high ^{68}Ga-FAPI–avid tumor burden and macrovascular invasion is associated with a shorter PFS, whereas an increased tumor ^{68}Ga-FAPI burden coupled with bone metastases predicted poor OS.

The communication is complicated between tumor metabolism and heterogeneous stromal components in the tumor microenvironment. Previous studies showed that ^{68}Ga-FAPI PET uptake and distribution

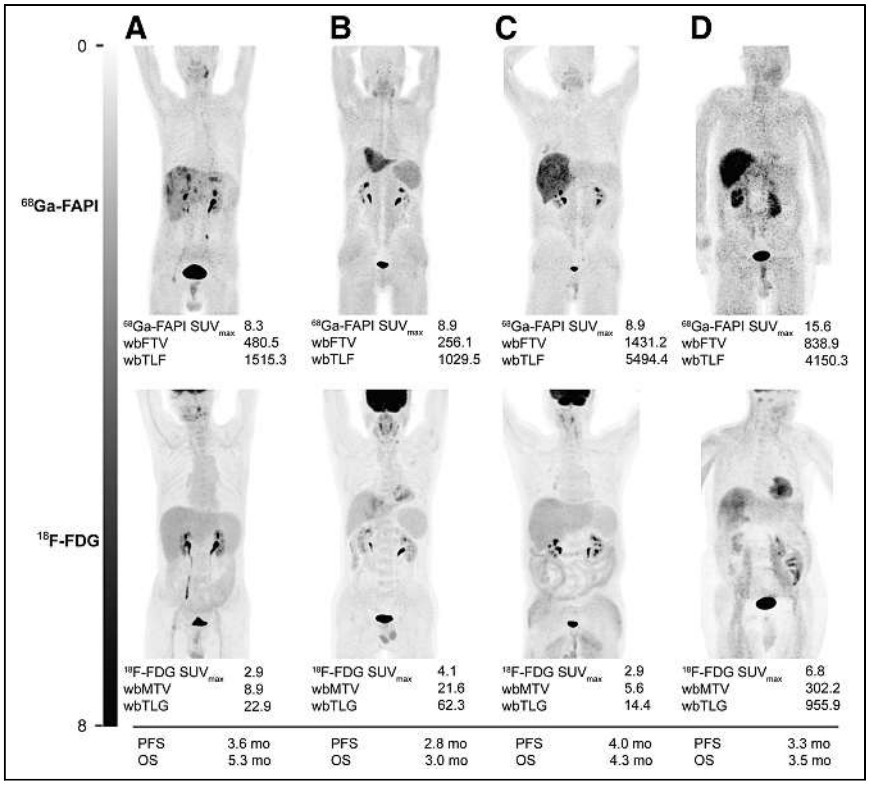

FIGURE 4. Representative baseline ^{68}Ga-FAPI and ^{18}F-FDG PET/CT images of patients with NDB. (A) A 63-y-old man with diffuse HCC. (B) A 69-y-old man with multiple intrahepatic HCC, portal vein invasion, and lung and bone metastases. (C) A 69-y-old man with diffuse right-lobe HCC, portal vein invasion, and lymph node metastases. Patients in A–C showed high ^{68}Ga-FAPI avidity and low metabolic tumor burden. (D) A 71-y-old man with diffuse right-lobe HCC and portal vein invasion showing high ^{68}Ga-FAPI avidity and metabolic tumor burden. All 4 patients progressed on first evaluation after 2–3 cycles of PD-1 inhibitor and had OS of <6 mo. wb = whole body.

strongly correlated with FAP expression characterized by immunohistochemistry in tumor tissues (*10,16*). FAP-positive cancer-associated fibroblast subsets contribute to immunosuppression through multiple pathways, including assisting differentiation of monocytes to M2-like macrophages, secreting chemokine (C-X-C motif) ligand 12, enhancing recruitment of myeloid-derived suppressor cells, and promoting generation of regulatory T cells (*17–20*). The current study showcased the potential of ^{68}Ga-FAPI quantification and stromal FAP expression to predict response to ICB in uHCC. The role of FAP-positive cells in HCC immune response is to be further elucidated.

In HCC characterization, ^{18}F-FDG PET/CT is limited by low uptake in well-differentiated HCC and background physiologic activity in the liver. However, a strong correlation between ^{18}F-FDG uptake by primary HCC and tumor differentiation makes ^{18}F-FDG PET/CT valuable in survival prediction. Previous studies found a significant association between pretreatment ^{18}F-FDG uptake or tumor metabolic burden and poor survival in HCC patients treated with transplantation, regional therapy, or targeted therapy (*6–8*). In this study, we also found that tumor metabolic burden is a prognosticator of OS, extending the prognostic value of ^{18}F-FDG PET in uHCC patients treated with ICB. Importantly, 2 patients (Figs. 4A and 4C) with negligible ^{18}F-FDG–avid lesions and substantial ^{68}Ga-FAPI uptake showed poor survival of less than 6 mo. FTV was higher than MTV in this cohort because more lesions were detected with ^{68}Ga-FAPI PET. The improved sensitivity of intrahepatic lesion detection over ^{18}F-FDG PET can facilitate a better representation of HCC tumor quantification.

The utility of PET/CT in HCC management has been limited. ^{68}Ga-FAPI PET has brought additional value for not merely

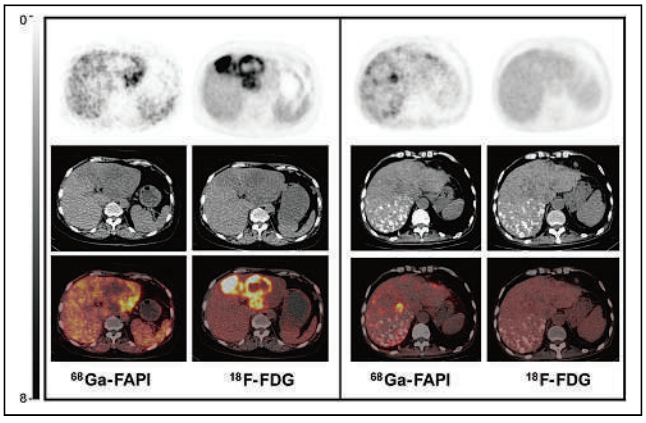

FIGURE 5. Axial PET, CT, and PET/CT images of patients in Figures 3A (left) and 4A (right).

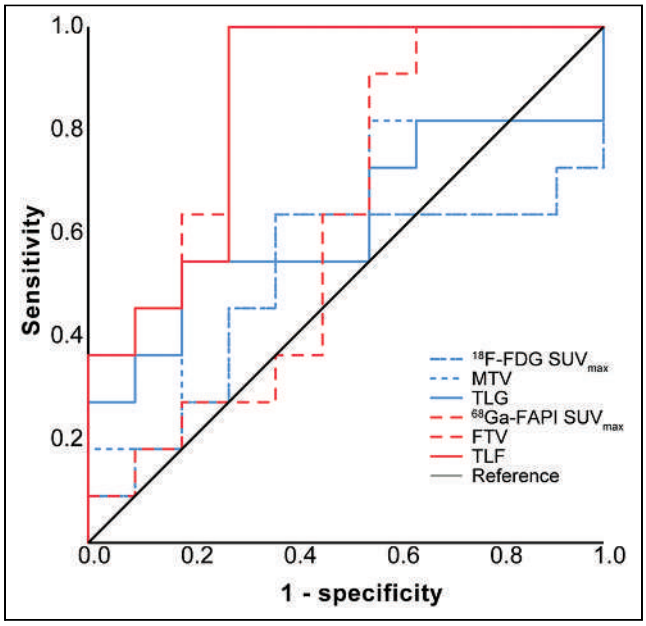

FIGURE 6. Receiver-operating-characteristic analysis curve for ^{18}F-FDG SUV_{max}, TLG, and MTV and for ^{68}Ga-FAPI SUV_{max}, TLF, and FTV for predicting NDB.

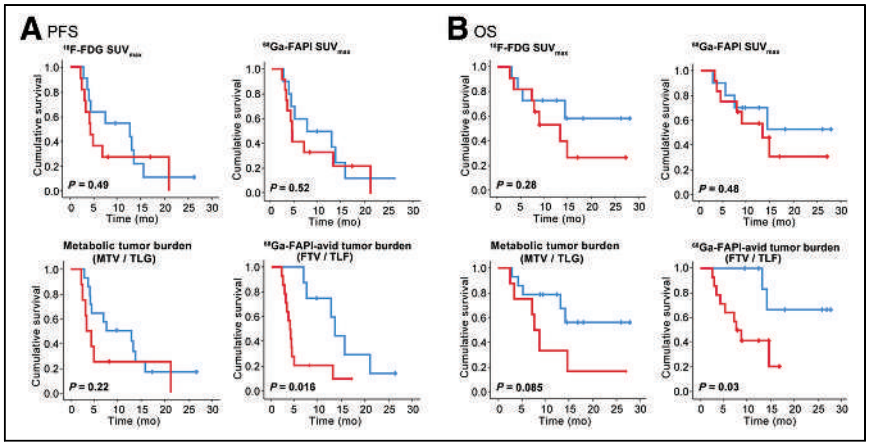

FIGURE 7. Kaplan–Meier curves for PFS (A) and OS (B) in uHCC patients stratified by optimal cutoffs for ^{18}F-FDG SUV_{max}, MTV/TLG, ^{68}Ga-FAPI SUV_{max}, and FTV/TLF.

primary diagnosis, staging, and restaging but also response and survival prediction for HCC, regardless of tumor differentiation. The value of ^{68}Ga-FAPI PET should be further investigated in phase 3 uHCC clinical trials.

Our study had several limitations. First, the study was limited to a small cohort and different PD-1 regimens. Second, previous treatment for HCC was applied in half the cohort and could potentially have impacted the imaging results and clinical outcomes. Third, regional treatment was incorporated as a combination regimen in some patients. Conversion surgery was applied in 4 patients. The heterogeneous treatment strategies may affect response assessment and outcomes. Only a subset of patients underwent biopsy before combination therapy because of the invasive nature of biopsy. In clinical practice, the sequence of local, regional, and systemic therapies for HCC can significantly differ depending on tumor size and stage and on the patient's condition, making evaluation of the impact of a single treatment option difficult. The independent value of ^{68}Ga-FAPI PET in patient prognosis should be further investigated in prospective clinical trials. Last, elevated background liver ^{68}Ga-FAPI was found in some patients with

TABLE 3
Cox Proportional-Hazards Regression Analysis for PFS and OS

	PFS				OS			
	Univariable		Multivariable		Univariable		Multivariable	
Predictor	HR	*P*	HR	*P*	HR	*P*	HR	*P*
Age > 65 y	1.01 (0.35–2.91)	0.99			1.85 (0.54–6.41)	0.33		
Male	2.24 (0.50–9.96)	0.29			6.42 (0.23–30.40)	0.36		
HBsAg (+)	1.90 (0.54–6.74)	0.32			2.64 (0.34–20.80)	0.36		
Ascites	1.66 (0.58–4.79)	0.35			2.66 (0.76–9.24)	0.12		
Cirrhosis	2.96 (1.03–8.49)	0.038	2.27 (0.62–8.28)	0.22	1.66 (0.48–5.69)	0.42		
ECOG PS 2	4.34 (1.01–18.6)	0.046	2.83 (0.66–12.21)	0.16	2.91 (0.57–14.72)	0.20		
Child–Pugh class B	1.98 (0.71–5.51)	0.19			3.45 (1.02–11.66)	0.054	1.43 (0.35–5.79)	0.62
AFP > 200 ng/mL	1.46 (0.56–3.74)	0.43			1.27 (0.39–4.19)	0.69		
Macrovascular invasion	3.60 (1.01–12.85)	0.048	4.00 (1.06–15.14)	0.039	2.17 (0.46–10.16)	0.33		
Extrahepatic spread	0.71 (0.27–1.86)	0.49			1.22 (0.37–4.02)	0.75		
Distant-organ metastases	0.93 (0.32–2.66)	0.89			2.07 (0.63–6.83)	0.23		
Bone metastases	2.21 (0.60–8.21)	0.24			4.27 (1.05–17.25)	0.037	5.88 (1.33–25.93)	0.022
BCLC stage C	1.48 (0.34–6.49)	0.61			1.63 (0.21–12.78)	0.64		
Prior regional treatment	0.58 (0.23–1.50)	0.26			0.74 (0.22–2.42)	0.61		
Prior targeted therapy	0.39 (0.11–1.37)	0.14			0.25 (0.03–1.96)	0.19		
^{18}F-FDG SUV_{max} > 6.69	1.39 (0.55–3.52)	0.49			1.94 (0.57–6.66)	0.29		
MTV > 206.80 cm^3 or TLG > 693.53 $SUV_{bw}{\cdot}cm^3$	1.81 (0.69–4.76)	0.23			2.74 (0.83–9.07)	0.10	2.80 (0.83–9.42)	0.10
^{68}Ga-FAPI SUV_{max} > 7.04	1.36 (0.53–3.45)	0.52			1.55 (0.45–5.30)	0.49		
FTV > 230.46 cm^3 or TLF > 961.74 $SUV_{bw}{\cdot}cm^3$	3.54 (1.20–10.45)	0.015	3.88 (1.26–12.01)	0.020	4.83 (1.02–22.88)	0.048	5.92 (1.19–29.42)	0.035

HBsAg (+) = hepatitis B surface antigen A–positive; ECOG PS = Eastern Cooperative Oncology Group performance status; AFP = α-fetoprotein; BCLC = Barcelona Clinic Liver Cancer.

Data in parentheses are 95% CIs.

cirrhosis, and manual contours were carefully applied. The value of cirrhosis-mediated FAP activity in HCC prognosis warrants further investigation (*21*).

CONCLUSION

Volumetric indices on baseline ^{68}Ga-FAPI PET/CT were potentially independent prognostic factors to predict DCB, PFS, and OS in uHCC patients treated with a combination of PD-1 inhibitor and lenvatinib. Baseline ^{68}Ga-FAPI PET/CT may facilitate selection of uHCC patients for the combination of ICB and targeted therapy.

DISCLOSURE

This work was sponsored in part by the National Natural Science Foundation of China (82071967), the CAMS innovation fund for medical science (CIFMS-2021-I2 M-1-025, CIFMS-2021-I2 M-1-002, CIFMS-2021-I2 M-1-061, and CIFMS-2022-I2 M-C&T-A-003), and National High Level Hospital Clinical Research Funding (2022-PUMCH-B-070). No other potential conflict of interest relevant to this article was reported.

KEY POINTS

QUESTION: Can baseline ^{68}Ga-FAPI PET predict response and survival in uHCC patients treated with ICB-based combination therapy?

PERTINENT FINDINGS: Volumetric indices on baseline ^{68}Ga-FAPI PET/CT can potentially predict DCB, PFS, and OS in uHCC patients treated with a combination of PD-1 inhibitor and lenvatinib.

IMPLICATIONS FOR PATIENT CARE: Baseline ^{68}Ga-FAPI PET/CT may facilitate uHCC patient selection for the combination of ICB and targeted therapy.

REFERENCES

1. Yang C, Zhang H, Zhang L, et al. Evolving therapeutic landscape of advanced hepatocellular carcinoma. *Nat Rev Gastroenterol Hepatol.* 2023;20:203–222.
2. Reig M, Forner A, Rimola J, et al. BCLC strategy for prognosis prediction and treatment recommendation: the 2022 update. *J Hepatol.* 2022;76:681–693.
3. Cheng AL, Hsu C, Chan SL, Choo SP, Kudo M. Challenges of combination therapy with immune checkpoint inhibitors for hepatocellular carcinoma. *J Hepatol.* 2020;72:307–319.
4. Yau T, Park JW, Finn RS, et al. Nivolumab versus sorafenib in advanced hepatocellular carcinoma (CheckMate 459): a randomised, multicentre, open-label, phase 3 trial. *Lancet Oncol.* 2022;23:77–90.
5. Asman Y, Evenson AR, Even-Sapir E, Shibolet O. [^{18}F]fludeoxyglucose positron emission tomography and computed tomography as a prognostic tool before liver transplantation, resection, and loco-ablative therapies for hepatocellular carcinoma. *Liver Transpl.* 2015;21:572–580.
6. Lee JW, Oh JK, Chung YA, et al. Prognostic significance of ^{18}F-FDG uptake in hepatocellular carcinoma treated with transarterial chemoembolization or concurrent chemoradiotherapy: a multicenter retrospective cohort study. *J Nucl Med.* 2016;57:509–516.
7. Na SJ, Oh JK, Hyun SH, et al. ^{18}F-FDG PET/CT can predict survival of advanced hepatocellular carcinoma patients: a multicenter retrospective cohort study. *J Nucl Med.* 2017;58:730–736.
8. Sung PS, Park HL, Yang K, et al. ^{18}F-fluorodeoxyglucose uptake of hepatocellular carcinoma as a prognostic predictor in patients with sorafenib treatment. *Eur J Nucl Med Mol Imaging.* 2018;45:384–391.
9. Peltier A, Seban RD, Buvat I, Bidard FC, Mechta-Grigoriou F. Fibroblast heterogeneity in solid tumors: from single cell analysis to whole-body imaging. *Semin Cancer Biol.* 2022;86:262–272.
10. Shi X, Xing H, Yang X, et al. Fibroblast imaging of hepatic carcinoma with ^{68}Ga-FAPI-04 PET/CT: a pilot study in patients with suspected hepatic nodules. *Eur J Nucl Med Mol Imaging.* 2021;48:196–203.
11. Shi X, Xing H, Yang X, et al. Comparison of PET imaging of activated fibroblasts and ^{18}F-FDG for diagnosis of primary hepatic tumours: a prospective pilot study. *Eur J Nucl Med Mol Imaging.* 2021;48:1593–1603.
12. Heimbach JK, Kulik LM, Finn RS, et al. AASLD guidelines for the treatment of hepatocellular carcinoma. *Hepatology.* 2018;67:358–380.
13. Zhou J, Sun HC, Wang Z, et al. Guidelines for diagnosis and treatment of primary liver cancer in China (2017 edition). *Liver Cancer.* 2018;7:235–260.
14. Lindner T, Loktev A, Altmann A, et al. Development of quinoline-based theranostic ligands for the targeting of fibroblast activation protein. *J Nucl Med.* 2018;59:1415–1422.
15. Lencioni R, Llovet JM. Modified RECIST (mRECIST) assessment for hepatocellular carcinoma. *Semin Liver Dis.* 2010;30:52–60.
16. Hirmas N, Hamacher R, Sraieb M, et al. Fibroblast-activation protein PET and histopathology in a single-center database of 324 patients and 21 tumor entities. *J Nucl Med.* 2023;64:711–716.
17. Kraman M, Bambrough PJ, Arnold JN, et al. Suppression of antitumor immunity by stromal cells expressing fibroblast activation protein-alpha. *Science.* 2010;330:827–830.
18. Feig C, Jones JO, Kraman M, et al. Targeting CXCL12 from FAP-expressing carcinoma-associated fibroblasts synergizes with anti-PD-L1 immunotherapy in pancreatic cancer. *Proc Natl Acad Sci USA.* 2013;110:20212–20217.
19. Fearon DT. The carcinoma-associated fibroblast expressing fibroblast activation protein and escape from immune surveillance. *Cancer Immunol Res.* 2014;2:187–193.
20. Lakins MA, Ghorani E, Munir H, Martins CP, Shields JD. Cancer-associated fibroblasts induce antigen-specific deletion of CD8 (+) T cells to protect tumour cells. *Nat Commun.* 2018;9:948.
21. Pirasteh A, Periyasamy S, Meudt JJ, et al. Staging liver fibrosis by fibroblast activation protein inhibitor PET in a human-sized swine model. *J Nucl Med.* 2022;63:1956–1961.

^{68}Ga-SSO-120 PET for Initial Staging of Small Cell Lung Cancer Patients: A Single-Center Retrospective Study

David Kersting[1,2], Patrick Sandach[1,2], Miriam Sraieb[1,2], Marcel Wiesweg[2,3], Martin Metzenmacher[2,3], Kaid Darwiche[4], Filiz Oezkan[4], Servet Bölükbas[5], Martin Stuschke[2,6], Lale Umutlu[2,7], Michael Nader[1,2], Rainer Hamacher[2,3], Wolfgang P. Fendler[1,2], Johannes Wienker[4,8], Wilfried E.E. Eberhardt[2,3,8], Martin Schuler[2,3,8], Ken Herrmann[1,2], and Hubertus Hautzel[1,2]

[1]Department of Nuclear Medicine, West German Cancer Center, University Hospital Essen, University of Duisburg–Essen, Essen, Germany; [2]German Cancer Consortium, Partner Site University Hospital Essen, Essen, Germany; [3]Department of Medical Oncology, West German Cancer Center, University Hospital Essen, University of Duisburg–Essen, Essen, Germany; [4]Department of Pulmonary Medicine, Section of Interventional Pulmonology, West German Cancer Center, University Medicine Essen–Ruhrlandklinik, University of Duisburg–Essen, Essen, Germany; [5]Department of Thoracic Surgery and Thoracic Endoscopy, West German Cancer Center, University Medicine Essen–Ruhrlandklinik, University of Duisburg–Essen, Essen, Germany; [6]Department of Radiotherapy, West German Cancer Center, University Hospital Essen, University of Duisburg–Essen, Essen, Germany; [7]Institute of Diagnostic and Interventional Radiology and Neuroradiology, West German Cancer Center, University Hospital Essen, University of Duisburg–Essen, Essen, Germany; and [8]Division of Thoracic Oncology, West German Lung Center, University Medicine Essen–Ruhrlandklinik, University of Duisburg–Essen, Essen, Germany

PET imaging using the somatostatin receptor 2 (SSTR2) antagonist satoreotide trizoxetan (SSO-120, previously OPS-202) could offer accurate tumor detection and screening for SSTR2-antagonist radionuclide therapy in patients with SSTR2-expressing small cell lung cancer (SCLC). The aim of this single-center study was to investigate tumor uptake and detection rates of ^{68}Ga-SSO-120 in comparison to ^{18}F-FDG PET in the initial staging of SCLC patients. **Methods:** Patients with newly diagnosed SCLC who underwent additional whole-body ^{68}Ga-SSO-120 PET/CT during the initial diagnostic workup were retrospectively included. The mean administered activity was 139 MBq, and the mean uptake time was 60 min. Gold-standard staging ^{18}F-FDG PET/CT was evaluated if available within 2 wk before or after ^{68}Ga-SSO-120 PET if morphologic differences in CT images were absent. ^{68}Ga-SSO-120– or ^{18}F-FDG–positive lesions were reported in 7 anatomic regions (primary tumor, thoracic lymph node metastases, and distant metastases including pleural, contralateral pulmonary, liver, bone, and other) according to the TNM classification for lung cancer (eighth edition). Consensus TNM staging (derived from CT, endobronchial ultrasound-guided transbronchial needle aspiration, PET, and brain MRI) by a clinical tumor board served as the reference standard. **Results:** Thirty-one patients were included, 12 with limited and 19 with extensive disease according to the Veterans Administration Lung Study Group classification. ^{68}Ga-SSO-120–positive tumor was detected in all patients (100%) and in 90 of the 217 evaluated regions (41.5%). Thirteen patients (42.0%) had intense average ^{68}Ga-SSO-120 uptake (region-based mean $SUV_{max} \geq 10$); 28 patients (90.3%) had average ^{68}Ga-SSO-120 uptake greater than liver uptake (region-based mean peak tumor-to-liver ratio > 1). In 25 patients with evaluable ^{18}F-FDG PET, primary tumor, thoracic lymph node metastases, and distant metastases were detected in 100%, 92%, and 64%, respectively, of all investigated patients by ^{68}Ga-SSO-120 and in 100%, 92%, and 56%, respectively, by ^{18}F-FDG PET. ^{68}Ga-SSO-120 PET detected additional contralateral lymph node, liver, and brain metastases in 1, 1, and 2 patients, respectively (no histopathology available), and ^{18}F-FDG PET detected additional contralateral lymph node metastases in 3 patients (1 confirmed, 1 systematic endobronchial ultrasound-guided transbronchial needle aspiration–negative, and 1 without available histopathology). None of these differences altered Veterans Administration Lung Study Group staging. The region-based monotonic correlation between ^{68}Ga-SSO-120 and ^{18}F-FDG uptake was low (Spearman $\rho = 0.26$–0.33). **Conclusion:** ^{68}Ga-SSO-120 PET offers high diagnostic precision with comparable detection rates and additional complementary information to the gold standard, ^{18}F-FDG PET. Consistent uptake in most patients warrants exploration of SSTR2-directed radionuclide therapy.

Key Words: ^{68}Ga-SSO-120; ^{68}Ga-OPS-202; PET; SCLC; SSTR

J Nucl Med 2023; 64:1540–1549
DOI: 10.2967/jnumed.123.265664

Small cell lung cancer (SCLC) is a highly aggressive tumor with a dismal prognosis and comprises about 15% of lung cancer diagnoses (*1*). SCLC tumor cells typically show a distinct molecular profile compared with other lung cancers and often exhibit neuroendocrine characteristics (*2*). Molecular imaging of glucose metabolism using ^{18}F-FDG PET/CT is the gold standard imaging in multidisciplinary management of SCLC patients, as it offers more accurate staging than conventional CT and bone scintigraphy (*3,4*) and accuracy can be crucial in deciding between curative or palliative treatment. Because SCLCs frequently express somatostatin receptors (SSTRs), particularly type 2 SSTRs (SSTR2), they are potentially also amenable to SSTR-directed theranostics (*5*).

Molecular imaging using SSTR agonists such as ^{68}Ga-DOTATATE or ^{68}Ga-DOTATOC is well established for both gastroenteropancreatic neuroendocrine tumors (NETs) (*6*) and pulmonary NETs (*7*). In a theranostic approach, peptide receptor radionuclide therapy using ^{177}Lu-DOTATATE or ^{177}Lu-DOTATOC can be performed and has been approved for treatment of gastroenteropancreatic NETs (*8,9*). In SCLC patients, mixed results were described, with

Received Mar. 6, 2023; revision accepted May 24, 2023.
For correspondence or reprints, contact David Kersting (david.kersting@uni-due.de).
Published online Jul. 20, 2023.

high PET tracer accumulation in only a subgroup of patients (*10*), indicating inter- and intraindividually variable SSTR expression and a generally lower level of SSTR expression than in NETs. SSTR-agonist peptide receptor radionuclide therapy was performed on small patient groups and without resounding success (*10,11*). Therefore, neither SSTR-targeting molecular imaging nor radionuclide therapy has yet found its way into the routine management of patients with SCLC.

SSTR2 antagonists such as ^{68}Ga-SSO-120/^{177}Lu-SSO-110 (international nonproprietary name: ^{68}Ga-satoreotide trizoxetan/^{177}Lu-satoreotide tetraxetan, also known as ^{68}Ga-OPS-202/^{177}Lu-OPS-201 or ^{68}Ga-NODAGA-JR11/^{177}Lu-DOTA-JR11) offer promising novel theranostic options. They show higher tumor uptake and longer retention times than SSTR agonists, probably because they bind to SSTRs not only in active states but also in inactive states (*12*). In the first clinical applications in NETs, this characteristic resulted in a higher tumor-to-background ratio and sensitivity in PET imaging (*13,14*) and high tumor-absorbed doses in radionuclide therapy (*15–17*). Thus, tumors with lower SSTR2 expression than NETs might also become susceptible to SSTR-directed theranostics (*12*). We therefore hypothesized that ^{68}Ga-SSO-120 PET allows precise tumor detection and screening for SSTR2-antagonist radionuclide therapy in patients with SSTR2-expressing SCLC.

Since ^{68}Ga-SSO-120 PET became available at our institution, we have routinely performed ^{68}Ga-SSO-120 PET and ^{18}F-FDG PET for staging and restaging of SCLC patients. We here report the first, to our best knowledge, evaluation of clinical ^{68}Ga-SSO-120 PET/CT imaging in SCLC patients. The aim of the study was to investigate tumor detection rates and tracer uptake on ^{68}Ga-SSO-120 PET in comparison to ^{18}F-FDG PET.

MATERIALS AND METHODS

Patients and Ethics

We retrospectively screened our institutional database for patients who underwent clinical ^{68}Ga-SSO-120 PET/CT for staging of SCLC with neuroendocrine differentiation (based on immunohistochemistry for CD56, synaptophysin SP11, and thyroid transcription factor 1). For further analysis, we selected patients whose primary diagnosis had been received within 3 mo before the ^{68}Ga-SSO-120 PET and who were at the beginning of their first-line therapy (allowing PET imaging before, within, or after a first cycle of primary chemotherapy). Additional staging ^{18}F-FDG PET/CT was used for comparison if available within 2 wk before or after ^{68}Ga-SSO-120 PET and if no major morphologic differences were observed on the CT images (stable disease according to RECIST 1.1). Patients gave written informed consent to undergo clinical PET examinations. The local institutional ethics committee (University of Duisburg–Essen, medical faculty) approved the study (ethics protocol 22-11013-BO) and waived the need for study-specific consent.

PET/CT Imaging

PET/CT images were acquired on a Biograph Vision 600 (Siemens Healthineers), a Biograph mCT (Siemens Healthineers), or a Vereos (Philips Healthcare) PET/CT system. The mean administered activity (±SD) was 139 ± 27 MBq of ^{68}Ga-SSO-120, and the mean uptake time was 60 ± 18 min, in accordance with the dose recommendations from a phase I/II study on patients with gastroenteropancreatic NETs (*18*). Before the PET acquisition, a contrast-enhanced whole-body CT scan was performed if not clinically available within 4 wk before the examination date; otherwise, a low-dose CT scan without application of contrast medium was acquired for attenuation correction and anatomic localization of PET uptake. The PET/CT acquisition and image reconstruction were performed according to our clinically established PET protocols for ^{68}Ga-based tracers (*19*).

PET Image Analysis

All PET images were analyzed by 2 nuclear medicine physicians with several years of experience in PET reporting. When the findings were discrepant, the images were reevaluated for consensus decision making. ^{68}Ga-SSO-120– or ^{18}F-FDG–positive lesions were reported for each patient separately in 7 different anatomic categories according to the TNM classification (World Health Organization/International Association for the Study of Lung Cancer, eighth edition) (*20*) for staging of lung cancer patients (primary tumor, thoracic lymph node metastases, and distant metastases including pleural, contralateral pulmonary, liver, bone, and other lesions). ^{68}Ga-SSO-120/^{18}F-FDG positivity was defined as visually markedly increased lesion uptake compared with local background; local background was used for this comparison because if a global reference was used, the characteristics of ^{68}Ga-SSO-120 PET (e.g., very low physiologic cerebral uptake and high physiologic adrenal gland uptake) would impede an accurate detectability comparison to ^{18}F-FDG PET (showing a different physiologic uptake pattern). Region-based detection rates were calculated using the total number of regions that were ^{68}Ga-SSO-120– and/or ^{18}F-FDG–positive as a reference. Our interdisciplinary clinical tumor board (in which certified board members from interventional pneumology, thoracic surgery, oncology, radiotherapy, radiology, nuclear medicine, and pathology participate) derived the consensus TNM stage from thoracoabdominal CT, brain MRI, whole-body PET, and endobronchial ultrasound-guided transbronchial needle aspiration, and this consensus stage served as the reference standard for validation of a lesion that was ^{68}Ga-SSO-120– or ^{18}F-FDG–positive.

For semiquantitative analysis, the SUV_{max} and SUV_{peak} of the hottest lesion in each of the predefined TNM regions that were ^{68}Ga-SSO-120–/^{18}F-FDG–positive were determined (in regions with multiple lesions, only the hottest lesion was evaluated). To calculate SUV_{max} and SUV_{peak} tumor-to-liver ratios (TLR_{max} and TLR_{peak}, respectively), SUV_{mean} was determined in a spheric volume of interest of 14 mL (3 cm in diameter) in the right liver lobe as suggested in PERCIST 1.0, and the following definitions were used (*21,22*):

$$TLR_{max} = \frac{SUV_{max}}{SUV_{mean,\ liver}}$$

and

$$TLR_{peak} = \frac{SUV_{peak}}{SUV_{mean,\ liver}}.$$

Patient-based mean SUV_{max} was defined as the mean of the SUV_{max} of the hottest lesions from all ^{68}Ga-SSO-120– or ^{18}F-FDG–positive regions per patient.

COMPARISON OF ^{68}GA-SSO-120 AND ^{18}F-FDG PET

In patients with available ^{18}F-FDG PET, patient- and region-based detection rates were compared between ^{68}Ga-SSO-120 and ^{18}F-FDG PET. For the region-based analysis, N-status and M-status were determined following the TNM classification for lung cancer patients (World Health Organization/International Association for the Study of Lung Cancer, eighth edition) (*20*), whereas analysis of the primary tumor (T) was restricted to positive (T1) or negative (T0), as PET imaging does not allow exact determination of local tumor extent.

Semiquantitative measures (SUV_{max}, SUV_{peak}, TLR_{max}, and TLR_{peak}) were compared between ^{68}Ga-SSO-120 and ^{18}F-FDG PET in a region-based analysis. Moreover, the region-based monotonic correlation between ^{68}Ga-SSO-120– and ^{18}F-FDG–positive findings

was evaluated. Adrenal gland and brain metastases were not included in these comparisons because their high physiologic uptake on ^{68}Ga-SSO-120 or ^{18}F-FDG PET, respectively, would bias the analysis. Distant metastases (pleural, contralateral pulmonary, liver, bone, and other) were summarized into a single category indicating the uptake value of the hottest lesion.

For a patient-based analysis, region-based mean SUV_{max} and TLR_{peak} (mean of SUV_{max} and TLR_{peak}, respectively, from all positive regions per patient) were calculated and compared between ^{68}Ga-SSO-120 and ^{18}F-FDG PET.

Statistics and Software

All statistical evaluations were performed using R statistical software, version 4.1.2 (R Foundation for Statistical Computing). For comparison of differences in SUV and TLR between ^{68}Ga-SSO-120 and ^{18}F-FDG, a Mann–Whitney *U* test was applied. Beforehand, the data were tested with the Shapiro–Wilk test for parametric distribution. The monotonic correlation of SUV and TLR across ^{68}Ga-SSO-120 and ^{18}F-FDG PET was analyzed using Spearman ρ. *P* values of 0.05 or less were regarded as statistically significant. The graphical abstract was created using BioRender.com.

RESULTS

Patient Characteristics

Between May 2022 and January 2023, 76 patients underwent PET imaging for staging or restaging of SCLC at our institution (University Hospital Essen). Of these, 47 were investigated for initial staging and 32 underwent additional ^{68}Ga-SSO-120 PET/CT. One patient was excluded because the diagnosis of SCLC had been changed to non–small cell lung cancer after ^{68}Ga-SSO-120 PET/CT. Details are presented in Figure 1.

Of 31 included patients, 4 were in TNM stage IIIA (12.9%), 4 in IIIB (12.9%), 4 in IIIC (12.9%), and 19 in IV (61.3%) (*20*); 12 patients showed limited (38.7%) and 19 extensive (61.3%) disease according to the Veterans Administration Lung Study Group (VALG) classification (referring to clinical primary staging by thoracoabdominal CT, head MRI, whole-body PET, and endobronchial ultrasound-guided transbronchial needle aspiration). Detailed patient characteristics, including TNM stages, are given in Table 1.

Evaluable additional staging ^{18}F-FDG PET was available for 25 patients (80.6%), with a median interval between ^{18}F-FDG and ^{68}Ga-SSO-120 PET of 3 d (range, −7 to 14 d). In 15 patients (60.0%), ^{18}F-FDG PET was performed before, and in 5 patients (20.0%) after, ^{68}Ga-SSO-120 PET; in 5 patients (20.0%), both modalities were performed on the same day. In 15 patients (60.0%), treatment was initiated (ongoing first cycle of first-line chemotherapy) between ^{18}F-FDG PET and ^{68}Ga-SSO-120 PET.

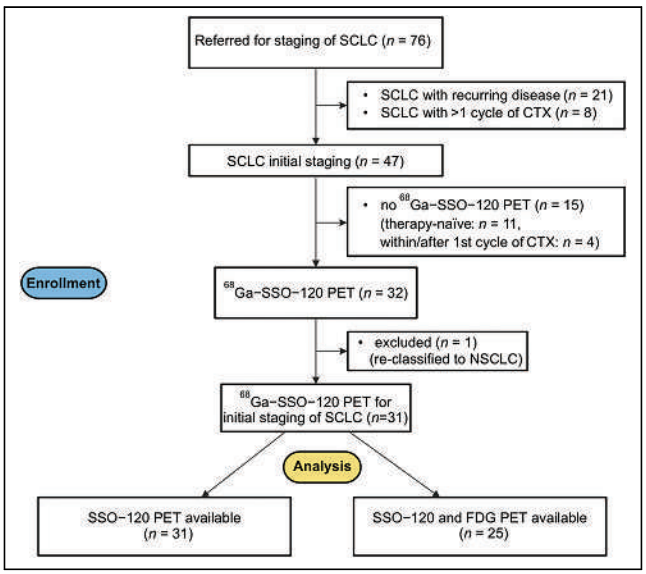

FIGURE 1. Flowchart for patients who underwent ^{68}Ga-SSO-120 PET at our institution (University Hospital Essen) between May 2022 and January 2023 and patients who were analyzed according to inclusion criteria. CTX = chemotherapy.

SSO-120 PET Imaging Results

In the patient-based analysis, all 31 patients (100%) showed ^{68}Ga-SSO-120–positive tumors (any lesion). In the region-based analysis, in 90 of the 217 evaluated TNM regions (41.5%), ^{68}Ga-SSO-120–positive tumor was detected. All 31 patients showed a ^{68}Ga-SSO-120–positive primary tumor (100%), whereas ^{68}Ga-SSO-120–positive thoracic lymph node metastases were detected in 29 of 31 patients (93.5%), and ^{68}Ga-SSO-120–positive distant metastases were detected in 19 of 31 patients (61.3%). Region-based semiquantitative ^{68}Ga-SSO-120 uptake ratios for primary tumor, thoracic lymph node metastases, and distant metastases are

TABLE 1
Patient Characteristics

Characteristic	Data
Age (y)	67 (50–81)
Sex	
Male	18 (58.1)
Female	13 (41.9)
T	
1	4 (12.9)
2	3 (9.7)
3	5 (16.1)
4	19 (61.3)
N	
0	3 (9.7)
1	0 (0)
2	12 (38.7)
3	16 (51.6)
M	
0	12 (38.7)
1	19 (51.3)
1a	4 (12.9)
1b	4 (12.9)
1c	11 (25.5)
Therapy	
Therapy-naïve	7 (22.6)
Within first cycle of chemotherapy	12 (38.7)
After first cycle of chemotherapy	12 (38.7)

Qualitative data are number and percentage; continuous data are median and range.

TABLE 2
Region-Based ^{68}Ga-SSO-120 Uptake

Region	SUV_{max}	SUV_{peak}	TLR_{max}	TLR_{peak}
Primary tumor	11.2 ± 8.8	9.0 ± 7.3	4.6 ± 4.4	3.7 ± 3.6
Thoracic lymph node metastases	11.9 ± 10.4	9.3 ± 8.6	5.1 ± 5.1	4.0 ± 4.1
Distant metastases	12.7 ± 12.8	9.8 ± 10.1	5.5 ± 6.7	4.2 ± 5.2

Data are mean ± SD.

presented in Table 2. In the category distant metastases, the table indicates mean $SUV/TLR_{max/peak}$ of the hottest distant metastasis per patient; full details indicating SUV and TLR for each of the metastatic subregions (pleural, contralateral pulmonary, liver, bone, and other) are given in Supplemental Table 1 (supplemental materials are available at http://jnm.snmjournals.org). Ten patients showed ^{68}Ga-SSO-120–positive other distant metastases (3 with brain metastases; 2 with abdominal lymph node metastases; 1 with cervical lymph node metastases; 1 with adrenal and brain metastases; 1 with soft-tissue metastases; 1 with diaphragm metastases; and 1 with adrenal, brain, peritoneal, and abdominal lymph node metastases).

Thirteen patients (42.0%) showed a high mean SUV_{max} (≥10), 10 patients (32.3%) an intermediate mean SUV_{max} (≥5 but <10), and 8 patients (25.7%) a low mean SUV_{max} (<5). Twenty-eight patients (90.3%) had average ^{68}Ga-SSO-120 uptake greater than liver uptake (region-based mean $TLR_{peak} > 1$), with markedly greater uptake (region-based mean $TLR_{peak} \geq 2$) in 18 patients (58.1%). Figure 2 shows image examples of patients with different ^{68}Ga-SSO-120 uptake patterns and the distribution of the ^{68}Ga-SSO-120 uptake groups. In 5 patients, brain metastases were detected on ^{68}Ga-SSO-120 PET: the SSTR expression level in the brain appeared to allow diagnostic findings there due to low background activity, whereas brain imaging is a well-known weakness of ^{18}F-FDG PET because of high physiologic cerebral glucose metabolism. In 2 patients, adrenal metastases were detectable by an irregular morphologic shape on CT and ^{68}Ga-SSO-120 PET images and an inhomogeneous ^{68}Ga-SSO-120 uptake pattern, whereas increased uptake on ^{68}Ga-SSO-120 PET was difficult to evaluate because of high physiologic adrenal SSTR expression.

Comparison of ^{68}Ga-SSO-120 and ^{18}F-FDG PET

In the patient-based analysis, all 25 patients (100%) showed ^{68}Ga-SSO-120– and ^{18}F-FDG–positive tumor (any lesion). In the region-based analysis, ^{68}Ga-SSO-120–positive tumor was detected in 71 of the 175 evaluated TNM regions (40.6%) and ^{18}F-FDG–positive tumor was detected in 68 regions (38.9%) (Fig. 3). Primary tumor, thoracic lymph node metastases, and distant metastases were detected in 25 of 25 patients (100%), 23 of 25 patients (92.0%), and 16 of 25 patients (64.0%), respectively, by ^{68}Ga-SSO-120 and in all patients (100%), 23 of 25 patients (92.0%), and 14 of 25 patients (56.0%), respectively, by ^{18}F-FDG PET. Detailed results, including subregions of distant metastases, are given in Supplemental Table 2. Region-based detection rates (calculated using the total number of regions that were ^{68}Ga-SSO-120– or ^{18}F-FDG–positive as a reference) were 100% for ^{68}Ga-SSO-120 PET and 95.8% for ^{18}F-FDG PET.

Regarding single lesions in the predefined regions with a potential influence on the TNM classification, in 1 patient a contralateral thoracic lymph node metastasis was detected only on ^{68}Ga-SSO-120 PET (TNM cN3 vs. cN2, not inducing differences in the region-based analysis), in 2 patients additional brain metastases were detected only on ^{68}Ga-SSO-120 PET (TNM cM1b vs. cM0), and in 1 patient liver metastases were detected only on ^{68}Ga-SSO-120 PET (TNM cM1c vs. cM1c). In 3 patients contralateral thoracic lymph node metastases were detected only on ^{18}F-FDG PET (TNM cN2 vs. cN3, not inducing differences in the region-based analysis). Of note, in 1 patient with additional brain metastases on ^{68}Ga-SSO-120 PET, the largest lesion showed no uptake but did show a discernable photopenic shape on ^{18}F-FDG PET. One additional metastasis on ^{18}F-FDG PET was histopathologically confirmed; for another one, systematic endobronchial ultrasound-guided transbronchial needle aspiration was negative. For the other additional lesions (1 on ^{18}F-FDG and 4 on ^{68}Ga-SSO-120 PET), histopathology was not available. These differences did not lead to changes in VALG staging or treatment strategies because other lesions were stage-determining or, in the case of brain metastases, previously known from MRI. Image examples of lesions that were detected only on ^{68}Ga-SSO-120 or ^{18}F-FDG PET and of brain and adrenal metastases are shown in Figures 4 and 5.

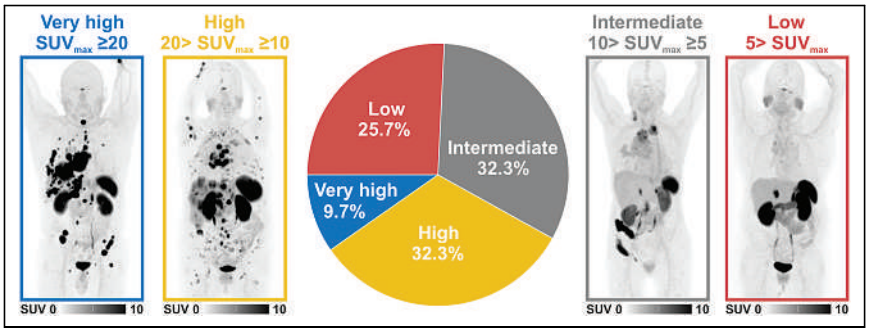

FIGURE 2. Distribution of ^{68}Ga-SSO-120 uptake patterns and image examples (maximum-intensity projections) of patients with very high, high, intermediate, and low ^{68}Ga-SSO-120 uptake. SUV_{max} refers to region-based mean SUV_{max} (mean from all ^{68}Ga-SSO-120–positive regions per patient).

Mean semiquantitative ^{18}F-FDG uptake was significantly higher than ^{68}Ga-SSO-120 uptake in primary tumors and thoracic lymph node metastases; uptake was comparable in distant metastases (Figs. 6A–6C for SUV_{max} and TLR_{max} and Supplemental Figs. 1A–1C for SUV_{peak} and TLR_{peak}). These differences are most likely an expression of the different molecular targets (glycolysis on ^{18}F-FDG PET vs. SSTR2 expression on ^{68}Ga-SSO-120 PET). Numeric results are

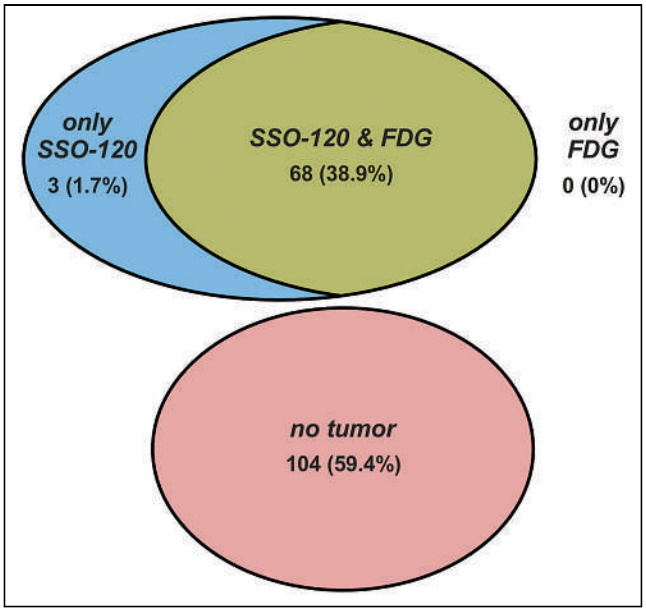

FIGURE 3. Venn diagram of region-based analysis showing numbers and distributions of only ^{68}Ga-SSO-120–positive regions, only ^{18}F-FDG–positive regions, ^{68}Ga-SSO-120– and ^{18}F-FDG–positive-regions, and regions in which no tumor was detected. In total, 175 regions were evaluated.

shown in Table 3 (SUV_{max} and TLR_{max}) and Supplemental Table 3 (SUV_{peak} and TLR_{peak}). Shapiro–Wilk test results are presented in Supplemental Table 4. Overall, ^{68}Ga-SSO-120 and ^{18}F-FDG SUV_{max}, SUV_{peak}, TLR_{max}, and TLR_{peak} showed a low monotonic correlation, with a Spearman ρ of 0.33 (SUV_{max}), 0.32 (SUV_{peak}), 0.28 (TLR_{max}), and 0.26 (TLR_{peak}), respectively (Fig. 6D for SUV_{max} and TLR_{max}; Supplemental Fig. 1D for SUV_{peak} and TLR_{peak}).

Moreover, the correlation analysis indicated that in a relevant number of patients, region-based ^{18}F-FDG uptake was high whereas ^{68}Ga-SSO-120 uptake was low, and in some patients region-based ^{68}Ga-SSO-120 uptake was high whereas ^{18}F-FDG was low (Fig. 6D; Supplemental Fig. D). We therefore sorted patients into different groups according to their region-based ^{68}Ga-SSO-120 and ^{18}F-FDG mean SUV_{max} (using a mean $SUV_{max} \geq 10$ as the cutoff). The analysis revealed 1 patient (4.0%) with high ^{68}Ga-SSO-120 uptake and low-to-intermediate ^{18}F-FDG uptake, 9 patients (36.0%) with both high ^{68}Ga-SSO-120 uptake and high ^{18}F-FDG uptake, 13 patients (52.0%) with low ^{68}Ga-SSO-120 uptake but high ^{18}F-FDG uptake, and 2 patients (8.0%) with both low ^{68}Ga-SSO-120 uptake and low ^{18}F-FDG uptake. A detailed presentation of patients with different ^{68}Ga-SSO-120/^{18}F-FDG uptake patterns, including image examples, is in Figure 7. Of note, 5 patients (20.0%) showed very low ^{68}Ga-SSO-120 uptake (mean $SUV_{max} < 5$) but high ^{18}F-FDG uptake (mean $SUV_{max} \geq 10$).

DISCUSSION

This is, to the best of our knowledge, the first description of SSTR2-antagonist PET imaging in SCLC patients. In the patient-based and region-based analyses, detection rates were comparable between ^{68}Ga-SSO-120 and ^{18}F-FDG PET, indicating that both are valuable tools for primary staging of SCLC patients. As ^{18}F-FDG PET is already well established, it will probably remain the mainstay of molecular imaging in SCLC patients. ^{68}Ga-SSO-120 PET likewise offers precise tumor detection and additional complementary information, as the region-based correlation between ^{68}Ga-SSO-120 and ^{18}F-FDG uptake was low (Fig. 6; Supplemental Fig. 1). In patients with sufficient SSTR2-antagonist uptake,

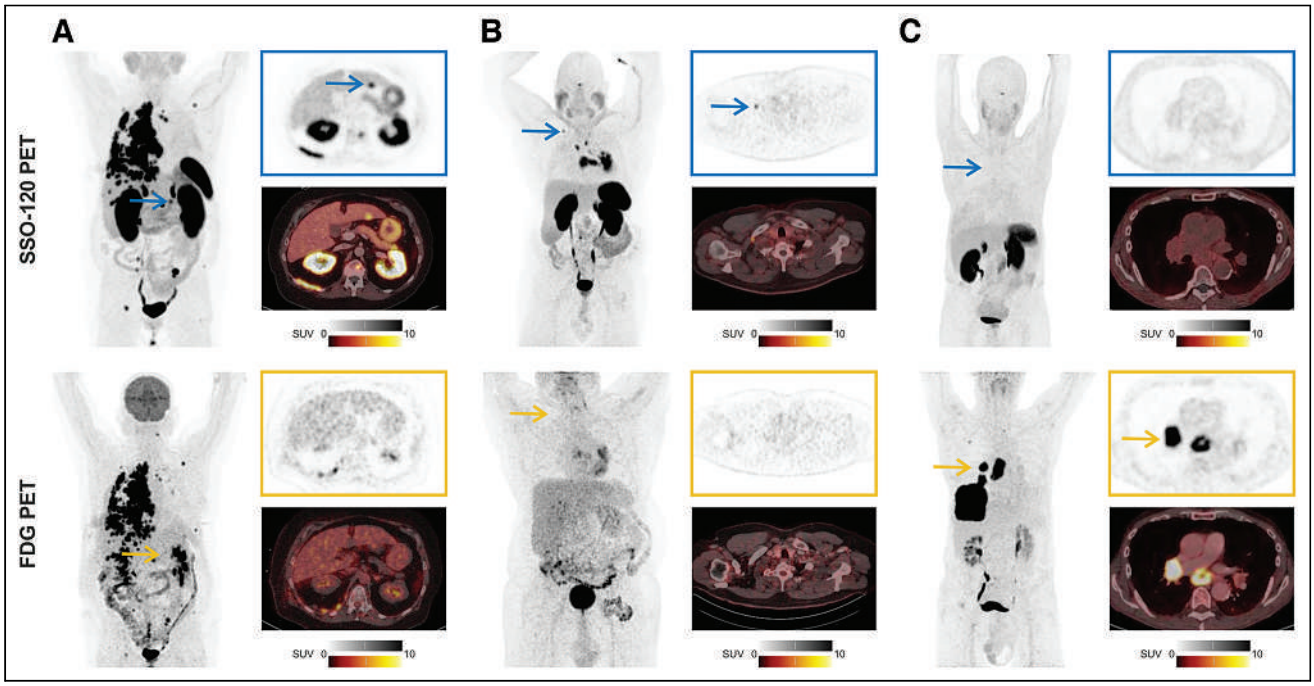

FIGURE 4. Image examples of liver and thoracic lymph node metastases in ^{68}Ga-SSO-120 in comparison to ^{18}F-FDG PET. Each panel shows maximum-intensity projections (left), transversal PET images (top right), and transversal PET/CT images (bottom right). (A) Liver metastases that were detected only on ^{68}Ga-SSO-120 PET. (B) Thoracic lymph node metastasis that was detected only on ^{68}Ga-SSO-120 PET. (C) Thoracic lymph node metastases that were detected only on ^{18}F-FDG PET.

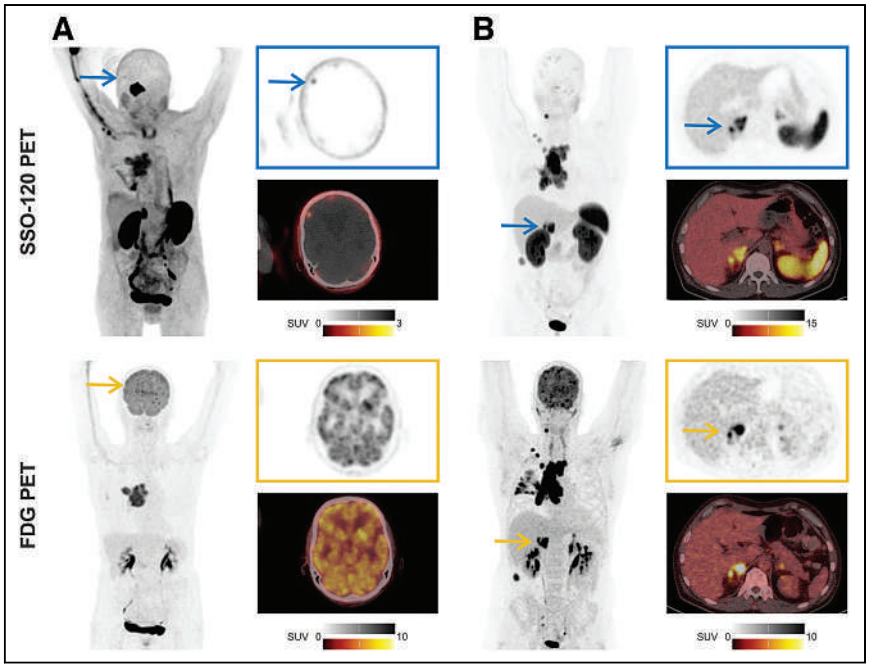

FIGURE 5. Image examples of brain and adrenal metastases on ^{68}Ga-SSO-120 PET in comparison to ^{18}F-FDG PET. Each panel shows maximum-intensity projections (left), transversal PET images (top right), and transversal PET/CT images (bottom right). (A) Brain metastasis that was detected only on ^{68}Ga-SSO-120 PET. (B) Adrenal metastasis that was detected on both ^{68}Ga-SSO-120 PET and ^{18}F-FDG PET.

targeted radionuclide therapy may be performed in a theranostic approach. Of note, the cutoff of mean SUV_{max} (≥10) used in this work to define high uptake is not an established standard for evaluating the applicability of SSTR2-directed radionuclide therapy but was chosen to compare the intensity of the uptake interindividually and in comparison to ^{18}F-FDG uptake. Moreover, Fendler et al. recently used an SUV_{max} cutoff of at least 10 in more than 50% of tumor lesions to select patients for systemic radionuclide therapy with the fibroblast activation protein inhibitor ^{90}Y-FAPI-46 (*23*).

A main goal of PET imaging in primary staging of SCLC patients is to distinguish limited disease from extensive disease to help determine the treatment (*24*). In this context, correct upstaging in binary VALG classification can prevent patients from undergoing ineffective surgery or radiotherapy. In this study, ^{68}Ga-SSO-120 PET detected more distant metastases, whereas ^{18}F-FDG PET detected more contralateral thoracic lymph node metastases (Figs. 3 and 4). However, the additionally detected metastases did not alter VALG staging. In 2 patients, additional brain metastases on ^{68}Ga-SSO-120 PET were already known from cerebral MRI. Another patient had not only liver metastases that were additionally detected on ^{68}Ga-SSO-120 PET but also pleural and bone manifestations. In larger patient cohorts, however, recognition of additional distant metastases could potentially influence patient management regarding the decision toward curative or palliative treatment intent.

In this context, a known limitation of ^{18}F-FDG PET in SCLC patients is detection of brain metastases, because they are barely discernible from high physiologic cerebral glucose uptake (*4*). ^{68}Ga-SSO-120 PET showed clearly detectable brain metastases in 5 patients, but in 1 patient a brain metastasis known from MRI was not detected. For 5 of these 6 patients, additional ^{18}F-FDG PET was available (Fig. 5A), and in 2 patients, ^{18}F-FDG uptake of brain metastases was observed. Of note, in 1 patient with several ^{68}Ga-SSO-120–positive brain metastases, the largest one showed no uptake but did show a discernable photopenic shape on ^{18}F-FDG PET. In contrast, ^{68}Ga-SSO-120 PET is limited for detection of adrenal metastases because of the adrenal glands' high physiologic uptake (*25*). In our cohort, in 2 patients adrenal metastases were detected by an irregular shape on morphologic CT and ^{68}Ga-SSO-120 PET images and by an inhomogeneous ^{68}Ga-SSO-120 uptake pattern, whereas elevated tracer uptake was difficult to evaluate (Fig. 5B).

Detection of additional thoracic lymph node metastases does not alter binary VALG staging but can, in patients with limited disease, evoke an extension of the target volume in radiotherapy planning (*26*). In this study, 3 patients were rated cN3 only on ^{18}F-FDG PET, compared with 1 patient rated cN3 only on ^{68}Ga-SSO-120 PET. Future studies are necessary to understand the potential clinical benefit of performing a dual-tracer approach in a purely diagnostic setting. It is noteworthy that a significant number of lesions had low ^{68}Ga-SSO-120 uptake but were still identifiable because they had clearly increased uptake compared with the surrounding background and also exhibited suggestive morphologic features. A relevant number of these lesions yet showed high ^{18}F-FDG uptake, with a general trend toward higher ^{18}F-FDG uptake for primary tumor and thoracic lymph node metastases, whereas uptake was comparable in distant metastases (Fig. 6; Supplemental Fig. 1).

All patients showed any ^{68}Ga-SSO-120 uptake, and about 40% of patients demonstrated high ^{68}Ga-SSO-120 uptake (Fig. 2), with 1 patient presenting high ^{68}Ga-SSO-120 uptake and low ^{18}F-FDG uptake (Fig. 7). In most patients, tumor ^{68}Ga-SSO-120 uptake was greater than liver uptake. We used region-based mean TLR_{peak} per patient as a suggested robust semiquantitative measure to evaluate lesion uptake in comparison to liver uptake. This measure was chosen on the basis of the visual Krenning score, which was originally introduced for octreotide scintigraphy and evaluates lesion uptake in comparison to physiologic reference tissue. Tumor uptake greater than liver uptake corresponds to a Krenning score of 3, and tumor uptake greater than spleen or kidney uptake corresponds to a score of 4 (*27*). Typically, peptide receptor radionuclide therapy can be applied to NETs if the Krenning score is at least 3. ^{68}Ga-SSO-120 uptake did not show a normal distribution (Supplemental Table 2), probably indicating different interindividual uptake patterns. Two previous studies used SSTR-agonist PET in SCLC patients. Both reports described enhanced tracer uptake in about half the included patients (*10,11*), and 1 report described any uptake in more than 80% of the evaluated lesions (*11*). The higher rates of patients with uptake on SSTR2-antagonist PET are in line with a previous comparison in patients with gastroenteropancreatic NETs describing an improved lesion-based detection rate for ^{68}Ga-SSO-120 compared with ^{68}Ga-DOTATOC PET, with a particular benefit for liver metastases (*13*).

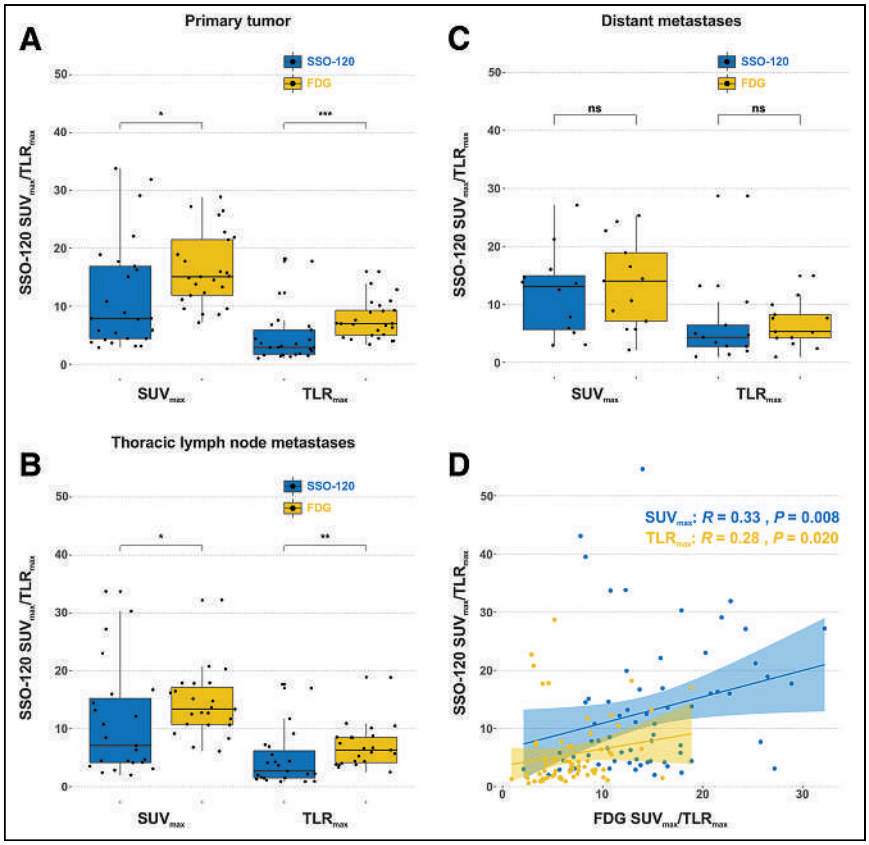

FIGURE 6. (A–C) Region-based box plot of ^{68}Ga-SSO-120 SUV_{max} and TLR_{max} in comparison to ^{18}F-FDG SUV_{max} and TLR_{max} for primary tumor (A), thoracic lymph node metastases (B), and distant metastases (C). Horizontal line indicates median, hinges indicate first and third quartiles, and whiskers indicate lowest and highest within 1.5 times interquartile range of hinge. (D) Scatterplot for region-based ^{68}Ga-SSO-120 SUV_{max}/TLR_{max} vs. ^{18}F-FDG SUV_{max}/TLR_{max}. ns = not statistically significant. *$P \leq 0.05$. **$P \leq 0.01$. ***$P \leq 0.001$. ****$P \leq 0.0001$.

Future evaluations of ^{68}Ga-SSO-120 PET in SCLC patients might point in 2 directions. First, immunohistochemical examination including determination of SSTR2 expression in lesions that have different ^{68}Ga-SSO-120 uptake and were previously biopsied or afterward resected might allow a deeper understanding of the various ^{68}Ga-SSO-120/^{18}F-FDG uptake patterns. Most SCLC cells express SSTR2 (*28*), with high-level SSTR2 expression occurring in almost half of SCLC patients (*29*), but expression varies in SCLC subtypes with different gene signatures of transcription factors (*30*). If high uptake on ^{68}Ga-SSO-120 PET can be predicted from histopathologic examination, patients who could benefit from this examination may be selected via the initial biopsy. The other way around, ^{68}Ga-SSO-120 PET may serve as a noninvasive tool to guide toward specific biopsy locations (if ^{68}Ga-SSO-120 uptake correlates with the genetic profile, particularly in advanced disease with clonal evolution and a heterogeneous uptake pattern). For ^{68}Ga-DOTATATE, a correlation between histologic SSTR2 expression and both SUV_{peak} and TLR values was described (*10*). Moreover, in the increasing field of personalized medicine and theranostic options, characterization of the molecular basics of tumor biology is decisive to select the most appropriate therapy, with radionuclide therapy using SSTR2 antagonists such as ^{177}Lu-SSO-110 being a possible new theranostic approach in SCLC patients. In this context, SSTR2 PET might be a more accurate screening tool for SSTR2 positivity than immunohistochemical examination, as—regarding intraindividual heterogeneity of expression levels—it enables whole-body examination and is not affected by sampling errors.

Second, mid- and long-term follow-up of patients who underwent ^{68}Ga-SSO-120 PET for initial tumor staging may allow investigation of the prognostic value of ^{68}Ga-SSO-120 PET. Patients with sufficient ^{68}Ga-SSO-120 uptake might potentially

TABLE 3
^{68}Ga-SSO-120 Vs. ^{18}F-FDG Uptake (SUV_{max}/TLR_{max})

Region	SUV_{max}		TLR_{max}	
	Mean	*P*	Mean	*P*
Primary tumor				
SSO-120 PET	11.7	≤0.05	4.8	≤0.001
FDG PET	16.4		7.7	
Thoracic lymph node metastases				
SSO-120 PET	11.1	≤0.05	4.8	≤0.01
FDG PET	14.3		6.9	
Distant metastases				
SSO-120 PET	15.2	0.84	6.6	0.40
FDG PET	13.6		6.6	

P values are for Mann–Whitney *U* test.

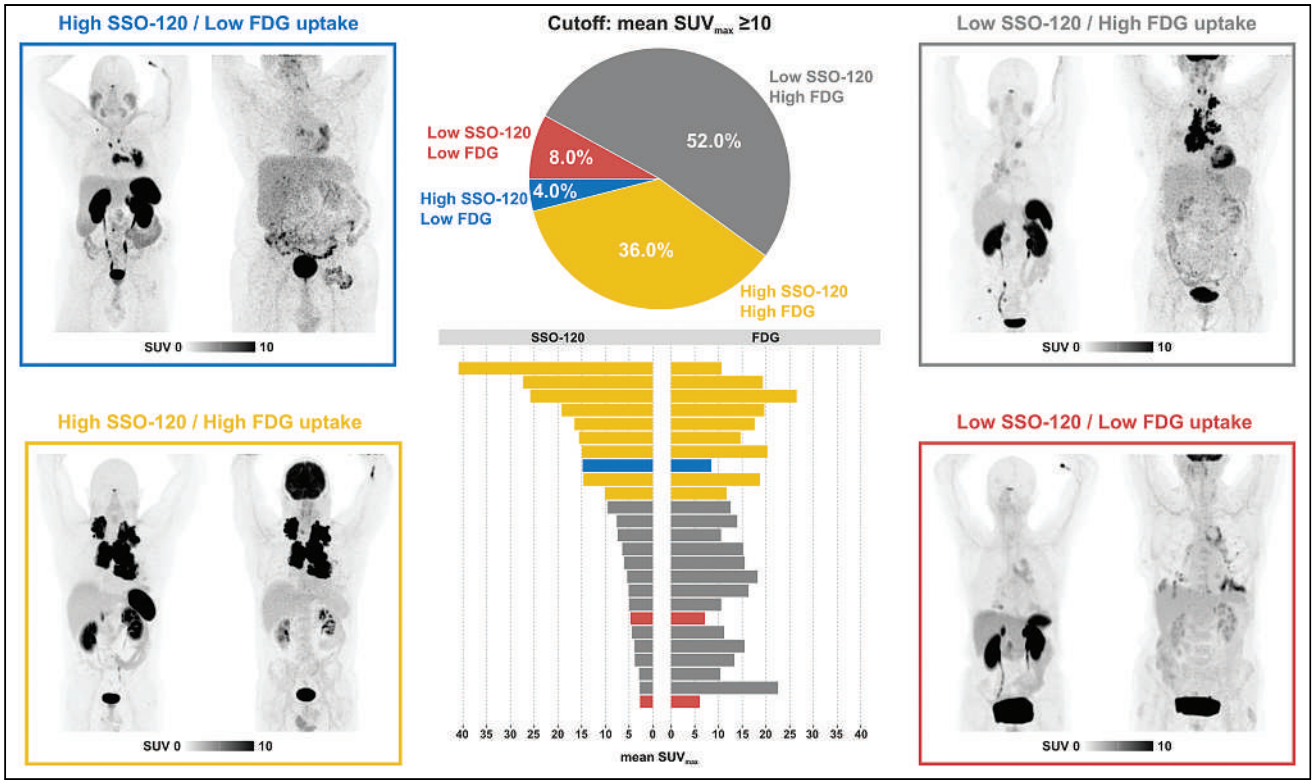

FIGURE 7. Patient-based comparison of ^{68}Ga-SSO-120 and ^{18}F-FDG uptake. Image examples (maximum-intensity projections) of patient groups show different patterns of low/high ^{68}Ga-SSO-120/^{18}F-FDG uptake. Low/high uptake was defined using mean SUV_{max} cutoff of ≥10. Graphs show distribution of different patient groups and comparison of mean ^{68}Ga-SSO-120 and mean ^{18}F-FDG SUV_{max} for every included patient. SUV_{max} refers to region-based mean SUV_{max} (mean from all ^{68}Ga-SSO-120–/^{18}F-FDG–positive regions per patient).

benefit from SSTR2-antagonist radionuclide therapy. The first investigations at our center indicated that the fraction of patients with high ^{68}Ga-SSO-120 uptake may be comparable between initial staging and restaging. It will be of particular interest to investigate whether SSTR2 expression remains stable in progressive disease, because other theranostic targets are frequently lost.

Thus far, to our knowledge, no applications of SSTR2-antagonist radionuclide therapy in SCLC patients have been described. SSTR agonists have been evaluated, but the results were not sufficient for broader clinical applications. For ^{90}Y-DOTATOC, in 6 SCLC patients no therapy response was observed (*31*). In a mixed cohort of 10 SCLC and NSCLC patients who underwent ^{90}Y-DOTA-lanreotide treatment, a response was described in 1 patient and stable disease in 5 patients (*32*). In another study, ^{90}Y-DOTATOC/DOTATATE was applied to 7 SCLC patients and ^{177}Lu-DOTATOC/DOTATATE was applied to 4 patients, but no treatment response was observed (*11*). In an evaluation of 4 SCLC patients who received ^{177}Lu-DOTATATE, 1 patient had a partial response and 1 patient had stable disease (*10*).

At this point, SSTR2 antagonists might be beneficial because they show increased uptake (in SCLC, an antagonist-to-agonist binding ratio of 4.5 was described) and prolonged residence times (*12*). In NET patients, application of ^{177}Lu-SSO-110 resulted in up to 10-fold increased tumor doses and favorable tumor-to-organ dose ratios compared with ^{177}Lu-DOTATATE (*15*), as well as promising response rates in a prospective phase I trial (*16*). However, an unexpectedly high rate of hematologic toxicity was problematic but was resolved by treatment with a reduced activity and by longer intervals between treatment cycles (*16*). In pretreated SCLC patients, careful monitoring should be performed, but SSTR2-antagonist radionuclide therapy can be justified in settings with exhausted standard-of-care options given the limited progression-free survival and overall survival of the disease. Moreover, considering the poor survival of patients with SCLC after first-line therapy and limited options in second-line therapy, SSTR2-directed radionuclide therapy might be an option in maintenance, such as in combination with immune checkpoint inhibitors (*33*). A multicenter phase I trial was designed to investigate ^{177}Lu-SSO-110 in SCLC and breast cancer patients but was terminated because of a high number of screening failures (NCT03773133); however, the only SCLC patient who was screened (but was excluded because of a brain metastasis) showed very good uptake in the primary tumor and (brain) metastases on ^{68}Ga-SSO-120 PET. As an alternative to ^{177}Lu-SSO-110, the SSTR2-antagonist ^{177}Lu-DOTA-LM3 did not induce high-grade adverse events in NET patients (*17*). Moreover, ^{161}Tb-labeled SSTR2 antagonists have the potential to open additional interesting theranostic opportunities due to their emitted low-energy and, thus, short-ranged β^--particles. In a preclinical study, ^{161}Tb-DOTA-LM3 showed greater effects on survival of SSTR-positive rat pancreatic AR42J cancer cells than did ^{177}Lu-DOTA-LM3, in both cell culture and subcutaneously inoculated cells in a mouse model (*34*).

Patient follow-up may also be used to investigate the prognostic value of ^{68}Ga-SSO-120 PET in primary staging of SCLC patients. Whereas SSTR expression in SCLC was previously assumed to be associated with less aggressive tumors and potential for favoring apoptosis (*5*), more recent in vitro and in vivo results suggest that in

this tumor entity SSTR may be a protumor survival signal (*29*). Consequently, in limited disease, patients with low SSTR expression showed improved survival (*29*). However, in a study including ^{68}Ga-DOTATATE PET, neither SUV metrics nor immunohistochemical scores were prognostic (*10*). This finding contrasts with ^{18}F-FDG PET–derived metabolic tumor volume and total lesion glycolysis, which were prognostic of overall and progression-free survival in a recent metaanalysis (*35*). In this context, it is of interest that the correlation between ^{18}F-FDG and ^{68}Ga-SSO-120 uptake was low (Fig. 6D; Supplemental Fig. 1D); therefore, ^{68}Ga-SSO-120 uptake cannot be predicted from ^{18}F-FDG uptake.

The study faces 2 main limitations. First, the timing between ^{18}F-FDG and ^{68}Ga-SSO-120 PET was heterogeneous, and some patients underwent treatment initiation between the 2 imaging modalities, potentially influencing ^{68}Ga-SSO-120 or ^{18}F-FDG uptake in the case of a hypothetical very early treatment response. However, the interval was short, with a maximum of 14 d between the 2 imaging modalities, and the CT images did not show major morphologic differences between ^{18}F-FDG and ^{68}Ga-SSO-120 PET (stable disease according to RECIST 1.1). Second, systemic histopathologic validation was not conducted for all lesions. However, we used a TNM classification from a clinical tumor board which was based on thoracoabdominal CT, brain MRI, whole-body PET, and endobronchial ultrasound-guided transbronchial needle aspiration to meet the highest demands of a reference standard in the setting of this retrospective analysis. Moreover, no direct comparison of the individual lesions on ^{68}Ga-SSO-120 and ^{18}F-FDG PET was performed. In the planning of the study, we intentionally chose a patient- and region-based analysis, as these parameters are clinically decisive for both primary staging and evaluation of global ^{68}Ga-SSO-120 uptake. In radionuclide therapy planning and restaging, however, a lesion-based comparison will be of additional interest to identify patients with ^{68}Ga-SSO-120/^{18}F-FDG mismatch, which might not be targeted by SSTR2-directed radionuclide therapy.

CONCLUSION

^{68}Ga-SSO-120 PET offers high diagnostic value in SCLC patients, with comparable detection rates and complementary information to the gold-standard, ^{18}F-FDG PET. ^{68}Ga-SSO-120 PET detected a slightly greater number of distant metastases, and ^{18}F-FDG PET detected a slightly greater number of contralateral thoracic lymph node metastases, without any changes in binary VALG classification. On ^{68}Ga-SSO-120 PET, brain metastases were well detectable, whereas the discernability of adrenal metastases could be limited. Consistent tumor uptake in most patients, with high uptake in 40%, highlights the theranostic potential of SSTR2 antagonists and warrants exploration of SSTR2-directed radionuclide therapy.

DISCLOSURE

This work was supported by the Universitätsmedizin Essen Clinician Scientist Academy (UMEA)/German Research Foundation (DFG, Deutsche Forschungsgemeinschaft) under grant FU356/12-2 to David Kersting. David Kersting also reports a research grant from Pfizer outside the submitted work. Marcel Wiesweg reports honoraria and an advisory role with Amgen, AstraZeneca, Daiichi Sankyo, GlaxoSmithKline, Janssen, Novartis, Pfizer, Roche, and Takeda and research funding from Bristol-Myers Squibb and Takeda outside the submitted work. Lale Umutlu is a speaker/advisory board member for Bayer Healthcare and Siemens Healthcare and received research grants from Siemens Healthcare outside the submitted work. Wolfgang Fendler reports fees from SOFIE Biosciences (research funding), Janssen (consultant, speaker), Calyx (consultant), Bayer (consultant, speaker, research funding), Parexel (image review), Novartis (speaker), and Telix (speaker) outside the submitted work. Martin Schuler reports honoraria for continuing medical education presentations from Amgen, Boehringer Ingelheim, Bristol-Myers Squibb, Janssen, MSD, Novartis, Roche, and Sanofi; research funding to the institution from AstraZeneca and Bristol Myers-Squibb; and a consultancy (compensated) from Amgen, AstraZeneca, Blueprint Medicines, Boehringer Ingelheim, Bristol Myers Squibb, GlaxoSmithKline, Janssen, Merck Serono, Novartis, Roche, Sanofi, and Takeda outside the submitted work. Ken Herrmann reports personal fees from Bayer, Sofie Biosciences, SIRTEX, Adacap, Curium, Endocyte, BTG, IPSEN, Siemens Healthineers, GE Healthcare, Amgen, Novartis, ymabs, Aktis Oncology, Theragnostics, and Pharma15; other fees from Sofie Biosciences; nonfinancial support from ABX; and grants from BTG outside the submitted work. No other potential conflict of interest relevant to this article was reported.

KEY POINTS

QUESTION: Is ^{68}Ga-SSO-120 PET a valuable imaging modality for primary staging of SCLC patients?

PERTINENT FINDINGS: ^{68}Ga-SSO-120 PET/CT images were evaluated for primary staging of SCLC in 31 patients and were compared with ^{18}F-FDG PET/CT in 25 patients. Per-patient and per-region tumor detection was comparable, with more distant metastases detected on ^{68}Ga-SSO-120 PET and more contralateral thoracic lymph node metastases detected on ^{18}F-FDG PET; the correlation of ^{68}Ga-SSO-120 and ^{18}F-FDG uptake was low.

IMPLICATIONS FOR PATIENT CARE: ^{68}Ga-SSO-120 PET offers comparable diagnostic precision and complementary information in SCLC patients when compared with the gold standard, ^{18}F-FDG PET. Tumor uptake greater than liver uptake in most patients, and high uptake in 40% of patients, highlight the theranostic potential of the SSTR2-antagonist pair ^{68}Ga-SSO-120/^{177}Lu-SSO-110.

REFERENCES

1. Herbst RS, Heymach JV, Lippman SM. Lung cancer. *N Engl J Med.* 2008;359:1367–1380.
2. Gazdar AF, Bunn PA, Minna JD. Small-cell lung cancer: what we know, what we need to know and the path forward. *Nat Rev Cancer.* 2017;17:725–737.
3. Fischer BM, Mortensen J, Langer SW, et al. A prospective study of PET/CT in initial staging of small-cell lung cancer: comparison with CT, bone scintigraphy and bone marrow analysis. *Ann Oncol.* 2007;18:338–345.
4. Brink I, Schumacher T, Mix M, et al. Impact of [^{18}F]FDG-PET on the primary staging of small-cell lung cancer. *Eur J Nucl Med Mol Imaging.* 2004;31:1614–1620.
5. Callison JC Jr, Walker RC, Massion PP. Somatostatin receptors in lung cancer: from function to molecular imaging and therapeutics. *J Lung Cancer.* 2011;10:69–76.
6. Sadowski SM, Neychev V, Millo C, et al. Prospective study of ^{68}Ga-DOTATATE positron emission tomography/computed tomography for detecting gastro-enteropancreatic neuroendocrine tumors and unknown primary sites. *J Clin Oncol.* 2016;34:588–596.
7. Kayani I, Conry BG, Groves AM, et al. A comparison of ^{68}Ga-DOTATATE and ^{18}F-FDG PET/CT in pulmonary neuroendocrine tumors. *J Nucl Med.* 2009;50:1927–1932.
8. Strosberg J, El-Haddad G, Wolin E, et al. Phase 3 trial of ^{177}Lu-dotatate for midgut neuroendocrine tumors. *N Engl J Med.* 2017;376:125–135.
9. Strosberg JR, Caplin ME, Kunz PL, et al. ^{177}Lu-dotatate plus long-acting octreotide versus highdose long-acting octreotide in patients with midgut neuroendocrine

tumours (NETTER-1): final overall survival and long-term safety results from an open-label, randomised, controlled, phase 3 trial. *Lancet Oncol.* 2021;22:1752–1763.
10. Lapa C, Hanscheid H, Wild V, et al. Somatostatin receptor expression in small cell lung cancer as a prognostic marker and a target for peptide receptor radionuclide therapy. *Oncotarget.* 2016;7:20033–20040.
11. Sollini M, Farioli D, Froio A, et al. Brief report on the use of radiolabeled somatostatin analogs for the diagnosis and treatment of metastatic small-cell lung cancer patients. *J Thorac Oncol.* 2013;8:1095–1101.
12. Fani M, Nicolas GP, Wild D. Somatostatin receptor antagonists for imaging and therapy. *J Nucl Med.* 2017;58(suppl 2):61S–66S.
13. Nicolas GP, Schreiter N, Kaul F, et al. Sensitivity comparison of ^{68}Ga-OPS202 and ^{68}Ga-DOTATOC PET/CT in patients with gastroenteropancreatic neuroendocrine tumors: a prospective phase II imaging study. *J Nucl Med.* 2018;59:915–921.
14. Zhu W, Cheng Y, Wang X, et al. Head-to-head comparison of ^{68}Ga-DOTA-JR11 and ^{68}Ga-DOTATATE PET/CT in patients with metastatic, well-differentiated neuroendocrine tumors: a prospective study. *J Nucl Med.* 2020;61:897–903.
15. Wild D, Fani M, Fischer R, et al. Comparison of somatostatin receptor agonist and antagonist for peptide receptor radionuclide therapy: a pilot study. *J Nucl Med.* 2014;55:1248–1252.
16. Reidy-Lagunes D, Pandit-Taskar N, O'Donoghue JA, et al. Phase I trial of well-differentiated neuroendocrine tumors (NETs) with radiolabeled somatostatin antagonist ^{177}Lu-satoreotide tetraxetan. *Clin Cancer Res.* 2019;25:6939–6947.
17. Baum RP, Zhang J, Schuchardt C, Muller D, Macke H. First-in-humans study of the SSTR antagonist ^{177}Lu-DOTA-LM3 for peptide receptor radionuclide therapy in patients with metastatic neuroendocrine neoplasms: dosimetry, safety, and efficacy. *J Nucl Med.* 2021;62:1571–1581.
18. Virgolini I, Bahri S, Kjaer A, et al. A randomized, factorial phase II study to determine the optimal dosing regimen for ^{68}Ga-satoreotide trizoxetan as an imaging agent in patients with gastroenteropancreatic neuroendocrine tumors. *J Nucl Med.* 2022;63:376–383.
19. Weber M, Jentzen W, Hofferber R, et al. Evaluation of [^{68}Ga]Ga-PSMA PET/CT images acquired with a reduced scan time duration in prostate cancer patients using the digital biograph vision. *EJNMMI Res.* 2021;11:21.
20. Nicholson AG, Chansky K, Crowley J, et al. The International Association for the Study of Lung Cancer Lung Cancer Staging Project: proposals for the revision of the clinical and pathologic staging of small cell lung cancer in the forthcoming eighth ed. of the TNM classification for lung cancer. *J Thorac Oncol.* 2016;11:300–311.
21. Wahl RL, Jacene H, Kasamon Y, Lodge MA. From RECIST to PERCIST: evolving considerations for PET response criteria in solid tumors. *J Nucl Med.* 2009;50(suppl 1):122S–150S.
22. Hofheinz F, Butof R, Apostolova I, et al. An investigation of the relation between tumor-to-liver ratio (TLR) and tumor-to-blood standard uptake ratio (SUR) in oncological FDG PET. *EJNMMI Res.* 2016;6:19.
23. Fendler WP, Pabst KM, Kessler L, et al. Safety and efficacy of ^{90}Y-FAPI-46 radioligand therapy in patients with advanced sarcoma and other cancer entities. *Clin Cancer Res.* 2022;28:4346–4353.
24. Martucci F, Pascale M, Valli MC, et al. Impact of ^{18}F-FDG PET/CT in staging patients with small cell lung cancer: a systematic review and meta-analysis. *Front Med (Lausanne).* 2020;6:336.
25. Nicolas GP, Beykan S, Bouterfa H, et al. Safety, biodistribution, and radiation dosimetry of ^{68}Ga-OPS202 in patients with gastroenteropancreatic neuroendocrine tumors: a prospective phase I imaging study. *J Nucl Med.* 2018;59:909–914.
26. Guberina M, Darwiche K, Hautzel H, et al. Patterns of nodal spread in stage III NSCLC: importance of EBUS-TBNA and ^{18}F-FDG PET/CT for radiotherapy target volume definition. *Radiat Oncol.* 2021;16:176.
27. Krenning EP, Bakker WH, Breeman WA, et al. Localisation of endocrine-related tumours with radioiodinated analogue of somatostatin. *Lancet.* 1989;1:242–244.
28. Erlandsson A, Forssell-Aronsson E, Seidal T, Bernhardt P. Binding of TS1, an anti-keratin 8 antibody, in small-cell lung cancer after ^{177}Lu-DOTA-Tyr^3-octreotate treatment: a histological study in xenografted mice. *EJNMMI Res.* 2011;1:19.
29. Lehman JM, Hoeksema MD, Staub J, et al. Somatostatin receptor 2 signaling promotes growth and tumor survival in small-cell lung cancer. *Int J Cancer.* 2019;144:1104–1114.
30. Gay CM, Stewart CA, Park EM, et al. Patterns of transcription factor programs and immune pathway activation define four major subtypes of SCLC with distinct therapeutic vulnerabilities. *Cancer Cell.* 2021;39:346–360.e7.
31. Pless M, Waldherr C, Maecke H, Buitrago C, Herrmann R, Mueller-Brand J. Targeted radiotherapy for small cell lung cancer using ^{90}yttrium-DOTATOC, an yttrium-labelled somatostatin analogue: a pilot trial. *Lung Cancer.* 2004;45:365–371.
32. Virgolini I, Britton K, Buscombe J, Moncayo R, Paganelli G, Riva P. In- and Y-DOTA-lanreotide: results and implications of the MAURITIUS trial. *Semin Nucl Med.* 2002;32:148–155.
33. Kim C, Liu SV, Subramaniam DS, et al. Phase I study of the ^{177}Lu-DOTA^0-Tyr^3-octreotate (Lutathera) in combination with nivolumab in patients with neuroendocrine tumors of the lung. *J Immunother Cancer.* 2020;8:e000980.
34. Borgna F, Haller S, Rodriguez JMM, et al. Combination of terbium-161 with somatostatin receptor antagonists: a potential paradigm shift for the treatment of neuroendocrine neoplasms. *Eur J Nucl Med Mol Imaging.* 2022;49:1113–1126.
35. Hope TA, Bergsland EK, Bozkurt MF, et al. Appropriate use criteria for somatostatin receptor PET imaging in neuroendocrine tumors. *J Nucl Med.* 2018;59:66–74.

The Association Between [^{68}Ga]PSMA PET/CT Response and Biochemical Progression in Patients with High-Risk Prostate Cancer Receiving Neoadjuvant Therapy

Mengxia Chen*[1,2], Yao Fu*[3], Shan Peng[3], Shiming Zang[4], Shuyue Ai[4], Junlong Zhuang[1,2], Feng Wang[4], Xuefeng Qiu[1,2], and Hongqian Guo[1,2]

[1]*Department of Urology, Affiliated Drum Tower Hospital, Medical School of Nanjing University, Nanjing, China;* [2]*Institute of Urology, Nanjing University, Nanjing, China;* [3]*Department of Pathology, Affiliated Drum Tower Hospital, Medical School of Nanjing University, Nanjing, China; and* [4]*Department of Nuclear Medicine, Nanjing First Hospital, Nanjing Medical University, Nanjing, China*

Our previous study found that the prostate-specific membrane antigen (PSMA) PET/CT response of primary prostate cancer (PCa) to neoadjuvant therapy can predict the pathologic response. This study was designed to investigate the association between [^{68}Ga]PSMA PET/CT changes and biochemical progression-free survival (bPFS) in high-risk patients who underwent neoadjuvant therapy before radical prostatectomy (RP). **Methods:** Seventy-five patients with high-risk PCa in 2 phase II clinical trials who received neoadjuvant therapy before RP were included. The patients received androgen deprivation therapy plus docetaxel ($n = 33$) or androgen deprivation therapy plus abiraterone ($n = 42$) as neoadjuvant treatment. All patients had serial [^{68}Ga]PSMA PET/CT scans before and after neoadjuvant therapy. Age, initial prostate-specific antigen level, nadir prostate-specific antigen level before RP, tumor grade at biopsy, treatment regimen, clinical T stage, PET imaging features, pathologic N stage, and pathologic response on final pathology were included for univariate and multivariate Cox regression analyses to identify independent predictors of bPFS. **Results:** With a median follow-up of 30 mo, 18 patients (24%) experienced biochemical progression. Multivariate Cox regression analyses revealed that only SUV_{max} derived from posttreatment [^{68}Ga]PSMA PET/CT and pathologic response on final pathology were independent factors for the prediction of bPFS, with hazard ratios of 1.02 (95% CI, 1.00–1.04; $P = 0.02$) and 0.12 (95% CI, 0.02–0.98; $P = 0.048$), respectively. Kaplan–Meier analysis revealed that patients with a favorable [^{68}Ga]PSMA PET/CT response (posttreatment $SUV_{max} < 8.5$) or a favorable pathologic response (pathologic complete response or minimal residual disease) had a significantly lower rate of 3-y biochemical progression. **Conclusion:** Our results indicated that [^{68}Ga]PSMA PET/CT response was an independent risk factor for the prediction of bPFS in patients with high-risk PCa receiving neoadjuvant therapy and RP, suggesting [^{68}Ga]PSMA PET/CT to be an ideal tool to monitor response to neoadjuvant therapy.

Key Words: [^{68}Ga]PSMA PET/CT; prostate cancer; neoadjuvant therapy; biochemical progression; prediction

J Nucl Med 2023; 64:1550–1555
DOI: 10.2967/jnumed.122.265368

Patients with high-risk prostate cancer (PCa) have a significant risk of biochemical recurrence and distant metastases after radical prostatectomy (RP) (*1*), despite the standard therapies of external-beam radiation therapy in combination with long-term androgen deprivation therapy (ADT) and RP plus extended lymph node dissection (*2*). Though neoadjuvant therapy before RP for patients with high-risk PCa still remains investigational, results from phase II trials have indicated a favorable pathologic response to neoadjuvant ADT combined with new-generation androgen receptor pathway inhibitors (*3–8*) or docetaxel chemotherapy (*9,10*).

A favorable pathologic response, defined as a pathologic complete response (pCR) or minimal residual disease (residual tumor ≤ 0.5 cm), has been widely applied as the primary endpoint to evaluate the efficacy of neoadjuvant therapy (*3,4,6,8*). A significant correlation between pCR and improved long-term oncologic outcomes has been verified in breast (*11*) and bladder cancer (*12*). However, whether a favorable pathologic response after neoadjuvant therapy can translate to better long-term oncologic outcomes, such as progression-free and metastasis-free survival, remains unclear in patients with high-risk PCa.

Prostate-specific membrane antigen (PSMA)–based PET is a promising technique for both initial staging (*13*) and restaging of biochemical recurrence (*14,15*). Recently, accumulative evidence also indicated that [^{68}Ga]PSMA PET/CT could be applied to monitor response in patients receiving systematic therapies (*16–19*). Our previous study demonstrated that [^{68}Ga]PSMA PET/CT performed better than prostate-specific antigen (PSA) in diagnosing a pathologic response to neoadjuvant ADT plus abiraterone, with SUV_{max} being an independent predictive factor for a favorable pathologic response (*19*). However, the relationship between [^{68}Ga]PSMA PET/CT changes and oncologic outcomes in neoadjuvant settings remains unknown.

To investigate the potential relationship between [^{68}Ga]PSMA PET/CT response and biochemical progression, this study analyzed patients with high-risk localized or locally advanced PCa treated with neoadjuvant therapy and RP who, in 2 clinical trials, had serial [^{68}Ga]PSMA PET/CT scans before and after neoadjuvant therapy.

MATERIALS AND METHODS

Study Design and Participants

Our center conducted 2 phase II clinical trials (NCT04356430 and NCT04869371) that were designed to investigate the efficacy of

Received Jan. 2, 2023; revision accepted May 10, 2023.
For correspondence or reprints, contact Hongqian Guo (dr.ghq@nju.edu.cn) or Xuefeng Qiu (xuefeng_qiu@nju.edu.cn).
*Contributed equally to this work.
Published online Jul. 20, 2023.

neoadjuvant ADT plus docetaxel or abiraterone for patients with high-risk localized or advanced PCa. Patients who met the following criteria were included: ADT plus docetaxel or abiraterone as neoadjuvant treatment; serial [^{68}Ga]PSMA PET/CT scans before and after neoadjuvant therapy; and at least 12 mo of follow-up since randomization, unless biochemical progression had occurred. The exclusion criterion was any adjuvant treatment (ADT or radiotherapy) after RP or persistence of PSA after RP (PSA > 0.2 ng/mL 8 wk after RP). Finally, 75 patients were included for analysis; the study flowchart is shown in Figure 1. The study was approved by the Ethics Committee of the Drum Tower Hospital (2019-214 and 2020-314), and all patients provided written informed consent. Clinical covariates including initial age, PSA level during each visit, preoperative clinical T stage, and International Society of Urological Pathology grade at biopsy were documented.

Treatment Intervention

Patients received 2 different therapies: ADT plus docetaxel or ADT plus abiraterone according to previously published protocols (*3,9*). Briefly, ADT was applied by a luteinizing hormone–releasing hormone analog every 12 wk. The ADT-plus-docetaxel group was additionally administered docetaxel, 75 mg/m^2 of body surface area, every 3 wk for 6 cycles plus 5 mg of prednisone acetate twice a day. The ADT-plus-abiraterone group took an additional 1,000 mg of abiraterone acetate and 5 mg of prednisone acetate orally once a day. After 6 mo of neoadjuvant therapy, the participants underwent robot-assisted RP and extended lymph node dissection. The median interval between the first PET/CT scan and the initiation of neoadjuvant therapy was 8 d (interquartile range [IQR], 6–12 d), the median interval between the initiation of neoadjuvant therapy and the second PET/CT scan was 165 d (IQR, 157–179 d), and the median interval from the second PET/CT scan to surgery was 9 d (IQR, 4–11 d).

Follow-up and Outcomes

PSA and testosterone levels were assessed every 4 wk during neoadjuvant treatment, 2 d before RP, and every 4 wk after RP. Biochemical progression was defined as a postoperative serum PSA level greater than 0.2 ng/mL on 2 separate occasions at minimally 2-wk intervals (*20*). Biochemical progression-free survival (bPFS) was defined as the time from randomization to biochemical progression or death.

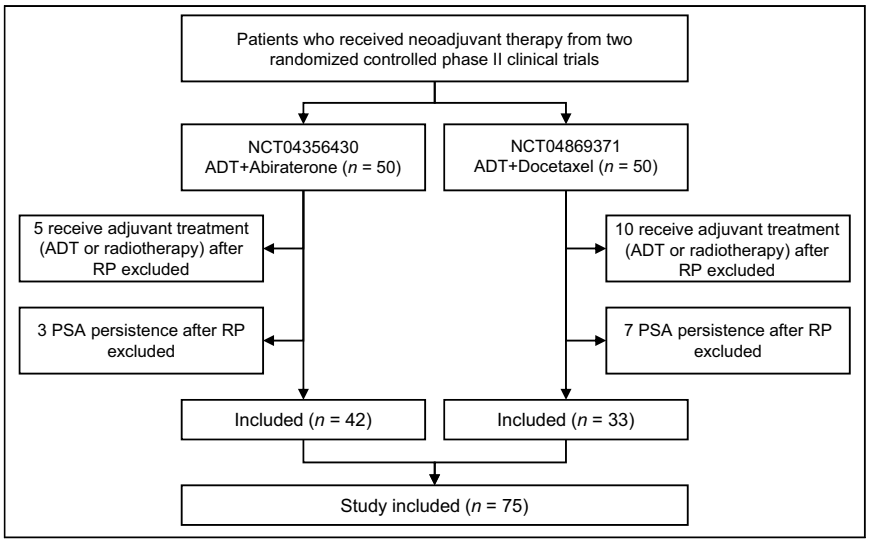

FIGURE 1. Study flowchart with excluded patients and reason for exclusion.

PET/CT Imaging Acquisition and Evaluation

[^{68}Ga]PSMA-11 PET/CT scanning was performed 1 h after intravenous injection of [^{68}Ga]PSMA-11. With a uMI 780 PET/CT scanner (United Imaging Healthcare), a CT scan (130 keV, 80 mAs) and a static emission scan were performed from the vertex to the proximal legs, corrected for dead time, scatter, and decay (*19*). [^{68}Ga]PSMA-ligand PET/CT images were reviewed by 2 nuclear medicine physicians with over 10 y of reading experience in the interpretation of PSMA-targeted PET. Lesions were delineated by higher uptake than background by a RadiAnt DICOM viewer (version 2022.1.1; Medixant). The PSMA intensity of the lesions was measured as the SUV_{max} in the delineated area. For patients with multiple lesions, the one with the highest SUV_{max} was recognized as the index tumor and recorded. For patients with no obvious PSMA uptake after neoadjuvant therapy, SUV_{max} was determined at the location of the same tumor as found on the first scan, by comparing the anatomic position through other tissues such as bladder or bone and excluding respective normal organs that demonstrate high uptake as part of normal biodistribution, including the bladder. Twelve patients did not have any obvious uptake on follow-up scans, with a median SUV_{max} of 3.06 (IQR, 2.23–3.37). The median time frame between 2 subsequent scans was 179 d (IQR, 169–188 d). The change in SUV_{max} between the 2 scans was defined as the SUV_{max} decline percentage, which was calculated by $\frac{\text{pretreatment SUV}_{max} - \text{posttreatment SUV}_{max}}{\text{pretreatment SUV}_{max}} \times 100\%$.

Whole-Mount Histologic Imaging and Pathologic Response

After robot-assisted RP, a whole-mount histologic sample was fixed and stained as previously described (*19,21*). To obtain the final pathologic result, all whole-mount histology slides were subsequently digitalized by a scanning system (NanoZoomer Digital Pathology) and interpreted by 2 dedicated genitourinary pathologists masked to clinical information. Residual tumors in the posttreatment surgical resection specimen were determined from the bidimensional diameters of the primary tumor bed as previously described (*22*). A favorable pathologic response was defined as pCR or as minimal residual disease whose largest cross-sectional dimension was less than 5 mm (*22*). Pathologic T stage, lymph node metastasis, and a positive margin were also recorded.

Statistical Analysis

Continuous nonnormally distributed variables were reported by median and IQRs. Univariable and multivariable Cox regression was applied to identify factors associated with clinical outcomes. The cutoff for the posttreatment SUV_{max} of the index tumor for prediction of bPFS was determined by X-tile plotting (*23*). Kaplan–Meier analysis was used to test the ability of selected variables to determine the survival probability, and the log-rank test was used to compare differences among groups. A significance level of 5% was applied. All analyses were conducted by SPSS software (version 22.0; IBM Corp.)

RESULTS

Patient Characteristics

The clinical and pathologic variables of the 75 patients are shown in Table 1. The median age was 70 y (IQR, 65–73 y). The initial PSA level before biopsy was 40.10 ng/mL (IQR, 19.24–80.02 ng/mL), followed by a nadir PSA of 0.04 ng/mL (IQR, 0.01–0.12 ng/mL) before RP. Thirty-three patients (44%) received ADT plus docetaxel, and 42 (56%) received ADT plus abiraterone. According to final pathology, 22 patients (29.3%) showed lymph node metastases and 15 patients

TABLE 1
Pre- and Postoperative Characteristics of 75 High-Risk PCa Patients with [^{68}Ga]PSMA PET/CT Scanning Before and After Neoadjuvant Treatment

Characteristic	Value
Age (y)	70 (65–73)
Initial PSA (ng/mL)	40.10 (19.24–80.02)
Nadir PSA before RP (ng/mL)	0.04 (0.01–0.12)
Neoadjuvant treatment	
ADT + chemotherapy	33 (44)
ADT + abiraterone	42 (56)
ISUP grade at biopsy	
2	3 (4)
3	13 (17.3)
4	39 (52.0)
5	20 (26.7)
Initial clinical T stage	
T2	23 (30.7)
T3a	11 (14.7)
T3b	41 (54.7)
Postoperative characteristics	
Pathologic T stage	
T2	38 (50.6)
T3a	13 (17.3)
T3b	24 (32.0)
Pathologic N stage	
N0	53 (70.7)
N1	22 (29.3)
Positive margin	
Positive	15 (20.0)
Negative	60 (80.0)
pCR or MRD	
No	50 (66.7)
Yes	25 (33.3)

ISUP = International Society of Urological Pathology; MRD = minimal residual disease.

Qualitative data are number and percentage; continuous data are median and IQR.

(20.0%) had a positive surgical margin. Notably, 25 patients (33.3%) achieved a favorable pathologic response (pCR or minimal residual disease) on the final pathology. Most index tumor lesions underwent a significant decline in [^{68}Ga]PSMA-11 intensity, from a median pretreatment SUV_{max} of 18.9 (IQR, 12.45–27.6) to a median posttreatment SUV_{max} of 5.61 (IQR, 4.51–7.91). The median follow-up for all participants was 30 mo (IQR, 20.0–41.5 mo). Eighteen patients (24%) experienced biochemical progression at a median follow-up of 30 mo since randomization.

Univariate and Multivariate Cox Regression Analyses of Clinical and PET Imaging Parameters for Prediction of bPFS

Among all incorporated variables, clinical staging of T3b, pretreatment SUV_{max}, posttreatment SUV_{max}, SUV_{max} decline percentage, and a favorable pathologic response on final pathology were significantly associated with bPFS according to Cox proportional-hazards regression (Table 2), with hazard ratios of 4.68 (95% CI, 1.04–21.02; $P = 0.04$), 1.02 (95% CI, 1.00–1.05; $P = 0.02$), 1.04 (95% CI, 1.02–1.06; $P = 0.00$), 1.00 (95% CI, 0.99–1.00; $P = 0.05$), and 0.10 (95% CI, 0.01–0.65; $P = 0.02$), respectively.

To avoid the possible dependence of different PET-based variables, we made the multivariate model of pathologic response with each SUV-based variable separately (Table 3). We found that only posttreatment SUV_{max} and a favorable pathologic response on final pathology were independent variables for the prediction of bPFS, with hazard ratios of 1.02 (95% CI, 1.00–1.04; $P = 0.02$) and 0.12 (95% CI, 0.02–0.98; $P = 0.048$), respectively (model 2). However, when posttreatment SUV_{max} was not included in the model, only a favorable pathologic response on final pathology was an independent variable for the prediction of bPFS, with hazard ratios of 0.11 (95% CI, 0.01–0.89; $P = 0.04$) in model 1 and 0.10 (95% CI, 0.01–0.80; $P = 0.03$) in model 3.

Predictive Value of PET Imaging Parameters and Pathologic Response for bPFS

With a cutoff of 8.5, Kaplan–Meier analysis revealed a significant difference in bPFS between patients with a posttreatment SUV_{max} of more than 8.5 and of less than 8.5, with a 36-mo biochemical progression-free rate of 29.4% (IQR, 7.6%–51.2%) and 97.6% (IQR, 92.6%–100%), respectively (log-rank $P < 0.001$) (Fig. 2A). Patients with and without a favorable pathologic response also had a significant difference in bPFS ($P = 0.002$), with a 36-mo biochemical recurrence-free rate of 100% (IQR, 100%–100%) and 55.2% (IQR, 35.0%–75.4%), respectively (Fig. 2B). Two representative cases, with and without biochemical progression, are shown in Supplemental Figures 1 and 2, respectively (supplemental materials are available at http://jnm.snmjournals.org). The patient who experienced biochemical progression had a higher posttreatment SUV_{max} and an unfavorable pathologic response.

DISCUSSION

This study was designed to investigate the relationship between response on [^{68}Ga]PSMA PET/CT and bPFS in patients with high-risk localized or locally advanced PCa who received neoadjuvant therapy and RP. Our results indicated that [^{68}Ga]PSMA PET/CT–derived SUV_{max} after neoadjuvant therapy was an independent risk factor for the prediction of bPFS. Patients with favorable responses on [^{68}Ga]PSMA PET/CT after neoadjuvant therapy ($SUV_{max} < 8.5$) had better bPFS than those with unfavorable responses. This is the first study, to our knowledge, to suggest that response on [^{68}Ga]PSMA PET/CT could be applied as an ideal tool to predict the oncologic outcomes of PCa patients receiving neoadjuvant therapy.

The pathologic response was set as the primary endpoint in several phase II clinical trials designed to investigate the efficacy and safety of neoadjuvant ADT in combination with androgen receptor pathway inhibitors for high-risk localized PCa. In addition, pCR was set as the coprimary endpoint in the ongoing phase III clinical trial, which was designed to determine whether treatment with apalutamide plus ADT before and after RP in patients with high-risk localized or locally advanced PCa (NCT03767244, PROTEUS trial) can bring benefit to those patients. In breast cancer and bladder cancer, the pathologic response has been well indicated to correlate significantly with improved long-term oncologic outcomes (*11,12*). Moreover, residual breast cancer burden after neoadjuvant

TABLE 2
Univariate Cox Regression Analyses for Risk of Biochemical Progression

Variable	HR	*P*
Age (y)	0.99 (0.92–1.05)	0.68
Initial PSA	1.00 (0.99–1.01)	0.90
Nadir PSA before RP	1.32 (0.98–1.77)	0.07
ISUP grade at biopsy	1.27 (0.65–2.47)	0.48
Treatment intervention (ADT + abiraterone vs. ADT + docetaxel)	0.98 (0.31–3.10)	0.98
Initial clinical T stage		
T2		0.03*
T3a	0.62 (0.06–6.86)	0.69
T3b	4.68 (1.04–21.02)	0.04*
SUV_{max} before treatment	1.02 (1.00–1.05)	0.02*
SUV_{max} after treatment	1.04 (1.02–1.06)	0.00*
SUV_{max} decline percentage	1.00 (0.99–1.00)	0.05*
Pathologic N stage (pN1 vs. pN0)	1.44 (0.50–4.18)	0.50
pCR or minimal residual disease (yes vs. no)	0.10 (0.01–0.65)	0.02*

ISUP = International Society of Urological Pathology.
Data in parentheses are 95% CIs.

therapy has been shown capable of predicting oncologic outcomes after neoadjuvant chemotherapy (*22*). Therefore, the pathologic response was set as the primary endpoint to evaluate the efficacy of neoadjuvant therapies in these cancers (*24–27*). However, the positive association between a favorable pathologic response and better long-term oncologic outcomes, such as bPFS and metastasis-free survival, remains unclear (*28*). In a pooled analysis, a favorable pathologic response after neoadjuvant therapy was demonstrated to be significantly associated with a better 3-y biochemical recurrence-free survival (*4,5*). In our study, a favorable pathologic response, defined as pCR or minimal residual disease, was found to be significantly associated with a lower rate of biochemical progression in a median follow-up of 30 mo, a finding that was consistent with previously published data (*4*).

Significant heterogeneity was found in pathologic response after neoadjuvant therapy, with a favorable pathologic response rate of 15.7%–62% in the previously published studies (*3–6,19*). Though some preliminary results suggested pathologic response as a surrogate endpoint to evaluate the efficacy of neoadjuvant therapy, efficacy could be revealed only after RP. A noninvasive biomarker to monitor response during or after neoadjuvant therapy is urgently needed to adopt novel treatment approaches and identify candidates for the subsequent RP.

PSMA PET/CT is currently recommended by guidelines for initial staging and restaging because of its high sensitivity and specificity (*13–15*). Patterns of change in PSMA PET/CT have been well indicated to be significantly associated with response in patients with metastatic hormone-sensitive or castration-resistant

TABLE 3
Multivariate Cox Regression Analyses for Risk of Biochemical Progression with SUV-Based Variable

	Model 1		Model 2		Model 3	
Variable	HR	*P*	HR	*P*	HR	*P*
Initial clinical T stage						
T2		0.09		0.15		0.08
T3a	0.42 (0.04–4.78)	0.48	0.38 (0.03–4.35)	0.43	0.39 (0.03–4.54)	0.46
T3b	2.98 (0.66–13.51)	0.16	2.39 (0.0–11.28)	0.27	2.95 (0.65–13.48)	0.16
SUV_{max} before treatment	1.01 (0.99–1.04)	0.35	—		—	
SUV_{max} after treatment	—	—	1.02 (1.00–1.04)	0.02*	—	
SUV_{max} decline percentage	—	—	—	—	1.00 (1.00–1.00)	0.46
pCR or MRD (yes vs. no)	0.11 (0.01–0.89)	0.04*	0.12 (0.02–0.98)	0.048*	0.10 (0.01–0.80)	0.03*

*Statistically significant value.
HR = hazard ratio; MRD = minimal residual disease
Data in parentheses are 95% CIs.

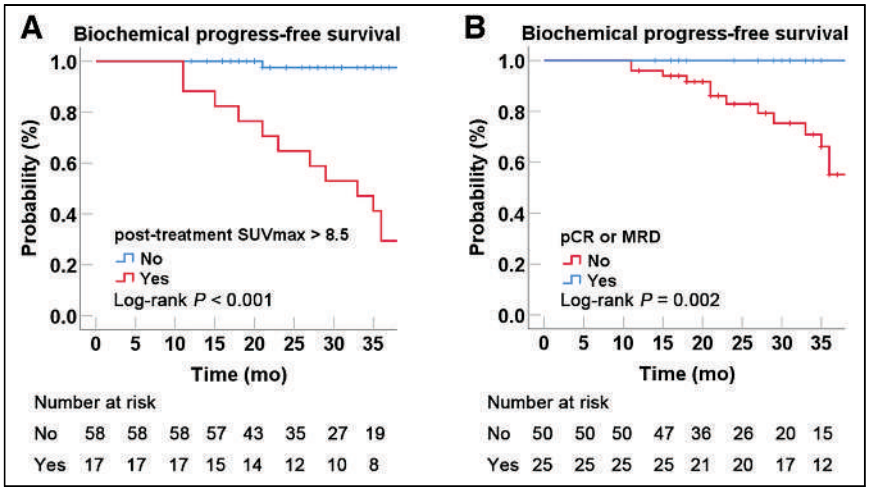

FIGURE 2. bPFS in patients with different pathologic responses on final pathology (A) and after neoadjuvant therapy [^{68}Ga]PSMA PET/CT (B). Favorable pathologic response was defined as pCR or minimal residual disease < 0.5 cm (pCR or minimal residual disease), whereas favorable [^{68}Ga]PSMA PET/CT response was defined as posttreatment SUV_{max} < 8.5 on [^{68}Ga]PSMA PET/CT.

PCa to docetaxel chemotherapy or new-generation androgen receptor pathway inhibitors (*29–33*). Unlike pathologic response, which could be revealed only after RP, [^{68}Ga]PSMA PET/CT, as a noninvasive and repeatable imaging tool, could provide predictive information during or after neoadjuvant therapy, suggesting [^{68}Ga]PSMA PET/CT to be an ideal biomarker to monitor treatment response. In fact, we previously reported the utility of [^{68}Ga]PSMA PET/CT in the prediction of pathologic response in patients with high-risk localized or locally advanced PCa receiving neoadjuvant ADT plus abiraterone for 6 mo (*19*). With a median follow-up of 30 mo, the present study revealed that PSMA uptake on PET/CT after neoadjuvant treatment was an independent risk factor to predict bPFS. In addition, patients with a better response on [^{68}Ga]PSMA PET/CT after neoadjuvant therapy (SUV_{max} < 8.5) had a significantly lower rate of biochemical progression than those with poor responses. Our results further verified the positive association between the response of [^{68}Ga]PSMA PET/CT and response in high-risk patients receiving neoadjuvant therapies. Of interest, SUV decline was not an independent risk factor for the prediction of bPFS in the multivariate analysis, though it was associated with biochemical progression in univariate analysis. Apparently, posttreatment SUV_{max} could better reflect residual tumor burden, which has been demonstrated to be significantly associated with longer oncologic outcomes (*19*).

The inherent limitation of this study is the limited sample size because of the relatively strict inclusion criteria. However, with patients pooled from 2 prospective cohorts, basic characteristics and treatment procedures were well balanced and standardized despite the retrospective design. Another limitation is the relatively short follow-up time, allowing us to apply only bPFS as the clinical outcome and not longer oncologic outcomes such as metastasis-free survival or castration-resistant PCa–free survival. A larger prospective study with longer follow-up is needed for further validation. In addition, we included only [^{68}Ga]PSMA PET/CT–derived SUV in the Cox regression analysis. The role of [^{68}Ga]PSMA PET/CT–derived radiomics in predicting bPFS needs to be further investigated. However, to our knowledge, our study is the first to reveal the role of [^{68}Ga]PSMA PET/CT response in the prediction of oncologic outcomes in high-risk patients receiving neoadjuvant therapy.

CONCLUSION

Our study indicated the predictive role of PSMA PET for patients with high-risk localized or locally advanced PCa receiving neoadjuvant therapies. Patients with better responses on [^{68}Ga]PSMA PET/CT after neoadjuvant therapies had significantly longer bPFS than did those with poor responses. Combined with our previous results indicating the association between [^{68}Ga]PSMA PET/CT changes and pathologic response, our studies suggest that [^{68}Ga]PSMA PET/CT is an ideal tool to monitor the response of primary PCa to neoadjuvant therapies and that patients with a higher posttreatment SUV_{max} (>8.5) could get limited benefits from neoadjuvant therapy after RP. Radiotherapy might be a better option for these patients. In addition, posttreatment SUV_{max} could be considered an idea biomarker for adjustment of neoadjuvant therapy regimens.

DISCLOSURE

This study is supported by grants from the National Natural Science Foundation of China (82172639, 81972388), the Mobility Programme of the National Natural Science Foundation of China (M-0670), and the Natural Science Foundation of Jiangsu Province (BK 20210023). No other potential conflict of interest relevant to this article was reported.

KEY POINTS

QUESTION: Could response on [^{68}Ga]PSMA PET/CT be a surrogate endpoint for patients with high-risk localized PCa receiving neoadjuvant therapy?

PERTINENT FINDINGS: In this pooled cohort of 75 patients from 2 clinical trials evaluating the efficacy of neoadjuvant treatment in high-risk PCa, we found that SUV_{max} derived from posttreatment [^{68}Ga]PSMA PET/CT and pathologic response on final pathology were independent factors for the prediction of bPFS.

IMPLICATIONS FOR PATIENT CARE: [^{68}Ga]PSMA PET/CT is an ideal tool to monitor response to neoadjuvant therapy.

REFERENCES

1. Rider JR, Sandin F, Andrén O, Wiklund P, Hugosson J, Stattin P. Long-term outcomes among noncuratively treated men according to prostate cancer risk category in a nationwide, population-based study. *Eur Urol.* 2013;63:88–96.
2. Mottet N, van den Bergh RCN, Briers E, et al. EAU-EANM-ESTRO-ESUR-SIOG guidelines on prostate cancer: 2020 update. Part 1: screening, diagnosis, and local treatment with curative intent. *Eur Urol.* 2021;79:243–262.
3. Taplin ME, Montgomery B, Logothetis CJ, et al. Intense androgen-deprivation therapy with abiraterone acetate plus leuprolide acetate in patients with localized high-risk prostate cancer: results of a randomized phase II neoadjuvant study. *J Clin Oncol.* 2014;32:3705–3715.
4. McKay RR, Berchuck J, Kwak L, et al. Outcomes of post-neoadjuvant intense hormone therapy and surgery for high risk localized prostate cancer: results of a pooled analysis of contemporary clinical trials. *J Urol.* 2021;205:1689–1697.
5. McKay RR, Montgomery B, Xie W, et al. Post prostatectomy outcomes of patients with high-risk prostate cancer treated with neoadjuvant androgen blockade. *Prostate Cancer Prostatic Dis.* 2018;21:364–372.

6. McKay RR, Ye H, Xie W, et al. Evaluation of intense androgen deprivation before prostatectomy: a randomized phase II trial of enzalutamide and leuprolide with or without abiraterone. *J Clin Oncol.* 2019;37:923–931.
7. Maluf FC, Schutz FA, Cronemberger EH, et al. A phase 2 randomized clinical trial of abiraterone plus ADT, apalutamide, or abiraterone and apalutamide in patients with advanced prostate cancer with non-castrate testosterone levels (LACOG 0415). *Eur J Cancer.* 2021;158:63–71.
8. Montgomery B, Tretiakova MS, Joshua AM, et al. Neoadjuvant enzalutamide prior to prostatectomy. *Clin Cancer Res.* 2017;23:2169–2176.
9. Ross RW, Galsky MD, Febbo P, et al. Phase 2 study of neoadjuvant docetaxel plus bevacizumab in patients with high-risk localized prostate cancer: a Prostate Cancer Clinical Trials Consortium trial. *Cancer.* 2012;118:4777–4784.
10. Fizazi K, Faivre L, Lesaunier F, et al. Androgen deprivation therapy plus docetaxel and estramustine versus androgen deprivation therapy alone for high-risk localised prostate cancer (GETUG 12): a phase 3 randomised controlled trial. *Lancet Oncol.* 2015;16:787–794.
11. Cortazar P, Zhang L, Untch M, et al. Pathological complete response and long-term clinical benefit in breast cancer: the CTNeoBC pooled analysis. *Lancet.* 2014; 384:164–172.
12. Petrelli F, Coinu A, Cabiddu M, Ghilardi M, Vavassori I, Barni S. Correlation of pathologic complete response with survival after neoadjuvant chemotherapy in bladder cancer treated with cystectomy: a meta-analysis. *Eur Urol.* 2014;65: 350–357.
13. Hofman MS, Lawrentschuk N, Francis RJ, et al. Prostate-specific membrane antigen PET-CT in patients with high-risk prostate cancer before curative-intent surgery or radiotherapy (proPSMA): a prospective, randomised, multicentre study. *Lancet.* 2020;395:1208–1216.
14. Fendler WP, Calais J, Eiber M, et al. Assessment of ^{68}Ga-PSMA-11 PET accuracy in localizing recurrent prostate cancer: a prospective single-arm clinical trial. *JAMA Oncol.* 2019;5:856–863.
15. Calais J, Ceci F, Eiber M, et al. ^{18}F-fluciclovine PET-CT and ^{68}Ga-PSMA-11 PET-CT in patients with early biochemical recurrence after prostatectomy: a prospective, single-centre, single-arm, comparative imaging trial. *Lancet Oncol.* 2019; 20:1286–1294.
16. Onal C, Guler OC, Torun N, Reyhan M, Yapar AF. The effect of androgen deprivation therapy on ^{68}Ga-PSMA tracer uptake in non-metastatic prostate cancer patients. *Eur J Nucl Med Mol Imaging.* 2020;47:632–641.
17. Vaz S, Hadaschik B, Gabriel M, Herrmann K, Eiber M, Costa D. Influence of androgen deprivation therapy on PSMA expression and PSMA-ligand PET imaging of prostate cancer patients. *Eur J Nucl Med Mol Imaging.* 2020;47:9–15.
18. Fassbind S, Ferraro DA, Stelmes JJ, et al. ^{68}Ga-PSMA-11 PET imaging in patients with ongoing androgen deprivation therapy for advanced prostate cancer. *Ann Nucl Med.* 2021;35:1109–1116.
19. Chen M, Zhuang J, Fu Y, et al. Can ^{68}Ga-PSMA-11 positron emission tomography/computerized tomography predict pathological response of primary prostate cancer to neoadjuvant androgen deprivation therapy? A pilot study. *J Urol.* 2021;205: 1082–1089.
20. Roberts MJ, Morton A, Donato P, et al. ^{68}Ga-PSMA PET/CT tumour intensity preoperatively predicts adverse pathological outcomes and progression-free survival in localised prostate cancer. *Eur J Nucl Med Mol Imaging.* 2021;48:477–482.
21. McNeal JE, Haillot O. Patterns of spread of adenocarcinoma in the prostate as related to cancer volume. *Prostate.* 2001;49:48–57.
22. Symmans WF, Peintinger F, Hatzis C, et al. Measurement of residual breast cancer burden to predict survival after neoadjuvant chemotherapy. *J Clin Oncol.* 2007;25: 4414–4422.
23. Camp RL, Dolled-Filhart M, Rimm DL. X-tile: a new bio-informatics tool for biomarker assessment and outcome-based cut-point optimization. *Clin Cancer Res.* 2004;10:7252–7259.
24. Ahn HK, Sim SH, Suh KJ, et al. Response rate and safety of a neoadjuvant pertuzumab, atezolizumab, docetaxel, and trastuzumab regimen for patients with ERBB2-positive stage II/III breast cancer: the Neo-PATH phase 2 nonrandomized clinical trial. *JAMA Oncol.* 2022;8:1271–1277.
25. Huober J, Barrios CH, Niikura N, et al. Atezolizumab with neoadjuvant anti-human epidermal growth factor receptor 2 therapy and chemotherapy in human epidermal growth factor receptor 2-positive early breast cancer: primary results of the randomized phase III IMpassion050 trial. *J Clin Oncol.* 2022;40:2946–2956.
26. Reijers ILM, Menzies AM, van Akkooi ACJ, et al. Personalized response-directed surgery and adjuvant therapy after neoadjuvant ipilimumab and nivolumab in high-risk stage III melanoma: the PRADO trial. *Nat Med.* 2022;28:1178–1188.
27. Hussain SA, Lester JF, Jackson R, et al. Addition of nintedanib or placebo to neoadjuvant gemcitabine and cisplatin in locally advanced muscle-invasive bladder cancer (NEOBLADE): a double-blind, randomised, phase 2 trial. *Lancet Oncol.* 2022;23:650–658.
28. Devos G, Devlies W, De Meerleer G, et al. Neoadjuvant hormonal therapy before radical prostatectomy in high-risk prostate cancer. *Nat Rev Urol.* 2021;18: 739–762.
29. Seitz AK, Rauscher I, Haller B, et al. Preliminary results on response assessment using ^{68}Ga-HBED-CC-PSMA PET/CT in patients with metastatic prostate cancer undergoing docetaxel chemotherapy. *Eur J Nucl Med Mol Imaging.* 2018;45: 602–612.
30. Anton A, Kamel Hasan O, Ballok Z, et al. Use of prostate-specific membrane antigen positron-emission tomography/CT in response assessment following upfront chemohormonal therapy in metastatic prostate cancer. *BJU Int.* 2020;126:433–435.
31. Has Simsek D, Kuyumcu S, Karadogan S, et al. Can PSMA-based tumor burden predict response to docetaxel treatment in metastatic castration-resistant prostate cancer? *Ann Nucl Med.* 2021;35:680–690.
32. Zukotynski KA, Emmenegger U, Hotte S, et al. Prospective, single-arm trial evaluating changes in uptake patterns on prostate-specific membrane antigen-targeted^{18}F-DCFPyL PET/CT in patients with castration-resistant prostate cancer starting abiraterone or enzalutamide. *J Nucl Med.* 2021;62:1430–1437.
33. Plouznikoff N, Artigas C, Sideris S, et al. Evaluation of PSMA expression changes on PET/CT before and after initiation of novel antiandrogen drugs (enzalutamide or abiraterone) in metastatic castration-resistant prostate cancer patients. *Ann Nucl Med.* 2019;33:945–954.

^{68}Ga-PSMA PET/CT for Response Evaluation of ^{223}Ra Treatment in Metastatic Prostate Cancer

Anouk C. de Jong*[1,2], Marcel Segbers*[2], Sui Wai Ling[2], Laura H. Graven[2], Niven Mehra[3], Paul Hamberg[4], Tessa Brabander[2], Ronald de Wit[1], and Astrid A.M. van der Veldt[1,2]

[1]*Department of Medical Oncology, Erasmus MC Cancer Institute, Rotterdam, The Netherlands;* [2]*Department of Radiology and Nuclear Medicine, Erasmus MC, Rotterdam, The Netherlands;* [3]*Department of Medical Oncology, Radboud UMC, Nijmegen, The Netherlands; and* [4]*Department of Internal Medicine, Franciscus Gasthuis and Vlietland, Rotterdam, The Netherlands*

CT and bone scintigraphy are not useful for response evaluation of bone metastases to ^{223}Ra treatment in metastatic castration-resistant prostate cancer (mCRPC). PET using ^{68}Ga prostate-specific membrane antigen 11 (^{68}Ga-PSMA) is a promising tool for response evaluation of mCRPC. The aim of this study was to determine the utility of ^{68}Ga-PSMA PET/CT for response evaluation of ^{223}Ra treatment in patients with mCRPC. **Methods:** Within this prospective, multicenter, imaging discovery study, 28 patients with mCRPC, eligible for ^{223}Ra treatment, were included between 2019 and 2022. Patients received ^{223}Ra according to the standard of care. Study procedures included CT, bone scintigraphy, and ^{68}Ga-PSMA PET/CT at baseline, after 3 and 6 cycles of ^{223}Ra treatment, and on treatment failure. Response to ^{223}Ra treatment was visually assessed on all 3 imaging modalities. Total tumor volume within bone (TTV_{bone}) was determined on ^{68}Ga-PSMA PET/CT. Intrapatient heterogeneity in response was studied using a newly developed image-registration tool for sequential images of PET/CT. Results were compared with failure-free survival (good responders vs. poor responders; cutoff, 24 wk) and alkaline phosphatase (ALP) response after 3 cycles. **Results:** Visual response assessment criteria could not distinguish good responders from poor responders on ^{68}Ga-PSMA PET/CT and bone scintigraphy. For ^{68}Ga-PSMA PET/CT, TTV_{bone} at baseline was lower in good responders than in poor responders, whereas TTV_{bone} increased in both groups during treatment. TTV_{bone} was higher in patients with new extraosseous metastases during ^{223}Ra treatment. Although TTV_{bone} and ALP correlated at baseline, changes in TTV_{bone} and ALP on treatment did not. ^{68}Ga-PSMA response of TTV_{bone} showed intrapatient heterogeneity in most patients. **Conclusion:** mCRPC patients with lower TTV_{bone} on ^{68}Ga-PSMA PET/CT have the best clinical outcome after ^{223}Ra treatment. Response is highly heterogeneous in most patients. A decrease in ALP, which occurred in most patients, was not correlated with a decrease in TTV_{bone}, which might make one question the value of ALP for disease monitoring during ^{223}Ra treatment in clinical practice.

Key Words: ^{68}Ga-PSMA PET/CT; prostate cancer; ^{223}Ra; response evaluation

J Nucl Med 2023; 64:1556–1562
DOI: 10.2967/jnumed.123.265489

Because bone metastases, which occur in up to 90% of patients with metastatic prostate cancer, are associated with severe pain and pathologic fractures, effective treatment is needed (*1,2*). However, the value of diagnostic CT (dCT) and bone scintigraphy is hampered for early response evaluation of bone metastases. On dCT, bone metastases of prostate cancer, which are often osteoblastic, cannot be distinguished from osteosclerosis (*3,4*). In addition, bone scintigraphy has a low specificity and is prone to flare phenomena. Therefore, confirmation of progressive bone metastases is required on a second bone scintigraphy after the start of treatment according to the Prostate Cancer Working Group 3 criteria (*5–7*).

PET using ^{68}Ga prostate-specific membrane antigen 11 (^{68}Ga-PSMA) is a useful imaging modality for diagnosis, staging, and response evaluation of prostate cancer (*8–11*). Correlations between ^{68}Ga-PSMA uptake, prostate-specific antigen, and patient survival have been reported for patients with metastatic castration-resistant prostate cancer (mCRPC) (*12–18*). In comparison with conventional imaging, at least one advantage of ^{68}Ga-PSMA PET/CT is image acquisition by a single machine.

^{223}Ra, an α-emitting radionuclide, is indicated for treatment of patients with mCRPC and bone metastases without visceral metastases (*19,20*). However, besides the limited value of dCT and bone scintigraphy for early response evaluation of bone metastases, blood-based biomarkers, including prostate-specific antigen, cannot predict a response to ^{223}Ra. Serum alkaline phosphatase (ALP) is the best biomarker to date but correlates only moderately with patient overall survival after ^{223}Ra treatment (*6,21*). Therefore, new tools are needed to evaluate bone metastases and to guide clinical decision-making on continuation of ^{223}Ra treatment.

In this prospective imaging and biomarker discovery study, we investigated the use of ^{68}Ga-PSMA PET/CT for response evaluation after ^{223}Ra treatment in patients with mCRPC. Images of ^{68}Ga-PSMA PET/CT were compared with images of conventional modalities, and changes in total tumor volume during ^{223}Ra treatment were analyzed. In addition, we developed a widely applicable image-registration tool to merge sequential PET/CT images and to quantify intrapatient heterogeneity of ^{68}Ga-PSMA uptake to measure the response in bone metastases.

MATERIALS AND METHODS

Study Design

This multicenter study (Radium223Insight, Dutch Trial Register NL7380) included patients at the Erasmus Medical Center Cancer Institute, Franciscus Gasthuis and Vlietland Hospital, and Radboud

Received Jan. 19, 2023; revision accepted May 31, 2023.
For correspondence or reprints, contact Astrid van der Veldt (a.vanderveldt@erasmusmc.nl).
*Contributed equally to this work.
Published online Aug. 3, 2023.

University Medical Center, The Netherlands. The study was approved by the institutional review boards (MEC 18-1562). Patients received 6 consecutive injections with ^{223}Ra at an interval of 4 wk. In the case of progression of disease, based on the Prostate Cancer Working Group 3 criteria, or severe toxicity, treatment was discontinued. Study procedures consisted of blood draws, tumor tissue biopsies, and imaging, including sequential ^{68}Ga-PSMA PET/CTs, dCT of the thorax and abdomen, and bone scintigraphy (Supplemental Fig. 1; supplemental materials are available at http://jnm.snmjournals.org). All patients provided written informed consent before the start of the study procedures.

Patients

Patients with mCRPC and predominantly bone metastases were eligible if they had progressive disease, received at least 2 prior treatment lines (unless the patient was not able or willing to receive other treatments), and had not received prior chemotherapy other than docetaxel. Detailed inclusion and exclusion criteria are described in the supplemental materials. Because of the explorative nature of the study, the sample size was arbitrarily set at 30 patients. However, because of delayed inclusion due to the coronavirus disease 2019 pandemic, the decision was made to close the trial for further accrual after the inclusion of 28 patients with completed follow-up between February 2019 and January 2022.

Study Endpoints

The primary endpoint was failure-free survival (FFS), defined as the time from the start of ^{223}Ra treatment to the next line of treatment, best supportive care, or death. The next treatment or best supportive care was started on clinical, biochemical, or radiologic signs of progressive disease, according to the Prostate Cancer Working Group 3 criteria (*7*). A composite endpoint was chosen because a reliable parameter of disease response and progression during ^{223}Ra treatment is lacking. To avoid bias in treatment decisions, treating physicians were unaware of the results of ^{68}Ga-PSMA PET/CT, except for the baseline scan. Detection of visceral metastases or other significant findings was reported by the nuclear medicine physician to the treating physician.

Here, we report on the primary endpoint and parameters based on sequential ^{68}Ga-PSMA PET/CT, dCT, and bone scintigraphy and longitudinal measurements of serum ALP (Supplemental Fig. 1). Other endpoints and parameters will be reported in later publications.

Image Acquisition

^{68}Ga-PSMA PET/CT, dCT, and bone scintigraphy were performed at baseline, after 3 cycles of ^{223}Ra treatment, at the end of the treatment (after 6 cycles of ^{223}Ra treatment), and at treatment failure (Supplemental Fig. 1). Details on image acquisition are described in the supplemental materials (*22*).

Image Analyses

Longitudinal ^{68}Ga-PSMA PET/CT, dCT of the thorax and abdomen, and bone scintigraphy images were visually assessed. In addition, semiautomatic assessment of total tumor volume within bone (TTV_{bone}) and analyses of heterogeneity in response were performed for ^{68}Ga-PSMA PET/CT. The 3 imaging modalities were mutually compared and correlated with FFS and ALP response. Details are described in the supplemental materials (*4,7,23*).

Visual Response Evaluation. ^{68}Ga-PSMA PET/CT images were examined by nuclear medicine physicians according to adapted PERCIST (*24,25*). The dCT and bone scintigraphy were assessed according to RECIST version 1.1 and the 2 + 2 rule, respectively (*4,7*).

Semiautomatic Assessment of TTV_{bone}. TTV_{bone} on ^{68}Ga-PSMA PET images was semiautomatically measured using a PERCIST-based lesion selection tool (Hermes Hybrid3D 3.0.1). In addition to assessing FFS and ALP response, we compared patients with and without new extraosseous metastases during treatment.

Analyses of Heterogeneity in Response. An image-registration tool was developed to merge 2 sequential PET/CT images. The difference in ^{68}Ga-PSMA uptake between baseline and follow-up was calculated per voxel for all previously selected tumor lesions using TTV_{bone}. All voxels within the merged tumor mask of an individual patient were categorized on the basis of changes in ^{68}Ga-PSMA uptake over time, and the intrapatient distribution of the categories was explored.

Statistical Analyses

Patients were categorized as good or poor responders using a cutoff at 24 wk of FFS, which is similar to the period of 6 cycles of 4 weekly injections with ^{223}Ra. Baseline characteristics, clinical outcomes, and parameters of ^{68}Ga-PSMA were described as mean ± SD, median and interquartile

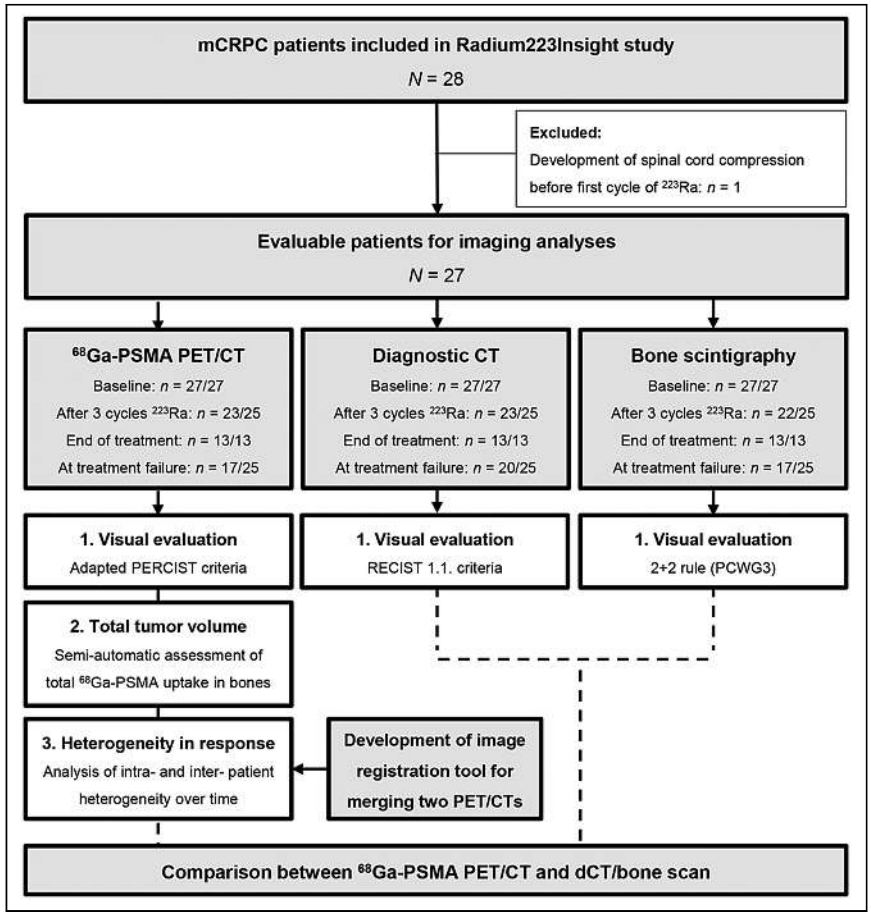

FIGURE 1. Flowchart of patient inclusion: description of patient inclusion, evaluable scans, and performed analyses. ^{68}Ga-PSMA PET/CT, dCT, and bone scintigraphy were visually assessed according to adapted PERCIST, RECIST version 1.1, and 2 + 2 rule as described in Prostate Cancer Working Group 3 criteria, respectively.

range (IQR), or number of events and percentage. Depending on the format and normality distribution of the data, the appropriate statistical tests were used. Applied statistical tests are described in the figure legends. All *P* values were 2-sided, and a *P* value of 0.05 or less was considered to be significant. No corrections for multiple testing were performed.

RESULTS

Patient Characteristics and Clinical Outcomes

Of the 28 included patients, 27 patients were evaluable (Fig. 1). On the basis of FFS, patients were categorized as good ($n = 13$) or poor responders ($n = 12$). Two patients, who discontinued treatment because of hematologic adverse events, were not included in the responder assessments. No significant differences between good and poor responders were found in baseline clinical characteristics. Serum lactate dehydrogenase at baseline was significantly higher in poor responders than in good responders (262 U/L [IQR, 229–330 U/L] vs. 201 U/L [IQR, 186–231 U/L]; $P = 0.001$), whereas serum prostate-specific antigen and ALP were not different (Supplemental Table 1).

Median FFS was 25.9 wk (IQR, 25.0–35.1 wk) and 11.7 wk (IQR, 10.0–17.3 wk) for good and poor responders, respectively ($P < 0.001$). Four of 13 (31%) good responders developed extraosseous disease during treatment, whereas this occurred in 8 of 12 (67%) poor responders ($P = 0.068$). Good responders had a longer median overall survival than poor responders (91.0 wk [IQR, 67.1–102.3 wk] vs. 27.0 wk [IQR, 16.4–48.0 wk], $P = 0.004$). Dynamics in prostate-specific antigen and ALP were not different between the 2 groups (Table 1).

Visual Response Evaluation of ^{68}Ga-PSMA PET/CT, dCT, and Bone Scintigraphy

All scans were visually assessed (Fig. 1; Supplemental Table 2). Of the 21 patients who underwent all 3 imaging modalities, 17 (81%) and 4 (19%) patients had progressive disease and stable disease on ^{68}Ga-PSMA PET/CT (PERCIST) (*24*), respectively, whereas the combination of dCT (RECIST version 1.1) (*4*) and bone scintigraphy (2 + 2 rule) (*7*) resulted in progressive disease, nonprogressive disease, and nonevaluable disease in 2 (10%), 10 (48%), and 9 (43%) of 21 patients after 3 cycles of ^{223}Ra treatment, respectively. Two patients with progressive disease on conventional imaging also had progressive disease on ^{68}Ga-PSMA PET/CT, whereas 15 patients with progressive disease on ^{68}Ga-PSMA PET/CT had nonprogressive disease or were not evaluable on conventional imaging (Fig. 2). At the end of treatment and at treatment failure, all patients had progressive disease on ^{68}Ga-PSMA PET/CT, whereas 15% and 43% of patients, respectively, also had progressive disease on conventional imaging (Supplemental Fig. 2).

For those patients who discontinued treatment because of progressive disease and underwent all 3 imaging modalities ($n = 20$), FFS was compared between the response categories after 3 cycles of ^{223}Ra treatment of each imaging modality. For ^{68}Ga-PSMA PET/CT, the median FFS for patients with progressive disease and stable disease was 23 wk (IQR, 17–26 wk; $n = 17$) and 35 wk (IQR, 25–43 wk; $n = 3$), respectively ($P = 0.362$). For dCT, the median FFS was higher in patients with nonevaluable disease than in patients with progressive disease (25 wk [IQR, 20–27 wk; $n = 16$] vs. 11 wk [IQR, 11–17 wk; $n = 2$]; $P = 0.001$), whereas FFS was comparable in patients with stable disease (19 wk [IQR, 19–25 wk; $n = 2$]; $P = 0.090$). For bone scintigraphy, the median FFS was comparable for at least 2 or more new lesions and fewer than 2 new lesions (23 wk [IQR, 16–27 wk; $n = 9$] vs. 25 wk [IQR, 20–35 wk; $n = 11$]; $P = 0.396$; Fig. 3A). The median change in ALP after 3 cycles of ^{223}Ra treatment was not different between the response categories for any of the 3 imaging modalities (Fig. 3B).

TABLE 1
Clinical Outcomes of Included Patients

Clinical outcome	Good responder ($n = 13$)	Poor responder ($n = 12$)	*P*
Number of ^{223}Ra injections			NA
1–3	0 (0%)	7 (58%)	
4–5	0 (0%)	5 (42%)	
6	13 (100%)	0 (0%)	
FFS (wk)	25.9 (25.0–35.1)	11.7 (10.0–17.3)	<0.001*
Reason for treatment failure			0.068†
Progression of bone disease	9 (69%)	3 (25%)	
Development of extraosseous metastases, with/without progression of bone disease	4 (31%)	8 (67%)	
Unspecified progression of disease	0 (0%)	1 (8%)	
Overall survival (wk)	91.0 (67.1–102.3)	27.0 (16.4–48.0)	0.004*
ALP response	8 (62%)	5 (42%)	0.434†
PSA response	0 (0%)	2 (17%)	0.220†
Time to ALP progression (wk)	39.9 (28.7–NR)	NA	NA
Time to PSA progression (wk)	15.0 (14.7–15.0)	16.0 (13.9–NA)	0.114*

*Log-rank test.
†χ^2 test.
NA = not applicable; PSA = prostate-specific antigen; NR = not reached.
Two patients discontinued treatment because of toxicity and were not included in table. Qualitative data are number and percentage; continuous data are median and IQR. ALP and prostate-specific antigen response was defined as ≤–30% change from baseline.

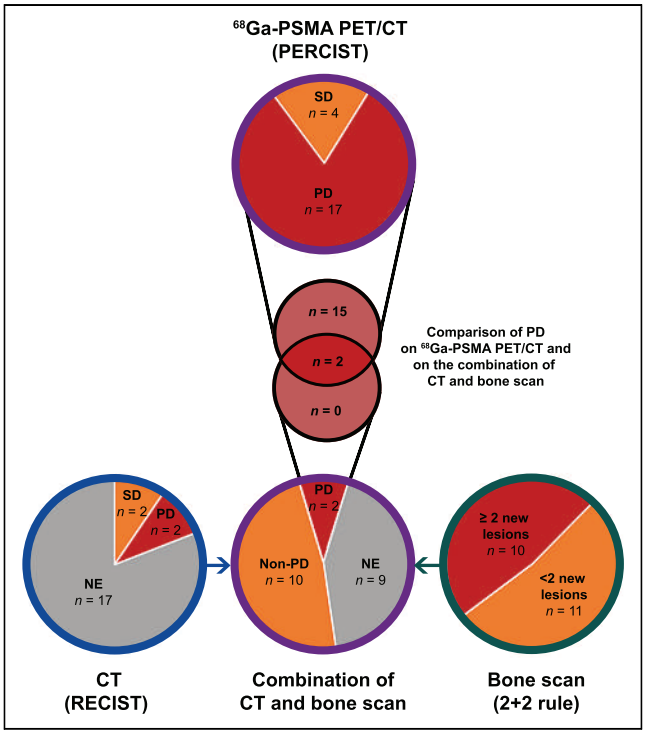

FIGURE 2. Visual response evaluation after 3 cycles of ^{223}Ra treatment. ^{68}Ga-PSMA PET/CT, dCT, and bone scintigraphy were visually assessed according to adapted PERCIST, RECIST version 1.1, and 2 + 2 rule as described in Prostate Cancer Working Group 3 criteria. Visual response evaluation results are after 3 cycles of ^{223}Ra treatment for patients who were evaluable for all 3 imaging modalities (n = 21). NE = nonevaluable disease; PD = progressive disease; SD = stable disease.

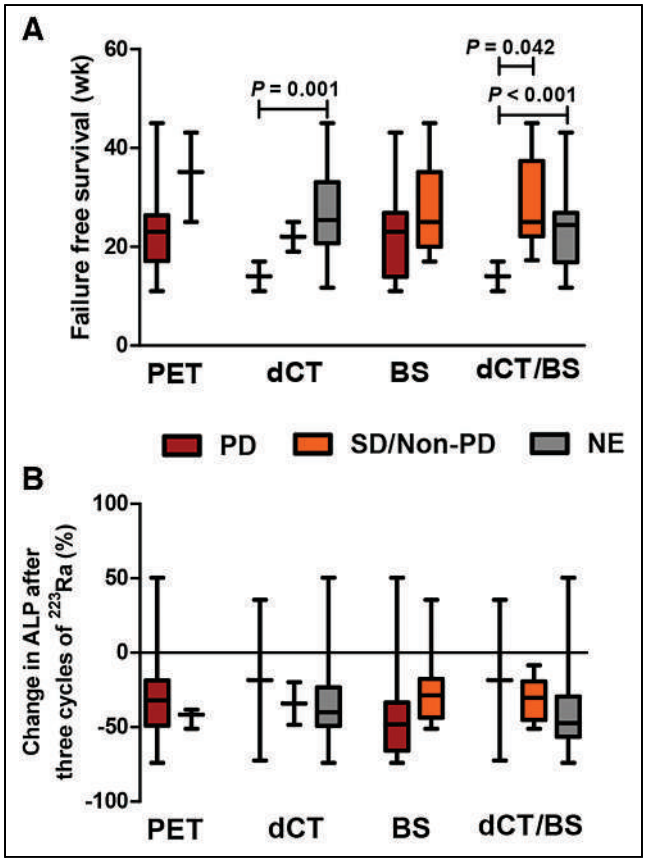

FIGURE 3. Visual response evaluation after 3 cycles of ^{223}Ra treatment in relation to FFS and ALP response. (A) FFS in response evaluation categories of 3 imaging modalities. All patients who underwent all 3 imaging modalities and discontinued treatment because of progression of disease (and not because of toxicity) were included (n = 20). FFS was compared between response categories within each imaging modality using log-rank test. (B) ALP response after 3 cycles of ^{223}Ra treatment (n = 20) was compared between response categories within each imaging modality using Kruskal–Wallis test. PD = progressive disease; SD = stable disease; NE = nonevaluable disease; PET = ^{68}Ga-PSMA PET/CT; BS = bone scan.

Semiautomatic Assessment of TTV_{bone} on ^{68}Ga-PSMA PET/CT

At baseline and after 3 cycles of ^{223}Ra treatment, the good responders had lower median TTV_{bone} than the poor responders: 90 cm^3 (IQR, 48–385 cm^3; n = 13) versus 372 cm^3 (IQR, 227–2,664 cm^3; n = 12) (P = 0.0208) and 161 cm^3 (IQR, 84–515 cm^3; n = 13) versus 926 cm^3 (IQR, 405–2,941 cm^3; n = 9) (P = 0.0384), respectively (Fig. 4A; Supplemental Fig. 3A). For good and poor responders, the median absolute change in TTV_{bone} after 3 cycles of ^{223}Ra treatment was +56 cm^3 (IQR, 12–237 cm^3; n = 13) and +348 cm^3 (IQR, −45 to +817 cm^3; n = 9) (P = 0.3853), whereas the median relative changes were +61% (IQR, +7% to +107%; n = 13) and +77% (IQR, −12% to +93%; n = 9) (P = 0.8938), respectively (Fig. 4B; Supplemental Fig. 3B). Three poor responders did not undergo ^{68}Ga-PSMA PET/CT after 3 cycles of ^{223}Ra treatment because of earlier treatment failure (n = 2) and patient withdrawal (n = 1). TTV_{bone} at other time points is shown in Supplemental Figures 3A–3F.

At the time of treatment failure, TTV_{bone} was higher in patients with extraosseous disease than in patients without extraosseous disease during treatment with ^{223}Ra (median, 1,835 cm^3 [IQR, 466–2,948 cm^3; n = 7] vs. 308 cm^3 [IQR, 150–697 cm^3; n = 9]; P = 0.0115; Supplemental Fig. 3H). This association was also seen at baseline (median TTV_{bone}, 311 cm^3 [IQR, 167–2,572 cm^3; n = 12] vs. 151 cm^3 [IQR, 59–380 cm^3; n = 12]; P = 0.1206) and after 3 cycles of ^{223}Ra treatment (median TTV_{bone}, 926 cm^3 [IQR, 182–2,823 cm^3; n = 9] vs. 159 cm^3 [IQR, 72–624 cm^3; n = 12]; P = 0.0302; Fig. 4C; Supplemental Figs. 3G and 3H).

TTV_{bone} and ALP were positively correlated at baseline and after 3 cycles, with Spearman correlation coefficients of 0.5413 (n = 27; P = 0.0035) and 0.6500 (n = 23; P = 0.0008), respectively (Supplemental Figs. 3I and 3J). Nevertheless, after 3 cycles of ^{223}Ra treatment, most patients showed a decrease in ALP, whereas TTV_{bone} increased, resulting in a Spearman correlation coefficient of 0.1739 (n = 23; P = 0.4274; Fig. 4D).

Heterogeneity on ^{68}Ga-PSMA PET/CT in Response to ^{223}Ra Treatment

During visual response evaluation, mixed responses in individual patients were observed. Therefore, we developed an image-registration tool that merges 2 sequential images of ^{68}Ga-PSMA PET/CT to visualize and quantify heterogeneity in response over time (Fig. 5; Supplemental Figs. 4 and 5; Supplemental Video 1).

After 3 cycles of ^{223}Ra treatment, ^{68}Ga-PSMA uptake decreased, stabilized, and increased with a median of 32% (IQR, 18%–40%), 21% (IQR, 12%–26%), and 53% (IQR, 29%–65%), respectively, of TTV_{bone} (n = 21; Fig. 6; Supplemental Fig. 4A). A higher fraction of decreased ^{68}Ga-PSMA uptake was correlated with a higher decrease in TTV_{bone} after 3 cycles of ^{223}Ra treatment (Spearman

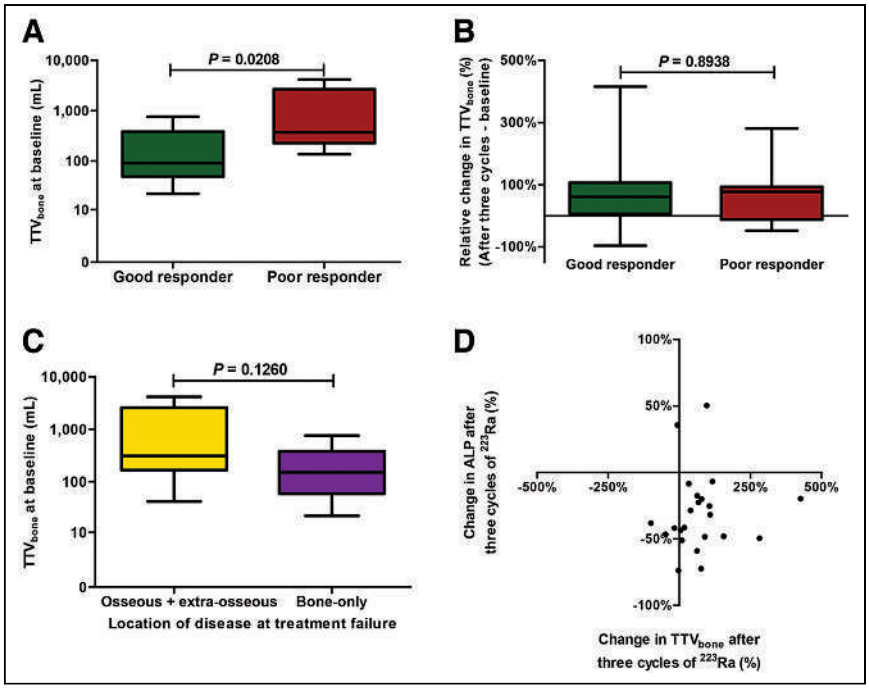

FIGURE 4. TTV$_{bone}$ on ^{68}Ga-PSMA PET/CT. (A) Absolute TTV$_{bone}$ in good responders (n = 13) and poor responders (n = 12) at baseline. (B) Relative change in TTV$_{bone}$ from baseline to after 3 cycles of ^{223}Ra treatment in good (n = 13) and poor responders (n = 9). (C) TTV$_{bone}$ in patients with and without new extraosseous metastases during ^{223}Ra treatment at baseline (n = 12 and 12, respectively; 1 not specified because of absence of imaging at time of treatment failure). Groups were compared using Mann–Whitney U test. (D) Relative change in ALP and TTV$_{bone}$ after 3 cycles of ^{223}Ra treatment did not correlate (Spearman correlation coefficient, 0.1739; n = 23; P = 0.4274).

correlation coefficient, −0.8156; n = 21; P < 0.0001; Supplemental Fig. 4G). At the time of treatment failure compared with after 3 cycles of ^{223}Ra treatment, the fraction of progressive ^{68}Ga-PSMA uptake increased from 53% (IQR, 28%–67%) to 78% (IQR, 56%–84%; n = 13) (P = 0.001; Supplemental Fig. 4E).

The fraction of decreased ^{68}Ga-PSMA uptake after 3 cycles of ^{223}Ra treatment did not correlate with TTV$_{bone}$ at baseline (Spearman correlation coefficient, −0.04880; n = 21; P = 0.8336) and was comparable between good and poor responders (median, 32% [IQR, 14%–40%; n = 13] vs. 29% [IQR, 18%–55%; n = 8]; P = 0.547; Fig. 6; Supplemental Fig. 4F). However, the fraction of decreased ^{68}Ga-PSMA uptake and change in ALP after 3 cycles of ^{223}Ra treatment showed a significant correlation (Spearman correlation coefficient, −0.4580; n = 21; P = 0.0368; Supplemental Fig 4H).

DISCUSSION

In this prospective multicenter study, we investigated the value of ^{68}Ga-PSMA PET/CT to evaluate mCRPC during treatment with ^{223}Ra.

To compare ^{68}Ga-PSMA PET/CT with conventional techniques, such as dCT and bone scintigraphy, we visually assessed all 3 imaging modalities, using standardized evaluation criteria. After 3 cycles of ^{223}Ra treatment, bone scintigraphy could not distinguish good responders from poor responders to ^{223}Ra treatment. In addition, many patients were nonevaluable on the basis of conventional imaging, because at least 2 new lesions on bone scintigraphy needed confirmation on a second scan according to the 2 + 2 rule, and dCT is not suitable for response evaluation of bone-only disease. ^{68}Ga-PSMA PET/CT has an increased diagnostic accuracy and the advantage of tomography in comparison with planar bone scintigraphy (*11*). However, when PERCIST was used for ^{68}Ga-PSMA PET/CT, most patients had progressive disease due to the development of at least 1 new bone lesion. In addition, we observed intrapatient heterogeneity in response, which was not reflected by PERCIST. Therefore, PERCIST was not considered sufficient to distinguish good responders from poor responders to ^{223}Ra treatment, and we decided to assess novel parameters of ^{68}Ga-PSMA PET/CT.

Using semiautomatic assessment of tumor volume on ^{68}Ga-PSMA PET/CT, we found that good responders had a lower TTV$_{bone}$ than poor responders at baseline and after 3 cycles of ^{223}Ra treatment. However, since a baseline tumor load is associated with the prognosis of patients with mCRPC in general, this finding might not be specific for ^{223}Ra treatment (*26*). Nevertheless, higher TTV$_{bone}$ was associated with new extraosseous disease during treatment, which might be considered at the start of ^{223}Ra treatment. Although improved clinical outcome is, in general, associated with radiologic response, a comparable increase in TTV$_{bone}$ after 3 cycles of ^{223}Ra treatment was observed in both good and poor responders. This might be caused by the arbitrary cutoff for responders at 24 wk of FFS and by confounding factors such as baseline tumor load and the development of extraosseous metastases. Therefore, validation of the association between TTV$_{bone}$ and clinical outcome, including the correction of confounding factors, in a larger patient cohort is required to further clarify the value of ^{68}Ga-PSMA PET/CT for response evaluation during treatment with ^{223}Ra.

Remarkably, a decrease in TTV$_{bone}$ was not associated with a decrease in ALP, whereas absolute ALP values did correlate with TTV$_{bone}$. This might be caused by the fact that ALP reflects the activity of osteoblasts, which are targeted by ^{223}Ra, but does not directly reflect the tumor load. In the ALSYMPCA trial, it was shown that ALP dynamics during treatment with ^{223}Ra correlate with the risk of death but cannot be used as a surrogate for overall survival (*21*). Thus, in clinical practice, an ALP decrease after ^{223}Ra treatment is not necessarily associated with tumor response on ^{68}Ga-PSMA PET/CT and could coexist with radiologic disease progression.

Using our in-house–developed image-registration tool, we gained more insight into the unexpected changes in TTV$_{bone}$. Remarkably, most patients had a significant intrapatient heterogeneity, showing a typical pattern of decreased ^{68}Ga-PSMA uptake in the original region of the bone metastasis and increased ^{68}Ga-PSMA uptake in the surrounding bone tissue after ^{223}Ra treatment (Supplemental Fig. 5). Although the distinct dynamics in ^{68}Ga-PSMA uptake over time suggest a change in tumor load and location, the upregulating effect of irradiation on PSMA expression in tumor cells should be considered as a potential factor in measuring tumor volume on ^{68}Ga-PSMA PET/CT (*27*). In addition, PSMA is expressed not only on prostate cancer cells but also on the neovasculature of several solid tumors, including prostate cancer (*28,29*). Because radiation can

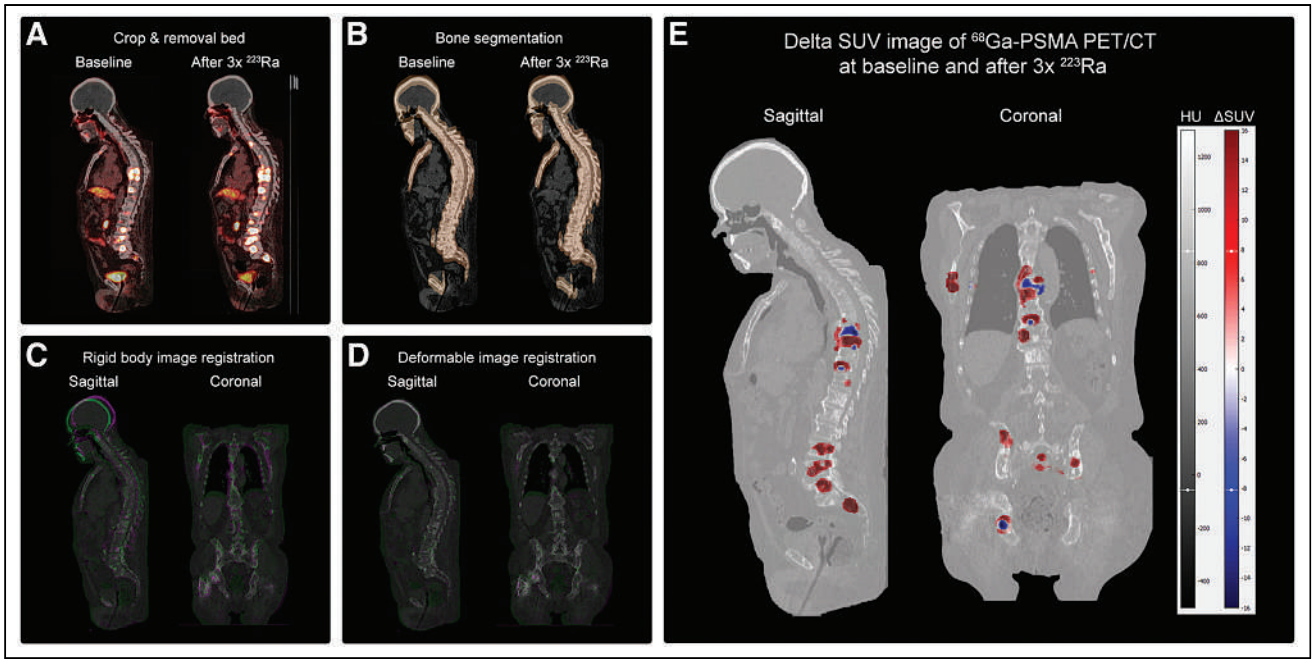

FIGURE 5. In-house–developed image-registration tool for visualization and quantification of heterogeneity in tumor response. Image registration to merge 2 sequential images of ^{68}Ga-PSMA PET/CT consists of 4 steps. (A) Both scans are cropped to comparable field of view, and bed is removed from images. (B) Bone masks are obtained by region-growing algorithm with threshold of 150 Hounsfield units on low-dose CT. (C) Initial alignment of both images is performed by rigid-body registration. (D) To correct for differences in patient posture between scans, deformable B-spline registration is applied using isotropic mesh size of ~10-cm distance between nodes. (E) Transformations are subsequently applied to associated PET images and tumor mask that were obtained during TTV_{bone} assessment. Changes in SUVs of ^{68}Ga-PSMA are color-scaled, showing increasing (i.e., red color) and decreasing (i.e., blue color) ^{68}Ga-PSMA uptake over time. HU = Hounsfield units.

induce angiogenesis, the increased PSMA expression in the surrounding bone tissue might also be the result of neovascularization in response to treatment with ^{223}Ra (*30,31*).

On the basis of our results, we hypothesized that the correlation between ALP and TTV_{bone} disappears because of the interruption of the osteoblast–tumor interaction by ^{223}Ra, as explained in Supplemental Figure 6 (*32*). This hypothesis is further supported by the known increase in ALP after discontinuation of ^{223}Ra treatment, suggesting the recovery of the activating tumor–osteoblast interaction (*32*). In addition, the typical shift of ^{68}Ga-PSMA uptake to the borders of the original tumor lesion on treatment with ^{223}Ra might suggest that the irradiated osteoblasts are no longer a suitable tumor microenvironment, whereas the adjacent undamaged bone tissue still is. Application of the image-registration tool in patients who received other systemic therapies could help to further improve our understanding of heterogeneity in response evaluation in bone metastases.

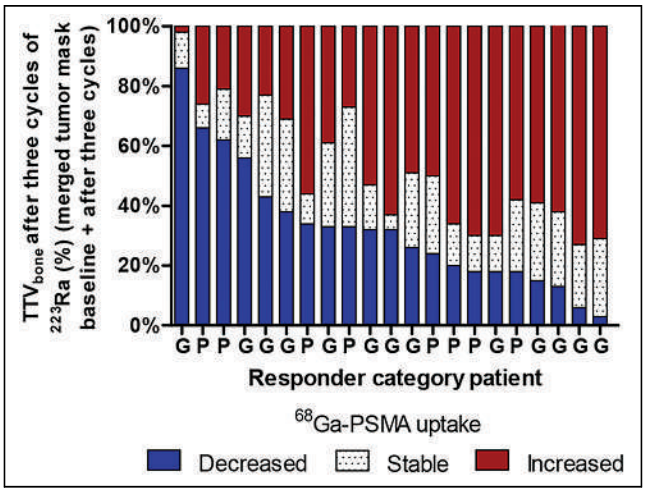

FIGURE 6. Quantification of heterogeneity in tumor response on ^{68}Ga-PSMA PET/CT after 3 cycles of ^{223}Ra treatment. Changes in SUV of ^{68}Ga-PSMA are categorized for every voxel within TTV_{bone} according to decreased ^{68}Ga-PSMA uptake (baseline to follow-up SUV $\leq -30\%$), stable ^{68}Ga-PSMA uptake (baseline to follow-up SUV $= -30\%$ to $+30\%$), and increased ^{68}Ga-PSMA uptake (baseline to follow-up SUV $\geq 30\%$) and visualized for good and poor responders after 3 cycles of ^{223}Ra treatment (n = 13 and 8). G = good responder; P = poor responder.

Other strengths of this study are the prospective design, the extensive follow-up with in-depth imaging, and the masking of ^{68}Ga-PSMA PET/CT to prevent bias on the clinical outcome. Response evaluation of bone metastases was complicated by the clinical endpoint, as extraosseous disease also determines FFS, whereas this is not targeted by ^{223}Ra. Nevertheless, other reliable endpoints directly related to bone metastases and ^{223}Ra are lacking. Therefore, we still consider a clinical endpoint, such as FFS, as the most relevant outcome for ^{223}Ra treatment in current clinical practice.

CONCLUSION

^{68}Ga-PSMA PET/CT could be a useful all-in-one imaging modality for response prediction in patients with mCRPC and predominantly bone disease during treatment with ^{223}Ra. Patients with a lower TTV_{bone} on ^{68}Ga-PSMA PET/CT appear to have the best clinical outcome and lowest chance of developing new extraosseous metastases during treatment. Response to ^{223}Ra shows intra- and intertumor heterogeneity in almost all patients. Remarkably, a decrease in ALP, which occurred in most patients, was not correlated with a decrease in

TTV_{bone}, which might make one question the value of ALP for disease monitoring during ^{223}Ra treatment in clinical practice.

DISCLOSURE

This research was financially supported by an unrestricted grant from Bayer and the Foundation Dutch Uro-Oncology Study Group (DUOS) and by the fundraising action Running Stairs for Cancer. Niven Mehra reports institutional grants from Roche, Astrazeneca, MSD, Astellas, BMS, and Pfizer and personal fees from Astrazeneca, MSD, Janssen, Bayer, and Pfizer, all outside the submitted work. Ronald de Wit has speaker roles for Sanofi and Astellas and advisory roles for Merck and Sanofi and received institutional research grants from Sanofi and Bayer. Astrid van der Veldt has received consultancy fees (all paid to the institute) from BMS, MSD, Pierre Fabre, Roche, Pfizer, Sanofi, Novartis, Eisai, and Ipsen. No other potential conflict of interest relevant to this article was reported.

ACKNOWLEDGMENTS

We thank Fred Guurink for organizing the fundraising action Running Stairs for Cancer. Additionally, we acknowledge Stefan Klein for sharing his expertise on image-registration tools and Daniela Oprea-Lager and Elisabeth de Vries for their advice on the manuscript.

KEY POINTS

QUESTION: Can ^{68}Ga-PSMA PET/CT be used for response evaluation of ^{223}Ra treatment in patients with mCRPC?

PERTINENT FINDINGS: Within this prospective imaging study, response to ^{223}Ra treatment showed high intrapatient heterogeneity on ^{68}Ga-PSMA PET/CT, though patients with a lower TTV_{bone} had the best clinical outcome. Remarkably, changes in TTV_{bone} and ALP were not correlated.

IMPLICATIONS FOR PATIENT CARE: ^{68}Ga-PSMA PET/CT is a useful all-in-one imaging tool for response prediction of ^{223}Ra treatment in patients with mCRPC.

REFERENCES

1. Bubendorf L, Schopfer A, Wagner U, et al. Metastatic patterns of prostate cancer: an autopsy study of 1,589 patients. *Hum Pathol.* 2000;31:578–583.
2. Sottnik JL, Keller ET. Understanding and targeting osteoclastic activity in prostate cancer bone metastases. *Curr Mol Med.* 2013;13:626–639.
3. Sailer V, Schiffman MH, Kossai M, et al. Bone biopsy protocol for advanced prostate cancer in the era of precision medicine. *Cancer.* 2018;124:1008–1015.
4. Eisenhauer EA, Therasse P, Bogaerts J, et al. New response evaluation criteria in solid tumours: revised RECIST guideline (version 1.1). *Eur J Cancer.* 2009;45:228–247.
5. Ryan CJ, Shah S, Efstathiou E, et al. Phase II study of abiraterone acetate in chemotherapy-naive metastatic castration-resistant prostate cancer displaying bone flare discordant with serologic response. *Clin Cancer Res.* 2011;17:4854–4861.
6. Keizman D, Fosboel MO, Reichegger H, et al. Imaging response during therapy with radium-223 for castration-resistant prostate cancer with bone metastases: analysis of an international multicenter database. *Prostate Cancer Prostatic Dis.* 2017; 20:289–293.
7. Scher HI, Morris MJ, Stadler WM, et al. Trial design and objectives for castration-resistant prostate cancer: updated recommendations from the Prostate Cancer Clinical Trials Working Group 3. *J Clin Oncol.* 2016;34:1402–1418.
8. Satapathy S, Singh H, Kumar R, Mittal BR. Diagnostic accuracy of ^{68}Ga-PSMA PET/CT for initial detection in patients with suspected prostate cancer: a systematic review and meta-analysis. *AJR.* 2021;216:599–607.
9. von Eyben FE, Picchio M, von Eyben R, Rhee H, Bauman G. ^{68}Ga-labeled prostate-specific membrane antigen ligand positron emission tomography/computed tomography for prostate cancer: a systematic review and meta-analysis. *Eur Urol Focus.* 2018;4:686–693.
10. FDA approves first PSMA-targeted PET drug. *J Nucl Med.* 2021;62(2):11N.
11. Thomas L, Balmus C, Ahmadzadehfar H, Essler M, Strunk H, Bundschuh RA. Assessment of bone metastases in patients with prostate cancer: a comparison between ^{99m}Tc-bone-scintigraphy and [^{68}Ga]Ga-PSMA PET/CT. *Pharmaceuticals (Basel).* 2017;10:68.
12. Zukotynski KA, Emmenegger U, Hotte S, et al. Prospective, single-arm trial evaluating changes in uptake patterns on prostate-specific membrane antigen (PSMA)-targeted ^{18}F-DCFPyL PET/CT in patients with castration-resistant prostate cancer starting abiraterone or enzalutamide. *J Nucl Med.* 2021;62:1430–1437.
13. Seitz AK, Rauscher I, Haller B, et al. Preliminary results on response assessment using ^{68}Ga-HBED-CC-PSMA PET/CT in patients with metastatic prostate cancer undergoing docetaxel chemotherapy. *Eur J Nucl Med Mol Imaging.* 2018;45: 602–612.
14. Grubmüller B, Senn D, Kramer G, et al. Response assessment using ^{68}Ga-PSMA ligand PET in patients undergoing ^{177}Lu-PSMA radioligand therapy for metastatic castration-resistant prostate cancer. *Eur J Nucl Med Mol Imaging.* 2019;46: 1063–1072.
15. Heinzel A, Boghos D, Mottaghy FM, et al. ^{68}Ga-PSMA PET/CT for monitoring response to ^{177}Lu-PSMA-617 radioligand therapy in patients with metastatic castration-resistant prostate cancer. *Eur J Nucl Med Mol Imaging.* 2019;46:1054–1062.
16. Michalski K, Klein C, Brueggemann T, Meyer PT, Jilg CA, Ruf J. Assessing response to [^{177}Lu]PSMA radioligand therapy using modified PSMA PET progression criteria. *J Nucl Med.* 2021;62:1741–1746.
17. Grubmüller B, Rasul S, Baltzer P, et al. Response assessment using [^{68}Ga]Ga-PSMA ligand PET in patients undergoing systemic therapy for metastatic castration-resistant prostate cancer. *Prostate.* 2020;80:74–82.
18. Ahmadzadehfar H, Azgomi K, Hauser S, et al. ^{68}Ga-PSMA-11 PET as a gatekeeper for the treatment of metastatic prostate cancer with ^{223}Ra: proof of concept. *J Nucl Med.* 2017;58:438–444.
19. Jong JM, Oprea-Lager DE, Hooft L, et al. Radiopharmaceuticals for palliation of bone pain in patients with castration-resistant prostate cancer metastatic to bone: a systematic review. *Eur Urol.* 2016;70:416–426.
20. Parker C, Nilsson S, Heinrich D, et al. Alpha emitter radium-223 and survival in metastatic prostate cancer. *N Engl J Med.* 2013;369:213–223.
21. Sartor O, Coleman RE, Nilsson S, et al. An exploratory analysis of alkaline phosphatase, lactate dehydrogenase, and prostate-specific antigen dynamics in the phase 3 ALSYMPCA trial with radium-223. *Ann Oncol.* 2017;28:1090–1097.
22. Boellaard R, Delgado-Bolton R, Oyen WJ, et al. FDG PET/CT: EANM procedure guidelines for tumour imaging—version 2.0. *Eur J Nucl Med Mol Imaging.* 2015; 42:328–354.
23. Lowekamp BC, Chen DT, Ibáñez L, Blezek D. The design of SimpleITK. *Front Neuroinform.* 2013;7:45.
24. Wahl RL, Jacene H, Kasamon Y, Lodge MA. From RECIST to PERCIST: evolving considerations for PET response criteria in solid tumors. *J Nucl Med.* 2009; 50(suppl 1):122S–150S.
25. O JH, Lodge MA, Wahl RL. Practical PERCIST: a simplified guide to PET response criteria in solid tumors 1.0. *Radiology.* 2016;280:576–584.
26. Perez-Lopez R, Lorente D, Blackledge MD, et al. Volume of bone metastasis assessed with whole-body diffusion-weighted imaging is associated with overall survival in metastatic castration-resistant prostate cancer. *Radiology.* 2016;280:151–160.
27. Sheehan B, Neeb A, Buroni L, et al. Prostate-specific membrane antigen expression and response to DNA damaging agents in prostate cancer. *Clin Cancer Res.* 2022;28:3104–3115.
28. Chang SS, Reuter VE, Heston WD, Bander NH, Grauer LS, Gaudin PB. Five different anti-prostate-specific membrane antigen (PSMA) antibodies confirm PSMA expression in tumor-associated neovasculature. *Cancer Res.* 1999;59:3192–3198.
29. Uijen MJM, Derks YHW, Merkx RIJ, et al. PSMA radioligand therapy for solid tumors other than prostate cancer: background, opportunities, challenges, and first clinical reports. *Eur J Nucl Med Mol Imaging.* 2021;48:4350–4368.
30. Marques FG, Poli E, Rino J, et al. Low doses of ionizing radiation enhance the angiogenic potential of adipocyte conditioned medium. *Radiat Res.* 2019;192:517–526.
31. Subbiah V, Anderson PM, Kairemo K, et al. Alpha particle radium 223 dichloride in high-risk osteosarcoma: a phase I dose escalation trial. *Clin Cancer Res.* 2019; 25:3802–3810.
32. Heinrich D, Bruland O, Guise TA, Suzuki H, Sartor O. Alkaline phosphatase in metastatic castration-resistant prostate cancer: reassessment of an older biomarker. *Future Oncol.* 2018;14:2543–2556.

The Diagnostic Value of the Sentinel Node Procedure to Detect Occult Lymph Node Metastases in PSMA PET/CT Node–Negative Prostate Cancer Patients

Jan J. Duin[1,2], Hilda A. de Barros[1,2], Maarten L. Donswijk[3], Eva E. Schaake[4], Tim M. van der Sluis[2,5], Esther M.K. Wit[1,2], Fijs W.B. van Leeuwen[1,6], Pim J. van Leeuwen[1,2], and Henk G. van der Poel[1,2,5]

[1]*Department of Urology, Netherlands Cancer Institute–Antoni van Leeuwenhoek Hospital, Amsterdam, The Netherlands;* [2]*Prostate Cancer Network The Netherlands, Amsterdam, The Netherlands;* [3]*Department of Nuclear Medicine, Netherlands Cancer Institute–Antoni van Leeuwenhoek Hospital, Amsterdam, The Netherlands;* [4]*Department of Radiation Oncology, Netherlands Cancer Institute–Antoni van Leeuwenhoek Hospital, Amsterdam, The Netherlands;* [5]*Department of Urology, Amsterdam University Medical Center, Amsterdam, The Netherlands; and* [6]*Interventional Molecular Imaging Laboratory, Department of Radiology, Leiden University Medical Center, Leiden, The Netherlands*

Our objective was to assess the diagnostic value of the sentinel node (SN) procedure for lymph node staging in primary intermediate- and high-risk prostate cancer patients with node-negative results on prostate-specific membrane antigen PET/CT (miN0). **Methods:** From 2016 to 2022, 154 patients with primary, miN0 PCa were retrospectively included. All patients had a Briganti nomogram–assessed nodal risk of more than 5% and underwent a robot-assisted SN procedure for nodal staging. The prevalence of nodal metastases at histopathology and the occurrence of surgical complications according to the Clavien–Dindo classification were evaluated. **Results:** The SN procedure yielded 84 (14%) tumor-positive lymph nodes with a median metastasis size of 3 mm (interquartile range, 1–4 mm). In total, 55 patients (36%) were reclassified as pN1. A complication of Clavien–Dindo grade 3 or higher occured in 1 patient (0.6%). **Conclusion:** The SN procedure classified 36% of patients with miN0 prostate cancer with an elevated risk of nodal metastases as pN1.

Key Words: sentinel node; lymph node metastases; prostate cancer; PSMA PET

J Nucl Med 2023; 64:1563–1566
DOI: 10.2967/jnumed.123.265556

The presence of lymph node (LN) metastases has a great impact on the prognosis and management of prostate cancer (PCa) (*1*). Therefore, nodal sampling is recommended for primary PCa patients with a nomogram-assessed risk of LN metastases of more than 5% undergoing radical prostatectomy (*2*). The gold standard for LN staging in PCa is an extended pelvic LN dissection (ePLND) (*2*). As this procedure is associated with morbidity (*3*), alternative options are being explored. The sentinel node (SN) procedure is a procedure in which the first draining LNs are located, removed, and histopathologically assessed for metastases. By yielding a similar diagnostic accuracy and extending nodal detection to aberrant locations, the SN procedure has proven to be a less invasive alternative to ePLND (*4,5*) but is still considered experimental because of a lack of high-quality evidence supporting its oncologic efficacy (*2*).

Most studies assessing the diagnostic value of the SN procedure in PCa nodal staging have been performed on patients staged with conventional imaging (*4,6*). Due to its superior accuracy in detecting macrometastases, prostate-specific membrane antigen (PSMA) PET/CT has now set the new standard in noninvasive PCa staging (*7*). An intrinsic limitation of this modality is its inability to accurately detect metastases smaller than 3 mm (*8,9*). Relying on PSMA-based target identification is therefore prone to missing of micrometastases (*10*). Thus, patients with node-negative PSMA PET/CT (miN0) may still benefit from an SN procedure.

The aim of this study was to investigate the prevalence of LN metastases at final histopathologic examination in miN0 intermediate- and high-risk PCa patients undergoing SN procedures. The secondary outcome was 90-d Clavien–Dindo surgical complications after the SN procedure.

MATERIALS AND METHODS

This retrospective, single-center study was conducted at The Netherlands Cancer Institute. The institutional review board (IRBdm21-216) approved this retrospective study, and the requirement to obtain informed consent was waived. Patients were included if they had biopsy-proven PCa, a Briganti 2012 nomogram–assessed risk of nodal invasion of more than 5% (*11*), and no evidence of metastases on preoperative staging PSMA PET/CT and underwent the SN procedure before radiotherapy between 2016 and 2022. Patients were excluded if the primary tumor was not visible on PSMA PET/CT. As all patients opted for primary radiotherapy, none received ePLND.

PSMA PET/CT imaging was performed either at our hospital or at the referring hospital. At our center, PET/CT imaging was performed as previously described (*12*). All PSMA PET/CT scans were reviewed by an experienced nuclear medicine physician in line with PROMISE (*13*) and discussed in multidisciplinary meetings.

SN procedures were performed as described previously (*6*), with injection of the hybrid tracer indocyanine green–^{99m}Tc-nanocolloid (*14*) transrectally in 4 quadrants of the prostate under ultrasound guidance. Subsequently, lymphoscintigrams (15 min and 2 h after injection) and SPECT/low-dose CT (SPECT/CT) were performed (Figs. 1A and 1B).

Received Feb. 6, 2023; revision accepted May 31, 2023.
For correspondence or reprints, contact Hilda A. de Barros (h.d.barros@nki.nl).
Published online Jul. 6, 2023.

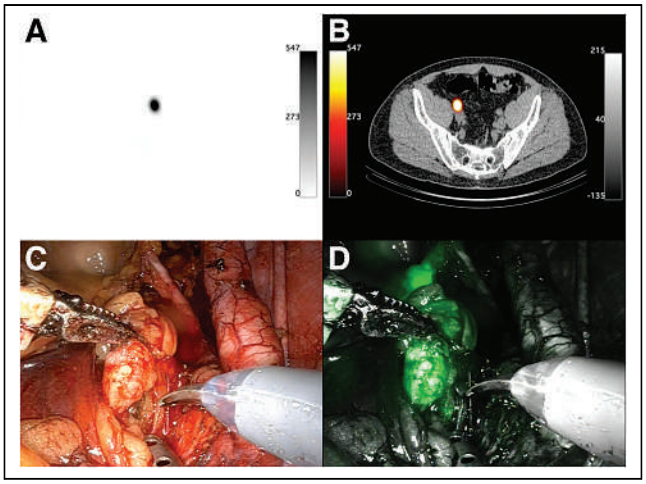

FIGURE 1. SPECT (A), SPECT/CT (B), intraoperative white light (C), and fluorescence imaging (D) of iliac SN, which harbored 3-mm metastasis on histopathology (pN1).

Experienced urologists performed robot-assisted surgery using the da Vinci Si Surgical System (Intuitive Surgical Inc.). Intraoperatively, SNs were localized using a laparoscopic γ-probe (Europrobe 2; Eurorad) and fluorescence imaging with the robot-integrated Firefly camera (Intuitive Surgical; Figs. 1C–1D).

All specimens were fixed in formalin, embedded in paraffin, sectioned at 2 mm, cut at 3 planes (150-μm intervals), stained with hematoxylin and eosin, and histopathologically examined for metastatic deposits. The CAM5.2 monoclonal antibody was used for immunohistochemical evaluation of PSMA expression in LN metastases measuring at least 5 mm.

Median and interquartile range were reported for continuous variables, and frequency and percentage were reported for categoric variables. Unpaired *t* tests or Mann–Whitney *U* nonparametric tests was used to compare continuous variables between pN0 and pN1 patients. χ^2 or Fisher exact tests was used to compare discrete variables. All statistical analyses were performed with SPSS statistics, version 27.0 (IBM Corp).

RESULTS

In total, 154 patients met the inclusion criteria and were included in the analysis (Fig. 2; Table 1). Preoperative SPECT/CT highlighted 445 SNs (median, 3 SNs per patient [interquartile range, 2–4]). Patients with unilateral ($n = 32$) or bilateral ($n = 12$) nonvisualization on SPECT/CT underwent ipsilateral ($n = 11$) or bilateral ($n = 11$) ePLND up to the ureter-vessel crossing, indocyanine green–guided node dissection ($n = 20$), or a unilateral SN procedure ($n = 2$). In patients with multiple SNs on SPECT/CT, SNs located in difficult-to-reach anatomic locations (e.g., pararectal or paraaortic) were left in situ ($n = 42$).

In total, 618 LNs were surgically excised (403 SNs and 215 non-SNs), of which 84 (14%) harbored metastases (75 SNs and 9 non-SNs; median metastasis size, 3 mm [Fig. 3]). Nodal metastases were located in the obturator fossa (52%; 44/84), external iliac (39%; 33/84), internal iliac (4%; 3/84), paravesical (2%; 2/84), presacral (1%; 1/84), and pararectal (1%; 1/84) regions. SNs were the only tumor-bearing nodes in 50 (91%) patients.

In total, 55 patients (36%) were upstaged to pN1 on the basis of the outcome of the SN procedure. Sixteen metastases were at least 5 mm, and all showed PSMA expression immunohistochemically.

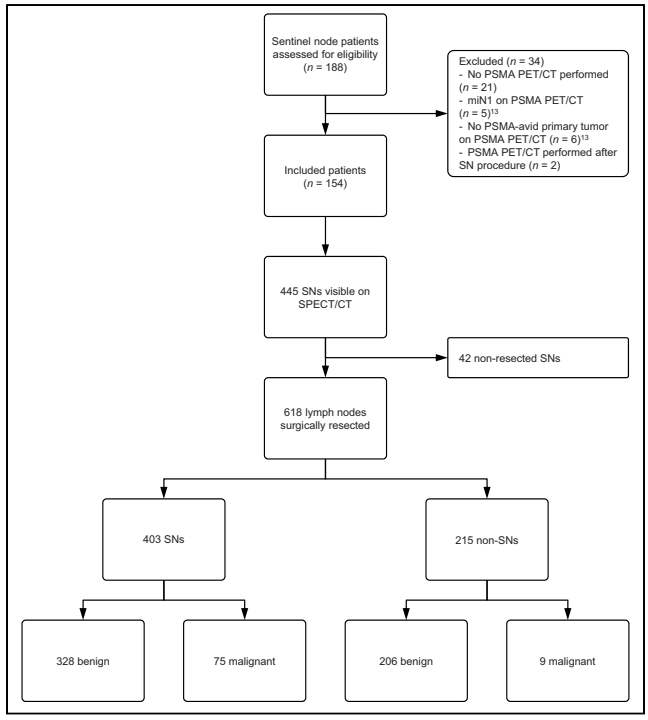

FIGURE 2. Consolidated Standards of Reporting Trials (CONSORT) diagram.

Only 1 (0.6%) patient had a high-grade complication (Clavien–Dindo ≥ 3; Table 2).

DISCUSSION

Using the SN procedure in PCa patients with increased nodal risk and miN0 disease on PSMA PET/CT resulted in upstaging of 55 (36%) patients to pN1, which may alter treatment recommendations. Our institute adjusts the radiation target volume for primary PCa patients according to the histologic outcome of the SN procedure. pN0 patients receive prostate-only radiotherapy, and pN1 patients receive additional pelvic radiotherapy and androgen deprivation therapy intensification. The oncologic benefit of such SN-based radiotherapy field adjustment (*15*) may also apply to miN0 patients. We believe the high-grade complication rate of 0.6% of the SN procedure justifies its use for nodal staging and subsequent treatment allocation.

The diagnostic value of the SN procedure in miN0 PCa patients treated with radical prostatectomy was previously evaluated (*12*). The SN procedure detected nodal metastases in 6 (19%) miN0 patients (median metastasis size, 2.0 mm; interquartile range, 1.0–3.0 mm). Building on these results, we demonstrate the diagnostic value of the SN procedure in an expanded cohort of miN0 PCa patients opting for primary radiotherapy.

SN procedures provide a means of mapping the most likely tumor lymphatic drainage, thus allowing detection of metastases and micrometastases that are not yet reached by the vascular supply and might be missed by PSMA targeting (*10*). In our study, 16 metastases measuring at least 5 mm were missed by PSMA PET/CT. Nearly one third of these positive nodes consisted of multiple micrometastases on histopathology; therefore, although the cross-sectional diameter of the metastasis may be more than 5 mm, the total volume may be too small to be detected by PSMA

TABLE 1
Patient and Diagnostic Characteristics

Characteristic	All patients (n = 154)	pN0 patients (n = 99)	pN1 patients (n = 55)	P
Age (y)	68 (63–72)	68 (63–72)	69 (63–73)	0.52
Initial PSA (μg/L)	12 (7–21)	11 (6–19)	14 (8–34)	0.03
Clinical tumor stage				0.01
cT1c	19 (12)	14 (14)	5 (9)	
cT2	83 (54)	60 (61)	23 (42)	
cT3	46 (30)	23 (23)	23 (42)	
cT4	5 (3)	1 (1)	4 (7)	
cTx	1 (1)	1 (1)	0 (0)	
Radiologic tumor stage*				<0.001
mT2	57 (37)	48 (49)	9 (16)	
mT3	90 (58)	49 (50)	41 (75)	
mT4	7 (5)	2 (2)	5 (9)	
ISUP grade group				0.007
1	1 (1)	1 (1)	0 (0)	
2	22 (14)	13 (13)	9 (16)	
3	56 (36)	43 (43)	13 (24)	
4	37 (24)	26 (26)	11 (20)	
5	38 (25)	16 (16)	22(40)	
EAU risk group				0.003
Intermediate	30 (19)	25 (25)	5 (9)	
High	73 (47)	50 (51)	23 (42)	
Locally advanced	51 (33)	24 (24)	27 (49)	
Briganti risk of LN metastasis	29 (15–52)	21 (13–41)	47 (28–75)	<0.001
PSMA tracer				0.75
^{68}Ga-PSMA-11	65 (42)	44 (44)	21 (38)	
^{18}F-DCFPyl	48 (31)	31 (31)	17 (31)	
^{18}F-PSMA-1007	30 (19)	19 (19)	11 (20)	
^{18}F-JK-PSMA-7	11 (7)	5 (5)	6 (11)	
Interval, PSMA to SN (d)	63 (43–78)	63 (44–84)	64 (42–78)	0.86
SPECT/CT-identified SNs	3 (2–4)	3 (2–4)	3 (2–4)	0.50
SNs removed	3 (2–4)	2 (2–4)	3 (2–4)	0.15
SNs positive			1 (1–2)	
Metastasis size (mm)			3 (1–4)	
Distribution SN/non-SN				
Positive SNs only			50 (91)	
Positive SNs + non-SNs			1 (2)	
Positive non-SNs only			4 (7)	

*Based on MRI.
PSA = prostate-specific antigen; ISUP = International Society of Uropathology; EAU = European Association of Urology.
Qualitative data are number and percentage; continuous data are median and interquartile range.

PET/CT. The median time between PSMA PET/CT and the SN procedure was not significantly different in patients with a metastasis of at least 5 mm and those with a metastasis of less than 5 mm. Therefore, tumor progression is unlikely to explain why macrometastases were missed.

Several limitations of this study are noteworthy. First, different scanning protocols and different PSMA-targeting tracers may have influenced interpretation of PET/CT scans. Second, nodal metastases smaller than 5 mm were not reassessed for PSMA expression. Third, since no ePLND was performed after the SN procedure, we

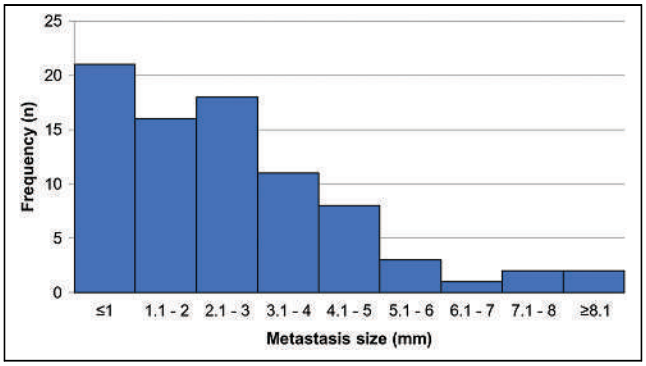

FIGURE 3. LN metastasis size distribution.

TABLE 2
90-D Complications After SN Procedure

Clavien–Dindo grade	Complication	Patients (*n*)
1		14 (9%)
	Obturator nerve–related weakness or pain	10
	Lymphedema	3
	Diverticulitis	1
2		18 (12%)
	Urinary tract infection	16
	Fever of unknown etiology	2
3a		1 (1%)
	Infected lymphocele	1
Any complication		33 (21%)
Total		154 (100%)

do not know the rate of false-negative SN biopsies. Lastly, oncologic outcomes cannot yet be accurately assessed because many patients received 3 y of androgen deprivation therapy and the current median follow-up is 2 y.

CONCLUSION

Our results demonstrate that the SN procedure detects nodal metastases in more than one third of patients with node-negative PSMA PET/CT. Smaller nodal metastases detected by examination of SNs are readily missed by PSMA PET/CT. Further studies are needed to evaluate the oncologic outcomes of SN-dependent PCa treatment in a prospective setting.

DISCLOSURE

No potential conflict of interest relevant to this article was reported.

KEY POINTS

QUESTION: Can SN biopsy improve nodal staging in PSMA PET/CT node-negative PCa patients with an increased risk of nodal invasion?

PERTINENT FINDINGS: SN biopsy upstaged 55 (36%) primary PSMA PET/CT node-negative PCa patients to pN1.

IMPLICATIONS FOR PATIENT CARE: Implementation of SN biopsy in primary PCa improves the detection of metastatic nodes, providing valuable information for further treatment guidance.

REFERENCES

1. Touijer KA, Mazzola CR, Sjoberg DD, Scardino PT, Eastham JA. Long-term outcomes of patients with lymph node metastasis treated with radical prostatectomy without adjuvant androgen-deprivation therapy. *Eur Urol.* 2014;65:20–25.
2. Mottet N, van den Bergh RCN, Briers E, et al. EAU-EANM-ESTRO-ESUR-SIOG guidelines on prostate cancer—2020 update. Part 1: screening, diagnosis, and local treatment with curative intent. *Eur Urol.* 2021;79:243–262.
3. Cacciamani GE, Maas M, Nassiri N, et al. Impact of pelvic lymph node dissection and its extent on perioperative morbidity in patients undergoing radical prostatectomy for prostate cancer: a comprehensive systematic review and meta-analysis. *Eur Urol Oncol.* 2021;4:134–149.
4. Wit EMK, Acar C, Grivas N, et al. Sentinel node procedure in prostate cancer: a systematic review to assess diagnostic accuracy. *Eur Urol.* 2017;71:596–605.
5. Acar C, Kleinjan GH, van den Berg NS, Wit EM, van Leeuwen FW, van der Poel HG. Advances in sentinel node dissection in prostate cancer from a technical perspective. *Int J Urol.* 2015;22:898–909.
6. Grivas N, Wit E, Pos F, et al. Sentinel lymph node dissection to select clinically node-negative prostate cancer patients for pelvic radiation therapy: effect on biochemical recurrence and systemic progression. *Int J Radiat Oncol Biol Phys.* 2017; 97:347–354.
7. Hofman MS, Lawrentschuk N, Francis RJ, et al. Prostate-specific membrane antigen PET-CT in patients with high-risk prostate cancer before curative-intent surgery or radiotherapy (proPSMA): a prospective, randomised, multicentre study. *Lancet.* 2020;395:1208–1216.
8. Jansen BHE, Bodar YJL, Zwezerijnen GJC, et al. Pelvic lymph-node staging with ^{18}F-DCFPyL PET/CT prior to extended pelvic lymph-node dissection in primary prostate cancer: the SALT trial. *Eur J Nucl Med Mol Imaging.* 2021;48:509–520.
9. Sprute K, Kramer V, Koerber SA, et al. Diagnostic accuracy of ^{18}F-PSMA-1007 PET/CT imaging for lymph node staging of prostate carcinoma in primary and biochemical recurrence. *J Nucl Med.* 2021;62:208–213.
10. van Leeuwen FWB, Winter A, van Der Poel HG, et al. Technologies for image-guided surgery for managing lymphatic metastases in prostate cancer. *Nat Rev Urol.* 2019;16:159–171.
11. Briganti A, Larcher A, Abdollah F, et al. Updated nomogram predicting lymph node invasion in patients with prostate cancer undergoing extended pelvic lymph node dissection: the essential importance of percentage of positive cores. *Eur Urol.* 2012;61:480–487.
12. Hinsenveld FJ, Wit EMK, van Leeuwen PJ, et al. Prostate-specific membrane antigen PET/CT combined with sentinel node biopsy for primary lymph node staging in prostate cancer. *J Nucl Med.* 2020;61:540–545.
13. Eiber M, Herrmann K, Calais J, et al. Prostate cancer molecular imaging standardized evaluation (PROMISE): proposed miTNM classification for the interpretation of PSMA-ligand PET/CT. *J Nucl Med.* 2018;59:469–478.
14. KleinJan GH, van den Berg NS, Brouwer OR, et al. Optimisation of fluorescence guidance during robot-assisted laparoscopic sentinel node biopsy for prostate cancer. *Eur Urol.* 2014;66:991–998.
15. de Barros HA, Duin JJ, Mulder D, et al. Sentinel node procedure to select clinically localized prostate cancer patients with occult nodal metastases for whole pelvis radiotherapy. *Eur Urol Open Sci.* 2023;49:80–89.

Radiation Safety Considerations of Household Waste Disposal After Release of Patients Who Have Received [^{177}Lu]Lu-PSMA-617

Stephen A. Graves

Departments of Radiology, Radiation Oncology, and Biomedical Engineering, University of Iowa, Iowa City, Iowa

Patients with metastatic prostate cancer are more likely than other groups to present for radiopharmaceutical therapy with urinary incontinence due to complications from prior local prostate cancer treatment. A consequence of urinary incontinence in patients receiving radiopharmaceutical therapy is the potential production of contaminated solid waste, which must be managed by the licensee and, at home, managed by and disposed of by the patient. Prolonging the patient stay in the treating facility after radiopharmaceutical therapy administration, until the first urinary void or potentially overnight, may moderately reduce the quantity of contaminated waste being managed by the patient at home. However, this approach does not fully mitigate the need for a patient waste-management strategy. In this brief communication, the relative radiation safety merits of contaminated waste disposal in the normal household waste stream in comparison to other waste management strategies are evaluated.

Key Words: PSMA; patient waste; incontinence; prostate cancer; Pluvicto

J Nucl Med 2023; 64:1567–1569
DOI: 10.2967/jnumed.123.265750

When patients with metastatic prostate cancer present for radiopharmaceutical therapy, they are more likely than others to have urinary incontinence due to complications from prior local prostate cancer treatment, including external-beam radiotherapy, permanent-implant low-dose-rate brachytherapy, radical prostatectomy, or some combination of these treatments. Rates of significant urinary incontinence after radiotherapy and radical prostatectomy have been reported to be as high as 52% based on patient-reported outcome surveys (*1*). After the recent Food and Drug Administration approval of [^{177}Lu]Lu-PSMA-617 (Pluvicto; Novartis Inc.) for treatment of patients with metastatic castration-resistant prostate cancer, a significant increase is expected in the number of patients with urinary incontinence receiving radiopharmaceutical therapy.

Peptide-based radiopharmaceutical therapies, including [^{177}Lu]Lu-PSMA-617, are rapidly excreted from the body primarily by renal elimination into urine. Whole-body elimination of [^{177}Lu]Lu-PSMA-617 is approximately biexponential: on average, 73% of administered activity is eliminated with a half-life of 0.071 d and the remaining 27% is eliminated with a half-life of 1.71 d (*2*). In a patient with full urinary continence, most of the administered activity will be flushed into municipal wastewater, which is the generally preferred approach to management of such waste. Among such patients, however, a significant fraction of excreted activity may remain as solid contaminated waste (adult diapers, clothing, bed linens, etc.), thereby complicating the issue of waste management. In the case of solid waste that is generated outside the radioactive material licensee's control (i.e., in the patient's own home), 3 options exist for waste management. In option A, the patient retains the waste in plastic trash bags in the home until radioactive decay is complete and the waste can be disposed of normally (i.e., as nonradioactive waste). In option B, the patient contains the waste in sanitary trash bags and immediately disposes of it in the normal household waste stream. In option C, the patient retains the waste in plastic trash bags at home and contacts the licensee to arrange waste pickup.

Option C may be logistically intractable for many medical providers. If required, and if fewer centers are able to offer therapy as a result, this approach to waste management could limit patient access to valuable medical care. Therefore, we focus on options A and B as being preferable if radiation risks to the public are sufficiently minimal.

OPTION A: DECAY IN STORAGE

For the scenario in which the patient is instructed to retain waste in the home for decay in storage, the maximally exposed member of the public is likely to be a member of the patient's household. Cumulative radiation exposure (D) to a household member can be estimated as follows:

$$D = \int_0^\infty \Gamma \left(\frac{A_p(t)\, E_p}{r_p^2} + \frac{A_w(t)\, E_w}{r_w^2} \right) dt, \qquad \text{Eq. 1}$$

where Γ is the exposure rate constant for ^{177}Lu (7.6 μSv m^2/GBq h [0.028 mrem m^2/mCi h]); $A_p(t)$ is the activity in the patient as a function of time; E_p is the occupancy factor of an individual relative to the patient, that is, the fraction of time spent near the patient; r_p is the distance (m) between the household member and the patient; $A_w(t)$ is waste activity stored in the house as a function time; E_w is occupancy factor relative to the waste, that is, the fraction of time spent near the waste; and r_w is the distance between the household member and the waste.

$A_p(t)$ is approximated by $A_0(F_1 e^{-\lambda_1 t} + F_2 e^{-\lambda_2 t})$, where A_0 is the administered activity (typically 7.4 GBq] 200 mCi]), F_1 and F_2 are the fractions of activity administered in the early and late elimination

Received Mar. 17, 2023; revision accepted May 31, 2023.
For correspondence or reprints, contact Stephen A. Graves (stephen-a-graves@uiowa.edu).
Published online Jul. 13, 2023.

phases ($F_1 = 0.730$ and $F_2 = 0.270$), and λ_1 and λ_2 are the elimination rate constants ($\lambda_1 = 0.4107\ h^{-1}$ and $\lambda_2 = 0.0169\ h^{-1}$) (*2*).

Evaluation of the integral in Equation 1 therefore yields the following:

$$D = \frac{\Gamma\ E_p}{r_p^2}\ A_0\left(\frac{F_1}{\lambda_1} + \frac{F_2}{\lambda_2}\right) + \frac{\Gamma\ E_w}{r_w^2}\ W\frac{A_w}{\lambda_p}, \qquad \text{Eq. 2}$$

where W is the fraction of activity excreted in the urine that ends up as contaminated solid waste, A_w is the total activity excreted by the patient, and λ_p is the physical decay constant for ^{177}Lu ($0.004345\ h^{-1}$).

It can be shown that A_w is calculated as follows:

$$A_w = A_0\left(1 - \frac{\frac{F_1}{\lambda_1} + \frac{F_2}{\lambda_2}}{\frac{1}{\lambda_p}}\right) = 0.923\ A_0. \qquad \text{Eq. 3}$$

This formulation implies that 92.3% of the injected activity is excreted, on average, and 7.7% decays in vivo.

Substituting the result of Equation 3 into Equation 2, and using some reasonable assumptions for occupancy and distance factors ($E_p = 0.25$; $r_p = 1$ m; $E_w = 1.00$; $r_w = 3$ m), the estimated exposure to a household member after release of a patient treated with 7.4 GBq (200 mCi) of [^{177}Lu]Lu-PSMA-617 is 249 μSv (24.9 mrem) from activity in the patient and 330 μSv (33.0 mrem) from activity in the waste, resulting in a total estimated exposure of 579 μSv (57.9 mrem) per treatment.

OPTION B: IMMEDIATE WASTE DISPOSAL

For the situation in which a patient with urinary incontinence is instructed to dispose of solid radioactive waste in the ordinary household waste stream with no delay, the radiation exposure to the sanitation worker who collects and transports the waste is of primary relevance. If one assumes that there is, on average, 24 h between waste creation and waste collection, the portion of administered activity that is collected by the sanitation worker is given by $A_w e^{-\lambda_p \times 24}$, or approximately 83.1% of the administered activity (A_0). Conservatively assuming that the household member is the individual who transports the waste outside the home for collection, taking 1 min to do so, and keeping all other considerations the same as above, the household member is expected to receive 36 μSv (3.6 mrem) from activity in the waste per treatment.

Assuming negligible radioactive decay during waste transport and an occupancy factor of 1, the radiation exposure to the sanitation worker can be expressed as

$$D = 0.831 \times \mathrm{W}\ \mathrm{A}_0\ \Gamma\left(\frac{t_c}{r_c^2} + \frac{\alpha\ t_T}{r_T^2}\right), \qquad \text{Eq. 4}$$

where t_c is the time (h) required to manually collect and empty the waste container into the sanitation truck, r_c is the distance (m) to the waste during container collection and emptying, t_T is the time (h) required to transport the waste to a waste facility, r_T is the distance (m) to the waste during transport, and α is the radiation transmission factor through the adjacent waste and the truck during transport.

The radiation transmission factor (α) can be conservatively estimated using Equation 5 for the approximate steel thickness of a sanitation truck wall ($x = \sim 0.476$ cm [$^3/_{16}$ in]), the mass attenuation coefficient of elemental iron for 208-keV photons ($\mu/\rho = 0.143\ cm^2/g$) (*3*), and the appropriate scatter build-up factor for the relevant energy and number of mean free pathlengths ($B = 1.28$) (*4*).

$$\alpha \approx Be^{\left(-\frac{\mu}{\rho}\times\rho\times x\right)} = (1.28)\ e^{-\left(0.143\frac{cm^2}{g}\right)\left(7.85\frac{g}{cm^3}\right)(0.476\ cm)} = 0.750. \qquad \text{Eq. 5}$$

This transmission estimate is conservative, as it ignores obliquity with respect to the ^{177}Lu γ-rays striking the truck wall, attenuation of lower-energy ^{177}Lu emissions (i.e., 113 keV), and attenuation by waste within the truck.

Some assumptions may be made regarding the time required to collect and transport the waste to a local municipal facility. Collection and transport times (t_c and t_T) may be estimated as 30 s (0.0083 h) and 4 h, respectively. Distances from the waste during collection and transport (r_c and r_T) may be estimated as 0.25 m and 2.0 m, respectively. Evaluating Equation 4 using these values yields a sanitation worker exposure estimate of 10.3 μSv (1.03 mrem) per patient treatment (assuming $A_0 = 7.4$ GBq [200 mCi]) or approximately 61.7 μSv (6.2 mrem) for a total of 6 treatments ($A_{total} = 44.4$ GBq [1,200 mCi]).

It is possible that a sanitation worker may provide services to multiple households that have patients undergoing treatment with [^{177}Lu]Lu-PSMA-617. According to the U.S. Bureau of Labor Statistics, approximately 138,700 "refuse and recyclable material collectors" provided services to the approximately 122,354,219 households in the United States in 2021. This implies that each sanitation worker may provide services to 882 households; however, there may be overlap (i.e., waste collection and recycling collection may be provided separately for each household), therefore, to be conservative we can assume that each sanitation worker provides services to 3,000 households.

There are approximately 268,490 new cases of prostate cancer each year in the United States, approximately 5.6% of which (15,035) will present as, or progress to the point of being, metastatic prostate cancer (*5*). If we assume that all individuals who develop metastatic prostate cancer receive [^{177}Lu]Lu-PSMA-617 and that 24% have urinary incontinence (weighted average from Daugherty et al. (*1*)), this amounts to a total of 3,608 patients with incontinence from whom sanitation workers might collect waste annually. The per-household probability of having a patient undergoing treatment is therefore 7,818 of 122,354,219, or roughly $P = 0.0029\%$ per year. Based on the assumption that individual sanitation workers service 3,000 homes, the probability of encountering N patients in a given year is given by the following binomial probability:

$$P(N) = p^N(1-p)^{3,000-N}\binom{3,000}{N}. \qquad \text{Eq. 6}$$

A conservative estimate of the probability that a sanitation worker will provide services to N patients is therefore as follows: $P(0) = 91.7\%$, $P(1) = 7.98\%$, $P(2) = 0.347\%$, $P(3) = 0.010\%$, $P(4) = 0.0002\%$, and $P(5) = 0.000004\%$.

Based on the calculation result from Equation 4, to exceed the typical regulatory limit of 1 mSv (100 mrem) a sanitation worker would need to provide services to at least 16 homes containing patients receiving [^{177}Lu]Lu-PSMA-617 in a given year. The probability of this occurring is approximately given by

$$P(N \geq 16) = 1 - \sum_{N=0}^{15} p^N(1-p)^{3,000-N}\binom{3,000}{N} = 4.56\times10^{-31}. \qquad \text{Eq. 7}$$

The number of sanitation workers who would be expected to exceed 100 mrem is therefore $(4.56\times10^{-31})(138,700) \approx 0$.

SUMMARY AND CONCLUSIONS

When a [^{177}Lu]Lu-PSMA-617 patient is incontinent, the expected excess effective dose to a member of the household is expected to be approximately 330 μSv (33 mrem) per 7.4 GBq (200 mCi) of treatment if waste is retained for decay within the household. By comparison, if the waste is disposed of in the normal household waste stream, the maximally exposed sanitation worker is expected to receive approximately 10.3 μSv (1.03 mrem) per 7.4 GBq (200 mCi) of treatment, and the household member exposure is reduced to 36 μSv (3.6 mrem). Therefore, disposal of solid contaminated waste in the normal waste stream results in approximately a 10-fold reduction in estimated household member exposure, with respect to the waste, with only a marginal increase in sanitation worker exposure relative to natural background radiation (~8 μSv/d [~0.8 mrem/d]).

The estimated exposures presented here are conservative, and true exposures are likely to be lower, both for decay in storage and for immediate household waste disposal. Household members are unlikely to spend 100% of their time at a distance of 3 m from the radioactive waste. A more conservative estimate might be 50% occupancy at a distance of 5 m, which would reduce exposure by a factor of approximately 5. In the case of a sanitation worker collecting waste, waste receptacle emptying is often automated (not performed by hand), and attenuation within the surrounding waste may be significant, likely more than 1 m of compacted waste, with a density of up to approximately 600 kg/m^3. These factors have the potential to decrease sanitation worker exposure by a factor of more than approximately 6. Additionally, the calculations provided in this paper assume immediate release from medical care after [^{177}Lu]Lu-PSMA-617 administration, whereas many patients will void before release, thereby reducing the exposure estimates in both scenarios A and B by approximately 30%. (*2*) Although not considered in this work, it is also possible that the patient could be catheterized for several days after administration, allowing for urine discharge into the sewage system. Although feasible, and some practices may consider this option, catheterization increases infection risk and reduces patient comfort, thereby potentially reducing the overall quality of care.

Regardless of the conservative nature of these calculations, it seems clear that the pragmatic approach to [^{177}Lu]Lu-PSMA-617 solid-waste management is to instruct patients to contain the waste in sanitary trash bags and to dispose of contaminated waste in the standard household waste stream. This approach is expected to minimize radiation exposure to members of the public, and cumulative exposures are expected to be well below regulatory limits.

DISCLOSURE

No potential conflict of interest relevant to this article was reported.

ACKNOWLEDGMENT

The author acknowledges substantial contributions from Pat B. Zanzonico, including the discussions that inspired this article, as well as his review and revision of the final draft.

KEY POINTS

QUESTION: What instructions should be provided to patients regarding contaminated solid waste after administration of [^{177}Lu]Lu-PSMA-617?

PERTINENT FINDINGS: Disposal of contaminated solid waste in the normal municipal waste stream is likely to minimize public radiation exposure, and the exposure received by the maximally exposed sanitation worker is expected to be approximately 10 μSv (~1 mrem) per administration.

IMPLICATIONS FOR PATIENT CARE: Prostate cancer patients with urinary incontinence can be safely treated, and they do not need to retain contaminated solid waste in their homes.

REFERENCES

1. Daugherty M, Chelluri R, Bratslavsky G, Byler T. Are we underestimating the rates of incontinence after prostate cancer treatment? Results from NHANES. *Int Urol Nephrol.* 2017;49:1715–1721.
2. Kurth J, Krause B, Schwarzenböck S, Stegger L, Schäfers M, Rahbar K. External radiation exposure, excretion, and effective half-life in ^{177}Lu-PSMA-targeted therapies. *EJNMMI Res.* 2018;8:32.
3. Hubbell JH, Seltzer SM. X-ray mass attenuation coefficients. National Institute of Standards and Technology website. https://www.nist.gov/pml/x-ray-mass-attenuation-coefficients. Updated July 2004. Accessed June 20, 2023.
4. Kiyani A, Karami AA, Bahiraee M, Moghadamian H. Calculation of gamma buildup factors for point sources. *Adv Mat Res.* 2013;2:93–98.
5. Desai MM, Cacciamani GE, Gill K, et al. Trends in incidence of metastatic prostate cancer in the US. *JAMA Netw Open.* 2022;5:e222246.

[^{177}Lu]Lu-PSMA-617 Therapy in a Patient with Chronic Kidney Disease

Lorenzo Mercolli[1], Clemens Mingels[1], Giulia Manzini[1], Paul Cumming[1,2], Konstantinos Zeimpekis[1], Song Xue[1], Ian Alberts[1], Dominik Uehlinger[3], Axel Rominger[1], Kuangyu Shi[1], and Ali Afshar-Oromieh[1]

[1]Department of Nuclear Medicine, Bern University Hospital, University of Bern, Bern, Switzerland; [2]School of Psychology and Counselling, Queensland University of Technology, Brisbane, Queensland, Australia; and [3]Department of Nephrology and Hypertension, Bern University Hospital, University of Bern, Bern, Switzerland

We report the dosimetric evaluation of prostate-specific membrane antigen–based radioligand therapy (RLT) for metastatic prostate cancer in a patient with autosomal-dominant polycystic kidney disease. **Methods:** The patient received hemodialysis during each of 6 RLT cycles while staying as an inpatient. We used voxel dosimetry and blood sampling for the dose calculation. **Results:** The patient responded well to the RLT, as indicated by the prostate-specific antigen level decreasing from 298 to 7.1 ng/mL. The doses per cycle ranged from 0.19 to 0.4 Gy/GBq for the parotid gland, 0.14 to 0.28 Gy/GBq for the submandibular gland, 0.03 to 0.11 Gy/GBq per kidney, and 0.10 to 0.15 Gy/GBq for the red bone marrow. **Conclusion:** This case suggests that [^{177}Lu]Lu-PSMA–based RLT can be applied successfully and safely to a patient with chronic kidney disease undergoing hemodialysis.

Key Words: chronic kidney disease; kidney failure; dosimetry; ^{177}Lu; prostate-specific membrane antigen; radioligand therapy

J Nucl Med 2023; 64:1570–1573
DOI: 10.2967/jnumed.123.265577

Prostate-specific membrane antigen (PSMA) is a glycoprotein with high expression on healthy prostate epithelial cells but is extremely upregulated in prostate cancer (*1–3*). This makes PSMA an ideal target for diagnostic and therapeutic applications. As a third-line treatment of metastatic castration-resistant prostate cancer, radioligand therapy (RLT) with [^{177}Lu]Lu-PSMA-617 or analogs has proven to be effective, imparting substantial benefits for the overall survival of patients (*4,5*).

The international guidelines for PSMA-based RLT do not include recommendations for patients with comorbid chronic kidney disease (CKD), who need hemodialysis during RLT. In theory, impaired kidney function could alter the pharmacokinetics of the radiopharmaceutical. In this paper, we report on the treatment with [^{177}Lu]Lu-PSMA-617 of a metastatic castration-resistant prostate cancer patient with comorbid stage 4 CKD according to the Kidney Disease: Improving Global Outcomes scale. His RLT was performed under a compassionate-use program. Apart from exploring the practical aspects of performing hemodialysis in a nuclear medicine ward, we present the organ dosimetry and effective half-life of [^{177}Lu]Lu-PSMA-617 in the patient. To the best of our knowledge, this is the first description of radiation dosimetry for a CKD patient underdoing PSMA-based RLT.

MATERIALS AND METHODS

Informed consent was obtained from the patient presented in this brief communication.

Clinical Status of the Patient

A 63-y-old patient with metastatic castration-resistant prostate cancer was referred to our hospital for [^{177}Lu]Lu-PSMA-617 RLT after all available options of first- and second-line treatments had been exhausted.

We established the indication for RLT on the basis of the high binding of the PSMA ligand [^{18}F]F-PSMA-1007 in the metastases. During the 4 y before RLT, the patient had received hemodialysis 3 times per week because of CKD with autosomal-dominant polycystic kidney disease. Supplemental Table 1 reports the renal-function data before each RLT cycle (supplemental materials are available at http://jnm.snmjournals.org).

RLT Procedure with Hemodialysis

The patient underwent 6 RLT cycles at our department between October 2021 and August 2022. In each cycle, the patient received between 7.71 and 8.07 GBq of [^{177}Lu]Lu-PSMA-617 (cumulative activity, 47.3 GBq), which was administered by intravenous injection. He stayed in the therapy ward for approximately 72 h after each cycle.

During the first RLT cycle, the patient received 3 hemodialyses while in the therapy ward. In the subsequent cycles, the patient maintained his regular hemodialysis schedule, corresponding to 2 hemodialyses during each ward visit (Table 1). With no access to treated water for dialysis at our facility, we replaced regular dialysis sessions with hemodiafiltration sessions using a Prismaflex device (Baxter International Inc.). We compensated for the lower clearance with an increased treatment time of 6.2–7.6 h, resulting in a clearance time per volume of 0.9 (*6*). The dialysate volume ranged from 40.3 to 57.0 L (Table 1). To assess the ^{177}Lu clearance from the blood, we measured the radioactivity concentration in the blood samples collected at the beginning of every hemodialysis and before the patient was discharged from the clinic.

Dosimetry

We performed the dose calculation for the organs at risk with the voxel dosimetry application of Hermes (Hermes Medical Solutions) (*7*) using SPECT/CT images (Siemens Healthineers Intevo Bold; medium-energy collimator, 128 × 128 matrix; Siemens Healthineers xSPECT reconstruction) acquired at 1, 2, 3, and 10 d after injection for 30 min of scan time in each session. A nuclear medicine resident physician segmented the parotid gland, submandibular gland, left colic flexure, and right kidney on the dose maps obtained from Hermes.

Received Mar. 8, 2023; revision accepted Jun. 12, 2023.
For correspondence or reprints, contact Lorenzo Mercolli (lorenzo.mercolli@insel.ch).
Published online Aug. 24, 2023.

TABLE 1
Therapy and Hemodialysis Data

Cycle	A_{th} (GBq)	Dialysis no.	t_{pi} (h)	V_{dia} (L)	A_{begin} (kBq/mL)	A_{end} (kBq/mL)
1	7.906	1	1.88	52.40	326.0 ± 34.0	131.0 ± 14.0
		2	24.60	40.28	68.2 ± 7.1	38.5 ± 4.0
		3	47.18	44.35	29.4 ± 3.1	16.9 ± 1.8
2	8.074	4	2.10	57.00	351.0 ± 37.0	117.0 ± 12.0
		5	49.60	49.36	46.7 ± 4.9	22.6 ± 2.4
3	7.889	6	1.71	51.18	300.0 ± 31.0	116.0 ± 12.0
		7	47.83	56.80	42.1 ± 4.4	25.0 ± 2.6
4	7.711	8	2.16	40.80	290.0 ± 30.0	136.0 ± 14.0
		9	50.88	51.29	46.4 ± 4.9	22.9 ± 2.4
5	7.806	10	1.27	50.43	271.0 ± 28.0	104.0 ± 11.0
		11	48.33	51.48	34.3 ± 3.6	19.1 ± 2.0
6	7.882	12	1.58	51.10	263.0 ± 27.0	103.0 ± 11.0
		13	49.58	50.67	35.4 ± 3.7	19.0 ± 2.0

A_{th} = administered activity; t_{pi} = time after injection to start of hemodialysis; V_{dia} = total dialysate volume; A_{begin} = activity concentration in dialysate at beginning of each hemodialysis; A_{end} = activity concentration in dialysate at end of each hemodialysis.

Following previous work (*8,9*), we used blood sampling to estimate the red bone marrow (RM) radioactivity dose. We opted for a Bayesian fit of a single-exponential function to the data (Gaussian likelihood, Gaussian priors of 0.1 ± 0.025 h^{-1} for a mean half-life and 0.89 ± 0.38 MBq/mL for the amplitude) to determine the time-integrated activity from which we performed the dose calculation according to previous data (*8*).

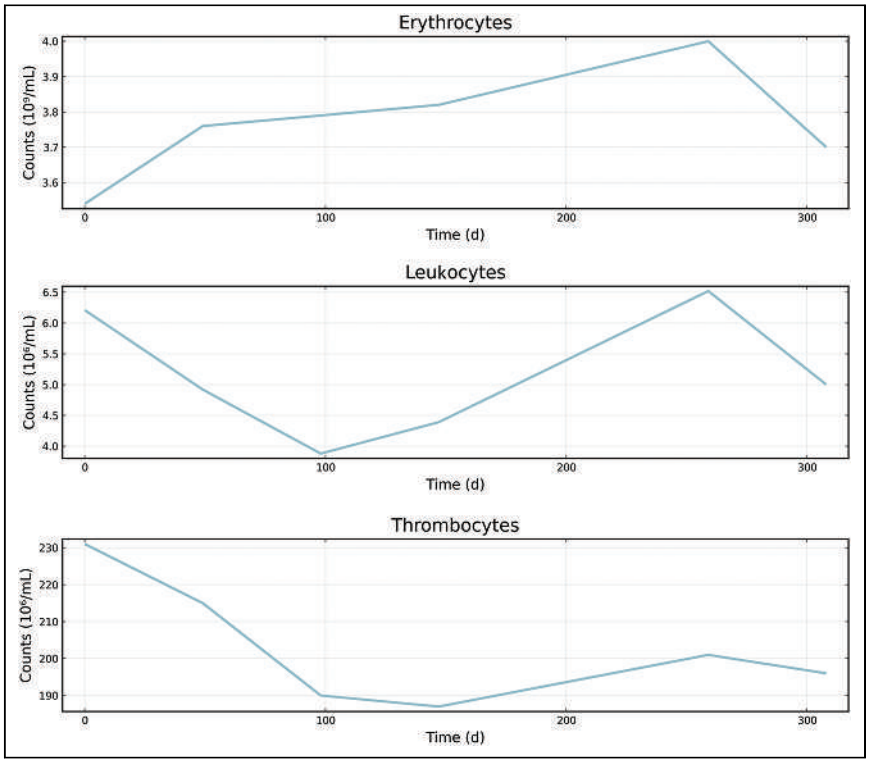

FIGURE 1. Time course of blood cell count data throughout 6 RLT cycles.

Radiation Protection

The therapy was conducted according to the standard radiation protection requirements for [^{177}Lu]Lu-PSMA-617 (*10*). While the nurse performed the hemodialysis, we monitored the whole-body effective dose with an electronic personal dosimeter to assess the additional radiation burden (*11*). We measured the dose rate of the patient before each discharge from the clinic and instructed him to follow radiation protection measures according to the Swiss regulations (www.bag.admin.ch/str-wegleitungen). Furthermore, we advised the personnel routinely performing the hemodialysis to follow standard radiation protection measures outside the therapy ward for 9 d after injection (use of disposable gloves and exclusion of pregnant women from performing the hemodialysis). We measured the residual activity in the dialysate at the beginning and at end of each hemodialysis with a calibrated γ-counter.

RESULTS

Therapy

During each RLT, a nephrologist closely monitored the patient's hemodialysis. The patient tolerated the [^{177}Lu]Lu-PSMA-617 RLT well. There were no adverse events according to the Common Terminology Criteria for Adverse Events (https://ctep.cancer.gov/protocolDevelopment/adverse_effects.htm). The prostate-specific antigen trend indicated a good tumor response for up to 4 cycles, with serum prostate-specific antigen levels decreasing from 298 to 7.1 ng/mL. However, after a longer intercycle time of 16 wk between

TABLE 2
Doses for Organs at Risk for Each Therapy Cycle

Organ	D_1	D_2	D_3	D_4	D_5	D_6
Left colic flexure	0.49	0.68	0.51	0.57	1.00	0.59
Parotid gland left	0.40	0.34	0.31	0.34	0.29	0.18
Parotid gland right	0.29	0.33	0.37	0.38	0.19	0.19
Submandibular gland left	0.23	0.27	0.28	0.13	0.17	0.14
Submandibular gland right	0.21	0.26	0.26	0.14	0.18	0.16
Right kidney	0.05	0.06	0.11	0.04	0.06	0.03
RM	0.15	0.10	0.11	0.12	0.14	0.11

D_1 to D_6 are the doses in Gy/GBq.

the fourth and fifth cycles (due to a global shortage of [^{177}Lu]Lu-PSMA-617), the prostate-specific antigen values rose again to 157 ng/mL, suggesting a relapse of the prostate cancer. There were no abnormalities found in the blood cell count data (Fig. 1).

Dosimetry

We report the organ doses of the patient in Table 2 and illustrate them in Figure 2. We do not report the dose of the left kidney because of its vicinity to the left colic flexure, which showed a much higher value in the dose map. The activity in the blood samples and the fit predictions are shown in Supplemental Figure 1. The blood effective half-life by cycle ranged from 13.8 ± 2.3 to 17.5 ± 4.1 h; Supplemental Table 2 shows the complete fit results.

Radiation Protection

The Prismaflex device was releasable from the controlled area immediately after the last hemodialysis because of the absence of detectable radioactive contamination. Therefore, only solid waste (i.e., tubing and dialysis fluid bags) showed detectable contamination with ^{177}Lu and was placed in a decay storage room for safe disposal.

The dose rate at 1 m at chest height before the patient's release (about 72 h after injection) ranged from 4.5 to 13.3 μSv/h. The individuals who performed the hemodialysis accumulated an effective dose between 8 and 42 μSv, which is consistent with previous results (*11*). For the first hemodialysis of each cycle, 24.8 ± 12.0 μSv were registered, whereas the hemodialysis performed 2 d after injection led to an effective dose of 12.7 ± 8.6 μSv. We report the radioactivity concentration in the dialysate medium at the beginning and at the end of each hemodialysis cycle in Table 1.

DISCUSSION

There is prior documentation of successful [^{177}Lu]Lu-PSMA-617 treatment of patients with reduced renal function, including a dosimetric evaluation (*12*) and, more recently, a report on hemodialyzed patients (*11*). However, these latter references focused on the practical implementation of a hemodialysis, without providing any dosimetry or blood and renal clearance data.

The doses to the salivary glands reported in Table 2 are very much comparable to those reported in the literature for typical RLT patients (*11*), but the kidney doses are almost an order of magnitude lower than the literature values (*10*). The values for the blood effective half-life somewhat exceed the 10.8 ± 2.5 h previously reported (*2*), whereas the RM doses are higher than the reported literature values (*8*). This scenario is consistent with the expectations of stage 4 renal failure and consequently slower clearance of ^{177}Lu due to the intermittent hemodialysis.

The dose limits for the salivary glands, kidney, and RM specified in the European Association of Nuclear Medicine guidelines (*10*) safely exceed what we observed in our patient (Fig. 2). The maximal RM dose was 1.1 Gy (in cycle 1), which still falls below the specified limit of 2 Gy for a single exposure (*10*). The absence of changes in the blood cell counts (Fig. 1) does not suggest an excessive radiation exposure of the RM.

On the basis of a preliminary organs-at-risk dose analysis, we reduced the number of hemodialyses in the therapy ward from 3 to 2. Across all therapy cycles, the intercycle variability of the organs-at-risk doses did not indicate any significant dependence on the number of hemodialyses performed during the RLT. Dosimetry of the hemodialysis practitioners did not indicate any untoward radiation exposure.

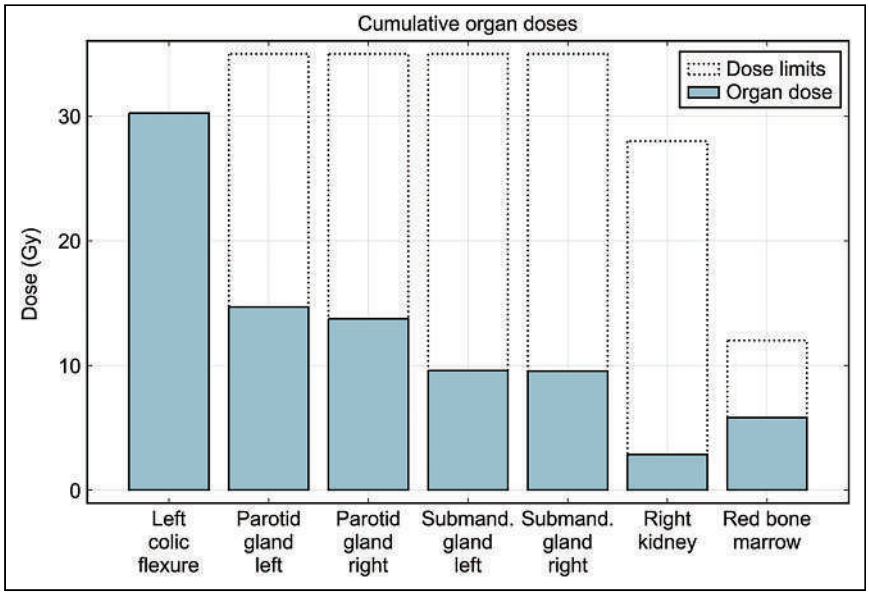

FIGURE 2. Visualization of cumulative organs-at-risk doses to patient with corresponding dose limits according to European Association of Nuclear Medicine guidelines (*10*). We multiplied single-exposure dose limit of 2 Gy for RM by factor of 6 to reflect all therapy cycles.

CONCLUSION

We report the successful treatment with [^{177}Lu]Lu-PSMA-617 of a prostate cancer patient with comorbid stage 4 CKD according to the Kidney Disease: Improving Global Outcomes scale. There were no adverse events, and the RLT was tolerated well by the patient. The organs-at-risk doses consistently fell within the dose limits of the European Association of Nuclear Medicine guidelines. This case suggests

that hemodialysis treatment for chronic renal failure should not exclude metastatic castration-resistant prostate cancer patients from obtaining RLT and that the procedure presents little radiation exposure for hemodialysis staff.

DISCLOSURE

Axel Rominger has received research support and speaker honoraria from Siemens. No other potential conflict of interest relevant to this article was reported.

KEY POINTS

QUESTION: Can [^{177}Lu]Lu-PSMA-617 therapy be applied to a patient with stage 4 CKD according to the Kidney Disease: Improving Global Outcomes scale while undergoing hemodialysis in the therapy ward?

PERTINENT FINDINGS: We applied 6 RLT cycles successfully and safely to a patient with stage 4 CKD according to the Kidney Disease: Improving Global Outcomes scale. The organ doses were well below the recommended dose limits.

IMPLICATIONS FOR PATIENT CARE: The case suggests that [^{177}Lu]Lu-PSMA-617 treatment of a patient with stage 4 CKD according to the Kidney Disease: Improving Global Outcomes scale can be performed effectively and safely and without exceeding organ dose limits.

REFERENCES

1. Afshar-Oromieh A, Malcher A, Eder M, et al. PET imaging with a [^{68}Ga]gallium-labelled PSMA ligand for the diagnosis of prostate cancer: biodistribution in humans and first evaluation of tumour lesions. *Eur J Nucl Med Mol Imaging.* 2013;40:486–495.
2. Kabasakal L, Toklu T, Yeyin N, et al. Lu-177-PSMA-617 prostate-specific membrane antigen inhibitor therapy in patients with castration-resistant prostate cancer: stability, bio-distribution and dosimetry. *Mol Imaging Radionucl Ther.* 2017;26:62–68.
3. Fendler WP, Rahbar K, Herrmann K, Kratochwil C, Eiber M. ^{177}Lu-PSMA radioligand therapy for prostate cancer. *J Nucl Med.* 2017;58:1196–1200.
4. Hofman MS, Violet J, Hicks RJ, et al. [^{177}Lu]-PSMA-617 radionuclide treatment in patients with metastatic castration-resistant prostate cancer (LuPSMA trial): a single-centre, single-arm, phase 2 study. *Lancet Oncol.* 2018;19:825–833.
5. Sartor O, de Bono J, Chi KN, et al. Lutetium-177–PSMA-617 for metastatic castration-resistant prostate cancer. *N Engl J Med.* 2021;385:1091–1103.
6. Daugirdas JT. Second generation logarithmic estimates of single-pool variable volume Kt/V: an analysis of error. *J Am Soc Nephrol.* 1993;4:1205–1213.
7. Hippeläinen E, Tenhunen M, Sohlberg A. Fast voxel-level dosimetry for ^{177}Lu labelled peptide treatments. *Phys Med Biol.* 2015;60:6685–6700.
8. Sjögreen Gleisner K, Chouin N, Gabina PM, et al. EANM dosimetry committee recommendations for dosimetry of ^{177}Lu-labelled somatostatin-receptor- and PSMA-targeting ligands. *Eur J Nucl Med Mol Imaging.* 2022;49:1778–1809.
9. Hindorf C, Glatting G, Chiesa C, et al. EANM dosimetry committee guidelines for bone marrow and whole-body dosimetry. *Eur J Nucl Med Mol Imaging.* 2010;37:1238–1250.
10. Kratochwil C, Fendler WP, Eiber M, et al. EANM procedure guidelines for radionuclide therapy with ^{177}Lu-labelled PSMA-ligands (^{177}Lu-PSMA-RLT). *Eur J Nucl Med Mol Imaging.* 2019;46:2536–2544.
11. Kneer H, Kull T, Beer AJ, Prasad V. Planning and organization of radioiodine or lutetium therapy for patients requiring dialysis [in German]. *Nucl Med (Stuttg).* 2022;61:205–206.
12. Zhang J, Kulkarni HR, Singh A, et al. ^{177}Lu-PSMA-617 radioligand therapy in metastatic castration-resistant prostate cancer patients with a single functioning kidney. *J Nucl Med.* 2019;60:1579–1586.

Clinical Experience with [^{225}Ac]Ac-PSMA Treatment in Patients with [^{177}Lu]Lu-PSMA–Refractory Metastatic Castration-Resistant Prostate Cancer

Nalan Alan-Selcuk[1], Gamze Beydagi[1], Emre Demirci[1,2], Meltem Ocak[3], Serkan Celik[4], Bala B. Oven[4], Turkay Toklu[1], Ipek Karaaslan[5], Kaan Akcay[1], Omer Sonmez[1], and Levent Kabasakal[1,6]

[1]Department of Nuclear Medicine, Faculty of Medicine, Yeditepe University, Istanbul, Turkey; [2]Department of Radiology, University of Missouri, Columbia, Missouri; [3]Molecular Imaging and Theranostics Center, University of Missouri, Columbia, Missouri; [4]Department of Medical Oncology, Faculty of Medicine, Yeditepe University, Istanbul, Turkey; [5]Department of Physics, Yeditepe University, Istanbul, Turkey; and [6]Department of Nuclear Medicine, Cerrahpasa Medical Faculty, Istanbul University, Istanbul, Turkey

For patients with advanced-stage metastatic castration-resistant prostate cancer (mCRPC) who do not respond to [^{177}Lu]Lu-PSMA therapy, there are limited treatment options. Clinical results obtained with [^{225}Ac]Ac-PSMA are promising. We retrospectively analyzed the outcomes of patients treated with [^{225}Ac]Ac-PSMA between December 2018 and October 2022. **Methods:** We evaluated the treatment results of 23 patients (mean age, 70.3 ± 8.8 y) with mCRPC who were refractory to treatment with [^{177}Lu]Lu-PSMA (2–9 cycles). The safety profile was assessed according to Common Technology Criteria for Adverse Events version 5.0. Treatment efficacy was assessed using prostate-specific membrane antigen PET progression criteria and prostate-specific antigen (PSA) response according to Prostate Cancer Working Group 2 criteria after the first cycle of [^{225}Ac]Ac-PSMA treatment. **Results:** All patients received androgen-deprivation therapy, whereas 22 (96%) and 19 (83%) patients received chemotherapy and second-generation antiandrogen therapy, respectively. One patient received 4 cycles, 2 received 3 cycles, 8 received 2 cycles, and 12 received 1 cycle of [^{225}Ac]Ac-PSMA. The median interval between cycles was 13 wk (range, 8–28 wk). [^{225}Ac]Ac-PSMA was administered with a mean activity of 7.6 MBq (range, 6.2–10.0 MBq) in each cycle. Patients were at an advanced stage of disease, and tumor burden was very high. Although the best PSA response was observed in 5 patients (26%) after [^{225}Ac]Ac-PSMA treatment, there was at least some level of decline in PSA observed in 11 patients (58%; n = 19). Treatment response was assessed in patients who underwent [^{68}Ga]Ga-PSMA PET/CT imaging. After the first cycle of treatment (n = 18), 50% of patients (n = 9) showed disease progression according to prostate-specific membrane antigen PET progression criteria, and the disease control rate was calculated to be 50%. Median progression-free survival was 3.1 mo, and median overall survival was 7.7 mo. Grade 3 hematologic toxicity occurred in 1 patient, and grade 3 nephrotoxicity was observed in another patient. Parotid SUV_{max} decreased by 33%, although all patients complained of dry mouth before treatment. **Conclusion:** We observed that [^{225}Ac]Ac-PSMA therapy was safe and showed potential even in cases with advanced-stage mCRPC in which all other treatment options were completed.

Key Words: [^{225}Ac]Ac-PSMA; actinium-targeted α-therapy; PSMA; [^{177}Lu]Lu-PSMA; prostate cancer

Received Jan. 31, 2023; revision accepted Jun. 13, 2023.
For correspondence or reprints, contact Levent Kabasakal (lkabasakal@tsnm.org).
Published online Aug. 24, 2023.

J Nucl Med 2023; 64:1574–1580
DOI: 10.2967/jnumed.123.265546

Prostate cancer is the most common malignancy in men and the second leading cause of cancer-related deaths (*1*). In the last decade, several new agents have been approved for the treatment of metastatic castration-resistant prostate cancer (mCRPC). Current standard treatment options for mCRPC include taxane-based chemotherapy (docetaxel and cabazitaxel) (*2,3*), novel androgen axis drug treatment (abiraterone or enzalutamide) (*4,5*), and bone-seeking [^{223}Ra]$RaCl_2$ therapy (*6*), which are approved by the European Medicines Agency and the U.S. Food and Drug Administration.

Prostate-specific membrane antigen (PSMA) is a glycoprotein overexpressed on prostate cancer cells. Radiolabeled PSMA inhibitors have been used for theranostic applications in the last decade. [^{177}Lu]Lu-PSMA, which emits β-particles, has been shown to be effective and safe in the treatment of mCRPC (*7,8*). An international multicenter phase III (VISION) clinical trial of [^{177}Lu]Lu-PSMA-617 demonstrated prolonged overall survival (OS) in patients with advanced PSMA-positive mCRPC and has been approved by the European Medicines Agency and U.S. Food and Drug Administration (*9*). However, currently, there are limited treatment options for patients with advanced-stage mCRPC who do not respond to treatment with [^{177}Lu]Lu-PSMA.

Radionuclides with high linear energy transfer have a cell-killing effect many times greater than that of particles with low linear energy transfer. Targeted α-therapy has the advantage of targeting any metastatic tissue and offers a good application perspective in small tumors, scattered cancers, and micrometastases (*10,11*).

^{225}Ac is an α-emitting radionuclide that can be successfully labeled with a variety of theranostic agents (*12*). The clinical results obtained with [^{225}Ac]Ac-PSMA are promising. Recent clinical trials using ^{225}Ac-labeled PSMA ligands ([^{225}Ac]Ac-PSMA-617 or [^{225}Ac]Ac-PSMA-I&T) have achieved remarkable therapeutic results. Therefore, [^{225}Ac]Ac-PSMA radioligand therapy may be an effective option for mCRPC that is resistant to β-emitting [^{177}Lu]Lu-PSMA (*13–21*).

The efficacy and safety of treatments with [^{225}Ac]Ac-PSMA, including chemotherapy and [^{177}Lu]Lu-PSMA–naïve patients, have been reported in the literature. The purpose of this retrospective

study is to evaluate the efficacy and safety of treatment with [^{225}Ac]Ac-PSMA in mCRPC patients who have not responded to chemotherapy and [^{177}Lu]Lu-PSMA treatment.

MATERIALS AND METHODS

Patients

From December 2018 to October 2022, 23 patients treated with [^{225}Ac]Ac-PSMA were enrolled in this single-center retrospective study. Inclusion criteria for [^{225}Ac]Ac-PSMA treatment were completion of first- and second-line therapies such as abiraterone, enzalutamide, and taxane-based chemotherapy and disease progression after at least 2 cycles of [^{177}Lu]Lu-PSMA treatment. Disease progression was verified by a more than 30% increase in prostate-specific antigen (PSA), a worsening of the patient's clinical condition such as pain or weight loss, or observation of new lesions on [^{68}Ga]Ga-PSMA PET/CT scans. All patients had an Eastern Cooperative Oncology Group performance status of 3 or lower, a white blood cell count of more than 2,000/μl, a red blood cell count of more than 3,000,000/μl, a hemoglobin value greater than 6 g/dL, and a serum creatinine level of less than 2 mg/dL. All patients had a high uptake in all of their metastatic lesions with [^{68}Ga]Ga-PSMA PET/CT, which was higher than liver uptake. Treatment with [^{225}Ac]Ac-PSMA was discussed individually by three experienced nuclear medicine physicians and recommended by a tumor board.

Exclusion criteria included urinary tract obstruction and bone marrow suppression as defined by Common Terminology Criteria for Adverse Events version 5.0. All patients were informed of the potential adverse events, including xerostomia, bone marrow suppression, and renal impairment. All patients gave written informed consent for treatment with [^{225}Ac]Ac-PSMA. The study was approved by the institutional ethics committee (reference no. 1736).

Preparation of [^{225}Ac]Ac-PSMA-617

[^{225}Ac]$AcCl_3$ and [^{225}Ac]$Ac(NO_3)_3$ were provided by Oak Ridge National Laboratory and the Institute of Physics and Power Engineering, respectively. In-house radiolabeling was performed in a hot cell using ^{225}Ac (1 MBq/16 nmol PSMA-617) with 0.1-M Tris buffer and 20% ascorbic acid. Radiolabeling was performed at 95°C for 20 min. After the reaction vessel cooled to room temperature, 0.3 mL of sterile diethylenetriaminepentaacetic acid solution (3 mg mL^{-1} of diethylenetriaminepentaacetic acid in saline) was added to the reaction vessel. The solution was sterilized and filtered (0.22 μM) under aseptic conditions, and the total volume was increased to 4–5 mL with sterile saline. The integrity of the filter was checked by a bubble-point test. The radiochemical yield was determined by instant thin-layer chromatography silica gel with 0.05 M citric acid as the solvent. The radiochemical yield was determined by measuring the activity of the 218-keV γ-emission from ^{221}Fr using a Captus 3000 well-type γ-counter (Capintec Inc.) after 45 min of labeling. The measured radiochemical yields of [^{225}Ac]Ac-PSMA were greater than 97% after 45 min of labeling.

Stability of [^{225}Ac]Ac-PSMA

In saline at 37°C, 1 MBq of [^{225}Ac]Ac-PSMA was incubated for up to 6 h (n = 3). At specific time points, a sample from the incubating solution was analyzed with reversed-phase high-pressure liquid chromatography (RP-HPLC) to evaluate the in vitro stability of [^{225}Ac]Ac-PSMA. HPLC fractions were measured in the γ-counter at least 20 h after collection. Fractions measured with 440-keV γ-emission from ^{213}Bi were plotted in agreement with the tube numbers from the RP-HPLC analysis. We used blood samples collected at 0–10 min and urine samples collected up to 3 h after injection to assess the in vivo stability in 3 patients. Blood samples collected from patients were precipitated with acetonitrile (1:1) and then vortexed. The precipitate was separated by a 5-min centrifugation. For RP-HPLC analysis, the supernatant was diluted with double-distilled water (1:1) and then injected into the RP-HPLC tube. Collected urine samples from patients were diluted with double-distilled water, filtered, and immediately analyzed using RP-HPLC. The measured counts of the fractions were plotted according to their tube number from the RP-HPLC analysis.

Treatment

Patients received a fluid infusion of 1,000 mL of 0.9% saline for 30 min before treatment. [^{225}Ac]Ac-PSMA was injected via slow infusion over 5 min. The amount of injected activity was 100 kBq/kg (*13*). Whole-body images were obtained between 4 and 24 h after injection using γ-rays of ^{221}Fr (218 keV) and ^{213}Bi (440 keV) with an energy window of 20%. A Discovery NM/CT 670 Pro (GE Healthcare) system with high-energy general-purpose collimators was used to obtain the images. The imaging method was a step and shoot with 15 min per step. The patients

TABLE 1
Patient Characteristics

Characteristic	Value
Age (y)	70.3 ± 8.8
PSA (ng/mL)	103.79 (0.349–727.8)
ALP (U/L)	95 (45–1,184)
LDH (U/L)	268.5 (98–2,374)
Hemoglobin (g/dL)	10.1 (7.0–12.2)
Platelet (count/μL)	154,500 (12,000–385,000)
WBC (count/μL)	5,740 (3,200–14,140)
ISUP grade group (n = 23)	
Group 1	0%
Group 2	9%
Group 3	26%
Group 4	9%
Group 5	43%
Undefined	13%
Sites of metastasis (n = 23)	
Bone	91%
Lymph node	56%
Liver	13%
Lung	22%
Leptomeningeal	4%
Subcutaneous metastasis	4%
Prior therapies (n = 23)	
Radical prostatectomy	48%
EBRT	70%
ADT	100%
Abiraterone or enzalutamide	83%
Docetaxel	96%
Cabazitaxel	43%
[^{177}Lu]Lu-PSMA	100%

ALP = alkaline phosphatase; LDH = lactate dehydrogenase; WBC = white blood cell; ISUP = International Society of Urological Pathology; EBRT = external-beam radiation therapy; ADT = androgen-deprivation therapy.

Continuous data are median and range or mean ± SD.

were observed every 60 min for 5 h to record vital signs such as blood pressure, body temperature, and pulse rate. Additionally, patients were monitored for any complaints of pain, vomiting, and nausea for 24 h according to the standard institutional protocol for all in-patient treatments.

Response Evaluation, Survival, and Toxicity

Response to [^{225}Ac]Ac-PSMA treatment was determined from serial measurements of serum PSA levels 1 wk before and every 4 wk after [^{225}Ac]Ac-PSMA treatment and by [^{68}Ga]Ga-PSMA PET/contrast-enhanced CT within 4 wk before and 8–12 wk after treatment. Response was assessed according to Prostate Cancer Clinical Trials Working Group 2 criteria (*22*) as a PSA decrease of at least 50% and a decrease from baseline. [^{68}Ga]Ga-PSMA PET/CT was repeated 8–12 wk after each treatment cycle and until disease progression or death. Radiologic evidence of disease progression was assessed according to PSMA PET progression criteria (*23*). Progression-free survival (PFS) and OS were calculated from the date of the first [^{225}Ac]Ac-PSMA administration to disease progression or death. Adverse events were documented according to Common Terminology Criteria for Adverse Events version 5.0. The total tumor volume (TTV) was determined from [^{68}Ga]Ga-PSMA PET/CT images using LIFEx version 7.2.0 (LIFExsoft) (*24*). A SUV threshold of at least 3.0 was used for tumor segmentation. The mean SUV_{max} of the parotid glands at baseline and at follow-up [^{68}Ga]Ga-PSMA PET/CT scans was calculated using a threshold value of 42% of maximum pixel value.

Statistical Analysis

Statistical analysis was performed using SPSS version 25.0 (IBM). PFS and OS with a 95% CI were estimated by the Kaplan–Meier method. Multivariate analysis was performed using Cox regression analysis in sequential order of statistical significance, variables that were found to be significant in the univariate analysis, followed by the interactive terms. Baseline factors included age, cumulative [^{225}Ac]Ac-PSMA activity, International Society of Urological Pathology grade group classification, baseline PSA levels, a PSA level with at least a 50% decline, lymph node, bone, visceral, and liver metastases, TTV, baseline hemoglobin levels, white blood cell counts, platelet counts, alkaline phosphatase levels, and lactic dehydrogenase levels. We also dichotomized the following clinical covariates: International Society of Urological Pathology grade group, PSA decline of at least 50%, and the presence of lymph node, bone, and liver metastasis. A *P* value of less than 0.05 was considered statistically significant. A Wilcoxon signed-rank test was performed to reveal changes in both TTV and SUV_{max} of the salivary glands before and after treatment with [^{68}Ga]Ga-PSMA PET/CT.

RESULTS

Patient Characteristics

All patients treated in the study were in advanced stages of mCRPC. The mean age of the patients was 70.3 ± 8.8 y. According to the International Society of Urological Pathology grade group classification, most patients were diagnosed as grade group 5. Descriptions of patient characteristics are shown in Table 1.

All patients had undergone a median of 4.5 cycles (range, 2–9 cycles) of [^{177}Lu]Lu-PSMA treatment. All patients did not respond to [^{177}Lu]Lu-PSMA treatment and had disease progression according to PSA levels and [^{68}Ga]Ga-PSMA PET/CT images obtained before [^{225}Ac]Ac-PSMA treatment. Patients who had experienced biochemical and clinical progression after [^{177}Lu]Lu-PSMA treatment were discussed with the hospital tumor board, and [^{225}Ac]Ac-PSMA treatment was decided. The mean interval between [^{177}Lu]Lu-PSMA and [^{225}Ac]Ac-PSMA treatment was 10 wk (range, 6–26 wk).

One patient received 4 cycles, 2 received 3 cycles, 8 received 2 cycles, and 12 received 1 cycle of [^{225}Ac]Ac-PSMA (a total of 34 cycles). The median interval between [^{225}Ac]Ac-PSMA treatment cycles was 13 wk (range, 8–28 wk). The mean administered activity of [^{225}Ac]Ac-PSMA was 7.6 MBq (range, 6.2–10.0 MBq) in each cycle. Although the interval between cycles was planned to be 8–10 wk, some patients were unable to initiate treatment in a timely manner because of ^{225}Ac supply shortages and travel restrictions during the coronavirus disease 2019 pandemic.

Stability of [^{225}Ac]Ac-PSMA

RP-HPLC analyses of the saline incubation samples showed a single radioactivity peak corresponding to [^{225}Ac]Ac-PSMA. However, a slight decrease of the in vitro stability of [^{225}Ac]Ac-PSMA was observed after 6 h in the saline incubation (Figs. 1A and 1B). A slight decrease of the in vitro stability was also observed with instant thin-layer chromatography, but still the radiochemical yield was higher than 95%.

RP-HPLC analyses of the blood and urine samples showed a single radioactivity peak corresponding to [^{225}Ac]Ac-PSMA; however, a slight decrease of the in vivo stability was also observed in the blood and urine after the injection (Figs. 1C and 1D). Stability in the blood could be checked only 10 min after the injection, and [^{225}Ac]Ac-PSMA remained stable for up to 10 min.

Toxicity and Side Effects

[^{225}Ac]Ac-PSMA administration was well tolerated. We did not observe any complications during the injection. No changes in blood pressure, body temperature, or pulse rate were observed for 5 h.

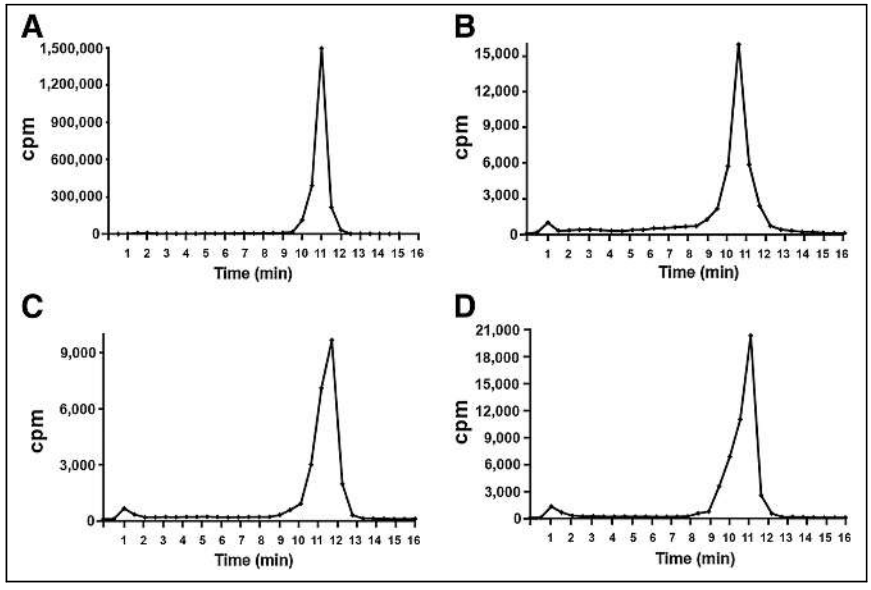

FIGURE 1. RP-HPLC profiles of 1 MBq of [^{225}Ac]Ac-PSMA from reaction vial (A), incubated in saline at 6 h (B), in blood after 8-MBq injection of radioligand in patient at 0–10 min (C), and in urine after 8-MBq injection of radioligand in patient at 3 h (D). cpm = counts per minute.

Before the [^{225}Ac]Ac-PSMA therapy, 2 patients had grade 3 nephrotoxicity; the remaining patients had grade 1 or 2 hematologic toxicity, and 4 patients had grade 1 or grade 2 nephrotoxicity due to previous treatments. In 1 patient, grade 1 to grade 3 hematologic toxicity was observed after 3 cycles of treatment. In 3 patients, grade 1 to grade 2 hematologic toxicity was observed after the first cycle of treatment. In 1 patient, grade 1 to grade 3 nephrotoxicity was observed after 2 cycles of treatment. The nephrotoxicity rate was 7%, and the total hematotoxicity rate was 28%.

All patients complained of dry mouth before and after treatment, but none of them complained from dysphagia as defined in Common Terminology Criteria for Adverse Events version 5.0. Mean parotid SUV_{max} was 12.2 ± 3.9 before treatment and decreased to 8.2 ± 2.8 (33% decrease) after the first cycle of [^{225}Ac]Ac-PSMA treatment ($n = 18$, $P = 0.001$).

Efficacy and Survival

According to the [^{68}Ga]Ga-PSMA PET/CT images obtained 8–12 wk after the first treatment cycle ($n = 18$), 50% of patients ($n = 9$) showed disease progression according to the PSMA PET progression criteria, and the disease control rate was calculated to be 50%. [^{68}Ga]Ga-PSMA PET/CT was not available to 5 patients because of an immediate deterioration of their clinical condition. After the first cycle of treatment, a decrease in PSA was observed in 11 of 19 patients (58%), and a decrease in PSA of more than 50% was observed in 5 of 19 patients (26%) (Fig. 2A).

The median baseline TTV ($n = 17$) on [^{68}Ga]Ga-PSMA PET/CT was 1,265 cm^3 (range, 99–6,450 cm^3), whereas the TTV after the first cycle of [^{225}Ac]Ac-PSMA treatment was 1,085 cm^3 (range, 85–5,170 cm^3). The change in TTV is shown in Figure 2B. The total number of patients in this analysis was 17 because the baseline images of 1 patient could not be processed with LIFEx software.

Univariate analysis showed that decreases in PSA of more than 50%, the presence of visceral and liver metastases, baseline TTV, baseline hemoglobin levels, and alkaline phosphatase and lactic dehydrogenase levels were significantly associated with OS ($P < 0.05$, 95% CI). Multivariate analysis showed that baseline TTV remained an individual predictor of OS ($P = 0.038$, 95% CI). On the other hand, the International Society of Urological Pathology grade group, baseline PSA levels, and bone metastases were found to be related to PFS ($P < 0.05$, 95% CI; Table 2).

For all patients, based on the first [^{225}Ac]Ac-PSMA treatment, the median PFS and median OS were 3.1 and 7.7 mo, respectively (Fig. 3). The estimated median OS plots for the selected parameters of the univariate analysis are shown in Figure 4.

TABLE 2
Univariate Analysis of Correlation Between Analyzed Variables and Survival

Variable	*P*	
	PFS	OS
Age (y)	0.341	0.994
Cumulative activity	0.395	0.233
ISUP grade group	0.010*	0.591
Baseline PSA level	0.033*	0.391
PSA ≥ 50% decline	0.081	0.005*
Lymph node metastasis	0.518	0.125
Bone metastasis	0.029*	0.461
Visceral metastasis	0.431	0.021*
Liver metastasis	0.170	<0.001*
TTV	0.058	<0.001*
Hemoglobin	0.359	0.007*
White blood cell count	0.964	0.964
Platelet count	0.226	0.330
ALP	0.058	0.016*
LDH	0.108	0.038*

*Statistically significant.
ISUP = International Society of Urological Pathology; ALP = alkaline phosphatase; LDH = lactate dehydrogenase.

DISCUSSION

Treatment with α-particle radiation has distinct advantages over treatment with β-particles, including a shorter range and a high linear energy transfer property. In addition, α-emitting isotopes are less dependent on the oxygen content of the tumor. These biologic advantages may explain why targeted α-therapy is superior to β-therapy. However, because of the short range of α-particles, the cross-fire effect may be less than with β-particles. Combination therapy with α- and β-particles may compensate for the lack of a cross-fire effect (*25*). The radiobiologic properties of ^{225}Ac for labeling with the PSMA molecule may provide a reasonable alternative. In this study, we investigated the in vivo and in vitro stability of [^{225}Ac]Ac-PSMA. The radiolabeling process of [^{225}Ac]Ac-PSMA is very similar to that of [^{177}Lu]Lu-PSMA and remains quite stable in vivo and in vitro. The in vitro stability of [^{225}Ac]Ac-PSMA decreased slightly in saline, but the radiochemical yield was still higher than 95% after 6 h of incubation in saline. [^{225}Ac]Ac-PSMA remained stable for up to 10 min in the blood and for up to 3 h in urine. In addition, we observed no side effects during injection and no change in patients' vital signs for at least 5 h after injection of [^{225}Ac]Ac-PSMA.

Treatment with [^{177}Lu]Lu-PSMA is well established in mCRPC patients. However, many of these patients become resistant to [^{177}Lu]Lu-PSMA treatment, and there are limited treatment options left for this patient group. [^{225}Ac]Ac-PSMA treatment is a new

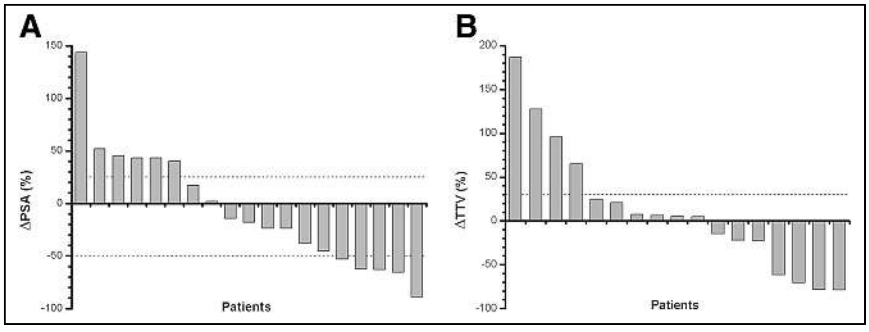

FIGURE 2. Waterfall plot demonstrating percentage change of PSA (A) and TTV (B) after first cycle of [^{225}Ac]Ac-PSMA treatment.

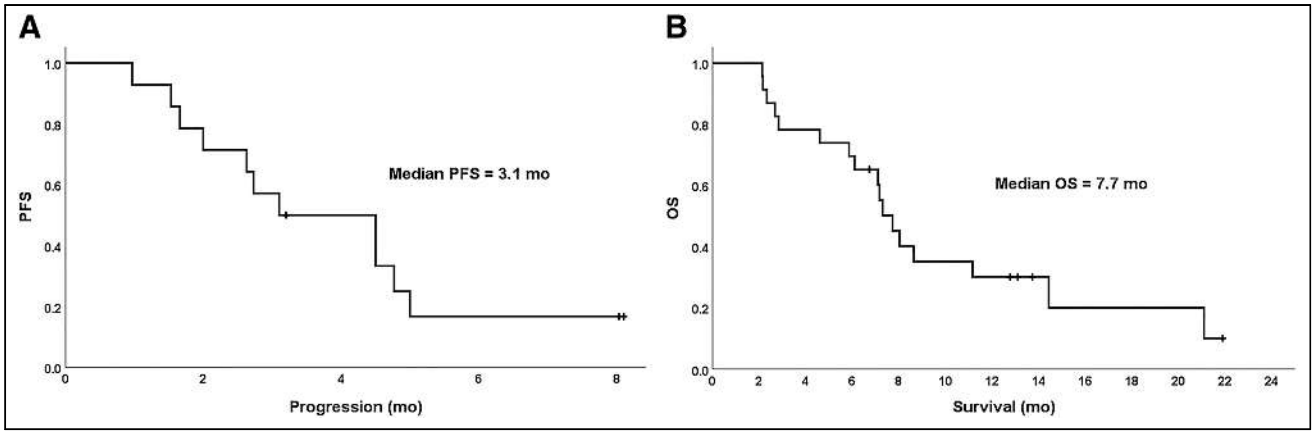

FIGURE 3. PFS (A) and OS (B) estimates from Kaplan–Meier analysis based on first [^{225}Ac]Ac-PSMA treatment date.

radionuclide treatment option, but there are very few publications in the literature on the topic. In the first report of [^{225}Ac]Ac-PSMA therapy, which included 2 patients, the serum PSA levels were shown to have decreased below detectable levels with limited toxicity in both patients, and both patients responded completely to [^{68}Ga]Ga-PSMA imaging (*13*). This early observation is promising in this area. In the analysis of 38 patients, some PSA decline was observed in 33 patients (87%), and there was a PSA decline of more than 50% in 24 patients (63%) (*26*). The median duration of tumor control was 9 mo. In another study of 73 patients with mCRPC, some PSA decline was observed in 60 patients (82%), and there was a PSA decline of more than 50% in 51 patients (70%) (*17*). The estimated median PFS and OS were 15.2 and 18 mo, respectively. In our study, after the first cycle of [^{225}Ac]Ac-PSMA treatment, a PSA response of at least 50% was observed in 5 patients (26%) (Fig. 5), with some decline in PSA in 11 patients (58%). The survival times were shorter, and the PSA response rates were relatively lower. We believe that the explanation for the lower response rate is related to patient-selection criteria. These studies included chemotherapy or [^{177}Lu]Lu-PSMA–naïve patients. In our study, all patients underwent all standard treatment options and also showed disease progression after at least 2 cycles of [^{177}Lu]Lu-PSMA treatment. On the contrary,

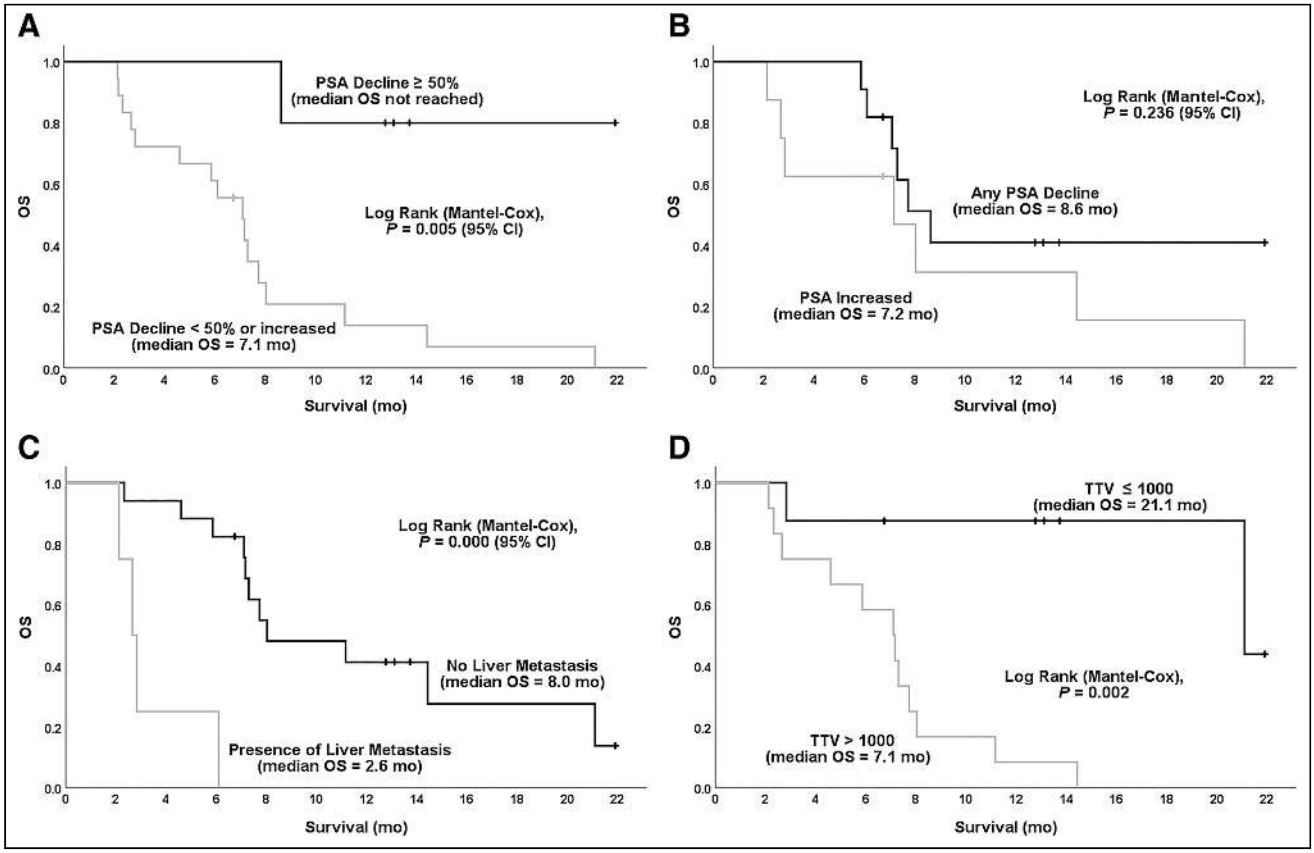

FIGURE 4. Survival analysis of patients who showed more than 50% PSA decline (A), any PSA decline (B), liver metastasis (C), and TTV of more than 1,000 cm^3 (D).

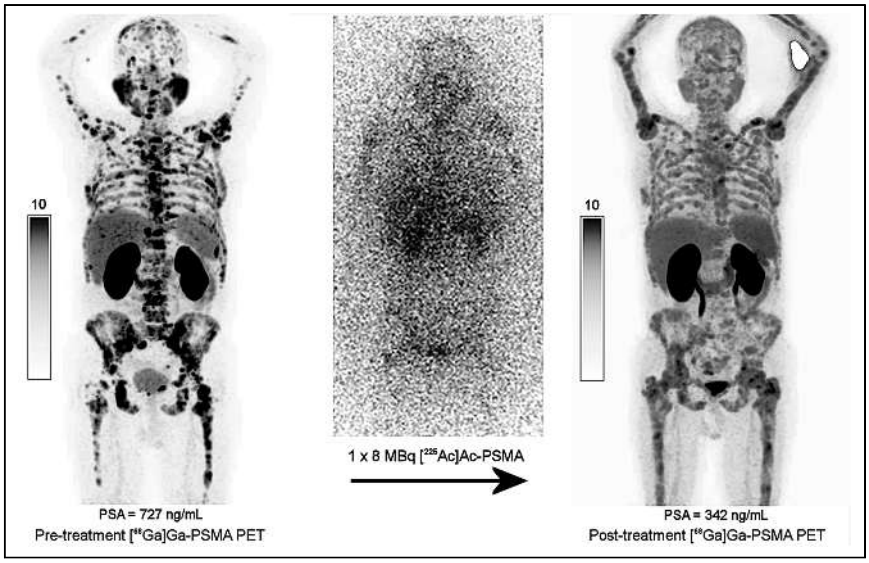

FIGURE 5. Pretreatment and posttreatment [^{68}Ga]Ga-PSMA PET maximum-intensity projection images of patient showing partial response.

the study by Feuerecker (*20*), which treated a cohort of patients similar to that in our study, showed that the median PSA PFS, clinical PFS, and OS were 3.5, 4.1, and 7.7 mo, respectively, which were similar to our study. Consistent with our study, they also showed that liver metastases were associated with shorter PSA PFS (median, 1.9 vs. 4.0 mo; $P = 0.02$), clinical PFS (median, 1.8 vs. 5.2 mo; $P = 0.001$), and OS (median, 4.3 vs. 10.4 mo; $P = 0.01$) (Figs. 3 and 4).

Rosar et al. (*27*) examined the importance of assessing early molecular-imaging response based on total viable tumor burden and its relationship to OS. Alkaline phosphatase levels, Eastern Cooperative Oncology Group classification, and biochemical and molecular-imaging response assessments were all significantly associated with OS according to univariate analysis. They showed that molecular-imaging response assessment, high alkaline phosphatase levels of at least 220 U/L, and an Eastern Cooperative Oncology Group of 2 or higher remained independent predictors of OS, with hazard ratios of 2.76, 3.08, and 2.21, respectively. Similarly, we demonstrated that the presence of liver metastasis, a high total tumor burden, and the absence of a PSA response decline of more than 50% shortened OS. Disease progression occurred earlier in patients with bone metastases and high baseline PSA levels. In our study, tumor burden was quite high (median TTV, 1,265 cm^3), which was due to our end-stage patient population. Accordingly, multivariate analysis showed that baseline TTV remained an independent predictor of OS ($P < 0.05$, 95% CI). This finding may suggest that an early treatment decision may be beneficial, and better outcomes may be achieved when patients with lower TTV receive [^{225}Ac]Ac-PSMA therapy.

In the safety analysis, no relevant hematologic toxicity was observed, and xerostomia was the only clinical side effect worth mentioning (*13*). On the other hand, in a recent metaanalysis (*28*), the rate of hematotoxicity after [^{225}Ac]Ac-PSMA treatment was calculated to be 30%, which is comparable to that in our study. We observed grade 3 and grade 2 hematotoxicity in 7% and 21% of patients, respectively. As for nephrotoxicity, grade 3 nephrotoxicity was observed in 1 patient (7%) in our study. In the same metaanalysis, a nephrotoxicity rate of 21% was reported. Regarding nephrotoxicity, our results were quite low when compared with the metaanalysis.

In a recent article, Lawal et al. (*21*) also reported low hematologic toxicity in patients with extensive skeletal metastases and a relatively high TTV. They found that age, number of treatment cycles, and the presence of renal dysfunction predicted hematologic toxicity. Although prior therapies such as chemotherapy or [^{177}Lu]Lu-PSMA therapies had an impact on the occurrence of hematologic toxicity in univariate analysis, it did not appear to be a predictive factor in multivariate analysis in their study. Our toxicity results were similar to those reported in their study. However, the average number of treatment cycles with [^{225}Ac]Ac-PSMA was lower in our study. Therefore, the toxicity results should be interpreted with caution.

The most common reason for discontinuation of [^{225}Ac]Ac-PSMA treatment was xerostomia, which may affect up to 10% of patients, according to published studies (*13*). We observed that salivary gland uptake in [^{68}Ga]Ga-PSMA PET/CT images decreased significantly after the first cycle of treatment. Cooling of the salivary glands with ice has been widely used to prevent xerostomia (*29*). However, the beneficial effect of cooling in the prevention of xerostomia has not yet been reported in the literature. Therefore, we did not use cooling, which is quite uncomfortable for patients. None of our patients discontinued treatment because of xerostomia, and we did not observe the patients to have any swallowing problems. However, all patients complained of dry mouth before and after treatment.

The main limitations of this study are that it is a retrospective study of a single center and the cohort is small. The toxicity results of this study should be interpreted with caution because a substantial number of patients were treated with only 1 cycle of [^{225}Ac]Ac-PSMA therapy. On the other hand, most of these patients had very large TTVs and were treated intensively before [^{225}Ac]Ac-PSMA therapy. Nevertheless, these patients did not develop significant toxicity. Long-term toxicity is also unknown because of the limited duration of the follow-up. Because of the pandemic and a group of patients who had to travel from abroad, follow-up data were lacking for some patients. However, the available data were sufficient to draw a conclusion for the short-term period.

CONCLUSION

We observed that [^{225}Ac]Ac-PSMA therapy was safe and effective, and toxicities were manageable. The treatment has potential even in advanced-stage mCRPC patients in whom almost all treatment options were completed. In patients with liver metastases and high TTV, an association with low OS was noted, and the benefits and risks of [^{225}Ac]Ac-PSMA treatment should be carefully weighed.

DISCLOSURE

No potential conflict of interest relevant to this article was reported.

KEY POINTS

QUESTION: Is treatment with [^{225}Ac]Ac-PSMA safe and effective in patients with mCRPC who are refractory to [^{177}Lu]Lu-PSMA?

PERTINENT FINDINGS: Treatment with [^{225}Ac]Ac-PSMA appears to be safe and may be particularly effective in patients with low TTV and in patients without liver metastases.

IMPLICATIONS FOR PATIENT CARE: [^{225}Ac]Ac-PSMA treatment may be an alternative for patients who have no other options.

REFERENCES

1. Siegel RL, Miller KD, Fuchs HE, Jemal A. Cancer statistics, 2021. *CA Cancer J Clin*. 2021;71:7–33.
2. de Bono JS, Oudard S, Ozguroglu M, et al. Prednisone plus cabazitaxel or mitoxantrone for metastatic castration-resistant prostate cancer progressing after docetaxel treatment: a randomised open-label trial. *Lancet.* 2010;376:1147–1154.
3. Tannock IF, Horti J, Oudard S, James ND, Rosenthal MA. Docetaxel plus prednisone or mitoxantrone plus prednisone for advanced prostate cancer. *N Engl J Med.* 2004;351:1502–1512.
4. de Bono JS, Logothetis CJ, Molina A, et al. Abiraterone and increased survival in metastatic prostate cancer. *N Engl J Med.* 2011;364:1995–2005.
5. Scher HI, Fizazi K, Saad F, et al. Increased survival with enzalutamide in prostate cancer after chemotherapy. *N Engl J Med.* 2012;367:1187–1197.
6. Parker C, Nilsson S, Heinrich D, et al. Alpha emitter radium-223 and survival in metastatic prostate cancer. *N Engl J Med.* 2013;369:213–223.
7. Mayor N, Sathianathen NJ, Buteau J, et al. Prostate-specific membrane antigen theranostics in advanced prostate cancer: an evolving option. *BJU Int.* 2020;126:525–535.
8. Hofman M, Emmett L, Sandhu S, et al. [^{177}Lu]Lu-PSMA-617 versus cabazitaxel in patients with metastatic castration-resistant prostate cancer (TheraP): a randomised, open-label, phase 2 trial. *Lancet.* 2021;397:797–804.
9. Sartor O, de Bono J, Chi K, et al. Lutetium-177–PSMA-617 for metastatic castration-resistant prostate cancer. *N Engl J Med.* 2021;385:1091–1103.
10. Ma J, Li L, Liao T, et al. Efficacy and safety of ^{225}Ac-PSMA-617-targeted alpha therapy in metastatic castration-resistant prostate cancer: a systematic review and meta-analysis. *Front Oncol.* 2022;12:796657.
11. Rizvi SMA, Chang FQ, Song YJ, Raja C, Allen BJ. In vivo studies of pharmacokinetics and efficacy of bismuth-213 labeled antimelanoma monoclonal antibody 9.2.27. *Cancer Biol Ther.* 2005;4:763–768.
12. Hooijman EL, Chalashkan Y, Ling SW, et al. Development of [^{225}Ac]Ac-PSMA-I&T for targeted alpha therapy according to GMP guidelines for treatment of mCRPC. *Pharmaceutics.* 2021;13:715.
13. Kratochwil C, Bruchertseifer F, Giesel FL, et al. ^{225}Ac-PSMA-617 for PSMA-targeted α-radiation therapy of metastatic castration-resistant prostate cancer. *J Nucl Med.* 2016;57:1941–1944.
14. Sathekge M, Bruchertseifer F, Knoesen O, et al. ^{225}Ac-PSMA-617 in chemotherapy-naive patients with advanced prostate cancer: a pilot study. *Eur J Nucl Med Mol Imaging.* 2019;46:129–138.
15. Yadav MP, Ballal S, Sahoo RK, Tripathi M, Seth A, Bal C. Efficacy and safety of ^{225}Ac-PSMA-617 targeted alpha therapy in metastatic castration-resistant prostate cancer patients. *Theranostics.* 2020;10:9364–9377.
16. Zacherl MJ, Gildehaus FJ, Mittlmeier L, et al. First clinical results for PSMA-targeted α-therapy using ^{225}Ac-PSMA-I&T in advanced-mCRPC patients. *J Nucl Med.* 2021;62:669–674.
17. Sathekge M, Bruchertseifer F, Vorster M, et al. Predictors of overall and disease-free survival in metastatic castration-resistant prostate cancer patients receiving ^{225}Ac-PSMA-617 radioligand therapy. *J Nucl Med.* 2020;61:62–69.
18. van der Doelen MJ, Mehra N, van Oort IM, et al. Clinical outcomes and molecular profiling of advanced metastatic castration-resistant prostate cancer patients treated with ^{225}Ac-PSMA-617 targeted alpha-radiation therapy. *Urol Oncol.* 2021;39:729.e7–729.e16.
19. Satapathy S, Mittal BR, Sood A, et al. Health-related quality-of-life outcomes with actinium-225-prostate-specific membrane antigen-617 therapy in patients with heavily pretreated metastatic castration-resistant prostate cancer. *Indian J Nucl Med.* 2020;35:299–304.
20. Feuerecker B, Tauber R, Knorr K, et al. Activity and adverse events of actinium-225-PSMA-617 in advanced metastatic castration-resistant prostate cancer after failure of lutetium-177-PSMA. *Eur Urol.* 2021;79:343–350.
21. Lawal IO, Morgenstern A, Vorster M, et al. Hematologic toxicity profile and efficacy of [^{225}Ac]Ac-PSMA-617 α-radioligand therapy of patients with extensive skeletal metastases of castration-resistant prostate cancer. *Eur J Nucl Med Mol Imaging.* 2022;49:3581–3592.
22. Scher HI, Halabi S, Tannock I, et al. Design and end points of clinical trials for patients with progressive prostate cancer and castrate levels of testosterone: recommendations of the Prostate Cancer Clinical Trials Working Group. *J Clin Oncol.* 2008;26:1148–1159.
23. Fanti S, Hadaschik B, Herrmann K. Proposal for systemic-therapy response-assessment criteria at the time of PSMA PET/CT imaging: the PSMA PET progression criteria. *J Nucl Med.* 2020;61:678–682.
24. Nioche C, Orlhac F, Boughdad S, et al. LIFEx: a freeware for radiomic feature calculation in multimodality imaging to accelerate advances in the characterization of tumor heterogeneity. *Cancer Res.* 2018;78:4786–4789.
25. Rosar F, Krause J, Bartholoma M, et al. Efficacy and safety of [^{225}Ac]Ac-PSMA-617 augmented [^{177}Lu]Lu-PSMA-617 radioligand therapy in patients with highly advanced mCRPC with poor prognosis. *Pharmaceutics.* 2021;13:722.
26. Kratochwil C, Bruchertseifer F, Rathke H, et al. Targeted α-therapy of metastatic castration-resistant prostate cancer with ^{225}Ac-PSMA-617: swimmer-plot analysis suggests efficacy regarding duration of tumor control. *J Nucl Med.* 2018;59:795–802.
27. Rosar F, Wenner F, Khreish F, et al. Early molecular imaging response assessment based on determination of total viable tumor burden in [^{68}Ga]Ga-PSMA-11 PET/CT independently predicts overall survival in [^{177}Lu]Lu-PSMA-617 radioligand therapy. *Eur J Nucl Med Mol Imaging.* 2022;49:1584–1594.
28. Ling SW, Blois E, Hooijman E, Veldt A, Brabander T. Advances in ^{177}Lu-PSMA and ^{225}Ac-PSMA radionuclide therapy for metastatic castration-resistant prostate cancer. *Pharmaceutics.* 2022;14:2166.
29. Rathke H, Kratochwil C, Hohenberger R, et al. Initial clinical experience performing sialendoscopy for salivary gland protection in patients undergoing ^{225}Ac-PSMA-617 RLT. *Eur J Nucl Med Mol Imaging.* 2019;46:139–147.

In Vivo Cerebral Imaging of Mutant Huntingtin Aggregates Using ^{11}C-CHDI-180R PET in a Nonhuman Primate Model of Huntington Disease

Daniele Bertoglio*[1,2], Alison R. Weiss*[3], William Liguore[3], Lauren Drew Martin[4], Theodore Hobbs[4], John Templon[5], Sathya Srinivasan[6], Celia Dominguez[7], Ignacio Munoz-Sanjuan[7], Vinod Khetarpal[7], Jeroen Verhaeghe[2], Steven Staelens[2], Jeanne Link[5], Longbin Liu[7], Jonathan A. Bard[7], and Jodi L. McBride[3,8]

[1]*Bio-Imaging Lab, University of Antwerp, Antwerp, Belgium;* [2]*Molecular Imaging Center Antwerp, University of Antwerp, Antwerp, Belgium;* [3]*Division of Neuroscience, Oregon National Primate Research Center, Beaverton, Oregon;* [4]*Division of Animal Resources and Research Support, Oregon National Primate Research Center, Beaverton, Oregon;* [5]*Center for Radiochemistry Research, Oregon Health and Science University, Portland, Oregon;* [6]*Integrated Pathology Core, Oregon National Primate Research Center, Beaverton, Oregon;* [7]*CHDI Management/CHDI Foundation, Los Angeles, California; and* [8]*Department of Behavioral Neuroscience, Oregon Health and Science University, Portland, Oregon*

Huntington disease (HD) is a neurodegenerative disorder caused by an expanded polyglutamine (CAG) trinucleotide expansion in the huntingtin (*HTT*) gene that encodes the mutant huntingtin protein (mHTT). Visualization and quantification of cerebral mHTT will provide a proxy for target engagement and a means to evaluate therapeutic interventions aimed at lowering mHTT in the brain. Here, we validated the novel radioligand ^{11}C-labeled 6-(5-((5-methoxypyridin-2-yl)methoxy)-benzo[d]oxazol-2-yl)-2-methylpyridazin-3(2H)-one (^{11}C-CHDI-180R) using PET imaging to quantify cerebral mHTT aggregates in a macaque model of HD. **Methods:** Rhesus macaques received MRI-guided intrastriatal delivery of a mixture of AAV2 and AAV2.retro viral vectors expressing an HTT fragment bearing 85 CAG repeats (85Q, $n = 5$), a control HTT fragment bearing 10 CAG repeats (10Q, $n = 4$), or vector diluent only (phosphate-buffered saline, $n = 5$). Thirty months after surgery, 90-min dynamic PET/CT imaging was used to investigate ^{11}C-CHDI-180R brain kinetics, along with serial blood sampling to measure input function and stability of the radioligand. The total volume of distribution was calculated using a 2-tissue-compartment model as well as Logan graphical analysis for regional quantification. Immunostaining for mHTT was performed to corroborate the in vivo findings. **Results:** ^{11}C-CHDI-180R displayed good metabolic stability (51.4% ± 4.0% parent in plasma at 60 min after injection). Regional time–activity curves displayed rapid uptake and reversible binding, which were described by a 2-tissue-compartment model. Logan graphical analysis was associated with the 2-tissue-compartment model ($r^2 = 0.96$, $P < 0.0001$) and used to generate parametric volume of distribution maps. Compared with controls, animals administered the 85Q fragment exhibited significantly increased ^{11}C-CHDI-180R binding in several cortical and subcortical brain regions (group effect, $P < 0.0001$). No difference in ^{11}C-CHDI-180R binding was observed between buffer and 10Q animals. The presence of mHTT aggregates in the 85Q animals was confirmed histologically. **Conclusion:** We validated ^{11}C-CHDI-180R as a radioligand to visualize and quantify mHTT aggregated species in a HD macaque model. These findings corroborate our previous work in rodent HD models and show that ^{11}C-CHDI-180R is a promising tool to assess the mHTT aggregate load and the efficacy of therapeutic strategies.

Key Words: mHTT; Huntington disease; nonhuman primate; PET; brain

J Nucl Med 2023; 64:1581–1587
DOI: 10.2967/jnumed.123.265569

Huntington disease (HD) is an autosomal dominant neurodegenerative disorder caused by an expanded polyglutamine (CAG) repeat in exon 1 of the huntingtin (*HTT*) gene (*1*,*2*). This mutated gene encodes the mutant huntingtin protein (mHTT), which is cleaved into N-terminal fragments, accumulates into intracellular inclusion bodies, and plays a pathophysiologic role in neurodegeneration (*3*–*6*). These neuropathologic features are known to severely impact the caudate and putamen (collectively, the striatum) but are also evident in several other cortical and subcortical brain regions (*3*,*7*,*8*). Several promising therapeutic candidates aimed at lowering mHTT in the brain have been developed and are undergoing clinical evaluation (*9*–*11*). In this context, quantifying the brainwide spatial distribution of mHTT protein with region-level resolution offers a proxy for target engagement and evaluation of the regional pharmacologic effects of such therapeutic interventions (*9*). Toward this goal, we evaluated ^{11}C-labeled 6-(5-((5-methoxypyridin-2-yl)methoxy)benzo[d]oxazol-2-yl)-2-methylpyridazin-3(2H)-one (^{11}C-CHDI-180R) as a ligand specific for mHTT aggregates that is cell- and brain-permeable and has high affinity (1–3 nM) and selectivity (*12*–*14*). Recently, we reported that ^{11}C-CHDI-180R PET imaging can noninvasively quantify mHTT brain aggregates in HD mouse models and offers insight into the time-, dose-, and region-specific pharmacodynamic activity in distinct mHTT-lowering interventional paradigms (*15*).

Application of ^{11}C-CHDI-180R in larger animal models of HD would be beneficial in monitoring future HTT-lowering efficacy studies. We recently created an adeno-associated virus (AAV)–mediated

Received Feb. 7, 2023; revision accepted Jun. 13, 2023.
For correspondence or reprints, contact Daniele Bertoglio (daniele.bertoglio@uantwerpen.be) or Alison Weiss (weissa@ohsu.edu).
*Contributed equally to this work.
Published online Aug. 17, 2023.

rhesus macaque model of HD wherein mHTT is expressed throughout the caudate, putamen, and several cortical and subcortical brain regions, in a pattern similar to that observed in people with HD (*16*). Immunohistochemical studies using monoclonal antibodies for (m)HTT in this model have verified the formation of EM48- and 2B4-positive mHTT aggregates in these same brain regions (*16*,*17*). Furthermore, this macaque model shows working memory impairment and motor dysfunction (chorea, dystonia, tremor, incoordination) and develops structural and functional corticostriatal changes including mild atrophy, increased white matter diffusivity, reduced cerebral glucose metabolism, and altered striatal $D_{2/3}$ receptor density (*17*,*18*).

Here, we investigated the novel radioligand ^{11}C-CHDI-180R using PET imaging at 30 mo after surgery in the HD macaque model and controls. Specifically, we assessed the plasma profile of ^{11}C-CHDI-180R, examined kinetic models for the volume of distribution (V_T) estimation, and explored its capability for quantification of mHTT aggregates and correspondence with behavioral phenotypes.

MATERIALS AND METHODS

Animals

Fourteen rhesus macaques (aged 7–14 y; weight, 5.5–13.6 kg; 10 female and 4 male) were used in this study. All animals received MRI-guided stereotactic injections of a 1:1 mixture of AAV2.retro and AAV2 at a titer of 1e12 vg/mL (2e12 vg/mL combined) expressing a fragment of mHTT with 85 CAG repeats (85Q), a control fragment of HTT with 10 CAG repeats (10Q), or a buffered saline injection w/F-Pluronic (BASF Corp.) (5 with AAV2:2retro-HTT85Q, 4 with AAV2:2retro-HTT10Q, and 5 with phosphate-buffered saline). Viral vectors were infused into the caudate and putamen (2 injections per region per hemisphere; total of 8 injections per animal), for a total volume of 330 μL per hemisphere, as reported in detail previously (*17*).

The guidelines specified in the National Institutes of Health Guide for the Care and Use of Laboratory Animals were strictly followed. All experimental procedures were approved by the Institutional Animal Care and Use Committee and the Institutional Biosafety Committee at the Oregon National Primate Research Center and Oregon Health and Science University.

Tracer Radiosynthesis

^{11}C-CHDI-180R was synthesized using an automated module (TRACERlab FXC; GE Healthcare) by adapting a method we previously described (*15*). The CHDI-180R precursor was radiolabeled by mixing the precursor (0.5–1.2 mg) with dimethylsulfoxide (100 ± 50 μL) and 4–10 mg of cesium carbonate (Cs_2CO_3). Then, ^{11}C-CH_3I was synthesized using a TRACERlab FX2-MEI box and bubbled into the vented reaction vial. The reaction was heated at 60°C ± 5°C for 1 min, after which 0.9 mL of the preparative mobile phase (0.10 M ammonium formate:acetonitrile; 60:40 v/v) was added to the reaction and the reaction mixture was injected onto a semipreparative high-performance liquid chromatography (HPLC) column (BetaBasic C18 7.6-mm outer diameter × 250-mm length; Thermo Scientific) at a flow rate of 1–1.5 mL/min. The radioactive product was passed through a sterilizing 0.2-μm filter in a volume of 1–1.5 mL to an empty sterile vial. The product radioactivity was assayed and diluted with sterile, preservative-free 0.9% saline. The mass of ^{11}C-CHDI-180R in the product was analyzed using HPLC mass spectrometry with ultraviolet and radiation detection to determine product radiochemical purity, chemical purity, injected mass, and identity. ^{11}C-CHDI-180R was synthesized with a radiochemical purity of more than 99% and a molar activity of 1,412 ± 556 GBq/μmol (mean ± SEM) at the end of synthesis.

Dynamic PET/CT Acquisition

Dynamic 90-min PET/CT imaging was performed using a Discovery MI 710 PET/CT imaging system (GE Healthcare). The animals were anesthetized with ketamine HCl (10–15 mg/kg intramuscularly), intubated, and maintained on 1%–2% isoflurane in oxygen. A saphenous intravenous catheter was placed for ligand administration, and a saphenous artery catheter, for blood collection. Before each PET scan, an 8-s CT scan was acquired using 100 kV and 50 mA for coregistration, attenuation, and scatter correction. A bolus of radioligand (131.3 ± 46.9 MBq) was injected manually over a 30-s interval immediately after the start of the 90-min dynamic PET scan. The resulting total injected mass was 0.055 ± 0.03 μg/kg. Detailed information on the animal and dosing parameters is provided in Supplemental Table 1 (supplemental materials are available at http://jnm.snmjournals.org). No significant difference in any of the dosing parameters was observed among the experimental groups. Dynamic PET data were acquired in list-mode format and were subsequently reconstructed into 28 frames of increasing length (4 × 15 s, 4 × 30 s, 4 × 60 s, 4 × 120 s, 9 × 300 s, and 3 × 600 s) using the GE Healthcare software (Q.clear technology). Normalization, scatter, dead time, and CT-based attenuation corrections were applied. PET image frames were reconstructed on a 120 × 100 × 52 grid with 1.823 × 1.823 × 2.780 mm voxels.

Input Function and Radiometabolite Analysis

In parallel to the PET acquisition, serial arterial blood samples were obtained to calculate arterial input functions and correct for the presence of plasma radiometabolites (*15*). Sixteen blood samples (1 mL each) at 0.25, 0.5, 0.75, 1, 1.5, 2, 2.5, 3, 5, 8, 15, 30, 45, 60, 75, and 90 min after injection were collected in 3-mL heparinized syringes. At each time point, radioactivity was measured in 300 μL of whole blood and 300 μL of plasma in a cross-calibrated γ-counter (Wizard2; PerkinElmer) and used to calculate the plasma–to–whole-blood ratio. An additional 1.0 mL of arterial blood was collected at 5, 15, 30, 45, 60, 75, and 90 min after injection to measure the parent fraction during the scan and correct the plasma input function for radiometabolites. After separation via a centrifuge (×3,000 relative centrifugal force for 5 min), 100 μL of deproteinated plasma supernatant were loaded onto a preconditioned reverse-phase HPLC column (Phenomenex Luna C18 (*2*) 5-μm HPLC column [250 × 4.6 mm] plus Phenomenex security guard precolumn) and eluted with sodium acetate buffer (0.05 M, pH 5.5) and acetonitrile (55:45 v/v) for 12 min at a flow rate of 1 mL/min. After elution, 2-min HPLC fractions were collected and measured in the γ-counter for quantification of the radiometabolite and parent fractions. The radioactivity associated with each peak was expressed as a percentage of the total area of the peaks based on the radiochromatograms to allow determination of the percentage contribution of the parent ligand to the total radioactivity signal at each sampling time.

With PMOD software (version 4.2; PMOD Technologies), individual metabolite-corrected plasma arterial input function for kinetic modeling of the PET data were obtained by correcting individual input functions by parent fraction values fitted with a sigmoid curve, as well as correcting for the plasma-to-whole blood ratios. The plasma free fraction was assessed (Supplemental Fig. 1) but not considered for quantification given the limited accuracy when measured through ultrafiltration.

Image Processing and Analysis

PET data were analyzed and processed using PMOD software. Spatial normalization of PET images to ONPRC18 MRI template space (*19*) was performed using individual T2-weighted MR images collected as part of an ongoing longitudinal study with the same animals (*17*). Once the dynamic PET images were normalized to the template space, the volumes of interest defined by the template were used to extract regional time–activity curves for cerebral gray and white matter regions.

This animal model displays only a mild atrophy (~5% volume change over time) in the striatum and cortex; therefore, partial volume correction was not needed (*17*).

In line with our previous observation in mice (*15*), ^{11}C-CHDI-180R kinetics were described by a 2-tissue-compartment model or Logan plot method (*20*). Thus, quantification of the total V_T was achieved using a 2-tissue-compartment model with blood volume fraction (V_B) fixed at 4%, after testing 3.5% and 4.5%, based on fitting of the model. The linear phase for the Logan plot was determined from the curve fitting based on 10% maximal error. For 1 animal (ID12), blood data were not available for the first 2.5 min; therefore, 2-tissue-compartment model data were not available for this animal.

To evaluate the time stability of the V_T estimates, PET data were reanalyzed by excluding the last 10 min of the PET acquisition from 90 to 40 min. The V_T estimates obtained using the 90-min PET acquisition were considered the reference outcome with which values from shorter acquisitions were compared. V_T estimates were considered acceptable if the mean percentage difference compared with the 90-min PET acquisition was below 10%, with an interindividual SD lower than 5%.

Parametric images were generated with PMOD software using the pixelwise modeling tool (PXMOD) through voxel-based graphical analysis (Logan plot). Parametric maps are not smoothed and are represented as group averages and overlaid onto the study-specific MRI brain template for anatomic reference. Voxelwise statistical analysis of the parametric V_T maps was performed using statistical parametric mapping (SPM, version 12; Wellcome Department of Imaging Neuroscience). Statistical T-maps were calculated for a peak voxel threshold of $P = 0.01$ (uncorrected) and a cluster of at least 10 voxels ($k > 10$). First, we confirmed the lack of significantly increased or decreased voxels between control groups (buffer and 10Q); next, we combined the control groups and compared them with the 85Q. The 85Q group did not display any reduced voxels; therefore, only clusters of increased binding are reported.

Behavioral Measures

As part of a previous longitudinal experiment, all 14 animals involved in this study completed a behavioral assessment of motor and cognitive function a few weeks before ^{11}C-CHDI-180R scanning (*17*). Briefly, motor phenotypes were assessed with a nonhuman-primate (NHP)–specific rating scale modified from the Unified Huntington's Disease Rating Scale, and cognitive capacities were measured using the 3-Choice Spatial Delayed Response task. Full methodologic details on these tasks are included in a previous work (*17*).

Immunostaining

Brain sections were immunohistochemically stained as previously described (*16*). Briefly, 40-μm-thick sections were incubated with the 2B4 antibody against (m)HTT (1-82aa, MAB5492, 1:1,000; Millipore) and a goat antimouse secondary antibody (BA-9200, 1:500; Vector Laboratories). The signal was developed using a standard Vectastain ABC kit (PK6100; Vector Laboratories) with subsequent incubation in 3,3′-diaminobenzidine (112080050; Sigma) and nickel (II) sulfate hexahydrate (N4882; Sigma) intensification. Images magnified to ×4 and ×20 were captured on an Olympus BX51 microscope with an Olympus DP72 camera controlled by the Olympus cellSens program from representative cases.

Statistical Analysis

A 2-way ANOVA with Holm–Šidák multiple comparison testing was applied to compare ^{11}C-CHDI-180R scan parameters and V_T among experimental groups in the different brain structures. Pearson correlation tests were used to compute all correlations. Statistical analyses were performed using Prism (version 9; GraphPad) and SPSS (version 28.0; IBM). Data are represented as mean ± SD. All tests were 2-tailed, and significance was set at a P value of less than 0.05.

RESULTS

Blood Analysis

Serial blood samples were collected from animals in all groups during each scan to derive the individual metabolite-corrected plasma arterial input function for kinetic modeling of the PET data. No apparent difference in radiometabolite profile of the radioligand was observed among the 3 experimental groups. After intravenous injection, the overall parent fraction (^{11}C-CHDI-180R) appeared to decrease slowly with time (Fig. 1A), accounting for 51.4% ± 4.0% of the total plasma radioactivity at 60 min after injection (Fig. 1B); the decline profile was described by a sigmoid fit. With radio-HPLC, only polar radiometabolites could be identified, suggesting low potential for brain-penetrant species. Finally, the plasma–to–whole-blood ratio did not show any apparent change over time (Fig. 1C), although, at the group level, it was best described by a quadratic fit (Fig. 1D). The plasma free fraction was 44.2% ± 9.3% and did not differ among the 3 experimental groups (Supplemental Fig. 1).

Description of ^{11}C-CHDI-180R by a 2-Tissue-Compartment Model

We evaluated ^{11}C-CHDI-180R kinetics in animals from all groups by performing 90-min dynamic PET acquisitions after intravenous injection. Representative brain regions with high (putamen) and low (cerebellum) ^{11}C-CHDI-180R uptake during the 90-min acquisition are reported in Figure 2A. ^{11}C-CHDI-180R displayed rapid cerebral uptake, peaking within 3 min after injection, with fast washout. Reversible kinetics were described by a 2-tissue-compartment model (Fig. 2A). A description of microparameters and goodness of fit is available in Supplemental Table 2. In line with the rodent findings (*15*), the Logan graphical analysis was a valid alternative to obtain V_T estimates based on 4 different brain regions ($r^2 = 0.96$, $P < 0.0001$) (Fig. 2B).

In a second exploratory analysis, data from the 90-min scans were reanalyzed, assessing scanning intervals ranging from 90 to 40 min. The time stability of V_T estimates based on Logan graphical analysis

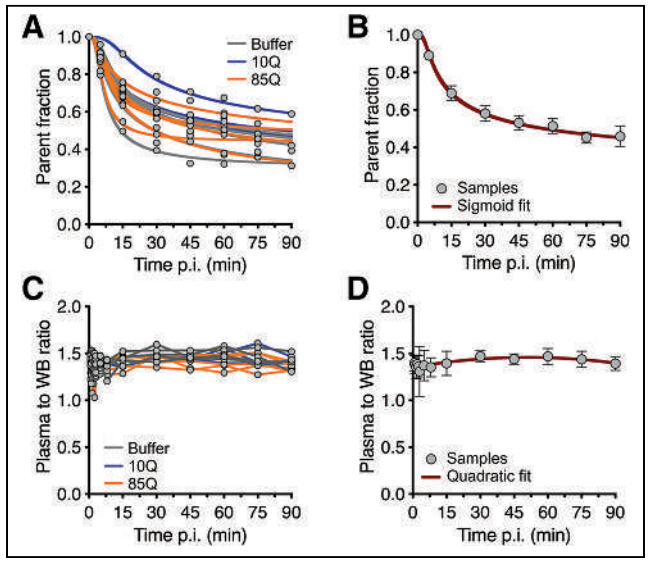

FIGURE 1. Blood analysis of ^{11}C-CHDI-180R in NHPs. Parent fraction profile in plasma for individual subjects (A) as well as group profile (B). Plasma–to–whole-blood ratio for individual subjects (C) as well as group profile (D) over time after intravenous injection of ^{11}C-CHDI-180R. Not all samples were available at 90 min because of radioactive decay. Data in B and D are mean ± SD ($n = 14$). p.i. = after injection; WB = whole blood.

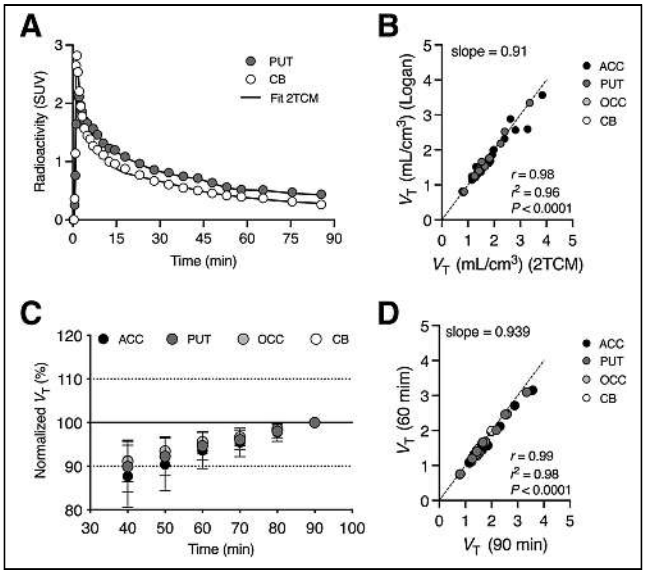

FIGURE 2. Kinetic modeling of ^{11}C-CHDI-180R in NHPs (n = 13). (A) Two-tissue-compartment model describes SUV time–activity curves of ^{11}C-CHDI-180R in regions with both high (putamen) and low (cerebellum) cerebral uptake in 85Q animal. (B) Comparison of ^{11}C-CHDI-180R V_T estimates using 2-tissue-compartment model and Logan plot for ^{11}C-CHDI-180R quantification in 4 different brain regions (anterior cingulate cortex and occipital cortex). (C) V_T estimates using Logan plot with different scan durations normalized to values obtained with 90-min acquisition. (D) Comparison of ^{11}C-CHDI-180R V_T estimates using Logan plot based on 90- or 60-min scan acquisition. 2TCM = 2-tissue-compartment model; ACC = anterior cingulate cortex; CB = cerebellum; OCC = occipital cortex; PUT = putamen.

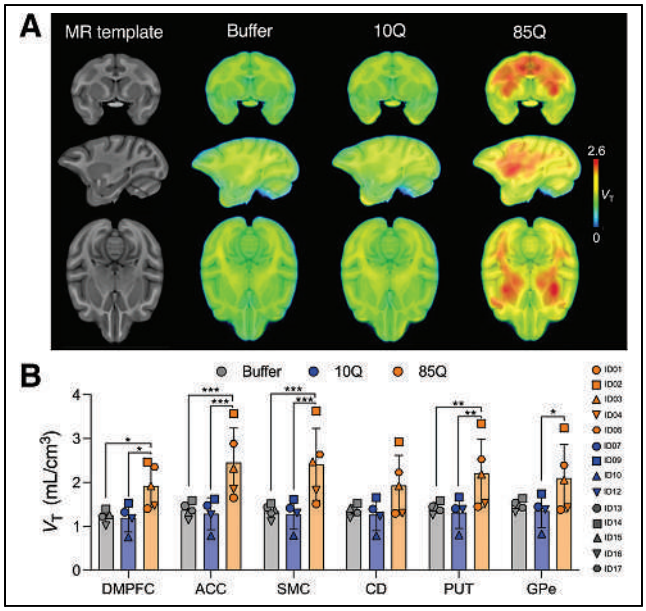

FIGURE 3. PET imaging using ^{11}C-CHDI-180R in NHPs. (A) Averaged parametric V_T maps in coronal (top), sagittal (middle), and axial (bottom) planes are overlaid onto ONPRC18 MRI T1-weighted rhesus macaque brain template. Animals in 85Q group show higher ^{11}C-CHDI-180R V_T than animals in control groups (buffer or 10Q). (B) Quantification of ^{11}C-CHDI-180R V_T in relevant brain structures. 85Q group displayed significantly higher ^{11}C-CHDI-180R V_T than control groups (buffer or 10Q). No statistical difference between buffer and 10Q was observed. (Buffer, n = 5; 10Q, n = 4; 85Q, n = 5.) ACC = anterior cingulate cortex; CD = caudate; DMPFC = dorsomedial prefrontal cortex; GPe = external segment of globus pallidus; PUT = putamen; SMC = supplemental motor cortex. *P < 0.05. **P < 0.01. ***P < 0.001.

indicated an underestimation of the outcome parameter with shortening of the scan acquisition (Fig. 2C). Nonetheless, V_T estimates based on a 60-min acquisition were comparable to the values obtained with the 90-min acquisition with a deviation of −5.3% ± 3.2%. This was also confirmed by the strong correlation in V_T measures obtained with the different scan durations (slope = 0.939, r^2 = 0.98, P < 0.0001) (Fig. 2D), indicating that a scan acquisition of a minimum of 60 min is reliable for estimation of ^{11}C-CHDI-180R V_T.

Detection of mHTT in an NHP Model of HD by ^{11}C-CHDI-180R PET Imaging

We previously demonstrated that intrastriatal delivery of AAV2 or AAV2.retro expressing 85Q leads to transduction of the caudate and putamen and of several other brain structures, resulting in the expression of mHTT and the formation of 2B4- and EM48-postitive mHTT aggregates in these brain regions (*16*,*17*). Accordingly, evident binding in the parametric ^{11}C-CHDI-180R V_T map for the 85Q group was visible in several cerebral structures compared with the buffer or 10Q-injected control groups (Fig. 3A). Regional analysis of ^{11}C-CHDI-180R V_T revealed a statistically significant main effect of group ($F_{(2,748)}$ = 165.1, P < 0.0001), with no effect of brain region ($F_{(67,748)}$ = 1.226, P = 0.1127) or interaction (group × brain region) ($F_{(134,748)}$ = 0.205, P > 0.99). Post hoc group analysis indicated a statistically significant difference between 85Q and control groups (buffer or 10Q) in several brain regions (Fig. 3B), whereas no differences were observed between buffer and 10Q in any volumes of interest, as expected given the lack of the target in the control groups. Group V_T values and post hoc statistical comparisons for all gray matter structures are shown in Supplemental Figure 2 and reported in Supplemental Table 3, respectively.

Next, we used a voxelwise analysis to investigate the subregional binding of ^{11}C-CHDI-180R. The voxelwise analysis detected significantly increased clusters of ^{11}C-CHDI-180R in 85Q animals compared with controls (Fig. 4) in the brain regions reported in the volume-of-interest–based analysis. Specifically, the voxel-based approach also identified subregional areas of increased ^{11}C-CHDI-180R binding, including the head of the caudate, the dorsolateral and ventrolateral prefrontal cortices, the dorsal premotor cortex, and the insular cortex (Fig. 4).

To confirm the expression of (m)HTT and formation of mHTT aggregates in transduced brain regions, 2B4 immunohistochemistry was performed on tissue collected at necropsy shortly after the conclusion of these PET studies (~31 mo after surgery). Figure 5 shows the presence of soluble and aggregated mHTT in representative cases from 85Q animals in regions of significantly increased ^{11}C-CHDI-180R V_T (Supplemental Fig. 3 shows individual cases and quantification). No (m)HTT aggregates were observed in the control groups (buffer and 10Q). Increased ^{11}C-CHDI-180R V_T in white matter structures was also detected both at the regional level (Supplemental Fig. 4; Supplemental Table 4) and at the voxel level (Fig. 5). Histologic investigation of white matter confirmed the presence of 2B4-positive (m)HTT aggregates in these brain structures (Supplemental Fig. 5), supporting the specificity of ^{11}C-CHDI-180R binding. Although mHTT accumulation in white matter was not anticipated, the formation of mHTT aggregates appears to be limited to the regions in and adjacent to the needle tracts created during AAV-vector delivery.

Finally, as part of a previous longitudinal study, the same animals completed behavioral assessments of motor and cognitive function a

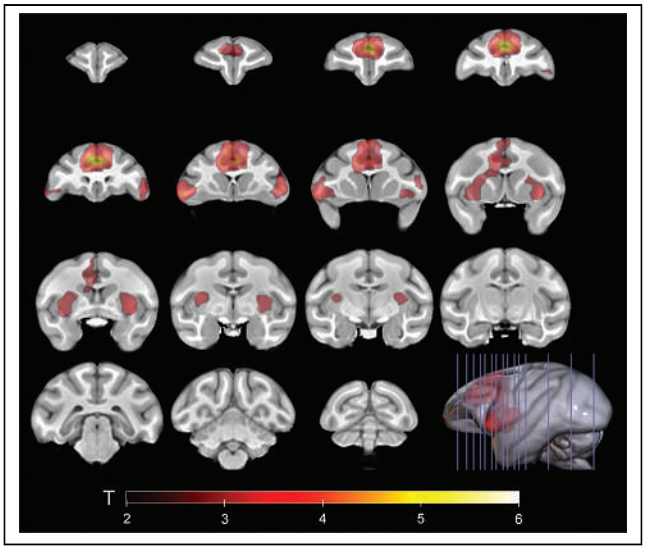

FIGURE 4. Increased voxelwise ^{11}C-CHDI-180R binding in 85Q NHPs compared with control groups combined. Clusters of significantly increased ^{11}C-CHDI-180R V_T in 85Q animals are overlaid onto ONPRC18 MRI template (threshold of $P < 0.01$, cluster size > 10). Scale bar represents T scores. (Buffer, $n = 5$; 10Q, $n = 4$; 85Q, $n = 5$.)

few weeks before ^{11}C-CHDI-180R scanning (*17*). We inquired whether behavioral deficits were associated with ^{11}C-CHDI-180R binding. Analyses revealed that there was a significant correlation between behavioral scores and V_T values in several cortical and subcortical regions, such that animals with greater behavioral deficits (higher neurologic rating scores and lower working memory scores) had higher levels of ^{11}C-CHDI-180R binding (Table 1).

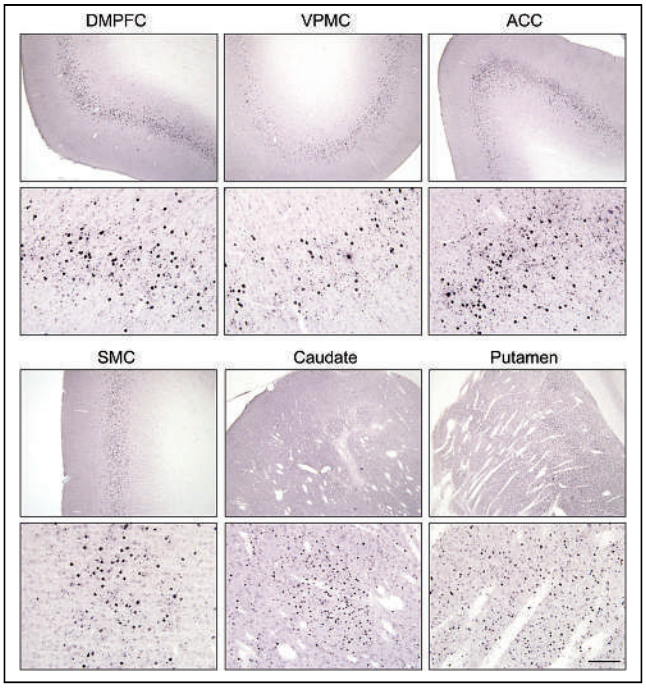

FIGURE 5. 2B4 immunostaining in 85Q NHPs showed agreement with areas of increased ^{11}C-CHDI-180R V_T. Images at ×4 (top) and ×20 (bottom) of mHTT aggregates detected by 2B4 staining in same brain regions show increased ^{11}C-CHDI-180R V_T in 85Q primates, including regions distal from injection sites (caudate and putamen) such as dorsal medial prefrontal cortex, ventral premotor cortex, anterior cingulate cortex, and supplemental motor cortex. Scale bar = 100 μm. ACC = anterior cingulate cortex; DMPFC = dorsal medial prefrontal cortex; SMC = supplemental motor cortex; VPMC = ventral premotor cortex.

DISCUSSION

Various new therapeutic approaches for HD focus on the modulation of mHTT levels (*9*,*11*,*21*). To determine whether these approaches are achieving target engagement in the relevant brain structures, and whether they are leading to lowering mHTT levels in vivo, the development of noninvasive quantification of mHTT is needed (*12–14*,*22*,*23*). We recently demonstrated that ^{11}C-CHDI-180R PET imaging is able to quantify mHTT aggregates in HD mouse models (*15*). Here, we offer evidence that ^{11}C-CHDI-180R is applicable in a large NHP model of HD bearing mHTT aggregates and behavioral phenotypes (*16*,*17*).

In contrast to previous preclinical mouse studies (*15*), analysis of the plasma profile of NHPs revealed the formation of at least one radiometabolite more polar than ^{11}C-CHDI-180R. This radiometabolite polarity, together with the measured brain time–activity curves, suggested no evidence of brain-penetrant radiometabolite species. This is important validation for the use of this ligand in humans and lays the foundation for future studies to use this NHP model to test the efficacy of therapeutic interventions designed to lower mHTT in the brain.

The results of both regional and voxelwise quantification of ^{11}C-CHDI-180R revealed significantly increased binding in several brain regions in the 85Q group compared with the buffer and 10Q control groups, suggesting specific binding to mHTT aggregates. It was previously demonstrated that the intrastriatal delivery of a mixture of AAV2 and AAV2.retro leads to transduction in the caudate and putamen as well as several cortical structures (as a result of the retrograde transport capability of AAV2.retro), forming detectable mHTT aggregates in all of these regions (*16*,*17*). This distribution profile is closely recapitulated by the binding pattern of ^{11}C-CHDI-180R PET imaging, with the putamen, anterior cingulate cortex, and supplemental motor cortex representing the most affected gray matter structures in this model (*16*,*17*). Importantly, we found an association between the increased binding pattern of ^{11}C-CHDI-180R PET imaging and the behavioral assessments of motor and cognitive function in the 85Q group.

Compared with genetically engineered animal models of HD, in which mHTT expression tends to be uniform throughout the brain, viral vector-based models often result in mHTT expression in specific targeted brain regions or subregions. Accordingly, voxel-based analyses in the AAV2:AAV2retro-based macaque HD model identified significant ^{11}C-CHDI-180R binding in subregions of several brain structures, some of which were not identified using the region-of-interest-based approach. This finding suggests that voxel-based analyses may also be useful in human HD studies, in which mHTT aggregates are more concentrated in subregions of certain structures, such as the lateral putamen and in deeper layers of the cerebral cortex (*5*,*24*). Additionally, should PET imaging be used in future studies to demonstrate target engagement of HTT-lowering therapeutics, voxel-based analysis may be able to discern HTT changes when therapeutic constructs reach only subregions of brain structures after delivery.

We performed a postmortem histologic investigation to confirm the formation of 2B4-positive mHTT aggregates in brain regions that showed significantly increased ^{11}C-CHDI-180R V_T. However, an important limitation of such a comparison is that this

TABLE 1
Correlations Between Behavioral Scores and ^{11}C-CHDI-180R V_T Values in Gray Matter Structures

	Neurologic rating		Working memory	
Gray matter structure	Correlation	*P*	Correlation	*P*
Dorsolateral prefrontal cortex	0.522	0.056	−0.6120	0.034*
Ventrolateral prefrontal cortex	0.533	0.050*	−0.6220	0.031*
Orbitofrontal cortex	0.406	0.150	−0.5770	0.050*
Ventromedial prefrontal cortex	0.443	0.112	−0.5550	0.0610
Dorsomedial prefrontal cortex	0.672	0.008†	−0.6630	0.019*
Anterior cingulate cortex	0.703	0.005†	−0.6370	0.026*
Dorsal premotor cortex	0.504	0.066	−0.5870	0.045*
Ventral premotor cortex	0.594	0.025*	−0.5980	0.040*
Supplemental motor cortex	0.667	0.009†	−0.6130	0.034*
Primary motor cortex	0.451	0.106	−0.5550	0.061
Superior temporal cortex	0.419	0.136	−0.5450	0.067
Inferior temporal cortex	0.406	0.150	−0.5360	0.072
Rhinal cortex	0.374	0.187	−0.5270	0.078
Insular cortex	0.566	0.035*	−0.5680	0.054
Somatosensory cortex	0.432	0.123	−0.5540	0.062
Parietal cortex	0.388	0.170	−0.5350	0.073
Posterior cingulate cortex	0.46	0.098	−0.5650	0.056
Occipital cortex	0.375	0.187	−0.5160	0.086
Caudate	0.51	0.063	−0.5720	0.052
Putamen	0.589	0.027*	−0.5930	0.042*
Internal globus pallidus	0.458	0.100	−0.5310	0.076
External globus pallidus	0.511	0.062	−0.5570	0.060
Lateral thalamus	0.402	0.155	−0.5210	0.082
Medial thalamus	0.387	0.172	−0.5060	0.093
Hippocampus	0.434	0.121	−0.5390	0.071
Amygdala	0.473	0.088	−0.5520	0.063
Substantia nigra	0.43	0.125	−0.5740	0.051
Cerebellum	0.423	0.132	−0.5370	0.072

*$P < 0.05$.
†$P < 0.01$.
Higher neurologic rating scores, and lower working memory scores, are associated with greater impairment. Correlations are 2-tailed Pearson. (Buffer, $n = 5$; 10Q, $n = 4$; 85Q, $n = 5$.)

radioligand does not bind to large mHTT species, as detected by the common antibodies used for histologic assessment, such as EM48 and 2B4. We have previously demonstrated binding to mHTT-derived fibrils and to mHTT aggregates expressed in mouse HD models and human HD samples, whose precise state has yet to be defined (*12*,*13*,*15*). Given that radioligand and antibodies do not recognize the same mHTT species, a direct association between readouts is not possible. Therefore, histologic analysis was performed to confirm the presence of mHTT aggregates in relevant brain regions.

Accordingly, in 85Q animals, 2B4-positive aggregates were detected in the regions of injection (caudate and putamen) and in several cortical gray matter structures that send afferent projections to the striatum. The anterior-to-posterior cortical gradient observed on immunostaining aligns with a similar distribution observed with PET imaging and recapitulates the previously described distribution of the AAV2:AAV2.retro viral vector mixture (*16*). We also detected increased ^{11}C-CHDI-180R binding in the white matter of 85Q-treated animals, a finding that was not anticipated given the lack of white matter binding observed during in vitro ^{3}H-CHDI-180 autoradiography studies in mouse models and human postmortem tissue (*12*,*13*,*15*). Histologic evaluation shows 2B4-positive mHTT aggregates in white matter tracts in, and near, visible needle tracts. This finding is not surprising, given that the infusion pump was run while the needle was lowered into the caudate and putamen to maintain positive pressure, prevent infusate backflow, and prevent tissue damage.

Autoradiography has been used in genetic mouse models and human HD brain tissue samples, in combination with immunohistochemistry, to confirm regional and subregional binding of CHDI-180R. Although tissue was not available in the current

study to perform autoradiography, pilot studies on 4 adult macaques injected with either AAV2retro-85Q (left hemisphere) and diluent (right hemisphere) or AAV2retro-10Q (left hemisphere) and diluent (right hemisphere) used autoradiography to demonstrate specific binding in the putamen, globus pallidus, and cortex of 85Q-injected animals but not in 10Q- or diluent-injected controls.

CONCLUSION

Our study demonstrated the validity of ^{11}C-CHDI-180R as a reliable radioligand to visualize and quantify the region-specific distribution of mHTT aggregated species in the HD macaque model with high spatial resolution. These findings corroborate our previous work in rodent HD models and further support ongoing investigation of ^{11}C-CHDI-180R as a pharmacodynamic biomarker in HD.

DISCLOSURE

Daniele Bertoglio was supported by the Research Foundation Flanders (FWO) (1229721N and K201222N) and the University of Antwerp (FFB210050). Daniele Bertoglio, Jeroen Verhaeghe, and Steven Staelens are members of the μNeuro Research Centre of Excellence at the University of Antwerp. Alison Weiss was supported by a postdoctoral fellowship (NIH/NIA T32AG055378). Jodi McBride is supported by NIH grant P51OD011092, and the creation of the NHP model of HD used in this project was supported by NIH grant NS099136. Microscopy was supported in part by the Imaging and Morphology Core at the Oregon National Primate Research Center (S10OD025002-01). Radiolabeling was done using the Oregon Health and Science University Center for Radiochemistry Research Core Facility. This work was funded by the CHDI Foundation, Inc. (https://chdifoundation.org/). Vinod Khetarpal, Longbin Liu, Celia Dominguez, Ignacio Munoz-Sanjuan, and Jonathan Bard are employed by CHDI Management, Inc., as advisors to CHDI Foundation, Inc., a privately funded nonprofit biomedical research organization dedicated exclusively to collaboratively developing therapeutics that improve the lives of those affected by HD. No other potential conflict of interest relevant to this article was reported.

KEY POINTS

QUESTION: Can we quantify mHTT aggregates in an NHP model of HD in vivo?

PERTINENT FINDINGS: In this study, we demonstrated that the regional accumulation of mHTT aggregates in the brain can be quantified using PET imaging with ^{11}C-CHDI-180R in a macaque model of HD.

IMPLICATIONS FOR PATIENT CARE: ^{11}C-CHDI-180R PET imaging quantifies the regional accumulation of mHTT aggregates and offers a promising new avenue to examine the efficacy of mHTT-lowering therapeutic strategies.

REFERENCES

1. The Huntington's Disease Collaborative Research Group. A novel gene containing a trinucleotide repeat that is expanded and unstable on Huntington's disease chromosomes. *Cell.* 1993;72:971–983.
2. Saudou F, Humbert S. The biology of Huntingtin. *Neuron.* 2016;89:910–926.
3. Vonsattel JP, Myers RH, Stevens TJ, Ferrante RJ, Bird ED, Richardson EP Jr. Neuropathological classification of Huntington's disease. *J Neuropathol Exp Neurol.* 1985;44:559–577.
4. Arrasate M, Mitra S, Schweitzer ES, Segal MR, Finkbeiner S. Inclusion body formation reduces levels of mutant huntingtin and the risk of neuronal death. *Nature.* 2004;431:805–810.
5. DiFiglia M, Sapp E, Chase KO, et al. Aggregation of huntingtin in neuronal intranuclear inclusions and dystrophic neurites in brain. *Science.* 1997;277:1990–1993.
6. DiFiglia M, Sena-Esteves M, Chase K, et al. Therapeutic silencing of mutant huntingtin with siRNA attenuates striatal and cortical neuropathology and behavioral deficits. *Proc Natl Acad Sci USA.* 2007;104:17204–17209.
7. Sapp E, Kegel KB, Aronin N, et al. Early and progressive accumulation of reactive microglia in the Huntington disease brain. *J Neuropathol Exp Neurol.* 2001;60:161–172.
8. Waldvogel HJ, Kim EH, Tippett LJ, Vonsattel JP, Faull RL. The neuropathology of Huntington's disease. *Curr Top Behav Neurosci.* 2015;22:33–80.
9. Tabrizi SJ, Ghosh R, Leavitt BR. Huntingtin lowering strategies for disease modification in Huntington's disease. *Neuron.* 2019;101:801–819.
10. Wild EJ, Tabrizi SJ. Therapies targeting DNA and RNA in Huntington's disease. *Lancet Neurol.* 2017;16:837–847.
11. Tabrizi SJ, Flower MD, Ross CA, Wild EJ. Huntington disease: new insights into molecular pathogenesis and therapeutic opportunities. *Nat Rev Neurol.* 2020;16:529–546.
12. Liu L, Prime ME, Lee MR, et al. Imaging mutant Huntingtin aggregates: development of a potential PET ligand. *J Med Chem.* 2020;63:8608–8633.
13. Herrmann F, Hessmann M, Schaertl S, et al. Pharmacological characterization of mutant huntingtin aggregate-directed PET imaging tracer candidates. *Sci Rep.* 2021;11:17977.
14. Bertoglio D, Verhaeghe J, Miranda A, et al. Longitudinal preclinical evaluation of the novel radioligand [^{11}C]CHDI-626 for PET imaging of mutant huntingtin aggregates in Huntington's disease. *Eur J Nucl Med Mol Imaging.* 2022;49:1166–1175.
15. Bertoglio D, Bard J, Hessmann M, et al. Development of a ligand for in vivo imaging of mutant huntingtin in Huntington's disease. *Sci Transl Med.* 2022;14:eabm3682.
16. Weiss AR, Liguore WA, Domire JS, Button D, McBride JL. Intra-striatal AAV2.-retro administration leads to extensive retrograde transport in the rhesus macaque brain: implications for disease modeling and therapeutic development. *Sci Rep.* 2020;10:6970.
17. Weiss AR, Liguore WA, Brandon K, et al. A novel rhesus macaque model of Huntington's disease recapitulates key neuropathological changes along with motor and cognitive decline. *eLife.* 2022;11:e77568.
18. Weiss AR, Bertoglio D, Liguore WA, et al. Reduced D_2/D_3 receptor binding and glucose metabolism in a macaque model of Huntington's disease. *Mov Disord.* 2023;38:143–147.
19. Weiss AR, Liu Z, Wang X, Liguore WA, Kroenke CD, McBride JL. The macaque brain ONPRC18 template with combined gray and white matter labelmap for multimodal neuroimaging studies of nonhuman primates. *Neuroimage.* 2021;225:117517.
20. Logan J, Fowler JS, Volkow ND, et al. Graphical analysis of reversible radioligand binding from time-activity measurements applied to [N-^{11}C-methyl]-(−)-cocaine PET studies in human subjects. *J Cereb Blood Flow Metab.* 1990;10:740–747.
21. Tabrizi SJ, Estevez-Fraga C, van Roon-Mom WMC, et al. Potential disease-modifying therapies for Huntington's disease: lessons learned and future opportunities. *Lancet Neurol.* 2022;21:645–658.
22. Liu L, Johnson PD, Prime ME, et al. [^{11}C]CHDI-626, a PET tracer candidate for imaging mutant Huntingtin aggregates with reduced binding to AD pathological proteins. *J Med Chem.* 2021;64:12003–12021.
23. Liu L, Johnson PD, Prime ME, et al. Design and evaluation of [^{18}F]CHDI-650 as a positron emission tomography ligand to image mutant Huntingtin aggregates. *J Med Chem.* 2023;66:641–656.
24. Gutekunst CA, Li SH, Yi H, et al. Nuclear and neuropil aggregates in Huntington's disease: relationship to neuropathology. *J Neurosci.* 1999;19:2522–2534.

Development of a PET Tracer for OGA with Improved Kinetics in the Living Brain

Brendon E. Cook[1], Sangram Nag[2,3], Ryosuke Arakawa[2,3], Edward Yin-Shiang Lin[1], Nancy Stratman[1], Kevin Guckian[1], Heike Hering[1], Mukesh Lulla[1], Jinkuk Choi[1], Cristian Salinas[1], Nathan E. Genung[1], Anton Forsberg Morén[2,3], Martin Bolin[2,3], Giulia Boscutti[4], Christophe Plisson[4], Laurent Martarello[1], Christer Halldin[2,3], and Maciej A. Kaliszczak[1]

[1]*Biogen, Cambridge, Massachusetts;* [2]*Department of Clinical Neuroscience, Center for Psychiatry Research, Karolinska Institutet, Stockholm, Sweden;* [3]*Stockholm County Council, Stockholm, Sweden; and* [4]*Invicro, London, United Kingdom*

O-GlcNAcylation is thought to play a role in the development of tau pathology in Alzheimer's disease because of its ability to modulate tau's aggregation propensity. *O*-GlcNAcylation is regulated by 2 enzymes: *O*-GlcNAc transferase and *O*-GlcNAcase (OGA). Development of a PET tracer would therefore be an essential tool for developing therapeutic small-molecule inhibitors of OGA, enabling clinical testing of target engagement and dose selection. **Methods:** A collection of small-molecule compounds was screened for inhibitory activity and high-affinity binding to OGA, as well as favorable PET tracer attributes (multidrug resistance protein 1 efflux, central nervous system PET multiparameter optimization, etc.). Two lead compounds with high affinity and selectivity for OGA were selected for further profiling, including OGA binding to tissue homogenate using a radioligand competition binding assay. In vivo pharmacokinetics were established using a microdosing approach with unlabeled compounds in rats. In vivo imaging studies were performed in rodents and nonhuman primates (NHPs) with ^{11}C-labeled compounds. **Results:** Two selected candidates, BIO-735 and BIO-578, displayed promising attributes in vitro. After radiolabeling with tritium, [^{3}H]BIO-735 and [^{3}H]BIO-578 binding in rodent brain homogenates demonstrated dissociation constants of 0.6 and 2.3 nM, respectively. Binding was inhibited, concentration-dependently, by homologous compounds and thiamet G, a well-characterized and structurally diverse OGA inhibitor. Imaging studies in rats and NHPs showed both tracers had high uptake in the brain and inhibition of binding to OGA in the presence of a nonradioactive compound. However, only BIO-578 demonstrated reversible binding kinetics within the time frame of a PET study with a ^{11}C-labeled molecule to enable quantification using kinetic modeling. Specificity of tracer uptake was confirmed with a 10 mg/kg blocking dose of thiamet G. **Conclusion:** We describe the development and testing of 2 ^{11}C PET tracers targeting the protein OGA. The lead compound BIO-578 demonstrated high affinity and selectivity for OGA in rodent and human postmortem brain tissue, leading to its further testing in NHPs. NHP PET imaging studies showed that the tracer had excellent brain kinetics, with full inhibition of specific binding by thiamet G. These results suggest that the tracer [^{11}C]BIO-578 is well suited for further characterization in humans.

Key Words: OGA; *O*-GlcNAcase; Alzheimer; PET

Received Feb. 22, 2023; revision accepted May 31, 2023.

For correspondence or reprints, contact Maciej Kaliszczak (maciej.kaliszczak@biogen.com).

Published online Jul. 6, 2023.

J Nucl Med 2023; 64:1588–1593
DOI: 10.2967/jnumed.122.265225

A key feature of Alzheimer's disease is the presence of fibrillar deposits of phosphorylated tau protein, so-called neurofibrillary tangles (*1*). Recent natural history studies in Alzheimer's disease patients have shown that increased tau pathology is associated with more severe disease, spurring efforts to develop treatments that may slow or prevent neurofibrillary tangle formation (*2,3*).

Glucose hypometabolism is directly correlated with tau pathology in Alzheimer's disease (*4*). Cellular glucose availability regulates a posttranslational modification known as *O*-GlcNAcylation (*5,6*). *O*-GlcNAcylation of tau has been demonstrated to attenuate the propensity of tau to aggregate, and increased *O*-GlcNAcylation can be achieved by inhibiting the enzyme responsible for the removal of *O*-GlcNAc residues from proteins, *O*-GlcNAcase (OGA) (*7–9*). The availability of an OGA PET radiotracer is important as an early clinical development tool to determine target occupancy of OGA inhibitors, aiding drug development and dose selection in patients.

To date, there have been 2 disclosed examples of OGA PET tracers, though existing limitations necessitate further optimization of an OGA PET tracer that can provide information on dose selection and target engagement of OGA inhibitors in the clinic (*10–14*). To this end, we developed 2 OGA PET ligands with favorable kinetics. The lead compound [^{11}C]BIO-578 was deemed suitable for clinical application.

MATERIALS AND METHODS

Animal studies were performed at either Invicro in the United Kingdom or Karolinska Institutet in Sweden and were reviewed and approved by respective institutional animal care and use committees (or equivalent) in accordance with all institutional and governmental regulations.

Homogenate Binding

Detailed protocols are listed in the supplemental materials (supplemental materials are available at http://jnm.snmjournals.org). In brief, tritiated radioligand binding studies were performed in 96-well plate–based assays with cytosolic brain homogenates for rodent and human brain studies or with whole-brain crude homogenates for human T-cells isolated from healthy volunteer blood in a steady-state reaction performed at room temperature. Reactions were terminated by rapid vacuum filtration

using a 96-well plate–based harvester. Filters containing bound ligand were assessed for radioactivity using scintillation counting techniques. Competition binding studies were also performed with the reference standards thiamet G, *O*-(2-acetamido-2-deoxy-D-glucopyranosylidenamino) *N*-phenylcarbamate, BIO-735, and BIO-578 (*7,15*).

Microdose Biodistribution

Three Sprague–Dawley rats per time point were injected by intravenous bolus with 10 μg/kg BIO-735 or BIO-578. After injection, the frontal cortex, striatum, cerebellum, and rest of the brain were excised at baseline and 30, 60, 90, 120, 150, and 180 min. The amount of BIO-735 or BIO-578 was measured in plasma and each brain region by liquid chromatography tandem mass spectrometry.

Labeling with ^{11}C

Synthesis of [^{11}C]BIO-735 or [^{11}C]BIO-578 was performed using either compound 1 or compound 2 as a precursor, respectively. Detailed synthesis protocols are provided in the supplemental materials. To summarize, [^{11}C]CH_3I was first produced according to previously published protocols (*16*). Precursor compound 1 or 2 was combined with anhydrous tetrahydrofuran and [^{11}C]CH_3I and heated to 125°C for 8 min. The reaction mixture was diluted, and the final radiolabeled product was isolated by reverse-phase, high-performance liquid chromatography. The collected fraction was diluted in sterile water, passed through a Sep-Pak tC18 cartridge (Waters), washed with sterile water, and eluted with 1 mL of ethanol into 9 mL of sterile saline.

PET Imaging in Rats

A detailed imaging protocol for the rodent study is presented in the supplemental materials. In brief, an adult male Sprague–Dawley rat received 2 PET scans using the tracer [^{11}C]BIO-735. The first scan was a baseline scan, with the tracer (10 MBq, 0.16 μg) administered by intravenous bolus under isoflurane anesthesia. The second scan was performed 4 h later, with the rat first given a 0.3 mg/kg dose of BIO-735 by intravenous bolus and then 5 min later dosed with the tracer [^{11}C]BIO-735 (8 MBq, 0.09 μg) and scanned. Both PET scans were dynamic acquisitions 0–60 min after injection of the tracer. Arterial blood sampling was performed, and a parent plasma input function was derived for both scans.

PET Imaging in Nonhuman Primates (NHPs)

A detailed protocol for NHP studies is presented in the supplemental materials. In brief, each NHP was scanned twice, receiving first a baseline scan and then a pretreatment blocking scan later the same day. The tracer was injected by intravenous bolus. Approximately 7 min before the blocking scans, either BIO-735 or thiamet G was administered intravenously, followed by intravenous administration of the tracer. Dynamic PET scans were acquired for 93 min immediately after intravenous injection of the tracer, with arterial blood sampling at time points throughout the duration of the scan (*17*).

RESULTS

Selection of Initial Compound

From the Biogen compound collection, 366 OGA inhibitors were filtered to select promising candidates as potential PET tracers (Fig. 1A). Compounds that had a high efflux ratio in the MDR1 Madin–Darby canine kidney cell assay were removed from consideration because of their likelihood of having poor central nervous system (CNS) penetrance, leaving 125 compounds. This was narrowed down on the basis of the CNS PET multiparameter optimization score of the compounds, a computational scoring function designed to select compounds with optimal PET tracer physicochemical properties (*18*). Further filtering was done by removing compounds that bound plasma proteins (the protein-free fraction

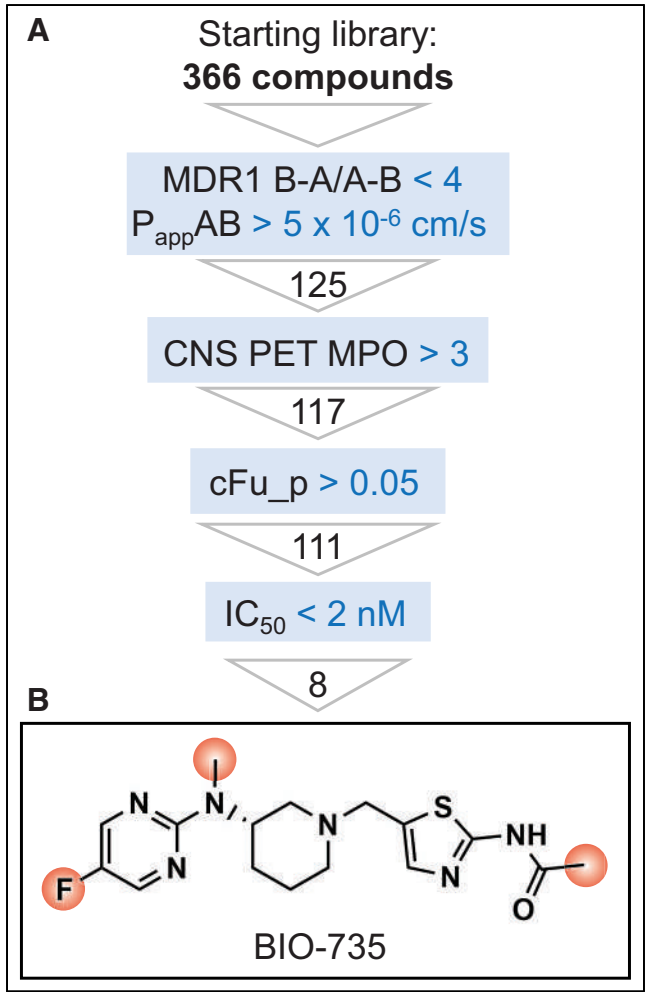

FIGURE 1. (A) Flowchart of selection process based on starting collection of compounds. (B) Lead compound selected was BIO-735, with potential sites for radiolabeling in red. cFu_p = plasma protein free fraction; IC_{50} = half maximal inhibitory constant; MDR1 = multidrug resistance protein 1; MPO = multiparameter optimization; P_{app} = apparent permeability.

cFu_p) greater than 95% to reduce the likelihood the candidate would have high nonspecific binding. Finally, because OGA concentration in the brain typically ranges from 5 to 50 nM, we screened out any compound with a half maximal inhibitory concentration (IC_{50}) greater than 2 nM while ensuring the total density of target receptor B_{max}/dissociation constant (K_d) would be greater than 10 (*19*). The remaining 8 compounds were then inspected to ensure facile introduction of a PET radiolabel, leaving BIO-735 as the lead candidate because of its ability to be labeled with either ^{11}C or ^{18}F (Fig. 1B). A summary of assay results (including plasma protein binding and MDR1 efflux transport) is provided in Supplemental Table 1.

In Vitro Screening of BIO-735

The OGA protein sequence is highly conserved in eukaryotes; therefore, cross-reactivity of the tracer molecule is expected in all species used for in vitro and in vivo testing (mouse, rat, NHP, and human) (*7*). In addition, B_{max} in the brain across these species was similar, allowing better comparison of tracer performance (Supplemental Figs. 1 and 2). Mouse brain homogenate binding with

[^{3}H]BIO-735 (Supplemental Fig. 3A) was used to determine K_d of 0.6 nM, which agreed with surface plasmon resonance (SPR) K_d (0.92 nM). Further binding studies with rat brain regional homogenates (including the striatum, cortex, hippocampus, and cerebellum) showed consistent K_d (0.6–0.7 nM) but differences in B_{max} (Supplemental Fig. 3B). These correlate with known differences in OGA concentration among the regions (*13*).

Next, competition binding studies with [^{3}H]BIO-735 were performed to determine the inhibition constants of 2 known inhibitors of OGA (*O*-(2-acetamido-2-deoxy-D-glucopyranosylidenamino) *N*-phenylcarbamate and thiamet G), as well as unlabeled BIO-735 as the homologous compound (Supplemental Figs. 1D, 3C, and 3D). Binding of [^{3}H]BIO-735 was inhibited by all 3 compounds with affinities for OGA, consistent with published observations, indicating the tracer was binding to the same site on OGA (*7,15*).

Finally, K_d for BIO-735 was tested in human frontal cortex homogenate (Supplemental Fig. 1A), with K_d (0.6 nM) and B_{max} (39 nM) comparable to the results in rat homogenate. In addition, these parameters were tested in human T-cell homogenates (Supplemental Fig. 1B). Human T-cell homogenate was found to have a B_{max} of 42 nM, presenting a potential challenge for quantification. Because OGA is expressed in circulating T-cells, it is possible a change in the tracer-free fraction could occur if peripheral OGA is blocked after administration of a nonradioactive drug (Supplemental Fig. 1D). Furthermore, typical input function analysis to calculate the volume of distribution relies on analysis of plasma, which will not account for potential tracer binding to OGA expressed on circulating T-cells. This must be considered given its potential implications in the quantification of the brain PET signal as measured by the volume of distribution (*20*).

In Vivo Rat Testing of BIO-735

With promising in vitro results for BIO-735, an in vivo pharmacokinetic study under microdosing conditions was performed in rats. A concentration of 10 μg/kg was chosen to avoid saturating OGA binding sites and to study the kinetic behavior of the compound in different regions of the brain (Fig. 2A) (*18,21,22*). OGA binding was shown to differ from region to region, and the striatum and the cerebellum had the highest and the lowest uptake, respectively. This pattern of BIO-735 distribution is consistent with the relative concentration of OGA in the regions measured (Supplemental Fig. 3B). Plasma kinetics showed rapid clearance of BIO-735, with most cleared by 60 min after injection, although because plasma does not contain OGA-expressing T-cells, clearance will likely be faster than in whole blood. The concentration of BIO-735 in the brain was highest in the striatum, followed by the frontal cortex, and the cerebellum had the lowest uptake.

The tracer candidate BIO-735 was radiolabeled with the PET isotope ^{11}C (half-life, 20.4 min) at high radiochemical purity (94%–95%) and molar activity (30–50 GBq/μmol). The tracer [^{11}C]BIO-735 was injected intravenously (8–10 MBq, 0.09–0.16 μg) into a naïve rat, first as a baseline scan and then after a 0.3 mg/kg blocking dose of BIO-735. The rat underwent a dynamic PET scan 0–60 min after injection, followed by a CT scan for anatomic reference (Fig. 2B).

Coronal images and time–activity curves showed measured uptake of the tracer in all sampled brain regions. Baseline time–activity curves showed that the tracer was rapidly taken up in the brain with little washout during the scan duration, suggesting strong affinity toward its target (Supplemental Fig. 4). Retention of the tracer varied in different brain regions. Regions such as the striatum and the hypothalamus were associated with relatively high tracer uptake and slow off-rate kinetics, whereas some regions, such as the cerebellum, were associated with relatively low tracer uptake and faster off-rate kinetics. The self-blocking scan showed tracer uptake followed by rapid clearance from the CNS, with a reduction in whole-brain SUV 50–60 min after injection from 2.9 at baseline to 0.3 after blocking, suggesting near-total saturation of the target (Supplemental Fig. 4). No regional difference could be seen in tracer uptake during the self-block scan.

PET Imaging of [^{11}C]BIO-735 in NHPs

With good evidence of brain uptake and saturable binding in rats, the tracer [^{11}C]BIO-735 was tested in a cynomolgus NHP. The tracer was synthesized at high radiochemical purity (>99%) and molar activity (35–60 GBq/μmol at the end of synthesis) and either administered intravenously alone as a baseline scan or coinjected with 1 mg/kg BIO-735 as a homologous block (for baseline, 36 MBq, 2.0 μg; for pretreatment, 95 MBq, 3.3 μg). A dynamic PET scan was acquired 0–90 min after injection with the arterial input function and parent fraction analysis. An MR image was also obtained as an anatomic frame of reference, and regions of interest for brain regions were drawn manually (Fig. 3A).

The baseline scan showed tracer uptake throughout the brain, with a gradient of SUV across brain regions consistent with the OGA expression level. Uptake was highest in the putamen and lowest in the thalamus (Fig. 3B). The second PET scan followed pretreatment with a 1 mg/kg self-block, which dramatically reduced uptake within all brain regions, allowing quick washout of the tracer. The initial SUV (0–5 min) was increased after treatment with the self-block, suggesting a change in the input function consistent with the blocking of OGA in the periphery and allowing more free radiotracer to be present in the blood and brain. This is likely because the tracer was bound to OGA expressed on circulating T-cells in the baseline scan and then inhibited by pretreatment with the self-block scan. Although there was no observed difference in the plasma parent fraction between the 2 scans (Supplemental Fig. 5), this is likely because of the lack of T-cells (and therefore OGA) in the plasma. This reinforces the need for an appropriate input function of quality to derive the volume of distribution and quantify the signal with confidence.

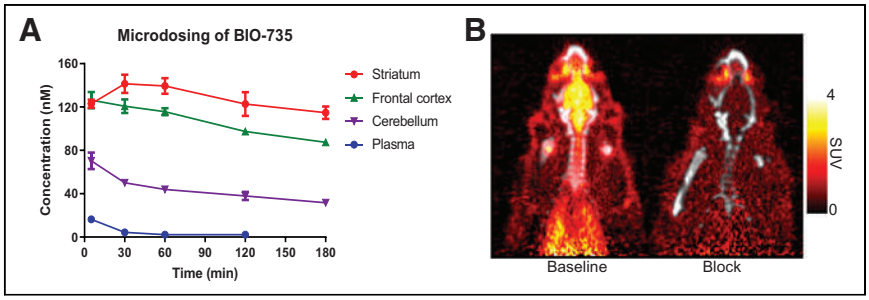

FIGURE 2. (A) Results of microdosing study where rats (n = 3 per time point) were administered BIO-735 by intravenous bolus (10 μg/kg) and tissues were analyzed for compound concentration by liquid chromatography tandem mass spectrometry. (B) Coronal PET images of rat administered [^{11}C]BIO-735 as either baseline scan (left) or blocking scan (right) after pretreatment with 0.3 mg/kg BIO-735, summed for 0–60 min.

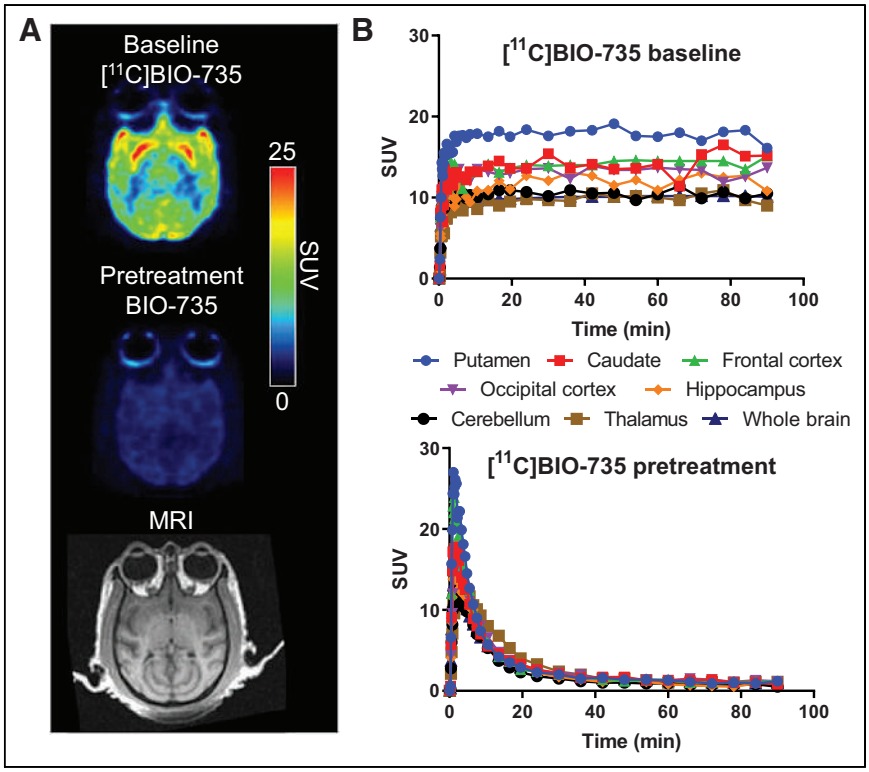

FIGURE 3. PET/MRI data of NHP scanned with [^{11}C]BIO-735. (A) PET images summed for 10–93 min: from top to bottom, baseline scan, blocking scan after pretreatment with 1 mg/kg BIO-735, and MR image for anatomic reference. (B) Regional time–activity curve for brain subregions after baseline scan (top) and blocking scan (bottom).

Although the tracer in NHP showed excellent specific uptake and binding, the time–activity curves for the baseline scan showed no observable clearance from the brain during the 90-min scan after initial uptake. This suggests that once bound, the off-rate for the tracer is very slow, making potential quantification of the volume of distribution challenging. Thus, BIO-735 was deemed suboptimal as a PET tracer candidate and was optimized toward reduced OGA affinity to facilitate release from the target and accelerate clearance without affecting selectivity or specificity.

Optimization of Lead Compound BIO-578

The original structure of BIO-735 was modified by replacing a single nitrogen with carbon (Fig. 4A), moving from pyrimidine to pyridine and reducing the compound's affinity for OGA without adversely affecting the CNS PET multiparameter optimization score or other key properties (Supplemental Table 1). The new compound, BIO-578, had a CNS PET multiparameter optimization score of 4.7 and SPR K_d of 6.15 nM, about 7-fold higher than that of BIO-735. This was confirmed by homogenate binding in a mouse brain with a K_d of 2.3 nM, about 4 times higher than that of BIO-735 (Supplemental Fig. 2A). The new compound was tested as before, with inhibition constant measurements showing specific and concentration-dependent inhibition of binding to OGA (Supplemental Figs. 2B and 2C).

A microdosed pharmacokinetic study in rats showed that BIO-578 accumulated in the brain with a pattern similar to what was observed for BIO-735, though with faster apparent clearance (Fig. 4B). BIO-578 was shown to have an approximately 4-fold decrease in striatum concentration over 3 h, whereas BIO-735 remained relatively constant.

PET Imaging of Lead Compound [^{11}C]BIO-578 in NHPs

BIO-578 was labeled with ^{11}C, and the tracer [^{11}C]BIO-578 was dosed intravenously (for baseline, 28 MBq, 0.9 μg; for pretreatment, 132 MBq, 1.6 μg). A baseline PET scan was acquired, as well as a 1 mg/kg blocking scan after pretreatment with nonradioactive BIO-735 (Fig. 5A). These were each acquired with the arterial input function and parent fraction analysis, as well as an MR image for anatomic reference. All brain regions measured showed uptake and retention of the tracer. Tracer uptake was also variable in different regions of the brain. High uptake in the putamen and low uptake in the cerebellum were observed, similar to trends observed by other OGA tracers (*11*). The signal was subsequently blocked after administration of a mass dose of BIO-735, demonstrating selectivity for the target (Fig. 5B). A higher initial SUV (0–5 min), a phenomenon noted in the [^{11}C]BIO-735 scans and a feature of PET tracers specific to OGA, was also observed.

In the baseline scan, all brain regions demonstrated observable clearance over the 90-min scan. With a measurable off-rate, [^{11}C]BIO-578 exhibited a desired profile for a PET tracer. Metabolite analysis demonstrated that the intact parent tracer accounted for approximately 10% of the total radioactivity measured in the plasma 60 min after administration (Supplemental Figs. 6 and 7).

To confirm the in vivo specificity of [^{11}C]BIO-578, a NHP PET study was conducted, using thiamet G as the blocking compound (Fig. 6). A baseline and a 10 mg/kg thiamet G pretreatment PET scan were each acquired (for baseline, 40 MBq, 1.1 μg; for pretreatment, 108 MBq, 1.0 μg). The dose of thiamet G was selected on the basis of published data showing pretreatment leads to an approximately 90% reduction in PET tracer binding to OGA (*11*). As before, the baseline scan showed uptake throughout the brain (Fig. 6). The thiamet G pretreatment scan showed substantial clearance from all brain regions, indicating that [^{11}C]BIO-578 binding is successfully blocked by thiamet G.

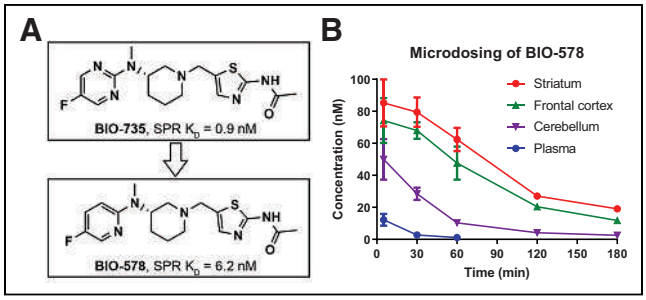

FIGURE 4. (A) Molecular structures of BIO-735 and BIO-578, showing replacement of pyrimidine with pyridine and resultant decrease in affinity by SPR. (B) Results of microdosing study where rats (n = 3 per time point) were administered BIO-578 by intravenous bolus (10 μg/kg) and tissues were analyzed by LC-MS/MS.

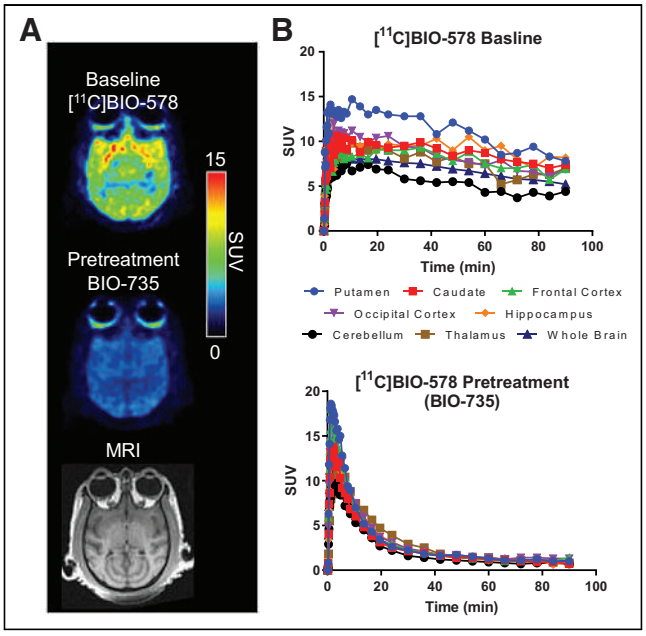

FIGURE 5. PET/MRI data of NHP scanned with [^{11}C]BIO-578 and pretreated with BIO-735. (A) Representative axial slices of PET/MR images after dosing of [^{11}C]BIO-578 in NHP. PET images were summed from 10 to 93 min: from top to bottom, baseline scan, blocking scan after pretreatment with 1 mg/kg BIO-735, and MR image for anatomic reference. (B) Regional time–activity curve for brain subregions after baseline scan (top) and blocking scan (bottom).

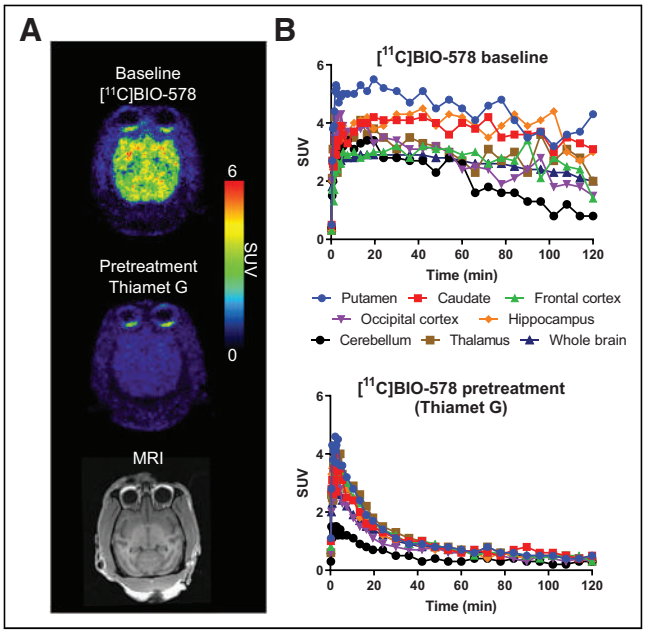

FIGURE 6. PET/MRI data of NHP scanned with [^{11}C]BIO-578 and pretreated with thiamet G. (A) Representative axial slices of PET/MR images after dosing of [^{11}C]BIO-578 in NHP. PET images were summed for 10–120 min: from top to bottom, baseline scan, blocking scan after pretreatment with 10 mg/kg thiamet G, and MR image for anatomic reference. (B) Regional time–activity curve for brain subregions after baseline scan (top) and blocking scan (bottom).

DISCUSSION

There is a precedence for the development of OGA PET tracers. One of the previously published OGA PET tracers, [^{18}F]MK-8553, has little data disclosed outside of conference proceedings. A more recent tracer, [^{18}F]LSN3316612, showed promise in preclinical imaging studies in rodents and NHPs published by Lu et al. (*13*) and Paul et al. (*11*) and was tested clinically in healthy human volunteers (*23*). Although the scope of the studies did not involve determination of target occupancy of an OGA inhibitor, the tracer showed promising imaging properties to provide information on dosing regimens, leading the authors to conclude that it could be suitable for clinical research on OGA. However, the ligand exhibits a slow off-rate, leading to the slow clearance kinetics observed in both NHP and human studies and complicating efforts to robustly quantify uptake because of the lack of a reference region (*24*). Furthermore, the relatively long time that it takes the tracer to reach equilibrium necessitates longer time frames for PET acquisition. This, combined with ^{18}F as the labeling isotope, limits the number of PET scans that could theoretically be performed on a subject in a single day. The efforts described here were in pursuit of finding a suitable OGA PET tracer that does not bear these limitations, enabling robust quantification of target occupancy to support drug development efforts.

The first compound tested, BIO-735, demonstrated high affinity toward OGA in both SPR and homogenate binding studies, as well as in vitro properties suggesting blood–brain barrier permeability and low efflux. An in vivo pharmacokinetic study using a microdose of BIO-735 exhibited uptake and slow clearance from the brain, with uptake in brain regions consistent with the previously determined B_{max} for those regions. Although the 10 μg/kg dose is approximately 10–20 times higher than the typical mass of the tracer injected during imaging, it was demonstrated that microdose kinetics and uptake were still consistent with a radiolabeled tracer dose. These results suggest that such microdosed pharmacokinetic studies could be valuable for screening other CNS PET tracers without the need to radiolabel them (*18,22,25*). This is particularly applicable for targets that have a differential expression in different compartments of the brain. We hypothesize that factors such as lower target B_{max} or presence of an off-target sink could negatively affect the microdose approximation by affecting tracer kinetics more than the larger microdose. This strategy could be extended to peripheral tissues, though it would be limited to targets of known protein expression and distribution that are naturally expressed in relative abundance.

After radiolabeling with ^{11}C, PET imaging studies were performed in rats and NHPs. However, as with the rat, clearance from the NHP of [^{11}C]BIO-735 in the baseline scan was very slow such that there was no observable decrease in SUV over the 90-min scan duration. This presented significant challenges for quantification and modeling, similar to challenges faced by Paul et al. (*11*). It was hypothesized that this may result from the high affinity of BIO-735 toward OGA, with a K_d of 0.9 nM by SPR.

After modifications to the original structure, the new compound, BIO-578, displayed a nearly 7-fold reduction in affinity. Results from the microdosed pharmacokinetic study in rats provided evidence of a faster off-rate and clearance from the CNS. A PET imaging study in NHPs with the radiolabeled tracer [^{11}C]BIO-578 confirmed this improved clearance, with the baseline scan showing uptake and binding to OGA, followed by about 50% washout over 90 min, as well as displaceable binding and rapid clearance in a scan after a 1 mg/kg pretreatment with BIO-735.

The PET tracer [^{11}C]BIO-578 demonstrated specific, reversible binding to OGA and kinetics favorable for target occupancy calculations, suggesting that [^{11}C]BIO-578 could serve as a tool for evaluating small-molecule inhibitors of OGA in the clinic. In addition to improved clearance, the tracer's labeling with ^{11}C results in lower radiation dosimetry than with ^{18}F and allows multiple same-day scans of the same patient, presenting a significant advantage over both [^{18}F]LSN3316612 and [^{18}F]MK-8553.

Also of note was the determination of OGA B_{max} in human T-cells, because this has the potential to affect quantification and is not captured in a typical plasma input function workflow. It is also worth considering when developing other tracers for targets that may be expressed in circulating immune cells.

CONCLUSION

Two ^{11}C PET tracers were developed targeting OGA, an enzyme with a known role in the *O*-GlcNAcylation of tau protein and potentially implicated in tau aggregation in Alzheimer's disease. Although the off-rate of the first tracer, [^{11}C]BIO-735, was suboptimal for clinical translation, the second tracer, [^{11}C]BIO-578, proved more promising. Testing through a series of in vitro and in vivo rat experiments demonstrated the high affinity and specificity of the tracer toward OGA, whereas in vivo NHP studies confirmed that the tracer is suitable for testing in patients.

DISCLOSURE

Authors are or were used or contracted by Biogen and may hold stock in the company. Work was paid for in full by Biogen. No other potential conflict of interest relevant to this article was reported.

KEY POINTS

QUESTION: Can a PET tracer be designed for OGA that can support target occupancy and dose selection studies of therapeutic OGA inhibitors in clinical trials?

PERTINENT FINDINGS: A PET tracer, [^{11}C]BIO-578, was developed and validated preclinically in rodent and NHP studies. Its optimized kinetics will enable robust calculation of target occupancy in future investigations.

IMPLICATIONS FOR PATIENT CARE: This PET tracer will provide critical data on target occupancy and dose selection during clinical development of OGA inhibitors for the treatment of Alzheimer's disease.

REFERENCES

1. Despres C, Byrne C, Qi H, et al. Identification of the tau phosphorylation pattern that drives its aggregation. *Proc Natl Acad Sci USA.* 2017;114:9080–9085.
2. Ossenkoppele R, Reimand J, Smith R, et al. Tau PET correlates with different Alzheimer's disease-related features compared to CSF and plasma p-tau biomarkers. *EMBO Mol Med.* 2021;13:e14398.
3. La Joie R, Visani AV, Baker SL, et al. Prospective longitudinal atrophy in Alzheimer's disease correlates with the intensity and topography of baseline tau-PET. *Sci Transl Med.* 2020;12:eaau5732.
4. Hammes J, Bischof GN, Drzezga A. Molecular imaging in early diagnosis, differential diagnosis and follow-up of patients with neurodegenerative diseases. *Clin Transl Imaging.* 2017;5:465–471.
5. Yang X, Qian K. Protein *O*-GlcNAcylation: emerging mechanisms and functions. *Nat Rev Mol Cell Biol.* 2017;18:452–465.
6. Mergenthaler P, Lindauer U, Dienel GA, Meisel A. Sugar for the brain: the role of glucose in physiological and pathological brain function. *Trends Neurosci.* 2013; 36:587–597.
7. Yuzwa SA, Macauley MS, Heinonen JE, et al. A potent mechanism-inspired *O*-GlcNAcase inhibitor that blocks phosphorylation of tau in vivo. *Nat Chem Biol.* 2008;4:483–490.
8. Graham DL, Gray AJ, Joyce JA, et al. Increased *O*-GlcNAcylation reduces pathological tau without affecting its normal phosphorylation in a mouse model of tauopathy. *Neuropharmacology.* 2014;79:307–313.
9. Hastings NB, Wang X, Song L, et al. Inhibition of *O*-GlcNAcase leads to elevation of *O*-GlcNAc tau and reduction of tauopathy and cerebrospinal fluid tau in rTg4510 mice. *Mol Neurodegener.* 2017;12:39.
10. Li W, Salinas C, Riffel K, et al. The discovery and characterization of [^{18}F]MK-8553, a novel PET tracer for imaging *O*-GlcNAcase (OGA). Paper presented at: Neuroreceptor Mapping; 2016; Boston, MA.
11. Paul S, Haskali MB, Liow J-S, et al. Evaluation of a PET radioligand to image *O*-GlcNAcase in brain and periphery of rhesus monkey and knock-out mouse. *J Nucl Med.* 2019;60:129–134.
12. Smith SM, Struyk A, Jonathan D, et al. O2-13-04: early clinical results and preclinical validation of the *O*-GlcNAcase (OGA) inhibitor Mk-8719 as a novel therapeutic for the treatment of tauopathies. *Alzheimers Dement.* 2016;12:P261.
13. Lu S, Haskali MB, Ruley KM, et al. PET ligands [^{18}F]LSN3316612 and [^{11}C]LSN3316612 quantify *O*-linked-β-*N*-acetyl-glucosamine hydrolase in the brain. *Sci Transl Med.* 2020;12:eaau2939.
14. Wang X, Li W, Marcus J, et al. MK-8719, a novel and selective *O*-GlcNAcase inhibitor that reduces the formation of pathological tau and ameliorates neurodegeneration in a mouse model of tauopathy. *J Pharmacol Exp Ther.* 2020;374: 252–263.
15. Haltiwanger RS, Grove K, Philipsberg GA. Modulation of *O*-linked *N*-acetylglucosamine levels on nuclear and cytoplasmic proteins in vivo using the peptide *O*-GlcNAc-beta-*N*-acetylglucosaminidase inhibitor *O*-(2-acetamido-2-deoxy-D-glucopyranosylidene)amino-*N*-phenylcarbamate. *J Biol Chem.* 1998;273:3611–3617.
16. Andersson J, Truong P, Halldin C. In-target produced [^{11}C]methane: increased specific radioactivity. *Appl Radiat Isot.* 2009;67:106–110.
17. Moein MM, Nakao R, Amini N, Abdel-Rehim M, Schou M, Halldin C. Sample preparation techniques for radiometabolite analysis of positron emission tomography radioligands; trends, progress, limitations and future prospects. *Trends Analyt Chem.* 2019;110:1–7.
18. Zhang L, Villalobos A. Strategies to facilitate the discovery of novel CNS PET ligands. *EJNMMI Radiopharm Chem.* 2017;1:13.
19. Eckelman WC, Kilbourn MR, Mathis CA. Discussion of targeting proteins in vivo: in vitro guidelines. *Nucl Med Biol.* 2006;33:449–451.
20. Abramowitz LK, Hanover JA. T cell development and the physiological role of *O*-GlcNAc. *FEBS Lett.* 2018;592:3943–3949.
21. Bergstrom M. The use of microdosing in the development of small organic and protein therapeutics. *J Nucl Med.* 2017;58:1188–1195.
22. Chernet E, Martin LJ, Li D, et al. Use of LC/MS to assess brain tracer distribution in preclinical, in vivo receptor occupancy studies: dopamine D2, serotonin 2A and NK-1 receptors as examples. *Life Sci.* 2005;78:340–346.
23. Lee J-H, Liow J-S, Paul S, et al. PET quantification of brain *O*-GlcNAcase with [^{18}F]LSN3316612 in healthy human volunteers. *EJNMMI Res.* 2020;10:20.
24. Innis RB, Cunningham VJ, Delforge J, et al. Consensus nomenclature for in vivo imaging of reversibly binding radioligands. *J Cereb Blood Flow Metab.* 2007;27: 1533–1539.
25. Sandhu P, Vogel JS, Rose MJ, et al. Evaluation of microdosing strategies for studies in preclinical drug development: demonstration of linear pharmacokinetics in dogs of a nucleoside analog over a 50-fold dose range. *Drug Metab Dispos.* 2004; 32:1254–1259.

Automated Brain Tumor Detection and Segmentation for Treatment Response Assessment Using Amino Acid PET

Robin Gutsche[1,2], Carsten Lowis[1], Karl Ziemons[3], Martin Kocher[1,4], Garry Ceccon[5], Cláudia Régio Brambilla[1,6], Nadim J. Shah[1,6,7], Karl-Josef Langen[1,8,9], Norbert Galldiks[1,5,9], Fabian Isensee[10,11], and Philipp Lohmann[1]

[1]Institute of Neuroscience and Medicine, Forschungszentrum Juelich GmbH, Juelich, Germany; [2]RWTH Aachen University, Aachen, Germany; [3]Medical Engineering and Technomathematics, FH Aachen University of Applied Sciences, Juelich, Germany; [4]Department of Stereotaxy and Functional Neurosurgery, Faculty of Medicine and University Hospital Cologne, University of Cologne, Cologne, Germany; [5]Department of Neurology, Faculty of Medicine and University Hospital Cologne, University of Cologne, Cologne, Germany; [6]JARA-BRAIN-Translational Medicine, Aachen, Germany; [7]Department of Neurology, University Hospital RWTH Aachen, Aachen, Germany; [8]Department of Nuclear Medicine, University Hospital RWTH Aachen, Aachen, Germany; [9]Center for Integrated Oncology, Universities of Aachen, Bonn, Cologne, and Duesseldorf, Germany; [10]Applied Computer Vision Lab, Helmholtz Imaging, Heidelberg, Germany; and [11]Division of Medical Image Computing, German Cancer Research Center, Heidelberg, Germany

Evaluation of metabolic tumor volume (MTV) changes using amino acid PET has become an important tool for response assessment in brain tumor patients. MTV is usually determined by manual or semiautomatic delineation, which is laborious and may be prone to intra- and interobserver variability. The goal of our study was to develop a method for automated MTV segmentation and to evaluate its performance for response assessment in patients with gliomas. **Methods:** In total, 699 amino acid PET scans using the tracer *O*-(2-[^{18}F]fluoroethyl)-L-tyrosine (^{18}F-FET) from 555 brain tumor patients at initial diagnosis or during follow-up were retrospectively evaluated (mainly glioma patients, 76%). ^{18}F-FET PET MTVs were segmented semiautomatically by experienced readers. An artificial neural network (no new U-Net) was configured on 476 scans from 399 patients, and the network performance was evaluated on a test dataset including 223 scans from 156 patients. Surface and volumetric Dice similarity coefficients (DSCs) were used to evaluate segmentation quality. Finally, the network was applied to a recently published ^{18}F-FET PET study on response assessment in glioblastoma patients treated with adjuvant temozolomide chemotherapy for a fully automated response assessment in comparison to an experienced physician. **Results:** In the test dataset, 92% of lesions with increased uptake (n = 189) and 85% of lesions with iso- or hypometabolic uptake (n = 33) were correctly identified (F1 score, 92%). Single lesions with a contiguous uptake had the highest DSC, followed by lesions with heterogeneous, noncontiguous uptake and multifocal lesions (surface DSC: 0.96, 0.93, and 0.81 respectively; volume DSC: 0.83, 0.77, and 0.67, respectively). Change in MTV, as detected by the automated segmentation, was a significant determinant of disease-free and overall survival, in agreement with the physician's assessment. **Conclusion:** Our deep learning–based ^{18}F-FET PET segmentation allows reliable, robust, and fully automated evaluation of MTV in brain tumor patients and demonstrates clinical value for automated response assessment.

Key Words: FET PET; volumetry; machine learning; artificial intelligence; AI; neurooncology

J Nucl Med 2023; 64:1594–1602
DOI: 10.2967/jnumed.123.265725

Received Mar. 14, 2023; revision accepted May 31, 2023.
For correspondence or reprints, contact Philipp Lohmann (p.lohmann@fz-juelich.de).
Published online Aug. 10, 2023.

In recent years, several studies have demonstrated the clinical potential of volumetric response assessment in patients with brain tumors, particularly since the development of artificial neural networks has enabled this laborious task to be conducted in a fully automated way and with quality comparable to an experienced physician performing manual volumetry (*1–3*). For example, Kickingereder et al. (*4*) demonstrated the superior performance of an artificial neural network for the assessment of response to bevacizumab plus lomustine therapy for glioma patients based on structural MRI compared with the response assessment performed by a physician based on the Response Assessment in Neuro-Oncology criteria. The full integration of this method into the clinical workflow and the complete automatization allow for a more efficient, standardized, and reproducible volumetric evaluation of tumor burden, yielding great potential for response assessment in future clinical trials.

Although the clinical importance of structural MRI for response assessment is undisputed, there are known limitations for differentiation between treatment-related changes and tumor progression and for delineation of tumor extent, especially in cases of nonenhancing tumor portions (*5–7*). Because of its ability to overcome these shortcomings, amino acid PET has become an important diagnostic tool in patients with brain tumors. Specifically, amino acid PET is recommended by the Response Assessment in Neuro-Oncology group for response assessment in glioma patients at all disease stages (*8,9*). Among the amino acid PET tracers for patients with brain tumors, *O*-(2-[^{18}F]fluoroethyl)-L-tyrosine (^{18}F-FET) is the most widely used and evaluated PET tracer in Europe but is also gaining international importance, especially in the United States.

A prospective study conducted by Suchorska et al. on 79 patients with newly diagnosed glioblastoma showed that the metabolic tumor volume (MTV) assessed by ^{18}F-FET PET before initiation of temozolomide chemoradiation was a strong prognostic factor for progression-free and overall survival, independent of the extent of resection (*10*). Recently, Ceccon et al. (*11*) found that in contrast to the MRI-based response assessment according to Response Assessment in Neuro-Oncology criteria and tumor-to-brain ratios (TBRs) for ^{18}F-FET PET evaluation, MTV changes were predictive for the early identification of metabolic responders in patients undergoing adjuvant temozolomide chemotherapy. Furthermore, Wollring et al. (*12*)

TABLE 1
Patient Characteristics

Characteristic	Training dataset	Test dataset
Patients	399	156
Lesions	496	205
Mean age ± SD (y)	51 ± 14	49 ± 14
Sex		
Male	219	83
Female	180	73
Median MTV (cm^3)	11.1 (range, 0.03–109.4)	10.6 (range, 0.1–98.8)
Patients with multifocal lesions	20	19
Patients without pathologic uptake (beyond clinically established threshold)	20	38
Patients with nonmalignant uptake (e.g., treatment-related changes, inflammation, encephalitis)	27	17
Gliomas		
Astrocytoma, IDH-mutant	35	10
CNS WHO grade 2	11	—
CNS WHO grade 3	19	6
CNS WHO grade 4	5	4
Astrocytoma, not otherwise specified	76	30
CNS WHO grade 2	27	12
CNS WHO grade 3	49	18
CNS WHO grade 4	—	—
Oligodendroglioma, IDH-mutant, 1p/19q-codeleted	24	4
CNS WHO grade 2	14	3
CNS WHO grade 3	10	1
Oligodendroglioma, not otherwise specified	18	7
CNS WHO grade 2	14	4
CNS WHO grade 3	4	3
Glioblastoma, IDH wild-type	63	45
Glioblastoma, not otherwise specified	89	22
Brain metastases	68	26
Lung	27	12
Breast	11	5
Melanoma	9	7
Renal	5	—
Gastrointestinal	3	—
Unknown	13	2
Other		
Ependymoma	—	1
Lymphoma	2	—
Ganglioma	1	—
Meningioma	1	—
Nonmalignant neoplasm	—	2
Inflammation, encephalitis	3	1
Unknown	19	8

IDH = isocitrate dehydrogenase; CNS WHO = central nervous system World Health Organization.
Data are number, unless otherwise specified.

showed that MTV changes on ^{18}F-FET PET are also an important factor for predicting response to lomustine-based chemotherapy in patients with recurrent gliomas. Despite these interesting findings, 3-dimensional assessment of MTV is not part of the routine clinical evaluation of amino acid PET, which is based mainly on TBR extracted from manually or semiautomatically generated 2-dimensional regions of interest (*13*). The fact that MTV is not routinely assessed in clinical practice suggests that the time and effort required for volumetric amino acid PET segmentation still exceed the clinical benefit. The number of studies investigating the clinical value of amino acid PET MTV needs to increase to demonstrate its clinical value and ultimately lead to the inclusion of volumetric amino acid PET assessment in consensus guidelines and recommendations.

To foster the clinical translation of volumetric amino acid PET evaluation, our study aimed to develop and evaluate an artificial neural network using the self-configuring no new U-Net (*14*) for the automated 3-dimensional segmentation of brain tumors using ^{18}F-FET PET. Furthermore, the network was applied to a recently published ^{18}F-FET PET study on response assessment in newly diagnosed glioblastoma patients treated with adjuvant temozolomide chemotherapy (*11*) for a fully automated response assessment in comparison to an experienced physician.

MATERIALS AND METHODS

Detailed methods can be found in the supplemental materials (available at http://jnm.snmjournals.org) (*11,13–22*).

Ethics

The study adhered to the standards established in the Declaration of Helsinki. The local ethics committees approved the retrospective analysis of imaging data (EK 055/19). All patients provided written informed consent before each ^{18}F-FET PET investigation.

Patient Characteristics

Our database comprising 4,381 patients who underwent diagnostic ^{18}F-FET PET scans at initial diagnosis, suspected tumor relapse, or treatment response assessment in our institution between November 2005 to April 2021 was retrospectively evaluated in this study. Of these ^{18}F-FET PET scans, only those for which segmentations of MTV were available were included. Further, to evaluate the performance of the segmentation algorithm in patients lacking an increased ^{18}F-FET uptake, 59 patients with iso- or hypometabolic ^{18}F-FET PET scans were added. In total, 699 ^{18}F-FET PET scans from 555 patients were investigated in the study. Detailed patient characteristics are presented in Table 1.

Data Sharing

The dataset, including ^{18}F-FET PET image data and segmentations, is available on request. In addition, data analysis scripts in Python are available on request. The trained network (JuST_BrainPET) is available at https://github.com/MIC-DKFZ/nnUNet/tree/nnunetv1#useful-resources.

RESULTS

^{18}F-FET Uptake Characteristics

Of the 476 ^{18}F-FET PET scans in the training dataset, 20 (4%) showed no pathologic uptake, 20 (4%) showed multifocal lesions, and 49 (10%) showed increased uptake due to nonmalignant lesions, for example, treatment-related changes. Of the 223 ^{18}F-FET PET scans in the test dataset, 39 (17%) showed no pathologic uptake, 19 (9%) showed multifocal lesions, and 26 (12%) showed nonmalignant lesions.

Network Performance for Lesion Detection

Of the 205 lesions with increased ^{18}F-FET uptake, 189 were correctly identified by the network. Of 39 scans without increased uptake, only 6 were erroneously considered to show tumors by the network. Importantly, none of the anatomic regions that showed a physiologically increased uptake, such as in the superior sagittal sinus, were considered to be tumors by the network. This resulted in a mean F1 score of 92%, a sensitivity of 93%, and a positive predictive value of 95% for lesion detection. Patient examples showing lesions missed by the network, false detections, and examples of regions showing physiologically increased uptake are provided in Figure 1.

Network Performance for Lesion Segmentation

The median tumor volume was 11.1 cm^3 (range, 0.03–109.4 cm^3) for the training set and 10.6 cm^3 (range, 0.1–98.8 cm^3) for the test set (Table 1). In the training set, the mean volume Dice similarity coefficient (DSC) during 5-fold cross validation was 0.75 ± 0.03, and the mean surface DSC was 0.87 ± 0.03 without prior brain extraction. In the test set, the median volume DSC was 0.81 (interquartile range, 0.70–0.89), and the surface DSC was 0.96 (interquartile range, 0.89–0.99). With prior brain extraction, the mean volume DSC in the training set after 5-fold cross validation was 0.74 ± 0.03, and the mean surface DSC was 0.85 ± 0.02. In the test set, the median volume DSC was 0.80 (interquartile range, 0.68–0.88), and the median surface DSC was 0.93 (interquartile range, 0.87–0.98). Since brain extraction had no statistically significant effect on

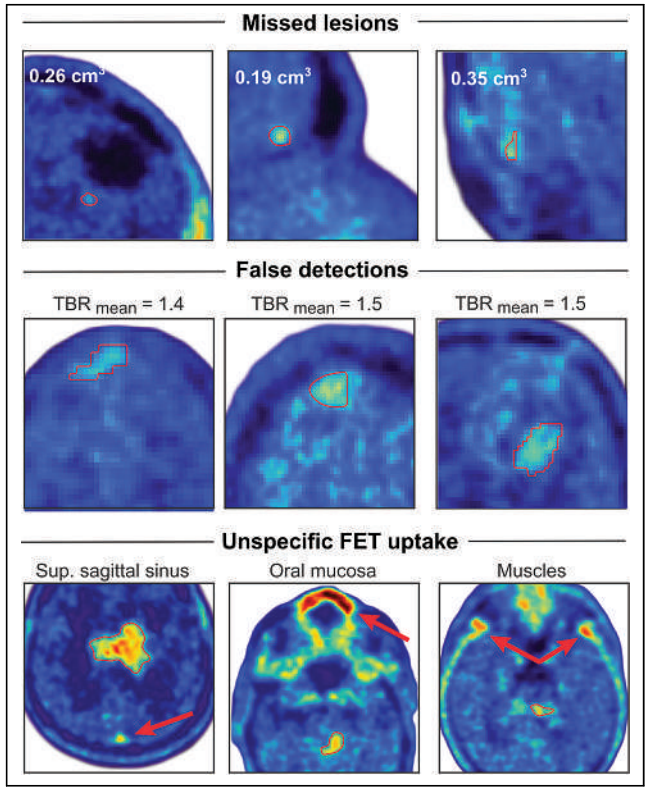

FIGURE 1. Network performance for lesion detection: ground truth segmentations of lesions that have not been detected by network, nonmalignant lesions with slightly increased but not pathologic uptake (mean TBR < 1.6) that have been erroneously detected as malignant lesions by network, and anatomic regions that show physiologically increased uptake that have always been correctly identified as such by network. TBRmean = mean TRB.

TABLE 2
Performance of Network in Training and Test Datasets

Parameter	Without brain extraction		With brain extraction	
	Volume DSC	Surface DSC*	Volume DSC	Surface DSC*
Training dataset (476 scans)				
1-fold	0.76	0.88	0.74	0.85
2-fold	0.78	0.88	0.77	0.87
3-fold	0.75	0.87	0.72	0.83
4-fold	0.76	0.89	0.76	0.87
5-fold	0.70	0.82	0.70	0.83
Mean ± SD	0.75 ± 0.03	0.87 ± 0.03	0.74 ± 0.03	0.85 ± 0.02
Test dataset (223 scans)				
Median	0.81	0.96	0.80	0.93
IQR, 25%–75%	0.70–0.89	0.89–0.99	0.68–0.88	0.87–0.98

*Tolerance of 3 mm.
IQR = interquartile range.

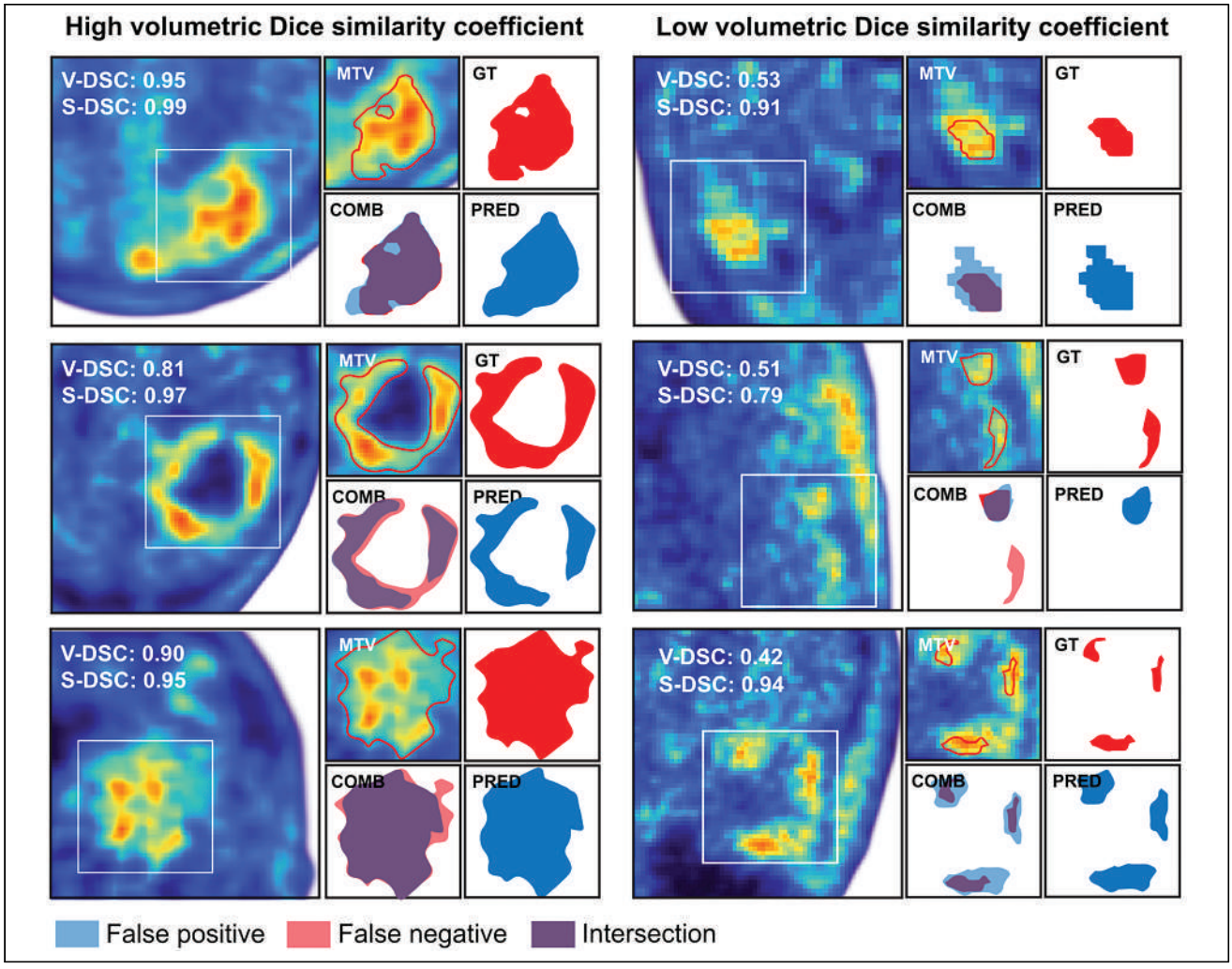

FIGURE 2. Representative examples of lesion segmentations with high and low volume DSC. COMB = combination of ground truth and network segmentation; GT = ground truth segmentation; PRED = segmentation predicted by network; S-DSC = surface DSC; V-DSC = volume DSC.

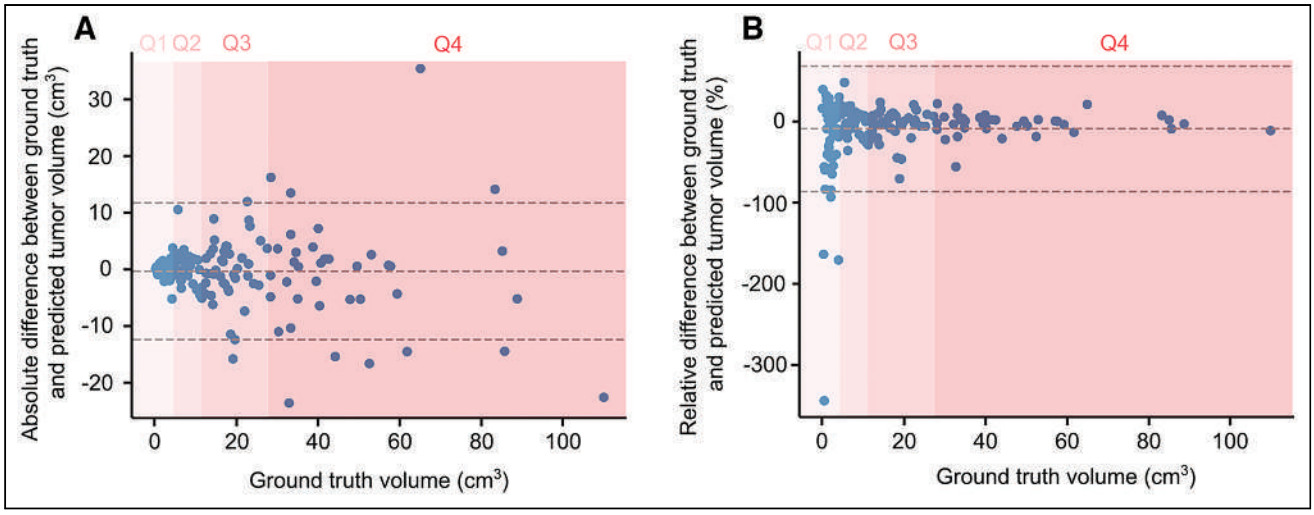

FIGURE 3. Absolute (A) and relative (B) differences between ground truth and predicted MTV of test dataset. Q1–Q4 = quartiles 1–4.

network performance ($P > 0.05$), the results in the following are based on the network trained without prior brain extraction. The network performance is summarized in Table 2. Some representative examples of tumor segmentations yielding low and high volume DSC and surface DSC are presented in Figure 2.

The volume DSC and surface DSC were lowest for small lesions with a volume of between 0.1 and 3.3 cm^3, which is equivalent to the first quartile of lesion volumes (median volume DSC, 0.65; interquartile range, 0.50–0.78; median surface DSC, 0.92; interquartile range, 0.78–0.99). For lesions of the second and third quartiles of lesion volumes (volume, 3.3–22.0 cm^3), the median volume DSC was 0.80 (interquartile range, 0.71–0.88), and the median surface DSC was 0.93 (interquartile range, 0.88–0.99). The network showed the best performance for lesions from the fourth quartile of lesion volumes with a volume of between 22.0 and 98.0 cm^3 (median volume DSC, 0.87 [interquartile range, 0.83–0.90]; median surface DSC, 0.97 [interquartile range, 0.94–0.99]).

Lesions with a larger MTV showed relatively low discrepancies between the predicted and the ground truth segmentations, compared with lesions with a smaller MTV (Fig. 3). This finding is also supported by a slight bias of the network in oversegmenting smaller MTVs, for example, the number of false-positive voxels was higher than that of false-negative voxels in smaller MTVs.

The number of false-positive voxels segmented by the network for the first, second/third, and fourth quartiles of lesion volumes was 65%, 21%, and 11%, respectively, and the number of false-negative voxels was 28%, 22%, and 15%, respectively. Single lesions were segmented with a better performance than nonmalignant and multifocal lesions (median volume DSC: 0.83, 0.77, and 0.67, respectively; median surface DSC: 0.96, 0.93, and 0.81, respectively) (Supplemental Fig. 3).

Automated Versus Manual Response Assessment

The ^{18}F-FET PET parameter mean TBR extracted by the network was 2.1 ± 0.2 at baseline and 2.1 ± 0.2 at follow-up. The ^{18}F-FET PET parameter mean TBR as evaluated by the physician was 2.0 ± 0.2 at baseline and 2.0 ± 0.2 at follow-up. The network and the physician agreed well in the assessment of MTV and in the clinical ^{18}F-FET PET parameter mean TBR for both the baseline and the follow-up scans, with correlation coefficients ranging from 0.81 to 0.95 (Fig. 4).

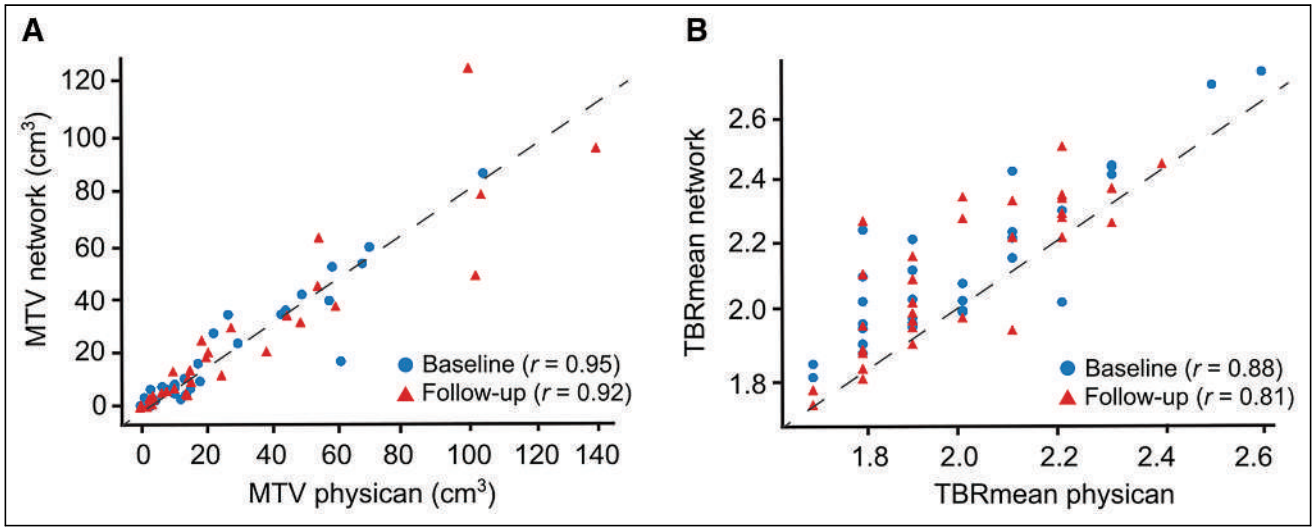

FIGURE 4. Correlation between manual and automatic assessment of MTV (A) and mean TBR (B).

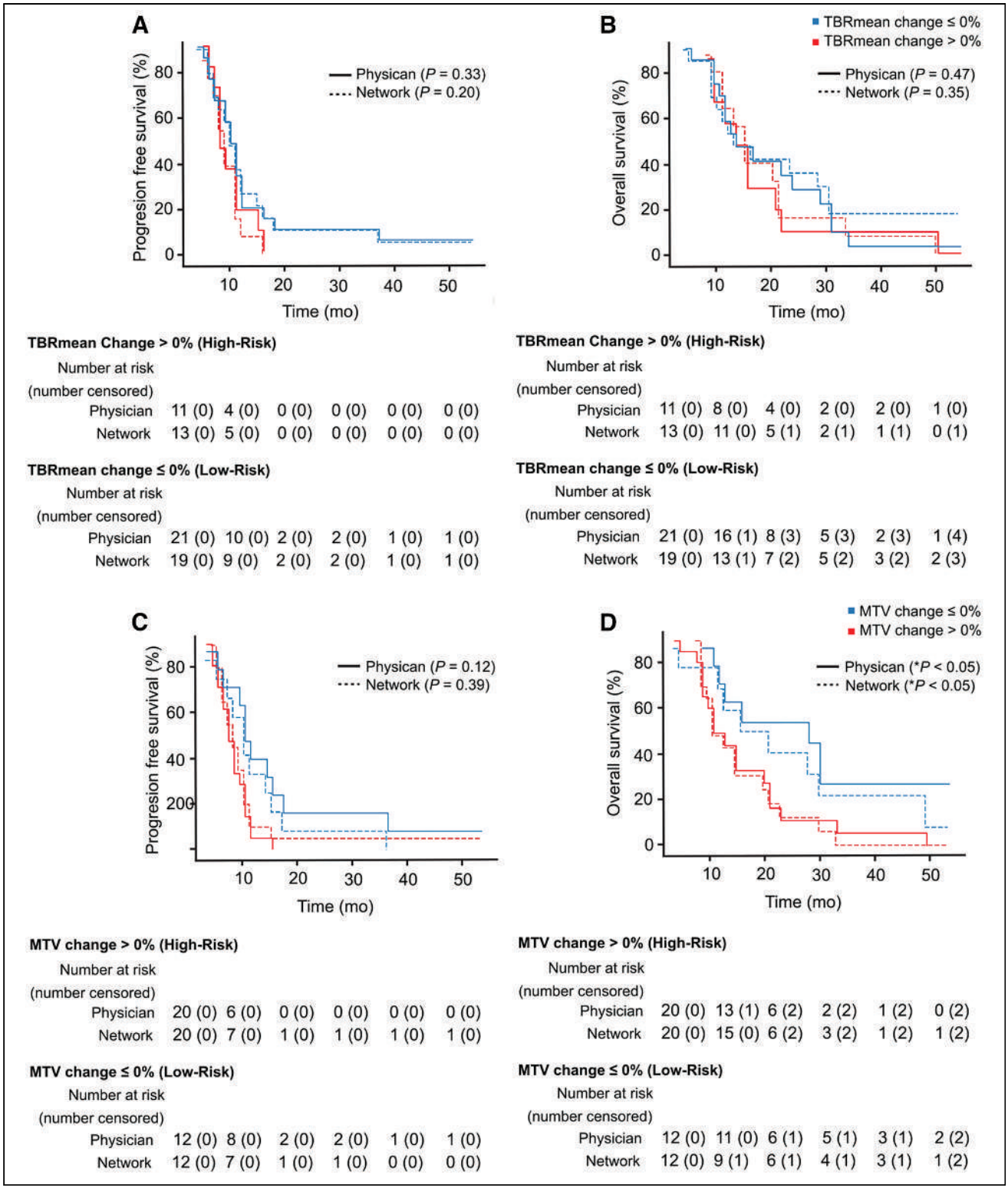

FIGURE 5. Comparison of Kaplan–Meier curves for progression-free survival and overall survival assessed automatically by network and manually by experienced physician on basis of changes in mean TBR (A and C) and MTV (B and D).

The 33 patients (median age, 50 y; range, 20–79 y; 17 women) had a median progression-free survival of 10 mo (range, 4–54 mo) and a median overall survival of 14 mo (range, 5–54 mo). The predicted baseline median MTV was 8.0 cm^3 (range, 0.6–84.0 cm^3), compared with a predicted follow-up median MTV of 12.6 cm^3 (range, 0.6–121.4 cm^3). The manually segmented median MTVs were 13.3 cm^3 (range, 0.6–103.2 cm^3) at baseline and 15.2 cm^3 (range, 0.6–137.1 cm^3) in the follow-up scans.

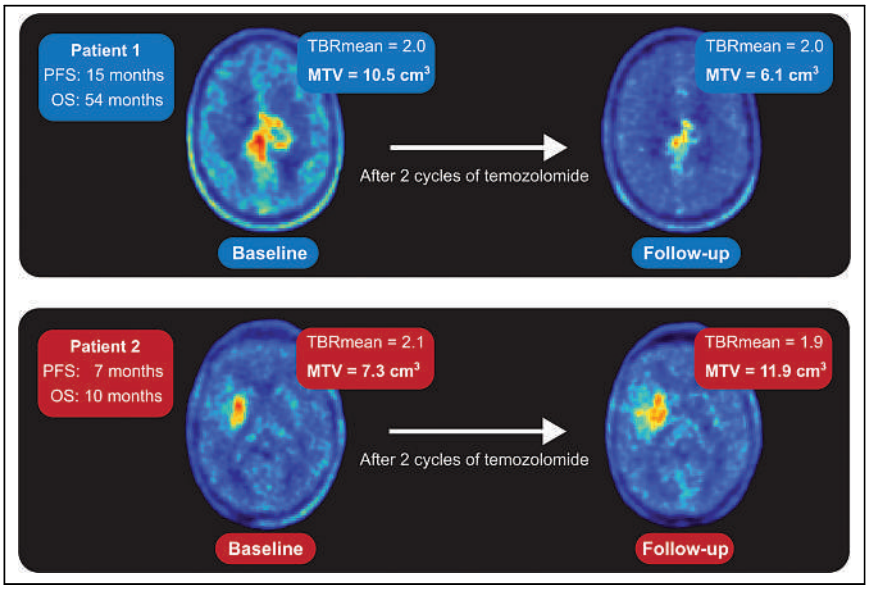

FIGURE 6. Representative ^{18}F-FET PET images at baseline and follow-up of glioma patients with favorable (top row) and unfavorable (bottom row) outcomes after 2 cycles of adjuvant temozolomide. OS = overall survival; PFS = progression-free survival; TBRmean = mean TRB.

The network identified any decrease in MTV after temozolomide chemoradiation as an independent predictor for a significantly longer overall survival in glioma patients ($P < 0.05$). Relative changes in other parameters showed no significant predictive capability for a longer progression-free survival or overall survival. These findings were in line with the manual response assessment performed by an experienced physician. The corresponding Kaplan–Meier curves for progression-free survival and overall survival, along with representative ^{18}F-FET PET images of patients with favorable and unfavorable prognoses, are shown in Figures 5 and 6.

DISCUSSION

The main finding of our study is that our deep learning–based neural network allows reliable and fully automated detection and 3-dimensional segmentation of brain tumors investigated by ^{18}F-FET PET. Furthermore, the network demonstrated its clinical value for a fully automated ^{18}F-FET PET assessment of response to temozolomide chemoradiation in glioma patients, whereby the network yielded results similar to the manual assessment performed by an experienced physician. This finding highlights the value of the network for improvement and automatization of clinical decision-making based on the volumetric evaluation of amino acid PET.

Currently, only a single study has investigated deep learning–based segmentation of brain tumors in adults using ^{18}F-FET PET. Blanc-Durand et al. (*23*) demonstrated the potential of a 3-dimensional U-Net convolutional neural network for the automated detection of gliomas. Although the network achieved a comparable volume DSC of 0.79 in the validation set, the dataset comprised only a small number of patients ($n = 37$). Hence, the generalizability and clinical applicability of this approach remain questionable and require further verification.

The network developed in our study was able to correctly detect most tumors in the test dataset, resulting in high diagnostic performance (F1 score, 92%). Importantly, these results were obtained from a dataset that, in addition to patients with brain tumors and increased uptake, included patients with nonmalignant lesions that showed only slightly increased uptake, patients with no increased uptake, and even patients with photopenic defects (*24*).

Our network erroneously detected and segmented 6 of 39 nonmalignant lesions, for example, treatment-related changes, which showed a slightly increased uptake with a mean TBR of 1.5, which is just below the threshold of 1.6 that was used to generate the ground truth segmentations (Fig. 3B). Identifying these lesions unequivocally on the basis of ^{18}F-FET PET imaging alone is a major challenge even for experienced nuclear medicine physicians, a fact that should be considered when evaluating the performance of our network. Furthermore, the lesions that were not correctly detected by the network were relatively small, with a mean MTV of 0.3 cm^3. Hence, it seems that our network detected and segmented larger lesions more accurately (Fig. 3). This possibility is also supported by a slight bias of the network toward oversegmenting smaller MTVs; for example, the number of false-positive voxels was higher than the number of false-negative voxels in smaller MTVs, a fact that was already described by Blanc-Durand et al. (*23*).

These findings are in line with a recent study from Ladefoged et al. (*25*) in which an artificial neural network was developed and trained on ^{18}F-FET PET and MRI scans from 233 adult brain tumor patients and applied to a dataset of 66 pediatric brain tumor patients for automated tumor segmentation. The authors also found the largest relative errors for tumor segmentations for small tumors with a volume of less than 10 cm^3. Although the network demonstrated excellent performance in pediatric tumor patients, a few cases were reported in which the network erroneously delineated anatomic regions showing a high physiologic uptake. Such was not the case in our study, possibly because of the much larger number of patients used for training and the fact that our network was trained and evaluated on ^{18}F-FET PET data from adults.

Of note, the fact that Ladefoged et al. (*25*) also included contrast-enhanced T1-weighted MR images as input images for the network might have had a positive effect on model performance. Since standardized anatomic MRI data were available for only a subset of patients in our study, we preferred to use a larger number of patients and omitted the addition of MRI. Nevertheless, the influence of the addition of MRI data should be investigated in future studies.

Another important finding of our study is the successful application of our fully automated ^{18}F-FET PET tumor segmentation for the assessment of response in glioma patients after temozolomide chemoradiation. Similar to the manual response assessment performed by an experienced physician, our network also showed that a decrease in MTV was associated with a favorable outcome (Figs. 5 and 6). Beyond MTV, the evaluation of conventional ^{18}F-FET PET parameters, especially TBRs, already plays an important role in the assessment of treatment response in clinical routine (*8*). In our study, we found a strong correlation in TBRs between the network and the manual assessment (Fig. 4).

The retrospective evaluation of our database revealed that MTV segmentation is still performed predominantly 2-dimensionally because

of lack of 3-dimensional methods for the clinic. Availability of an automated method for 3-dimensional segmentation of MTV suitable for daily clinical use should therefore be in demand. Our network performs fully automated 3-dimensional segmentation of a single ^{18}F-FET PET scan on a conventional graphics processing unit–equipped computer in less than 2 min without preprocessing, suggesting its suitability for successful implementation into clinical routine.

One limitation of our study is the uncertainty of the ground truth segmentation. Even though the segmentations were carefully performed according to the current guidelines for the evaluation of amino acid PET in brain tumor patients, interrater variability cannot be excluded. Nonetheless, this limitation is inherent in all work on segmentation and can hardly be overcome. Yet, ground truth uncertainties should be considered when the performance of a segmentation algorithm is being evaluated. A potential source of bias is patient selection, which was limited to patients for whom volumetric tumor segmentation was already available, rather than patients from a random sampling of a larger cohort, as might become possible if an automated 3-dimensional method of MTV segmentation were available. Another limitation—the low spatial resolution of PET—has a direct impact on the quality of the segmentations. To partly account for this limitation, development of our network was based on routinely acquired ^{18}F-FET PET data from 2 PET scanners with different spatial resolutions. In the future, the addition of structural MRI might offer ways to minimize this effect. A further limitation might be that the network was trained on only ^{18}F-FET PET data; its value for other commonly used amino acid PET tracers remains to be evaluated.

A general limitation is the comparatively low availability of amino acid PET. Another factor preventing wider use of amino acid PET is that it requires experienced users for an objective and comparable diagnosis. In this regard, our approach could play an important role because it provides, for the first time, to our knowledge, an objective and easy-to-use way to volumetrically evaluate amino acid PET data from brain tumor patients. We are confident that the availability of the method to the public will further promote amino acid PET internationally and emphasize its value for clinical decision-making.

CONCLUSION

Our deep learning–based ^{18}F-FET PET segmentation allows a reliable, robust, and fully automated evaluation of MTV in patients with brain tumors. The method alleviates the need for extensive image preprocessing, and its potential for an automated response assessment in patients with gliomas has been demonstrated, fostering translation of volumetric amino acid PET evaluation to clinical routine.

DISCLOSURE

This work was supported by the Deutsche Forschungsgemeinschaft (DFG, German Research Foundation; projects 428090865/SPP 2177 [Robin Gutsche, Norbert Galldiks, and Philipp Lohmann] and 491111487). Part of this work was funded by Helmholtz Imaging, a platform of the Helmholtz "Incubator on Information and Data Science." Norbert Galldiks and Philipp Lohmann received honoraria for lectures from Blue Earth Diagnostics. Norbert Galldiks received honoraria for advisory board participation from Telix Pharmaceuticals. No other potential conflict of interest relevant to this article was reported.

ACKNOWLEDGMENTS

We thank Silke Frensch, Suzanne Schaden, Trude Plum, Natalie Judov, Kornelia Frey, and Lutz Tellmann for assistance with the patient studies, and we thank Johannes Ermert, Silke Grafmüller, Erika Wabbals, and Sascha Rehbein for radiosynthesis of ^{18}F-FET.

KEY POINTS

QUESTION: In patients with gliomas, can a fully automated response assessment based on amino acid PET achieve results similar to those of an expert?

PERTINENT FINDINGS: A deep learning–based tumor detection and segmentation tool based on 699 ^{18}F-FET PET scans from 555 patients with brain tumors showed high accuracy for lesion detection and segmentation. Further, changes in MTV as evaluated and outlined by the automated segmentation tool were a significant determinant of disease-free and overall survival, in agreement with manual assessment by an expert.

IMPLICATIONS FOR PATIENT CARE: The tumor detection and segmentation tool allows for a fully automated, easy-to-use, objective brain tumor diagnosis and response assessment based on amino acid PET and has the potential to be an important building block to further promote amino acid PET and to strengthen its clinical value.

REFERENCES

1. Chang K, Beers AL, Bai HX, et al. Automatic assessment of glioma burden: a deep learning algorithm for fully automated volumetric and bidimensional measurement. *Neuro Oncol.* 2019;21:1412–1422.
2. Di Ieva A, Russo C, Liu S, et al. Application of deep learning for automatic segmentation of brain tumors on magnetic resonance imaging: a heuristic approach in the clinical scenario. *Neuroradiology.* 2021;63:1253–1262.
3. Tampu IE, Haj-Hosseini N, Eklund A. Does anatomical contextual information improve 3D U-net-based brain tumor segmentation? *Diagnostics (Basel).* 2021;11:1159.
4. Kickingereder P, Isensee F, Tursunova I, et al. Automated quantitative tumour response assessment of MRI in neuro-oncology with artificial neural networks: a multicentre, retrospective study. *Lancet Oncol.* 2019;20:728–740.
5. Langen KJ, Galldiks N, Hattingen E, Shah NJ. Advances in neuro-oncology imaging. *Nat Rev Neurol.* 2017;13:279–289.
6. Galldiks N, Law I, Pope WB, Arbizu J, Langen KJ. The use of amino acid PET and conventional MRI for monitoring of brain tumor therapy. *Neuroimage Clin.* 2016;13:386–394.
7. Lohmann P, Stavrinou P, Lipke K, et al. FET PET reveals considerable spatial differences in tumour burden compared to conventional MRI in newly diagnosed glioblastoma. *Eur J Nucl Med Mol Imaging.* 2019;46:591–602.
8. Albert NL, Weller M, Suchorska B, et al. Response Assessment in Neuro-Oncology Working Group and European Association for Neuro-Oncology recommendations for the clinical use of PET imaging in gliomas. *Neuro Oncol.* 2016;18:1199–1208.
9. Galldiks N, Niyazi M, Grosu AL, et al. Contribution of PET imaging to radiotherapy planning and monitoring in glioma patients: a report of the PET/RANO group. *Neuro Oncol.* 2021;23:881–893.
10. Suchorska B, Jansen NL, Linn J, et al. Biological tumor volume in ^{18}FET-PET before radiochemotherapy correlates with survival in GBM. *Neurology.* 2015;84:710–719.
11. Ceccon G, Lohmann P, Werner JM, et al. Early treatment response assessment using 18F-FET PET compared with contrast-enhanced MRI in glioma patients after adjuvant temozolomide chemotherapy. *J Nucl Med.* 2021;62:918–925.
12. Wollring MM, Werner JM, Bauer EK, et al. Prediction of response to lomustine-based chemotherapy in glioma patients at recurrence using MRI and FET PET. *Neuro Oncol.* 2023;25:984–994.
13. Law I, Albert NL, Arbizu J, et al. Joint EANM/EANO/RANO practice guidelines/SNMMI procedure standards for imaging of gliomas using PET with radiolabelled amino acids and [^{18}F]FDG: version 1.0. *Eur J Nucl Med Mol Imaging.* 2019;46:540–557.

14. Isensee F, Jaeger PF, Kohl SAA, Petersen J, Maier-Hein KH. nnU-Net: a self-configuring method for deep learning-based biomedical image segmentation. *Nat Methods.* 2021;18:203–211.
15. Pauleit D, Floeth F, Hamacher K, et al. O-(2-[^{18}F]fluoroethyl)-L-tyrosine PET combined with MRI improves the diagnostic assessment of cerebral gliomas. *Brain*. 2005;128:678–687.
16. Langen KJ, Bartenstein P, Boecker H, et al. German guidelines for brain tumour imaging by PET and SPECT using labelled amino acids [in German]. *Nuklearmedizin*. 2011;50:167–173.
17. Herzog H, Langen KJ, Weirich C, et al. High resolution BrainPET combined with simultaneous MRI [in German]. *Nuklearmedizin*. 2011;50:74–82.
18. Caldeira L, Kops ER, Yun SD, et al. The Julich experience with simultaneous 3T MR-BrainPET: methods and technology. *IEEE Trans Radiat Plasma Med Sci*. 2019;3:352–362.
19. Rota Kops E, Hautzel H, Herzog H, Antoch G, Shah NJ. Comparison of template-based versus CT-based attenuation correction for hybrid MR/PET scanners. *IEEE Trans Nucl Sci*. 2015;62:2115–2121.
20. Lohmann P, Herzog H, Rota Kops E, et al. Dual-time-point O-(2-[^{18}F]fluoroethyl)-L-tyrosine PET for grading of cerebral gliomas. *Eur Radiol*. 2015;25:3017–3024.
21. Isensee F, Schell M, Pflueger I, et al. Automated brain extraction of multisequence MRI using artificial neural networks. *Hum Brain Mapp*. 2019;40:4952–4964.
22. Nikolov S, Blackwell S, Zverovitch A, et al. Deep learning to achieve clinically applicable segmentation of head and neck anatomy for radiotherapy. arXiv website. https://arxiv.org/abs/1809.04430. Published September 12, 2017. Revised January 13, 2021. Accessed January 17, 2023.
23. Blanc-Durand P, Van Der Gucht A, Schaefer N, Itti E, Prior JO. Automatic lesion detection and segmentation of ^{18}F-FET PET in gliomas: a full 3D U-Net convolutional neural network study. *PLoS One.* 2018;13:e0195798.
24. Galldiks N, Unterrainer M, Judov N, et al. Photopenic defects on O-(2-[^{18}F]-fluoroethyl)-L-tyrosine PET: clinical relevance in glioma patients. *Neuro Oncol.* 2019;21:1331–1338.
25. Ladefoged CN, Henriksen OM, Mathiasen R, et al. Automatic detection and delineation of pediatric gliomas on combined [^{18}F]FET PET and MRI. *Front Nucl Med.* 2022;2:960820.

Stacking Ensemble Learning–Based [^{18}F]FDG PET Radiomics for Outcome Prediction in Diffuse Large B-Cell Lymphoma

Shuilin Zhao*[1–4], Jing Wang*[1–3], Chentao Jin*[1–3], Xiang Zhang[1–3], Chenxi Xue[1–3], Rui Zhou[1–3], Yan Zhong[1–3], Yuwei Liu[1–3], Xuexin He[5], Youyou Zhou[1–3], Caiyun Xu[6], Lixia Zhang[6], Wenbin Qian[7], Hong Zhang[1–3,8,9], Xiaohui Zhang[1–3], and Mei Tian[1–3,10]

[1]Department of Nuclear Medicine and PET Center, Second Affiliated Hospital of Zhejiang University School of Medicine, Hangzhou, China; [2]Institute of Nuclear Medicine and Molecular Imaging of Zhejiang University, Hangzhou, China; [3]Key Laboratory of Medical Molecular Imaging of Zhejiang Province, Hangzhou, China; [4]Cancer Center, Department of Radiology, Zhejiang Provincial People's Hospital, Affiliated People's Hospital, Hangzhou Medical College, Hangzhou, China; [5]Department of Medical Oncology, Huashan Hospital of Fudan University, Shanghai, China; [6]Department of Nuclear Medicine, First Affiliated Hospital of Zhejiang Chinese Medical University (Zhejiang Provincial Hospital of Traditional Chinese Medicine), Hangzhou, China; [7]Department of Hematology, Second Affiliated Hospital of Zhejiang University School of Medicine, Hangzhou, China; [8]College of Biomedical Engineering and Instrument Science, Zhejiang University, Hangzhou, China; [9]Key Laboratory for Biomedical Engineering of Ministry of Education, Zhejiang University, Hangzhou, China; and [10]Human Phenome Institute, Fudan University, Shanghai, China

This study aimed to develop an analytic approach based on [^{18}F]FDG PET radiomics using stacking ensemble learning to improve the outcome prediction in diffuse large B-cell lymphoma (DLBCL). **Methods:** In total, 240 DLBCL patients from 2 medical centers were divided into the training set (n = 141), internal testing set (n = 61), and external testing set (n = 38). Radiomics features were extracted from pretreatment [^{18}F]FDG PET scans at the patient level using 4 semiautomatic segmentation methods (SUV threshold of 2.5, SUV threshold of 4.0 [SUV4.0], 41% of SUV_{max}, and SUV threshold of mean liver uptake [PERCIST]). All extracted features were harmonized with the ComBat method. The intraclass correlation coefficient was used to evaluate the reliability of radiomics features extracted by different segmentation methods. Features from the most reliable segmentation method were selected by Pearson correlation coefficient analysis and the LASSO (least absolute shrinkage and selection operator) algorithm. A stacking ensemble learning approach was applied to build radiomics-only and combined clinical–radiomics models for prediction of 2-y progression-free survival and overall survival based on 4 machine learning classifiers (support vector machine, random forests, gradient boosting decision tree, and adaptive boosting). Confusion matrix, receiver-operating-characteristic curve analysis, and survival analysis were used to evaluate the model performance. **Results:** Among 4 semiautomatic segmentation methods, SUV4.0 segmentation yielded the highest interobserver reliability, with 830 (66.7%) selected radiomics features. The combined model constructed by the stacking method achieved the best discrimination performance. For progression-free survival prediction in the external testing set, the areas under the receiver-operating-characteristic curve and accuracy of the stacking-based combined model were 0.771 and 0.789, respectively. For overall survival prediction, the stacking-based combined model achieved an area under the curve of 0.725 and an accuracy of 0.763 in the external testing set. The combined model also demonstrated a more distinct risk stratification than the International Prognostic Index in all sets (log-rank test, all $P < 0.05$). **Conclusion:** The combined model that incorporates [^{18}F]FDG PET radiomics and clinical characteristics based on stacking ensemble learning could enable improved risk stratification in DLBCL.

Key Words: PET; diffuse large B-cell lymphoma; prognosis; machine learning; radiomics

J Nucl Med 2023; 64:1603–1609
DOI: 10.2967/jnumed.122.265244

Diffuse large B-cell lymphoma (DLBCL) is the most common subtype of aggressive non-Hodgkin lymphoma. Rituximab plus cyclophosphamide, doxorubicin, vincristine, and prednisone represents the current first-line treatment, which is effective in approximately 60%–70% of patients (*1*). Patients with refractory disease or relapse after initial treatment have a low probability of cure and dismal outcomes due to the modest response rates for salvage regimens (*2*). Therefore, early identification of those high-risk patients is essential for designing individualized therapeutic intervention. Current prognostic scoring systems, such as the International Prognostic Index (IPI) and the National Comprehensive Cancer Network–IPI, have been the basis for determining prognosis in DLBCL (*3,4*). However, those models are inaccurate in predicting refractory disease, possibly because of their lack of intratumoral metabolic and functional information.

[^{18}F]FDG PET/CT, a type of molecular imaging and a means to "transpathology" (*5*), has been recommended for staging and response assessment in DLBCL (*6,7*). Quantitative parameters on PET/CT, particularly total metabolic tumor volume (TMTV) and total lesion glycolysis, are considered to have prognostic significance in DLBCL (*8,9*). These parameters may allow for the assessment of whole-body tumor burden but remain limited in their ability to characterize phenotypical profiles such as shape, morphology, spatial distribution, and heterogeneity across individual lesions. For PET/CT image analysis, radiomics has recently been proposed as a novel high-throughput, noninvasive approach that could quantify tumor phenotype at a microscale level via extracting thousands of imaging-derived features (*10*). With the

Received Nov. 23, 2022; revision accepted May 31, 2023.
For correspondence or reprints, contact Mei Tian (tianmei@fudan.edu.cn) or Xiaohui Zhang (zhanghui4127@zju.edu.cn).
*Contributed equally to this work.
Published online Jul. 27, 2023.

assistance of artificial intelligence, such as machine learning, radiomics offers a promising tool for diagnosis, therapeutic response assessment, and outcome prediction in various tumor types (*11*), including DLBCL (*12–16*). Preliminary studies have suggested that the application of machine learning algorithms, such as LASSO (least absolute shrinkage and selection operator) regression (*16*), ridge regression (*13*), and random forest (*17*), may contribute to the improved radiomics feature selection and prognostic modeling in DLBCL. However, most of those studies focused on evaluating a single machine learning approach, whereas only a minority used cross combination of different machine learning algorithms (*14*) or adopted ensemble machine learning (*15*). Stacking, an ensemble approach that combines different base classifiers into 1 metaclassifier, has been suggested to provide optimized performance and simplicity (*18*). In the present study, we aimed to develop an analytic approach based on [^{18}F]FDG PET radiomics using stacking ensemble learning to improve the outcome prediction in DLBCL.

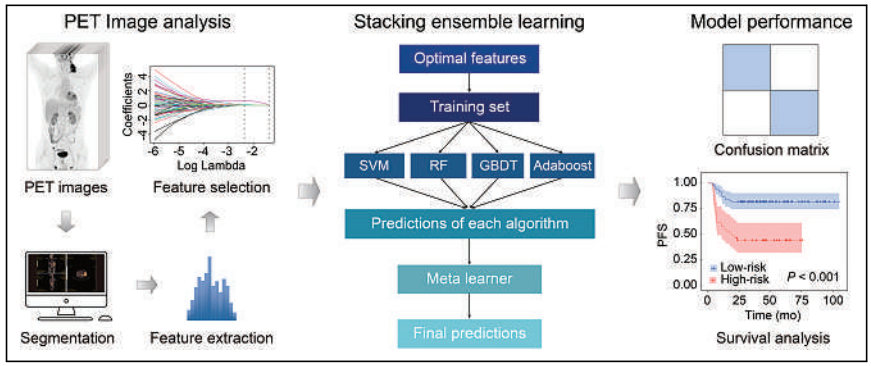

FIGURE 1. Radiomics workflow.

MATERIALS AND METHODS

Study Population

We retrospectively enrolled 240 consecutive patients with newly diagnosed DLBCL at 2 medical centers, including 202 patients at center 1 (the Second Affiliated Hospital of Zhejiang University School of Medicine) and 38 patients at center 2 (the First Affiliated Hospital of Zhejiang Chinese Medical University). Detailed information about the study population is shown in the supplemental materials (available at http://jnm.snmjournals.org) (*19,20*). The flowchart of patient enrollment is shown in Supplemental Figure 1. This study was approved by the Institutional Review Board at each institution, and the requirement to obtain written informed consent was waived.

PET/CT Imaging Protocol

Image acquisition and reconstruction were in accordance with the guidelines of European Association of Nuclear Medicine, version 2.0 (*21*). Patients fasted for at least 6 h and had a blood glucose level below 200 mg/dL before PET/CT examination. They were scanned at about 60 min after intravenous injection of [^{18}F]FDG (3.70 MBq/kg). All PET images were corrected for attenuation using acquired low-dose CT data. Acquisitions differed between the 2 institutions in terms of PET/CT scanners, acquisition protocols, and reconstruction settings (Supplemental Table 1).

PET Image Segmentation and Feature Extraction

PET/CT images were reviewed by 2 independent nuclear medicine physicians, who were masked to patients' clinical outcome. The volumes of interest were semiautomatically delineated using LIFEx software (version 6.30, https://www.lifexsoft.org/index.php) (*22*). Four different segmentation methods were applied to delineate lesions, including an SUV threshold of 2.5, an SUV threshold of 4.0 (SUV4.0), 41% of SUV_{max}, and $SUV_{PERCIST}$ (1.5 × liver SUV_{mean} + 2 SDs) (*21,23*). SUV was calculated as (tissue radioactivity concentration [Bq/mL]) × (body weight [g])/(injected radioactivity [Bq]). According to the European Association of Nuclear Medicine guidelines, the liver SUV_{mean} should be between 1.3 and 3.0 (*21*). Conventional PET parameters including SUV_{max}, SUV_{peak}, TMTV, and total lesion glycolysis of each patient were recorded. The distance between the largest lesion and the lesion farthest from that bulk was also recorded (*16*).

Before feature extraction, all PET images were resampled to a voxel size of 3 × 3 × 3 mm using bilinear interpolation (*24*) and were discretized with a fixed bin size of 0.25 SUV (*25*). In total, 1,245 radiomics features were extracted from the entire segmented disease (patient level) via the open-source toolbox PyRadiomics (version 3.0.1) (*16,26*), consistent with the Image Biomarker Standardization Initiative (*27*). Detailed descriptions of the extracted features are presented in Supplemental Table 2. The radiomics workflow is shown in Figure 1.

Feature Selection

The interobserver repeatability of radiomics features was evaluated using the intraclass correlation coefficient (ICC) in 100 randomly selected patients from center 1. Features with an ICC above 0.80 were considered robust and retained for subsequent analysis. The segmentation method with the maximum number of selected features was considered to be the most reliable method.

The ComBat harmonization method was applied to pool all conventional PET parameters and radiomics features derived from images acquired on the 2 different PET/CT scanners (*28*). Pearson correlation coefficient analysis followed by the LASSO algorithm were applied to select features. Details on feature selection are presented in the supplemental materials.

Stacking Ensemble Learning–Based Model Construction

Stacking ensemble learning is a complex machine learning algorithm that combines the result of several base learners to generate predictions into the metalearner to improve predictive accuracy (*18*). In this study, random forest, support vector machine, gradient boosting decision tree, and adaptive boosting were set as the base learners (first level), whereas random forest served as the metalearner (second level). The methodologic details are presented in the supplemental materials. Logistic regression was also applied to generate predictions. Confusion matrix analytics (including accuracy, F1 score, recall, and precision) were used to compare the performance of different machine learning algorithms. The detailed parameters of these algorithms are presented in Supplemental Table 3.

We evaluated the predictive value of 5 different models, including the radiomics model, the combined clinical–radiomics model, IPI, the model based on TMTV, the distance between the largest lesion and the lesion farthest from that bulk, and SUV_{peak} (*17*), as well as the International Metabolic Prognostic Index (*29*). Receiver-operating-characteristic (ROC) curve analysis was used to compare the predictive performance of different models.

TABLE 1
Patient Characteristics

Characteristic	Training set (n = 141)	Internal testing set (n = 61)	External testing set (n = 38)	P
Sex				0.225
Female	67	30	24	
Male	74	31	14	
Mean age ± SD (y)	57.6 ± 15.1	60.6 ± 13.4	64.3 ± 13.6	0.093
Age (y)				0.269
≤60	70	25	14	
>60	71	36	24	
Ann Arbor stage				0.381
I–II	51	21	18	
III–IV	90	40	20	
B symptoms				0.231
Yes	39	19	16	
No	102	42	22	
Performance status				0.324
<2	102	45	32	
≥2	39	16	6	
Extranodal sites				0.432
<2	88	39	28	
≥2	53	22	10	
LDH				0.217
Normal	61	34	20	
Elevated	80	27	18	
β2-microglobulin				0.745
Normal	95	38	24	
Elevated	46	23	14	
IPI				0.900
≤2	77	35	22	
>2	64	26	16	
Cell of origin				0.182
GCB	59	21	10	
Non-GCB	82	40	28	
Therapy regimens				0.560
R-CHOP	126	54	36	
R-EPOCH	15	7	2	
Endpoints				
2-y PFS (%)	69.5	72.1	71.1	0.855
2-y OS (%)	76.6	80.3	73.7	0.569

LDH = lactate dehydrogenase; GCB = germinal center B-cell–like; R-CHOP = rituximab plus cyclophosphamide, doxorubicin, vincristine, and prednisone; R-EPOCH = rituximab plus etoposide, prednisone, vincristine, cyclophosphamide, and doxorubicin.

Data are n unless otherwise indicated. P values were calculated by 1-way ANOVA for continuous variables, χ^2 test for categoric variables, and log-rank test for survival rates.

Statistical Analysis

All statistical analysis was performed using SPSS (version 26.0), R (version 4.0.5, http://www.R-project.org), and Python (version 3.10). Progression-free survival (PFS) was defined as the time from diagnosis until lymphoma progression or death from any cause. Overall survival (OS) was defined as the time from diagnosis to death from any cause or to the last follow-up. Patients still alive were censored at the date of last contact. The differences in clinical characteristics were

TABLE 2
AUCs of Different Models

Model	Training set		Internal testing set		External testing set	
	PFS	OS	PFS	OS	PFS	OS
Combined	0.791 (0.725–0.857)	0.843 (0.786–0.899)	0.762 (0.618–0.906)	0.741 (0.572–0.911)	0.771 (0.594–0.948)	0.725 (0.534–0.916)
Radiomics	0.765 (0.697–0.834)	0.787 (0.724–0.850)	0.715 (0.559–0.870)	0.637 (0.447–0.827)	0.707 (0.515–0.899)	0.661 (0.450–0.871)
IPI	0.715 (0.624–0.807)	0.729 (0.734–0.823)	0.717 (0.569–0.864)	0.670 (0.497–0.843)	0.715 (0.531–0.900)	0.689 (0.495–0.884)
TMTV + $Dmax_{bulk}$ + SUV_{peak}	0.696 (0.604–0.789)	0.720 (0.623–0.817)	0.623 (0.457–0.788)	0.722 (0.551–0.893)	0.652 (0.452–0.851)	0.640 (0.432–0.848)
IMPI	0.765 (0.681–0.849)	0.765 (0.676–0.854)	0.699 (0.546–0.851)	0.659 (0.479–0.839)	0.660 (0.470–0.850)	0.689 (0.495–0.884)

$Dmax_{bulk}$ = distance between largest lesion and lesion farthest from that bulk; IMPI = International Metabolic Prognostic Index.
Data in parentheses are 95% CIs.

assessed using the χ^2 test and 1-way ANOVA, when appropriate. Patients were stratified into high- and low-risk groups using ROC curve analysis and maximizing the Youden index (*30*). Survival curves were estimated by the Kaplan–Meier analysis, and survival distributions were compared using the log-rank test. A *P* value of less than 0.05 was considered statistically significant.

RESULTS

Patient Characteristics and Outcome

Patients' clinical characteristics are summarized in Table 1. No clinical characteristic had statistically significant differences among different datasets (all $P > 0.05$). The median follow-up intervals for the training, internal testing, and external testing sets were 41 mo (range, 4–105 mo), 44 mo (range, 6–104 mo), and 39 mo (range, 4–69 mo), respectively. By the end of follow-up, relapse and progression occurred in 56, 21, and 14 patients in the training, internal testing and external testing sets, respectively, whereas 45, 16, and 10 patients, respectively, had died.

Feature Selection

Among 4 segmentations, SUV4.0 segmentation showed the highest reliability, with 830 features (66.7%) retained in the context of an ICC of more than 0.8 (Supplemental Table 4). After the Pearson correlation coefficient test, 88 radiomics features were selected for SUV4.0 segmentation. The optimal features were obtained by the LASSO algorithm for construction of different stacking models (Supplemental Table 5).

Model Performance Evaluation

The model performance for 2-y PFS prediction based on different machine learning algorithms is shown in Supplemental Table 6. For the radiomics model, the stacking classifier showed better performance than the other 4 base classifiers and logistic regression,

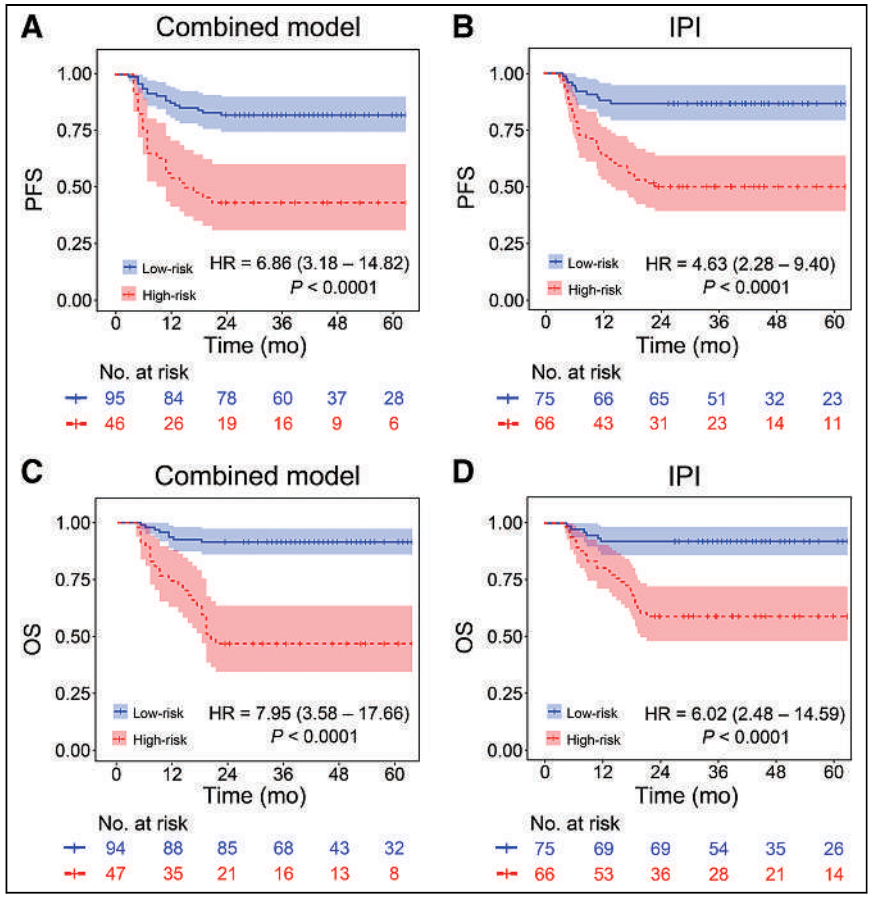

FIGURE 2. Kaplan–Meier curves for PFS of combined model (A), PFS of IPI (B), OS of combined model (C), and OS of IPI (D) in training set. Hazard ratio with 95% CI and log-rank *P* value are reported. HR = hazard ratio.

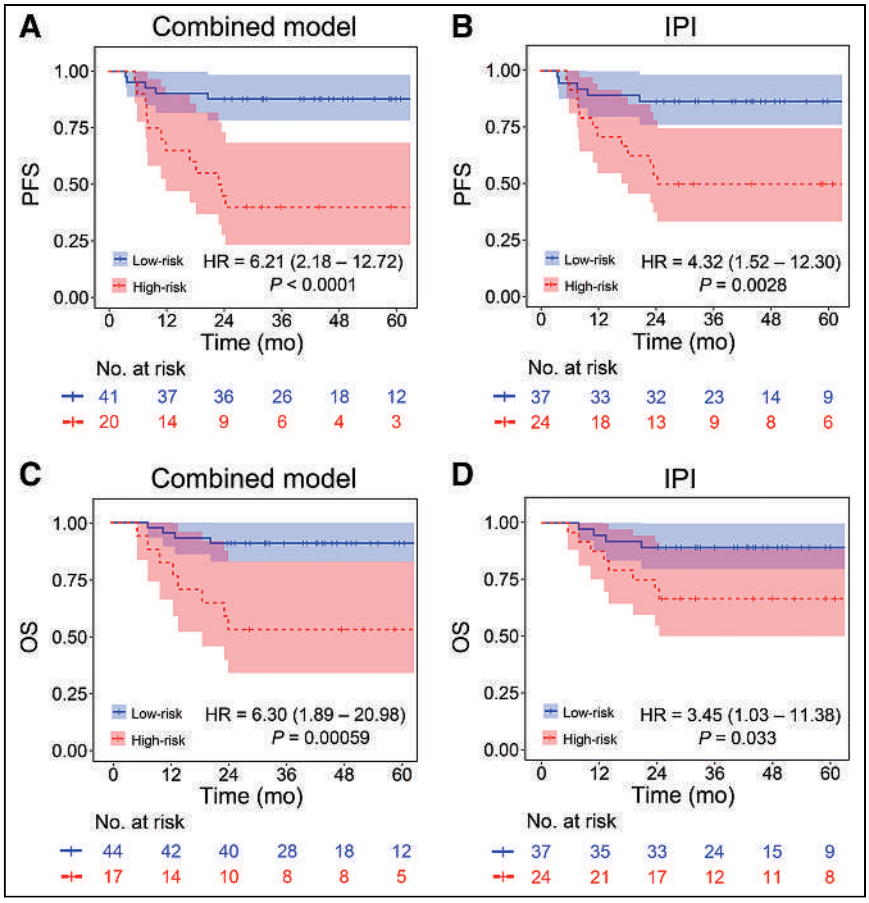

FIGURE 3. Kaplan–Meier curves for PFS of combined model (A), PFS of IPI (B), OS of combined model (C), and OS of IPI (D) in internal testing set. Hazard ratio with 95% CI and log-rank *P* value are reported. HR = hazard ratio.

except for recall in the training set. For the combined model, the stacking classifier also demonstrated better performance than the other classifiers in the training set, internal testing set, and external testing set. Furthermore, the stacking-based combined model had higher predictive power than the radiomics model and IPI across nearly all evaluation metrics.

The model performance for 2-y OS prediction is shown in Supplemental Table 7. For the radiomics model, the stacking classifier demonstrated superior performance to the other base classifiers and logistic regression, except for precision in the internal testing set and accuracy and recall in the external testing set. For the combined model, the stacking classifier had relatively balanced performance in the training set but outperformed the other base classifiers in the internal testing set and the external testing set. Moreover, the stacking-based combined model performed better than the radiomics model and IPI.

We compared the performance of the stacking-based combined models by various combinations of base classifiers. As shown in Supplemental Tables 8 and 9, the combination of 4 base classifiers had a more balanced performance for PFS and OS prediction than did the other combinations. We also evaluated the performance of the radiomics and combined models trained on PFS prediction for predicting OS and vice versa; the results are shown in Supplemental Tables 10 and 11.

The results of ROC analysis are shown in Table 2. The combined model outperformed the other models for PFS prediction, with the area under the ROC curve (AUC) being 0.791, 0.762, and 0.771 in the training set, internal testing set, and external testing set, respectively. A similar trend was observed for OS prediction (the AUCs of the combined model were 0.843, 0.741, and 0.725 for the training set, internal testing set, and external testing set, respectively).

Survival Prediction

Kaplan–Meier survival estimates of the combined model and IPI in the training set, internal testing set, and external testing set are shown in Figures 2, 3, and 4, respectively. The Kaplan–Meier survival estimates of the radiomics model are shown in Supplemental Figure 2. The differences in survival rates between low- and high-risk groups were significant except for OS in the radiomics model in the external testing set ($P = 0.053$). Moreover, the combined model demonstrated a more distinct risk stratification than the radiomics model and IPI, with larger differences between subgroups for both PFS and OS prediction (all $P < 0.05$).

DISCUSSION

In this study, we developed an analytic approach based on [^{18}F]FDG PET radiomics using stacking ensemble learning for outcome prediction in DLBCL. Radiomics and combined clinical–radiomics models constructed by the stacking method outperformed those built on other single machine learning classifiers. Furthermore, the combined models integrating radiomics features and clinical information exhibited predictive performance superior to that of radiomics-only models and IPI.

To the best of our knowledge, this was the first study to evaluate the prognostic effect of [^{18}F]FDG PET radiomics through a stacking ensemble learning approach in patients with DLBCL. Several previous studies have found that machine learning–based PET radiomics could be of prognostic importance in DLBCL (*12–14*). A multicenter study with 317 DLBCL patients suggested that the radiomics model based on LASSO logistic regression was predictive of 2-y time to progression, with an AUC of 0.76 (*16*). Another study using a LASSO-Cox algorithm reported an AUC of 0.748 for the radiomics model in the test set for PFS prediction (*12*). In a recent study, Jiang et al. used cross combination of 7 different machine learning algorithms for feature selection and found that the radiomics signature obtained by the support vector machine–support vector machine was highly predictive of PFS (AUC, 0.757) (*14*). Despite these encouraging findings, a recently developed ensemble learning approach has revealed diagnostic and prognostic advantages over a single machine learning method by aggregating multiple algorithms to achieve higher prediction accuracy (*31,32*). In our current study, the radiomics model built on a stacking ensemble learning approach outperformed those developed by the other 4 base classifiers and logistic regression, with AUCs of 0.715 and 0.707 for PFS prediction in the internal and external testing sets, respectively. This finding is consistent with

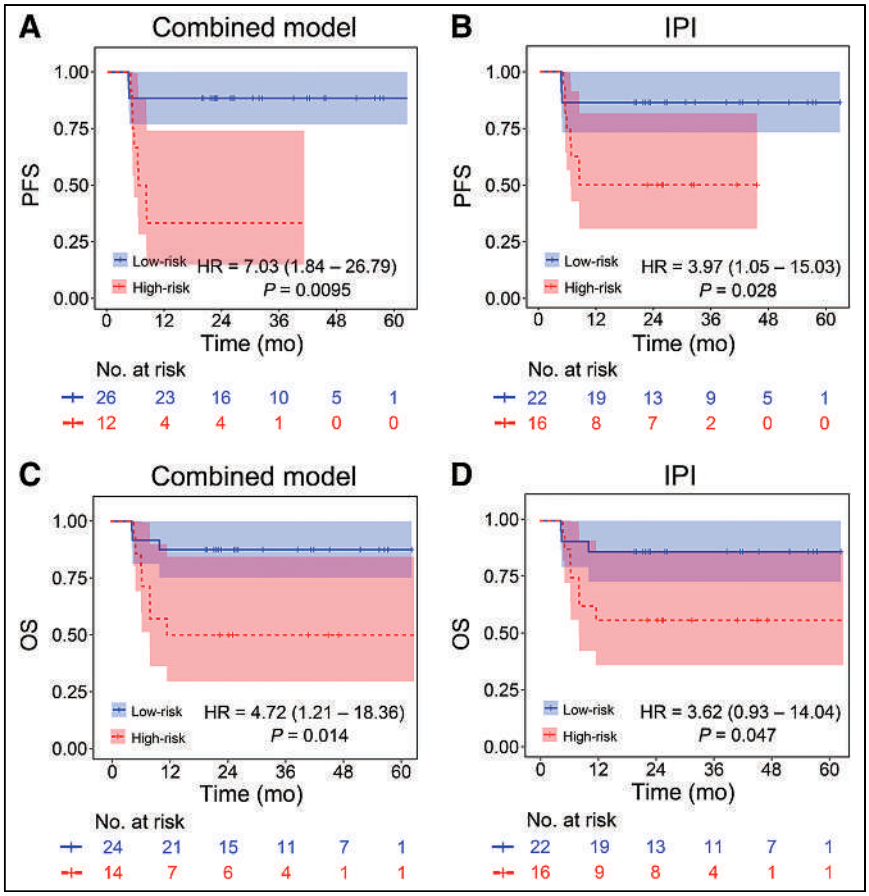

FIGURE 4. Kaplan–Meier curves for PFS of combined model (A), PFS of IPI (B), OS of combined model (C), and OS of IPI (D) in external testing set. Hazard ratio with 95% CI and log-rank *P* value are reported. HR = hazard ratio.

the results from a recent radiomics study on DLBCL, in which a soft voting ensemble–based model showed higher accuracy than those based on single machine learning classifiers for 2-y event-free survival prediction (*15*). Notably, voting considers only linear relationships among classifiers whereas stacking is able to learn complex associations when individual base classifiers are heterogeneous (*33*). In our study, the combined model developed by 4 classifiers showed a more balanced performance than the other combinations, supporting the potential of stacking ensemble learning for radiomics analysis in DLBCL.

Our study also demonstrated that the combined models incorporating patient-level PET radiomics and clinical characteristics yielded higher AUCs and more distinct risk stratifications than IPI for outcome prediction in DLBCL, which is in line with previous observations (*12,14,16*). Recent studies suggested that the predictive ability of IPI has been weakened in the rituximab era (*4*). In this context, PET radiomics might add a new perspective on the phenotypic characteristics of DLBCL through profiling the intratumoral metabolic heterogeneity. Therefore, it is likely that considering both clinical and imaging features in analysis may offer a deeper understanding of the complex biologic properties of malignancy and thereby provide a better prognosis estimation.

Radiomics analysis in lymphoma remains challenging because of the lack of a primary site and the complexity of lesion delineation, particularly for disseminated disease. To date, no consensus has been reached on which segmentation method for lesion delineation in DLBCL is preferable. Although the 41%-of-SUV_{max} method has been recommended by the European Association of Nuclear Medicine for TMTV evaluation (*21*), this method is more likely to be influenced by interobserver variability (*34*). Other studies indicated that the SUV4.0 method could give a good approximation of TMTV for prediction of disease progression (*35*). On top of these, the impact of different segmentations on radiomics features for prognosis prediction in DLBCL remains to be explored. In our study, we compared the reliability of radiomics features based on 4 different segmentation methods. The SUV4.0 method yielded the highest interobserver reliability, with 830 features (66.7%) retained in ICC analysis, which is in line with the results from a recent study suggesting that SUV4.0 is the most stable approach (with excellent reliability for 84.8% of all features) among 6 semiautomatic segmentation methods (*36*). By contrast, the interobserver reliability of radiomics features based on 41%-of-SUV_{max} segmentation was the lowest in the current study, with only 46 features (3.7%) having excellent reliability. This discrepancy may correlate with differences in TMTV delineation. Previous studies demonstrated that variations in segmentation methods could have a marked effect on the outer contour of the segmentation, thereby influencing radiomics features, especially morphologic metrics (*36,37*). In our study, the SUV4.0 method exhibited a higher TMTV estimation and more stable radiomics features than the 41%-of-SUV_{max} method, indicating that a higher TMTV may cause the segmentation method to have less of an impact on radiomics features.

Several limitations of our study deserve mention. First, since this was a retrospective study with a relatively small sample size, our results need to be further validated in prospective multicenter studies involving a larger cohort of patients. Second, we applied only patient-level radiomics analysis; further studies are required to compare the impact of different lesion selection methods on radiomics analysis. Third, we applied ICC, Pearson correlation analysis, and LASSO for feature selection; further studies will be required to assess the performance of other strategies, for example, minimum redundancy maximum relevance and ReliefF. Fourth, to facilitate comparison with previous results, we used only PET images for radiomics analysis. A combination of PET and CT images may lead to the discovery of radiomics features that are more predictive. Fifth, Ki-67 expression and MYC/BCL-2 double-hit status are established prognostic factors but were not assessed in this study because of the incompleteness of the available data.

CONCLUSION

In the present study, we proposed an analytic approach using stacking ensemble learning for outcome prediction in DLBCL

based on [^{18}F]FDG PET radiomics. The stacking-based combined model that incorporates radiomics features and clinical characteristics could enable improved risk stratification in DLBCL patients.

DISCLOSURE

This study was partially supported by the National Natural Science Foundation of China (32027802), the National Key R&D Program of China (2021YFE0108300 and 2022YFE0118000), and the Key R&D Program of Zhejiang (2022C03071). No other potential conflict of interest relevant to this article was reported.

KEY POINTS

QUESTION: Can stacking ensemble learning–based [^{18}F]FDG PET radiomics improve outcome prediction in patients with DLBCL?

PATIENT FINDINGS: In a retrospective study of 240 DLBCL patients, a stacking ensemble learning–based model that incorporates radiomics features and clinical characteristics enabled improved risk stratification.

IMPLICATIONS FOR PATIENT CARE: The stacking ensemble learning–based model incorporating PET radiomics and clinical information can be useful for better survival prediction and therapeutic decision making.

REFERENCES

1. Tilly H, Gomes da Silva M, Vitolo U, et al. Diffuse large B-cell lymphoma (DLBCL): ESMO Clinical Practice Guidelines for diagnosis, treatment and follow-up. *Ann Oncol.* 2015;26(suppl 5):v116–v125.
2. Crump M, Neelapu SS, Farooq U, et al. Outcomes in refractory diffuse large B-cell lymphoma: results from the international SCHOLAR-1 study. *Blood.* 2017;130:1800–1808.
3. International Non-Hodgkin's Lymphoma Prognostic Factors Project. A predictive model for aggressive non-Hodgkin's lymphoma. *N Engl J Med.* 1993;329:987–994.
4. Zhou Z, Sehn LH, Rademaker AW, et al. An enhanced International Prognostic Index (NCCN-IPI) for patients with diffuse large B-cell lymphoma treated in the rituximab era. *Blood.* 2014;123:837–842.
5. Tian M, He X, Jin C, et al. Transpathology: molecular imaging-based pathology. *Eur J Nucl Med Mol Imaging.* 2021;48:2338–2350.
6. Barrington SF, Kluge R. FDG PET for therapy monitoring in Hodgkin and non-Hodgkin lymphomas. *Eur J Nucl Med Mol Imaging.* 2017;44(suppl 1):97–110.
7. Zhang X, Jiang H, Wu S, et al. Positron emission tomography molecular imaging for phenotyping and management of lymphoma. *Phenomics.* 2022;2:102–118.
8. Cottereau AS, Lanic H, Mareschal S, et al. Molecular profile and FDG-PET/CT total metabolic tumor volume improve risk classification at diagnosis for patients with diffuse large B-cell lymphoma. *Clin Cancer Res.* 2016;22:3801–3809.
9. Toledano MN, Desbordes P, Banjar A, et al. Combination of baseline FDG PET/CT total metabolic tumour volume and gene expression profile have a robust predictive value in patients with diffuse large B-cell lymphoma. *Eur J Nucl Med Mol Imaging.* 2018;45:680–688.
10. Lambin P, Leijenaar RTH, Deist TM, et al. Radiomics: the bridge between medical imaging and personalized medicine. *Nat Rev Clin Oncol.* 2017;14:749–762.
11. Bi WL, Hosny A, Schabath MB, et al. Artificial intelligence in cancer imaging: clinical challenges and applications. *CA Cancer J Clin.* 2019;69:127–157.
12. Zhang X, Chen L, Jiang H, et al. A novel analytic approach for outcome prediction in diffuse large B-cell lymphoma by [^{18}F]FDG PET/CT. *Eur J Nucl Med Mol Imaging.* 2022;49:1298–1310.
13. Frood R, Clark M, Burton C, et al. Discovery of pre-treatment FDG PET/CT-derived radiomics-based models for predicting outcome in diffuse large B-cell lymphoma. *Cancers (Basel).* 2022;14:1711.
14. Jiang C, Li A, Teng Y, et al. Optimal PET-based radiomic signature construction based on the cross-combination method for predicting the survival of patients with diffuse large B-cell lymphoma. *Eur J Nucl Med Mol Imaging.* 2022;49:2902–2916.
15. Ritter Z, Papp L, Zámbó K, et al. Two-year event-free survival prediction in DLBCL patients based on in vivo radiomics and clinical parameters. *Front Oncol.* 2022;12:820136.
16. Eertink JJ, van de Brug T, Wiegers SE, et al. ^{18}F-FDG PET baseline radiomics features improve the prediction of treatment outcome in diffuse large B-cell lymphoma. *Eur J Nucl Med Mol Imaging.* 2022;49:932–942.
17. Eertink JJ, Zwezerijnen GJC, Cysouw MCF, et al. Comparing lesion and feature selections to predict progression in newly diagnosed DLBCL patients with FDG PET/CT radiomics features. *Eur J Nucl Med Mol Imaging.* 2022;49:4642–4651.
18. Naimi AI, Balzer LB. Stacked generalization: an introduction to super learning. *Eur J Epidemiol.* 2018;33:459–464.
19. Chawla NV, Bowyer KW, Hall LO, Kegelmeyer WP. SMOTE: synthetic minority over-sampling technique. *J Artif Intell Res.* 2002;16:321–357.
20. Bergstra J, Bengio Y. Random search for hyper-parameter optimization. *J Mach Learn Res.* 2012;13:281–305.
21. Boellaard R, Delgado-Bolton R, Oyen WJ, et al. FDG PET/CT: EANM procedure guidelines for tumour imaging—version 2.0. *Eur J Nucl Med Mol Imaging.* 2015;42:328–354.
22. Nioche C, Orlhac F, Boughdad S, et al. LIFEx: a freeware for radiomic feature calculation in multimodality imaging to accelerate advances in the characterization of tumor heterogeneity. *Cancer Res.* 2018;78:4786–4789.
23. Wahl RL, Jacene H, Kasamon Y, Lodge MA. From RECIST to PERCIST: evolving considerations for PET response criteria in solid tumors. *J Nucl Med.* 2009;50(suppl 1):122S–150S.
24. Shiri I, Vafaei Sadr A, Amini M, et al. Decentralized distributed multi-institutional PET image segmentation using a federated deep learning framework. *Clin Nucl Med.* 2022;47:606–617.
25. Pfaehler E, van Sluis J, Merema BBJ, et al. Experimental multicenter and multivendor evaluation of the performance of PET radiomic features using 3-dimensionally printed phantom inserts. *J Nucl Med.* 2020;61:469–476.
26. van Griethuysen JJM, Fedorov A, Parmar C, et al. Computational radiomics system to decode the radiographic phenotype. *Cancer Res.* 2017;77:e104–e107.
27. Zwanenburg A, Vallières M, Abdalah MA, et al. The Image Biomarker Standardization Initiative: standardized quantitative radiomics for high-throughput image-based phenotyping. *Radiology.* 2020;295:328–338.
28. Orlhac F, Boughdad S, Philippe C, et al. A postreconstruction harmonization method for multicenter radiomic studies in PET. *J Nucl Med.* 2018;59:1321–1328.
29. Mikhaeel NG, Heymans MW, Eertink JJ, et al. Proposed new dynamic prognostic index for diffuse large B-cell lymphoma: International Metabolic Prognostic Index. *J Clin Oncol.* 2022;40:2352–2360.
30. Ruopp MD, Perkins NJ, Whitcomb BW, Schisterman EF. Youden index and optimal cut-point estimated from observations affected by a lower limit of detection. *Biom J.* 2008;50:419–430.
31. Chassagnon G, Vakalopoulou M, Battistella E, et al. AI-driven quantification, staging and outcome prediction of COVID-19 pneumonia. *Med Image Anal.* 2021;67:101860.
32. Papp L, Spielvogel CP, Grubmuller B, et al. Supervised machine learning enables non-invasive lesion characterization in primary prostate cancer with [^{68}Ga]Ga-PSMA-11 PET/MRI. *Eur J Nucl Med Mol Imaging.* 2021;48:1795–1805.
33. Heisler M, Karst S, Lo J, et al. Ensemble deep learning for diabetic retinopathy detection using optical coherence tomography angiography. *Transl Vis Sci Technol.* 2020;9:20.
34. Ilyas H, Mikhaeel NG, Dunn JT, et al. Defining the optimal method for measuring baseline metabolic tumour volume in diffuse large B cell lymphoma. *Eur J Nucl Med Mol Imaging.* 2018;45:1142–1154.
35. Barrington SF, Zwezerijnen B, de Vet HCW, et al. Automated segmentation of baseline metabolic total tumor burden in diffuse large B-cell lymphoma: which method is most successful? A study on behalf of the PETRA consortium. *J Nucl Med.* 2021;62:332–337.
36. Eertink JJ, Pfaehler EAG, Wiegers SE, et al. Quantitative radiomics features in diffuse large B-cell lymphoma: does segmentation method matter? *J Nucl Med.* 2022;63:389–395.
37. Belli ML, Mori M, Broggi S, et al. Quantifying the robustness of [^{18}F]FDG-PET/CT radiomic features with respect to tumor delineation in head and neck and pancreatic cancer patients. *Phys Med.* 2018;49:105–111.

Impact of Single-Time-Point Estimates of ^{177}Lu-PRRT Absorbed Doses on Patient Management: Validation of a Trained Multiple-Linear-Regression Model in 159 Patients and 477 Therapy Cycles

Alexandre Chicheportiche[1], Moshe Sason[1], Mahmoud Zidan[1], Jeremy Godefroy[1], Yodphat Krausz[1], David J. Gross[2], Simona Grozinsky-Glasberg[2], and Simona Ben-Haim[1,3]

[1]*Department of Nuclear Medicine and Biophysics, Hadassah Medical Organization and Faculty of Medicine, Hebrew University of Jerusalem, Jerusalem, Israel;* [2]*Neuroendocrine Tumor Unit, ENETS Center of Excellence, Hebrew University of Jerusalem, Jerusalem, Israel; and* [3]*University College London, London, United Kingdom*

Dosimetry after ^{177}Lu-DOTATATE peptide receptor radionuclide therapy (PRRT) enables estimation of radiation doses absorbed by normal organs and target lesions. This process is time-consuming and requires multiple posttreatment studies on several subsequent days. In a previous study, we described a newly developed multiple-linear-regression model to predict absorbed doses (ADs) from a single-time-point (STP) posttreatment study acquired 168 h after the first infusion and 24 h after the following ones, with similar results to the standard multiple-time-point (MTP) protocol. The present study aimed to validate this model in a large patient cohort and to assess whether STP dosimetry affects patient management decisions compared with our MTP protocol. **Methods:** Quantitative ^{177}Lu-DOTATATE SPECT/CT post-PRRT data from 159 consecutive patients (172 therapies, 477 therapy cycles) were retrospectively analyzed. ADs obtained from an STP model were compared with those obtained using an MTP model. We evaluated the impact of the STP model on the decision on whether PRRT should be stopped because of an expected kidney AD exceeding the safety threshold. We hypothesized that patient management based on the STP model does not differ from that based on the MTP model in at least 90% of the cases. **Results:** There was no difference in management decisions between the MTP and STP models in 170 of 172 therapies (98.8%). A Fisher χ^2 test for combined probabilities produced a composite *P* value of 0.0003. Mean cumulative AD relative differences between the STP and MTP models were 0.8% ± 8.0%, −7.7% ± 4.8%, 0.0% ± 11.4%, −2.8% ± 6.3%, and −2.1% ± 18.4% for kidneys, bone marrow, liver, spleen, and tumors, respectively (Pearson $r = 0.99$ for all), for patients who underwent 4 therapy cycles. Similar results were obtained with fewer therapy cycles. **Conclusion:** Estimated radiation ADs and patient management decisions were similar with the STP and MTP models. The STP model can simplify the dosimetry process while also reducing scanner and staff time and improving patient comfort.

Key Words: peptide receptor radionuclide therapy; PRRT; ^{177}Lu-DOTATATE; SPECT/CT; single time point; internal dosimetry

J Nucl Med 2023; 64:1610–1616
DOI: 10.2967/jnumed.122.264923

Peptide receptor radionuclide therapy (PRRT) with the radionuclide ^{177}Lu-DOTATATE is effective in the management of neuroendocrine neoplasms (*1–3*). Currently, PRRT is administered following an empiric protocol of 4 fixed doses of 7.4 GBq (200 mCi) of ^{177}Lu-DOTATATE, as approved by the Food and Drug Administration (*4*). However, because the absorbed dose (AD) to critical organs is highly variable, the therapy dose or number of therapy cycles might be increased, thereby increasing the AD to tumor sites without exceeding the critical healthy-organ safety thresholds (*5,6*). Several studies have assessed personalized PRRT based on the patient-specific AD (*5–8*)—that is, adjusting the number of therapy cycles—with low toxicity and promising efficacy (*6,8*).

Dosimetry calculation after PRRT is essential, but the process requires multiple posttreatment SPECT acquisitions corrected for photon attenuation (using CT attenuation maps) on several subsequent days, followed by complex image processing and calculation of ADs. The European Association of Nuclear Medicine/MIRD guidelines for quantitative ^{177}Lu imaging (*9*) require 3 quantitative SPECT/CT studies at a time 1 (t_1) of 24 h, a time 2 of 96 h, and a time 3 (t_3) of 168 h after the first treatment cycle and a single SPECT/CT examination at t_1 after the following cycles. In a recent study (*10*), we trained a multiple-linear-regression (MLR) model on a set of 40 consecutive patients for prediction of radiation ADs using a single posttreatment SPECT/CT study performed at a t_3 of 168 h after the first therapy cycle and at a t_1 of 24 h after the subsequent cycles, with small mean relative differences from our standard multiple-time-point (MTP) protocol for kidneys, bone marrow, liver, spleen, and tumor sites. The aim of the present study was to confirm the accuracy of single-time-point (STP) dosimetry in a large patient cohort receiving PRRT and to define whether it guides management decisions similarly to the results obtained with MTP measurements.

MATERIALS AND METHODS

Patient Population

Between November 2011 and March 2022, 297 consecutive patients with neuroendocrine neoplasms received 1,041 PRRT treatment cycles with ^{177}Lu-DOTATATE at our institution.

The study inclusion criteria were, first, patients who started and completed their series of treatments during the defined period; second, patients who underwent MTP dosimetry following our standard

Received Oct. 23, 2022; revision accepted May 31, 2023.
For correspondence or reprints, contact Alexandre Chicheportiche (alexandre@hadassah.org.il).
Published online Jul. 27, 2023.

TABLE 1
Patients' Demographic and Clinical Data

Characteristic	Training dataset (*10*)	Test dataset
Total number of patients	40	159
Age (y)	63 ± 12 (range, 16–86)	60 ± 15 (range, 12–88)
Weight (kg)	69 ± 13	72 ± 17
Height (cm)	167 ± 9	170 ± 10
Sex		
Male	22	95
Female	18	64
Primary tumor site		
Pancreas	13	69
Small bowel	7	12
Lung	5	21
Pheochromocytoma	3	6
Unknown	3	20
Thymus	2	7
Stomach	2	12
Rectum	2	7
Carotid paraganglioma	1	0
Appendix	0	1
Colon	1	4
Paraganglioma	0	2
Esophagus	0	4
Skin	0	3
Sites of metastases		
Liver	28	135
Lymph nodes	18	89
Bones	25	70
Lungs	7	26
Peritoneum	3	15
Retroperitoneum	0	9
Thyroid	1	0
Adrenal glands	1	4
Pelvis	0	4
Spleen	0	2
Pancreas	0	23

Qualitative data are number; continuous data are mean ± SD.

protocol, including 3 quantitative SPECT/CT studies at a t_1 of 24 h, a t_2 of 98 h, and a t_3 of 168 h or 2 SPECT/CT studies at t_1 and t_3 after the first therapy cycle and a single SPECT/CT study at t_1 after the subsequent cycles; and third, patients who were not included in the training dataset used to generate the STP MLR model (*10*).

A total of 281 patients had PRRT during this period. Three patients were excluded because of missing data in the hospital archiving system. Of 278 remaining patients, 178 underwent MTP dosimetry with SPECT/CT in the appropriate acquisition times described above. Nineteen patients, included in the training dataset of the previous study, were excluded from the present study. The remaining 159 patients (95 men; average age, 60 y; range, 12–88 y) with 477 therapy cycles (5 cycles in 2 patients, 4 cycles in 57, 3 cycles in 45, 2 cycles in 36, and 1 cycle in 32) and a total of 172 PRRTs (13 salvage therapies) were included in this study. In 107 patients who did not complete 4 cycles of PRRT, 27 (25%) stopped receiving the therapy because the expected kidney dose after the following cycle exceeded 25 Gy, 24 (22%) died before completing PRRT, 10 (9%) had disease progression, and 7 (7%) had general deterioration. The clinical characteristics of the patients included in the training dataset (*10*) and in the test dataset of the present study are summarized in Table 1.

SPECT/CT data were used to calculate the cumulative radiation ADs for 167 kidneys (right and left), 170 livers, and 150 spleens. Five kidney pairs, 2 livers, and 20 spleens were excluded because of missing archived data, and 20 patients underwent splenectomy. Additional measurements were performed in the bone marrow of 27 patients (145 were excluded because of inappropriate timing of sampling) and 311 tumors using both standard MTP dosimetry and the STP MLR model.

This study was approved by the Institutional Review Board in accordance with the 1964 Declaration of Helsinki and its later amendments or comparable ethical standards. The requirement to obtain informed consent was waived.

PRRT Therapy

Infusion of 1.5 L of amino acid solution started at least 30 min before radiopharmaceutical administration and continued for 5–6 h. ^{177}Lu-DOTA-octreotate (Isorad Ltd., Soreq Nuclear Research Center [396 therapy cycles]; S.R.Y Medical Services Ltd. [81 cycles]) was coadministered intravenously over 30 min (*11*). The mean injected activity per treatment cycle was 7.2 ± 0.7 MBq. The median cumulative activity per patient was 21.9 GBq (range, 5.7–37.5 GBq). The interval between treatment cycles was 5–28 wk (median, 7 wk).

Posttreatment Imaging

SPECT/CT studies of the abdomen, including kidneys, liver, and spleen, were acquired after each cycle of treatment, as previously described (*10*,*12*). When necessary for extraabdominal tumor sites, an additional field of view was acquired.

Acquisition parameters and camera calibration were previously described (*10*). Briefly, studies were acquired either on an Infinia SPECT/CT (GE Healthcare) (n = 12, February to September 2012) or

TABLE 2
Regression Coefficients of STP MLR Model in Solid Organs and Tumors

	First therapy cycle (t_s = 168 h)			Subsequent therapy cycles (t_s = 24 h)		
Site	$\alpha_{0,k}$ (ln[cm^3·mGy/37·MBq])	$\alpha_{1,k}$ (no units)	$\alpha_{2,k}$ (h^{-1})	$\alpha_{0,k}$ (ln[cm^3·mGy/37·MBq])	$\alpha_{1,k}$ (no units)	$\alpha_{2,k}$ (h^{-1})
Kidneys	11.86	0.85	0.0111	12.01	0.91	0.0153
Liver	12.26	0.90	0.0090	12.37	0.96	0.0205
Spleen	12.51	0.95	0.0094	12.21	1.00	0.0336
Tumors	12.80	0.99	0.0086	12.80	0.99	0.0086

TABLE 3
Regression Coefficients of STP MLR Model in Bone Marrow

Therapy cycle	$\Theta_{BM,BM}$ (cm^3·mGy/37·MBq·h)	$\Theta_{BM,RM}$ (cm^3·mGy/37·MBq·h)	$\beta_{0,BM}$ (ln[h])	$\beta_{1,BM}$ (no units)	$\beta_{2,BM}$ (h^{-1})
First (t_s = 168 h)	1,879	316	4.59	0.90	0.0101
Subsequent (t_s = 24 h)	1,868	319	4.26	1.07	0.0241

on a Discovery NM/CT 670 (GE Healthcare) (n = 147) with a 20% energy window around the main 208-keV photopeak of ^{177}Lu and medium-energy general-purpose collimators.

Image Reconstruction and Analysis

SPECT images were reconstructed with the ordered-subsets expectation maximization algorithm (2 iterations, 10 subsets), CT attenuation correction, scatter correction, and resolution recovery (for blurring) and were processed using the Dosimetry Toolkit (GE Healthcare) software on the Xeleris 3.0 workstation (GE Healthcare) as previously described (*12*). Volumes of interest were placed over the entire healthy organs of interest and over tumor sites.

Standard MTP Dosimetry Calculation

Of the 172 PRRTs with MTP dosimetry, 162 (94%) were performed using 3 time points, and in 10 therapies 2-time-point dosimetry was performed. We previously demonstrated that ADs obtained using a 2-time-point dosimetry protocol (24 and 168 h) show mean relative differences lower than 1.0% compared with the European Association of Nuclear Medicine/MIRD protocol (*10*).

MTP ADs were computed using an in-house interactive data language code, taking as input the output file of the Dosimetry Toolkit, including the volume and activity concentrations in each volume of interest at every time point. The code performs monoexponential curve fitting from MTPs (2 or 3) after the first cycle and from an STP for the following cycles, assuming an unchanged effective half-life between cycles (*13*,*14*), and calculates residence times in the different organs and tumors. For organs, the MIRD formalism (*15*) was used for AD calculation. For tumors, only self-ADs are considered (*16*). Briefly, the ADs (mGy) were obtained by multiplying the tumor radioactivity concentration residence time ([MBq · s]/[MBq · kg]) by the dose concentration factor (0.0236 [mGy · kg]/[MBq · s]) and by the administered activity (MBq). For bone marrow, AD blood samples were drawn at a t_1 of 24 h and a t_3 of 168 h after the first cycle and at t_1 after subsequent cycles. Blood activity concentrations were measured using a NaI(Tl) well γ-counter (Wizard 1480 3″; Perkin Elmer). The blood activity concentration was fitted by a monoexponential curve and integrated to infinity to estimate the self-AD to the bone marrow, assuming that the activity concentration in the latter is similar to blood (*17*).

STP Dosimetry Calculation

Organ and tumor radiation ADs were estimated from a single SPECT/CT study using the MLR model previously developed (*10*). This model takes 2 independent variables as input (time of imaging after treatment and ^{177}Lu-DOTATATE activity concentration in a given organ or tumor) and predicts the corresponding ADs for solid organs, bone marrow, and tumors. When comparing cumulative kidney dosimetry results obtained using the MTP model and the STP MLR model, the best agreement was achieved using a single SPECT/CT study acquired at a t_3 of 168 h after the first therapy cycle and at a t_1 of 24 h after the following ones (*10*). These same time points were used in the present study to predict the AD by solid organs, tumors, and bone marrow.

Solid Organs and Tumors. Radiation ADs by the kidneys, liver, spleen, and tumors (r_k) were predicted using the following model with a single SPECT/CT study:

$$D(r_k) \sim [a_k(t_s)]^{\alpha_{1,k}} \cdot e^{\alpha_{2,k}\, t_s + \alpha_{0,k}}, \quad \text{Eq. 1}$$

with $D(r_k)$ being the AD by r_k (mGy), t_s being the time of imaging (h), $a_k(t_s)$ being the activity concentration in r_k at time t_s (MBq/cm^3) and $\alpha_{0,k}$ (ln[kg·mGy/MBq]), $\alpha_{1,k}$ having no units, and $\alpha_{2,k}$ (s^{-1}) being the regression coefficients at t_s.

Bone Marrow. The largest contribution to the AD is derived from the self-AD conveyed by the blood, followed by the cross-dose from the remainder of the body (*18*). Therefore, the model takes as input the activity concentration in blood and in the remainder of the body (MBq/cm^3) at time t_s: $a_{blood}(t_s)$ and $a_{RM}(t_s)$, respectively.

$$D(\mathrm{BM}) \sim [a_{blood}(t_s) \cdot \theta_{BM,BM} + a_{RM}(t_s) \cdot \theta_{BM,RM}]^{\beta_{1,BM}} \cdot e^{\beta_{2,BM}\, t_s + \beta_{0,BM}}, \quad \text{Eq. 2}$$

where $\theta_{BM,BM}$ and $\theta_{BM,RM}$ are in kg·mGy/MBq·s; $\beta_{0,k}$ (ln(s)), $\beta_{1,k}$ having no units, and $\beta_{2,k}$(s^{-1}) being the regression coefficients of the bone marrow (BM) model at time t_s.

Equations 1 and 2 were used for prediction of the radiation ADs by 167 kidneys (462 therapies), 150 spleens (412 therapies), 170 livers (467 therapies), 27 bone marrows (67 therapies), and 311 tumors using a t_s of 168 h for the first therapy cycles (n = 172) and a t_s of 24 h for the following ones (n = 305). Tables 2 and 3 summarize the regression coefficients used for solid organs, bone marrow, and tumors.

Patient Management from Expected Cumulative Kidney Radiation AD

After each therapy cycle number n, the expected cumulative kidney AD after the following cycle (n + 1) was defined by adding the mean ADs of the previous n therapy cycles to

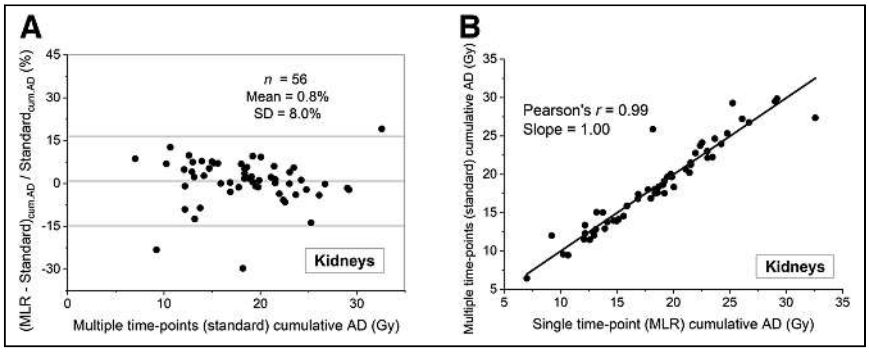

FIGURE 1. Bland–Altman (A) and correlation (B) plots between cumulative kidney ADs after 4 PRRT cycles calculated with STP and MTP protocols.

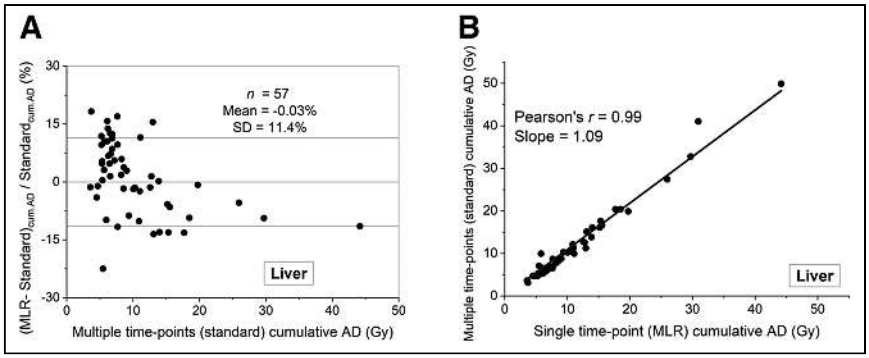

FIGURE 2. Bland–Altman (A) and correlation (B) plots between cumulative liver ADs after 4 PRRT cycles calculated with STP and MTP protocols.

the cumulative AD of the n therapies. When the expected cumulative AD exceeded 25 Gy ± 5%, PRRT was stopped, unless decided otherwise by a multidisciplinary team. Management decisions based on STP MLR calculation were compared with decisions based on MTP dosimetry.

Statistical Analysis

Patients were separated into 4 independent groups according to the number of cycles administered (group 1, 1 cycle [32 patients]; group 2, 2 cycles [36 patients]; group 3, 3 cycles [45 patients]; and group 4, 4 cycles [57 patients]).

Differences between cumulative ADs obtained with MTP and STP MLR-based protocols were assessed with Bland–Altman analysis for each patient group. Median relative differences and range were also calculated. The Pearson r correlation coefficient and the angular coefficient a (slope of the linear regression line) were used for correlation between methods.

To test the hypothesis that patient management based on an STP protocol does not differ from that based on an MTP protocol in at least 90% of the therapies, an exact 1-tailed binomial test was performed separately on each group. A Fisher χ^2 test for combined probabilities (*19*) was performed to combine the P values from the different groups into a single composite P value. A Fisher P value lower than 0.05 was considered statistically significant. For the 2 patients who received 5 cycles, only mean ± SD was calculated, and patient management was not evaluated. SPSS Statistics (IBM Corp., Version 29.0) for Microsoft Windows was used for the analysis.

RESULTS

Relative differences and correlations between the cumulative ADs calculated using our standard MTP model and the STP MLR model are respectively shown in Figures 1, 2, 3, and 4 for kidneys, liver, spleen, and tumor sites for patients who received 4 cycles of treatment (group 4). For these patients, mean relative differences of 0.8% ± 8.0%, −7.7% ± 4.8%, 0.03% ± 11.4%, −2.8% ± 6.3%, and −2.1% ± 18.4% were obtained for 56 kidneys, 5 bone marrows, 57 livers, 48 spleens, and 101 tumors, respectively (Pearson r = 0.99 for all). For other patients, similar mean relative differences were obtained. Table 4 summarizes the mean relative differences, median, range, and angular coefficients obtained between both methodologies for organ and tumor cumulative ADs for patients who received 1–5 therapy cycles (Pearson r = 0.99 for all).

Effective half-lives of 53 ± 10 h (range, 36–100 h), 73 ± 13 h (range, 35–109 h), 72 ± 12 h (range, 41–112 h), and 84 ± 26 h (range, 24–159 h) were obtained with the standard MTP protocol for kidneys, liver, spleen, and tumors, respectively. The regression coefficient $\alpha_{2,k}$ (Eq. 1; Table 2) corresponds to the effective decay constant λ_k for a given organ or tumor k (*10*). Comparing the STP model effective half-life $\ln(2)/\alpha_{2,k}$ with the effective half-life obtained from our MTP protocol, we obtained similar values of 62, 77, 73, and 81 h with a t_s of 168 h for kidneys, liver, spleen, and tumors, respectively.

Patient management based on the expected kidney cumulative ADs after the next treatment, calculated with the STP MLR model, was similar to that for the MTP model in 170 of 172 PRRTs. In 1.2% (2/172) of the PRRT therapies, there were different management decisions, including 1 of 32 patients in group 1 (3.1%) and 1 of 36 in group 2 (2.7%). The agreement was well over 90%, but the differences were not statistically significant at the 0.05 level (0.156 and 0.113, respectively). For groups 3 (n = 45) and 4 (n = 57), there was no difference in management (P = 0.009 and 0.002, respectively). The Fisher χ^2 test for combined probabilities produced a composite P value of 0.0003 for the 4 groups.

DISCUSSION

We previously described an MLR model that predicted radiation ADs by organs and tumors from a single SPECT/CT study acquired 1 wk after the first post-PRRT cycle and 1 d after subsequent cycles, in 32 consecutive neuroendocrine neoplasm patients (*10*). In the present study, the model was evaluated in 159 patients, 172 therapies, and 477 cycles. To the best of our knowledge, this was the first study assessing an STP model after PRRT in a large patient cohort. When the STP MLR model was used, patient management decisions differed from those made using the MTP model in only 2 of 172 therapies (1.2%). A composite Fisher P value of 0.03% for the groups of patients who underwent between 1 and 4 therapy cycles was obtained. Of note, the independent P values for groups 1 and 2 (each with 1 patient mismanaged) were expected to be higher than 0.05 in view of the relatively low number of patients

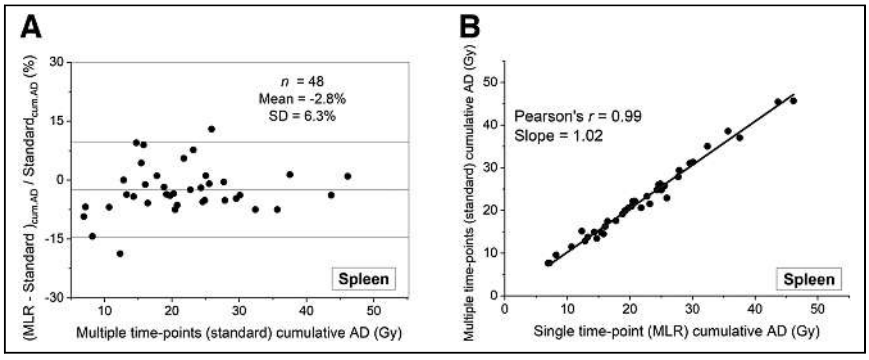

FIGURE 3. Bland–Altman (A) and correlation (B) plots between cumulative spleen ADs after 4 PRRT cycles calculated with STP and MTP protocols.

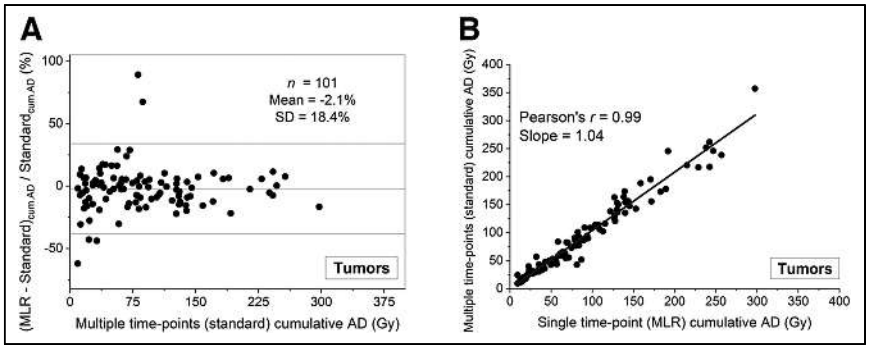

FIGURE 4. Bland–Altman (A) and correlation (B) plots between cumulative tumor ADs after 4 PRRT cycles calculated with STP and MTP protocols.

in these groups. However, both mismanaged patients had high kidney ADs after the first PRRT, underestimated by the STP model (11.8 and 10 Gy vs. 14.2 and 14.4 Gy with our standard MTP, respectively). The expected cumulative ADs exceeded the 25-Gy threshold after the second therapy cycle with the standard MTP model and after the third cycle with the STP model. The mean kidney AD with our MTP model in the present study was 5.2 Gy. Patients with high predicted kidney ADs after the first PRRT cycle should be managed carefully, and the MTP methodology should be used for the remaining treatment cycles. Recent studies reported cumulative ADs of as high as 40 Gy (*6*,*8*,*20*,*21*) with no renal toxicity. Therefore, the STP model with the kidney threshold set at 25 Gy is not expected to lead to significant safety problems even for the 1% of patients managed differently.

There were 3 outlier cumulative kidney ADs, underestimated by the STP MLR model. In 2 patients, PRRT was stopped after a single treatment cycle because of deterioration in the patients' clinical status. No safety issues are expected in this case. The last patient presented a high kidney effective half-life of 89 h, likely due to obstructive uropathy, which may have caused the relatively large difference in the cumulative AD obtained from both methods. However, such cases are rare.

Hänscheid et al. (*22*) have previously demonstrated in 29 patients that a single posttreatment SPECT/CT study performed 4 d after PRRT provides a reliable time-integrated activity estimation (self-AD), with median errors of 5%, 6%, 8%, and 6% for kidneys, liver, spleen, and lesions, respectively. In the present study, including 172 PRRTs, median errors in cumulative AD estimates were significantly lower (kidneys, 0.2%; liver, 1.8%; spleen, −2.5%; and tumors, −0.9%). Jackson et al. (*23*) estimated in 29 patients

TABLE 4
Differences Between STP and Our MTP Calculations

STP MLR vs. MTP	Kidneys (n = 167)	Bone marrow (n = 27)	Liver (n = 170)	Spleen (n = 150)	Tumors (n = 311)
Group 1, one cycle (n = 32)					
Relative difference	−1.6% ± 13.1% (n = 32)	−0.8% ± 11.0% (n = 12)	0.4% ± 8.3% (n = 32)	1.6% ± 2.4% (n = 28)	−9.0% ± 17.9% (n = 56)
Median	−3.6%	−2.0%	1.2%	2.4%	−3.1%
Range	−31%–33%	−17%–31%	−21%–17%	−15%–22%	−69%–11%
Angular coefficient	1.03	0.99	0.98	0.97	0.98
Group 2, two cycles (n = 36)					
Relative difference	−0.3% ± 2.5% (n = 33)	2.9% (n = 1)	2.5% ± 4.7% (n = 36)	−3.2% ± 4.9% (n = 34)	−1.3% ± 9.3% (n = 63)
Median	−0.9%	—	2.5%	−2.4%	0.1%
Range	−12%–12%	—	−8%–15%	−15%–4%	−33%–21%
Angular coefficient	1.03	—	1.00	1.05	1.00
Group 3, three cycles (n = 45)					
Relative difference	−0.8% ± 5.5% (n = 45)	−1.3% ± 2.8% (n = 8)	2.5% ± 8.7% (n = 43)	−2.5% ± 6.2% (n = 38)	−2.0% ± 13.5% (n = 87)
Median	−0.2%	−1.1%	3.9%	−3.7%	−1.3%
Range	−13%–17%	−6%–2%	−21%–23%	−19%–13%	−41%–32%
Angular coefficient	1.03	1.01	1.07	1.02	1.07
Group 4, four cycles (n = 57)					
Relative difference	0.8% ± 8.0% (n = 56)	−7.7% ± 4.8% (n = 5)	−0.0% ± 11.4% (n = 57)	−2.8% ± 6.3% (n = 48)	−2.1% ± 18.4% (n = 101)
Median	1.5%	−6.7%	0.9%	−2.9%	−1.9%
Range	−30%–19%	−15%–3%	−21%–18.3%	−23%–11%	−62%–89%
Angular coefficient	1.00	1.10	1.09	1.02	1.04
Five cycles (n = 2), relative difference	−4.6% (n = 1)	−3.0% (n = 1)	2.4% ± 4.8% (n = 2)	−2.6% ± 1.4% (n = 2)	−9.2% ± 11.2% (n = 4)

time-integrated activities from tissue-specific dose conversion factors obtained from the normalization of existing time–activity curves to a single measurement. Recently, Devasia et al. (*24*) and Hardiansyah et al. (*25*) estimated in 8 patients the radiation ADs from an STP model using a physiologically based pharmacokinetic model and a nonlinear mixed effect model.

The present study showed that our STP MLR model produces similar dosimetry results and persistent patient management decisions compared with MTP dosimetry. It does not necessarily prove the accuracy of the dosimetry approach or its precision for preventing toxicity. This STP model could potentially be incorporated into clinical trials to evaluate whether safety can be estimated from a single posttreatment imaging study. However, in view of the relatively high SD obtained in the Bland–Altman analysis, it may present challenges for prediction of toxicity at the individual level.

A limitation of the present study is that our MTP protocol includes multiple SPECT/CT studies only after the first therapy cycle and not after each treatment. The model needs to be further tested with MTP dosimetry after each treatment cycle. In addition, 10 of 172 (6%) dosimetry calculations were performed with 2-time-point dosimetry, compared with 162 therapies (94%) with 3 time points. We previously demonstrated mean relative differences in ADs lower than 1.0% ± 4.0% between the 2- and the 3-time-point protocols (*26*). Although the difference in the cumulative AD obtained in the present study with STP was somewhat higher (−3.0% to 1.5%), it had the same order of magnitude.

CONCLUSION

The present study, performed on a large cohort of 159 patients, showed that dosimetry results derived from a single post-PRRT SPECT/CT study were similar to our standard MTP protocol, with a 1.2% difference in management decisions. STP dosimetry is feasible and can be used with confidence, avoiding the use of laborious software, simplifying calculations, improving patient comfort, and optimizing departmental workflow and productivity.

KEY POINTS

QUESTION: Can radiation ADs by organs and tumors after PRRT be estimated from a single SPECT/CT study?

PERTINENT FINDINGS: Quantitative ^{177}Lu-DOTATATE SPECT/CT data from 159 consecutive patients were retrospectively analyzed to test an STP MLR model predicting the radiation AD from a single posttherapy SPECT/CT study in a large patient group. Cumulative ADs had a mean relative difference from the standard MTP of 0.8% ± 8.0%, −7.7% ± 4.8%, 0.0% ± 11.4%, −2.8% ± 6.3%, and −2.1% ± 18.4% for kidneys, bone marrow, liver, spleen, and tumors, respectively, for patients who underwent 4 therapy cycles. Similar results were obtained with fewer therapy cycles. Differences in management decisions between our standard protocol and the STP model occurred in 1.2% (2/172) of the therapies.

IMPLICATIONS FOR PATIENT CARE: Dosimetry calculations using our MLR model for AD estimation with a single quantitative SPECT/CT study after PRRT are similar to the results obtained using the standard MTP protocol. The MLR model simplifies the dosimetry process, reduces scanner and technician time, and shortens the AD calculation process for the medical physicist. It may optimize departmental workflow and productivity and improve patient comfort.

DISCLOSURE

No potential conflict of interest relevant to this article was reported.

ACKNOWLEDGMENTS

We thank Prof. Ora Israel for her critical review of the manuscript and useful suggestions, and we thank Prof Norman B. Grover for his statistical suggestions.

REFERENCES

1. Strosberg J, El-Haddad G, Wolin E, et al. Phase 3 trial of ^{177}Lu-dotatate for midgut neuroendocrine tumors. *N Engl J Med.* 2017;376:125–135.
2. Strosberg JR, Caplin ME, Kunz PL, et al. ^{177}Lu-dotatate plus long-acting octreotide versus high-dose long-acting octreotide in patients with midgut neuroendocrine tumours (NETTER-1): final overall survival and long-term safety results from an open-label, randomised, controlled, phase 3 trial. *Lancet Oncol.* 2021;22:1752–1763.
3. Kwekkeboom DJ, de Herder WW, Kam BL, et al. Treatment with the radiolabeled somatostatin analog [^{177}Lu-DOTA^{0},Tyr^{3}]octreotate: toxicity, efficacy, and survival. *J Clin Oncol.* 2008;26:2124–2130.
4. FDA approves lutetium Lu 177 dotatate for treatment of GEP-NETS. U.S. Food and Drug Administration website. https://www.fda.gov/drugs/informationondrugs/approveddrugs/ucm594105.htm. Revised January 26, 2018. Accessed July 10, 2023.
5. Del Prete M, Buteau F-A, Beauregard J-M. Personalized ^{177}Lu-octreotate peptide receptor radionuclide therapy of neuroendocrine tumours: a simulation study. *Eur J Nucl Med Mol Imaging.* 2017;44:1490–1500.
6. Sundlöv A, Gleisner KS, Tennvall J, et al. Phase II trial demonstrates the efficacy and safety of individualized, dosimetry-based ^{177}Lu-DOTATATE treatment of NET patients. *Eur J Nucl Med Mol Imaging.* 2022;49:3830–3840.
7. Del Prete M, Buteau F-A, Arsenault F, et al. Personalized ^{177}Lu-octreotate peptide receptor radionuclide therapy of neuroendocrine tumours: initial results from the P-PRRT trial. *Eur J Nucl Med Mol Imaging.* 2019;46:728–742.
8. Sundlöv A, Sjögreen-Gleisner K, Svensson J, et al. Individualised ^{177}Lu-DOTATATE treatment of neuroendocrine tumours based on kidney dosimetry. *Eur J Nucl Med Mol Imaging.* 2017;44:1480–1489.
9. Ljungberg M, Celler A, Konijnenberg MW, et al. MIRD pamphlet no. 26: joint EANM/MIRD guidelines for quantitative ^{177}Lu SPECT applied for dosimetry of radiopharmaceutical therapy. *J Nucl Med.* 2016;57:151–162.
10. Chicheportiche A, Sason M, Godfroy J, et al. Simple model for estimation of radiation absorbed dose by organs and tumors after PRRT from a single SPECT/CT study. *EJNMMI Phys.* 2021;8:63.
11. Hope TA, Abbott A, Colucci K, et al. NANETS/SNMMI procedure standard for somatostatin receptor–based peptide receptor radionuclide therapy with ^{177}Lu-DOTATATE. *J Nucl Med.* 2019;60:937–943.
12. Chicheportiche A, Artoul F, Schwartz A, et al. Reducing the number of CTs performed to monitor personalized dosimetry during peptide receptor radionuclide therapy (PRRT). *EJNMMI Phys.* 2018;5:10.
13. Garske U, Sandström M, Johansson S, et al. Minor changes in effective half-life during fractionated ^{177}Lu-octreotate therapy. *Acta Oncol.* 2012;51:86–96.
14. Willowson KP, Eslick E, Ryu H, Poon A, Bernard EJ, Bailey DL. Feasibility and accuracy of single time point imaging for renal dosimetry following ^{177}Lu-DOTATATE ('Lutate') therapy. *EJNMMI Phys.* 2018;5:33.
15. Bolch WE, Eckerman KF, Sgouros G, Thomas SR. MIRD pamphlet no. 21: a generalized schema for radiopharmaceutical dosimetry—standardization of nomenclature. *J Nucl Med.* 2009;50:477–484.
16. Sandström M, Garske U, Granberg D, Sundin A, Lundqvist H. Individualized dosimetry in patients undergoing therapy with ^{177}Lu-DOTA-D-Phe^{1}-Tyr^{3}-octreotate. *Eur J Nucl Med Mol Imaging.* 2010;37:212–225.
17. Forrer F, Krenning EP, Kooij PP, et al. Bone marrow dosimetry in peptide receptor radionuclide therapy with [^{177}Lu-DOTA^{0},Tyr^{3}]octreotate. *Eur J Nucl Med Mol Imaging.* 2009;36:1138–1146.
18. Sandström M, Garske-Román U, Granberg D, et al. Individualized dosimetry of kidney and bone marrow in patients undergoing ^{177}Lu-DOTA-octreotate treatment. *J Nucl Med.* 2013;54:33–41.
19. Fisher RA. *Statistical Methods for Research Workers.* 5th ed. Oliver and Boyd; 1934:103.
20. Bodei L, Cremonesi M, Ferrari M, et al. Long-term evaluation of renal toxicity after peptide receptor radionuclide therapy with ^{90}Y-DOTATOC and

^{177}Lu-DOTATATE: the role of associated risk factors. *Eur J Nucl Med Mol Imaging*. 2008;35:1847–1856.
21. Konijnenberg M, Melis M, Valkema R, Krenning E, de Jong M. Radiation dose distribution in human kidneys by octreotides in peptide receptor radionuclide therapy. *J Nucl Med*. 2007;48:134–142.
22. Hänscheid H, Lapa C, Buck AK, Lassmann M, Werner RA. Dose mapping after endoradiotherapy with ^{177}Lu-DOTATATE/DOTATOC by a single measurement after 4 days. *J Nucl Med*. 2018;59:75–81.
23. Jackson PA, Hofman MS, Hicks RJ, Scalzo M, Violet J. Radiation dosimetry in ^{177}Lu-PSMA-617 therapy using a single posttreatment SPECT/CT scan: a novel methodology to generate time- and tissue-specific dose factors. *J Nucl Med*. 2020;61:1030–1036.
24. Devasia TP, Dewaraja YK, Frey KA, Wong KK, Schipper MJ. A novel time–activity information-sharing approach using nonlinear mixed models for patient-specific dosimetry with reduced imaging time points: application in SPECT/CT after ^{177}Lu-DOTATATE. *J Nucl Med*. 2021;62:1118–1125.
25. Hardiansyah D, Riana A, Beer AJ, Glatting G. Single-time-point estimation of absorbed doses in PRRT using a non-linear mixed-effects model. *Z Med Phys*. 2023;33:70–81.
26. Chicheportiche A, Ben-Haim S, Grozinsky-Glasberg S, et al. Dosimetry after peptide receptor radionuclide therapy: impact of reduced number of post-treatment studies on absorbed dose calculation and on patient management. *EJNMMI Phys*. 2020;7:5.

Choosing the Right Metrics for Evaluation of Radiopharmaceutical Therapy Dosimetry Methodologies

Joshua S. Scheuermann[1] and Daniel A. Pryma[1,2]

[1]*Division of Nuclear Medicine Imaging and Therapy, Department of Radiology, Perelman School of Medicine at the University of Pennsylvania, Philadelphia, Pennsylvania; and* [2]*Abramson Cancer Center at the University of Pennsylvania, Philadelphia, Pennsylvania*

In this issue of *The Journal of Nuclear Medicine,* Chicheportiche et al. (*1*) compare radiation dosimetry calculated from single-time-point (STP) imaging to that obtained with multiple-time-point (MTP) imaging and conclude that they are highly correlated and that, therefore, the simpler method can be used "with confidence." The justifications underpinning their desire to simplify dosimetry image acquisition are valid, namely the resource intensiveness of MTP dosimetry and the potential inconvenience and discomfort for patients. Conversely, they highlight the improved efficiency and patient experience by moving to STP. Currently in most nuclear medicine departments, scanner and staff availability are scaled to diagnostic imaging volumes, with little incremental bandwidth for time-intensive dosimetry acquisitions. Additionally, returning over several days for multiple imaging sessions is not a common patient experience in radiology or nuclear medicine. Thus, we are currently in a self-fulfilling prophecy wherein dosimetry is not widely used because of the complexity, and because it is not widely used, it is thought to be not particularly impactful. Studies exploring ways to simplify and streamline the dosimetry process and improve the patient experience are important for increasing the likelihood that dosimetry will be adopted by more institutions for more therapeutic procedures. However, it is of vital importance to be clear on the intended use of dosimetry and to ensure that the testing methodology matches the use case. Radiopharmaceutical dosimetry can be used to estimate average radiation exposure across a population (common with diagnostic radiopharmaceuticals), in which situation individual outliers are of relatively little consequence and comparing the average of results from one method to another is perfectly adequate and appropriate. For radiopharmaceutical therapy (RPT), dosimetry could be applied to the individual patient to make treatment decisions, and in this case, outlier or discordant measurements can have considerable impact, potentially even leading to life-threatening or fatal adverse events.

Although the work by Chicheportiche et al. is interesting, rigorous, and compelling, it is important to underscore that it shows that the 2 methods get the same answer on average. Because the error bars are still relatively wide, the answer can be discrepant or inaccurate in any individual. In external-beam radiotherapy, the expectation is that absorbed dose estimates are accurate to within 5% or better (*2*). That is, every individual measurement—not the average of the measurements across a population—is accurate to within 5%. These treatments, whether external beam or radiopharmaceutical, have a relatively narrow therapeutic window, and inaccurate dosimetry puts patients at risk for serious side effects if overdosed and at risk for ineffective or suboptimally effective treatment if underdosed. Therefore, to be used to make clinical decisions in individual patients, dosimetry needs to be both accurate and precise. Unfortunately, even for MTP dosimetry many studies highlight that the uncertainty is likely more than 5% (*3*–*5*); therefore, even if MTP and STP agree perfectly, it is not clear whether the answer has sufficient precision to alter clinical decisions based on the results. So, it is difficult to make the claim that STP dosimetry data can be used to make treatment safer or more effective when the comparator MTP dosimetry results are unlikely sufficiently precise for that task. Even when provided with the same data, users achieve results outside the 5% threshold when performing MTP dosimetry; greater standardization and rigor are therefore required (*6*).

In the article, the authors indicate an expectation that STP dosimetry will result in the same clinical choice as MTP dosimetry in at least 90% of patients. This likely falls short of what is needed for adoption as a standard patient management strategy (assuming for the moment that MTP dosimetry could or should be used to make clinical choices). The outliers are potentially very important. If up to 10% of the patient population will be "mismanaged" with STP dosimetry, it would be helpful to understand whether the patients in whom STP will be less reliable (or come to a different answer from MTP) can be identified and undergo MTP instead. The authors indicate that in some cases STP dosimetry significantly underestimated the absorbed dose compared with MTP dosimetry; thus, using a threshold for organ-at-risk dose to flag potentially discordant STP dosimetry results may not be adequate for some of the population. As the authors point out, this concern likely is not at issue for the currently accepted toxicity thresholds but may be more significant should those toxicity thresholds be raised. Said another way, these discordances do not matter today for ^{177}Lu-peptide receptor radionuclide therapy because we likely underdose a majority of patients. Indeed, especially for the current kidney dose threshold derived from external-beam radiotherapy (*7*)—a threshold that appears to substantially underestimate the renal tolerance to RPT (and in particular RPT given over multiple cycles) (*8*)—a spuriously low STP dosimetry result is unlikely to result in patient harm. However, if we were to incorporate dosimetry into dose selection (whether administered activity per treatment or number of cycles per patient) along with a future empirically derived organ limit, these underestimates could be quite clinically significant.

Received Aug. 22, 2023; revision accepted Aug. 28, 2023.
For correspondence or reprints, contact Daniel A. Pryma (dpryma@pennmedicine.upenn.edu).

DOI: 10.2967/jnumed.123.266304

As the authors discuss, because there is currently very little renal toxicity resulting from clinical ^{177}Lu-peptide receptor radionuclide therapy, dosimetry may not be an important patient management tool in the current treatment setting. However, increased high-quality dosimetry within the field as a whole will allow for a better understanding of absorbed doses across larger populations and for the development of toxicity thresholds based on absorbed dose from RPT, rather than trying to adapt toxicity thresholds developed from fractionated external-beam radiation therapy. If there is a better understanding of the true absorbed dose levels at which we can expect a 5% or 15% complication rate, this would allow for potential dose escalation, which may increase the likelihood of a satisfactory therapeutic response. As a corollary to gaining a better understanding of the organ-at-risk toxicity thresholds, high-quality dosimetry on larger patient populations will allow for a better assessment of absorbed doses to tumors and, potentially, the development of expected therapeutic response as a function of RPT absorbed dose. This may allow for dosimetry to be used not only to assess the likelihood of complications due to RPT but also to determine an expected number of cycles to get the desired response. It could help us move away from empiric dosing and toward individualized treatment planning. At first glance, one may infer that at least at the population level, STP could be used for this purpose, but this use would be valid only if toxicity or tumor response is also aggregated at a population level to mitigate the effects of outlier measurements. Ideally, future development of normal-tissue complication probability curves and tumor control probability curves will rely on high-quality dosimetry data that are unlikely to be obtained from STP methodologies (or maybe even from SPECT/CT dosimetry in general).

Finally, the idea that MTP is too inconvenient or uncomfortable for a patient should be revisited. In radiation oncology, patients generally undergo several diagnostic studies before their decision to receive external-beam radiotherapy. They get at least a CT simulation as part of the treatment planning process and potentially additional PET, MRI, or ultrasound studies over one or more days. Then, they return several days or weeks later for daily treatments that can last for 8 wk or longer. This is certainly inconvenient for the patient but important for their anticipated successful outcome (and less inconvenient than cancer death). If RPT were approached similarly to fractionated external-beam therapy in radiation oncology, where the patient's expectations are set from the initial discussions about the treatment planning and delivery process, MTP dosimetry may not be viewed as an inconvenience but as an important part of the treatment planning and administration process that is integral to ensuring the best possible outcome. Improving scanning and reconstruction technologies to reduce the imaging time required while maintaining high-quality image data will be important for improving the patient experience.

Certainly, the issues around dosimetry imaging acquisition are complex and include reimbursement, standardization, reproducibility, and accessibility; they will need to be addressed. We will then need evidence that patient-specific dosing, informed by dosimetry, is superior to population-level dose administration. To realize that goal, RPT dosimetry must be accurate and precise not only across a population but also at the individual level. The simpler the better, but simplification cannot be achieved at the expense of reliability in a significant subset of patients.

DISCLOSURE

Daniel Pryma is on the scientific advisory board for MTTI and Trevarx, receives personal fees from Curium, is a member of the Independent Data and Safety Monitoring Board for PSI Pharma, and receives clinical trial funding from Lantheus, POINT Biopharma, and Fusion Pharmaceuticals. No other potential conflict of interest relevant to this article was reported.

REFERENCES

1. Chicheportiche A, Sason M, Zidan M, et al. Impact of single-time-point estimates of ^{177}Lu-PRRT absorbed doses on patient management: validation of a trained multiple-linear-regression model in 159 patients and 477 therapy cycles. *J Nucl Med.* 2023;64:1610–1616.
2. Absorbed dose determination in external beam radiotherapy: an international code of practice for dosimetry based on standards of absorbed dose to water. International Atomic Energy Agency website. https://www-pub.iaea.org/MTCD/Publications/PDF/TRS398_scr.pdf. Published 2000. Accessed August 30, 2023.
3. Brolin G, Gustafsson J, Ljungberg M, Gleisner KS. Pharmacokinetic digital phantoms for accuracy assessment of image-based dosimetry in ^{177}Lu-DOTATATE peptide receptor radionuclide therapy. *Phys Med Biol.* 2015;60:6131–6149.
4. Finocchiaro D, Gear JI, Fioroni F, et al. Uncertainty analysis of tumour absorbed dose calculations in molecular radiotherapy. *EJNMMI Phys.* 2020;7:63.
5. He B, Du Y, Segars WP, et al. Evaluation of quantitative imaging methods for organ activity and residence time estimation using a population of phantoms having realistic variations in anatomy and uptake. *Med Phys.* 2009;36:612–619.
6. Uribe C, Peterson A, Van B, et al. An international study of factors affecting variability of dosimetry calculations, part 1: design and early results of the SNMMI Dosimetry Challenge. *J Nucl Med.* 2021;62(suppl 3):36S–47S.
7. Emami B, Lyman J, Brown A, et al. Tolerance of normal tissue to therapeutic irradiation. *Int J Radiat Oncol Biol Phys.* 1991;21:109–122.
8. Vegt E, de Jong M, Wetzels JF, et al. Renal toxicity of radiolabeled peptides and antibody fragments: mechanisms, impact on radionuclide therapy, and strategies for prevention. *J Nucl Med.* 2010;51:1049–1058.

Membrane and Nuclear Absorbed Doses from ^{177}Lu and ^{161}Tb in Tumor Clusters: Effect of Cellular Heterogeneity and Potential Benefit of Dual Targeting—A Monte Carlo Study

Alexandre Larouze[1], Mario Alcocer-Ávila[1], Clément Morgat[2], Christophe Champion[1], and Elif Hindié[2,3]

[1]*Université de Bordeaux–CNRS-CEA, Centre Lasers Intenses et Applications, UMR 5107, Talence, France;* [2]*Service de Médecine Nucléaire, CHU de Bordeaux, Université de Bordeaux, UMR CNRS 5287, INCIA, Talence, France; and* [3]*Institut Universitaire de France, Paris, France*

Early use of targeted radionuclide therapy to eradicate tumor cell clusters and micrometastases might offer cure. However, there is a need to select appropriate radionuclides and assess the potential impact of heterogeneous targeting. **Methods:** The Monte Carlo code CELLDOSE was used to assess membrane and nuclear absorbed doses from ^{177}Lu and ^{161}Tb (β^--emitter with additional conversion and Auger electrons) in a cluster of 19 cells (14-μm diameter, 10-μm nucleus). The radionuclide distributions considered were cell surface, intracytoplasmic, or intranuclear, with 1,436 MeV released per labeled cell. To model heterogeneous targeting, 4 of the 19 cells were unlabeled, their position being stochastically determined. We simulated situations of single targeting, as well as dual targeting, with the 2 radiopharmaceuticals aiming at different targets. **Results:** ^{161}Tb delivered 2- to 6-fold higher absorbed doses to cell membranes and 2- to 3-fold higher nuclear doses than ^{177}Lu. When all 19 cells were targeted, membrane and nuclear absorbed doses were dependent mainly on radionuclide location. With cell surface location, membrane absorbed doses were substantially higher than nuclear absorbed doses, both with ^{177}Lu (38–41 vs. 4.7–7.2 Gy) and with ^{161}Tb (237–244 vs. 9.8–15.1 Gy). However, when 4 cells were not targeted by the cell surface radiopharmaceutical, the membranes of these cells received on average only 9.6% of the ^{177}Lu absorbed dose and 2.9% of the ^{161}Tb dose, compared with a cluster with uniform cell targeting, whereas the impact on nuclear absorbed doses was moderate. With an intranuclear radionuclide location, the nuclei of unlabeled cells received only 17% of the ^{177}Lu absorbed dose and 10.8% of the ^{161}Tb dose, compared with situations with uniform targeting. With an intracytoplasmic location, nuclear and membrane absorbed doses to unlabeled cells were one half to one quarter those obtained with uniform targeting, both for ^{177}Lu and for ^{161}Tb. Dual targeting was beneficial in minimizing absorbed dose heterogeneities. **Conclusion:** To eradicate tumor cell clusters, ^{161}Tb may be a better candidate than ^{177}Lu. Heterogeneous cell targeting can lead to substantial heterogeneities in absorbed doses. Dual targeting was helpful in reducing dose heterogeneity and should be explored in preclinical and clinical studies.

Key Words: targeted radionuclide therapy; ^{177}Lu; ^{161}Tb; terbium-161; absorbed dose

J Nucl Med 2023; 64:1619–1624
DOI: 10.2967/jnumed.123.265509

Targeted radionuclide therapy (TRT) uses radiopharmaceuticals that bind to tumors to deliver targeted radiation. Significant successes have been recorded in recent years (*1*), notably in metastatic neuroendocrine tumors with the radiolabeled somatostatin analog ^{177}Lu-DOTATATE (*2*) and in castration-resistant metastatic prostate cancer with ^{177}Lu-PSMA (*3,4*). Currently, TRT is used mainly in advanced metastatic disease. There is, however, significant interest in moving TRT earlier with the hope of achieving cure, following the example of ^{131}I therapy in thyroid cancer (*5,6*).

Distant metastases start with the shedding of circulating tumor cells (CTCs) from the primary site into the blood, where CTCs are found as single cells or as clusters (2 to >50 cells) (*7,8*). CTC clusters can be homotypic (made of cancer cells only) or heterotypic (associating with other cells, such as macrophages, neutrophils, platelets, and fibroblasts) (*7,8*). CTC clusters have 20- to 100-fold greater metastatic potential than single CTCs because of an increased ability to survive within the bloodstream, evade the immune system, and initiate metastatic lesions at distant sites (*8*). Their presence in blood is generally associated with unfavorable clinical outcomes (*7,8*).

The use of TRT to eradicate CTC clusters, micrometastases, or minimal residual disease (*7–9*) is highly relevant. However, currently used radionuclides, emitting medium-energy (^{177}Lu, ^{131}I) or high-energy (^{90}Y) β^- particles, are suboptimal for TRT of tiny tumor lesions, as most of the energy will be deposited outside the lesions (*10–12*). Other radionuclides are now being explored, including more suitable β^- emitters, α-emitters, and Auger electron emitters.

^{161}Tb has relevant properties for TRT, including for small lesions (*12–17*). Indeed, in addition to a β^- spectrum (mean energy, 154 keV, comparable to ^{177}Lu 133 keV), ^{161}Tb emits multiple low-energy conversion electrons and very low-energy Auger electrons that confer an advantage to ^{161}Tb over ^{177}Lu at up to about 30 μm from the decay site (*14*). As radiolanthanides, ^{161}Tb and ^{177}Lu share similar chemistry (*13,17*). The ^{161}Tb half-life (6.96 d) is close to that of ^{177}Lu (6.65 d). Like ^{177}Lu, ^{161}Tb emits photons useful for imaging. Moreover, 2 isotopes (^{155}Tb, ^{152}Tb) offer the possibility for SPECT or PET imaging before therapy (*13,14*). The superiority of ^{161}Tb over ^{177}Lu has been documented in preclinical studies (*17*). Also, a recently published case report provided proof-of-concept clinical evidence of the therapeutic potential of ^{161}Tb-PSMA-617 in prostate cancer (*18*).

We previously showed that, when all cells in a tumor cluster are targeted, ^{161}Tb delivered 2- to 3-fold higher nuclear absorbed

Received Jan. 25, 2023; revision accepted May 11, 2023.
For correspondence or reprints, contact Elif Hindié (elif.hindie@chu-bordeaux.fr) or Christophe Champion (christophe.champion@u-bordeaux.fr).
Published online Jun. 15, 2023.

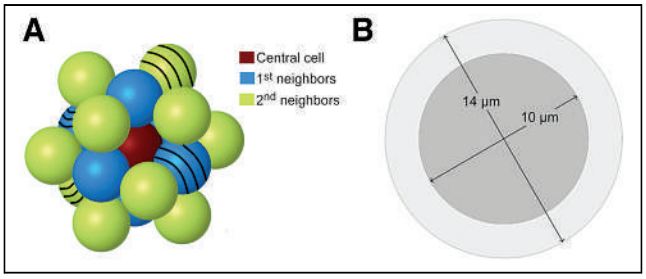

FIGURE 1. Tumor cluster model. In present study, hatched cells (4/19) contained no activity. (Adapted from (*15*).)

doses than ^{177}Lu (*15*). However, cell targeting can be nonuniform, such as when some cells lose the target that allows the radiopharmaceutical (radioligand) to be recognized or attached. This nonuniformity should lead to heterogeneity in absorbed dose (*19–21*). Thus, we here modeled situations of uniform and nonuniform targeting with ^{177}Lu and ^{161}Tb within tumor clusters. We assessed nuclear absorbed doses in labeled and unlabeled cells (*19,20,22*). We also assessed absorbed doses to the cell membrane, another important target for TRT (*23,24*). Finally, as multitargeting is now widely used in oncology to counter tumor heterogeneity (*25*) and has been suggested in TRT (*1,26,27*), we assessed through Monte Carlo modeling whether a second targeting radiopharmaceutical, the distribution of which is independent of the first, may reduce absorbed dose heterogeneities.

MATERIALS AND METHODS

We assessed absorbed doses from simulations performed with CELLDOSE (*11,28*). ^{177}Lu and ^{161}Tb electron emissions were taken from the International Commission on Radiological Protection publication 107 (*29*). The whole β^- spectrum was considered, as well as all conversion and Auger electrons with a probability greater than 0.01%. The tumor cluster consisted of 19 cells with a central cell surrounded by 6 immediate neighbors and a second layer of 12 neighbors (Fig. 1A). Each cell had a 14-μm diameter, a 10-nm-thick membrane, and a centered nucleus of 10 μm (Fig. 1B). Three distributions of the radionuclide were investigated: cell surface, intracytoplasmic, and intranuclear. We assessed absorbed doses to cell nuclei and cell membranes (with an intranuclear radionuclide location, only nuclear absorbed doses were assessed). For each cell, we individualized the self-dose and the cross-dose from surrounding cells (*22*).

CELLDOSE is a homemade Monte Carlo track-structure code for simulating the transport of electrons in water, based on differential and total interaction cross sections describing the elastic scattering, electronic excitation, and ionization (*11,12,14*). This code has been validated against experimental data and benchmarked against various codes. Photons are neglected. This is also the case in other studies on cell clusters, given the negligible energy deposited by x and γ photons (*20,22*). The energy transferred from primary and secondary electrons to the medium is scored event by event until their kinetic energy falls below 7.4 eV (i.e., the excitation threshold of the water molecule in liquid phase), and residual energy is assumed to be deposited locally (*11*). This ability of CELLDOSE to follow electrons until a low-energy level allows assessing absorbed dose in the 10-nm-thick cell membrane. The uncertainty associated with the energy deposits of subcutoff electrons (<7.4 eV) becomes relevant only when considering subnanometer structures (*30*).

Because electron energy per decay differs between ^{177}Lu (147.9 keV) and ^{161}Tb (202.5 keV), simulations were normalized considering that 1,436 MeV were released per labeled cell from either cell surface, cytoplasm, or nucleus (9,709 decays of ^{177}Lu or 7,091 decays of ^{161}Tb). The figure of 1,436 MeV was selected considering cell volume (1,436 μm^3) and 1 MeV released per cubic micrometer (*12,14,15*).

We considered situations of uniform cell targeting, as well as situations of nonuniform targeting in which 4 of 19 cells in the clusters were unlabeled (hatched cells in Fig. 1A).

Finally, to assess the usefulness of dual targeting in counteracting dose heterogeneity from nonuniform targeting, we performed for each situation 2 simulations, one mimicking the first radiopharmaceutical and the other mimicking a second radiopharmaceutical. Both radiopharmaceuticals are labeled with the same radionuclide, either ^{177}Lu or ^{161}Tb, and distribute to similar compartments (cell surface, intracytoplasmic, or intranuclear compartment). However, they aim at 2 different targets. The expression of these targets on tumor cells are independent of one another. With each radiopharmaceutical, 4 cells are unlabeled, their position in the cluster being randomly selected. Thus, after successive simulations with the 2 radiopharmaceuticals, a cell can be double-labeled, single-labeled, or unlabeled. We took the mean absorbed dose from the 2 simulations.

RESULTS

Absorbed Doses Delivered by ^{177}Lu and ^{161}Tb When All Cells in the Cluster Are Labeled

When the radionuclide is at the cell surface, the absorbed doses to the cell membranes are high (^{177}Lu, 38–41 Gy; ^{161}Tb, 237–244 Gy), with a large contribution from self-dose (Table 1), whereas nuclear

TABLE 1
Absorbed Doses from ^{177}Lu and ^{161}Tb to Membrane of Cells Within Tumor Cluster,* Considering Various Distributions of Radionuclide

	Cell surface location of radionuclide (M ← CS)			Intracytoplasmic location of radionuclide (M ← Cy)		
Parameter	Central cell	First neighbors	Second neighbors	Central cell	First neighbors	Second neighbors
^{177}Lu	41.3	39.9	38.2	9.4	8.1	6.7
Self-dose	35 (85%)	35 (88%)	35 (92%)	3.7 (39%)	3.7 (46%)	3.7 (55%)
^{161}Tb	244	241	237	22.9	20.1	16.9
Self-dose	231 (95%)	231 (96%)	231 (97%)	11.6 (51%)	11.6 (58%)	11.6 (69%)
Dose ratio ^{161}Tb/^{177}Lu	5.9	6.0	6.2	2.4	2.5	2.5

*Given symmetry of system, cells of a given neighborhood receive same dose (Fig. 1).
Dose data are in grays. Self-dose represents dose that would be received by isolated tumor cell.

TABLE 2
Absorbed Doses from ^{177}Lu and ^{161}Tb to Nucleus of Cells Within Tumor Cluster,* Considering Various Distributions of Radionuclide

Parameter	Cell surface location of radionuclide (N ← CS)			Intracytoplasmic location of radionuclide (N ← Cy)			Intranuclear location of radionuclide (N ← N)		
	Central cell	First neighbors	Second neighbors	Central cell	First neighbors	Second neighbors	Central cell	First neighbors	Second neighbors
^{177}Lu	7.2	6.0	4.7	8.3	7.0	5.8	15.7	14.6	13.5
Self-dose	1.9 (26%)	1.9 (32%)	1.9 (40%)	3.0 (36%)	3.0 (43%)	3.0 (52%)	10.7 (68%)	10.7 (73%)	10.7 (79%)
^{161}Tb	15.1	12.4	9.8	17.9	15.3	12.9	47.8	45.2	43.1
Self-dose	5.0 (33%)	5.0 (40%)	5.0 (51%)	8.3 (46%)	8.3 (54%)	8.3 (64%)	38.6 (81%)	38.6 (85%)	38.6 (90%)
Dose ratio ^{161}Tb/^{177}Lu	2.1	2.1	2.1	2.2	2.2	2.2	3.0	3.1	3.2

*Given symmetry of system, cells of a given neighborhood receive same dose (Fig. 1).
Dose data are in grays. Self-dose represents dose that would be received by isolated tumor cell.

absorbed doses are comparatively low (^{177}Lu, 4.7–7.2 Gy; ^{161}Tb, 9.8–15.1 Gy) (Table 2). The dose to the membrane is heterogeneous, consisting of multiple impact points. Indeed, if we consider that local interactions around a decay point would occur mostly in a cylinder of 10-nm height (membrane thickness) and 10-nm radius, the ratio between the volume of this cylinder and that of the whole membrane is 5.1×10^{-7}. So, even after considering all decays (^{177}Lu, 9,709; ^{161}Tb, 7,091), local interactions involve 0.5% or less of the cell membrane. Also, as measured with CELLDOSE, the absorbed dose to a cylinder (10-nm height, 10-nm radius) from a decay occurring at its surface is extremely high (^{177}Lu, 3,585 Gy; ^{161}Tb, 37,555 Gy).

With the radionuclide in a intracytoplasmic location, absorbed doses to the cell membranes (^{177}Lu, 6.7–9.4 Gy; ^{161}Tb, 16.9–20.1 Gy) are comparable to nuclear absorbed doses (^{177}Lu, 5.8–8.3 Gy; ^{161}Tb, 12.9–17.9 Gy) (Tables 1 and 2). Finally, when the radionuclide is in an intranuclear location, nuclear absorbed doses are high (^{177}Lu, 13.5–15.7 Gy; ^{161}Tb, 43.1–47.8 Gy), with a large contribution from self-dose (Table 2).

In Figure 2, we plot membrane and nuclear absorbed doses to the central cell of the cluster for the different configurations. Absorbed doses delivered by ^{161}Tb are consistently higher than those delivered by ^{177}Lu. The highest ^{161}Tb/^{177}Lu absorbed dose ratio (~6.1) is for cell membranes when the radionuclide is on the cell surface (Table 1).

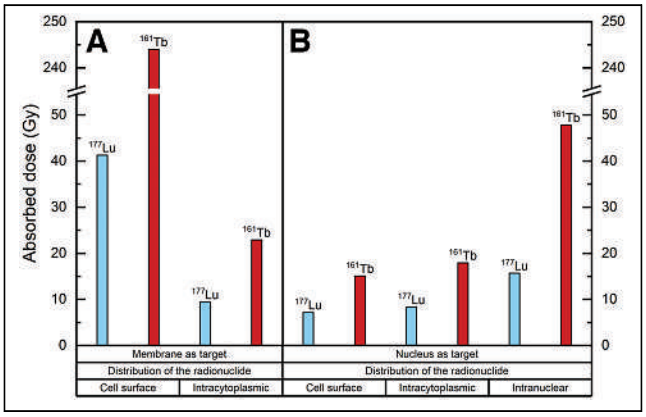

FIGURE 2. Absorbed doses to central cell of cluster from ^{177}Lu (blue) and ^{161}Tb (red).

Effect of Heterogeneous Cell Targeting on ^{177}Lu and ^{161}Tb Absorbed Doses

Figure 3 shows absorbed doses delivered by ^{177}Lu (Fig. 3A) and ^{161}Tb (Fig. 3B) in situations of uniform targeting and heterogeneous targeting. The mean absorbed dose is when all 19 cells are targeted, with doses to individual cells depending on their position within the cluster. The figure also indicates 50% of this mean dose (0.5D) and 25% (0.25D). When 4 cells are unlabeled, the cluster contains only 79% of the total activity. Absorbed doses to labeled cells are lower than with uniform targeting because of a reduced cross-dose. The impact on unlabeled tumor cells is more pronounced and is dependent mainly on the specific configuration of radionuclide location or target.

With an intracytoplasmic radionuclide location, membrane and nuclear absorbed doses to the 4 unlabeled cells ranged between 0.25D and 0.5D, both for ^{177}Lu and for ^{161}Tb (Fig. 3). The absorbed dose to a given cell also depends on its position and the labeling state of adjacent cells.

With the radionuclide at the cell surface, nonuniform targeting resulted in substantial heterogeneity in absorbed doses to cell membranes (Fig. 3). With ^{177}Lu, unlabeled cells received between 2.3 and 4.5 Gy, or on average only 9.6% of the mean dose for a homogeneously targeted cluster (38.9 Gy). With ^{161}Tb, heterogeneity is even more pronounced. Absorbed doses to membranes of unlabeled cells ranged between 5.0 and 12.4 Gy, or on average only 2.9% of the dose with uniform targeting (238 Gy). The impact on nuclear absorbed doses is here lower. The nuclei of unlabeled cells received on average 60% of the ^{177}Lu absorbed doses, or 48% of the ^{161}Tb doses, as compared with a cluster with uniform targeting (Fig. 3).

With intranuclear ^{177}Lu (Fig. 3), the nuclei of unlabeled cells received 1.7–3.0 Gy, or on average 17.2% of the dose expected with uniform targeting (14.0 Gy). With ^{161}Tb, unlabeled cells received 3.5–5.9 Gy, or only 10.8% of the dose expected with uniform cell targeting (44.0 Gy).

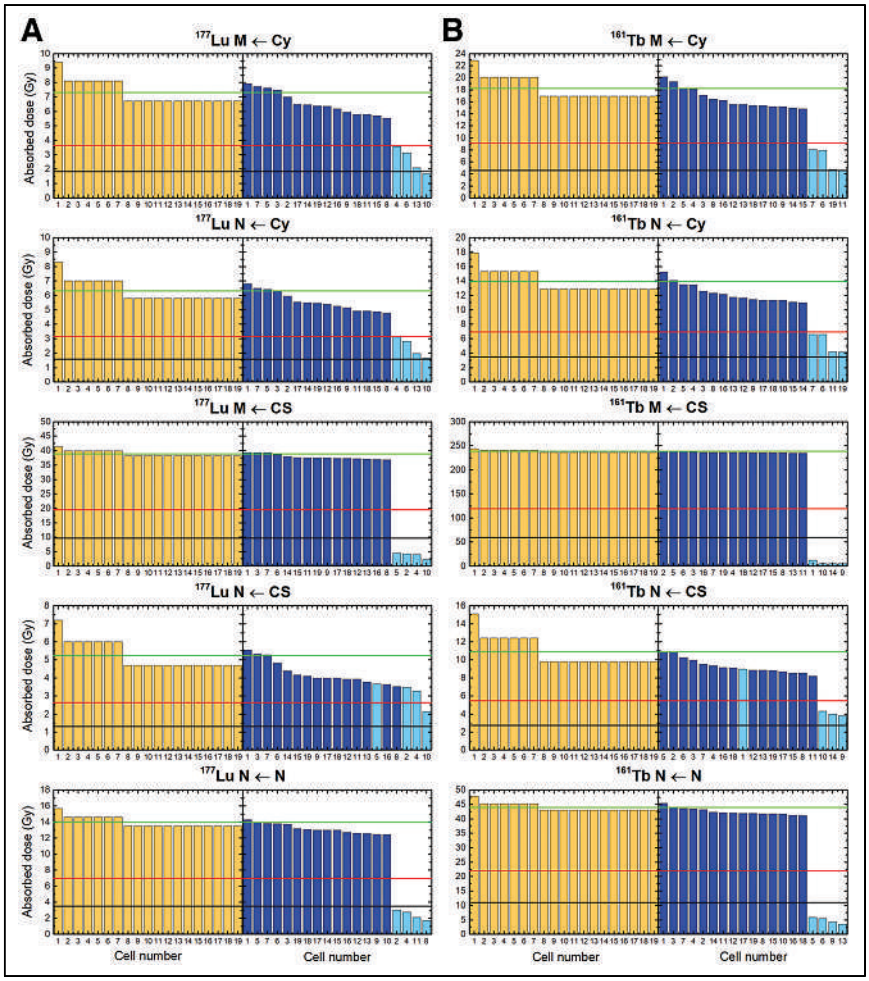

FIGURE 3. Absorbed doses from ^{177}Lu and ^{161}Tb to cell membranes and nuclei for situations of uniform cell targeting (amber) and nonuniform targeting (blue, with dark blue corresponding to labeled cells and light blue to 4 unlabeled cells) and for various distributions of radionuclide. Green line represents mean absorbed dose for uniform targeting; red line corresponds to 0.5D and black line to 0.25D. Cell 1 is central cell, cells 2–7 are first neighbors, and cells 8–19 are second neighbors. For a given radionuclide distribution (e.g., intracytoplasmic), same simulation allowed assessment of absorbed doses to cell membranes and to nuclei. CS = cell surface; Cy = cytoplasm; M = membranes; N = nuclei.

Assessment of Dual Targeting as a Strategy to Compensate for Heterogeneity

With an intracytoplasmic radionuclide, dual targeting minimized heterogeneities in membrane and nuclear absorbed doses (Fig. 4). Most unlabeled cells, which had dose levels between 0.25D and 0.5D, reached 0.5D with dual targeting. Because of the stochastic aspect, 1 cell in the ^{161}Tb simulation was untargeted by either radiopharmaceutical and stayed at about 0.25D. In our model (4/19 untargeted cells), the probabilities that clusters contain one or more cells missed by both radiopharmaceuticals are about 47% for 1 cell, 6.3% for 2 cells, 1.6% for 3 cells, and 0.03% for all 4 cells.

With the radionuclide at the cell surface, and the membrane as the target, dual targeting showed substantial benefit (Fig. 4). With ^{177}Lu, in 3 cells with a dose initially less than 12%, the mean dose reached 0.5D with the second radiopharmaceutical. With ^{161}Tb, again because of the stochastic aspect, only 2 cells received compensation, moving from 2.2% of the mean dose to 0.5D. As heterogeneities in nuclear absorbed doses were less pronounced, dual targeting had almost no impact (^{177}Lu) or only modest benefit (^{161}Tb) (Fig. 4).

With an intranuclear radionuclide location, dual targeting was beneficial in minimizing heterogeneities in nuclear absorbed doses (Fig. 4). With ^{161}Tb, for example, 3 of the 4 unlabeled cells, with a dose level well below 0.25D, reached 0.5D level at the second targeting. Compensation was accompanied by a decrease in absorbed dose to other cells in the cluster, which, however, remained above the 0.5D level.

DISCUSSION

Used as adjuvant therapy to target CTC and micrometastases, or as consolidation therapy for minimal residual disease, TRT has the potential to be curative (*5–9,31*). Radionuclides that can increase the absorbed dose in tiny tumors would be relevant in these settings. ^{161}Tb, a β^--emitter with coemissions of Auger electrons, is one interesting candidate (*12–17*). Interest in ^{161}Tb is growing, and 2 clinical trials on patients with advanced disease have started recruitment. The phase I/II trial VIOLET is assessing the safety and efficacy of ^{161}Tb-PSMA-I&T in men with castration-resistant prostate cancer (NCT05521412). A phase 0 proof-of concept study is measuring the therapeutic index of the somatostatin antagonist ^{161}Tb-DOTA-LM3, in comparison to ^{177}Lu-DOTATOC, in patients with gastroenteropancreatic neuroendocrine tumors (NCT05359146).

In our tumor cluster model, when all 19 cells were targeted, and depending on the location of the radionuclide, ^{161}Tb delivered a 2- to 3-fold higher nuclear absorbed doses than ^{177}Lu but also 2- to 6-fold higher absorbed doses to cell membranes (Tables 1 and 2; Fig. 2). Interaction of ionizing radiation with the cell membrane induces sphingomyelin hydrolysis to ceramide, initiating apoptosis (*32*). Since a number of radiopharmaceuticals reside on the membrane without being internalized (e.g., neuropeptide antagonist analogs and many antibodies), understanding the role of the cell membrane as a target becomes particularly important, specifically for TRT. Membrane irradiation by Auger electrons or α-particles is highly cytotoxic through various mechanisms (*23,24,33*). With the radionuclide at the cell surface, absorbed doses to cell membranes were higher than nuclear doses, both with ^{177}Lu (7.4-fold higher: 38–41 vs. 4.7–7.2 Gy) and with ^{161}Tb (22-fold higher: 237–244 vs. 9.8–15.1 Gy) (Tables 1 and 2). Also, ^{161}Tb showed substantial superiority (^{161}Tb/^{177}Lu dose ratio, ~6.1) (Table 1; Fig. 2). Importantly, a recent preclinical study showed highly enhanced efficacy for TRT with ^{161}Tb-labeled somatostatin antagonists that stay at the cell membrane (*34*).

Damage to membranes can also impair the motility and invasion abilities of cells (*35*), which may impact the fate of CTC. Therefore, the impact of radiopharmaceuticals in this regard also deserves investigation.

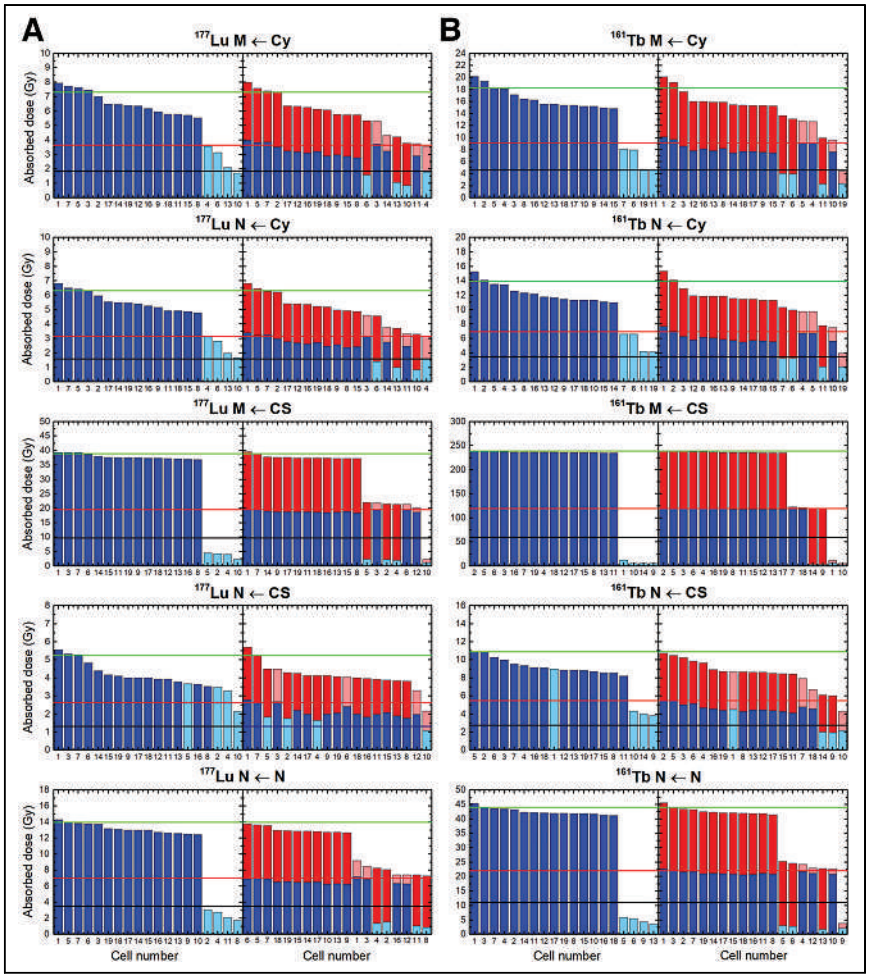

FIGURE 4. Absorbed doses in situations of nonuniform cell targeting: comparison between single and dual targeting. For single targeting, nonuniform targeting is in blue, with dark blue corresponding to labeled cells and light blue to 4 unlabeled cells. For dual targeting, absorbed doses from first radiopharmaceutical are in blue (dark blue for labeled cells and light blue for unlabeled cells), whereas absorbed doses delivered by second radiopharmaceutical are in red (dark red for labeled cells and light red for unlabeled cells). CS = cell surface; Cy = cytoplasm; M = membranes; N = nuclei.

When aiming to eradicate small tumors, the potential impact of nonuniform cell targeting should be assessed (*19–21*). Loss of target expression can be present from the outset or occur during disease evolution or under pressure from previous therapies. We modeled a situation of moderate nonuniformity in which 4 of 19 cells were unlabeled, their positions within the cluster being stochastically determined. With an intranuclear radionuclide, nuclear absorbed doses to unlabeled cells were on average only 17.2% (^{177}Lu) or 10.8% (^{161}Tb) those obtained with uniform targeting (Fig. 3), pointing to the importance of the self-dose (Table 2). Thus, efforts toward achieving an intranuclear location for Auger emitters (*36,37*) should also aim at targeting of all cells. With intracytoplasmic radionuclides, absorbed doses to the membranes and nuclei of unlabeled cells were 25%–50% those obtained with uniform targeting (Fig. 3). With cell surface radiopharmaceuticals, nonuniform targeting resulted in major heterogeneity in absorbed doses to cell membranes but not to nuclei. Membranes of unlabeled cells received about 9.6% of the ^{177}Lu absorbed dose or about 2.9% of the ^{161}Tb dose, compared with uniform targeting (Fig. 3).

Dual targeting is being actively investigated in cancer therapy to counter tumor heterogeneity (*25*). Multiple targeting is also possible with TRT (*1,26,27*). If the organs at risk differ, then an appropriate combination of 2 radiopharmaceuticals might also offer better tolerance (*1,26*). Through Monte Carlo simulation, we assessed whether dual targeting may minimize absorbed dose heterogeneities. With an intranuclear radionuclide location, dual targeting appeared helpful (Fig. 4). Developing many radiopharmaceuticals having an intranuclear location might not be simple, however. With an intracytoplasmic radionuclide, dual targeting showed some benefit (Fig. 4). With cell surface radiopharmaceuticals, dual targeting showed a major benefit in reducing cell membrane dose heterogeneities (Fig. 4), with little impact on nuclear absorbed doses. The benefit from dual targeting would thus depend on the relative importance of the cell membrane as a target (*23,24,34*). Dual targeting is feasible given the increasing number of identified cell surface targets and designed radioligands.

Our study had some limitations. We considered cells with a uniform size, spheric shape, and centered nucleus. Cell targeting was considered binary (labeled/unlabeled); activity content can be more nuanced. Only one simulation was performed for each situation. Our aim was simply to help understand the relative merit of diverse targeting strategies (Figs. 3 and 4). With dual targeting, we considered 2 radiopharmaceuticals in the same cell compartment, with the same radionuclide. Other approaches, such as combining internalizing and noninternalizing radiopharmaceuticals or different radionuclides, can be envisioned. In this work, we focused on 2 targets: the nucleus and the cell membrane (*23,24*). However, cytoplasmic organelles, such as mitochondria and lysosomes, can also play a role in inducing cell death from a dose deposit linked to internalizing peptides or antibodies that could have a strong cytotoxic effect when using Auger or α-emitters (*33,38*). In future work, we intend to also model the dose deposit in cytoplasm and cytoplasmic organelles with CELLDOSE from ^{177}Lu, ^{161}Tb, and Auger emitters. Finally, besides effects on targeted cells, TRT can also impact nontargeted cells through bystander effects or immune responses (*33,39,40*). Indeed, absorbed dose is only one step toward understanding the complexity of radiobiologic effects in TRT (*33,40*).

CONCLUSION

When aiming at CTC clusters, micrometastases, or minimal residual disease, ^{161}Tb is a better candidate than ^{177}Lu, delivering higher absorbed doses. The role of the cell membrane as a target deserves attention. With cell surface radiopharmaceuticals, doses to cell membranes are high—notably so with ^{161}Tb. Nonuniform

cell targeting leads to absorbed dose heterogeneity that can impact the efficacy of TRT. Dual targeting can minimize this heterogeneity and should be further investigated.

DISCLOSURE

This study was conducted in the framework of the University of Bordeaux IdEx "Investments for the Future" program RRI "NewMOON." No other potential conflict of interest relevant to this article was reported.

KEY POINTS

QUESTION: Is the novel radionuclide ^{161}Tb suitable for TRT of tumor cell clusters?

PERTINENT FINDINGS: Our Monte Carlo simulations showed that ^{161}Tb delivers higher absorbed doses than ^{177}Lu to nuclei and cell membranes, whatever the location of a radiopharmaceutical. Nonuniform cell targeting resulted in absorbed dose heterogeneity that could be countered through dual targeting.

IMPLICATIONS FOR PATIENT CARE: ^{161}Tb can be a better radionuclide for clinical trials aiming at eradicating tumor cell clusters and micrometastases.

REFERENCES

1. Aboagye EO, Barwick TD, Haberkorn U. Radiotheranostics in oncology: making precision medicine possible. *CA Cancer J Clin.* 2023;73:255–274.
2. Strosberg J, El-Haddad G, Wolin E, et al. Phase 3 trial of ^{177}Lu-dotatate for midgut neuroendocrine tumors. *N Engl J Med.* 2017;376:125–135.
3. Sartor O, de Bono J, Chi KN, et al. Lutetium-177-PSMA-617 for metastatic castration-resistant prostate cancer. *N Engl J Med.* 2021;385:1091–1103.
4. Hofman MS, Emmett L, Sandhu S, et al. [^{177}Lu]Lu-PSMA-617 versus cabazitaxel in patients with metastatic castration-resistant prostate cancer (TheraP): a randomised, open-label, phase 2 trial. *Lancet.* 2021;397:797–804.
5. Ruel E, Thomas S, Dinan M, Perkins JM, Roman SA, Sosa JA. Adjuvant radioactive iodine therapy is associated with improved survival for patients with intermediate-risk papillary thyroid cancer. *J Clin Endocrinol Metab.* 2015;100:1529–1536.
6. Hindié E, Zanotti-Fregonara P, Keller I, et al. Bone metastases of differentiated thyroid cancer: impact of early ^{131}I-based detection on outcome. *Endocr Relat Cancer.* 2007;14:799–807.
7. Aceto N, Bardia A, Miyamoto DT, et al. Circulating tumor cell clusters are oligoclonal precursors of breast cancer metastasis. *Cell.* 2014;158:1110–1122.
8. Schuster E, Taftaf R, Reduzzi C, Albert MK, Romero-Calvo I, Liu H. Better together: circulating tumor cell clustering in metastatic cancer. *Trends Cancer.* 2021;7:1020–1032.
9. Pantel K, Alix-Panabières C. Liquid biopsy and minimal residual disease: latest advances and implications for cure. *Nat Rev Clin Oncol.* 2019;16:409–424.
10. O'Donoghue JA, Bardiès M, Wheldon TE. Relationships between tumor size and curability for uniformly targeted therapy with beta-emitting radionuclides. *J Nucl Med.* 1995;36:1902–1909.
11. Champion C, Zanotti-Fregonara P, Hindié E. CELLDOSE: a Monte Carlo code to assess electron dose distribution—S values for ^{131}I in spheres of various sizes. *J Nucl Med.* 2008;49:151–157.
12. Hindié E, Zanotti-Fregonara P, Quinto MA, Morgat C, Champion C. Dose deposits from ^{90}Y, ^{177}Lu, ^{111}In, and ^{161}Tb in micrometastases of various sizes: implications for radiopharmaceutical therapy. *J Nucl Med.* 2016;57:759–764.
13. Gracheva N, Müller C, Talip Z, et al. Production and characterization of no-carrier-added ^{161}Tb as an alternative to the clinically-applied ^{177}Lu for radionuclide therapy. *EJNMMI Radiopharm Chem.* 2019;4:12.
14. Champion C, Quinto MA, Morgat C, Zanotti-Fregonara P, Hindié E. Comparison between three promising β-emitting radionuclides, ^{67}Cu, ^{47}Sc and ^{161}Tb, with emphasis on doses delivered to minimal residual disease. *Theranostics.* 2016;6:1611–1618.
15. Alcocer-Ávila ME, Ferreira A, Quinto MA, Morgat C, Hindié E, Champion C. Radiation doses from ^{161}Tb and ^{177}Lu in single tumour cells and micrometastases. *EJNMMI Phys.* 2020;7:33.
16. Bernhardt P, Svensson J, Hemmingsson J, et al. Dosimetric analysis of the short-ranged particle emitter ^{161}Tb for radionuclide therapy of metastatic prostate cancer. *Cancers (Basel).* 2021;13:2011.
17. Müller C, Umbricht CA, Gracheva N, et al. Terbium-161 for PSMA-targeted radionuclide therapy of prostate cancer. *Eur J Nucl Med Mol Imaging.* 2019;46:1919–1930.
18. Rosar F, Maus S, Schaefer-Schuler A, Burgard C, Khreish F, Ezziddin S. New horizons in radioligand therapy: ^{161}Tb-PSMA-617 in advanced mCRPC. *Clin Nucl Med.* 2023;48:433–434.
19. Neti PV, Howell RW. Isolating effects of microscopic nonuniform distributions of ^{131}I on labeled and unlabeled cells. *J Nucl Med.* 2004;45:1050–1058.
20. Falzone N, Lee BQ, Able S, et al. Targeting micrometastases: the effect of heterogeneous radionuclide distribution on tumor control probability. *J Nucl Med.* 2018;60:250–258.
21. Tamborino G, Nonnekens J, De Saint-Hubert M, et al. Dosimetric evaluation of the effect of receptor heterogeneity on the therapeutic efficacy of peptide receptor radionuclide therapy: correlation with DNA damage induction and in vivo survival. *J Nucl Med.* 2022;63:100–107.
22. Goddu SM, Rao DV, Howell RW. Multicellular dosimetry for micrometastases: dependence of self-dose versus cross-dose to cell nuclei on type and energy of radiation and subcellular distribution of radionuclides. *J Nucl Med.* 1994;35:521–530.
23. Pouget JP, Santoro L, Raymond L, et al. Cell membrane is a more sensitive target than cytoplasm to dense ionization produced by Auger electrons. *Radiat Res.* 2008;170:192–200.
24. Paillas S, Ladjohounlou R, Lozza C, et al. Localized irradiation of cell membrane by Auger electrons is cytotoxic through oxidative stress-mediated nontargeted effects. *Antioxid Redox Signal.* 2016;25:467–484.
25. Wang T, Tang Y, Cai J, et al. Coadministration of CD19- and CD22-directed chimeric antigen receptor T-cell therapy in childhood B-cell acute lymphoblastic leukemia: a single-arm, multicenter, phase II trial. *J Clin Oncol.* 2023;41:1670–1683.
26. Hobbs RF, Wahl RL, Frey EC, et al. Radiobiologic optimization of combination radiopharmaceutical therapy applied to myeloablative treatment of non-Hodgkin lymphoma. *J Nucl Med.* 2013;54:1535–1542.
27. Reubi JC, Maecke HR. Approaches to multireceptor targeting: hybrid radioligands, radioligand cocktails, and sequential radioligand applications. *J Nucl Med.* 2017;58(suppl 2):10S–16S.
28. Hindié E, Champion C, Zanotti-Fregonara P, et al. Calculation of electron dose to target cells in a complex environment by Monte Carlo code "CELLDOSE." *Eur J Nucl Med Mol Imaging.* 2009;36:130–136.
29. Eckerman K, Endo A. ICRP publication 107. Nuclear decay data for dosimetric calculations. *Ann ICRP.* 2008;38:7–96.
30. Alcocer Ávila ME, Hindié E, Champion C. How to explain the sensitivity of DNA double-strand breaks yield to ^{125}I position? *Int J Radiat Biol.* 2023;99:103–108.
31. Katugampola S, Wang J, Rosen A, Howell RW. MIRD pamphlet no. 27: MIRDcell V3, a revised software tool for multicellular dosimetry and bioeffect modeling. *J Nucl Med.* 2022;63:1441–1449.
32. Haimovitz-Friedman A, Kan CC, Ehleiter D, et al. Ionizing radiation acts on cellular membranes to generate ceramide and initiate apoptosis. *J Exp Med.* 1994;180:525–535.
33. Pouget JP, Constanzo J. Revisiting the radiobiology of targeted alpha therapy. *Front Med (Lausanne).* 2021;8:692436.
34. Borgna F, Haller S, Rodriguez JMM, et al. Combination of terbium-161 with somatostatin receptor antagonists: a potential paradigm shift for the treatment of neuroendocrine neoplasms. *Eur J Nucl Med Mol Imaging.* 2022;49:1113–1126.
35. Bouvet F, Ros M, Bonedeau E, et al. Defective membrane repair machinery impairs survival of invasive cancer cells. *Sci Rep.* 2020;10:21821.
36. Ku A, Facca VJ, Cai Z, Reilly RM. Auger electrons for cancer therapy—a review. *EJNMMI Radiopharm Chem.* 2019;4:27.
37. Chastel A, Worm DJ, Alves ID, et al. Design, synthesis, and biological evaluation of a multifunctional neuropeptide-Y conjugate for selective nuclear delivery of radiolanthanides. *EJNMMI Res.* 2020;10:16.
38. Bavelaar BM, Lee BQ, Gill MR, Falzone N, Vallis KA. Subcellular targeting of theranostic radionuclides. *Front Pharmacol.* 2018;9:996.
39. Xue LY, Butler NJ, Makrigiorgos GM, Adelstein SJ, Kassis AI. Bystander effect produced by radiolabeled tumor cells in vivo. *Proc Natl Acad Sci USA.* 2002;99:13765–13770.
40. Pouget JP, Santoro L, Piron B, et al. From the target cell theory to a more integrated view of radiobiology in targeted radionuclide therapy: the Montpellier group's experience. *Nucl Med Biol.* 2022;104–105:53–64.

Albumin-Binding and Conventional PSMA Ligands in Combination with ^{161}Tb: Biodistribution, Dosimetry, and Preclinical Therapy

Viviane J. Tschan*[1], Sarah D. Busslinger*[1], Peter Bernhardt[2], Pascal V. Grundler[1], Jan Rijn Zeevaart[3], Ulli Köster[4], Nicholas P. van der Meulen[1,5], Roger Schibli[1,6], and Cristina Müller[1,6]

[1]*Center for Radiopharmaceutical Sciences ETH–PSI, Paul Scherrer Institute, Villigen-PSI, Switzerland;* [2]*Department of Radiation Physics, Institution of Clinical Science, Sahlgrenska Academy, University of Gothenburg, Gothenburg, Sweden;* [3]*Radiochemistry, South African Nuclear Energy Corporation (Necsa), Brits, South Africa;* [4]*Institut Laue-Langevin, Grenoble, France;* [5]*Laboratory of Radiochemistry, Paul Scherrer Institute, Villigen-PSI, Switzerland; and* [6]*Department of Chemistry and Applied Biosciences, ETH Zurich, Zurich, Switzerland*

The favorable decay characteristics of ^{161}Tb attracted the interest of clinicians in using this novel radionuclide for radioligand therapy (RLT). ^{161}Tb decays with a similar half-life to ^{177}Lu, but beyond the emission of β^--particles and γ-rays, ^{161}Tb also emits conversion and Auger electrons, which may be particularly effective to eliminate micrometastases. The aim of this study was to compare the dosimetry and therapeutic efficacy of ^{161}Tb and ^{177}Lu in tumor-bearing mice using SibuDAB and PSMA-I&T, which differ in their blood residence time and tumor uptake. **Methods:** [^{161}Tb]Tb-SibuDAB and [^{161}Tb]Tb-PSMA-I&T were evaluated in vitro and investigated in biodistribution, imaging, and therapy studies using PC-3 PIP tumor–bearing mice. The ^{177}Lu-labeled counterparts served for dose calculations and comparison of therapeutic efficacy. The tolerability of RLT in mice was monitored on the basis of body mass, blood plasma parameters, blood cell counts, and the histology of relevant organs and tissues. **Results:** The prostate-specific membrane antigen (PSMA)–targeting radioligands, irrespective of whether labeled with ^{161}Tb or ^{177}Lu, showed similar in vitro data and comparable tissue distribution profiles. As a result of the albumin-binding properties, [^{161}Tb]Tb/[^{177}Lu]Lu-SibuDAB had an enhanced blood residence time and higher tumor uptake (62%–69% injected activity per gram at 24 h after injection) than [^{161}Tb]Tb/[^{177}Lu]Lu-PSMA-I&T (30%–35% injected activity per gram at 24 h after injection). [^{161}Tb]Tb-SibuDAB inhibited tumor growth more effectively than [^{161}Tb]Tb-PSMA-I&T, as can be ascribed to its 4-fold increased absorbed tumor dose. At any of the applied activities, the ^{161}Tb-based radioligands were therapeutically more effective than their ^{177}Lu-labeled counterparts, as agreed with the approximately 40% increased tumor dose of ^{161}Tb compared with that of ^{177}Lu. Under the given experimental conditions, no obvious adverse events were observed. **Conclusion:** The data of this study indicate the promising potential of ^{161}Tb in combination with SibuDAB for RLT of prostate cancer. Future clinical studies using ^{161}Tb-based RLT will shed light on a potential clinical benefit of ^{161}Tb over ^{177}Lu.

Key Words: PSMA; prostate cancer; ^{161}Tb; albumin-binding radioligand; radioligand therapy

J Nucl Med 2023; 64:1625–1631
DOI: 10.2967/jnumed.123.265524

Received Jan. 28, 2023; revision accepted May 31, 2023.
For correspondence or reprints, contact Cristina Müller (cristina.mueller@psi.ch).
*Contributed equally to this work.
Published online Jul. 13, 2023.

Radioligand therapy (RLT) using prostate-specific membrane antigen (PSMA)–targeting radioligands emerged as an effective means for the treatment of patients with metastatic castration-resistant prostate cancer (*1–3*). The positive outcome of a clinical phase III study (VISION; NCT0351166) using [^{177}Lu]Lu-PSMA-617 (*4*) led to the approval of this radioligand (Pluvicto; Novartis) for the treatment of patients with PSMA-positive metastatic castration-resistant prostate cancer. [^{177}Lu]Lu-PSMA-I&T, a similar radioligand, has also been used clinically for the treatment of metastatic castration-resistant prostate cancer (*5–7*).

Currently, several clinical trials are ongoing to investigate a potential benefit of ^{177}Lu-based RLT in patients at an earlier disease stage (*8–12*). β^--particles have a relatively long tissue range (^{177}Lu, 2 mm) and thus are suitable for the treatment of macrometastases; however, they are not effective enough to eliminate micrometastases, an ability that would be essential for these patients to achieve long-term disease control. RLT using an α-particle emitter may be an option to address this situation; however, severe side effects will prevent the use of ^{225}Ac-based RLT in patients with a generally good prognosis (*13,14*).

^{161}Tb has attracted the attention of clinicians and researchers alike. It shares similar chemical properties and physical decay characteristics (β^--particles and γ-ray emission) with ^{177}Lu but coemits low-energy conversion and Auger electrons. Since Auger electrons have an ultrashort tissue range (<500 nm) and, hence, a high linear energy transfer (4–26 keV/μm), they may be particularly effective to eliminate single and clustered cancer cells (*15,16*). In our previous work, we demonstrated that ^{161}Tb outperforms ^{177}Lu in cell-based in vitro assays irrespective of the applied targeting concept (*17–19*). Preclinical therapy studies using [^{161}Tb]Tb-PSMA-617 in xenografted mice showed a dose-dependent tumor growth delay and survival.

Currently, [^{161}Tb]Tb-PSMA-I&T (VIOLET; NCT05521412 (*20*)) and [^{161}Tb]Tb-PSMA-617 (REALITY; NCT04833517 (*21*) are applied to metastatic castration-resistant prostate cancer patients in phase I and II clinical studies and on a compassionate-use basis under the local regulatory framework (*22*).

At the Paul Scherrer Institute, we have developed several generations of albumin-binding PSMA ligands that are characterized by an enhanced blood circulation time and, as a result, higher tumor accumulation than for PSMA-617 or PSMA-I&T.

[^{177}Lu]Lu-PSMA-ALB-56, derivatized with a *p*-tolyl–based albumin binder, showed promising therapeutic efficacy in preclinical studies (*23*); however, the long blood residence time observed in patients affected the bone marrow dose unfavorably (*24*). [^{177}Lu]Lu-SibuDAB, the *S*-isomer of [^{177}Lu]Lu-Ibu-DAB-PSMA (*25,26*), was developed as an optimized PSMA ligand with moderate albumin-binding properties (*27*). The tolerability of this new class of ibuprofen-derivatized PSMA radioligands was in the same range as for conventional PSMA radioligands (*26*).

The goal of this study was to investigate SibuDAB in combination with ^{161}Tb and assess the potential benefit of this novel RLT concept. We performed preclinical studies to evaluate [^{161}Tb]Tb-SibuDAB and [^{161}Tb]Tb-PSMA-I&T in comparison to their ^{177}Lu-labeled counterparts with regard to dosimetry estimations and therapeutic efficacy.

MATERIALS AND METHODS

Detailed methods are presented as a supplemental data file (supplemental materials are available at http://jnm.snmjournals.org). This study was performed in agreement with national laws and the institutional internal guidelines on radiation safety.

Radioligand Preparation and In Vitro Characterization

SibuDAB (*S*-isomer of Ibu-DAB-PSMA (*27*)) and PSMA-I&T were labeled under standard conditions at molar activities of up to 50 MBq/nmol, with radiochemical purity of more than 98% (Supplemental Figs. 1 and 2). The radiolytic stability of [^{161}Tb]Tb-SibuDAB and [^{161}Tb]Tb/[^{177}Lu]Lu-PSMA-I&T, their distribution coefficients (logD values), and cell uptake in PSMA-positive PC-3 PIP and PSMA-negative PC-3 flu tumor cells (provided by Martin Pomper, Johns Hopkins University School of Medicine) were determined as previously reported for [^{177}Lu]Lu-SibuDAB (*27*). The in vitro albumin-binding capacity of the radioligands was determined according to an established protocol (*28*).

In Vivo Studies

All applicable international, national, or institutional guidelines for the care and use of laboratory animals were followed, and all animal experiments were performed according to the guidelines of Swiss Regulations for Animal Welfare. The preclinical studies were ethically approved by the Cantonal Committee of Animal Experimentation and permitted by the responsible cantonal authorities (license 75668).

Blood Clearance

The blood clearance of [^{161}Tb]Tb-SibuDAB (25 MBq, 1 nmol per mouse) was determined as previously reported for [^{177}Lu]Lu-SibuDAB using an immunocompetent mouse strain (FVB, Friend leukemia virus B) (*27*). The collected blood samples were measured to calculate the percentage injected activity (%IA) retained in the blood over 24 h, with the activity at $t = 0$ set as 100%.

Biodistribution Studies and Dosimetry Estimation

PC-3 PIP/flu tumor–bearing nude mice (BALB/c nude, Bagg Albino) were intravenously injected with the respective radioligand (5 MBq, 1 nmol per mouse). Tissues were collected, weighed, and counted for activity using a γ-counter. The decay-corrected results were listed as %IA per gram of tissue mass (%IA/g).

Dosimetry estimations were performed for tumors (assuming a sphere of 80 mm^3) and kidneys on the basis of the time-integrated activity concentration using non–decay-corrected biodistribution data for the ^{177}Lu-labeled PSMA ligands. The Monte Carlo code PENELOPE (penetration and energy loss of positrons and electrons) was used for determination of the energy deposits in the tissues (*29*).

Dual-Isotope SPECT/CT Imaging

Dual-isotope SPECT/CT was performed according to a previously established protocol using a small-animal SPECT/CT scanner (*27*). PC-3 PIP/flu tumor–bearing BALB/c nude mice were injected with a mixture of [^{161}Tb]Tb-SibuDAB and [^{177}Lu]Lu-SibuDAB or [^{161}Tb]Tb-PSMA-I&T and [^{177}Lu]Lu-PSMA-I&T (20 MBq, 1 nmol per mouse in total). The images were reconstructed on the basis of γ-lines of ^{161}Tb or ^{177}Lu or the combined γ-lines.

Therapy Study

PC-3 PIP tumor–bearing BALB/c nude mice were treated with either [^{161}Tb]Tb-SibuDAB or [^{177}Lu]Lu-SibuDAB (2, 5, or 10 MBq, 1 nmol per mouse) or with [^{161}Tb]Tb-PSMA-I&T or [^{177}Lu]Lu-PSMA-I&T (5 or 10 MBq, 1 nmol per mouse). Control mice received only vehicle (saline with 0.05% bovine serum albumin) (Supplemental Table 1). The body mass and tumor volume of the mice were monitored (*27*). The area under the curve of the relative tumor volume (AUC_{RTV}) for each mouse in a group was calculated and expressed as the average value per group. The median survival of mice was determined as a measure of the radioligands' therapeutic efficacy. Potential adverse events were determined on the basis of body mass, plasma parameters, blood cell counts, and analysis of histologic changes using a predefined scoring system (Supplemental Table 2).

Analysis and Statistical Methods

GraphPad Prism software (version 8) was used for data analysis, including determination of statistical significance ($P < 0.05$) and preparation of graphs.

RESULTS

In Vitro Characterization of Radioligands

The radioligands (25 MBq/nmol) were stable over 4 h in saline at room temperature (>95% of intact radioligand). The logD values of [^{161}Tb]Tb-SibuDAB (-2.5 ± 0.1) and [^{161}Tb]Tb-PSMA-I&T (<−4) were similar to those of [^{177}Lu]Lu-SibuDAB (-2.3 ± 0.1 (*27*)) and [^{177}Lu]Lu-PSMA-I&T (<−4), respectively.

PC-3 PIP tumor cell uptake and internalization of [^{161}Tb]Tb-SibuDAB (54% ± 1% and 18% ± 2%, respectively) and [^{161}Tb]Tb-PSMA-I&T (42% ± 6% and 11% ± 2%, respectively) were in the same range as for their respective ^{177}Lu-labeled counterparts (Fig. 1A). Negligible uptake of the radioligands (<1%) was observed in PC-3 flu cells.

The protein-bound fraction of [^{161}Tb]Tb-SibuDAB and [^{177}Lu]Lu-SibuDAB (*28*) was approximately 90% in undiluted mouse and human blood plasma (Figs. 1B and 1C) but much lower for [^{161}Tb]Tb-PSMA-I&T and [^{177}Lu]Lu-PSMA-I&T (50%–60%) (Figs. 1B and 1C). Affinity curves determined using variable serum albumin-to-radioligand molar ratios confirmed the strong plasma protein binding of SibuDAB as compared with only moderate binding of PSMA-I&T irrespective of the used radionuclide in both mouse and human plasma (Figs. 1B and 1C).

Blood Clearance and Biodistribution Data

Equal blood clearance curves were obtained for [^{161}Tb]Tb-SibuDAB as previously determined for [^{177}Lu]Lu-SibuDAB (*27*) in immunocompetent mice without tumors ($P > 0.05$; Fig. 2A).

The blood retention of [^{161}Tb]Tb-SibuDAB in tumor-bearing BALB/c nude mice (6.5 ± 3.7 %IA/g and 0.32 ± 0.05 %IA/g at 4 and 24 h after injection, respectively) was considerably enhanced as compared with that of [^{161}Tb]Tb-PSMA-I&T (<0.1%IA/g at 4 h after injection). As a result, the tumor uptake of [^{161}Tb]Tb-SibuDAB was almost twice as high (75 ± 5 %IA/g) as for [^{161}Tb]Tb-PSMA-I&T

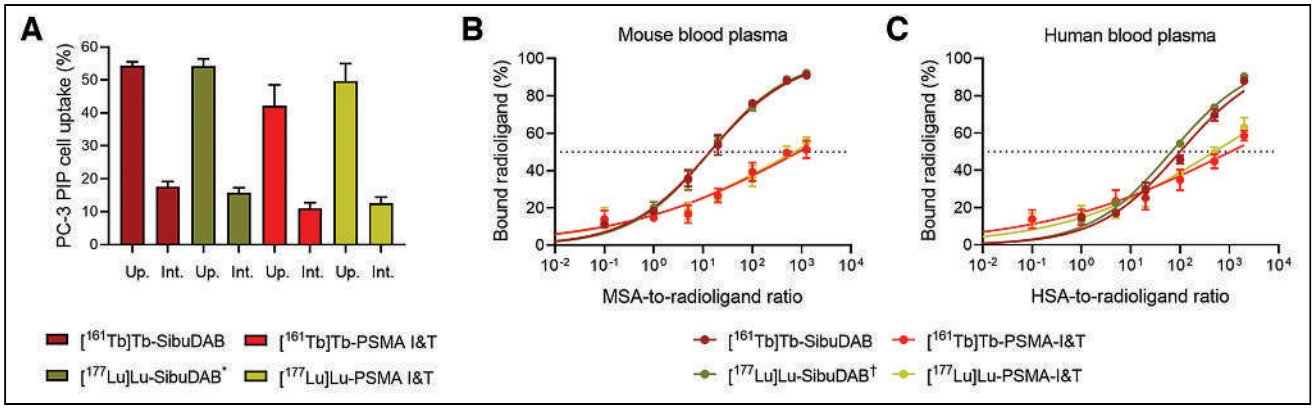

FIGURE 1. (A) Cell uptake and internalization of [^{161}Tb]Tb/[^{177}Lu]Lu-SibuDAB and [^{161}Tb]Tb/[^{177}Lu]Lu-PSMA-I&T in PC-3 PIP cells after 4 h of incubation (average ± SD). (B and C) In vitro albumin-binding curves of [^{161}Tb]Tb/[^{177}Lu]Lu-SibuDAB and [^{161}Tb]Tb/[^{177}Lu]Lu-PSMA-I&T in mouse (B) and human (C) blood plasma. Dashed line indicates half-maximum (i.e., 50%) binding. HSA = human serum albumin; Int. = internalization; MSA = mouse serum albumin; Up. = uptake. *Data were previously published (*27*). †Data were previously published (*28*).

(42 ± 14 %IA/g) at 4 h after injection (Fig. 2B; Supplemental Tables 3 and 4). Kidney retention of [^{161}Tb]Tb-SibuDAB (16 ± 1 %IA/g) was in a similar range to that for [^{161}Tb]Tb-PSMA-I&T (18 ± 3 %IA/g) at this same time point. At the 24-h time point, less than 7 %IA/g was retained in the kidneys for both radioligands. Uptake in the tumors and kidneys at 4 and 24 h after injection of the ^{161}Tb-based PSMA ligands did not significantly differ from that for the ^{177}Lu-based counterparts ($P > 0.05$; Supplemental Tables 3 and 4). At 4 h after injection of any of the radioligands, activity retention was already less than 2% in nontargeted tissues such as the liver, spleen, and bone (Fig. 2B).

Dual-Isotope SPECT Imaging Studies

The SPECT images reconstructed on the basis of the γ-lines of ^{161}Tb or ^{177}Lu showed equal distribution in the blood, tumor, and kidneys of the same mouse, irrespective of the used radionuclide (Fig. 3). At 1 h after injection of [^{161}Tb]Tb-SibuDAB/[^{177}Lu]Lu-SibuDAB, blood retention was increased as compared with that of [^{161}Tb]Tb-PSMA-I&T/[^{177}Lu]Lu-PSMA-I&T, whereas kidney retention appeared somewhat lower for the former. At the 4-h time point, the differences between radiolabeled SibuDAB and PSMA-I&T were less pronounced (Fig. 3).

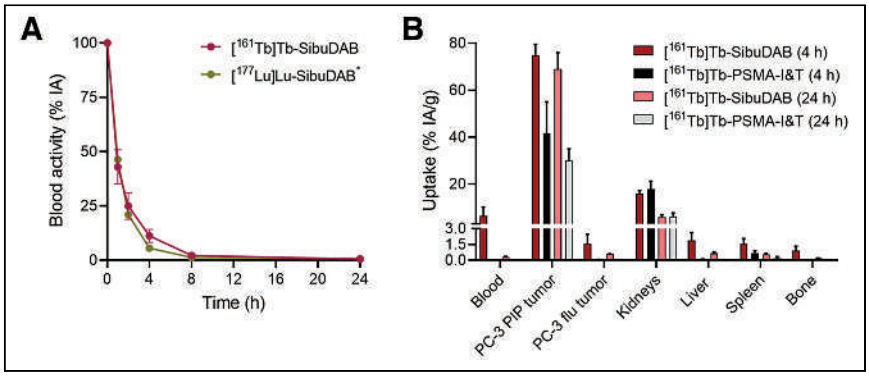

FIGURE 2. (A) Blood clearance of [^{161}Tb]Tb-SibuDAB and [^{177}Lu]Lu-SibuDAB over 24 h after injection. (B) Decay-corrected biodistribution data 4 and 24 h after injection of [^{161}Tb]Tb-SibuDAB and [^{161}Tb]Tb-PSMA-I&T. PC-3 flu = PSMA-negative tumor xenografts; PC-3 PIP = PSMA-positive tumor xenograft. *Data were previously published (*27*).

Dosimetry Estimations

Dosimetry data were calculated using extended biodistribution data acquired with the ^{177}Lu-based radioligands (Supplemental Tables 5 and 6), assuming equal distribution profiles for the ^{161}Tb- and ^{177}Lu-labeled counterparts (Figs. 2A and 3; Supplemental Tables 3 and 4). The mean absorbed PC-3 PIP tumor dose of [^{161}Tb]Tb-SibuDAB (10.8 ± 1.6 Gy/MBq) was about 40% higher than for [^{177}Lu]Lu-SibuDAB (7.7 ± 1.1 Gy/MBq), and the same held true for [^{161}Tb]Tb-PSMA-I&T (2.9 ± 0.3 Gy/MBq) as compared with [^{177}Lu]Lu-PSMA-I&T (2.1 ± 0.2 Gy/MBq). The mean absorbed kidney dose was 0.44 ± 0.04 Gy/MBq and 0.59 ± 0.04 Gy/MBq for the respective ^{161}Tb-labeled ligands and 0.32 ± 0.03 Gy/MBq and 0.43 ± 0.03 Gy/MBq for the ^{177}Lu-labeled counterparts. [^{161}Tb]Tb/[^{177}Lu]Lu-SibuDAB demonstrated an approximately 5-fold higher tumor-to-kidney dose ratio (~24.5) than [^{161}Tb]Tb/[^{177}Lu]Lu-PSMA-I&T (~4.8) (Supplemental Table 7).

Therapeutic Efficacy of Radioligands

In control mice, the tumors grew rapidly over time, with all mice reaching a predefined endpoint between days 14 and 28 (median survival, 18 d). ^{161}Tb-labeled PSMA ligands were consistently more effective at delaying tumor growth than the respective ^{177}Lu-labeled counterparts, irrespective of whether SibuDAB or PSMA-I&T was used (Fig. 4; Table 1). The increased therapeutic efficacy of [^{161}Tb]Tb-SibuDAB over [^{177}Lu]Lu-SibuDAB was most visible in mice that received 2 MBq, as demonstrated by a median survival of 32.5 versus 23 d, respectively. All mice treated with 5 MBq of [^{161}Tb]Tb-SibuDAB survived until study end, whereas 1 of 6 mice treated with 5 MBq [^{177}Lu]Lu-SibuDAB reached an endpoint on day 49. Treatment of the mice with 10 MBq of [^{161}Tb]Tb-SibuDAB resulted in complete tumor regression over the 2-mo observation period, whereas tumor regrowth was observed in 1 case approximately 6 wk after treatment with 10 MBq of [^{177}Lu]Lu-SibuDAB (Figs. 4A and 4C).

When the application was 5 MBq per mouse, 3 of 6 mice treated with [^{161}Tb]Tb-PSMA-I&T were alive at study end (median

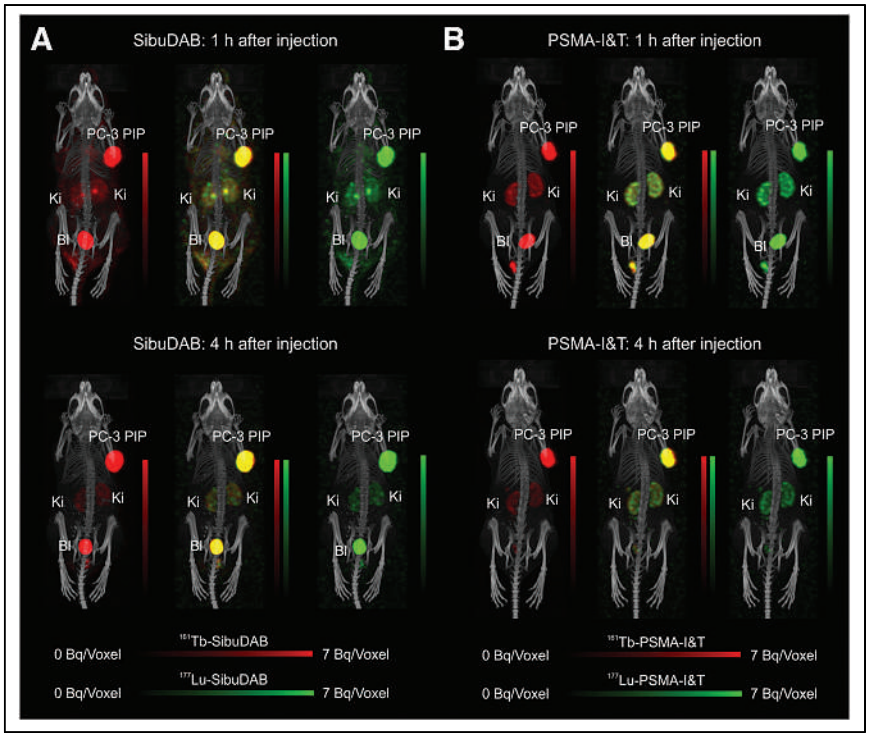

FIGURE 3. Dual-isotope SPECT/CT images of mice bearing PC-3 PIP (right shoulder) and PC-3 flu (left shoulder) tumor xenografts 1 and 4 h after injection of 1:1 mixture (20 MBq per mouse) of [^{161}Tb]Tb-SibuDAB and [^{177}Lu]Lu-SibuDAB (A) or [^{161}Tb]Tb-PSMA-I&T and [^{177}Lu]Lu-PSMA-I&T (B). Image reconstruction was based on γ-lines of ^{161}Tb (red), ^{177}Lu (green), or both (red/green overlay). Bl = bladder; Ki = kidneys; PC-3 flu = PSMA-negative tumor xenograft; PC-3 PIP = PSMA-positive tumor xenograft.

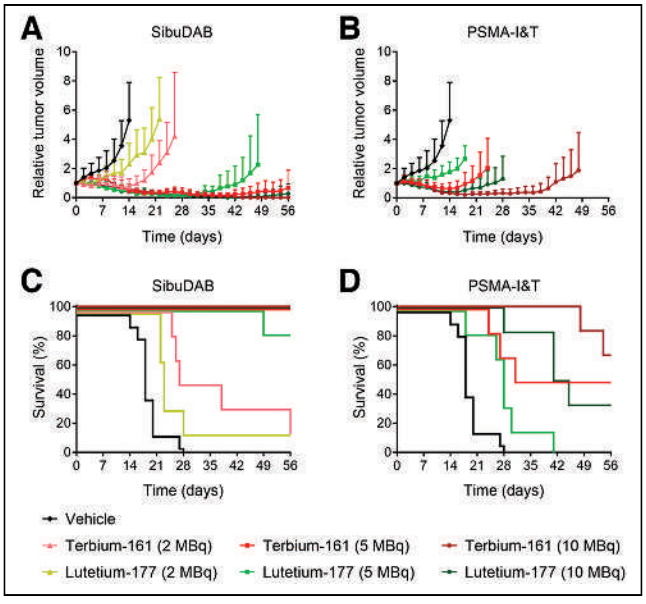

FIGURE 4. (A and B) Relative tumor growth curves shown until first mouse of respective group reached endpoint. (C and D) Kaplan–Meier plot (vertical offset was applied to improve readability). Mice received vehicle or were treated with [^{161}Tb]Tb-SibuDAB or [^{177}Lu]Lu-SibuDAB (A and C) or with [^{161}Tb]Tb-PSMA-I&T or [^{177}Lu]Lu-PSMA-I&T (B and D). (Data of control group and mice treated with 5 MBq and 10 MBq of [^{177}Lu]Lu-SibuDAB were previously published (*27,28*).)

survival, 43.5 d), whereas all mice treated with [^{177}Lu]Lu-PSMA-I&T reached an endpoint by day 41 (median survival, 28 d). When the application was 10 MBq, 4 of 6 mice injected with [^{161}Tb]Tb-PSMA-I&T were alive at study end, whereas only 1 of 6 mice in the group that received [^{177}Lu]Lu-PSMA-I&T was alive at study end (Figs. 4B and 4D).

The therapeutic efficacy was quantitatively expressed as the average of the AUC_{RTV} for mice in each group (Table 1). These values were 1.3-fold and 1.7-fold smaller for mice injected with 2 MBq or 5 MBq, respectively, of [^{161}Tb]Tb-SibuDAB than for mice treated ith equal activities of [^{177}Lu]Lu-SibuDAB. The AUC_{RTV} was 2.4- and 2.2-fold lower for mice that received 5 or 10 MBq of [^{161}Tb]Tb-PSMA-I&T, respectively, than for mice treated with equal activities of [^{177}Lu]Lu-PSMA-I&T.

Analysis of Potential Adverse Events During Therapy

The body mass of mice with effective tumor shrinkage increased over time, with the average body mass of mice treated with 10 MBq of radioligand being in the same range on the day of euthanasia as for untreated, non–tumor-bearing control mice of the same age ($P > 0.05$; Supplemental Fig. 3). In contrast, rapid tumor growth was associated with body mass loss, which was observed for PC-3 PIP tumor–bearing mice that received only vehicle and for mice treated with the lowest activity.

Blood urea nitrogen, albumin, alkaline phosphatase, and total bilirubin in blood plasma were in the same range for mice treated with 10 MBq of radioligands and non–tumor-bearing control mice. The same held true for blood cell counts ($P > 0.05$; Fig. 5; Supplemental Tables 8 and 9). The leukocyte, erythrocyte, and thrombocyte counts were in the reference range irrespective of the applied treatment. Histopathologic analysis of the kidneys, liver, salivary glands, spleen, and bone marrow did not indicate any changes after RLT (Supplemental Table 10).

DISCUSSION

Several preclinical studies demonstrated the superiority of ^{161}Tb over ^{177}Lu (*17,18,30*), which was supported by dose calculations that consistently proposed the benefit of the coemitted conversion and Auger electrons by ^{161}Tb (*15,16,31*). The fact that ^{161}Tb can be produced in large quantities, in analogy to ^{177}Lu (*32*), and the commercial interest of companies to produce ^{161}Tb make this radionuclide particularly attractive for clinical translation.

In agreement with our previous study performed with [^{161}Tb]Tb-PSMA-617 and [^{177}Lu]Lu-PSMA-617 (*18*), the in vitro properties and tissue distribution profiles of [^{161}Tb]Tb-SibuDAB and [^{161}Tb]Tb-PSMA-I&T were similar to their respective ^{177}Lu-labeled counterparts. Dosimetry estimations were thus based on data obtained with [^{177}Lu]Lu-SibuDAB and [^{177}Lu]Lu-PSMA-I&T. Estimation of the radiation dose of [^{161}Tb]Tb-SibuDAB and [^{161}Tb]Tb-PSMA-I&T would most likely be feasible also for clinical data currently being

TABLE 1
Parameters Indicative of Efficacy of Treatment

Treatment	Injected activity (MBq)	First mouse euthanized (d)*	Last mouse euthanized (d)*	Median survival (d)	Mice alive on day 56	AUC_{RTV}
Saline†	—	14	28	18	0/12	477 ± 148
[^{161}Tb]Tb-SibuDAB	2	25	56	32.5	1/6	233 ± 111
[^{177}Lu]Lu-SibuDAB	2	22	56	23	1/6	306 ± 172
[^{161}Tb]Tb-SibuDAB	5	56	56	>>56‡	6/6	29 ± 16
[^{177}Lu]Lu-SibuDAB†	5	49	56	>>56‡	5/6	50 ± 50
[^{161}Tb]Tb-SibuDAB	10	56	56	>>56‡	6/6	20 ± 5
[^{177}Lu]Lu-SibuDAB§	10	56	56	>>56‡	6/6	18 ± 8
[^{161}Tb]Tb-PSMA-I&T	5	24	56	43.5	3/6	147 ± 134
[^{177}Lu]Lu-PSMA-I&T	5	18	41	28	0/6	356 ± 177
[^{161}Tb]Tb-PSMA-I&T	10	48	56	>>56‡	4/6	49 ± 42
[^{177}Lu]Lu-PSMA-I&T	10	28	56	43	2/6	108 ± 81

*All mice that did not reach endpoint were euthanized on day 56.
†Data were previously published (*27*).
‡Exact median survival could not be defined, since more than half of mice survived until study end (day 56).
§Data were previously published (*28*).

acquired for [^{177}Lu]Lu-SibuDAB and already published for [^{177}Lu]Lu-PSMA-I&T (*33*). ^{161}Tb delivers a slightly higher dose to the tissue than ^{177}Lu because of the 15% increased β^--energy (average β^- energy, 154 vs. 134 keV). More importantly, the coemission of conversion and Auger electrons contributes substantially to the enhanced dose of ^{161}Tb depending on the sphere radius assumed for the tumor size (*15*). In the current study, the absorbed tumor dose estimated for the ^{161}Tb-based PSMA ligands was 40% higher than that of the ^{177}Lu-based counterparts. As a result, and in agreement with previous studies using other targeting agents (*17,30*), our data showed consistently enhanced antitumor efficacy and prolonged survival in mice treated with the ^{161}Tb-labeled versions of SibuDAB and PSMA-I&T as compared with mice that received their ^{177}Lu-labeled counterparts.

Because the albumin-binding properties of SibuDAB enhanced tumor uptake considerably, [^{161}Tb]Tb-SibuDAB demonstrated an approximately 4-fold higher absorbed tumor dose than [^{161}Tb]Tb-PSMA-I&T. [^{161}Tb]Tb-SibuDAB, applied at the same activity as [^{161}Tb]Tb-PSMA-I&T, thus showed better therapeutic efficacy as demonstrated by the 2.5- to 5-fold enhanced tumor growth inhibition quantified on the basis of the AUC_{RTV}. According to dosimetry calculations, a complete tumor response could most likely also be achieved with approximately 20 MBq of [^{161}Tb]Tb-PSMA-I&T or approximately 25 MBq of [^{177}Lu]Lu-PSMA-I&T applied under the given experimental conditions.

Since the absorbed kidney dose was similar for both radioligands, [^{161}Tb]Tb-SibuDAB showed a more favorable tumor-to-kidney dose ratio than [^{161}Tb]Tb-PSMA-I&T. Assuming 23 Gy as the kidney dose limit (*34*), 4–5 therapy cycles of 10 MBq of [^{161}Tb]Tb-SibuDAB or [^{161}Tb]Tb-PSMA-I&T could be safely applied; thus, no kidney toxicity was observed in our study. In agreement with other reported preclinical studies (*35*), kidney uptake was considerably higher for [^{161}Tb]Tb/[^{177}Lu]Lu-PSMA-I&T than for [^{161}Tb]Tb/[^{177}Lu]Lu-PSMA-617 tested in the same tumor mouse model (*18*). In patients, renal retention of [^{177}Lu]Lu-PSMA-I&T and [^{177}Lu]Lu-PSMA-617 was more similar (*36*) and radionephrotoxicity was only rarely reported in the literature (*37,38*).

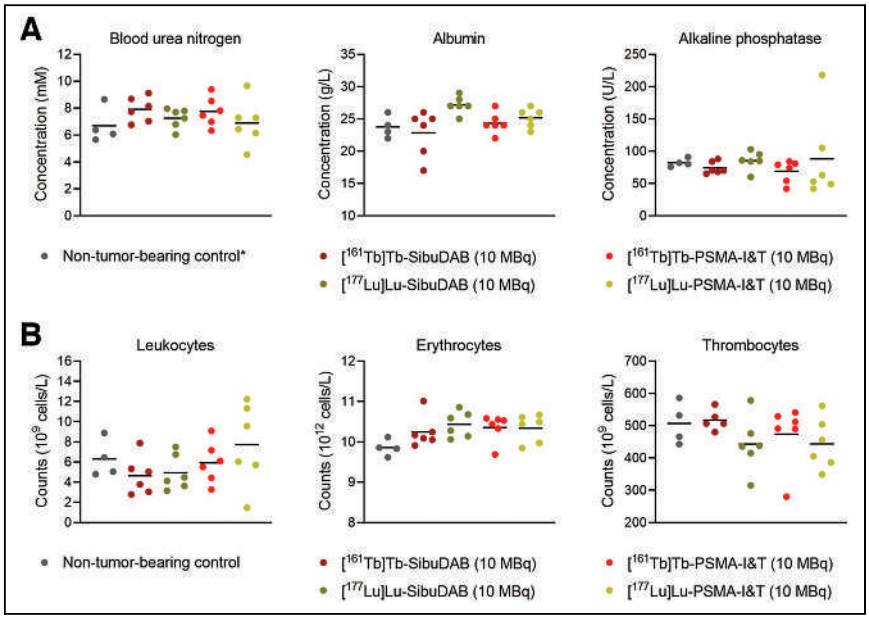

FIGURE 5. (A) Blood plasma parameters: blood urea nitrogen, albumin, and alkaline phosphatase. (B) Blood cell counts of leukocytes, erythrocytes, and thrombocytes. *Data were previously published (*28*).

Regarding other organs and tissues, the applied RLT in our study was well tolerated in mice, irrespective of the ligand and radionuclide applied. It is noteworthy, however, that salivary gland toxicity cannot be investigated in mice and therefore has to be carefully assessed in clinical studies conducted with ^{161}Tb-based RLT.

Because mice seem to be less susceptible to undesired effects of RLT than humans, much higher activities would probably be necessary to observe hematotoxicity (*39,40*). Indeed, previous experiments showed that [^{177}Lu]Lu-(*R/S*)-Ibu-DAB-PSMA (30 MBq per mouse) was well tolerated in immunocompetent mice over the first month after treatment (*26*).

Potential limitations of our study relate to the fact that an extrapolation from mice to men may not be easily feasible and that bone marrow dose calculations can hardly be performed for mice. It is likely, however, that bone marrow represents the dose-limiting organ for application of albumin-binding PSMA radioligands. Investigations of the tissue distribution profile of [^{161}Tb]Tb/[^{177}Lu]Lu-SibuDAB thus remain to be assessed in patients, and the favorable preclinical findings of using ^{161}Tb remain to be confirmed clinically. As the proposed benefit of using ^{161}Tb over ^{177}Lu refers mainly to the elimination of single cancer cells and micrometastases, ^{161}Tb-based radioligands should be tested in a follow-up study using mouse models of metastasized disease.

CONCLUSION

The superior therapeutic efficacy of ^{161}Tb over ^{177}Lu in combination with PSMA ligands agreed with the increased estimated absorbed tumor dose. The data of this study indicate particularly promising potential for [^{161}Tb]Tb-SibuDAB in the RLT of prostate cancer patients. Generally, the clinical translation of ^{161}Tb-based RLT appears promising, yet the therapeutic window for each of these radioligands must be carefully assessed.

DISCLOSURE

Viviane Tschan was funded by an iDoc grant from the Personalized Medicine and Related Technology program (PHRT-301; principal investigator, Cristina Müller). The research was supported by the Swiss Cancer Research Foundation (KFS-4678-02-2019-R; principal investigator, Cristina Müller) and by the Swiss National Science Foundation (310030_188978; principal investigator, Cristina Müller). Peter Bernhardt received grants from the Swedish Cancer Society, the Swedish Research Council, the King Gustav V Jubilee Clinic Cancer Research Foundation, and the Swedish state under the agreement between the Swedish government and the county councils (an ALF agreement). The project was further supported by ITM Isotope Technologies Munich SE, Germany, which delivered free ^{177}Lu for all the performed studies. The following is a competing financial interest: patent applications on albumin-binding PSMA ligands have been filed by ITM Isotope Technologies Munich SE, Germany, in which Roger Schibli and Cristina Müller are listed as coinventors. No other potential conflict of interest relevant to this article was reported.

ACKNOWLEDGMENTS

We thank Luisa M. Deberle, Anna E. Becker, Susan Cohrs, Fan Sozzi-Guo, Colin Hillhouse, and Rebekka Mayer for technical assistance with the experiments at Paul Scherrer Institute, Switzerland.

KEY POINTS

QUESTIONS: How effective is the therapeutic application of ^{161}Tb in combination with albumin-binding and conventional PSMA ligands in comparison to their respective ^{177}Lu-labeled analogs?

PERTINENT FINDINGS: These preclinical therapy studies confirmed the benefit of ^{161}Tb-based RLT over ^{177}Lu-based RLT in PSMA-positive tumor-bearing mice. It was also shown that [^{161}Tb]Tb-SibuDAB was more powerful than [^{161}Tb]Tb-PSMA-I&T because of its increased tumor uptake and, hence, absorbed tumor dose.

IMPLICATIONS FOR PATIENT CARE: These preclinical data set the basis for future clinical translation of ^{161}Tb-based RLT using albumin-binding and conventional PSMA radioligands.

REFERENCES

1. Kulkarni HR, Singh A, Schuchardt C, et al. PSMA-based radioligand therapy for metastatic castration-resistant prostate cancer: the Bad Berka experience since 2013. *J Nucl Med.* 2016;57(suppl 3):97S–104S.
2. Rahbar K, Ahmadzadehfar H, Kratochwil C, et al. German multicenter study investigating ^{177}Lu-PSMA-617 radioligand therapy in advanced prostate cancer patients. *J Nucl Med.* 2017;58:85–90.
3. Violet J, Sandhu S, Iravani A, et al. Long-term follow-up and outcomes of retreatment in an expanded 50-patient single-center phase II prospective trial of ^{177}Lu-PSMA-617 theranostics in metastatic castration-resistant prostate cancer. *J Nucl Med.* 2020;61:857–865.
4. Sartor O, de Bono J, Chi KN, et al. Lutetium-177-PSMA-617 for metastatic castration-resistant prostate cancer. *N Engl J Med.* 2021;385:1091–1103.
5. Weineisen M, Schottelius M, Simecek J, et al. ^{68}Ga- and ^{177}Lu-labeled PSMA I&T: optimization of a PSMA-targeted theranostic concept and first proof-of-concept human studies. *J Nucl Med.* 2015;56:1169–1176.
6. Chatalic KL, Heskamp S, Konijnenberg M, et al. Towards personalized treatment of prostate cancer: PSMA I&T, a promising prostate-specific membrane antigen-targeted theranostic agent. *Theranostics.* 2016;6:849–861.
7. Heck MM, Tauber R, Schwaiger S, et al. Treatment outcome, toxicity, and predictive factors for radioligand therapy with ^{177}Lu-PSMA-I&T in metastatic castration-resistant prostate cancer. *Eur Urol.* 2019;75:920–926.
8. Privé BM, Janssen MJR, van Oort IM, et al. Update to a randomized controlled trial of lutetium-177-PSMA in oligo-metastatic hormone-sensitive prostate cancer: the BULLSEYE trial. *Trials.* 2021;22:768.
9. Azad A, Dhiantravan N, Emmett L, et al. UpFrontPSMA: a randomized phase II study of sequential ^{177}Lu-PSMA617 and docetaxel versus docetaxel in metastatic hormone-naïve prostate cancer (mHNPC) [abstract]. *J Clin Oncol.* 2021;39(suppl): TPS180.
10. Alghazo O, Eapen R, Dhiantravan N, et al. Study of the dosimetry, safety, and potential benefit of ^{177}Lu-PSMA-617 radionuclide therapy prior to radical prostatectomy in men with high-risk localized prostate cancer (LuTectomy study) [abstract]. *J Clin Oncol.* 2021;39(suppl):TPS264.
11. Sartor AO, Tagawa ST, Saad F, et al. PSMAddition: a phase 3 trial to compare treatment with ^{177}Lu-PSMA-617 plus standard of care (SOC) versus SOC alone in patients with metastatic hormone-sensitive prostate cancer [abstract]. *J Clin Oncol.* 2022;40(suppl):TPS210.
12. Golan S, Frumer M, Zohar Y, et al. Neoadjuvant ^{177}Lu-PSMA-I&T radionuclide treatment in patients with high-risk prostate cancer before radical prostatectomy: a single-arm phase 1 trial. *Eur Urol Oncol.* 2023;6:151–159.
13. Feuerecker B, Tauber R, Knorr K, et al. Activity and adverse events of actinium-225-PSMA-617 in advanced metastatic castration-resistant prostate cancer after failure of lutetium-177-PSMA. *Eur Urol.* 2021;79:343–350.
14. Lee DY, Kim YI. Effects of ^{225}Ac-labeled prostate-specific membrane antigen radioligand therapy in metastatic castration-resistant prostate cancer: a meta-analysis. *J Nucl Med.* 2022;63:840–846.
15. Hindié E, Zanotti-Fregonara P, Quinto MA, Morgat C, Champion C. Dose deposits from ^{90}Y, ^{177}Lu, ^{111}In, and ^{161}Tb in micrometastases of various sizes: implications for radiopharmaceutical therapy. *J Nucl Med.* 2016;57:759–764.
16. Alcocer-Avila ME, Ferreira A, Quinto MA, Morgat C, Hindie E, Champion C. Radiation doses from ^{161}Tb and ^{177}Lu in single tumour cells and micrometastases. *EJNMMI Phys.* 2020;7:33.

17. Müller C, Reber J, Haller S, et al. Direct in vitro and in vivo comparison of ^{161}Tb and ^{177}Lu using a tumour-targeting folate conjugate. *Eur J Nucl Med Mol Imaging.* 2014;41:476–485.
18. Müller C, Umbricht CA, Gracheva N, et al. Terbium-161 for PSMA-targeted radionuclide therapy of prostate cancer. *Eur J Nucl Med Mol Imaging.* 2019;46: 1919–1930.
19. Borgna F, Barritt P, Grundler PV, et al. Simultaneous visualization of ^{161}Tb- and ^{177}Lu-labeled somatostatin analogues using dual-isotope SPECT imaging. *Pharmaceutics.* 2021;13:536.
20. Buteau JP, Kostos LK, Alipour R, et al. VIOLET: a phase I/II trial evaluation of radioligand treatment in men with metastatic castration-resistant prostate cancer with [^{161}Tb]Tb-PSMA-I&T [abstract]. *J Clin Oncol.* 2023;41(suppl):TPS281.
21. Rosar F, Maus S, Schaefer-Schuler A, Burgard C, Khreish F, Ezziddin S. New horizons in radioligand therapy: ^{161}Tb-PSMA-617 in advanced mCRPC. *Clin Nucl Med.* 2023;48:433–434.
22. Al-Ibraheem A, Doudeen RM, Juaidi D, Abufara A, Maus S. ^{161}Tb-PSMA radioligand therapy: first-in-human SPECT/CT imaging. *J Nucl Med.* February 9, 2023 [Epub ahead of print].
23. Umbricht CA, Benesova M, Schibli R, Müller C. Preclinical development of novel PSMA-targeting radioligands: modulation of albumin-binding properties to improve prostate cancer therapy. *Mol Pharm.* 2018;15:2297–2306.
24. Kramer V, Fernandez R, Lehnert W, et al. Biodistribution and dosimetry of a single dose of albumin-binding ligand [^{177}Lu]Lu-PSMA-ALB-56 in patients with mCRPC. *Eur J Nucl Med Mol Imaging.* 2021;48:893–903.
25. Deberle LM, Benesova M, Umbricht CA, et al. Development of a new class of PSMA radioligands comprising ibuprofen as an albumin-binding entity. *Theranostics.* 2020;10:1678–1693.
26. Tschan VJ, Borgna F, Busslinger SD, et al. Preclinical investigations using [^{177}Lu]Lu-Ibu-DAB-PSMA toward its clinical translation for radioligand therapy of prostate cancer. *Eur J Nucl Med Mol Imaging.* 2022;49:3639–3650.
27. Borgna F, Deberle LM, Busslinger SD, et al. Preclinical investigations to explore the difference between the diastereomers [^{177}Lu]Lu-SibuDAB and [^{177}Lu]Lu-RibuDAB toward prostate cancer therapy. *Mol Pharm.* 2022;19:2105–2114.
28. Busslinger SD, Tschan VJ, Richard OK, Talip Z, Schibli R, Müller C. [^{225}Ac]Ac-SibuDAB for targeted alpha therapy of prostate cancer: preclinical evaluation and comparison with [^{225}Ac]Ac-PSMA-617. *Cancers (Basel).* 2022;14:5651.
29. Salvat F. *PENELOPE-2014: A Code System for Monte Carlo Simulation of Electron and Photon Transport.* OECD; 2015:1–386.
30. Borgna F, Haller S, Rodriguez JMM, et al. Combination of terbium-161 with somatostatin receptor antagonists: a potential paradigm shift for the treatment of neuroendocrine neoplasms. *Eur J Nucl Med Mol Imaging.* 2022;49:1113–1126.
31. Bernhardt P, Svensson J, Hemmingsson J, et al. Dosimetric analysis of the short-ranged particle emitter ^{161}Tb for radionuclide therapy of metastatic prostate cancer. *Cancers (Basel).* 2021;13:2011.
32. Gracheva N, Müller C, Talip Z, et al. Production and characterization of no-carrier-added ^{161}Tb as an alternative to the clinically-applied ^{177}Lu for radionuclide therapy. *EJNMMI Radiopharm Chem.* 2019;4:12.
33. Okamoto S, Thieme A, Allmann J, et al. Radiation dosimetry for ^{177}Lu-PSMA I&T in metastatic castration-resistant prostate cancer: absorbed dose in normal organs and tumor lesions. *J Nucl Med.* 2017;58:445–450.
34. Haller S, Reber J, Brandt S, et al. Folate receptor-targeted radionuclide therapy: preclinical investigation of anti-tumor effects and potential radionephropathy. *Nucl Med Biol.* 2015;42:770–779.
35. Ruigrok EAM, van Vliet N, Dalm SU, et al. Extensive preclinical evaluation of lutetium-177-labeled PSMA-specific tracers for prostate cancer radionuclide therapy. *Eur J Nucl Med Mol Imaging.* 2021;48:1339–1350.
36. Schuchardt C, Zhang J, Kulkarni HR, Chen X, Muller D, Baum RP. Prostate-specific membrane antigen radioligand therapy using ^{177}Lu-PSMA I&T and ^{177}Lu-PSMA-617 in patients with metastatic castration-resistant prostate cancer: comparison of safety, biodistribution, and dosimetry. *J Nucl Med.* 2022;63:1199–1207.
37. Hartrampf PE, Weinzierl FX, Serfling SE, et al. Hematotoxicity and nephrotoxicity in prostate cancer patients undergoing radioligand therapy with [^{177}Lu]Lu-PSMA I&T. *Cancers (Basel).* 2022;14:647.
38. Hartrampf PE, Weinzierl FX, Buck AK, et al. Matched-pair analysis of [^{177}Lu]Lu-PSMA I&T and [^{177}Lu]Lu-PSMA-617 in patients with metastatic castration-resistant prostate cancer. *Eur J Nucl Med Mol Imaging.* 2022;49:3269–3276.
39. Fendler WP, Stuparu AD, Evans-Axelsson S, et al. Establishing ^{177}Lu-PSMA-617 radioligand therapy in a syngeneic model of murine prostate cancer. *J Nucl Med.* 2017;58:1786–1792.
40. Kristiansson A, Vilhelmsson Timmermand O, Altai M, et al. Hematological toxicity in mice after high activity injections of ^{177}Lu-PSMA-617. *Pharmaceutics.* 2022;14:731.

Tumor Control Probability and Small-Scale Monte Carlo Dosimetry: Effects of Heterogenous Intratumoral Activity Distribution in Radiopharmaceutical Therapy

Emma Mellhammar[1], Magnus Dahlbom[2], Oskar Vilhelmsson-Timmermand[1,3], and Sven-Erik Strand[1,4]

[1]Oncology, Department of Clinical Sciences Lund, Lund University, Lund, Sweden; [2]Department of Molecular and Medical Pharmacology, David Geffen School of Medicine, UCLA, Los Angeles, California; [3]Imaging Chemistry and Biology, King's College London, London, United Kingdom; and [4]Medical Radiation Physics, Department of Clinical Sciences Lund, Lund University, Lund, Sweden

In radiopharmaceutical therapy, intratumoral uptake of radioactivity usually leads to heterogeneous absorbed dose distribution. The likelihood of treatment success can be estimated with the tumor control probability (TCP), which requires accurate dosimetry, estimating the absorbed dose rate per unit activity to individual tumor cells. **Methods:** Xenograft cryosections of the prostate cancer cell line LNCaP treated with [^{177}Lu]Lu-PSMA-617 were evaluated with digital autoradiography and stained with hematoxylin and eosin. The digital autoradiography images were used to define the source in a Monte Carlo simulation of the absorbed dose, and the stained sections were used to detect the position of cell nuclei to relate the intratumoral absorbed dose heterogeneity to the cell density. Simulations were performed for ^{225}Ac, ^{177}Lu, and ^{90}Y. TCP was calculated to estimate the mean necessary injected activity for a high TCP. A hypothetical case of activity mainly taken up on the tumor borders was generated and used to simulate the absorbed dose. **Results:** The absorbed dose per decay to tumor cells was calculated from the staining and simulation results to avoid underestimating the tumor response from low absorbed doses in tumor regions with low cell density. The mean of necessary injected activity to reach a 90% TCP for ^{225}Ac, ^{177}Lu, and ^{90}Y was found to be 18.3 kBq (range, 18–22 kBq), 24.3 MBq (range, 20–29 MBq), and 5.6 MBq (range, 5–6 MBq), respectively. **Conclusion:** To account for the heterogeneous absorbed dose generated from nonuniform intratumoral activity uptake, dosimetry models can estimate the mean necessary activity to reach a sufficient TCP for treatment response. This approach is necessary to accurately evaluate the efficacy of suggested radiopharmaceuticals for therapy.

Key Words: Monte Carlo dosimetry simulation; radiopharmaceutical therapy; digital autoradiography; tumor control probability; heterogeneity

J Nucl Med 2023; 64:1632–1637
DOI: 10.2967/jnumed.123.265523

Radiopharmaceutical therapy has become a promising approach to treating metastatic cancers, such as metastatic castrate-resistant prostate cancer (*1,2*). Radiopharmaceuticals that target cell-specific epitopes emitting short-range radiation with high linear energy transfer can deliver high absorbed doses to tumors while sparing healthy tissues. Nonuniform uptake of radiopharmaceuticals in a targeted volume can cause heterogeneous energy depositions, leading to large variations in the absorbed dose experienced by the cells.

The MIRD formalism assumes uniform activity in the source and calculates an average absorbed dose to the target volumes (*3,4*). Although the formalism can be applied on any scale, macroscopic or microscopic, it is commonly used with data from γ-cameras or SPECT imaging, where spatial resolution and sensitivity are limited and mainly organs can be delineated. Instead, digital autoradiography (DAR) can detect the intratumoral distribution of radioactivity (*5–8*). Chouin et al. used an α-camera to estimate the absorbed dose to cells in micrometastases after treatment with a radioimmunoconjugate labeled with ^{211}At (*9*). Similar to the study presented here, they correlated the detected activity in cryosections to cells detected in adjacent sections stained with hematoxylin and eosin (HE).

Detailed dosimetry models in preclinical trials can help identify the most promising tracers for radiopharmaceutical therapy. Unexplained failure of tracers could be resolved by improving the tumor penetration of the tracer, optimizing for more homogeneous intratumoral distribution of the tracer, or changing the labeled radionuclide to one with longer-range emission. Our group previously improved the tumor uptake uniformity of ^{111}In-DOTA-hu5A10 by increasing the chelate-to-antibody molar ratio in the labeling process, thereby improving the therapeutic effect in treated xenografted mice (*10*). Similarly, Howe et al. showed that a combination of carriers labeled with ^{225}Ac with complementary intratumoral distributions generated improved radioactivity distribution and significantly reduced tumor growth compared with the same activity delivered by either of the 2 carriers alone (*11*).

The tumor control probability (TCP) estimates the probability of killing all cells in a lesion from absorbed dose and cell radiosensitivity data (*12–14*). The intratumoral radioactivity distribution affects TCP for short-range radiation (*15*). This paper aims to calculate TCP from dosimetry simulations of heterogeneous activity distributions measured with DAR.

Received Jan. 30, 2023; revision accepted Jun. 12, 2023.
For correspondence or reprints, contact Emma Mellhammar (emma.mellhammar@med.lu.se).
Published online Jul. 27, 2023.

MATERIALS AND METHODS

Sections from xenografts treated with [^{177}Lu]Lu-PSMA-617 from BALB/cAnNRj mice were used to build a dosimetry model. The activity detected in the DAR image pixels was used to define voxels in the source volume in a Monte Carlo simulation of the absorbed dose. By matching DAR and HE images, the cells segmented from the HE stain within an aligned DAR image pixel were assumed to receive the absorbed dose simulated to the corresponding target voxel. TCP, as a function of injected activity, was calculated considering the cell's simulated absorbed dose per decay (from now on called dose values or dose image). Detailed descriptions of radiolabeling, cell culturing, animal work, and autoradiography can be found in supplemental materials (supplemental materials are available at http://jnm.snmjournals.org).

Monte Carlo dose simulations of ^{177}Lu, ^{90}Y, and ^{225}Ac were performed in GATE version 8.1 (OpenGATE), which in turn uses Geant4 version 10.3.3 (European Organization for Nuclear Research) (*16*). All image and data processing were performed in MATLAB R2020b (MathWorks). Each tumor's 8 DAR images were decay-corrected to the same time point and aligned (coregistered), an average of the images was calculated, and grayscale values were normalized. The tumor borders were detected by thresholding the grayscale values. The resulting mask was used to coregister the DAR and HE images. Cell nuclei were segmented from the HE images (details in supplemental materials), and a cell density map was generated in which the number of cells within the corresponding pixel in the coregistered DAR image was calculated. A hypothetical case in which the activity is primarily taken up at the edge of the xenograft because of low tumor penetration was generated by filtering the mean DAR images (description and filter in Supplemental Fig. 1).

GATE Monte Carlo Simulations

The β-decay of both ^{177}Lu and ^{90}Y has a yield of 100%, and the primary β-emissions were included in the simulations. ^{177}Lu emits β-particles with maximum (endpoint) β energy ($E_{\beta(max)}$) of 497 keV (79.4%), 384 keV (8.9%), 247 keV (0.016%), and 176 keV (11.7%) (*17*). ^{90}Y emits β-particles with $E_{\beta(max)}$ of 2,279 keV (99.9%), 518 keV (0.01%), and 92 keV (0.0000014%) (*17*). The mean β-energy spectrums of these emissions considered for ^{177}Lu and ^{90}Y, shown in Supplemental Figure 2A, were collected from the International Atomic Energy Agency's Livechart of Nuclides (*17*)—originally computed by Betashape (*18,19*)—and defined in GATE as histogram sources. The histogram had a step width of 0.5 keV for ^{177}Lu and 0.3 keV for ^{90}Y. No other electron or γ-emissions were considered because it was assumed their contribution to the final absorbed dose was negligible.

For ^{225}Ac simulations, the highest-energy α-emission of 5.8 MeV was considered, together with the highest-energy α-emissions from the daughters ^{221}Fr (6.4 MeV), ^{217}At (7.1 MeV), and ^{213}Po (8.4 MeV), thereby simplifying and speeding up the simulation. The decay chain of ^{225}Ac is shown in Supplemental Figure 2B. The daughters were assumed to remain immobile relative to the mother nuclide. To generate a realistic distribution of these emissions, a discrete spectrum was defined in the GATE simulation, where the 4 α-energies all have the same probability of being emitted as primary particles. Again, no γ-particles or electrons were included in this simulation because they were assumed to be negligible.

In the simulation, the world was defined as a water cube. To build a source volume, each pixel of the mean DAR image was defined as a box-shaped, general-purpose source placed in the water volume as a grid of voxels. The energy spectrum of the simulated radionuclide was ascribed to the general-purpose sources. The intensity of each source voxel was set to the normalized grayscale pixel values of the mean DAR image, thereby giving the relative probability for the emission of a simulated particle. Their *x*- and *y*-dimensions remained 50 × 50 μm, like the DAR image pixel size. The *z*-dimension was set to twice the continuous slowing-down approximation range in liquid water of the maximum energy of the emission of the radionuclide, except for ^{90}Y. Instead, the range was limited to 10 mm, because no axis length of the included tumors was longer. For ^{225}Ac, the daughter ^{213}Po had the highest α-energy considered in the simulation, with an estimated continuous slowing-down approximation range of 0.085 mm (*20*). For ^{177}Lu, the $E_{\beta(max)}$ 496.8 MeV equated to a continuous slowing-down approximation range of 1.8 mm (*20*). The electromagnetic interactions of the primary and secondary emissions were simulated by the Geant4 physics list emstandard_opt3 (*16*).

The energy of simulated primary particles was sampled from the energy spectrum, and its origin was sampled from the voxel intensities. Simulations were run for 10^9 primary particle emissions. A GATE dose actor was defined that overlapped the source voxel volume with the same resolution as the source in the *x*- and *y*-direction (50 × 50 μm^2) and 10 μm in the *z*-direction, mimicking the tumor cryosection thickness. To convert the absorbed dose recorded in the target volume to the absorbed dose per decay (Gy Bq^{-1} s^{-1}), S_i in the *i*th voxel was calculated as the total number of nuclear transformations (decays), and the simulated absorbed dose was multiplied with the yield Y of the emissions and the number of primary particle emissions P in the simulation (Equation 1):

$$S_i = D_{\mathrm{sim},i} \cdot \frac{Y}{P}. \qquad \text{Eq. 1}$$

For ^{177}Lu and ^{90}Y, the yield Y equals 100%. For ^{225}Ac, the α-decay has a 100% yield. However, because of the included daughter α-emissions, 1 in 4 of the simulated primary particles originate from ^{225}Ac; therefore, the ^{225}Ac yield in the simulation can be described as 400%.

The cell density map was used to overlap the resulting simulated dose image. Cells detected in the corresponding target voxel were assumed to receive its absorbed dose per decay. Histograms of equal binning of target voxels and cell dose values were used to calculate the cumulated dose–volume histograms.

TCP, as a function of injected activity, was calculated from the cell dose values. For each dose value interval *j,* the absorbed dose D_j was calculated. It is defined by the MIRD formalism (*3*) as the product of the cumulated activity $\tilde{A}$ and the dose value:

$$D_j = \tilde{A} \cdot S_j = \frac{T_{1/2}}{\ln(2)} \cdot A_0 \cdot S_j. \qquad \text{Eq. 2}$$

where $T_{1/2}$ is the physical half-life.

The initial activity A_0 in the source volume was calculated as the product of the uptake U (percentage injected activity per gram), assuming instantaneous uptake; the injected activity A_{inj} (Bq); and the tumor source volume considered in the simulation V_{source} (g):

$$A_0 = U \cdot V_{\mathrm{source}} \cdot A_{\mathrm{inj}}. \qquad \text{Eq. 3}$$

To exemplify a realistic case, average activity uptake was assumed to be 3.6% per injected activity per gram of xenograft tissue, as previously measured by our group (*22*), with a tissue density of 1.0 g/cm^3.

The cumulated activity is the total number of decays from the fraction of the injected activity taken up by the tumor. To exemplify the use of DAR images for TCP calculations, we simplified the model. We assumed no biologic clearance and no redistribution within the tumor. All activity measured 3 d after injection was therefore assumed to have been taken up instantaneously without redistribution during the dose integration period. For a more realistic model, uptake should be measured at several time points to estimate the cumulated activity better. For each radionuclide, a range of injected activities was evaluated within relevant intervals; 0–100 MBq for ^{177}Lu, 0–30 MBq for ^{90}Y, and 0–100 kBq for ^{225}Ac.

The survival probability and TCP were calculated as previously described by Nahum (*13*) and Bernhardt et al. (*12*) and later summarized by Uusijärvi et al. (*14*). For each dose value interval *j,* the survival probability SP_j for the cells in that interval that were assumed to be identical was calculated as in Equation 1. A range of values for the radiosensitivity α in a relevant interval based on radiosensitivity measurements performed by Elgqvist et al. (*21*) was applied in the calculations to evaluate its effect on the resulting TCP:

$$SP_j = e^{-(\alpha \times D_j)}. \quad \text{Eq. 4}$$

Equation 4 is a simplification of the linear-quadratic model (*13*) and is applicable for radiation with high linear energy transfer, such as α-particles or β-particles delivering an absorbed dose of more than approximately 2 Gy.

TCP, defined as the probability to kill all cells, for all intervals *j*—normalized for the number of cells N_c in each interval receiving the absorbed dose D_j—is then given by the following equation:

$$\mathrm{TCP} = \prod_{j=1}^{N_c} (1 - SP_j). \quad \text{Eq. 5}$$

RESULTS

The results for tumor 3 are presented here. Results for tumors 1 and 2 are found in Supplemental Figures 3–25.

The mean of 8 aligned DAR images from tumor 3 is shown in Figure 1A. The modified DAR image, shown in Figure 1B, represents a case of reduced tumor penetration. Activity has been moved from the central parts of the tumor and concentrated on the edges. The cell density map of tumor 3 in Figure 1C found between 0 and 30 cells per pixel. Segmentation results are presented in Supplemental Table 1.

The resulting dose values in the dose actor voxels in tumor 3 are presented in Figure 2. The differing particle range of the 3 radionuclide emissions can be seen in the gradually smoother distribution as the range increases. The long range of the ^{90}Y β-particles generated a smooth dose image in which local variations in activity uptake were indistinguishable. In contrast, the α-particle emissions of ^{225}Ac and its daughters caused a more heterogeneous distribution with hot spots induced by local activity clusters. Effectively, cells residing in a voxel with low activity uptake could still receive a relatively high dose value when simulations were run for ^{90}Y but depended more on local uptake when ^{225}Ac was simulated. Similar results were seen for tumors 1 and 2 (Supplemental Fig. 4).

For simulations performed with the modified activity distributions, the maximum dose values for all radionuclides increased, as did the focus of higher dose values to voxels with higher source intensity. Although ^{90}Y generated the most homogeneous dose value distribution, differences between edges and central parts increased (Supplemental Fig. 5).

The cell dose value distribution, calculated by matching the dose value image to the cell density map, for ^{177}Lu in tumor 3 is presented in the histogram in Figure 3A. Although the mean absorbed dose rate per unit activity in cells was 2.2×10^{-10} Gy Bq^{-1} s^{-1}, it ranged from close to 0 to more than 4×10^{-10} Gy Bq^{-1} s^{-1}. This can be compared with the target voxel dose value distribution shown in Figure 3B, where the mean was 1.2×10^{-10} Gy Bq^{-1} s^{-1}. The shape of the histograms differs greatly, because the cell density varies over the tumor section. Many voxels experienced a low dose value, but these contained few cells, whereas the cell dose value distribution was approximately centered on its mean. The cumulated absorbed dose rate histograms for cells and voxels are plotted in Figure 3C.

The resulting cell dose value histograms of all tumors and radionuclides are shown in Supplemental Figure 15, and the modified activity distributions appear in Supplemental Figure 16. Comparing ^{90}Y and ^{177}Lu, the mean absorbed dose rate per unit activity was higher for ^{90}Y. However, between the two, the highest dose value was received by ^{177}Lu in tumor 2.

From the cell dose value histograms, TCP was calculated for all 3 tumors as a function of injected activity for ranges of activity realistic to inject in a mouse model. Elgqvist et al. investigated the radiosensitivity of several prostate cancer cell lines, including LNCaP (*21*). By fitting their data to Equation 4, LNCaP should have a radiosensitivity of 1.33 Gy^{-1} (95% CI, 0.96–1.70 Gy^{-1}) for α-particles and 0.21 Gy^{-1} (95% CI, 0.16–0.25 Gy^{-1}) for β-particles. Based on this, TCP was calculated as in Equation 5 for intervals of radiosensitivity of 0.5, 1.0, 1.3, and 2.0 Gy^{-1} for ^{225}Ac and 0.1, 0.2, 0.3, and 0.4 Gy^{-1} for ^{177}Lu and ^{90}Y. The resulting TCPs for tumor 3 are shown in Figure 4. Corresponding figures for tumors 1 and 2 can be found in Supplemental Figures 17–25. The necessary activities to be injected to reach a 90% TCP are summarized in Table 1, and the modified activity distributions are summarized in Table 2.

When treating tumor 3 with ^{225}Ac, as shown in Figure 4A, an injection of about 20–30 kBq should be expected to give a good tumor response. However, when the activity remained at the border of the tumor, as shown in Figure 1B, the injected activity needed to reach a 90% TCP greatly increased, as seen in Table 2. This TCP level was never reached for a radiosensitivity of 0.5 Gy^{-1}; however, this was a low estimate for radiosensitivity. The necessary activities to be injected might be so high that they cause damage to healthy tissues.

For treatment of tumor 3 with ^{177}Lu, as shown in Figure 4B, an injection of less than 30 MBq would unlikely be curative. The necessary activity for a high TCP increased when the activity distribution in the tumor was modified, as summarized in Table 2. For a radiosensitivity of 0.1 Gy^{-1}, no activity below 100 MBq was sufficient to reach a 90% TCP.

Finally, TCP for tumor 3 treated with ^{90}Y is shown in Figure 4C. The relative difference in activity needed for a 90% TCP when comparing the original and the modified activity distribution is smaller for ^{90}Y than for ^{177}Lu and ^{225}Ac because of its longer β-particle range.

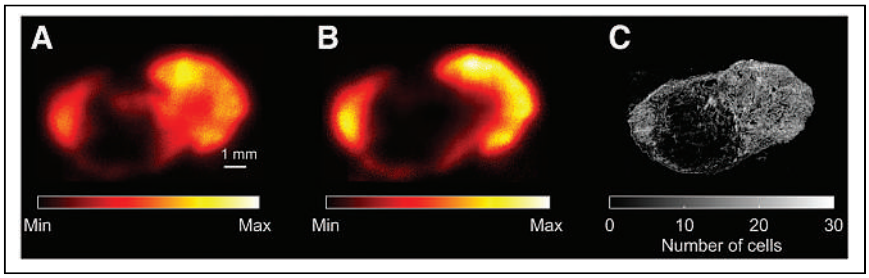

FIGURE 1. Mean DAR image (A), modified DAR image after filtering (B), and cell density map (C) for tumor 3. (A) Mean DAR image results from averaging 8 DAR sections after coregistration. (B) Hypothetical case of reduced tumor penetration. (C) Number of cells in corresponding target voxels in simulation.

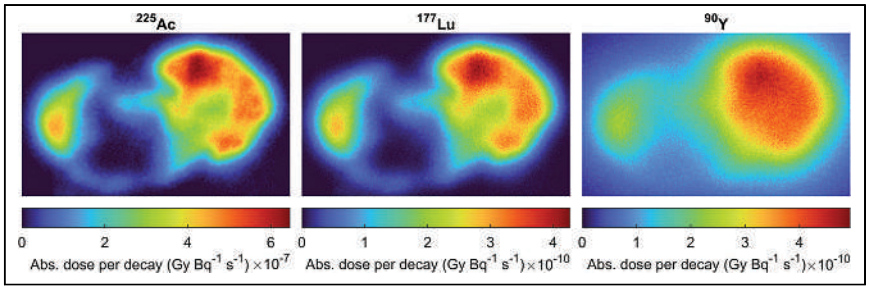

FIGURE 2. Simulated absorbed dose per unit activity in LNCaP tumor cryosections from tumor 3 for α- or β-emissions of ^{225}Ac, ^{177}Lu, and ^{90}Y. Abs. = absorbed.

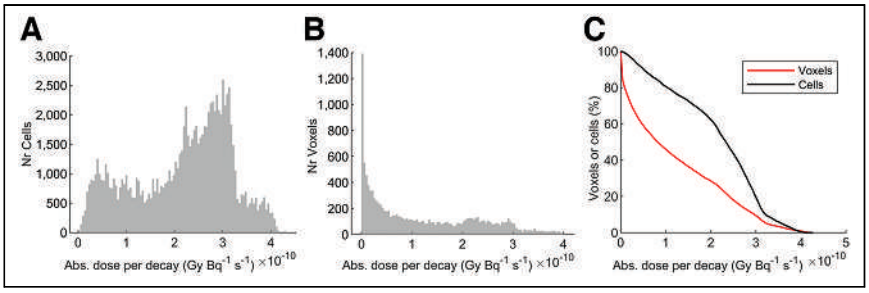

FIGURE 3. Cell dose value distribution for tumor 3 when treated with ^{177}Lu (A), compared with voxel dose value distribution (B), and cumulated dose–volume histograms of dose values for either cells or voxels (C). Abs. = absorbed; Nr = number.

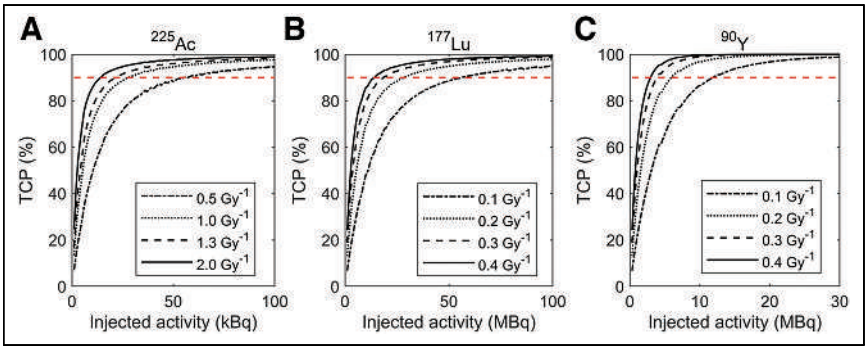

FIGURE 4. TCP vs. injected activity in tumor 3 investigated for radiosensitivities of 0.5–2.0 Gy^{-1} for ^{225}Ac (A) and 0.1–04 Gy^{-1} for ^{177}Lu (B) and ^{90}Y (C). Dashed line indicates 90% TCP level.

For comparison, if TCP was instead calculated from the voxel dose values, none of the investigated injected activities or radiosensitivities reached a TCP of at least 90% for ^{225}Ac or ^{177}Lu in tumor 3 (results in Supplemental Figs. 17, 20, and 23).

DISCUSSION

A common approach for tumor dosimetry in radiopharmaceutical therapy is to assume a sphere or ellipsoid of evenly distributed tumor cells with homogeneous radioactivity uptake. For short-range radiation, this oversimplification is inappropriate (*23*), because it risks miscalculating the absorbed dose to cells if activity uptake is heterogeneous. This is accounted for by performing voxel dosimetry, which still ignores the cellular distribution.

In preclinical trials, dosimetry models are necessary to evaluate which radiotracers have the potential to generate good treatment responses. However, overly simplified dosimetry models might mislead researchers instead of guiding their decision-making. An improvement considers intratumoral activity uptake and its relation to tumor cell distribution. Then, based on TCP calculations, realistic activities to be injected for optimal treatment effect can be estimated.

This study simulates heterogeneous absorbed dose distributions within xenografts treated with PSMA-617–ligated radioactivity. To improve calculations of TCP, we connect dose values to the number of cells experiencing them. This generates a dose value distribution that is different from the distribution generated when only voxels are considered, as seen in Figures 3A and 3B. This way, the treatment response to a wasted dose—that is, energy deposited in volumes where few cells reside—and the response of cells in volumes receiving less than necessary for tumor control will not be overestimated.

We estimate the minimum injected activities necessary to reach a 90% TCP for varying radiosensitivities. For ^{225}Ac, assuming a radiosensitivity of 1.3 Gy^{-1}, the mean injected activity would be 18.3 kBq (range, 18–22 kBq). For ^{177}Lu and ^{90}Y, assuming a radiosensitivity of 0.2 Gy^{-1}, a mean of 24.3 MBq (range, 20–29 MBq) and 5.6 MBq (range, 5–6 MBq), respectively, would

TABLE 1
Injected Activity of ^{225}Ac, ^{177}Lu, or ^{90}Y Necessary to Reach TCP of 90%

Radioactivity	^{225}Ac (kBq)				^{177}Lu (MBq)				^{90}Y (MBq)			
Radiosensitivity (Gy^{-1})	0.5	1.0	1.3	2.0	0.1	0.2	0.3	0.4	0.1	0.2	0.3	0.4
Tumor 1	39	20	15	10	40	20	13	10	9.5	5	3.5	2.5
Tumor 2	47	24	18	12	47	24	16	12	12	6	4	3
Tumor 3	55	28	22	14	56	29	19	14	12	6	4.5	3

Calculations were made for ranges of radiosensitivity of 0.5, 1.0, 1.3, and 2.0 Gy^{-1} for ^{225}Ac and 0.1, 0.2, 0.3, and 0.4 Gy^{-1} for ^{177}Lu and ^{90}Y.

TABLE 2
Injected Activity of ^{225}Ac, ^{177}Lu, or ^{90}Y Necessary to Reach TCP of 90% for Modified Activity Distribution

Radioactivity	^{225}Ac (kBq)				^{177}Lu (MBq)				^{90}Y (MBq)			
Radiosensitivity (Gy^{-1})	0.5	1.0	1.3	2.0	0.1	0.2	0.3	0.4	0.1	0.2	0.3	0.4
Tumor 1	—	90	34	29	78	39	26	20	11	6	4	3
Tumor 2	—	80	31	27	66	35	23	18	12	6	4	3
Tumor 3	—	86	66	42	—	77	52	39	14.5	7.5	5	4

Calculations were made for ranges of radiosensitivity of 0.5, 1.0, 1.3, and 2.0 Gy^{-1} for ^{225}Ac and 0.1, 0.2, 0.3, and 0.4 Gy^{-1} for ^{177}Lu and ^{90}Y.

be necessary. In the case of ^{177}Lu, these numbers agree with the injected activities that resulted in good tumor response when previously investigated by our group (*22*). The sample consists of only 3 tumors, so the resulting numbers are uncertain.

Along the slicing axis of the sectioned xenograft, the activity distribution and cell density change only slightly. This is an argument for the validity of our approach to evaluating the TCP of the tumor, because we assume the TCP of a section of the tumor is representative of the whole tumor.

We present here a general model; more parameters should be included to increase the accuracy. In our model, uptake is based on a single time point, and there is a lack of pharmacokinetics because we have included only the physical clearance of the radionuclides. Some biologic clearance is expected, so the results likely overestimate TCP. By measuring at several time points, one might improve the estimate of cumulated activity. In addition, no consideration of DNA damage repair, tumor repopulation, or differences in dose rate, which are relevant (*24*), is made.

Regions of varying cell density and cell type, necrotic areas, vascular structures, etc., are seen throughout the tumor volumes. In addition, the targeted epitopes of the tumor cells might not be equally available because of restricted tumor penetration or varying expression. Bordes et al. (*25*) used the measured uptake of rituximab by fluorescence microscopy in a multicellular aggregate of lymphoma cells, distinctly limited to the edges, to represent activity uptake in Monte Carlo simulations of the absorbed dose rate per activity unit in multicellular volumes (*25*). This method is favored by the greater resolution of fluorescence microscopy. However, it is not a direct measurement of actual activity uptake, because uptake might differ when labeling a tracer molecule to a radionuclide rather than a fluorophore.

For short-range radiation with high linear energy transfer, the microscopic energy deposition distribution can affect the absorbed dose to the cell nucleus. Cellular internalization can shorten the distance between decay and nucleus, thereby increasing energy deposited where it is most effective. The DAR images' pixel size limits the spatial resolution. Similar to the range of α-particles emitted in the ^{225}Ac decay chain, no microscale heterogeneity will be considered. However, Mínguez Gabiña et al. simulated TCP in a cluster of cells with varying ^{225}Ac-PSMA internal uptake and only found a small difference between activity on the cell surface and activity inside the cytoplasm (*26*).

CONCLUSION

We have shown how to improve preclinical dosimetry in radiopharmaceutical therapy by considering intratumoral activity uptake and its relation to tumor cell distributions. Realistic activities to be injected for optimal treatment effect can be determined with Monte Carlo simulations and TCP calculations. Examples are given for LNCaP xenografts treated with radiolabeled PSMA-617. Our approach, which considers the intratumoral distribution of cells rather than only the voxel volume, avoids underestimating the mean experienced absorbed dose rate per unit activity, because the influence of the wasted dose on the dose value calculations is reduced.

DISCLOSURE

This study was performed with support from the Swedish Cancer Society and Mrs. Berta Kamprad's Foundation. No other potential conflict of interest relevant to this article was reported.

ACKNOWLEDGMENTS

We thank Wahed Zedan for cell culturing and animal handling and Anders Örbom for help with DAR imaging.

KEY POINTS

QUESTION: Can combining DAR images with HE-stained xenograft sections in a Monte Carlo dosimetry model improve calculations of TCP?

PERTINENT FINDINGS: The model finds dose values experienced by cells in the tumor. We calculated TCP and estimated the necessary injected activity for LNCaP xenografts treated with PSMA-617 radiolabeled to ^{225}Ac, ^{177}Lu, and ^{90}Y.

IMPLICATIONS FOR PATIENT CARE: Improved dosimetry models are vital to evaluate radiotracers' potential in a preclinical phase.

REFERENCES

1. Fendler WP, Rahbar K, Herrmann K, Kratochwil C, Eiber M. ^{177}Lu-PSMA radioligand therapy for prostate cancer. *J Nucl Med.* 2017;58:1196–1200.
2. Kratochwil C, Bruchertseifer F, Giesel FL, et al. ^{225}Ac-PSMA-617 for PSMA-targeted alpha-radiation therapy of metastatic castration-resistant prostate cancer. *J Nucl Med.* 2016;57:1941–1944.
3. Bolch WE, Eckerman KF, Sgouros G, Thomas SR. MIRD pamphlet no. 21: a generalized schema for radiopharmaceutical dosimetry—standardization of nomenclature. *J Nucl Med.* 2009;50:477–484.
4. Sgouros G, Dewaraja YK, Escorcia F, et al. Tumor response to radiopharmaceutical therapies: the knowns and the unknowns. *J Nucl Med.* 2021;62(suppl 3): S12–S22.

5. Örbom A, Miller BW, Bäck T. Beta and alpha particle autoradiography. In: Ljungberg M, ed. *Handbook of Nuclear Medicine and Molecular Imaging for Physicists: Instrumentation and Imaging Procedures.* CRC Press/Balkema; 2021: 563–587.
6. Ljunggren K, Strand SE. Beta camera for static and dynamic imaging of charged-particle emitting radionuclides in biologic samples. *J Nucl Med.* 1990;31:2058–2063.
7. Bäck T, Jacobsson L. The alpha-camera: a quantitative digital autoradiography technique using a charge-coupled device for ex vivo high-resolution bioimaging of alpha-particles. *J Nucl Med.* 2010;51:1616–1623.
8. Örbom A, Ahlstedt J, Serén T, et al. Characterization of a double-sided silicon strip detector autoradiography system. *Med Phys.* 2015;42:575–584.
9. Chouin N, Lindegren S, Frost SH, et al. Ex vivo activity quantification in micrometastases at the cellular scale using the alpha-camera technique. *J Nucl Med.* 2013; 54:1347–1353.
10. Vilhelmsson Timmermand O, Örbom A, Altai M, et al. A conjugation strategy to modulate antigen binding and FcRn interaction leads to improved tumor targeting and radioimmunotherapy efficacy with an antibody targeting prostate-specific antigen. *Cancers (Basel).* 2021;13:3469.
11. Howe A, Bhatavdekar O, Salerno D, et al. Combination of carriers with complementary intratumoral microdistributions of delivered alpha-particles may realize the promise for ^{225}Ac in large, solid tumors. *J Nucl Med.* 2022;63:1223–1230.
12. Bernhardt P, Ahlman H, Forssell-Aronsson E. Model of metastatic growth valuable for radionuclide therapy. *Med Phys.* 2003;30:3227–3232.
13. Nahum AE. Microdosimetry and radiocurability: modelling targeted therapy with beta-emitters. *Phys Med Biol.* 1996;41:1957–1972.
14. Uusijärvi H, Bernhardt P, Forssell-Aronsson E. Tumour control probability (TCP) for non-uniform activity distribution in radionuclide therapy. *Phys Med Biol.* 2008; 53:4369–4381.
15. Falzone N, Lee BQ, Able S, et al. Targeting micrometastases: the effect of heterogeneous radionuclide distribution on tumor control probability. *J Nucl Med.* 2018; 60:250–258.
16. Sarrut D, Bardies M, Boussion N, et al. A review of the use and potential of the GATE Monte Carlo simulation code for radiation therapy and dosimetry applications. *Med Phys.* 2014;41:064301.
17. International Atomic Energy Agency. *LiveChart of Nuclides*. https://www-nds.iaea.org/relnsd/vcharthtml/VChartHTML.html (accessed July 2023).
18. Mougeot X. Towards high-precision calculation of electron capture decays. *Appl Radiat Isot.* 2019;154:108884.
19. Mougeot X. Erratum: reliability of usual assumptions in the calculation of beta and neutrino spectra [Phys. Rev. C 91, 055504 (2015)]. *Phys Rev C.* 2015;92:059902.
20. Berger MJ, Coursey JS, Zucker MA, Chang J. *ESTAR, PSTAR, and ASTAR: Computer Programs for Calculating Stopping-Power and Range Tables for Electrons, Protons, and Helium Ions.* National Institute of Standards and Technology; 2017.
21. Elgqvist J, Timmermand OV, Larsson E, Strand SE. Radiosensitivity of prostate cancer cell lines for irradiation from beta particle-emitting radionuclide ^{177}Lu compared to alpha particles and gamma rays. *Anticancer Res.* 2016;36:103–109.
22. Kristiansson A, Örbom A, Ahlstedt J, et al. ^{177}Lu-PSMA-617 therapy in mice, with or without the antioxidant alpha$_1$-microglobulin (A1M), including kidney damage assessment using ^{99m}Tc-MAG3 imaging. *Biomolecules.* 2021;11:263.
23. Sgouros G, Roeske JC, McDevitt MR, et al. MIRD pamphlet no. 22 (abridged): radiobiology and dosimetry of alpha-particle emitters for targeted radionuclide therapy. *J Nucl Med.* 2010;51:311–328.
24. Spoormans K, Crabbe M, Struelens L, De Saint-Hubert M, Koole M. A review on tumor control probability (TCP) and preclinical dosimetry in targeted radionuclide therapy (TRT). *Pharmaceutics.* 2022;14:2007.
25. Bordes J, Incerti S, Mora-Ramirez E, et al. Monte Carlo dosimetry of a realistic multicellular model of follicular lymphoma in a context of radioimmunotherapy. *Med Phys.* 2020;47:5222–5234.
26. Mínguez Gabiña P, Roeske JC, Mínguez R, Rodeño E, Gómez de Iturriaga A. Microdosimetry-based determination of tumour control probability curves for treatments with ^{225}Ac-PSMA of metastatic castration resistant prostate cancer. *Phys Med Biol.* 2020;65:235012.

Immuno-PET Detects Antibody–Drug Potency on Coadministration with Statins

Emma L. Brown*[1], Shayla Shmuel*[1], Komal Mandleywala*[2], Sandeep Surendra Panikar[1], Na-Keysha Berry[1], Yi Rao[2], Abbey Zidel[1,3], Jason S. Lewis[2,4–7], and Patrícia M.R. Pereira[1]

[1]*Department of Radiology, Mallinckrodt Institute of Radiology, Washington University School of Medicine, St. Louis, Missouri;* [2]*Department of Radiology, Memorial Sloan Kettering Cancer Center, New York, New York;* [3]*Department of Biology, Washington University School of Medicine, St. Louis, Missouri;* [4]*Department of Pharmacology, Weill Cornell Medical College, New York, New York;* [5]*Molecular Pharmacology Program, Memorial Sloan Kettering Cancer Center, New York, New York;* [6]*Department of Radiology, Weill Cornell Medical College, New York, New York; and* [7]*Radiochemistry and Molecular Imaging Probes Core, Memorial Sloan Kettering Cancer Center, New York, New York*

The human epidermal growth factor receptor 2 (HER2)–targeting trastuzumab emtansine (T-DM1) and trastuzumab deruxtecan (T-DXd) are antibody–drug conjugates (ADC) clinically used to treat HER2-positive breast cancer, with the latter receiving clinical approval in 2021 for HER2-positive gastric cancer. Lovastatin, a cholesterol-lowering drug, temporally elevates cell-surface HER2 in ways that enhance HER2-ADC binding and internalization. **Methods:** In an NCIN87 gastric xenograft model and a gastric patient–derived xenograft model, we used the ^{89}Zr-labeled or ^{64}Cu-labeled anti-HER2 antibody trastuzumab to investigate the dosing regimen of ADC therapy with and without coadministration of lovastatin. We compared the ADC efficacy of a multiple-dose ADC regime, which replicates the clinical dose regimen standard, with a single-dose regime. **Results:** T-DM1/lovastatin treatment inhibited tumor growth, regardless of multiple- or single-dose T-DM1 administration. Coadministration of lovastatin with T-DM1 or T-DXd as a single dose enhanced tumor growth inhibition, which was accompanied by a decrease in signal on HER2-targeted immuno-PET and a decrease in HER2-mediated signaling at the cellular level. DNA damage signaling was increased on ADC treatment in vitro. **Conclusion:** Our data from a gastric cancer xenograft show the utility of HER2-targeted immuno-PET to inform the tumor response to ADC therapies in combination with modulators of cell-surface target availability. Our studies also demonstrate that statins enhance ADC efficacy in both a cell-line and a patient-derived xenograft model in ways that enable a single-dose administration of the ADC.

Key Words: ADC; T-DM1; T-DXd; PET imaging

J Nucl Med 2023; 64:1638–1646
DOI: 10.2967/jnumed.122.265172

Treatment of human epidermal growth factor receptor 2 (HER2)–expressing metastatic breast cancer has been greatly improved using trastuzumab (*1*), an antibody targeting membrane HER2. In addition to trastuzumab, antibody–drug conjugates (*2,3*) (ADCs) enable a potent chemotherapeutic payload to be delivered directly to the tumor tissue (*4–6*). Examples of ADCs targeted toward HER2 include trastuzumab emtansine (T-DM1) and trastuzumab deruxtecan (T-DXd) (*6–8*).

HER2 is a potential therapeutic target not only in breast cancer but also in other HER2-expressing solid tumors, including those of the lung, bladder, and stomach (*3,5,7,9–12*). HER2 is overexpressed in approximately 20% of metastatic gastric cancers (*13*), and similar to HER2-positive breast cancer, adding chemotherapy to trastuzumab improved survival in the first-line metastatic setting in patients with gastric cancer (*14*). However, contrary to breast cancer, no improvement in overall survival was observed in patients with gastric cancer treated with T-DM1 (7.9 mo) versus taxane (8.6 mo) (*15*). Until recently, there was a lack of meaningful clinical response of HER2-targeted agents in treating gastric cancer. However, the latest results with T-DXd in HER2-low and HER2-high tumors brought a paradigm shift (*6*). T-DXd became Food and Drug Administration–approved in 2021 for treating patients with HER2-positive gastric cancer. T-DXd has also shown efficacy in HER2-low gastric tumors (ClinicalTrials.gov identifier NCT04379596) (*16*), with an objective response rate of up to 26.3% (*17*).

For T-DM1 and T-DXd to bind to tumors, the HER2 receptor must be available at the cancer cell membrane (*4*). However, gastric tumors are characterized by a heterogeneous expression of HER2 and nonpredominant staining of HER2 at the cell membrane that impairs antibody binding to tumors (*11,13,18*). Importantly, HER2 heterogeneity is associated with resistance to HER2-targeted therapies (*19*). HER2 membrane availability is in part regulated by caveolae-mediated endocytosis, which is often dysregulated in cancer cells, resulting in heterogeneous HER2 membrane expression, particularly in gastric cancer (*18,20*).

Statins are pharmacologic inhibitors of endocytosis, likely via temporal depletion of cholesterol (*21,22*). Lovastatin is a statin prodrug that is enzymatically hydrolyzed in the liver to its active form, which inhibits 3-hydroxy-3-methylglutaryl coenzyme A, a key enzyme in the mevalonate pathway that produces isoprene moieties needed for cholesterol biosynthesis (*23,24*). Lovastatin modulates endocytosis to increase cell-surface HER2 availability, resulting in increased antibody–tumor binding (*18*). Lovastatin increased T-DM1 efficacy in gastric tumor xenografts and a patient-derived xenograft (PDX) model from a gastric tumor resistant to anti-HER2 therapy in the clinic (*21*). In this previous study, mice were administered weekly doses of T-DM1, mimicking existing clinical dose regimes.

Received Nov. 16, 2022; revision accepted May 12, 2023.
For correspondence or reprints, contact Patrícia M.R. Pereira (ribeiropereirap@wustl.edu).
*Contributed equally to this work.
Published online Jun. 29, 2023.

Although using T-DM1 and T-DXd significantly increases the overall survival of some patients, clinical trials using multiple doses of T-DM1 and T-DXd have noted some significant side effects. T-DM1 causes cardiotoxicity in approximately 3.37% of breast cancer patients (*25*), whereas early clinical data on gastric cancer suggest that 10% of T-DXd–treated patients develop interstitial lung disease (*17*). These toxicities limit the number of dosing cycles that patients can tolerate and can result in dose reductions or termination of the treatment (*17,26*). Strategies that reduce toxic side effects caused by ADCs and predictive biomarkers of ADC toxicity are a currently unmet clinical need.

Therefore, this study had 2 objectives. The first was to determine whether a single dose of ADCs could be administered in combination with lovastatin to achieve therapeutic efficacy similar to that of a multiple-dose ADC regime in both a HER2-positive xenograft and PDX gastric cancer models of known resistance to anti-HER2 therapy. The second was to use HER2-targeted immuno-PET to monitor changes in HER2 expression after ADC therapy.

MATERIALS AND METHODS

Cell Culture and Treatments

The human gastric cancer cell line NCIN87 was purchased from the American Type Culture Collection. NCIN87 were cultured in RPMI 1640 growth medium supplemented with 10% fetal calf serum, 2 mM L-glutamine, 10 mM hydroxyethyl piperazineethanesulfonic acid, 1 mM sodium pyruvate, 4,500 mg L^{-1} glucose, 1,500 mg L^{-1} sodium bicarbonate, and 100 units mL^{-1} penicillin and streptomycin.

NCIN87 cells were treated with vehicle, T-DM1, or T-DXd for 48 h before lysates were extracted. Cells additionally given lovastatin were incubated with 25 μM of the active form of lovastatin (Millipore) for 4 h before addition of T-DM1 or T-DXd.

Western Blot Analysis

Total protein extracts from NCIN87 cells and tumors were prepared after tissue homogenization in radioimmunoprecipitation assay buffer (150 mM sodium chloride, 50 mM Tris hydrochloride, pH 7.5, 5 mM ethylene glycol tetraacetic acid, 1% Triton X-100 [Dow], 0.5% sodium deoxycholate, 0.1% sodium dodecyl sulfate, 2 mM phenylmethanesulfonyl, 2 mM iodoacetamide, and ×1 protease inhibitor cocktail [Roche]). After centrifugation at 18,000*g* for 16 min at 4°C, supernatants containing total protein extracts were collected and stored at −80°C. The amount of total protein in tumor extracts was quantified using the Pierce bicinchoninic acid protein assay kit (Thermo Fisher Scientific), followed by denaturation of the sample with NuPAGE lithium dodecyl sulfate sample buffer and NuPAGE sample reducing agent (Thermo Fisher Scientific). The denatured samples underwent gel electrophoresis and transfer to polyvinylidene difluoride membranes (Bio-Rad). The membranes were incubated in 5% (m/v) milk (Bio-Rad) or bovine serum albumin (Sigma) in tris-buffered saline buffer-polysorbate (EZ BioResearch). The membranes were then incubated with the primary antibodies: mouse anti-β-actin, 1:10,000 (A1978; Sigma); rabbit anti-HER2, 1:800 (ab131490; Abcam); rabbit anti-HER2 phospho Y1139, 1:500 (ab53290; Abcam); rabbit anti–epidermal growth factor receptor (EGFR), 1:1,000 (ab52894; Abcam); rabbit anti-EGFR phospho Y1068, 1:500 (ab40815; Abcam); rabbit anti-HER3, 1:500 (ab32121; Abcam); rabbit anti-HER3 phospho Y1289, 1:2,500 (ab76469; Abcam); mouse antiphosphotyrosine, 1:2,000 (05-321; Sigma); rabbit anti–poly(adenosine diphosphate ribose) polymerase (PARP), 1:1,000 (9542; Cell Signaling Technology); rabbit anti–histone H2A.X, 1:1,000 (2595; Cell Signaling Technology); or rabbit anti–phosphohistone H2A.X (Ser139), 1:1,000 (9718; Cell Signaling Technology). After washing of the membranes with tris-buffered saline buffer-polysorbate, the membranes were incubated with the secondary antibody goat anti-rabbit IgG (heavy- and light-chain) conjugated with AlexaFluor Plus 680 (Invitrogen) or goat anti-mouse IgG (heavy- and light-chain) conjugated with AlexaFluor Plus 800 (Invitrogen). Membranes were imaged on an Odyssey infrared imaging system (LI-COR Biosciences), and densiometric analysis of the respective bands was performed using ImageJ/FIJI. The supplemental materials (available at http://jnm.snmjournals.org) contain uncropped scans of the blots shown in the figures.

Conjugation and Radiolabeling of Trastuzumab

Trastuzumab (Herceptin; Roche) used in imaging and biodistribution studies was obtained from the Siteman Cancer Center pharmacy or the Memorial Sloan Kettering pharmacy.

^{89}Zr-Labeled Trastuzumab. As previously described (*18,21*), conjugation and radiolabeling of trastuzumab with zirconium-89 were achieved using the bifunctional chelate *p*-isothiocyanatobenzyl-desferrioxamine (DFO-Bz-NCS; Macrocyclics, Inc). [^{89}Zr]Zr-oxalate was obtained from the cyclotron at Memorial Sloan Kettering Cancer Center. The ^{89}Zr-labeled trastuzumab used in our studies had a radiochemical purity of 99% as determined by instant thin-layer chromatography, and the molar activity was 21.98 MBq/nmol.

^{64}Cu-Labeled Trastuzumab. Copper-64 was obtained from Washington University Cyclotron facility. Trastuzumab was buffer-exchanged in 0.1 M 4-(2-hydroxyethyl)-1-piperazineethanesulfonic acid buffer (pH 8.5) and was conjugated and radiolabeled as previously described (*27*). Briefly, conjugation and radiolabeling of trastuzumab with copper-64 were achieved by conjugating trastuzumab to *p*-SCN-Bn-NOTA (Macrocyclics) in 100% ethanol in a 20-fold molar excess, before incubation at 4°C overnight with slow agitation. The antibody–NOTA conjugate was purified and concentrated in 0.1 M ammonium acetate buffer (pH 6) and then radiolabeled with copper-64. The reaction mixture was incubated at 37°C for 1 h. The radiochemical yield and purity were determined as described above in a mixture of 0.1 M ammonium acetate buffer (pH 6) with 50 mM ethylenediaminetetraacetic acid as the mobile phase. The radiolabeled conjugates used for in vivo studies had a radiochemical purity of 99%, radiochemical yields ranging from 87% to 99%, and molar activities in the range of 47.4–69.6 MBq/nmol.

Tumor Xenografts and Animal Studies

The animal experiments were conducted at both Washington University in St. Louis and Memorial Sloan Kettering Cancer Center. All animals were treated according to the guidelines approved by the Research Animal Resource Center and Institutional Animal Care and Use Committee at Washington University School of Medicine at St. Louis or the Research Animal Resource Center and Institutional Animal Care and Use Committee at Memorial Sloan Kettering Cancer Center.

NCIN87 Gastric Xenografts. Eight- to 10-wk-old *nu/nu* female mice (Charles River Laboratories) were injected subcutaneously on the right shoulder with 5 million NCIN87 cells in a 200-μL cell suspension of a 1:1 (v/v) mixture of Matrigel (BD Biosciences). The mice were housed in type II polycarbonate cages, fed with a sterilized standard laboratory diet, and given sterile water ad libitum. The animals were housed at approximately 19°C–23°C, at 30%–70% relative humidity, and in a 12 h light/12 h dark cycle.

The tumor volume (V/mm^3) was estimated by external vernier caliper measurements of the longest axis, a/mm, and the axis perpendicular to the longest axis, b/mm. The tumors were assumed to be spheroid, and the volume was calculated in accordance with the equation $V = (4\pi/3) \times (a/2)^2 \times (b/2)$.

PDXs. A gastric PDX model was established by the Antitumor Assessment Core at Memorial Sloan Kettering Cancer Center from a patient with HER2-positive gastric cancer, collected under an approved institutional review board protocol by the Research Animal Resource Center and Institutional Animal Care and Use Committee at Memorial

Sloan Kettering Cancer Center. Tumor fragments were mixed with Matrigel and implanted subcutaneously in 6- to 8-wk-old female NSG mice (Jackson Laboratories). Once established, tumors were maintained and expanded by serial subcutaneous transplantation. Tumor samples were evaluated as described previously (*21*), to grade for HER2 expression and to exclude B-cell lymphomas in PDXs associated with Epstein–Barr virus.

In Vivo Therapeutic Efficacy

When tumor volumes reached approximately 200–500 mm^3, mice were randomly grouped into treatment cohorts (≥8 per group for T-DM1 treatments and ≥5 per group for T-DXd treatments). Supplemental Table 1 outlines the therapeutic studies conducted, the number of animals per group, and the imaging agents used.

Multiple-Treatment T-DM1 Schedule. The multiple-treatment schedule was published previously (*21*). Vehicle, T-DM1, lovastatin, or a combination of T-DM1 with lovastatin was administered to mice bearing NCIN87 or gastric PDX tumors. Intravenous T-DM1 administration was 5 mg/kg (once weekly, for 5 wk). Lovastatin (4.15 mg/kg, oral gavage) was administrated 12 h before and at the same time as the intravenous injection of T-DM1. Tumor volumes were determined by vernier caliper measurement twice a week.

Single-Treatment T-DM1 Schedule. A single dose of vehicle or T-DM1, 5 mg/kg, was administered, and tumor volumes were measured as described above. In cohorts of T-DM1 single-dose treatment combined with lovastatin, the lovastatin (4.15 mg/kg, oral gavage) was administrated 12 h before and at the same time as the intravenous injection of T-DM1.

T-DXd Treatment. Vehicle, T-DXd, or a combination of T-DXd with lovastatin was administered to mice bearing NCIN87 or gastric PDX tumors. The mice received an intravenous injection of T-DXd (5 mg/kg, single-dose). Lovastatin (4.15 mg/kg, oral gavage) was administrated 12 h before and at the same time as the intravenous injection of T-DXd. Tumor volumes were determined by vernier caliper measurement twice a week.

Acute Biodistribution Studies and Small-Animal PET

Supplemental Table 1 outlines the imaging agents used in each treatment cohort. Mice in the T-DM1/statin cohorts were administered ^{89}Zr-labeled trastuzumab on day 39 after initiating therapy. Acute biodistribution studies were performed 48 h after injection of radiolabeled [^{89}Zr]Zr-DFO-trastuzumab. The mice were sacrificed and organs were harvested and measured in the γ-counter. Radioactivity associated with each organ was expressed as percentage injected dose per gram of organ (%ID/g).

Mice in the T-DXd/statin cohorts were administered ^{64}Cu-labeled trastuzumab before initiating therapy or on day 29 after therapy.

PET imaging experiments at Memorial Sloan Kettering were conducted on a microPET Focus 120 scanner (Concorde Microsystems) at 48 h after intravenous injection of [^{89}Zr]Zr-DFO-trastuzumab. The mice were anesthetized by inhalation of 1.5%–2% isoflurane (Baxter Healthcare) in an oxygen gas mixture 10 min before recording PET images. PET data for each group ($n = 4$) were recorded with the mice under isoflurane anesthesia (1.5%–2%). Images were analyzed using ASIPro VM software (Concorde Microsystems).

PET imaging experiments at Washington University in St. Louis were conducted on a Mediso nanoScan PET/CT scanner (Mediso) at 24 h after injection of [^{64}Cu]Cu-NOTA-trastuzumab. PET images for each group ($n = 2$) were collected before therapy and on day 30 after therapy and were recorded with the mice under isoflurane anesthesia (1.5%–2%) as described above. Images were reviewed using 3D Slicer software (version 5.0.3).

Statistical Analysis

Data were analyzed using RStudio and GraphPad Prism, version 9.0. The volume fold-change for each tumor was calculated as the tumor volume at the endpoint (mm^3) divided the tumor volume at the start of therapy (mm^3). Differences in fold-change were analyzed by a 1-way ANOVA or an unpaired Student *t* test. Differences in tumor volume over time between treatment groups were calculated using a 2-way repeated-measures ANOVA. Mean activity in the tumor region of interest (%ID/g) was quantified using 3D Slicer, version 5.2.2. The correlation between mean %ID/g and tumor volume was calculated by the Pearson correlation coefficient.

RESULTS

A Single Dose of T-DM1 Combined with Statin Reduces Tumor Volume in Gastric Cancer Xenografts

Previous work has shown that statins enhanced trastuzumab accumulation in tumors (*18*) and that coadministration of the anti-HER2 ADC T-DM1 with statins enhanced efficacy in gastric cancer mouse models in a multiple-dose T-DM1 treatment regime that mimicked the weekly infusion schedules performed in clinics (*21*). In these previous studies, a multiple-dose regime of 5 weekly 5 mg/kg doses of T-DM1 was administered in combination with a 4.15 mg/kg dose of lovastatin administered twice, 12 h before and on the day of T-DM1 administration. This multiple-dose ADC regime significantly reduced NCIN87 tumor volumes compared with T-DM1 alone, statin alone, or control saline-treated tumor cohorts (*21*). Because of the possible side effects that a multiple-dose infusion schedule of T-DM1 can cause (*25*), we sought to investigate whether the enhanced potency of T-DM1 seen on coadministration with statins could enable fewer doses of T-DM1 to be given, without interfering with therapeutic efficacy.

We first determined whether using T-DM1/statin as a single dose effectively treated NCIN87 gastric tumor xenografts (Figs. 1A and 1B). In our current study, a single 5 mg/kg dose of T-DM1 was administered, with a 4.15 mg/kg dose of lovastatin administered twice. As performed in our previous studies, the statin was administered 12 h before and on the day of T-DM1 administration. NCIN87 tumor volumes monitored across a 60 d period from treatment initiation were significantly lower ($P < 0.001$) in T-DM1/statin cohorts, even with single-dose T-DM1 administration, than with control and T-DM1 administration alone (Fig. 1B; Supplemental Fig. 1). Both T-DM1/statin cohorts had a significantly lower ($P < 0.001$) tumor volume fold-change than the T-DM1–alone equivalent in both single- and multiple-dose regimes (Fig. 1C). The tumor volume fold-change was significantly lower ($P < 0.001$) in T-DM1/statin cohorts in a multiple-dose regime than in a single-dose regime (Fig. 1C).

Overall, we found that a single dose of T-DM1, when combined with a statin, controlled NCIN87 gastric xenografts over a period of 60 d.

PET Imaging Annotates Alterations in Tumoral HER2 in Response to T-DM1/statin Combination

Noninvasive PET imaging using [^{89}Zr]Zr-DFO-trastuzumab can annotate changes in HER2 expression in response to HER2-targeted therapies (*18,21*). Therefore, we next sought to determine whether PET imaging could visualize changes in HER2 tumoral expression accompanying the decrease in tumor volume in T-DM1–treated or T-DM1/statin-treated NCIN87 xenograft tumors.

[^{89}Zr]Zr-DFO-trastuzumab was injected at 39 d after treatment initiation, the time at which NCIN87 tumors develop resistance to weekly doses of T-DM1 (*21*). In our experiments, the radiolabeled trastuzumab binds to tumoral membrane HER2 in vivo, and PET images are acquired at 48 h after antibody injection. On the basis of data shown in Figure 1, we expected that a decrease in tumor

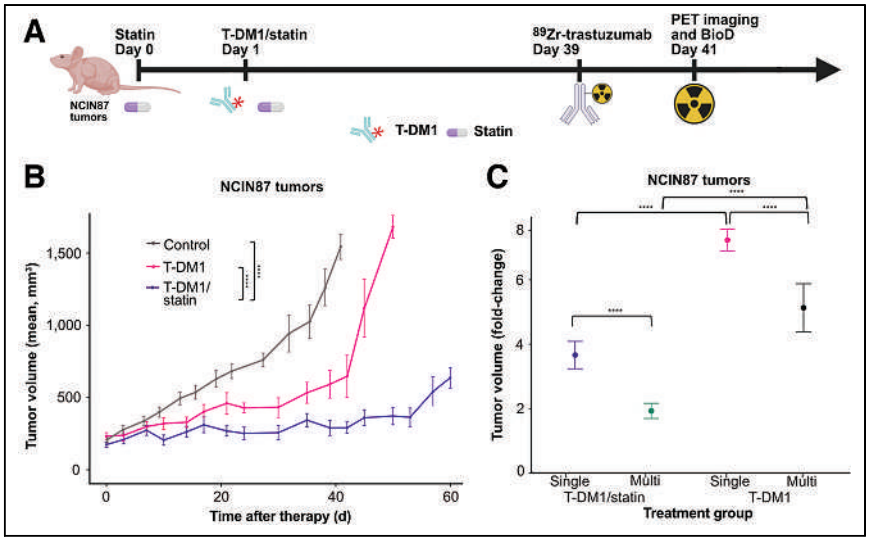

FIGURE 1 (A) Schematic illustrating T-DM1 and statin dose administration in single-dose ADC regime. NCIN87 gastric xenografts were established in female nude mice (≥8 per group). Once tumors reached 200–300 mm^3, intravenous T-DM1 administration at 5 mg/kg weekly (for 1 wk—single-treatment regime) was started on day 1. Lovastatin (4.15 mg/kg) was orally administered 12 h before and simultaneously with intravenous injection of T-DM1. [^{89}Zr]Zr-DFO-trastuzumab was intravenously administered on day 39, and PET images were collected at 41 d after treatment. Immediately after PET imaging, organs were harvested for ex vivo biodistribution. Tumors were excised at 43 d after initiating therapy and used for Western blot analyses. Schematic was created with Biorender.com. (B) Tumor volumes (mm^3) measured across 60 d for control, T-DM1 single-treatment regime, and T-DM1/statin single-treatment regime. Mean ± SD for at least 8 mice is shown. ****$P < 0.0001$ based on 2-way repeated measures ANOVA. (C) Fold-change in NCIN87 tumor volume for T-DM1 or T-DM1/statin (1 wk of therapy, single-treatment regime) and for T-DM1 or T-DM1/statin (5 wk, multiple-treatment regime reported (*21*)). Fold-change between day 0 and day 60 is displayed as mean ± SD ($n \geq 8$). ****$P < 0.0001$ based on 1-way ANOVA.

volume observed in T-DM1/statin cohorts would be accompanied by a reduction in HER2 expression as monitored by HER2-targeted immuno-PET. Immuno-PET after ADC therapy demonstrated decreased uptake of [^{89}Zr]Zr-DFO-trastuzumab in NCIN87 tumors on coadministration with statins, in both multiple- and single-dose T-DM1 regimens, indicating that T-DM1 therapy had reduced membrane tumoral HER2 expression at 39 d after therapy initiation (Fig. 2A). Ex vivo biodistribution of the tumors excised from mice after imaging quantified a 1.3-fold decrease in [^{89}Zr]Zr-DFO-trastuzumab uptake when statins were coadministered with T-DM1 compared with T-DM1 administration alone, which was significant in T-DM1 single-dose versus T-DM1/statin single-dose treatment ($P = 0.02$; Fig. 2B; Supplemental Fig. 2). [^{89}Zr]Zr-DFO-trastuzumab tumor uptake on PET images (measured at %ID/g) correlated with tumor volume ($r = 0.97$, $P = 0.03$; Fig. 2C), indicating a positive correlation between trastuzumab-tumor binding and tumor size at 39 d after therapy initiation.

Overall, T-DM1/statin combination therapy significantly reduced membrane HER2 tumoral expression compared with T-DM1 treatment alone, which can be annotated in vivo using immuno-PET.

Statins Enhance the Efficacy of the ADC T-DXd in HER2-Positive Gastric Tumors

Next, we sought to investigate whether including a statin could enhance the efficacy of the trastuzumab ADC T-DXd (*5,6*). T-DXd is showing excellent promise in treating gastric cancer, with initial clinical trials reporting a 51% objective response rate for HER2-positive gastric cancers (*17*). Initially using NCIN87 xenografts, we replicated the single-dose regime such that a single dose of T-DXd was administered at 5 mg/kg along with two doses of lovastatin (4.15 mg/kg) administered 12 h before and on the day of T-DXd administration (Fig. 3A). Both T-DXd and T-DXd/statin treatments reduced tumor volumes over the first 20 d of measurement, but in the next 14 d, T-DXd–treated tumors began to regrow, whereas T-DXd/statin-treated tumors remained controlled, resulting in a significant difference in growth between the two groups ($P = 0.006$; Fig. 3B; Supplemental Figs. 3 and 4). Tumor volume fold-change at 34 d after treatment initiation averaged 0.57 ± 0.09 T-DXd/statin compared with 1.31 ± 0.22 in tumors treated with T-DXd alone ($P = 0.008$; Fig. 3C).

To annotate changes in tumoral HER2 before and at 29 d after T-DXd therapy, we used [^{64}Cu]Cu-NOTA-trastuzumab before and after therapy, as the half-life of copper-64 is 12.7 h, allowing multiple imaging sessions during our therapy window. Additionally, recent studies have shown the ability of ^{64}Cu-labeled trastuzumab to monitor responder versus nonresponder tumors to ADC therapy (*28*). Immuno-PET imaging after therapy in NCIN87 tumors demonstrated a decrease in uptake of [^{64}Cu]Cu-NOTA-trastuzumab in both T-DXd and T-DXd/statin cohorts (Fig. 3D), and the mean %ID/g tumor values from both pretherapy and posttherapy imaging correlated with tumor volume ($r = 0.77$, $P = 0.03$; Supplemental Fig. 5).

Overall, T-DXd therapy was enhanced on coadministration with statins in HER2-positive NCIN87 tumors, and HER2 expression on immuno-PET could be monitored before and after therapy with ^{64}Cu-labeled trastuzumab.

ADC Single-Dose Coadministered with Statins Reduces Tumor Volume in a Trastuzumab-Resistant Gastric PDX Model

Cell-line xenograft models such as NCIN87 cancer cells are commercially available and can be used across multiple analyses for preclinical work. However, they do not always represent the heterogeneity observed in clinical samples. PDX models offer an alternative that can better represent patient tumor tissue and response to therapies (*29*). Gastric PDXs recapitulate patient tumor inter- and intratumoral heterogeneity in histology and genetic characteristics (*30*). Because of the preservation of tumoral heterogeneity, PDXs are thought of as avatars for patients when testing novel therapies (*31*). Therefore, we chose a previously established gastric PDX model with known clinical resistance to anti-HER2 therapy to test both the T-DM1/statin and the T-DXd/statin single-dose regimes (Fig. 4A) (*18,21*).

When the HER2-positive gastric PDX was treated with a single dose of T-DM1/statin (Fig. 4A), tumor volume was significantly reduced ($P < 0.001$) compared with T-DM1 alone and control cohorts (Fig. 4B; Supplemental Fig. 6). The volume fold-change of T-DM1/statin tumors was significantly lower ($P < 0.001$) than for the equivalent T-DM1–alone regime. No significant differences in tumor volume fold-change were observed between T-DM1/statin single-dose and multiple-dose regimes (Fig. 4C). Equally, when

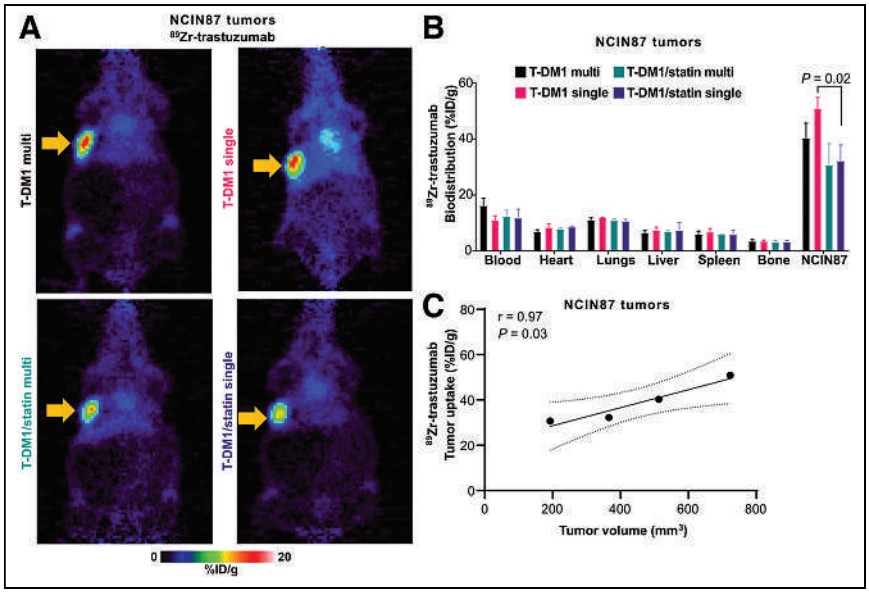

FIGURE 2. (A and B) Representative PET images (A) and biodistribution (B) of [^{89}Zr]Zr-DFO-trastuzumab displaying %ID/g acquired 48 h after radiolabeled trastuzumab injection on day 39 for T-DM1 single-treatment regime, T-DM1/statin single-treatment regime, T-DM1 multiple-treatment regime, and T-DM1/statin multiple-treatment regime. Tumor location is indicated by arrow. Data are mean ± SD (n = 4). Significant P values (<0.05) are displayed for tumor mean comparisons and were calculated by unpaired Student t test. (C) Scatterplot of mean %ID/g of [^{89}Zr]Zr-DFO-trastuzumab in tumor regions against tumor volume (mm^3). Pearson correlation coefficient (r) and P value are displayed. Line of best fit is displayed (solid black line) with 95% CIs (dotted black lines).

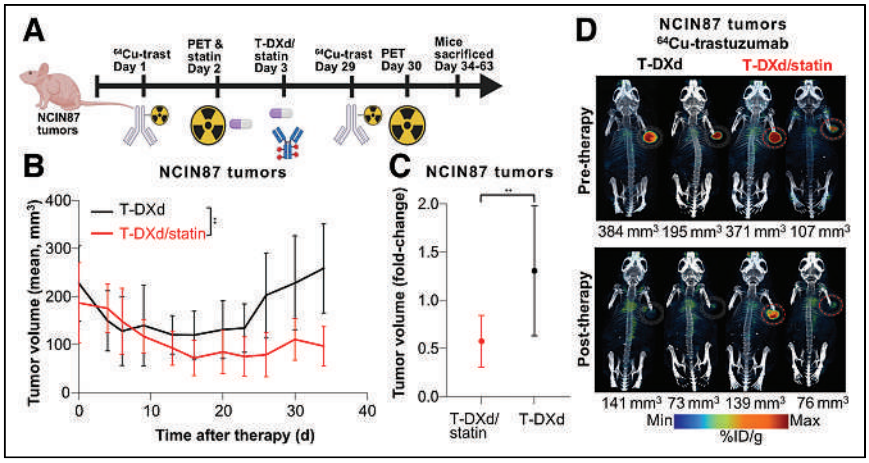

FIGURE 3. (A) Schematic illustrating T-DXd and statin dose administration across single-dose regime. NCIN87 gastric xenografts were established in female nude mice (9 per group). Once tumors reached about 200 mm^3, mice were intravenously administered T-DXd, 5 mg/kg weekly (for 1 wk—single-treatment regime). Lovastatin (4.15 mg/kg) was orally administrated 12 h before and simultaneously with intravenous injection of T-DXd. [^{64}Cu]Cu-NOTA-trastuzumab was intravenously administered on days 1 and 29, and PET images were collected before (day 2) and after (day 30) therapy. Mice were sacrificed 34–63 d after initiating therapy. Schematic was created with Biorender.com. (B) Tumor volumes (mm^3) were measured across 34 d for T-DXd and T-DXd/statin. Mean ± SD of 9 mice per group is shown. **P = 0.006 at endpoint based on 2-way repeated-measures ANOVA. (C) Tumor volume fold-change in NCIN87 tumor volume in T-DXd or T-DXd/statin. Fold-change between days 0 and 34 is displayed as mean ± SD. **P = 0.008 calculated by unpaired Student t test. (D) Representative PET images of [^{64}Cu]Cu-NOTA-trastuzumab displaying %ID/g acquired at 24 h after radiolabeled trastuzumab injection before therapy (day 2) and after therapy (day 30) for T-DXd and T-DXd/statin. Two different mice with varying tumor sizes from 73 to 384 mm^3 are displayed for each group and each time point. Tumors are encircled.

the HER2-positive gastric PDX was treated with a single dose of T-DXd/statin (Fig. 4A), there was a significant ($P < 0.001$) reduction in tumor volume compared with T-DXd alone (Fig. 4D; Supplemental Fig. 7). The tumor volume fold-change of T-DM1/statin PDXs was significantly lower ($P = 0.07$; Fig. 4E; Supplemental Fig. 8) than for the equivalent T-DXd–alone regime. Finally, both T-DXd single-dose and T-DXd/statin single-dose treatments were more effective at controlling gastric PDX tumor volumes than were the T-DM1 and T-DM1/statin single-dose regimes, as measured by tumor volume fold-change ($P < 0.0001$ for all comparisons; Supplemental Fig. 9).

Overall, both the T-DM1 and the T-DXd/statin single-dose regimes effectively reduced tumor volumes in a clinically representative gastric PDX model in which the originating patient tumor was previously resistant to anti-HER2 therapy.

ADC Therapy *Co*administered with Statin Downregulates HER2 Signaling and Increases DNA Damage

After observations that an ADC/statin single-dose regime is effective at reducing tumor volume and induces alterations in HER2 expression as detected via immuno-PET, we sought to annotate changes in HER2 signaling in total protein extracts once tumor tissue was excised on day 43 after ADC therapy. Western blot analysis of NCIN87 tumor extracts demonstrated depletion of HER2 and phospho-HER2/total HER2 after T-DM1 coadministration with statins, in both multiple- and single-dose regimes (Fig. 5A), with a 15- to 30-fold reduction compared with control tumors and tumors treated with T-DM1 alone (Fig. 5B). Additionally, other HER family receptors, including EGFR and HER3, were depleted in T-DM1/statin groups, with an 8-fold reduction in phospho-HER3/total HER3 and a 6-fold reduction in phospho-EGFR/total EGFR in comparison to control tumors (Figs. 5A and 5B). Tyrosine phosphorylation of multiple proteins was decreased in T-DM1/statin multiple- or single-dose tumors (Fig. 5A). The results shown in Figure 5 were further validated in 2 more independent analyses (Supplemental Figs. 10–13).

In addition to evaluating protein expression in T-DM1–treated tumors, we found that HER2 levels were 6-fold lower and barely detectable in T-DXd and T-DXd/statin-treated tumors harvested at 63 d after therapy induction compared with control tumors (Fig. 5C; Supplemental Fig. 14). Further analyses in NCIN87 cells treated

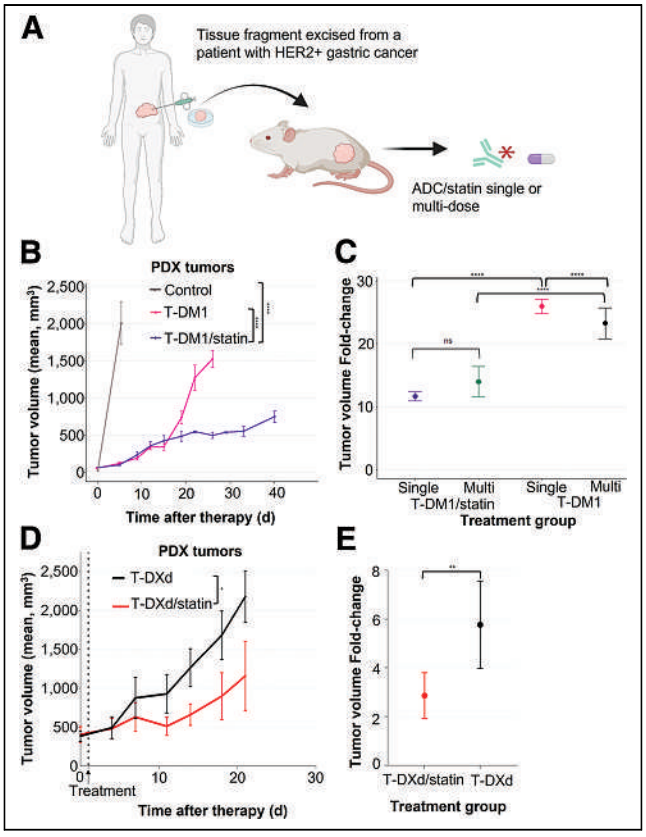

FIGURE 4. (A) Schematic displaying establishment of HER-positive gastric cancer PDX from patient tumor. Tumor fragments were implanted subcutaneously into NSG mice (≥8 per group). T-DM1/statin multiple- and single-dose schedules were administered as described in Figure 1. T-DXd/statin single-dose schedule was administered as described in Figure 3. Schematic was created with Biorender.com. (B) Tumor volumes (mm^3) were measured across 40 d for control, T-DM1 single-dose regime, and T-DM1/statin single-dose regime. Mean ± SD is shown ($n \geq 8$ per group). ****$P < 0.0001$ based on 2-way repeated measures ANOVA. (C) Tumor volume fold-change in gastric PDX for T-DM1 or T-DM1/statin (1 wk of therapy, single-treatment regime) and for T-DM1 or T-DM1/statin (5 wk, multiple-treatment regime reported (*21*)). Fold-change between first and last tumor volume measurements is displayed as mean ± SD ($n \geq 5$ per group). ns = not significant. ****$P < 0.0001$ based on 1-way ANOVA. (D) Tumor volumes (mm^3) were measured across 21 d for T-DXd single-dose regime and T-DXd/statin single-dose regime. Mean ± SD is shown ($n \geq 8$ per group). *$P = 0.02$ based on 2-way repeated measures ANOVA. (E) Tumor volume fold-change in gastric PDX for T-DXd or T-DXd/statin. Fold-change between first and last tumor volume measurements is displayed as mean ± SD ($n \geq 8$ per group). **$P = 0.007$ based on unpaired Student *t* test.

for 48 h with ADC alone or in combination with lovastatin demonstrated a 2- to 6.5-fold reduction in HER2 and a 2- to 3-fold reduction in phospho-HER2 (Fig. 5D; Supplemental Fig. 15). Phosphorylated tyrosines were downregulated in all treatments compared with control (Fig. 5D; Supplemental Fig. 16). Because the DXd chemotherapy is expected to induce DNA damage, expression of H2AX, phosphorylated H2AX, cleaved PARP, and full-length PARP was evaluated at the cellular level. All 4 treatments (T-DM1, T-DM1/statin, T-DXd, and T-DXd/statin) increased the expression of markers for DNA damage, showing a 3- to 6-fold increase in H2AX and a 1.6- to 3.5-fold increase in phosphorylated H2AX compared with control cells (Fig. 5D; Supplemental Fig. 17). Interestingly, levels of H2AX and phosphorylated H2AX were relatively high in T-DM1/statin-treated samples and in T-DXd–treated cells. Finally, the ratio of cleaved PARP/PARP in T-DM1/statin and T-DXd/statin-treated cells was 16-fold and 28-fold higher than in control cells (Fig. 5E; Supplemental Fig. 18), suggesting cleavage of full-length PARP in cells undergoing DNA damage.

Overall, Western blot analyses demonstrated depletion of HER2 and decreased phosphorylation of HER2 and multiple downstream targets on coadministration of T-DM1 or T-DXd with statin compared with control tumors. Additionally, Western blot analyses showed expression of DNA damage markers on acute treatment with HER2-targeting ADC-plus-statin therapies.

DISCUSSION

ADCs have become eminent in oncologic treatment schedules because of their ability to precisely target tumors with potent efficacy. Indeed, 14 ADCs have been approved for cancer treatment, and more than 100 different ADCs are being evaluated in clinical trials (*4*). T-DM1 and T-DXd are two Food and Drug Administration–approved anti-HER2 antibody conjugates, which are based on the antibody trastuzumab linked to a cytotoxic payload. T-DM1 comprises trastuzumab conjugated with a microtubule-targeting payload (DM1), whereas T-DXd contains trastuzumab linked to a topoisomerase-1 inhibitor payload. T-DM1 is effective in treating HER2-positive breast tumors, but in clinical trials it failed to treat HER2-expressing gastric cancers (*15*). Most recently, T-DXd demonstrated improved efficacy in HER2-positive advanced gastric tumors (*17*). A common characteristic of T-DM1 and T-DXd is that treatment schedules often require frequent infusions of the cold ADC to maintain therapy. Although ADCs are usually well tolerated, severe side effects can occur in patients, including low blood counts, liver damage, and lung damage (*32*). After our previous studies showing that cholesterol-depleting drugs (statins) enhance cell-surface HER2 availability (*18*) and ADC internalization (*20*) in ways that enhance anti-HER2 antibody–based therapies, we have now demonstrated here that statins can be used to reduce the number of infusion schedules of the cold ADC. In our studies, preclinical gastric tumors treated with a single dose of T-DM1 in combination with a statin achieve responses similar to multiple doses of T-DM1. Tumor growth inhibition in HER2-positive NCIN87 and PDX gastric tumors was achieved with a single dose of T-DXd, and growth inhibition was enhanced by coadministration with lovastatin.

We found that preclinical immuno-PET with radiolabeled trastuzumab can monitor HER2 tumoral levels on treatment with the T-DM1 or T-DXd. Recently, another study demonstrated the use of HER2 PET to monitor response to T-DM1 therapy in breast cancer mouse models, with a decrease in radiolabeled anti-HER2 antibody observed after treatment (*33*). In metastatic breast cancer patients, pretreatment imaging of HER2 targeting with ^{64}Cu-labeled trastuzumab (*28*) or ^{89}Zr-labeled trastuzumab (*34*) was predictive of treatment response, with higher uptake of radiolabeled antibody before treatment being predictive of a better response. Our current study showed a correlation between the %ID/g of ^{89}Zr-labeled trastuzumab or ^{64}Cu-labeled trastuzumab and volume in tumors treated with T-DM1 or T-DXd, respectively. Our preclinical data contribute to the accumulating evidence that HER2 PET can provide noninvasive insight into receptor tumoral levels.

Tumors of animals treated with T-DM1 or T-DXd plus statin showed growth suppression and demonstrated lower uptake on PET images after therapy. These imaging findings correlated with changes

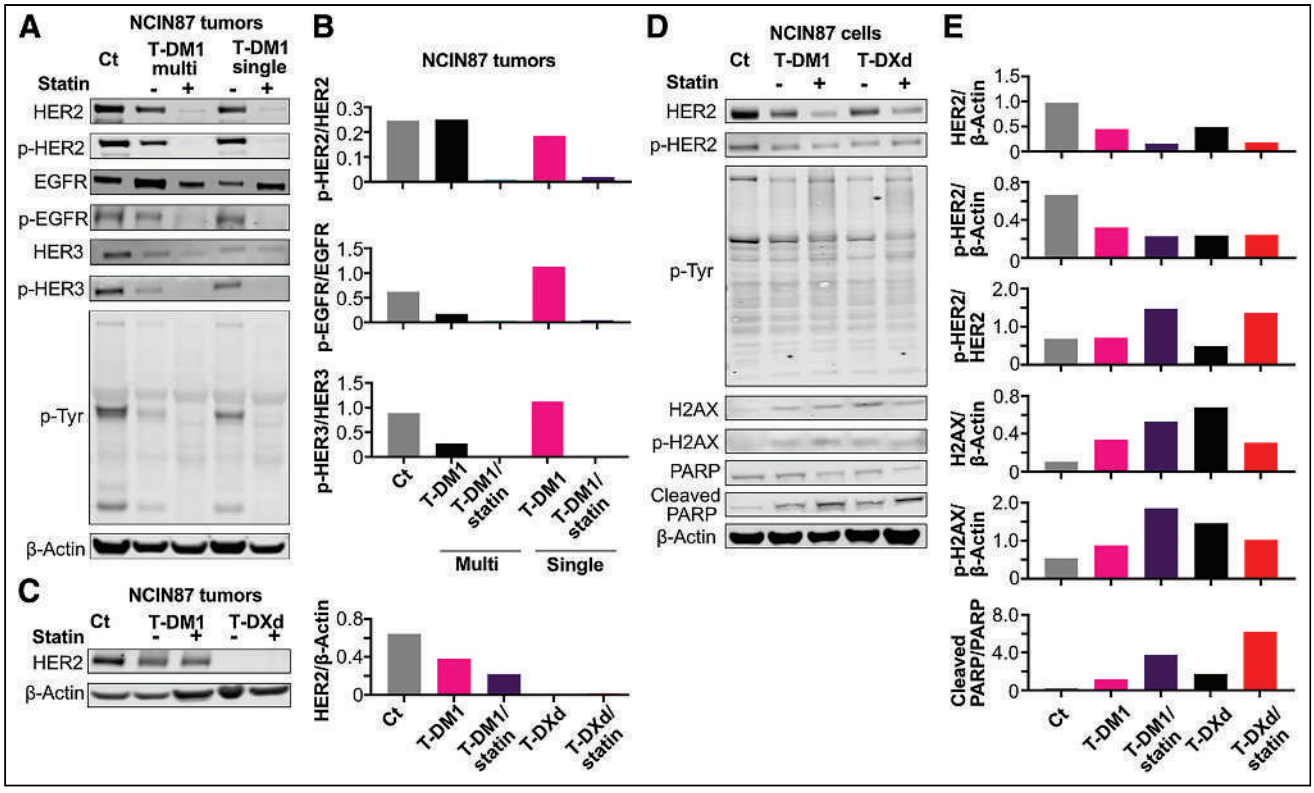

FIGURE 5. (A and B) Western blot analyses (A) and quantification (B) at 43 d after treatment of NCIN87 tumors for control, T-DM1 multiple-treatment regime, T-DM1/statin multiple-treatment regime, T-DM1 single-treatment regime, and T-DM1/statin single-treatment regime. Western blots show expression of proteins in HER2 downstream signaling pathways including HER2, phosphor-HER2, EGFR, phosphor-EGFR, HER3, phosphor-HER3, and phosphor-tyrosine. β-actin was used as loading control. Quantifications shown in B relate to A, and analyses for additional repeats are shown in supplemental materials. (C) HER2 Western blot analyses and quantification after treatment of NCIN87 tumors for control, T-DM1 single-treatment regime, T-DM1/statin single-treatment regime, T-DXd single-treatment regime, and T-DXd/statin single-treatment regime. β-actin was used as loading control. (D) Western blot analyses and (E) quantification for NCIN87 cells treated with vehicle, T-DM1, T-DM1/statin, T-DXd, and T-DXd/statin for 48 h. Western blots show expression of HER2, phosphor-HER2, phosphor-tyrosine, H2AX, phosphor-H2AX, cleaved PARP, and PARP. β-actin was used as loading control. Full membranes of all repeats are shown in supplemental materials. p-Tyr = phosphor-tyrosine.

in HER2 and HER2-mediated signaling in tumors, because we observed—by Western blot analyses—decreased HER2, HER2 phosphorylation, and phosphor-tyrosine phosphorylation in tumors. HER2 phosphorylation results in signaling activation, and further downstream phosphorylation of multiple proteins occurs, ultimately resulting in increased proliferation, survival, and migration of cancer cells that are driven by HER2 signaling (*35,36*). Our results indicate a suppression in HER-mediated signaling after T-DM1/statin and T-DXd/statin therapy.

Anti-HER2 ADC efficacy depends on a series of several sequential events: binding of the ADC to the cell-surface HER2, ability of the antibody to decrease HER2-mediated oncogenic signaling and to induce antibody-mediated cellular toxicity, ADC-HER2 internalization, and, finally, payload release inside the tumor cell (*37–39*). Our previous preclinical experiments are consistent with the hypothesis that surface-localized HER2s can be modulated to enhance trastuzumab and T-DM1 efficacy (*18,21*). Therefore, pharmacologic strategies that augment HER2 antibody tumor binding and further internalization may allow reducing the number of dose schedules of the therapeutic antibody or ADC. We observed that treating tumors with T-DM1 in combination with lovastatin enhances T-DM1 tumor binding and internalization in vitro, resulting in higher efficacy than with T-DM1 alone (*21*). Importantly, our results show that just a single dose of T-DM1/statin is efficacious in gastric tumor models and was just as effective as multiple doses of T-DM1/statin in a PDX gastric model (Fig. 4). Overall, our findings support a mechanism by which stabilization of membrane HER2 increases anti-HER2 ADC binding; consequently, internalization is enhanced, which in our studies allowed a lower number T-DM1 doses to achieve therapeutic efficacy in mice. If translated to the clinic, this strategy could potentially reduce the number of doses of T-DM1 and adverse events associated with T-DM1 treatment (*40*).

Although T-DM1 and T-DXd are composed of the same antibody (trastuzumab), several differences exist between these two ADCs: T-DXd has a higher drug-to-antibody ratio than T-DM1, two different linkers are used in the preparation of T-DM1 and T-DXd, the two cytotoxic payloads DM1 and DXd have a different mechanism of action, and DXd permeability allows for a bystander effect to the neighbor cells regardless of their expression for HER2. Coadministration of statin with an ADC enhanced the expression of the DNA damage markers PARP and H2AX. Additionally, PARP and H2AX were expressed in T-DM1/statin-treated cells but not in cells treated with T-DM1 alone, indicating induction of DNA damage with statins. Indeed, lipophilic statins such as lovastatin have previously been reported to sensitize cancer cells to radiotherapy via increased DNA damage. However, statins are also reported to protect against DNA damage in normal tissues by increasing DNA

double-strand break repair (*23,41*). This mechanism of action by statins requires further investigation with other preclinical tumor models.

In addition to modulating HER2 in tumors, it is possible that statins might also induce alterations in other HER2-expressing nontumor organs. Since trastuzumab does not bind the rodent homolog of HER2 (*42*), our study failed to address the effects of statin in trastuzumab binding to HER2-expressing murine tissues. Additionally, the pleiotropic effects of statins suggest that lovastatin has potential off-target effects in addition to HER2 modulation, none of which were determined in our study.

CONCLUSION

Our results showed that immuno-PET with radiolabeled trastuzumab can monitor HER2 tumoral levels on treatment with HER2-targeted ADCs in preclinical models. Our study also demonstrated that the combination of a statin with anti-HER2 ADC enhances therapeutic efficacy in preclinical HER2-expressing gastric tumor models in ways that allow reducing the number of ADC therapeutic doses. Considering that statins are prescribed to millions of people every year to reduce cholesterol levels (*43*), our findings have the potential to be translated to clinical trials to test the feasibility, safety, and efficacy of using statins in combination with HER2-targeting ADCs.

DISCLOSURE

The MSK Anti-Tumor Assessment Core and Molecular Cytology Core Facility is supported by NIH grant P30 CA08748. Abbey Zidel's contributions to the research were supported through Washington University's biology undergraduate research program (Bio 200/500) and MIR Summer Research Program. This research was supported by internal funds provided by the Mallinckrodt Institute of Radiology and the NIH (R01 CA244233-01A1). Patrícia Pereira acknowledges the NIH (R01 CA244233-01A1), American Cancer Society (IRG-21-133-64-03), Cancer Research Foundation (P22-03203), Elsa Pardee Foundation, Alvin J. Siteman Cancer Center through the Foundation for Barnes–Jewish Hospital, and National Cancer Institute (P30 CA091842). Jason Lewis acknowledges NIH NCI R35 CA232130 and NIH R01 CA244233-01A1. The Preclinical Imaging Facility at Washington University School of Medicine in St. Louis was supported by NIH/NCI Siteman Cancer Center support grant P30CA091842, NIH instrumentation grants S10OD018515 and S10OD030403, and internal funds provided by the Mallinckrodt Institute of Radiology. No other potential conflict of interest relevant to this article was reported.

ACKNOWLEDGMENTS

We thank the Washington University isotope production team for producing copper-64, and we thank the small-animal imaging facility for helping with small-animal PET/CT data generation. We also acknowledge the MSK Small-Animal Imaging Core Facility, the MSK Radiochemistry and Molecular Imaging Probe Core, and the MSK Anti-Tumor Assessment Core and Molecular Cytology Core Facility. We are grateful to Dr. Elisa De Stanchina and the entire team at the Antitumor Assessment Core at MSK for helping with the PDX models. We are thankful to Dr. Luis Batista for letting us use the Odyssey Infrared Imaging System. We thank Dr. Luke Carter for his help with the 3D Slicer software. We gratefully acknowledge the Siteman Cancer Center pharmacy for providing us with trastuzumab/Herceptin, T-DM1/Kadcyla (Genentech), and T-DXd/Enhertu (Daiichi Sankyo) antibodies.

KEY POINTS

QUESTION: Can HER2-targeted immuno-PET inform on the tumor response and dose regime of ADC therapy in combination with statins?

PERTINENT FINDINGS: Immuno-PET serves as a noninvasive tool to monitor HER2 depletion in vivo in response to T-DM1, T-DXd, T-DM1/statin, or T-DXd/statin administration.

IMPLICATIONS FOR PATIENT CARE: The enhanced potency of ADC therapy observed on coadministration with statins can be monitored with immuno-PET and enables lowering of ADC doses while achieving similar efficacy.

REFERENCES

1. Hudis CA. Trastuzumab: mechanism of action and use in clinical practice. *N Engl J Med.* 2007;357:39–51.
2. Modi S, Saura C, Yamashita T, et al. Trastuzumab deruxtecan in previously treated HER2-positive breast cancer. *N Engl J Med.* 2020;382:610–621.
3. Modi S, Saura C, Yamashita T, et al. Abstract PD3-06: updated results from DESTINY-breast01, a phase 2 trial of trastuzumab deruxtecan (T-DXd) in HER2 positive metastatic breast cancer [abstract]. *Cancer Res.* 2021;81(suppl):PD3-06.
4. Fu Z, Li S, Han S, Shi C, Zhang Y. Antibody drug conjugate: the "biological missile" for targeted cancer therapy. *Signal Transduct Target Ther.* 2022;7:93.
5. Ferraro E, Drago JZ, Modi S. Implementing antibody-drug conjugates (ADCs) in HER2-positive breast cancer: state of the art and future directions. *Breast Cancer Res.* 2021;23:84.
6. do Pazo C, Nawaz K, Webster RM. The oncology market for antibody-drug conjugates. *Nat Rev Drug Discov.* 2021;20:583–584.
7. Diéras V, Miles D, Verma S, et al. Trastuzumab emtansine versus capecitabine plus lapatinib in patients with previously treated HER2-positive advanced breast cancer (EMILIA): a descriptive analysis of final overall survival results from a randomised, open-label, phase 3 trial. *Lancet Oncol.* 2017;18:732–742.
8. Tarantino P, Carmagnani Pestana R, Corti C, et al. Antibody–drug conjugates: smart chemotherapy delivery across tumor histologies. *CA Cancer J Clin.* 2022;72:165–182.
9. Mamounas EP, Untch M, Mano MS, et al. Adjuvant T-DM1 versus trastuzumab in patients with residual invasive disease after neoadjuvant therapy for HER2-positive breast cancer: subgroup analyses from KATHERINE. *Ann Oncol.* 2021;32:1005–1014.
10. Iqbal N, Iqbal N. Human epidermal growth factor receptor 2 (HER2) in cancers: overexpression and therapeutic implications. *Mol Biol Int.* 2014;2014:852748.
11. Oh D-Y, Bang Y-J. HER2-targeted therapies: a role beyond breast cancer. *Nat Rev Clin Oncol.* 2020;17:33–48.
12. Li BT, Smit EF, Goto Y, et al. Trastuzumab deruxtecan in HER2-mutant non–small-cell lung cancer. *N Engl J Med.* 2022;386:241–251.
13. Grillo F, Fassan M, Sarocchi F, Fiocca R, Mastracci L. HER2 heterogeneity in gastric/gastroesophageal cancers: from benchside to practice. *World J Gastroenterol.* 2016;22:5879–5887.
14. Bang Y-J, Van Cutsem E, Feyereislova A, et al. Trastuzumab in combination with chemotherapy versus chemotherapy alone for treatment of HER2-positive advanced gastric or gastro-oesophageal junction cancer (ToGA): a phase 3, open-label, randomised controlled trial. *Lancet.* 2010;376:687–697.
15. Thuss-Patience PC, Shah MA, Ohtsu A, et al. Trastuzumab emtansine versus taxane use for previously treated HER2-positive locally advanced or metastatic gastric or gastro-oesophageal junction adenocarcinoma (GATSBY): an international randomised, open-label, adaptive, phase 2/3 study. *Lancet Oncol.* 2017;18:640–653.
16. Janjigian YY, Viglianti N, Liu F, Mendoza-Naranjo A, Croydon L. A phase Ib/II, multicenter, open-label, dose-escalation, and dose-expansion study evaluating trastuzumab deruxtecan (T-DXd, DS-8201) monotherapy and combinations in patients with HER2-overexpressing gastric cancer (DESTINY-Gastric03) [abstract]. *J Clin Oncol.* 2021;39(suppl):TPS261.
17. Shitara K, Bang Y-J, Iwasa S, et al. Trastuzumab deruxtecan in previously treated HER2-positive gastric cancer. *N Engl J Med.* 2020;382:2419–2430.

18. Pereira PMR, Sharma SK, Carter LM, et al. Caveolin-1 mediates cellular distribution of HER2 and affects trastuzumab binding and therapeutic efficacy. *Nat Commun.* 2018;9:5137.
19. Filho OM, Viale G, Stein S, et al. Impact of HER2 heterogeneity on treatment response of early-stage HER2-positive breast cancer: phase II neoadjuvant clinical trial of T-DM1 combined with pertuzumab. *Cancer Discov.* 2021;11:2474–2487.
20. Orr G, Hu D, Ozçelik S, Opresko LK, Wiley HS, Colson SD. Cholesterol dictates the freedom of EGF receptors and HER2 in the plane of the membrane. *Biophys J.* 2005;89:1362–1373.
21. Pereira PMR, Mandleywala K, Monette S, et al. Caveolin-1 temporal modulation enhances antibody drug efficacy in heterogeneous gastric cancer. *Nat Commun.* 2022;13:2526.
22. Guruswamy S, Rao CV. Synergistic effects of lovastatin and celecoxib on caveolin-1 and its down-stream signaling molecules: implications for colon cancer prevention. *Int J Oncol.* 2009;35:1037–1043.
23. Fritz G, Henninger C, Huelsenbeck J. Potential use of HMG-CoA reductase inhibitors (statins) as radioprotective agents. *Br Med Bull.* 2011;97:17–26.
24. Valentovic M. Lovastatin. Lovastatin. In: Enna SJ, Bylund DB, eds. *xPharm: The Comprehensive Pharmacology Reference.* Elsevier; 2007:1–5.
25. Pondé N, Ameye L, Lambertini M, Paesmans M, Piccart M, de Azambuja E. Trastuzumab emtansine (T-DM1)-associated cardiotoxicity: pooled analysis in advanced HER2-positive breast cancer. *Eur J Cancer.* 2020;126:65–73.
26. Abdel-Qadir H, Bobrowski D, Zhou L, et al. Statin exposure and risk of heart failure after anthracycline- or trastuzumab-based chemotherapy for early breast cancer: a propensity score–matched cohort study. *J Am Heart Assoc.* 2021;10:e018393.
27. Woo S-K, Jang SJ, Seo M-J, et al. Development of ^{64}Cu-NOTA-trastuzumab for HER2 targeting: a radiopharmaceutical with improved pharmacokinetics for human studies. *J Nucl Med.* 2019;60:26–33.
28. Mortimer JE, Bading JR, Frankel PH, et al. Use of ^{64}Cu-DOTA-trastuzumab PET to predict response and outcome of patients receiving trastuzumab emtansine for metastatic breast cancer: a pilot study. *J Nucl Med.* 2022;63:1145–1148.
29. Choi SYC, Lin D, Gout PW, Collins CC, Xu Y, Wang Y. Lessons from patient-derived xenografts for better in vitro modeling of human cancer. *Adv Drug Deliv Rev.* 2014;79–80:222–237.
30. Corso S, Isella C, Bellomo SE, et al. A comprehensive PDX gastric cancer collection captures cancer cell–intrinsic transcriptional MSI traits. *Cancer Res.* 2019;79:5884–5896.
31. Zeng M, Pi C, Li K, et al. Patient-derived xenograft: a more standard "Avatar" model in preclinical studies of gastric cancer. *Front Oncol.* 2022;12:898563.
32. Wolska-Washer A, Robak T. Safety and tolerability of antibody-drug conjugates in cancer. *Drug Saf.* 2019;42:295–314.
33. Massicano AVF, Lee S, Crenshaw BK, et al. Imaging of HER2 with [^{89}Zr]pertuzumab in response to T-DM1 therapy. *Cancer Biother Radiopharm.* 2019;34:209–217.
34. Gebhart G, Lamberts LE, Wimana Z, et al. Molecular imaging as a tool to investigate heterogeneity of advanced HER2-positive breast cancer and to predict patient outcome under trastuzumab emtansine (T-DM1): the ZEPHIR trial. *Ann Oncol.* 2016;27:619–624.
35. Arienti C, Pignatta S, Tesei A. Epidermal growth factor receptor family and its role in gastric cancer. *Front Oncol.* 2019;9:1308.
36. Roviello G, Aprile G, D'Angelo A, et al. Human epidermal growth factor receptor 2 (HER2) in advanced gastric cancer: where do we stand? *Gastric Cancer.* 2021;24:765–779.
37. Drago JZ, Modi S, Chandarlapaty S. Unlocking the potential of antibody–drug conjugates for cancer therapy. *Nat Rev Clin Oncol.* 2021;18:327–344.
38. Ogitani Y, Aida T, Hagihara K, et al. DS-8201a, a novel HER2-targeting ADC with a novel DNA topoisomerase I inhibitor, demonstrates a promising antitumor efficacy with differentiation from T-DM1. *Clin Cancer Res.* 2016;22:5097–5108.
39. Junttila TT, Li G, Parsons K, Phillips GL, Sliwkowski MX. Trastuzumab-DM1 (T-DM1) retains all the mechanisms of action of trastuzumab and efficiently inhibits growth of lapatinib insensitive breast cancer. *Breast Cancer Res Treat.* 2011;128:347–356.
40. Kowalczyk L, Bartsch R, Singer CF, Farr A. Adverse events of trastuzumab emtansine (T-DM1) in the treatment of HER2-positive breast cancer patients. *Breast Care (Basel).* 2017;12:401–408.
41. Efimova EV, Ricco N, Labay E, et al. HMG-CoA reductase inhibition delays DNA repair and promotes senescence after tumor irradiation. *Mol Cancer Ther.* 2018;17:407–418.
42. Lewis Phillips G, Guo J, Kiefer JR, et al. Trastuzumab does not bind rat or mouse ErbB2/neu: implications for selection of non-clinical safety models for trastuzumab-based therapeutics. *Breast Cancer Res Treat.* 2022;191:303–317.
43. Juarez D, Fruman DA. Targeting the mevalonate pathway in cancer. *Trends Cancer.* 2021;7:525–540.

Ambient Light Resistant Shortwave Infrared Fluorescence Imaging for Preclinical Tumor Delineation via the pH Low-Insertion Peptide Conjugated to Indocyanine Green

Benedict Edward Mc Larney[1], Mijin Kim*[1], Sheryl Roberts*[2], Magdalena Skubal*[1], Hsiao-Ting Hsu[1], Anuja Ogirala[1], Edwin C. Pratt[1,2], Naga Vara Kishore Pillarsetty[2,4], Daniel A. Heller[1,3], Jason S. Lewis[1–4], and Jan Grimm[1–5]

[1]*Molecular Pharmacology Program, Memorial Sloan Kettering Cancer Center, New York, New York;* [2]*Department of Radiology, Memorial Sloan Kettering Cancer Center, New York, New York;* [3]*Department of Pharmacology, Weill Cornell Medicine, New York, New York;* [4]*Department of Radiology, Weill Cornell Medicine, New York, New York; and* [5]*Molecular Imaging Therapy Service, Memorial Sloan Kettering Cancer Center, New York, New York*

Shortwave infrared (900–1,700 nm) fluorescence imaging (SWIRFI) has shown significant advantages over visible (400–650 nm) and near-infrared (700–900 nm) fluorescence imaging (reduced autofluorescence, improved contrast, tissue resolution, and depth sensitivity). However, there is a major lag in the clinical translation of preclinical SWIRFI systems and targeted SWIRFI probes. **Methods:** We preclinically show that the pH low-insertion peptide conjugated to indocyanine green (pHLIP ICG), currently in clinical trials, is an excellent candidate for cancer-targeted SWIRFI. **Results:** pHLIP ICG SWIRFI achieved picomolar sensitivity (0.4 nM) with binary and unambiguous tumor screening and resection up to 96 h after injection in an orthotopic breast cancer mouse model. SWIRFI tumor screening and resection had ambient light resistance (possible without gating or filtering) with outstanding signal-to-noise ratio (SNR) and contrast-to-noise ratio (CNR) values at exposures from 10 to 0.1 ms. These SNR and CNR values were also found for the extended emission of pHLIP ICG in vivo (>1,100 nm, 300 ms). **Conclusion:** SWIRFI sensitivity and ambient light resistance enabled continued tracer clearance tracking with unparalleled SNR and CNR values at video rates for tumor delineation (achieving a tumor-to-muscle ratio above 20). In total, we provide a direct precedent for the democratic translation of an ambient light resistant SWIRFI and pHLIP ICG ecosystem, which can instantly improve tumor resection.

Key Words: SWIR; fluorescence; surgery; preclinical; tumor

J Nucl Med 2023; 64:1647–1653
DOI: 10.2967/jnumed.123.265686

Shortwave infrared (SWIR, 900–1,700 nm, or the second near-infrared [NIR] window) fluorescence imaging (SWIRFI) is providing novel insights for preclinical and clinical biophotonic imaging (*1–5*). In the SWIR spectrum, tissue scattering, absorption, and autofluorescence are negligible, permitting higher contrast, deeper penetration, and improved resolution (*6–10*). By combining the spectral response of human eyes (380–720 nm) with SWIR detector insensitivity below 920 nm, SWIRFI can be performed without ambient light removal and with no effect on human vision (*11*). SWIRFI is undergoing rapid preclinical deployment but is hampered by system and dye unavailability for routine applications that are investigating complex and diverse biologic systems, a situation that is exacerbated in clinical settings. SWIRFI has characterized the extended emission of indocyanine green (ICG, >900 nm, which is invisible to silicon sensors), with improvements in resolution and contrast over silicon-based NIR fluorescence imaging (NIRFI) (*5*,*8*,*10*,*12–14*). Improved spatial resolution can be achieved with SWIRFI by using long-pass filters at 1,100 and 1,300 nm, and simply using the entire SWIRFI spectral response enables improved image quality over NIRFI (*15*). In addition, dedicated SWIR (>1,000 nm) fluorophores have been developed (*16*,*17*). Targeted clinical cancer resection could greatly benefit from SWIRFI, but novel SWIRFI cancer-targeting agents require further assessment before clinical deployment (*11*,*16*,*18*). Accordingly, clinical SWIRFI has focused on the nontargeted enhanced permeability and retention effect (second window) of ICG-based imaging. Here, SWIRFI has shown both image and patient outcome improvements over NIRFI for liver tumor surgery, glioma resection, cystic renal mass removal, and brain metastasis (*19–22*). However, there is an unmet need for a workhorse cancer-targeting agent for SWIRFI like that of ^{18}F-FDG for PET (*23*).

The pH low-insertion peptide (pHLIP) conjugated to ICG (pHLIP ICG), not yet validated for SWIRFI, is a tumor-targeting agent under clinical investigation for breast cancer resection (NCT05130801) (*24–27*). In acidic tumor microenvironments, pHLIP ICG inserts into cellular membranes, displays high selectivity and contrast over healthy tissues, and preclinically delineates various cancers (*24*). pHLIP is also amenable to other dyes or radiolabeling (*28*,*29*). Here, we combined commercial SWIRFI's video rate picomolar sensitivity to ICG with the tumor selectivity of pHLIP ICG. We achieved video rates with a high signal-to-noise ratio (SNR), a high contrast-to-noise ratio (CNR), and preclinical tumor screening and resection in an orthotopic murine breast model. SWIRFI displayed improved sensitivity over the current preclinical gold-standard NIRFI (IVIS; PerkinElmer) for pHLIP ICG, extending the video-guided surgical resection window from 24 up to 96 h (*24*,*30–32*). Surgical window extension enabled an increased tumor CNR, peaking 72–96 h after injection, with tumor screening and resection possible at exposures of 10–0.1 ms. This could be performed under cost-effective and facile ambient lighting conditions (no gating), enhancing clinical practicality, translation, and dissemination (*33*). The extended

Received Mar. 6, 2023; revision accepted Jun. 12, 2023.
For correspondence or reprints, contact Benedict Edward Mc Larney (mclarneb@mskcc.org) or Jan Grimm (grimmj@mskcc.org).
*Contributed equally to this work.
Published online Aug. 24, 2023.

emission of pHLIP ICG beyond 1,100 nm in vivo is also demonstrated. The CNR achieved by SWIRFI (mean tumor-to-muscle ratio of 22.6) provided binary and unambiguous tumor or no-tumor delineation, with implications for preclinical assessment of other cancer-targeting dyes. This work establishes the basis for SWIRFI's clinical translation via pHLIP ICG for targeted cancer resection, aiding the translation of other SWIRFI cancer-targeting agents.

MATERIALS AND METHODS

Ambient Light Resistant SWIRFI

A commercial preclinical SWIR hyperspectral system (IR-VIVO and PHySpec; Photon Etc.) permitted in vivo SWIRFI. Laser excitation (808 nm) was distributed over the mouse (90–450 mW/cm^2, measured using a laser power meter, PM100D; Thorlabs). Sensor settings were −70.0°C, high gain, 0 gain conversion, 8-MHz readout, no corrections, and 14-bit depth, and 30-Hz rates were achieved at exposure times of 10–0.1 ms. The in-built SWIR light-emitting diode (LED, 940 nm) was used for SWIR white light (anatomical reference) images (10 ms). A red, green, blue LED with a 650-nm short-pass filter (FES0650; Thorlabs) provided ambient lighting (70 μW/cm^2 at 488 nm).

SWIR Spectral Measurement of pHLIP ICG

The NIR absorbance of pHLIP ICG was measured on a plate reader (SpectraMax iD5; Molecular Devices). pHLIP ICG's SWIR emission spectra were assessed with and without 1-palmitoyl-2-oleoyl-sn-glycero-3-phosphocholine liposomes (POPC) (100 nm; T&T Scientific Corp.; Fig. 1D) (*24*,*25*). SWIR spectra were acquired using a home-built SWIRFI spectroscopy system and tunable white light source (SuperK Extreme supercontinuum white light laser; NKT Photonics), an inverted microscope (IX-71 microscope and ×20 SWIR objective; Olympus), and a 1-dimensional indium gallium arsenide NIR detector (iDus 1.7-μm InGaAs, Andor; Oxford Instruments). Light was collected at exposures of 0.1–5 s with 808 nm excitation. Wavelength-dependent emission intensity artifacts from the spectrometer, detector, and other optics were corrected via an HL-3-CAL-EXT halogen calibration light source (Ocean Optics).

Phantom Imaging

Commercial imaging phantoms (ICG-equivalent Reference Set; Quel Imaging) assessed resolution, sensitivity, and depth penetration of NIRFI and SWIRFI preclinical systems (*34*–*36*). Quel targets were analyzed by Quel's dedicated site (*35*). Custom prelens filter mounts and appropriate long-pass filters (FELH-1100, FELH-1200, and FELH-1300 with SM1L03; Thorlabs) enabled SWIRFI at longer wavelengths of 1,100, 1,200, and 1,300 nm, respectively.

NIRFI

NIRFI was performed on a gold-standard commercial system (IVIS Spectrum CT; PerkinElmer). System settings were low binning, f-stop 1, high lamp, and 745- and 820-nm excitation and emission filter sets, respectively. Raw (luminescent) tiff files were analyzed after dark-noise subtraction, with median filtering (outlier removal) and gaussian blur applied as for SWIRFI. Exposure times ranged from 10 to 10,000 ms.

Image Processing and Analysis

SWIRFI data (h5 format) were converted to 14-bit tiff files in ImageJ (*37*). Automated image processing consisted of dark-noise subtraction and 32-bit conversion, flat field correction with a normalized ICG (Cardiogreen, I2633; Sigma) image, dark and bright pixel removal via median filtering (outlier removal; kernel, 1; threshold, 500), LUT (Fire) application, gaussian blur (σ = 2 pixels), and thresholding. Single frames were quantified for all exposures. Analysis was performed in GraphPad Prism (version 9.3.1; GraphPad Software) and MATLAB

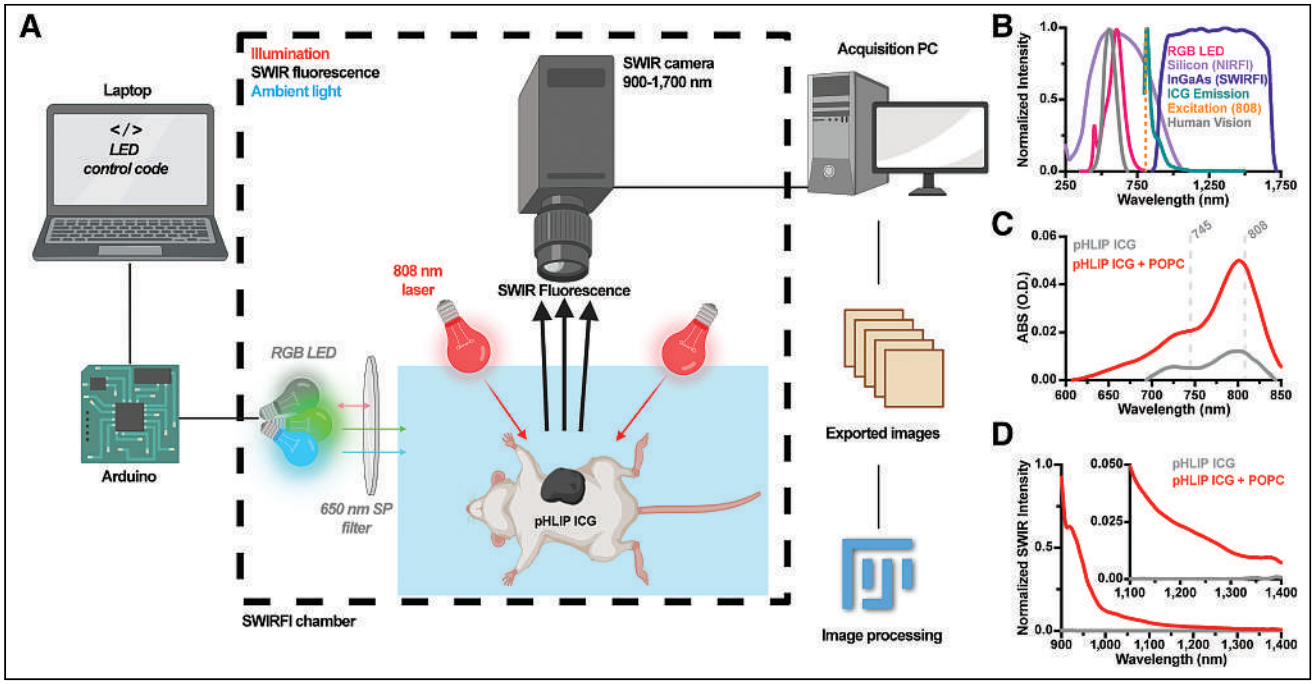

FIGURE 1. Ambient light resistant SWIRFI for pHLIP ICG detection. (A) SWIRFI setup for ambient light resistant imaging of pHLIP ICG. Images were automatically converted to tiff files for rapid image correction and analysis (ImageJ). Panel was created with Biorender.com. (B) Comparison of silicon (NIRFI), indium gallium arsenide (InGaAs; SWIRFI) sensors, and human vision responses with ICG laser excitation (808 nm), ICG, and LED emission profiles. (C) pHLIP ICG absorption (100 μL, 8 μM) with and without (bound and unbound) POPC liposomes. NIRFI (745 nm) and SWIRFI (808 nm) excitation wavelengths are shown. (D) SWIR emission of pHLIP ICG (normalized) in on and off states. (Inset) Emission from 1,100 to 1,400 nm. ABS (O.D.) = absorbance (optical density); PC = personal computer; RGB = red, green, blue; SP = short pass.

(2021b; MathWorks). SNR and CNR values (dB) were calculated (Excel, version 16.57; Microsoft) according to Equations 1 and 2:

$$\mathrm{SNR_{dB}} = 10 \times \log_{10}\left(\frac{\text{brightest ROI}_{\mathrm{Avg}} - \text{background ROI}_{\mathrm{Avg}}}{\text{background ROI}_{\mathrm{SD}}}\right) \quad \text{Eq. 1}$$

$$\mathrm{CNR_{dB}} = 10 \times \log_{10}\left(\frac{\text{tumor ROI}_{\mathrm{Avg}} - \text{body ROI}_{\mathrm{Avg}}}{\text{body ROI}_{\mathrm{SD}}}\right). \quad \text{Eq. 2}$$

Mouse Handling

Mouse handling, imaging, and housing were performed in accordance with the National Institutes of Health guidelines and approved by the Office of the Institutional Animal Care and Use Committee protocols at Memorial Sloan Kettering Cancer Center. Athymic female nude mice (n = 12, Foxn1^{nu}, 002019, inbred; the Jackson Laboratory) were housed under a 12-h on-and-off light cycle, with up to 5 mice per cage with food (trimethoprim–sulfamethoxazole [Sulfatrim] addition; TestDiet, #TD1810356-293) and water ad libitum. Mammary fat pad injection of 3.0 × 10^5 4T1 cells (ATCC, CRL-2539, STR-validated, *Mycoplasma*-free) suspended in 30 μL of Matrigel generated orthotopic breast tumor models. At tumor sizes of approximately 100 mm^3 (~7–9 d postinjection), mice intravenously received pHLIP ICG (0.5 mg/kg) and were imaged 1, 24, 48, 72, and 96 h after injection. Anesthesia was achieved in all cases via gaseous isoflurane inhalation (induction, 3%; maintenance, 1%–2% v/v). Euthanasia via CO_2 inhalation occurred at 96 h under approved protocols. Tumor resection (after euthanasia) was performed, with tumor excision confirmed via SWIRFI. SWIRFI necropsy biodistribution was performed for tumor, liver, kidneys, spleen, stomach, large and small intestines, brain, skin, bone, muscle, heart, and lungs. SWIRFI organ values from a noninjected (control) mouse were subtracted from injected mouse values. Two mice were excluded from all analyses because of a failed acquisition time point and insufficient tumor size, respectively. Hematoxylin and eosin (H&E) staining was performed in line with Supplemental Table 1 (supplemental materials are available at http://jnm.snmjournals.org).

RESULTS

Ambient Light Resistant SWIRFI for pHLIP ICG

SWIRFI's ambient lighting resistant setup and processing workflow were determined (Figs. 1A and 1B; Supplemental Fig. 1). Red, green, blue LED combinations without laser excitation found that green, blue, and green-blue (cyan) with and without a 650-nm short-pass filter and without gating were invisible to the sensor (there was no long-pass filter on the sensor; Supplemental Fig. 1). Red emission was barely detectable at 10 ms exposures (~5% of the sensor's dynamic range) and slightly dimmed by the 650 nm short-pass filter (Supplemental Fig. 1). The sensor's spectral response, human vision response, LED emission, laser excitation, and ICG emission combine to achieve ambient lighting resistant imaging under these conditions (Fig. 1B). pHLIP ICG NIR absorbance and SWIR emission spectra were determined on respective dedicated spectrometers (Figs. 1C and 1D). An 8 μM bound (with POPC liposomes) pHLIP ICG solution displayed characteristic ICG absorption (with a 802-nm peak). pHLIP ICG's SWIR fluorescence mechanism was in line with its previously reported NIR format and extended to approximately 1,400 nm, like that of naïve ICG, with the unbound solution, free of POPC liposomes, having minimal absorption or fluorescence, as expected (Figs. 1C and 1D) (*24*,*25*).

SWIRFI Advantages for pHLIP ICG

Phantoms enabled direct comparison between SWIRFI and NIRFI modalities in their ICG-optimized modes. Preclinical gold-standard NIRFI was performed on an IVIS system and found to be insensitive compared with SWIRFI. ICG-mimicking phantoms highlighted SWIRFI's improved sensitivity, improved depth (5.24 vs. 3.64 mm), and comparative resolution levels (2.5 line pairs/mm; Supplemental Fig. 2). This improvement was also found in custom pHLIP ICG phantoms in which SWIRFI had 100 times more sensitivity than NIRFI, both with and without tissue (Supplemental Fig. 3). SWIRFI achieved picomolar (0.4 nM) pHLIP ICG sensitivity at 10 ms (100 Hz equivalent) exposure times (Supplemental Fig. 4), at a third of the American National Standards Institute limit for laser fluence at 808 nm (ANSI, <330 mW/cm^2) (*38*).

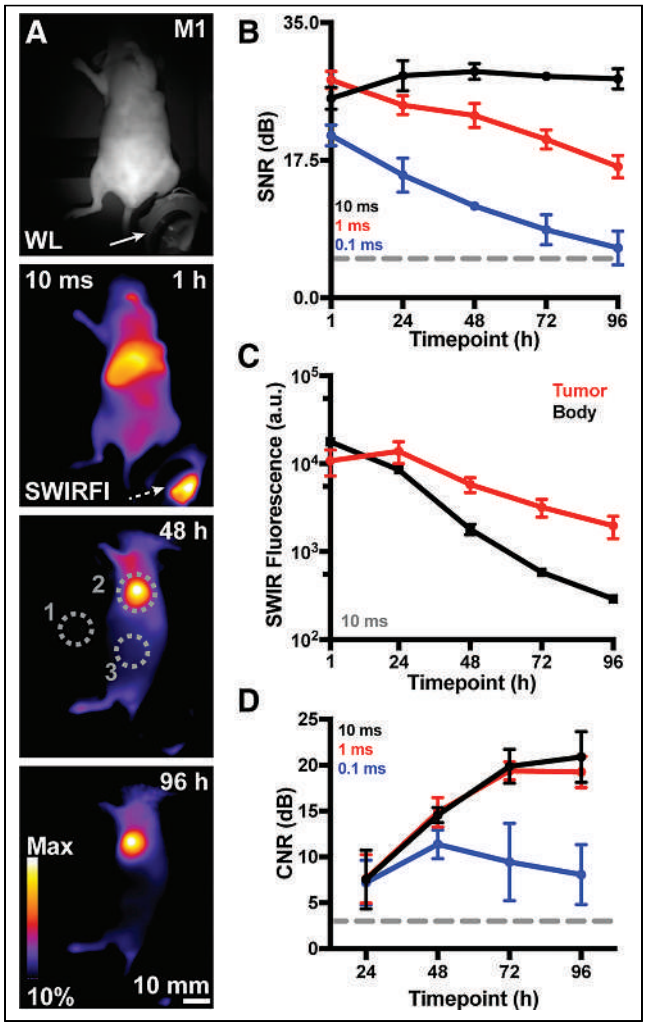

FIGURE 2. Ambient lighting resistant SWIRFI tumor screening via pHLIP ICG. (A) Representative white light (WL, in-built SWIR LED illumination, 940 nm) and SWIRFI detection of pHLIP ICG–injected mice (>900 nm, n = 4, 10 ms, 0.5 mg/kg) at 1, 48, and 96 h after injection. Negligible signal was detected from a control mouse (data not shown, noninjected, n = 1). (B) SNR (dB) of brightest point from all mice from 1 to 96 h at all exposures (10, 1, and 0.1 ms). (C) Values (10 ms) comparing tumor and body SWIRFI levels. Tumor fluorescence peaked at 24 h and was retained up to 96 h. (D) Tumor-to-body CNR (dB) increases past 24 h and peaks at 72 h. In all cases, mean and SD are shown (n = 4 biologic replicates) aside from D, up to 96 h with 0.1 ms exposure, where only n = 3 values are shown. a.u. = arbitrary unit; dotted arrow = fluorescence reflection from ambient LED; dotted gray circles = quantification regions of interest, where 1 is system noise (SNR), 2 is tumor values, and 3 is body values (CNR); Dotted line = acceptable thresholds (5 dB for SNR, 3 dB for CNR); M1 = mouse 1; Max = maximum; solid arrow = ambient light source (red, green, blue LED).

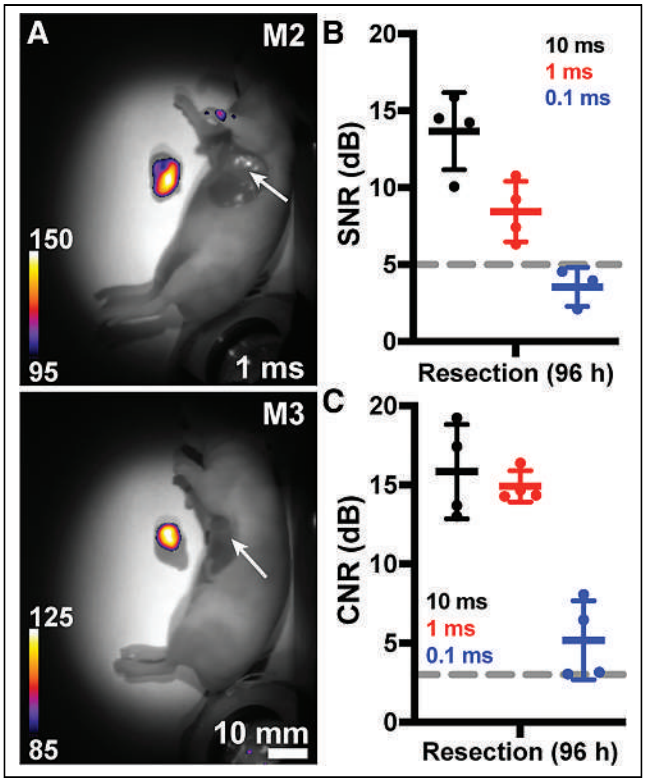

FIGURE 3. Ambient lighting resistant SWIRFI resection. (A) Representative SWIRFI white light (WL) overlaid with detection of tumor resection (after euthanasia) at 96 h. The tumor is clearly delineated from both the body and tumor bed (arrow). (B) Resected tumor SNR levels for all exposure times. (C) Resected tumor CNR levels for all exposure times. In all cases, mean and SD are shown (n = 4 biologic replicates, aside from B, 0.1 ms exposure, where only n = 3 are shown). Dotted line = acceptable thresholds (5 dB for SNR, 3 dB for CNR); M2 = mouse 2; M3 = mouse 3.

Improved Tumor Contrast via SWIRFI Under Ambient Lighting

Reanalysis of 0 to 48 h published NIRFI levels for pHLIP ICG biodistribution found competition between tumor and liver fluorescence, and after 48 h, tumor contrast should improve (Supplemental Fig. 5) (*24*). Because SWIRFI provided sufficient (picomolar) sensitivity to detect low probe levels, we assessed tumor contrast up to 96 h after injection. Nude mice bearing orthotopic breast tumors were used for facile SWIRFI of deep-seated organs through the skin (*24*). pHLIP ICG was administered intravenously (0.5 mg/kg), with SWIRFI performed every 24 h from 1 to 96 h. Signal collection from the deep-seated liver was aided by imaging above the ANSI fluence limit at 808 nm (450 mW/cm^2), removing the need to euthanize mice at later time points (*38*). SWIRFI of pHLIP ICG and the image processing pipeline displayed excellent tumor screening from 24 to 96 h (Fig. 2; Supplemental Figs. 6 and 7). As expected, liver fluorescence was strongest 1 h after injection, decreasing with time as tumor contrast and delineation simultaneously increased. SWIRFI consistently performed with high SNR values (~30 dB, 10 ms) above acceptable 5 dB thresholds (Fig. 2B). Tumor fluorescence levels peaked at 24 h compared with surrounding areas, with CNR values also above acceptable 3 dB thresholds. However, CNR values dramatically increased, peaking from 72 to 96 h with 10- and 1-ms exposures providing indistinguishable CNR values. A batch of mice imaged within the ANSI limit (300 mW/cm^2 at 808 nm) provided similar results (Supplemental Fig. 8) to aid clinical translation of these results. Gold-standard NIRFI required exposure of 1,000 ms to match the 1 ms SWIRFI SNR and CNR (Supplemental Fig. 9).

SWIRFI Tumor Resection via pHLIP ICG Under Ambient Lighting

Surgical resection (after euthanasia) was performed at 96 h. SWIRFI binarily delineated the tumor (Fig. 3A) and confirmed tumor-free beds with SNR and CNR above acceptable thresholds (Figs. 3B and 3C). SWIRFI biodistribution found tumors had significantly higher fluorescence than other tissues, confirming the improved clearance of pHLIP ICG from tissues other than the tumor (Fig. 4). Values for all organs from all mice are shown (Fig. 4), as are all organs with corresponding threshold levels from all mice (Supplemental Fig. 10). Images and values are combined from mice imaged at 808 nm fluence levels of either 450 or 300 mW/cm^2, with each corrected via noninjected organs. H&E staining was performed on select organs, confirming the characterization of tissues associated with residual agent uptake (Supplemental Fig. 11).

Extended SWIRFI (>1,100 nm) of pHLIP ICG In Vivo

We then investigated the emission of pHLIP ICG extended past 1,100 nm in vivo (Fig. 1D), similar to antibody-conjugated ICG imaging (*39*). First, a 4 μM pHLIP ICG solution with POPC liposomes, as before, was imaged in a multiwell plate. Imaging was performed with and without scattering medium (raw chicken breast) and various long-pass optical filters (Supplemental Fig. 12). A reduction of 1.98 mm in the full width at half maximum was found when imaging with a long-pass filter at 1,100 nm over 900 nm (no filter and sensor spectral response). This was further reduced by 2.27 mm when employing

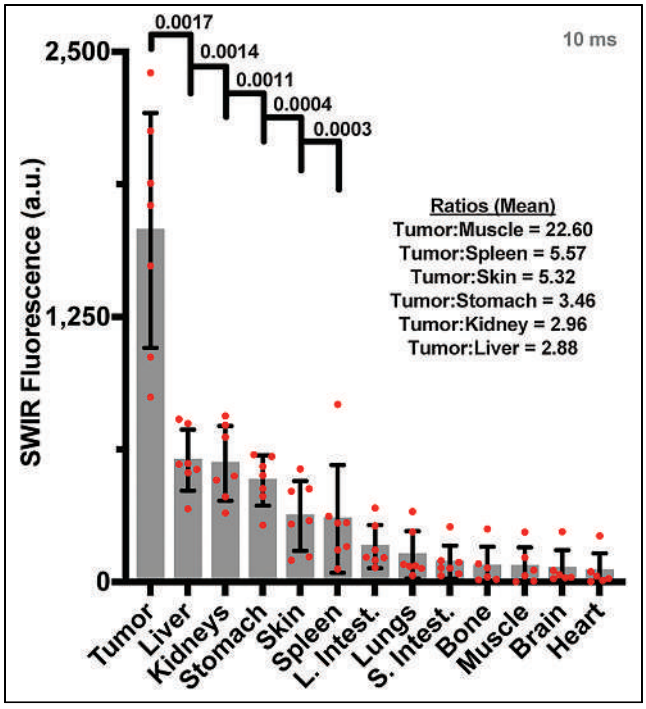

FIGURE 4. Ambient lighting resistant SWIRFI necropsy biodistribution. SWIRFI organ values. Respective endogenous values from control mice imaged under comparative conditions have been subtracted for each. Mean, standard deviation, and biologic replicates (n = 7) are shown, negative values after endogenous level subtraction are not shown. Select P values (<0.05, Welch 2-tailed t test, unpaired, parametric) and ratios comparing tumor to select tissues are shown. a.u. = arbitrary unit; L. Intest. = large intestine; S. Intest. = small intestine.

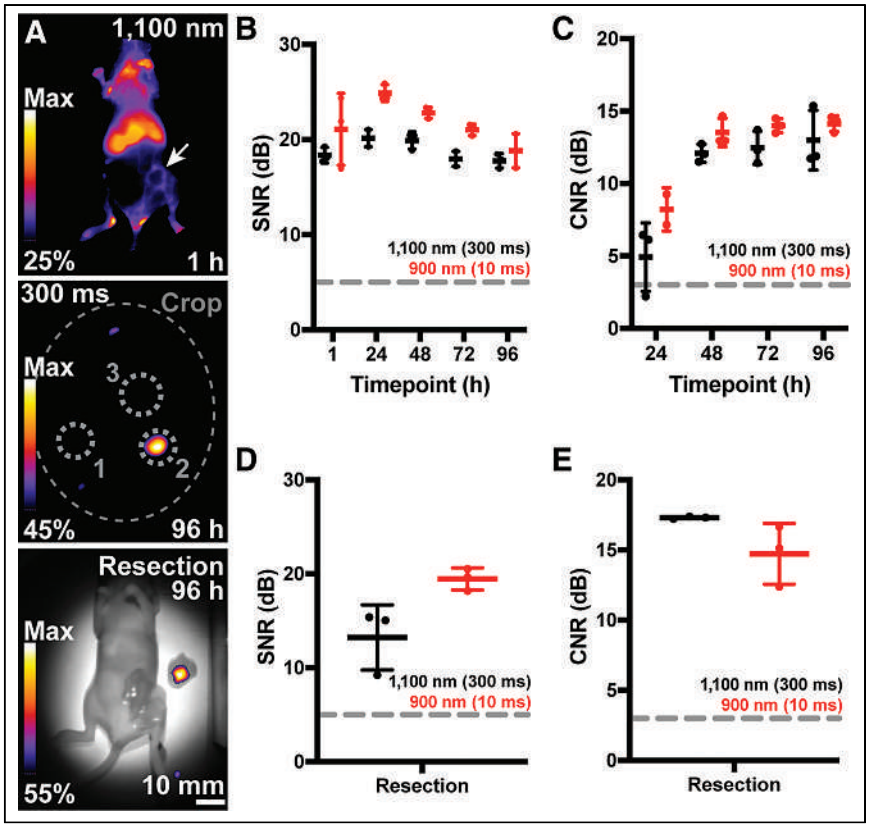

FIGURE 5. Ambient lighting resistant extended emission SWIRFI (>1,100 nm) of pHLIP ICG in vivo. (A, top) >1,100 nm representative image 1 h after pHLIP ICG (300 ms, 0.5 mg/kg). Gaussian blur has not been added to 1 h time point images. (A, middle) >1,100 nm image at 96 h. Regions of interest are shown as before. (A, bottom) >1,100 nm SWIRFI resection for complete tumor removal at 96 h. (B) SNR values of >1,100 nm (300-ms exposure) and >900 nm (10-ms exposure) from all mice at all time points. Exposures were selected at close to camera saturation at 1 h and then used for all time points. (C) Tumor CNR values from 24 to 96 h from all mice. (D and E) Comparative resection SNR and CNR values at both >1,100 and >900 nm for all mice. SD, mean, and individual replicates (n = 3) are shown. a.u. = arbitrary units; dotted gray circles = quantification regions of interest, where 1 is system noise (SNR), 2 is tumor values, and 3 is body values (CNR); large dotted gray oval = cropping because of long-pass filter; dotted lines = acceptable thresholds (5 dB for SNR, 3dB for CNR); Max = maximum; solid arrow = tumor location.

a long-pass filter at 1,300 nm. A final batch of mice was imaged using the 1,100 nm long-pass filter after pHLIP ICG administration, as before, with the extended SWIRFI emission of pHLIP ICG readily detected, albeit not at video rates (Fig. 5; Supplemental Figs. 13 and 14).

DISCUSSION

In this work, preclinical commercial SWIRFI's advantages for pHLIP ICG were shown in phantoms, along with its utility in tumor screening and resection. When compared in their respective ICG optimized modes, SWIRFI consistently outperformed a NIRFI system. The used SWIRFI system and developed image processing pipeline produced relevant and accurate images (Figs. 1–3 and 5; Supplemental Figs. 6–8, 10, and 13). The achieved sensitivity (Supplemental Figs. 2–4) facilitated video rate tumor detection, guided resection, and determined biodistribution at low probe levels up to 96 h after injection, highlighted by the high SNR and CNR levels at exposure times of 10, 1, and 0.1 ms (Figs. 2–4). The video rate picomolar sensitivity of SWIRFI was essential for validating the hypothesized increase in tumor CNR at later time points (Supplemental Fig. 4; Supplemental Video 1). The next iterations could use the minor decrease in SNR with comparative CNR at 1 versus 10 ms (Figs. 2 and 3), with gated laser emission to reduce exposure of the agent at no cost to tumor delineation, thus reducing photobleaching (*40–43*). The mean necropsy-based muscle-to-tumor ratio of 22.6 at 96 h provided binary and unambiguous tumor delineation, with tumor values that were statistically significant compared with liver values (Fig. 4; Supplemental Fig. 10). Considering the wide tumor-targeting capabilities of pHLIP ICG, other tumor models should be investigated (*24*).

All SWIRFI images and results presented here were performed under ambient lighting conditions with no detriment to signal accuracy (*17,18*). The LED (~$1) used in a green-blue combination was undetectable by the sensor with and without filtering (Fig. 1; Supplemental Fig. 1). This proof-of-principle work positions SWIRFI as an easily scalable, cost-effective, environmentally friendly, and democratic facile solution for ambient light resistant fluorescence guided surgery (FGS) without gating or filters (*33*). Future iterations should aim to assess various commercial LEDs for clinical deployment.

The spectral emission of pHLIP ICG extended past 1,100 nm is also shown. A direct comparison was made from mice consecutively imaged with 900 (sensor response) and 1,100 nm long-pass filters at all time points (Fig. 5; Supplemental Figs. 13 and 14). However, the 1,100-nm cutoff did not equate to an improved SNR or CNR over the 900 nm cutoff images because of tumor localization of pHLIP ICG at later time points, topical tumor location, and overall reduction in bulk sensitivity above 1,100 nm. SWIRFIs resolution improvement (>1,100 or >1,300 nm) is likely of more benefit to smaller-structure imaging (angiography, delineation of nerves, micrometastases) than to large tumor masses (*8,15*).

These results have implications for preclinical imaging, in which novel targeting agents (peptides, nanoparticles, small molecules, antibodies, etc.) can be evaluated via video rate SWIRFI by conjugating ICG, or novel SWIRFI dyes can be evaluated using the pHLIP (*16,44*). The achieved sensitivity may permit dose reduction for detection and simultaneously elongate imaging windows—improving tumor delineation (CNR), as shown here—and could be combined with multispectral SWIRFI for even further improvement (*45*). Clinical translation of the observed CNR increase could enable democratic dissemination of tumor resection techniques, with nonexperts (as in this work) being able to perform targeted FGS, with resection ambiguity being simultaneously eliminated for experienced surgeons. The ability to perform guided resection under ambient lighting via SWIRFI with minimal disruption to current workflows may aid surgeon uptake of FGS. The potential for direct clinical translation of these results has been established via laser intensities within the ANSI limit

(<330 mW/cm^2; Supplemental Fig. 8). However, this translation will require a custom SWIRFI device with a smaller footprint than current preclinical systems, as well as improvements in usability. Such a device should also be compared with current clinical NIRFI systems. At the time of writing, no SWIRFI device has received Food and Drug Administration approval or is routinely deployed clinically, especially in complex operating room environments. In addition, the LED setup should be scaled up for ambient lighting.

CONCLUSION

This work validates a pH-sensitive, peptide-based, tumor-targeting agent conjugated to ICG, which is in clinical trials, for SWIRFI. pHLIP conjugation to ICG retains both pHLIP's tumor selective mechanism and the extended emission of ICG in the SWIR region, where tissue scattering, absorbance, and autofluorescence are minimal (Figs. 1, 2, and 5; Supplemental Fig. 12) (*24*). Accordingly, SWIRFI was readily performed with minimal to no background interference from tissue and under ambient lighting conditions. SWIRFI provided unprecedented CNR and SNR at various exposure times (10–0.1 ms) that are at least 3 and up to 300 times faster than video rate requirements (30 ms). Combining SWIRFI sensitivity with extended probe clearance provides unambiguous and binary tumor delineation resistant to ambient lighting. This work calls for a clinically compatible system to further assess SWIRFI for clinical FGS. Such a system could provide video rate FGS under ambient lighting conditions at improved tissue depth and resolution with high confidence in complete tumor resection. This may have clinical implications for tumor visualization through blood pools or in highly optically scattering tissue environments, for example, brain gliomas or lymphatic mapping (*5*,*22*,*46*).

DISCLOSURE

This work was supported by the NIH (R56 EB030512 to Jan Grimm, R35 CA232130 to Jason Lewis, and F32 CA268912-01 to Edwin Pratt), the National Science Foundation CAREER Award (1752506 to Daniel Heller), the NCI (R01-CA215719 to Daniel Heller and Cancer Center Support Grant P30-CA008748, Selwyn Vickers/MSKCC), the NIBIB (R01-EB033651 to Daniel Heller), the American Cancer Society Research Scholar Grant (GC230452 to Daniel Heller), the Louis and Rachel Rudin Foundation (to Daniel Heller), the Experimental Therapeutics Center of MSKCC (to Daniel Heller), Mr. William H. Goodwin and Mrs. Alice Goodwin and the Commonwealth Foundation for Cancer Research (to Daniel Heller). Mijin Kim was supported by the NIH (K99-EB033580) and the Marie-Josée Kravis Women in Science Endeavor Postdoctoral Fellowship. Jason Lewis is a founder of and has shares in pHLIP, Inc. pHLIP, Inc. has provided funding for manufacturing of pHLIP ICG, safety, pharmacology, and toxicology studies and donated pHLIP ICG for this study. Jason Lewis has shares in Stryker Corp. Daniel Heller is a cofounder and officer with equity interest in Lime Therapeutics, Inc., and cofounder with equity interest in Selectin Therapeutics Inc. and Resident Diagnostics, Inc., and a member of the scientific advisory board of Concarlo Therapeutics, Inc., Nanorobotics Inc., and Mediphage Bioceuticals, Inc. No other potential conflict of interest relevant to this article was reported.

ACKNOWLEDGMENTS

We thank pHLIP, Inc., for the donation of pHLIP ICG to this investigation. The authors also thank the support of Memorial Sloan Kettering Cancer Center's Animal Imaging Core Facility.

KEY POINTS

QUESTION: Does pHLIP ICG, a cancer-targeting agent currently in clinical trials for FGS, serve as a suitable candidate for SWIRFI?

PERTINENT FINDINGS: This work compared commercially available preclinical systems in their optimized ICG detection modes and found SWIRFI readily outperformed the current NIRFI gold standard for both depth and sensitivity.

IMPLICATIONS FOR PATIENT CARE: The picomolar sensitivity of SWIRFI enabled video rate imaging of pHLIP ICG at lengthy time points (96 h). This resulted in a dramatic improvement in CNR, providing binary and unambiguous tumor delineation that was unaffected by ambient light. This work is a direct precedent for clinical SWIRFI deployment for tumor resection and has implications for preclinical probe development.

REFERENCES

1. Thimsen E, Sadtler B, Berezin MY. Shortwave-infrared (SWIR) emitters for biological imaging: a review of challenges and opportunities. *Nanophotonics.* 2017;6:1043–1054.
2. Vollmer M, Möllmann K-P, Shaw JA. The optics and physics of near infrared imaging. Paper presented at: Education and Training in Optics and Photonics; 2015; Bordeaux, France.
3. McLarney BE, Zhang Q, Pratt EC, et al. Detection of shortwave-infrared Cerenkov luminescence from medical isotopes. *J Nucl Med.* 2022;64:177–182.
4. Qi J, Sun C, Zebibula A, et al. Real-time and high-resolution bioimaging with bright aggregation-induced emission dots in short-wave infrared region. *Adv Mater.* 2018;30:e1706856.
5. Byrd BK, Marois M, Tichauer KM, et al. First experience imaging short-wave infrared fluorescence in a large animal: indocyanine green angiography of a pig brain. *J Biomed Opt.* 2019;24:080501.
6. Jacques SL. Optical properties of biological tissues: a review. *Phys Med Biol.* 2013;58:R37–R61.
7. Golovynskyi S, Golovynska I, Stepanova LI, et al. Optical windows for head tissues in near-infrared and short-wave infrared regions: approaching transcranial light applications. *J Biophotonics.* 2018;11:e201800141.
8. Carr JA, Aellen M, Franke D, So PT, Bruns OT, Bawendi MG. Absorption by water increases fluorescence image contrast of biological tissue in the shortwave infrared. *Proc Natl Acad Sci USA.* 2018;115:9080–9085.
9. Wang F, Ren F, Ma Z, et al. In vivo non-invasive confocal fluorescence imaging beyond 1,700 nm using superconducting nanowire single-photon detectors. *Nat Nanotechnol.* 2022;17:653–660.
10. Hong G, Antaris AL, Dai H. Near-infrared fluorophores for biomedical imaging. *Nat Biomed Eng.* 2017;1:0010.
11. Wang F, Qu L, Ren F, et al. High-precision tumor resection down to few-cell level guided by NIR-IIb molecular fluorescence imaging. *Proc Natl Acad Sci USA.* 2022;119:e2123111119.
12. Carr JA, Franke D, Caram JR, et al. Shortwave infrared fluorescence imaging with the clinically approved near-infrared dye indocyanine green. *Proc Natl Acad Sci USA.* 2018;115:4465–4470.
13. Cosco ED, Lim I, Sletten EM. Photophysical properties of indocyanine green in the shortwave infrared region. *ChemPhotoChem.* 2021;5:727–734.
14. Carr JA, Valdez TA, Bruns OT, Bawendi MG. Using the shortwave infrared to image middle ear pathologies. *Proc Natl Acad Sci USA.* 2016;113:9989–9994.
15. Wu Y, Suo Y, Wang Z, et al. First clinical applications for the NIR-II imaging with ICG in microsurgery. *Front Bioeng Biotechnol.* 2022;10:1042546.
16. Bandi VG, Luciano MP, Saccomano M, et al. Targeted multicolor in vivo imaging over 1,000 nm enabled by nonamethine cyanines. *Nat Methods.* 2022;19:353–358.
17. Cosco ED, Arús BA, Spearman AL, et al. Bright chromenylium polymethine dyes enable fast, four-color in vivo imaging with shortwave infrared detection. *J Am Chem Soc.* 2021;143:6836–6846.
18. Zhang L, Shi X, Li Y, et al. Visualizing tumors in real time: a highly sensitive PSMA probe for NIR-II imaging and intraoperative tumor resection. *J Med Chem.* 2021;64:7735–7745.

19. Hu Z, Fang C, Li B, et al. First-in-human liver-tumour surgery guided by multispectral fluorescence imaging in the visible and near-infrared-I/II windows. *Nat Biomed Eng.* 2020;4:259–271.
20. Shi X, Zhang Z, Zhang Z, et al. Near-infrared window II fluorescence image-guided surgery of high-grade gliomas prolongs the progression-free survival of patients. *IEEE Trans Biomed Eng.* 2022;69:1889–1900.
21. Cao C, Deng S, Wang B, et al. Intraoperative near-infrared II window fluorescence imaging-assisted nephron-sparing surgery for complete resection of cystic renal masses. *Clin Transl Med.* 2021;11:e604.
22. Teng CW, Cho SS, Singh Y, et al. Second window ICG predicts gross-total resection and progression-free survival during brain metastasis surgery. *J Neurosurg.* 2021;135:1026–1035.
23. Almuhaideb A, Papathanasiou N, Bomanji J. ^{18}F-FDG PET/CT imaging in oncology. *Ann Saudi Med.* 2011;31:3–13.
24. Crawford T, Moshnikova A, Roles S, et al. pHLIP ICG for delineation of tumors and blood flow during fluorescence-guided surgery. *Sci Rep.* 2020;10:18356.
25. Golijanin J, Amin A, Moshnikova A, et al. Targeted imaging of urothelium carcinoma in human bladders by an ICG pHLIP peptide ex vivo. *Proc Natl Acad Sci USA.* 2016;113:11829–11834.
26. Wyatt LC, Lewis JS, Andreev OA, Reshetnyak YK, Engelman DM. Applications of pHLIP technology for cancer imaging and therapy. *Trends Biotechnol.* 2017;35:653–664.
27. Pinker-Domenig, K. A study of multiparametric MRI and pHLIP® ICG in breast cancer imaging during surgery. ClinicalTrials.gov website. https://clinicaltrials.gov/study/NCT05130801. Updated June 15, 2023. Accessed July 25, 2023.
28. Roberts S, Strome A, Choi C, et al. Acid specific dark quencher QC1 pHLIP for multi-spectral optoacoustic diagnoses of breast cancer. *Sci Rep.* 2019;9:8550.
29. Bauer D, Visca H, Weerakkody A, et al. PET imaging of acidic tumor environment with ^{89}Zr-labeled pHLIP probes. *Front Oncol.* 2022;12:882541.
30. Hwang S-K, Tyszkiewicz C, Morin J, Point GR, Liu C-N. Novel in vivo and ex vivo hybrid in vivo imaging system (IVIS) imaging offers a convenient and precise way to measure the glomerular filtration rate in conscious mice. *J Pharmacol Toxicol Methods.* 2021;110:107084.
31. Spinelli AE, Kuo C, Rice BW, et al. Multispectral Cerenkov luminescence tomography for small animal optical imaging. *Opt Express.* 2011;19:12605–12618.
32. Ezra-Elia R, Obolensky A, Ejzenberg A, et al. Can an in vivo imaging system be used to determine localization and biodistribution of AAV5-mediated gene expression following subretinal and intravitreal delivery in mice? *Exp Eye Res.* 2018;176:227–234.
33. Sexton KJ, Zhao Y, Davis SC, Jiang S, Pogue BW. Optimization of fluorescent imaging in the operating room through pulsed acquisition and gating to ambient background cycling. *Biomed Opt Express.* 2017;8:2635–2648.
34. Davis SC, Pogue BW, Dehghani H, Paulsen KD. Contrast-detail analysis characterizing diffuse optical fluorescence tomography image reconstruction. *J Biomed Opt.* 2005;10:050501.
35. LaRochelle EPM, Streeter SS, Littler EA, Ruiz AJ. 3D-printed tumor phantoms for assessment of in vivo fluorescence imaging analysis methods. *Mol Imaging Biol.* 2023;25:212–220.
36. Ruiz AJ, Garg S, Streeter SS, et al. 3D printing fluorescent material with tunable optical properties. *Sci Rep.* 2021;11:17135.
37. Schindelin J, Arganda-Carreras I, Frise E, et al. Fiji: an open-source platform for biological-image analysis. *Nat Methods.* 2012;9:676–682.
38. American National Standards Institute. *American National Standard for Safe Use of Lasers.* Laser Institute of America; 2007.
39. Tsuboi S, Jin T. Shortwave-infrared (SWIR) fluorescence molecular imaging using indocyanine green–antibody conjugates for the optical diagnostics of cancerous tumours. *RSC Advances.* 2020;10:28171–28179.
40. Clutter ED, Chen LL, Wang RR. Role of photobleaching process of indocyanine green for killing neuroblastoma cells. *Biochem Biophys Res Commun.* 2022;589:254–259.
41. Yaqoob Z, McDowell EJ, Wu J, Heng X, Fingler JP, Yang C. Molecular contrast optical coherence tomography: a pump-probe scheme using indocyanine green as a contrast agent. *J Biomed Opt.* 2006;11:054017.
42. Holzer W, Mauerer M, Penzkofer A, et al. Photostability and thermal stability of indocyanine green. *J Photochem Photobiol B.* 1998;47:155–164.
43. Yeroslavsky G, Umezawa M, Okubo K, et al. Photostabilization of indocyanine green dye by energy transfer in phospholipid-PEG micelles. *J Photopolym Sci Technol.* 2019;32:115–121.
44. Lim I, Lin EY, Garcia J, et al. Shortwave infrared fluorofluorophores for multicolor in vivo imaging. *Angew Chem Int Ed Engl.* 2023;62:e202215200.
45. Waterhouse DJ, Privitera L, Anderson J, Stoyanov D, Giuliani S. Enhancing intraoperative tumor delineation with multispectral short-wave infrared fluorescence imaging and machine learning. *J Biomed Opt.* 2023;28:094804.
46. Takeuchi M, Sugie T, Abdelazeem K, et al. Lymphatic mapping with fluorescence navigation using indocyanine green and axillary surgery in patients with primary breast cancer. *Breast J.* 2012;18:535–541.

Preclinical Comparison of the ^{64}Cu- and ^{68}Ga-Labeled GRPR-Targeted Compounds RM2 and AMTG, as Well as First-in-Humans [^{68}Ga]Ga-AMTG PET/CT

Lena Koller[1], Markus Joksch[2], Sarah Schwarzenböck[2], Jens Kurth[2], Martin Heuschkel[2], Nadine Holzleitner[1], Roswitha Beck[1], Gunhild von Amsberg[3], Hans-Jürgen Wester[1], Bernd Joachim Krause*[2], and Thomas Günther*[1]

[1]Pharmaceutical Radiochemistry, Technical University of Munich, Garching, Germany; [2]Department of Nuclear Medicine, Rostock University Medical Center, Rostock, Germany; and [3]Department of Oncology, University Medical Center Hamburg–Eppendorf, Hamburg, Germany

Despite the recent success of prostate-specific membrane antigen (PSMA)–targeted compounds for theranostic use in prostate cancer (PCa), alternative options for the detection and treatment of PSMA-negative lesions are needed. We have recently developed a novel gastrin-releasing peptide receptor (GRPR) ligand with improved metabolic stability, which might improve diagnostic and therapeutic efficacy and could be valuable for PSMA-negative PCa patients. Our aim was to examine its suitability for theranostic use. We performed a comparative preclinical study on [^{64}Cu]Cu-/[^{68}Ga]Ga-AMTG ([^{64}Cu]Cu-/[^{68}Ga]Ga-α-Me-L-Trp^{8}-RM2) using [^{64}Cu]Cu-/[^{68}Ga]Ga-RM2 ([^{64}Cu]Cu-/[^{68}Ga]Ga-DOTA-Pip^{5}-Phe^{6}-Gln^{7}-Trp^{8}-Ala^{9}-Val^{10}-Gly^{11}-His^{12}-Sta^{13}-Leu^{14}-NH_2) as a reference compound and investigated [^{68}Ga]Ga-AMTG in a proof-of-concept study in a PCa patient. **Methods:** Peptides were labeled with ^{64}Cu (80 °C, 1.0 M NaOAc, pH 5.50) and ^{68}Ga (90 °C, 0.25 M NaOAc, pH 4.50). GRPR affinity (half-maximal inhibitory concentration, room temperature, 2 h) and GRPR-mediated internalization (37 °C, 60 min) were examined on PC-3 cells. Biodistribution studies were performed at 1 h after injection in PC-3 tumor–bearing mice. For a first-in-humans application, 173 MBq of [^{68}Ga]Ga-AMTG were administered intravenously and whole-body PET/CT scans were acquired at 75 min after injection. **Results:** ^{64}Cu- and ^{68}Ga-labeling proceeded almost quantitatively (>98%). All compounds revealed similarly high GRPR affinity (half-maximal inhibitory concentration, 1.5–4.0 nM) and high receptor-bound fractions (79%–84% of cell-associated activity). In vivo, high activity levels (percentage injected dose per gram) were found in the PC-3 tumor (14.1–15.1 %ID/g) and the pancreas (12.6–30.7 %ID/g), whereas further off-target accumulation was low at 1 h after injection, except for elevated liver uptake observed for both ^{64}Cu-labeled compounds. Overall biodistribution profiles and tumor-to-background ratios were comparable but slightly enhanced for the ^{68}Ga-labeled analogs in most organs. [^{68}Ga]Ga-AMTG confirmed the favorable pharmacokinetics—as evident from preclinical studies—in a patient with metastasized castration-resistant PCa showing intense uptake in several lesions. **Conclusion:** AMTG is eligible for theranostic use, as labeling with ^{64}Cu and ^{68}Ga, as well as ^{177}Lu (known from previous study), does not have a negative influence on its favorable biodistribution pattern. For this reason, further clinical evaluation is warranted.

Key Words: AMTG; first-in-humans; ^{68}Ga; ^{64}Cu; prostate cancer

J Nucl Med 2023; 64:1654–1659
DOI: 10.2967/jnumed.123.265771

Although prostate cancer (PCa) is associated with a high morbidity and mortality in metastasized castration-resistant PCa (mCRPC) (*1*), treatment has recently made some progress due to approval by the U.S. Food and Drug Administration and the European Medicines Agency of radioligand therapy (RLT) targeting the prostate-specific membrane antigen (PSMA) as a third-line therapy (*2,3*). However, in approximately 10%–20% of patients with recurrent PCa, a sufficiently high PSMA expression either is not present in PSMA-targeted PET imaging (*4,5*) or is lost in the course of subsequent treatment. Indeed, loss of PSMA expression may reflect aggressive transdifferentiation, a resistance mechanism to currently available standard therapies (*6,7*). In these patients, a PCa-atypical metastatic pattern is frequently observed (especially with visceral metastasis), whereas the classic adenocarcinoma features are often lost. Furthermore, PCa is known to be highly heterogeneous (*8*), which is why alternative compounds for imaging and RLT of PCa are required.

The gastrin-releasing peptide receptor (GRPR, bombesin-2 receptor) has been shown to be overexpressed in early, but more importantly in advanced and aggressive, PCa (*9,10*). Moreover, PCa patient cohorts that underwent both PSMA and GRPR PET revealed some metastases that were found only by the PSMA-targeted compound and others that were detected only by the GRPR-targeted compound; a complementary role for these targets in PCa is therefore anticipated (*11–14*). The GRPR-targeted radiopharmaceutical most often clinically applied, [^{68}Ga]Ga-RM2 ([^{68}Ga]Ga-DOTA-Pip^{5}-Phe^{6}-Gln^{7}-Trp^{8}-Ala^{9}-Val^{10}-Gly^{11}-His^{12}-Sta^{13}-Leu^{14}-NH_2), displayed favorable biodistribution patterns in humans, as high activity levels were found only in tumor lesions and the pancreas (*11,15,16*). Hence, its ^{177}Lu-labeled analog was used for RLT in PSMA-negative/GRPR-positive PCa patients, and this analog demonstrated promising dosimetry data (*17*). However, the limited metabolic stability of [^{68}Ga]Ga-RM2 has been discussed (*18*), being the motivation for our group to develop a RM2 derivative,

Received Mar. 24, 2023; revision accepted Jun. 12, 2023.
For correspondence or reprints, contact Thomas Günther (thomas.guenther@tum.de)
*Contributed equally to this work.
Published online Jul. 20, 2023.

[^{177}Lu]Lu-AMTG ([^{177}Lu]Lu-α-Me-L-Trp^{8}-RM2), which retained the favorable pharmacokinetics of [^{68}Ga]Ga-/[^{177}Lu]Lu-RM2 but showed distinctly increased metabolic stability in vivo and could thus improve therapeutic efficacy (*19*).

To confirm a sufficient GRPR expression on PCa cells before GRPR RLT, imaging of preferably PSMA-negative PCa patients is required first, which is why, with regard to a potential RLT using [^{177}Lu]Lu-AMTG, it would be advantageous to have a pendant for PET imaging. Due to the presence of a DOTA chelator, the use of the established theranostic pair ^{68}Ga and ^{177}Lu is well feasible. Besides ^{68}Ga, ^{64}Cu has recently emerged as an interesting alternative for PET imaging because of its longer half-life (12.7 h) and positron energy ($E_{\beta+,max}$, 653 keV), which is similar to the positron energy of ^{18}F and thus enables a high spatial resolution in PET despite its low positron decay probability of approximately 17% (*20*).

Hence, this study aimed to elucidate whether the AMTG peptide, originally designed for RLT, could also be used for PET imaging when labeled with either ^{64}Cu or ^{68}Ga. A comparative preclinical evaluation on [^{64}Cu]Cu-/[^{68}Ga]Ga-AMTG and [^{64}Cu]Cu-/[^{68}Ga]Ga-RM2 encompassed the determination of GRPR affinity (half-maximal inhibitory concentration [IC_{50}]) and GRPR-mediated internalization on PC-3 cells, lipophilicity (as evaluated by *n*-octanol/phosphate-buffered saline solution distribution coefficient distribution coefficients at pH 7.4 [log$D_{7.4}$]), and biodistribution in PC-3 tumor–bearing mice. Moreover, we selected [^{68}Ga]Ga-AMTG for clinical translation in a first-in-humans PET/CT examination in a patient with mCRPC.

MATERIALS AND METHODS

Chemical Synthesis and Labeling Procedures

A detailed description of the precursor synthesis is provided in the supplemental materials (available at http://jnm.snmjournals.org). Purification was accomplished via reversed-phase high-performance liquid chromatography (HPLC).

^{64}Cu and ^{68}Ga labeling was performed in analogy to an established protocol for ^{177}Lu labeling (*19*). A detailed description of the labeling procedures is provided in the supplemental materials. [^{64}Cu]$CuCl_2$ was purchased from DSD-Pharma GmbH. [^{68}Ga]$GaCl_3$ was provided by ITM Isotope Technologies Munich SE. The radiolabeled reference, *3*-[^{125}I]I-Tyr^{6}-MJ9 (Supplemental Fig. 1), was prepared according to reported procedures (*19,21*). Characterization of all GRPR ligands is provided in Supplemental Figures 2–4.

The synthesis of [^{68}Ga]Ga-AMTG according to good manufacturing practices for human PET/CT studies was performed using a good radiopharmaceutical practice module (Scintomics GmbH) while using an SC-01 gallium peptide labeling kit (ABX). [^{68}Ga]$GaCl_3$ was obtained from a GalliaPharm generator (Eckert & Ziegler) and was trapped on a PS-H^+ cartridge (ABX), which was eluted by a sodium chloride solution. The eluate was transferred in the reactor containing the AMTG precursor and the 4-(2-hydroxyethyl)-1-piperazineethanesulfonic acid (HEPES) buffer. The solution was heated and afterward transferred to a Sep-Pak C18 Light cartridge (Waters) for purification. After washing with water, the cartridge was eluted with ethanol and the solution was diluted with phosphate-buffered saline. The Cathivex-GV (Merck KGaA) was used as a sterile filter after the synthesis. Quality control included an instant thin-layer chromatography silica gel scan (NH_4OAc/MeOH; Agilent), as well as an HPLC measurement against the corresponding reference compound, [^{nat}Ga]Ga-AMTG. Compliance with the HEPES limit was determined by a spot test. Furthermore, a sterile filter integrity test, a limulus amebocyte lysate test, and a postapplication sterility test were performed. The ethanol concentration was measured by gas chromatography analysis.

In Vitro Experiments

All in vitro experiments (IC_{50} and log$D_{7.4}$) were performed according to a previously published procedure (*19*). A detailed description is provided in the supplemental materials.

In Vivo Experiments

Animal Experiments. All animal experiments were conducted according to a previously published protocol (*19*) and in accordance with general animal welfare regulations in Germany (German animal protection act, in the edition of the announcement dated May 18, 2006, as amended by article 280 of June 19, 2020, approval ROB-55.2-1-2532.Vet_02-18-109 by the General Administration of Upper Bavaria) and the institutional guidelines for the care and use of animals. Exclusion criteria for animals from an experiment were weight loss of more than 20%, a tumor size of more than 1,500 mm^3, ulceration of the tumor, respiratory distress, or a change in behavior. None of these criteria applied to any animal from the experiment. Neither randomization nor masking was applied in the allocation of the experiments. The health status of the animals was specific pathogen-free according to the recommendation of the Federation of European Laboratory Animal Science Associations. The study was performed in compliance with the ARRIVE guidelines (Animal Research: Reporting of In Vivo Experiments).

For biodistribution studies, approximately 2–4 MBq (100 pmol, 150 μL) of the ^{64}Cu-/^{68}Ga-labeled GRPR ligand were injected into the tail vein of anesthetized (2% isoflurane) 2- to 3-mo-old female PC-3 tumor–bearing CB17-SCID mice (n = 4). Organs were removed and weighed, and radioactivity was measured in a γ-counter (Perkin Elmer) after euthanasia at 1 h after injection.

Acquired data were statistically analyzed via a Student *t*-test via Excel (Microsoft Corp.) and OriginPro software (version 9.7) from OriginLab Corp. Acquired P values of less than 0.05 were considered statistically significant.

PET/CT in Patient. [^{68}Ga]Ga-AMTG was applied as an individual medical diagnostic test in a 72-y-old patient with advanced-stage mCRPC for whom no other diagnostic or therapeutic options were available. This use is allowed by the German Medical Act (§13 2b Arzneimittelgesetz), which waives the need for institutional review board approval. The legal and ethical compliance of this approach has recently been reviewed by the local ethics committee in the context of requesting approval for retrospective evaluation of therapy data obtained in this way (Ethics Committee at Rostock University, file no. A 2018-0240). The patient gave written informed consent after receiving comprehensive medical information from a board-certified nuclear medicine physician. The anonymized analyses were performed in accordance with the Declaration of Helsinki and its later amendments and with the legal considerations of clinical guidelines.

A detailed description of the patient's history is provided in the supplemental materials. The patient underwent [^{68}Ga]Ga-AMTG whole-body PET/CT using a Gemini TF 16 (Philips Healthcare) at 75 min after injection of 173 MBq of [^{68}Ga]Ga-AMTG. Whole-body CT imaging was performed as auxiliary CT (120 kVp, 40 mAs). PET datasets were reconstructed using the blob ordered-subsets time-of-flight protocol (3 iterations, 31 subsets), corrected for randoms, scatter, decay, and attenuation (using whole-body auxiliary CT).

RESULTS

Synthesis and Radiolabeling

Manual synthesis of RM2 and AMTG yielded 14% and 12% labeling precursor, respectively, after purification by reversed-phase HPLC (chemical purity > 98%, determined by reversed-phase

HPLC at λ = 220 nm). Complexation of all ligands with a 2.5-fold excess of [^{nat}Ga]Ga(NO_3)$_3$ and [^{nat}Cu]$CuCl_2$ each resulted in quantitative yields. The radiolabeled reference, 3-[^{125}I]I-Tyr^6-MJ9, was produced in a radiochemical yield and purity of 29% and more than 98%, respectively, after reversed-phase HPLC purification. Both ^{64}Cu- and ^{68}Ga-labeling was performed manually, each resulting in radiochemical yields and purities of more than 98% as well as molar activities of 55 ± 4 GBq/μmol (decay-corrected) and 35 ± 3 GBq/μmol (decay-corrected). Both ^{64}Cu- and ^{68}Ga-labeled RM2, as well as AMTG, were used without further purification.

The synthesized batch used for the patient yielded 409 MBq (~56% non–decay-corrected). All specifications were fulfilled. The pH of the 16 mL of solution was 7. The reference compound and the radiolabeled product displayed the same HPLC retention times. The radiochemical purity determined by HPLC was 98.7%, and the content of unbound [^{68}Ga]Ga-species was less than 0.3%. Thin-layer chromatography measurement was in line with less than 0.5% of unbound [^{68}Ga]Ga^{3+}.

In Vitro Characterization

The ^{nat}Cu- and ^{nat}Ga-labeled compounds exhibited high GRPR affinity on PC-3 cells, with IC_{50} values in the range of 1.5–4.0 nM (Fig. 1A; Supplemental Table 1; Supplemental Fig. 5). Although overall internalization was low for all GRPR ligands, the more affine ^{68}Ga-labeled compounds were internalized significantly higher within 1 h by PC-3 cells than were their ^{64}Cu-labeled counterparts ($P < 0.04$, Fig. 1B). It was evident for all analogs that a higher GRPR affinity led to increased internalized (Fig. 2A), as well as receptor-bound noninternalized, fractions (Fig. 2B), which is why the ratio of receptor-bound to internalized fraction was nearly constant, regardless of their GRPR affinity (Fig. 2C). Log$D_{7.4}$ was similar for all compounds (Fig. 1C). However, the ^{68}Ga-labeled ligands exhibited significantly lower lipophilicity than their ^{64}Cu-labeled analogs ($P < 0.01$).

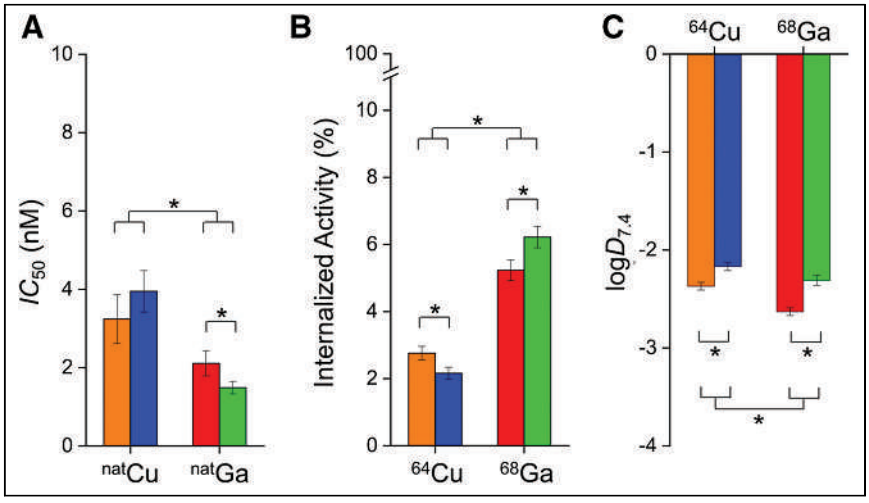

FIGURE 1. In vitro data of [$^{nat/64}$Cu]Cu-RM2 (orange), [$^{nat/68}$Ga]Ga-RM2 (red), [$^{nat/64}$Cu]Cu-AMTG (blue), and [$^{nat/68}$Ga]Ga-AMTG (green). Data are expressed as mean ± SD. (A) Affinity data on PC-3 cells (1.5×10^5 cells/mL/well) using 3-[^{125}I]I-Tyr^6-MJ9 (0.2 nM/well) as radiolabeled reference (2 h, room temperature, Hanks balanced salt solution plus 1% bovine serum albumin, *v/v*). (B) GRPR-mediated internalization (1.0 nM/well) on PC-3 cells as percentage of applied activity (incubation at 37 °C for 1 h, Dulbecco modified Eagle medium/F-12 plus 5% bovine serum albumin [*v/v*], 1.5×10^5 cells/mL/well). Data are corrected for nonspecific binding (10^{-3} M [^{nat}Lu]Lu-RM2). (C) Log$D_{7.4}$. *$P < 0.05$.

In Vivo Characterization

In vivo studies on PC-3 tumor–bearing mice at 1 h after injection (Fig. 3; Supplemental Table 2) revealed favorable biodistribution profiles with similarly low off-target accumulation for ^{64}Cu- and ^{68}Ga-labeled RM2 and AMTG in most organs. Although the highest uptake values were determined for all derivatives in the tumor (14.1%–15.1% injected dose per gram [%ID/g]) and the pancreas (12.6–30.7 %ID/g), significantly increased accumulation was observed for the ^{64}Cu-labeled analogs in the heart and the lung as compared with their ^{68}Ga-labeled counterparts ($P < 0.003$). Moreover, activity levels in the liver were distinctly enhanced for the ^{64}Cu-labeled compounds ($P < 0.001$). Uptake values were elevated in the pancreas for the ^{68}Ga-labeled analogs as compared with the ^{64}Cu-labeled analogs ($P < 0.05$). Accumulation in the adrenals was significantly higher for [^{64}Cu]Cu-/[^{68}Ga]Ga-AMTG than for [^{64}Cu]Cu-/[^{68}Ga]Ga-RM2 ($P < 0.03$) yet was on a very low level (1.9–2.8 vs. 1.0–1.1 %ID/g).

In general, tumor-to-background (T/B) ratios for the ^{68}Ga-labeled compounds were higher than for the ^{64}Cu-labeled derivatives (Fig. 4; Supplemental Table 3). Both [^{64}Cu]Cu-AMTG and [^{64}Cu]Cu-RM2 showed similar T/B ratios, except in the adrenals and kidneys, in which the ratio for the latter was slightly higher. Although [^{68}Ga]Ga-AMTG displayed enhanced T/B ratios in the muscle and the bone, [^{68}Ga]Ga-RM2 demonstrated higher T/B ratios in the spleen, the liver, and the adrenals. Because overall biodistribution patterns were comparable for both ^{68}Ga-labeled GRPR ligands, and [^{68}Ga]Ga-RM2 had already been applied in clinical studies, we selected [^{68}Ga]Ga-AMTG for PET imaging in a first-in-humans application.

Proof-of-Concept Study in Patient

[^{68}Ga]Ga-AMTG PET showed a favorable biodistribution, with uptake being highest in tumor lesions and the pancreas. Besides the bladder (because of excretion), no significant activity levels were found in other organs. One month previously, the patient had undergone [^{18}F]F-PSMA-1007 PET/CT, which showed only 1 subphrenic lesion with low [^{18}F]F-PSMA-1007 uptake (Fig. 5A; Supplemental Fig. 7). On [^{68}Ga]Ga-AMTG PET/CT, multiple lesions with intense focal uptake could be detected in the peritoneum, the subphrenic area adjacent to the liver, and between the left internal and external iliac arteries; these [^{68}Ga]Ga-AMTG–positive findings corresponded to soft-tissue lesions that were visualized on CT (Fig. 5B; Supplemental Fig. 7).

DISCUSSION

Based on the need for treatment options for PSMA-negative PCa patients, alternative targets such as the GRPR may become more relevant. We recently developed [^{177}Lu]Lu-AMTG, an RM2 derivative with noticeably increased metabolic stability in vivo (*19*), initially for an improved GRPR RLT. Because we additionally wanted to explore its potential for PET imaging, we performed a preclinical study on [^{64}Cu]Cu-/[^{68}Ga]Ga-AMTG and a first-in-humans application using [^{68}Ga]Ga-AMTG.

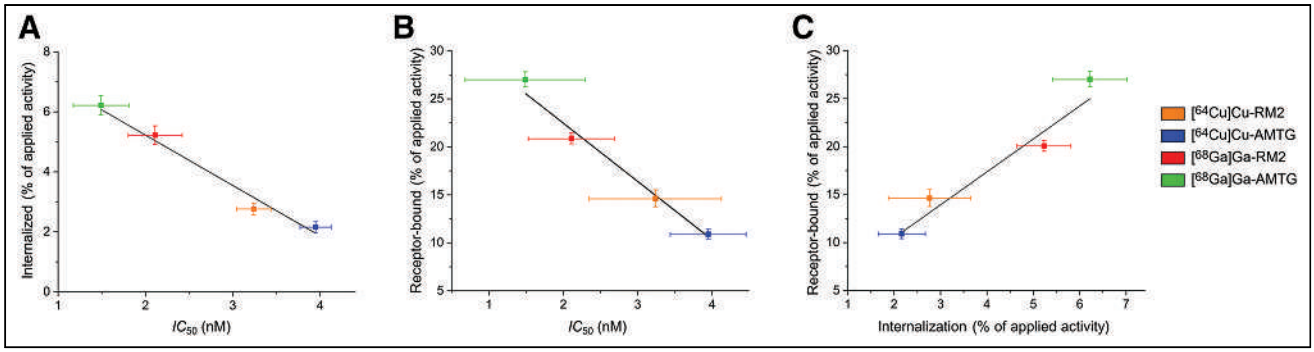

FIGURE 2. Internalization data of [^{64}Cu]Cu-RM2, [^{64}Cu]Cu-AMTG, [^{68}Ga]Ga-RM2, and [^{68}Ga]Ga-AMTG. Data are expressed as mean ± SD. (A) Ratio of IC_{50} and internalized fraction. (B) Ratio of IC_{50} and receptor-bound, noninternalized fraction. (C) Ratio of internalized and receptor-bound, noninternalized fraction.

Synthesis of the precursors was easily accessible via solid-phase peptide synthesis, and complexation with $^{nat/64}$Cu and $^{nat/68}$Ga proceeded quantitatively. The ^{nat}Cu- and ^{nat}Ga-labeled compounds were not purified before affinity studies, as we could show in a previous study that an excess of ions, such as Lu^{3+}, did not have any influence on GRPR affinity (*19*). Because of their structural similarity, all 4 compounds revealed comparably high GRPR affinity (IC_{50}, 1.5–4.0 nM), which met or even surpassed the values of their $^{nat/177}$Lu-labeled counterparts (IC_{50}, 3.0–3.5 nM) (*19*). The high receptor-bound fractions (79%–84% of cell-associated activity) found for all 4 analogs corroborated well with the values determined for [^{177}Lu]Lu-AMTG/RM2 (*19*) and are generally expected for antagonists (*22*). The log$D_{7.4}$ of the 4 compounds was in a range (−2.6 to −2.2) comparable to that of the previously published ^{177}Lu-labeled analogs (*19*).

Because we could show that a change in the radionuclide (^{64}Cu and ^{68}Ga instead of ^{177}Lu) had minimal impact on in vitro parameters, we expected in vivo properties similar to those of the previously reported [^{177}Lu]Lu-AMTG/RM2 (*19*). Indeed, the overall biodistribution profiles of [^{64}Cu]Cu-/[^{68}Ga]Ga-AMTG and [^{64}Cu]Cu-/[^{68}Ga]Ga-RM2 at 1 h after injection displayed high activity levels in the tumor and pancreas, whereas further off-target accumulation was either low or cleared rapidly within the first hour after injection. An exception was the liver, which revealed increased activity levels for the ^{64}Cu-labeled compounds as compared with the ^{68}Ga-labeled compounds. This increase was expected, since there are reports on the insufficient in vivo stability of the Cu-DOTA chelate (*23–25*), which led to a significant removal of ^{64}Cu from the DOTA chelator via transchelation to the superoxide dismutase in the liver and storage of free $^{64}Cu^{2+}$ ions in hepatocytes by metallothionein 1 and 2 (*26*). The instability of the ^{64}Cu-DOTA chelate could also explain the generally decreased T/B ratios of the ^{64}Cu-labeled ligands as compared with the ^{68}Ga-labeled ligands because of the thus higher off-target accumulation in most organs at 1 h after injection.

However, the high in vivo instability of the Cu-DOTA chelate in mice cannot be directly transferred to the human situation, because metabolism between these species is noticeably different. For example, high activity levels (~6 %ID/g) were found in the murine liver at 1 h after injection of [^{64}Cu]Cu-DOTATATE (*25*), whereas in humans slightly elevated activity levels observed in the liver did not hamper the detection of a variety of liver metastases (*27–29*). Dosimetry studies on [^{64}Cu]Cu-DOTATATE in 5 patients revealed that the dose delivered to the liver was similar to that delivered to the kidneys (0.161 vs. 0.139 Gy/GBq) (*27*), and this dose is indeed 2- to 4-fold higher than for [^{68}Ga]Ga-DOTATATE (0.045 and 0.092 Sv/GBq, respectively) but does not affect its clinical use (*30*).

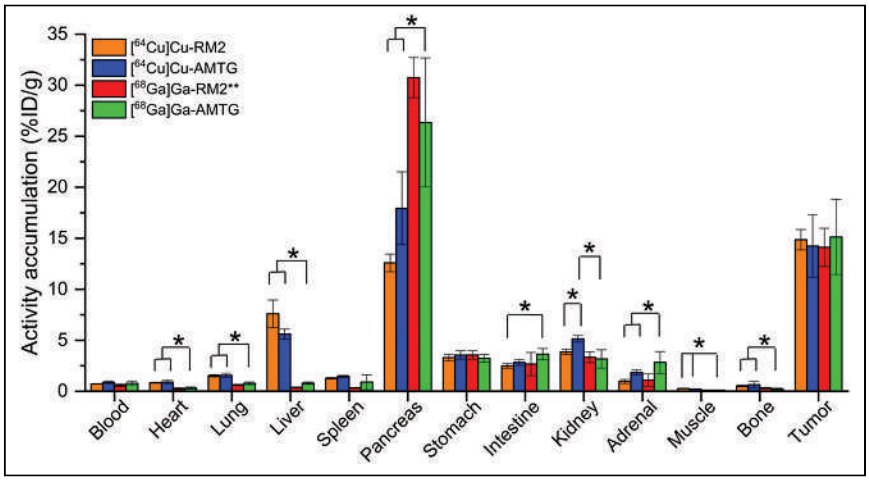

FIGURE 3. Biodistribution data of [^{64}Cu]Cu-RM2, [^{64}Cu]Cu-AMTG, [^{68}Ga]Ga-RM2, and [^{68}Ga]Ga-AMTG in selected organs at 1 h after injection in PC-3 tumor–bearing CB17-SCID mice (100 pmol each). Data are expressed as %ID/g, mean ± SD (n = 4). *P < 0.05. **10 pmol, NMRI nu/nu-mice, data taken from Mansi et al. (*31*). Statistical comparison with regard to [^{68}Ga]Ga-RM2 not applicable.

[^{68}Ga]Ga-AMTG (100 pmol, CB17-SCID mice) displayed a similar biodistribution profile (Supplemental Fig. 6) and thus comparable T/B ratios in most organs to the clinical standard for PET imaging of GRPR-expressing malignancies, [^{68}Ga]Ga-RM2 (10 pmol, NMRI nu/nu-mice, data taken from Mansi et al. (*31*)). The comparison of these 2 tracers is a limitation of this study, as biodistribution studies of [^{68}Ga]Ga-RM2 have been performed by another group using different mouse models and precursor amounts than we did for [^{68}Ga]Ga-AMTG. Because preclinical data, particularly overall pharmacokinetics, were mainly comparable for [^{64}Cu]Cu-/[^{68}Ga]Ga-AMTG and [^{64}Cu]Cu-/[^{68}Ga]Ga-RM2, both AMTG derivatives appear to be promising candidates for clinical translation. Although [^{68}Ga]Ga-AMTG

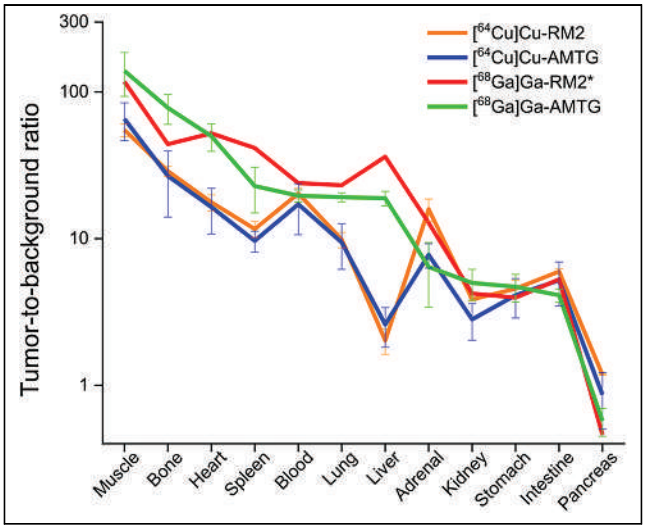

FIGURE 4. Graphical comparison of T/B ratios for selected organs for [^{64}Cu]Cu-RM2, [^{64}Cu]Cu-AMTG, [^{68}Ga]Ga-RM2, and [^{68}Ga]Ga-AMTG. Biodistribution studies were performed at 1 h after injection in PC-3 tumor–bearing CB17-SCID mice (100 pmol each). Data are expressed as mean ± SD (n = 4). *10 pmol, NMRI nu/nu-mice, data taken from Mansi et al. (*31*)

was selected for a first-in-humans investigation in a PCa patient, ^{64}Cu-labeled compounds might be superior to ^{68}Ga-labeled compounds in the future because of the longer half-life of ^{64}Cu (12.7 vs. 67.6 min), which would enable PET imaging over an extended time span. In addition, its lower positron energy ($E_{\beta+,max}$, 653 vs. 1,899 keV) allows for a higher resolution in PET (*20*). However, it remains to be seen whether the low positron decay probability of ^{64}Cu generates some drawbacks for PET imaging, such as with regard to counting statistics. Moreover, the current availability of ^{68}Ga (generator) is a significant advantage over ^{64}Cu (cyclotron).

For a first-in-humans application, good-manufacturing-practice synthesis of [^{68}Ga]Ga-AMTG was achieved within 36 min, yielded 409 MBq (~56% non–decay-corrected), and fulfilled all specifications (clear and particle-free solution, pH 7, radiochemical purity > 98%, unbound [^{68}Ga]Ga^{3+} ≤ 0.5%, HEPES limit, ethanol concentration, endotoxin limit, filter integrity).

[^{68}Ga]Ga-AMTG revealed a favorable biodistribution in a PET/CT scan of an mCRPC patient at 75 min after injection, with high uptake in tumor lesions and the pancreas, whereas further off-target accumulation was low. Moreover, [^{68}Ga]Ga-AMTG PET/CT revealed distinctly more lesions and increased SUVs than [^{18}F]F-PSMA-1007 in this mCRPC patient. An epithelial–mesenchymal transition is expected in PCa after several treatment lines including PSMA-targeted RLT (*32*), can lead to a loss of PSMA expression, and thus requires alternative treatment options. For such patients, GRPR-targeted compounds could offer an alternative option for imaging and RLT. The feasibility of [^{68}Ga]Ga-AMTG for such cases has been shown for only 1 patient to date—a limitation of this study and why further clinical evaluation has to be performed to confirm this promising preliminary result. Because [^{68}Ga]Ga-AMTG PET did not display noticeable uptake in organs other than the pancreas, and because pancreatic clearance is known to occur within the first hours after injection, this could open new possibilities for treatment of PCa, provided that GRPR expression is sufficient. Moreover, unlike PSMA inhibitors, GRPR-targeted compounds do not accumulate in the salivary glands and the kidneys, among others, which is why the use of ^{90}Y or α-particle–emitting radionuclides likely causes less severe side effects.

CONCLUSION

Both [^{64}Cu]Cu- and [^{68}Ga]Ga-AMTG revealed excellent preclinical data and might be valuable tools for PET imaging of PSMA-negative PCa in progressed disease stages, as well as in other cancer types such as breast cancer and glioblastoma multiforme. A first-in-humans examination in an mCRPC patient displayed favorable biodistribution patterns and did not show any biosafety issues or significant differences from the clinically established reference, [^{68}Ga]Ga-RM2. [^{68}Ga]Ga-AMTG PET/CT identified noticeably more lesions than [^{18}F]F-PSMA-1007, likely due to an aggressive transdifferentiation of PCa and, thus, limited PSMA expression. Because an enhanced in vivo stability was observed in previous studies for the AMTG peptide, an improved RLT might be achievable in these patients, rendering this peptide a valuable theranostic tool. Further patient studies will elucidate whether these promising results are reflected on a broader scale.

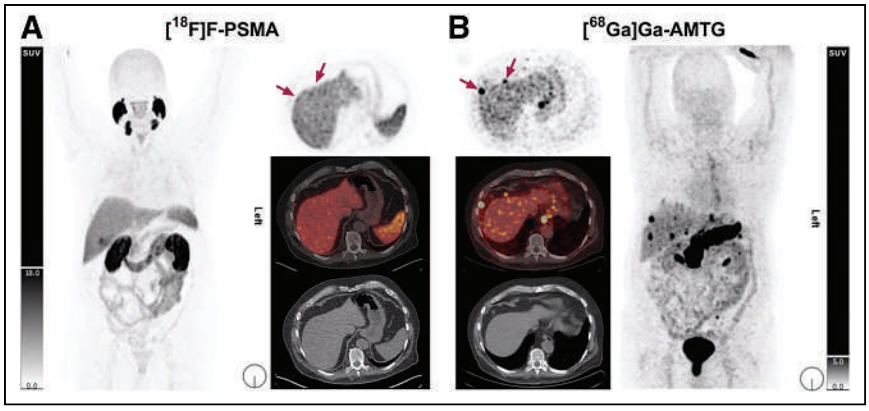

FIGURE 5. Patient with mCRPC after 4 cycles of [^{177}Lu]Lu-PSMA-617 RLT, with multiple small perihepatic and abdominal lymph node metastases that currently show no or only faint uptake on [^{18}F]F-PSMA-1007 PET/CT. (A) Left: PET maximum-intensity projection. Upper right: transaxial [^{18}F]F-PSMA-1007 PET. Middle right: transaxial fused PET/CT. Lower right: transaxial CT but intense uptake on [^{68}Ga]Ga-AMTG PET/CT. (B) Right: PET maximum-intensity projection. Upper left: transaxial [^{68}Ga]Ga-AMTG PET. Middle left: transaxial fused PET/CT. Lower left: transaxial CT.

DISCLOSURE

A patent application on modified GRPR-targeted ligands including AMTG, with Thomas Günther and Hans-Jürgen Wester as inventors, has been filed. Hans-Jürgen Wester is founder and shareholder of Scintomics GmbH. Bernd Joachim Krause is an advisor for Terumo, Rotop, AAA/Novartis, PSI CRO, ITM, Bayer, and Janssen; receives third-party funding from AAA/Novartis, AMGEN, and Eisai; receives travel support from AAA/Novartis; and receives royalties from AAA/Novartis, Bayer, and Janssen.

No other potential conflict of interest relevant to this article was reported.

KEY POINTS

QUESTION: Is the metabolically more stable peptide AMTG (as compared with RM2)—particularly designed for an improved RLT of GRPR-expression malignancies—also an option for imaging applying ^{64}Cu or ^{68}Ga?

PERTINENT FINDINGS: [^{64}Cu]Cu-/[^{68}Ga]Ga-AMTG and [^{64}Cu]Cu-/[^{68}Ga]Ga-RM2 displayed comparable pharmacokinetics preclinically, and [^{68}Ga]Ga-AMTG clinically, to those of the often used [^{68}Ga]Ga-RM2, rendering the AMTG peptide a promising theranostic tool for PET imaging and RLT.

IMPLICATIONS FOR PATIENT CARE: Although the clinical value of [^{64}Cu]Cu- and [^{68}Ga]Ga-AMTG (and [^{177}Lu]Lu-AMTG) has to be further elucidated, this study might pave the way for clinical use of an improved theranostic peptide and, thus, patient care.

REFERENCES

1. Prostate cancer prognosis. Johns Hopkins Medicine website. https://www.hopkinsmedicine.org/health/conditions-and-diseases/prostate-cancer/prostate-cancer-prognosis. Accessed June 30, 2023.
2. Sartor O, de Bono J, Chi KN, et al. Lutetium-177-PSMA-617 for metastatic castration-resistant prostate cancer. *N Engl J Med.* 2021;385:1091–1103.
3. FDA approves Pluvicto for metastatic castration-resistant prostate cancer. U.S. Food and Drug Administration website. https://www.fda.gov/drugs/resources-information-approved-drugs/fda-approves-pluvicto-metastatic-castration-resistant-prostate-cancer. Revised March 23, 2022. Accessed June 30, 2023.
4. Afshar-Oromieh A, Holland-Letz T, Giesel FL, et al. Diagnostic performance of ^{68}Ga-PSMA-11 (HBED-CC) PET/CT in patients with recurrent prostate cancer: evaluation in 1007 patients. *Eur J Nucl Med Mol Imaging.* 2017;44:1258–1268.
5. Eiber M, Maurer T, Souvatzoglou M, et al. Evaluation of hybrid ^{68}Ga-PSMA ligand PET/CT in 248 patients with biochemical recurrence after radical prostatectomy. *J Nucl Med.* 2015;56:668–674.
6. Hofman MS, Emmett L, Sandhu S, et al. TheraP: ^{177}Lu-PSMA-617 (LuPSMA) versus cabazitaxel in metastatic castration-resistant prostate cancer (mCRPC) progressing after docetaxel—overall survival after median follow-up of 3 years (ANZUP 1603) [abstract]. *J Clin Oncol.* 2022;40(suppl):5000.
7. Merkens L, Sailer V, Lessel D, et al. Aggressive variants of prostate cancer: underlying mechanisms of neuroendocrine transdifferentiation. *J Exp Clin Cancer Res.* 2022;41:46.
8. Macintosh CA, Stower M, Reid N, Maitland NJ. Precise microdissection of human prostate cancers reveals genotypic heterogeneity. *Cancer Res.* 1998;58:23–28.
9. Maina T, Bergsma H, Kulkarni HR, et al. Preclinical and first clinical experience with the gastrin-releasing peptide receptor-antagonist [^{68}Ga]SB3 and PET/CT. *Eur J Nucl Med Mol Imaging.* 2016;43:964–973.
10. Reubi JC, Wenger S, Schmuckli-Maurer J, Schaer JC, Gugger M. Bombesin receptor subtypes in human cancers: detection with the universal radioligand ^{125}I-[D-TYR^{6}, beta-ALA^{11}, PHE^{13}, NLE^{14}] bombesin(6-14). *Clin Cancer Res.* 2002;8:1139–1146.
11. Baratto L, Song H, Duan H, et al. PSMA- and GRPR-targeted PET: results from 50 patients with biochemically recurrent prostate cancer. *J Nucl Med.* 2021;62:1545–1549.
12. Touijer KA, Michaud L, Alvarez HAV, et al. Prospective study of the radiolabeled GRPR antagonist BAY86-7548 for positron emission tomography/computed tomography imaging of newly diagnosed prostate cancer. *Eur Urol Oncol.* 2019;2:166–173.
13. Fassbender TF, Schiller F, Zamboglou C, et al. Voxel-based comparison of [^{68}Ga]Ga-RM2-PET/CT and [^{68}Ga]Ga-PSMA-11-PET/CT with histopathology for diagnosis of primary prostate cancer. *EJNMMI Res.* 2020;10:62.
14. Heuschkel M, Kurth J, Hakenberg OW, Nitsch S, Schwarzenböck SM, Krause BJ. Monocentric intraindividual comparison of ^{68}Ga-RM2 and ^{68}Ga-PSMA PET/CT in mCRPC [abstract]. *Eur J Nucl Med Mol Imaging.* 2019;46:526.
15. Stoykow C, Erbes T, Maecke HR, et al. Gastrin-releasing peptide receptor imaging in breast cancer using the receptor antagonist ^{68}Ga-RM2 and PET. *Theranostics.* 2016;6:1641–1650.
16. Baratto L, Duan H, Mäcke H, Iagaru A. Imaging the distribution of gastrin-releasing peptide receptors in cancer. *J Nucl Med.* 2020;61:792–798.
17. Kurth J, Krause BJ, Schwarzenböck SM, Bergner C, Hakenberg OW, Heuschkel M. First-in-human dosimetry of gastrin-releasing peptide receptor antagonist [^{177}Lu]Lu-RM2: a radiopharmaceutical for the treatment of metastatic castration-resistant prostate cancer. *Eur J Nucl Med Mol Imaging.* 2020;47:123–135.
18. Roivainen A, Kahkonen E, Luoto P, et al. Plasma pharmacokinetics, whole-body distribution, metabolism, and radiation dosimetry of ^{68}Ga bombesin antagonist BAY 86-7548 in healthy men. *J Nucl Med.* 2013;54:867–872.
19. Günther T, Deiser S, Felber V, Beck R, Wester HJ. Substitution of L-tryptophan by a-methyl-L-tryptophan in ^{177}Lu-RM2 results in ^{177}Lu-AMTG, a high-affinity gastrin-releasing peptide receptor ligand with improved in vivo stability. *J Nucl Med.* 2022;63:1364–1370.
20. Braune A, Oehme L, Freudenberg R, et al. Comparison of image quality and spatial resolution between ^{18}F, ^{68}Ga, and ^{64}Cu phantom measurements using a digital Biograph Vision PET/CT. *EJNMMI Phys.* 2022;9:58.
21. Nakagawa T, Hocart SJ, Schumann M, et al. Identification of key amino acids in the gastrin-releasing peptide receptor (GRPR) responsible for high affinity binding of gastrin-releasing peptide (GRP). *Biochem Pharmacol.* 2005;69:579–593.
22. Borgna F, Haller S, Rodriguez JMM, et al. Combination of terbium-161 with somatostatin receptor antagonists: a potential paradigm shift for the treatment of neuroendocrine neoplasms. *Eur J Nucl Med Mol Imaging.* 2022;49:1113–1126.
23. Boswell CA, Sun X, Niu W, et al. Comparative in vivo stability of copper-64-labeled cross-bridged and conventional tetraazamacrocyclic complexes. *J Med Chem.* 2004;47:1465–1474.
24. Persson M, El Ali HH, Binderup T, et al. Dosimetry of ^{64}Cu-DOTA-AE105, a PET tracer for uPAR imaging. *Nucl Med Biol.* 2014;41:290–295.
25. Rylova SN, Stoykow C, Del Pozzo L, et al. The somatostatin receptor 2 antagonist ^{64}Cu-NODAGA-JR11 outperforms ^{64}Cu-DOTA-TATE in a mouse xenograft model. *PLoS One.* 2018;13:e0195802.
26. Persson M, Hosseini M, Madsen J, et al. Improved PET imaging of uPAR expression using new ^{64}Cu-labeled cross-bridged peptide ligands: comparative in vitro and in vivo studies. *Theranostics.* 2013;3:618–632.
27. Pfeifer A, Knigge U, Mortensen J, et al. Clinical PET of neuroendocrine tumors using ^{64}Cu-DOTATATE: first-in-humans study. *J Nucl Med.* 2012;53:1207–1215.
28. Pfeifer A, Knigge U, Binderup T, et al. ^{64}Cu-DOTATATE PET for neuroendocrine tumors: a prospective head-to-head comparison with ^{111}In-DTPA-octreotide in 112 patients. *J Nucl Med.* 2015;56:847–854.
29. Johnbeck CB, Knigge U, Loft A, et al. Head-to-head comparison of ^{64}Cu-DOTATATE and ^{68}Ga-DOTATOC PET/CT: a prospective study of 59 patients with neuroendocrine tumors. *J Nucl Med.* 2017;58:451–457.
30. Walker RC, Smith GT, Liu E, Moore B, Clanton J, Stabin M. Measured human dosimetry of ^{68}Ga-DOTATATE. *J Nucl Med.* 2013;54:855–860.
31. Mansi R, Wang X, Forrer F, et al. Development of a potent DOTA-conjugated bombesin antagonist for targeting GRPr-positive tumours. *Eur J Nucl Med Mol Imaging.* 2011;38:97–107.
32. Hu CD, Choo R, Huang J. Neuroendocrine differentiation in prostate cancer: a mechanism of radioresistance and treatment failure. *Front Oncol.* 2015;5:90.

[^{68}Ga]Ga-FAPI-46 PET for Visualization of Postinfarction Renal Fibrosis

Lena M. Unterrainer[1,2], Anthony E. Sisk, Jr.[3], Johannes Czernin[1], Brian M. Shuch[4], Jeremie Calais*[1], and Masatoshi Hotta*[1,5]

[1]Ahmanson Translational Theranostics Division, Department of Molecular and Medical Pharmacology, David Geffen School of Medicine, UCLA, Los Angeles, California; [2]Department of Nuclear Medicine, University Hospital, LMU Munich, Munich, Germany; [3]Department of Pathology, David Geffen School of Medicine, UCLA, Los Angeles, California; [4]Department of Urology, UCLA, Los Angeles, California; and [5]Division of Nuclear Medicine, Department of Radiology, National Center for Global Health and Medicine, Tokyo, Japan

Fibroblast activation protein (FAP)–targeted PET imaging is promising for cancers with a high content of cancer-associated fibroblasts (*1,2*). However, FAP is also expressed by activated fibroblasts involved in multiple fibroinflammatory nononcologic conditions. FAP is involved in remodeling processes by stimulating fibrosis and extracellular matrix remodeling after an infarction. After myocardial infarction, FAP inhibitor (FAPI) PET imaging can show the activated fibroblasts (*3*) in the territory of the occluded coronary artery (*4*). In the early stage of renal fibrosis, fibroblasts accumulate in the renal parenchyma. Preliminary experience with FAPI PET quantification of renal fibrosis has been reported (*5*).

Here, we report the case of an 83-y-old man with clear cell renal cell carcinoma of the left kidney with gross hematuria requiring blood transfusions and an emergency embolization of the left renal artery (Fig. 1). Subsequently nephrectomy was planned, and the patient preoperatively underwent both [^{18}F]FDG (26 d after embolization) and [^{68}Ga]Ga-FAPI-46 PET/CT (67 d after embolization) as part of the exploratory study (NCT04147494), which was approved by the institutional review board. The primary tumor had a slight hypermetabolism at its periphery ([^{18}F]FDG SUV_{max}, 5.9) without increased FAP uptake (FAPI SUV_{max}, 2.0). [^{68}Ga]Ga-FAPI-46 PET/CT showed increased uptake in the embolization area in the lower-pole left kidney parenchyma (SUV_{max}, 4.1 vs. 1.7 in the normal parenchyma). [^{18}F]FDG PET/CT showed significantly decreased uptake at the infarction site (SUV_{max}, 1.9 vs. 4.8 in the normal parenchyma). The FAP immunohistochemistry staining performed on the nephrectomy tissue showed an increased FAP expression in the ischemic areas that included reactive fibroblasts, whereas the primary tumor had no significant FAP expression. The corresponding hematoxylin and eosin staining showed the ischemic stromal cells and adjacent tumor. Our findings suggest that [^{68}Ga]Ga-FAPI-46 PET/CT molecular imaging can show FAP expression in fibrotic renal tissue and may represent a valuable biomarker for remodeling processes after infarction of the kidney.

DISCLOSURE

No potential conflict of interest relevant to this article was reported.

REFERENCES

1. Loktev A, Lindner T, Mier W, et al. A tumor-imaging method targeting cancer-associated fibroblasts. *J Nucl Med.* 2018;59:1423–1429.
2. Lindner T, Loktev A, Altmann A, et al. Development of quinoline-based theranostic ligands for the targeting of fibroblast activation protein. *J Nucl Med.* 2018;59:1415–1422.
3. Varasteh Z, Mohanta S, Robu S, et al. Molecular imaging of fibroblast activity after myocardial infarction using a ^{68}Ga-labeled fibroblast activation protein inhibitor, FAPI-04. *J Nucl Med.* 2019;60:1743–1749.
4. Notohamiprodjo S, Nekolla SG, Robu S, et al. Imaging of cardiac fibroblast activation in a patient after acute myocardial infarction using ^{68}Ga-FAPI-04. *J Nucl Cardiol.* 2022;29:2254–2261.
5. Conen P, Pennetta F, Dendl K, et al. [^{68}Ga] Ga-FAPI uptake correlates with the state of chronic kidney disease. *Eur J Nucl Med Mol Imaging.* 2022;49:3365–3372.

Received Mar. 1, 2023; revision accepted Mar. 24, 2023.
For correspondence or reprints, contact Lena M. Unterrainer (lunterrainer@mednet.ucla.edu).
*Contributed equally to this work.
Guest Editor: Todd Peterson, Vanderbilt University
Published online Jun. 15, 2023.

DOI: 10.2967/jnumed.123.265640

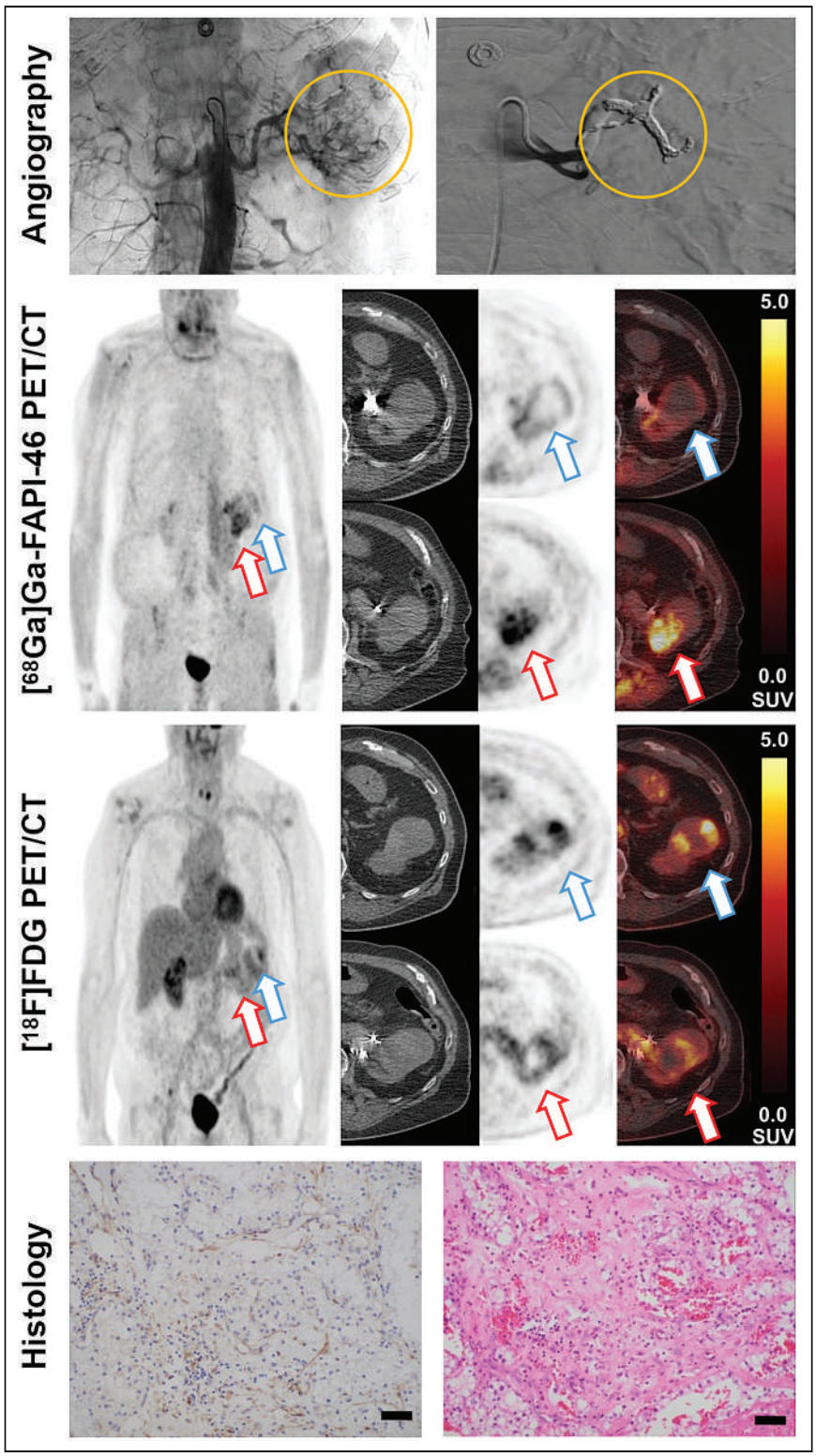

FIGURE 1. (Row 1) Preembolization angiography with contrast extravasation of lower branch of left renal artery and tumor-associated neovasculature (left panel, circle) and postembolization angiography showing occlusion of arterial vessels (right panel, circle). (Rows 2 and 3, from left to right) Maximum-intensity-projection, CT, PET, and PET/CT images obtained with [^{68}Ga]Ga-FAPI-46 and [^{18}F]FDG. Blue arrows denote primary tumor, and red arrows denote embolization area. (Row 4) Immunohistochemistry staining (left panel) and hematoxylin and eosin staining (right panel) (scale bars = 25 μm).

Not All Gatekeepers Are Theranostics

TO THE EDITOR: Sometimes we need to challenge the views of colleagues and friends, especially when their thinking has the effect of muddying the waters rather than providing greater insight and clarity. I believe this to be the case with the opinion piece by Weber et al. in the May 2023 issue of the journal (*1*).

The authors seek to redefine the term *theranostic.* They assert that this is any molecular imaging probe that provides actionable information for any subsequent therapeutic. This includes medical therapies, radiation therapy, surgery, or cell therapies.

I believe that, in doing so, they are losing the very essence of what a theranostic is.

I agree with the authors that the therapeutic component of a theranostic pair need not be a radionuclide therapy, but I contend that it must be the same (or a very similar) molecule or moiety. It could be carrying a toxic therapeutic or it may be an antibody that targets a protein (e.g., amyloid in the brain), but it has to be the same targeting moiety.

What the authors of this article are referring to as a theranostic imaging probe when used with a range of other therapies is more accurately described by the term *gatekeeper* or *companion diagnostic*. The imaging study validates the use of a certain therapeutic approach: this is not theranostics but simply a good use of medical imaging. The authors surely would not contend that a ventilation–perfusion lung scan demonstrating a pulmonary embolism that was subsequently treated with anticoagulation was a theranostic approach.

Definitions are important and help us to describe and conceptualize the strategy chosen to diagnose and treat diseases. Seeking to dilute the definition of a theranostic in the way the authors have done will have the effect of confusing the basis of the concept and will be unhelpful. The theranostic approach is an extremely powerful one and should be a major focus of future developments in molecular imaging and therapy. We need to keep the concepts clear and appreciate the differences between gatekeeper and theranostic approaches. They are both very important, but they are not the same. Not all gatekeepers are theranostics.

REFERENCE

1. Weber WA, Barthel H, Bengel F, Eiber M, Herrmann K, Schäfers M. What is theranostics? *J Nucl Med.* 2023;64:669–670.

Dale L. Bailey
Royal North Shore Hospital
Sydney, Australia
E-mail: dale.bailey@sydney.edu.au

Published online Jun. 29, 2023.
DOI: 10.2967/jnumed.123.266006

REPLY: We very much would like to thank Dr. Bailey for his valuable comments, which give us the opportunity to further explain our definition of theranostics.

Dr. Bailey writes that a meaningful definition of theranostics requires that the targeting moiety be the same or very similar for the imaging agent and the therapeutic agent. We are not sure if this is a reasonable requirement. For example, amyloid imaging agents are small molecules, whereas the therapeutics are full-size antibodies. Nevertheless, the identical molecular target is addressed, and the use of amyloid PET imaging to select patients for amyloid antibody therapy seems to be a perfect example of a theranostic approach. Conversely, minor chemical changes in a peptide can fundamentally alter its binding affinities. For example, somatostatin receptor antagonists are highly sensitive to N-terminal modifications of the peptide chain. As a consequence, the somatostatin receptor antagonist DOTA-JR11 has a more than 10-fold lower binding affinity when labeled with ^{68}Ga than when labeled with ^{177}Lu (*1*). Consequently, the combination of ^{68}Ga-DOTA-JR11/^{177}Lu-DOTA-JR11 is not an ideal theranostic pair (*2*). A better companion diagnostic for ^{177}Lu-DOTA-JR11 is ^{68}Ga-NODAGA-JR11, that is, a compound that is chemically less similar to ^{177}Lu-DOTA-JR11 than is ^{68}Ga-DOTA-JR11 (*3*).

Because similar molecules may be poor theranostic pairs and very different molecules may be excellent theranostic pairs, we do not think that the definition of theranostic agents should require that the imaging agent and the therapeutic agent be identical or very similar. A better definition may be that the imaging agent and the diagnostic agent have an identical target.

One can have different opinions on the question of whether the definition of theranostic imaging should be made even wider. We have argued in our article that the definition should be broad, especially for the development of new imaging agents. Imaging agents that are companion diagnostics for a specific therapy have a clear path for regulatory approval and reimbursement because they have an obvious impact on patient management. Whether one should use the term *theranostic* or *companion diagnostic* for this use of imaging can be debated. We would prefer *theranostic* because the term *companion diagnostic* is already broadly used for blood- or tissue-based biomarkers.

However, we would caution on use of the term *gatekeeper* to refer to theranostics or companion diagnostics. In fact, we believe that a theranostic imaging agent is the opposite of a gatekeeper—which limits therapeutic options—but rather is a facilitator that creates new opportunities to treat patients. In other words, no theranostic is a gatekeeper. We of course realize that this is often a matter of perspective: a theranostic agent that images the expression of a target for radiopharmaceutical therapy can be seen as a test that facilitates this therapy or as a gatekeeper that prevents an ineffective therapy in a patient who does not express the target. However, in other instances theranostic imaging clearly enables new therapies, for example, by detecting the site of recurrence in a patient with an elevated tumor marker. Therefore, we believe that theranostic imaging should be viewed as a facilitator, not a gatekeeper.

In conclusion, we appreciate the opportunity to further clarify our definition of theranostics and would maintain that theranostics is "a combination of imaging and therapy in which imaging provides actionable information that enables new or more effective therapies." (*4*)

REFERENCES

1. Fani M, Del Pozzo L, Abiraj K, et al. PET of somatostatin receptor-positive tumors using ^{64}Cu- and ^{68}Ga-Somatostatin antagonists: the chelate makes the difference. *J Nucl Med.* 2011;52:1110–1118.

2. Krebs S, O'Donoghue JA, Biegel E, et al. Comparison of ^{68}Ga-DOTA-JR11 PET/CT with dosimetric ^{177}Lu-satoreotide tetraxetan (^{177}Lu-DOTA-JR11) SPECT/CT in patients with metastatic neuroendocrine tumors undergoing peptide receptor radionuclide therapy. *Eur J Nucl Med Mol Imaging.* 2020;47:3047–3057.
3. Mansi R, Fani M. Design and development of the theranostic pair ^{177}Lu-OPS201/^{68}Ga-OPS202 for targeting somatostatin receptor expressing tumors. *J Labelled Comp Radiopharm.* 2019;62:635–645.
4. Weber WA, Barthel H, Bengel F, Eiber M, Herrmann K, Schäfers M. What is theranostics? *J Nucl Med.* 2023;64:669–670.

Wolfgang Andreas Weber*
Henryk Barthel
Frank M. Bengel
Matthias M. Eiber
Ken Herrmann
Michael Schäfers
**Technical University of Munich*
Munich, Germany
E-mail: w.weber@tum.de

Published online Jun. 29, 2023.
DOI: 10.2967/jnumed.123.266028

Potential of ^{188}Re as an Alternative to ^{177}Lu and Dosimetric Consequences

TO THE EDITOR: We read with interest the article "PSMA-GCK01: A Generator-Based ^{99m}Tc/^{188}Re Theranostic Ligand for the Prostate-Specific Membrane Antigen" in *The Journal of Nuclear Medicine* (*1*). It is noteworthy that kidney accumulation of ^{188}Re-PSMA-GCK01 in LNCaP tumor–bearing mice was found to be 14 times higher than tumor uptake 1 h after injection and 9 times higher 2 h after injection (*1*).

It is worthwhile to investigate ^{188}Re as an alternative to ^{177}Lu, because accredited ^{177}Lu radiopharmaceuticals are available and the amount of ^{177}Lu is limited. Further alternatives such as ^{161}Tb (*2*) or ^{67}Cu (*3*) are moving into the focus of clinical research and could have even better therapeutic properties because of the coemission of Auger–Meitner electrons.

However, the kidney geometry in small animals is not representative for humans regarding geometry and pathlengths of the β-emission. Recently, Vargas et al. presented a method to understand the heterogeneity of absorbed doses in the kidneys of mice (*4*). In humans, the heterogeneity of absorbed doses in, for example, kidneys is crucial for the application of therapeutic radiopharmaceuticals (*5*). Hence, studies in pigs (single kidney weight, 125 g for pig vs. 150 g for human) may be required. Further, most patients currently receive radionuclide therapy as the last line of treatment after previous hormone and chemotherapy, so that bone marrow and kidney function may already be predamaged. This effect, too, can neither be simulated nor reproduced in animal experiments but requires clinical testing.

In our own efforts on ^{188}Re-PSMA derivatives, we found that biokinetics must be considered in terms of the physical half-life of the applied isotopes: at 17 h (^{188}Re) versus 6.6 d (^{177}Lu), the initial phase is more significant for ^{188}Re, and this is the phase with the greatest renal accumulation or excretion. Dosimetric calculations for ^{177}Lu-PSMA by Kurth et al. revealed kidney doses between 2.9 and 3.7 Gy, depending on the therapeutic cycle (*6*). On the basis of the effective half-lives for the kidneys that were reported, we calculated the biologic half-life for PSMA in the kidneys. We identified the expected effective half-life for ^{188}Re-PSMA by assuming a biodistribution identical to that for ^{177}Lu-PSMA and using the physical half-life for ^{188}Re. The calculated number of ^{188}Re decay in the kidneys was found to be approximately 66% lower than that of ^{177}Lu-PSMA decay. Nevertheless, the S value, S(kidney←kidney), for ^{188}Re is 5 times higher than that for ^{177}Lu. This means that the dose to the kidney is expected to be 1.7 times higher when using the same activity for ^{188}Re-PSMA as for ^{177}Lu-PSMA. The dose would be even higher when the initial kidney biokinetic is considered more accurately by assuming a linear accumulation within the first 2 h (*6*).

Furthermore, radiation biology must be considered, as higher activity levels must be used to achieve the same dose because of the shorter half-life of ^{188}Re. The authors used the same activity of ^{188}Re-PSMA and ^{177}Lu-PSMA (3.7 GBq) (*1*). Assuming an identical tumor uptake in a lesion with a mass of 10 g, the absorbed dose of ^{188}Re will be only 51% of the absorbed dose of ^{177}Lu. Hence, in therapeutic applications, the activity of ^{188}Re must be twice the activity of ^{177}Lu to achieve the same tumor dose. Furthermore, the various effective half-lives must be considered with respect to cellular repair mechanisms. The biologically effective dose is expected to be about 25% higher from ^{188}Re than from ^{177}Lu for equal absorbed doses. In conclusion, it is necessary to consider the dosimetric consequences carefully when replacing ^{177}Lu with ^{188}Re as mentioned above.

REFERENCES

1. Cardinale J, Giesel FL, Wensky C, Rathke HG, Haberkorn U, Kratochwil C. PSMA-GCK01: a generator-based ^{99m}Tc/^{188}Re theranostic ligand for the prostate-specific membrane antigen. *J Nucl Med.* 2023;64:1069–1075.
2. Baum RP, Singh A, Kulkarni HR, et al. First-in-humans application of ^{161}Tb: a feasibility study using ^{161}Tb-DOTATOC. *J Nucl Med.* 2021;62:1391–1397.
3. Bailey DL, Willowson KP, Harris M, et al. ^{64}Cu treatment planning and ^{67}Cu therapy with radiolabelled SARTATE ([^{64}Cu/^{67}Cu]MeCOSAR-octreotate) in subjects with unresectable multifocal meningioma: initial results for human imaging, safety, biodistribution, and radiation dosimetry. *J Nucl Med.* 2023;64:704–710.
4. Vargas CS, Struelens L, D'Huyvetter M, Caveliers V, Covens P. A realistic multiregion mouse kidney dosimetry model to support the preclinical evaluation of potential nephrotoxicity of radiopharmaceutical therapy. *J Nucl Med.* 2023;64:493–499.
5. Hanaoka H, Hashimoto K, Watanabe S, et al. Comparative evaluation of radionuclide therapy using ^{90}Y and ^{177}Lu. *Ann Nucl Med.* 2023;37:52–59.
6. Kurth J, Heuschkel M, Tonn A, et al. Streamlined schemes for dosimetry of ^{177}Lu-labeled PSMA targeting radioligands in therapy of prostate cancer. *Cancers (Basel).* 2021;13:3884.

Marc Pretze*
Jörg Kotzerke
Robert Freudenberg
Claudia Brogsitter
Technical University Dresden
Dresden, Germany
**E-mail: marc.pretze@ukdd.de*

Published online Aug. 3, 2023.
DOI: 10.2967/jnumed.123.265782

REPLY: In our recent publication about the preclinical development and clinical translation of ^{99m}Tc- and ^{188}Re-PSMA-GCK01, we consciously withheld the presentation of dosimetry estimates, despite having serial planar images of patients available (*1*). One reason is the

limited quantitative accuracy of dosimetry based on planar scans. A SPECT/CT-based dosimetry study is already in preparation. Consequently, we saw no need to report preliminary results, which soon will become obsolete anyway. The other reason is the challenging interpretation of dosimetry data in predicting clinical consequences of systemic radioligand therapy. The latter issue is now addressed by Pretze et al., who mention various physical and radiation biologic aspects of this theme. We appreciate receiving such an instructive letter, stimulating a fruitful academic discussion.

First, Pretze et al. mention further radionuclides that could serve as alternatives to ^{177}Lu. Indeed, the amount of ^{176}Yb that is needed for the production of high-specific-activity ^{177}Lu without ^{177m}Lu impurities (half-life, 161 d) is limited. Consequently, the costs for producing no-carrier-added ^{177}Lu are relatively high. Routine availability of ^{161}Tb and ^{67}Cu is currently even worse than for ^{177}Lu. In contrast, ^{188}Re is readily available from a well-established generator system and, if generators are eluted regularly, converts it into reduced radionuclide costs by approximately a power of 10. The current shortage of ^{177}Lu-PSMA-617 in the United States (Pluvicto from Novartis has been on the Food and Drug Administration's shortage list since March 7, 2023) illustrates the logistic challenges of airfreight delivery even between well-developed countries. In regions with a lower airport density, just-in-time delivery of ^{177}Lu (half-life, 6.7 d) radiopharmaceuticals is likely an illusion, and the same applies to ^{161}Tb (half-life, 6.9 d) and ^{67}Cu (half-life, 2.6 d). Hence, the 70-d half-life of the ^{188}W/^{188}Re generator is the most reasonable option to have local access to PSMA radioligand therapy at all.

Next, the letter addresses the challenge of projecting absorbed doses based on small-animal studies to human beings. Hence, studies in pigs would be required. However, beyond radiation geometry, the specific expression of PSMA in the proximal kidney tubules has to be considered. A study comparing human PSMA with its rat and pig orthologs exhibits different glutamate carboxypeptidase II expression levels among the species studied (*2*). Therefore, we considered the theranostic approach a more responsible way to continue clinical development; that is, innocuous ^{99m}Tc-PSMA-GCK01 imaging will be used to extrapolate the dosimetry of ^{188}Re-PSMA-GCK01 therapy in men.

Pretze et al. estimated that the same activities of ^{188}Re-PSMA may convert into a 1.7 times higher kidney dose but only a 51% absorbed dose to tumors with a mass of 10 g when compared with ^{177}Lu-PSMA-617. This is not too much away from our own preliminary approximation. However, because of its higher β-energy, ^{188}Re theoretically performs better against larger tumor lesions (23–32 mm) than does ^{177}Lu (*3*). In a tumor model that is very similar to the typical clustered PSMA expression pattern in prostate cancer, the increased cross-fire effect of ^{188}Re improved its intercluster microdosimetry (*4*). Pretze et al. emphasized that the antitumor activity of ^{188}Re-PSMA could be about 25% higher than identical absorbed doses delivered by ^{177}Lu when dose-rate effects are considered. However, it is worth mentioning that the biologically effective dose concept, which is based on the linear-quadratic model, was developed for external-beam radiotherapy, but its appropriateness for radioligand therapy still needs confirmation.

In summary, considering the dosimetric consequences of replacing ^{177}Lu with ^{188}Re may not be enough because there are no validated tools to simulate the radiation biologic consequences. Even if physical absorbed doses—1 surrogate for the therapeutic index of a radiopharmaceutical—may be lower than for ^{177}Lu-PSMA-617, we consider it warranted to assess the antitumor activity of ^{188}Re-PSMA-GCK01 using a patient-related endpoint, for example, prostate-specific antigen response in a clinical trial.

REFERENCES

1. Cardinale J, Giesel FL, Wensky C, Rathke HG, Haberkorn U, Kratochwil C. PSMA-GCK01: a generator-based ^{99m}Tc/^{188}Re theranostic ligand for the prostate-specific membrane antigen. *J Nucl Med.* 2023;64:1069–1075.
2. Rovenská M, Hlouchová K, Sácha P, et al. Tissue expression and enzymologic characterization of human prostate specific membrane antigen and its rat and pig orthologs. *Prostate.* 2008;68:171–182.
3. O'Donoghue JA, Bardiès M, Wheldon TE. Relationships between tumor size and curability for uniformly targeted therapy with beta-emitting radionuclides. *J Nucl Med.* 1995;36:1902–1909.
4. Enger SA, Hartman T, Carlsson J, Lundqvist H. Cross-fire doses from beta-emitting radionuclides in targeted radiotherapy. A theoretical study based on experimentally measured tumor characteristics. *Phys Med Biol.* 2008;53:1909–1920.

Jens Cardinale*
Frederik L. Giesel
Christina Wensky
Hendrik G. Rathke
Uwe Haberkorn
Clemens Kratochwil
**University Hospital Heidelberg*
Heidelberg, Germany
E-mail: jens.cardinale@med.uni-duesseldorf.de

Published online Aug. 3, 2023.
DOI: 10.2967/jnumed.123.266195

Response to "Critique and Discussion of 'Multicenter Evaluation of Frequency and Impact of Activity Infiltration in PET Imaging, Including Microscale Modeling of Skin-Absorbed Dose'"

TO THE EDITOR: We read with interest a recent commentary printed in *Frontiers in Nuclear Medicine* entitled "Critique and Discussion of 'Multicenter Evaluation of Frequency and Impact of Activity Infiltration in PET Imaging, Including Microscale Modeling of Skin-Absorbed Dose'" (*1*) that took issue with the science presented in our recent publication in *The Journal of Nuclear Medicine* (*2*). We felt that a reply was in order, as although several relevant points were made, other criticisms appear to be unfounded or based on false assumptions.

The first clarification is the insinuation that the Society of Nuclear Medicine and Molecular Imaging "fostered" the work presented in the article. This is categorically not the case. The experimental idea, design, and execution was neither funded, suggested, coerced, nor otherwise influenced by the society or society leadership beyond expressing an interest that the research be published. Project design and leadership were primarily from the lead author. Coauthors on the paper were just that—significant active scientific and experimental contributors to the work.

The second clarification relates to the unjustified statement that the paper's conclusions started with an assumption that diagnostic radiopharmaceutical infiltrations are not a concern. To the contrary,

safety concerns were the primary justification for initiation of our study. After hearing about alleged 15%–20% infiltration rates, we initiated a safety review at our facility with about 50 patients to determine whether we were experiencing this reported frequency of problematic injections. We expanded our safety assessment to additional patients for confirmation. A subsequent literature review revealed 2 important scientific incongruities. The first was that several single-institution studies reported high rates (>15%) of activity infiltrations, which were inconsistent with our measurements. This finding was also inconsistent with reported rates of injection infiltrations in chemotherapy and CT contrast injections, which stand at around 0.2% (*3*,*4*). The second puzzling issue related to published reports of infiltrated injection with absorbed dose estimates above 10 Gy, a level at which one would expect to see literature reports of deterministic skin injury from external-beam radiation therapy. However, no such injuries have been reported from diagnostic administrations. The scientific method dictates that when current models do not correctly predict experimental results, new hypotheses and models be developed and tested that better fit and explain observed phenomena. Both the frequency of reported infiltrations and the safety aspects associated with dose infiltrations appeared to conflict with known science and data. No presumption of safety was made in any aspect of the study design or results.

The several typographic errors identified in the article are correctly identified, and we entirely accept responsibility for these. However, we do not believe they meaningfully detract from the substance of the research work presented.

Several methodologic concerns were expressed about both the frequency-of-infiltration study and the Monte Carlo dosimetry model.

MONTE CARLO DOSIMETRY MODEL

Regarding the Monte Carlo dosimetry model, significant concern was expressed that our geometry excluded muscle from the distribution volume of an infiltrated radiopharmaceutical injection. We stand behind our distribution model that limits activity to the subcutaneous tissue and, to a lesser extent, the dermis. Muscle is encapsulated in the epimysium, which is a thick connective tissue layer that is composed of coarse collagen fibers in a proteoglycan matrix. The epimysium surrounds the entire muscle and largely isolates it from macroscopic rapid exchange of fluids from surrounding tissue, even under pressure. Unless the radiopharmaceutical is accidentally directly injected into the muscle, there is no direct pathway into muscle tissue. Further, our review of PET/CT infiltrations invariably shows the infiltrate limited to the skin layer, with no detectable component in the muscle above expected background. Figure 6A of the article demonstrates that, in an animal model, fluid introduced under pressure in the subcutaneous tissue is contained within the fat space and does not enter muscle. We strongly disagree with the criticism that "the muscle tissue adjacent to the injection site is valid as both a source and target volume" and is "inappropriately ignored … in the dosimetry model." We stand by its inclusion as a target organ only. We agree that in the unlikely event of an intramuscular injection, muscle would need to be a source and target organ, but we would then exclude all skin structures as source volumes, as tissue exchange is improbable.

Even in the unlikely event of a direct intramuscular injection, the distribution volume in the muscle is large, which would dilute the infiltrate over a larger volume, thus reducing absorbed dose. Further, muscles are among the least proliferative and most radiation-resistant cells in the body. Only at doses in excess of 40 Gy (functional changes) (*5*) or 60–80 Gy (significant tissue injury) (*6*) do we see tissue effects in muscle tissue, and these absorbed doses are in excess of those achievable with diagnostic quantities of PET radiopharmaceuticals. The significant concern voiced for damage to muscle tissue as an unstudied risk is entirely unfounded and ignores decades of radiation biology experience from external-beam radiation therapy.

There was concern expressed that we did not compare our Monte Carlo results against existing published models. In fact, we did perform several dose estimates of the skin using several existing published models (not reported). The results of these dose calculations were entirely consistent with the literature, and only when simulating approximately 100% infiltration of administered activity did absorbed doses exceed values for which we would expect to see deterministic and observable skin reactions (2–10 Gy, mild temporary effects; >15 Gy, high probability of serious or permanent injury) (*7*). Yet we found no such reports in the literature for diagnostic PET radiopharmaceuticals. It was precisely the failure of conventional dosimetry methods to explain observed phenomena (or lack thereof) that prompted the development of the proposed model that accounts for skin tissue subanatomy. Modeling accounted for an approximately 40-min biologic half-life combined with the physical half-life of the radionuclide under study. The biologic half-life was derived from a typical 30-min combined biologic and physical half-life reported by Osborne (*8*).

We freely admit that this is only an early-phase model, but we think it holds promise to assess safety risk more accurately in the event of a significant infiltration event than do the current more simplistic methods, which appear to correctly calculate absorbed dose when using a somewhat arbitrarily assumed tissue mass but incorrectly predict risk. We are in the process of expanding the scope of simulation to include a wider range of radionuclides and geometries and expect these results to be published within a year.

The opinion piece further objects to our using a subcutaneous injection model to describe fluid dynamics when a radiopharmaceutical is infiltrated. They state, "Subcutaneous administrations are very different than intravenous and are not an appropriate basis for model definition." We agree fully that subcutaneous administrations are very different from intravenous injections. However, we do firmly believe that subcutaneous administrations are precisely analogous to infiltrated intravenous administrations. Veins accessed for intravenous administrations reside exclusively in the subcutaneous tissue, and when injectate leaks into surrounding tissue under pressure through a blown vein or from around the puncture site of the vein itself, the leakage will invariably enter the subcutaneous fat layer given the anatomic confines. The fat layer is a remarkably accommodating and elastic structure to contain the excess fluid introduced under pressure. References supporting this were provided in the original article. We maintain confidence in our geometric model defining the behavior of infiltrated injectate and its time course and disagree strongly that our model is inappropriate; we consider our approach to be a substantially more appropriate physical model than currently used approaches.

FREQUENCY-OF-INFILTRATION STUDY

Regarding the frequency-of-infiltration study, it was initiated because of the discordant results between our institution and the

reports in the literature describing much higher rates. It became apparent on reading the literature that the primary difference from our internal institutional analysis was that we measured activity at the injection site, where reports of significantly higher infiltration rates were based solely on "visualization" of activity.

We absolutely stand by our belief that visualization is an inappropriate criterion to characterize a meaningful infiltration event. The clinical utility of PET in oncologic applications is entirely dependent on the modality's exquisite sensitivity. Virtually all PET scanners will clearly visualize a 2-cm-diameter tumor with ^{18}F-FDG at an SUV of 4. With a typical injection activity and body weight, this tumor will have, very approximately, 37 kBq (1 μCi) of activity, or about 0.01% of the injected activity. This implies, particularly in the low-background injection site, that PET is capable of visualizing this amount of activity. Categorizing 0.01% of the injected activity as a reportable or significant infiltration event, by virtue of visibility, is categorically wrong and misleading, particularly since the activity could instead be trivially quantitated in less than a minute from the image data. It is based on these observations that we now believe we clearly understand the discrepancies between our institutional results and these other visualization-based literature reports, which we consider misleading for the above reasons.

Missing from the literature was a body of quantitative measurements of activity at the injection site. This was considered a significant information gap that this study intended to fill. The true incidence rate for significant infiltration events remains unanswered and will depend entirely on a formal definition, which is beyond the scope of the article and our expertise and responsibility. But it will hopefully be better informed because of the data reported.

Criticisms were made implying inherent bias in the data reported. We believe the study took reasonable efforts to avoid bias in data collection. Intentionally, a variety of institutions (10 total) were chosen, including an academic medical center, private radiology groups, private oncology groups, a community hospital, multispecialty groups, and a research facility. Consecutive patients who had the injection site in the field of view were studied. To avoid statistical overweighting, no single site was allowed to contribute more than 200 studies. Consistent analysis methods were used to quantitate activity at the injection site. Criticism was leveled that "training and experience levels of participating technologists" was not reported, and "an unknown number of images with injection sites outside of the field of view were excluded from the study." Regarding the latter concern, we believe strongly this did not in any way statistically bias results. With regard to technologist training (many sites were small enough to not have on-site reading physicians), we are confident that this diverse array of 10 different institutions represented an array of different technologist skill levels and is almost certainly a more accurate sampling of the technologist population than the largely single-center studies on which the author and his company base their estimates.

The critique further states that "The results from this paper only reflect what happened in these few centers during undefined observation periods and cannot be applied to the practice of nuclear medicine generally." As we believe ours is a largely unbiased sample, we believe strongly that it is entirely generalizable to the broader PET imaging community. Injection practices in the larger nuclear medicine community may or may not be similar, as we made no attempt to sample this broader space. However, regarding the Monte Carlo dose estimation methods, we do believe the approach is broadly applicable to the entire practice of nuclear medicine. This criticism about generalization from a well-sampled population is a particularly odd comment and concerning for several reasons. First, it flies in the face of the entire field of statistics, which is based on unbiased sampling of a much larger population where the sample is considered mathematically representative of that larger population—to within calculable confidence intervals. Second, this is a self-defeating argument coming from an individual and company who have continuously based comments to the Nuclear Regulatory Commission and other organizations on arithmetic extrapolation from much smaller, less controlled, and more statistically biased reports.

Finally, in our article we somewhat arbitrarily categorized infiltration of less than 1% of total activity at the injection site as being "not a clinically meaningful infiltration event" for the sake of simple statistical analysis. This in no way implies, nor means to imply, that an infiltration of more than 1% is a clinically meaningful infiltration event. The absorbed dose estimates from the Monte Carlo analysis suggest that even at a 100% injection infiltration, we would not expect a patient to experience deterministic skin injury, which is entirely consistent with the lack of reported events in the literature over the last several decades. The question of a threshold for compromised image quality or quantitation was not addressed by the article. As such, the frequencies of "clinically meaningful extravasations" calculated in the critique based on a 1% threshold are dramatically overstated.

DISCUSSION

We find that most of the criticisms leveled are unfounded and based on what we see as fundamental misconceptions regarding injection anatomy and physiology, radiation biology, and even statistics. We remain confident in the experimental methods used in the collection of injection infiltration frequency data in the PET imaging space, and we believe these methods are superior in quality to those of previously reported studies because of the number of patients studied, the variety of imaging sites sampled, and the actual measurement of activity at the injection site rather than simple reporting of visualized activity. We also believe the physical model used in our Monte Carlo model, accounting for major skin subanatomies, is a necessary addition to the infiltration skin dosimetry paradigm given the failure of current models to predict the lack of reported deterministic skin injury events in this space. We further stand by our Monte Carlo starting boundary conditions whereby we confine activity to the subcutaneous fat and dermis, and we disagree strongly that the exchange with muscle tissue is appropriate (although this would serve to reduce skin/epidermal dose, which is the primary tissue of concern).

REFERENCES

1. Knowland J. Critique and discussion of "Multicenter Evaluation of Frequency and Impact of Activity Infiltration in PET Imaging, Including Microscale Modeling of Skin-Absorbed Dose." *Front Nucl Med.* 2023;3:1240162.
2. Sunderland JJ, Graves SA, York DM, Mundt CA, Bartel TB. Multicenter evaluation of frequency and impact of activity infiltration in PET imaging, including microscale modeling of skin-absorbed dose. *J Nucl Med.* 2023;64:1095–1101.
3. Jackson-Rose J, Del Monte J, Groman A, et al. Chemotherapy extravasation: establishing a national benchmark for incidence among cancer centers. *Clin J Oncol Nurs.* 2017; 21:438–445.

4. Dykes TM, Bhargavan-Chatfield M, Dyer RB. Intravenous contrast extravasation during CT: a national data registry and practice quality improvement initiative. *J Am Coll Radiol.* 2015;12:183–191.
5. Lipps DB, Sachdev S, Strauss JB. Quantifying radiation dose delivered to individual shoulder muscles during breast radiotherapy. *Radiother Oncol.* 2017;122:431–436.
6. Hall EJ, Giaccia AJ. *Radiobiology for the Radiologist.* Lippincott Williams & Wilkins; 2006:334–335.
7. Jaschke W, Schmuth M, Trianni A, Bartal G. Radiation-induced skin injuries to patients: what the interventional radiologist needs to know. *Cardiovasc Intervent Radiol.* 2017;40:1131–1140.
8. Osborne D, Kiser JW, Knowland J, Townsend D, Fisher DR. Patient-specific extravasation dosimetry using uptake probe measurements. *Health Phys.* 2021;120:339–343.

John J. Sunderland*
Stephen A. Graves
Dusty M. York
Christine A. Mundt
Twyla B. Bartel
**University of Iowa*
Iowa City, Iowa
E-mail: john-sunderland@uiowa.edu

Published online Sep. 7, 2023.
DOI: 10.2967/jnumed.123.266596

Addendum to MIRD Pamphlet No. 28

TO THE EDITOR: The journal has recently published MIRD pamphlet no. 28, parts 1 and 2, which describe and provide validation for the nuclear medicine software code MIRDcalc, part of the MIRDsoft.org series of freely accessible software for the field of nuclear medicine (*1,2*). We wish this letter to serve as an addendum clarifying an important technical aspect of the work in regard to some of the graphical presentations of the library of phantom computational models used to generate radionuclide S values, which form the computational engine of organ dosimetry in the MIRDcalc code.

In both part 1 and part 2 of MIRD pamphlet no. 28, we reference 4 International Commission on Radiological Protection (ICRP) publications that provide key reference material for MIRDcalc: two regarding computational phantoms and two regarding values of specific absorbed fractions (or SAFs) from which radionuclide S values were computed. The ICRP phantoms used in MIRDcalc data are the ICRP publication 110 reference adult male and adult female voxel phantoms (*3*) and the ICRP publication 143 reference pediatric male and female phantoms (*4*). The corresponding ICRP official values of SAFs are included in ICRP publication 133 (for the adult publication 110 phantoms) and in an in-press ICRP publication (for the pediatric publication 143 phantoms) (*5,6*). Confusion might arise in that ICRP is also in the process of migrating from voxelized reference phantoms to mesh-type reference phantoms. The adult mesh-type reference phantoms, the next generation of the Publication 110 adult voxel phantoms, have been already published in ICRP publication 145, with pediatric mesh-based phantoms to appear in an upcoming ICRP document (*3,7,8*). We point out, however, that the only official ICRP values of photon, electron, and α-particle SAFs published by ICRP are those derived in the voxelized reference phantoms of publications 110 and 143, along with supplemental stylized models of the respiratory tract and alimentary tract. No updated SAFs have been published by the ICRP for the newer mesh-based reference phantoms.

These details are implicit in the text descriptions in both parts 1 and 2 of MIRD pamphlet no. 28, especially in regard to the references to ICRP publications 110, 133, 143, and the in-press document on pediatric SAFs. However, for graphical purposes—to include Figures 3 and 4 of part 1 and Figure 1 of part 2—we chose to display the ICRP reference phantoms using their mesh-type formats. In this addendum, we wish to clarify that showing the ICRP reference phantoms in their mesh-type formats does not imply that new SAFs were derived for the mesh-type phantoms during the development of the MIRDcalc software. As noted, the original source of the SAFs used for S-value calculation were clearly cited in both parts 1 and 2 of this MIRD pamphlet, and both ICRP documents themselves make clear that the voxel-type reference phantoms were used.

REFERENCES

1. Kesner AL, Carter LM, Ramos JCO, et al. MIRD Pamphlet No. 28, Part 1: MIRDcalc—a software tool for medical internal radiation dosimetry. *J Nucl Med.* 2023;64:1117–1124.
2. Carter LM, Ocampo Ramos JC, Olguin EA, et al. MIRD Pamphlet No. 28, Part 2: comparative evaluation of MIRDcalc dosimetry software across a compendium of diagnostic radiopharmaceuticals. *J Nucl Med.* 2023;64:1295–1303.
3. ICRP. Adult reference computational phantoms. ICRP Publication 110. Ann. ICRP. 2009;39(2).
4. ICRP. Paediatric computational reference phantoms. ICRP Publication 143. Ann. ICRP. 2020;49(1).
5. ICRP. The ICRP computational framework for internal dose assessment for reference adults: specific absorbed fractions. ICRP Publication 133. Ann. ICRP. 2016; 45(2), 1–74.
6. Jokisch DW, Bolch WE, Schwarz BC, et al. Specific absorbed fractions for reference paediatric individuals. *Ann ICRP.* In press.
7. ICRP. Adult mesh-type reference computational phantoms. ICRP Publication 145. Ann. ICRP. 2020;49(3).
8. Kim CH, Choi C, Bolch WE, et al. Paediatric mesh-type reference computational phantoms. Ann ICRP. In press.

Adam L. Kesner*
Lukas M. Carter
Wesley E. Bolch
**Memorial Sloan Kettering Cancer Center*
New York, New York
E-mail: kesnera@mskcc.org

Published online Aug. 10, 2023.
DOI: 10.2967/jnumed.123.266325

Erratum

In the article "Multicenter Evaluation of Frequency and Impact of Activity Infiltration in PET Imaging, Including Microscale Modeling of Skin-Absorbed Dose" by Sunderland et al. (*J Nucl Med*. 2023;64:1095–1101), the legend in Figure 2A mistakenly states units of MBq, whereas *kBq* are the correct units. Additionally, the *y*-axis in Figure 3 should read *0.41 MBq* rather than 0.83 MBq. The authors regret the errors.

Johan S. Masjhur, dr, SpPD-KEMD, SpKN-TM, 1942–2023

Johan Masjhur, dr, SpPD-KEMD, SpKN-TM, widely regarded as the father of nuclear medicine in Indonesia, died on May 13, 2023, in Bandung, Java. He was the first professor in medicine at Universitas Padjadjaran (UNPAD) in Bandung, the original home of nuclear science in Indonesia. He was appointed an emeritus professor at UNPAD in 2006.

Dr. Masjhur was born in Payakumbuh on the island of Sumatra in 1942. He graduated from medical school in 1967 from UNPAD, where he completed a residency in internal medicine in 1976. In 1977, he accepted a position in Indonesia's first nuclear medicine department, at the Dr. Hasan Sadikin Hospital (Bandung), and was funded to travel to The Netherlands to advance his studies in the field. He was appointed head of the Department of Nuclear Medicine at the Dr. Hasan Sadikin Hospital in 1980, a position he held for more than 25 y.

FIGURE 1. Indonesian nuclear medicine trainees at residential workshop organized by Dr. Masjhur (center front, dark shirt) in Bandung, Java, 1988.

In the early years of nuclear medicine in Indonesia, nuclear medicine specialization was not recognized as an independent discipline. The Indonesian Society of Nuclear Medicine and Biology was established in Bandung in 1978 with a multidisciplinary membership, including physicians, technologists, and nonclinical scientists, with Dr. Masjhur as founding president. In 1989, the Indonesian Society of Nuclear Medicine was established as a physician-only organization, with Dr. Masjhur serving as the first president and for 2 additional terms. With his junior colleagues, he struggled for recognition of nuclear medicine for nearly a decade. In 1997, thanks to his persistence and efforts, the role of nuclear medicine specialist was recognized by the Indonesian Medical Association as a distinct specialty. A year later, formal education for nuclear medicine specialists was established at the UNPAD/Dr. Hasan Sadikin Hospital. This remains the only avenue available in Indonesia for nuclear medicine specialist training. All current practicing nuclear medicine specialists in Indonesia were Dr. Masjhur's students (Fig. 1).

Dr. Masjhur served as vice president of the Asia Oceania Federation of Nuclear Medicine and Biology and as chair of the organizing committee of the fifth Asia Oceania Congress of Nuclear Medicine and Biology, held in Jakarta in 1992. He received a lifetime achievement award from the World Radiopharmaceuticals Therapy Council in 2008.

Twenty-four nuclear medicine facilities operate today in Indonesia, including 4 medical cyclotrons, 7 PET/CT scanners, and around 22 SPECT/CT systems. No one has made a more significant contribution to nuclear medicine in Indonesia than our dear friend and colleague Johan Masjhur.

Hussein S. Kartamihardja
Dr. Hasan Sadikin Hospital, Bandung, Indonesia
Dale L. Bailey
Royal North Shore Hospital, Sydney, Australia

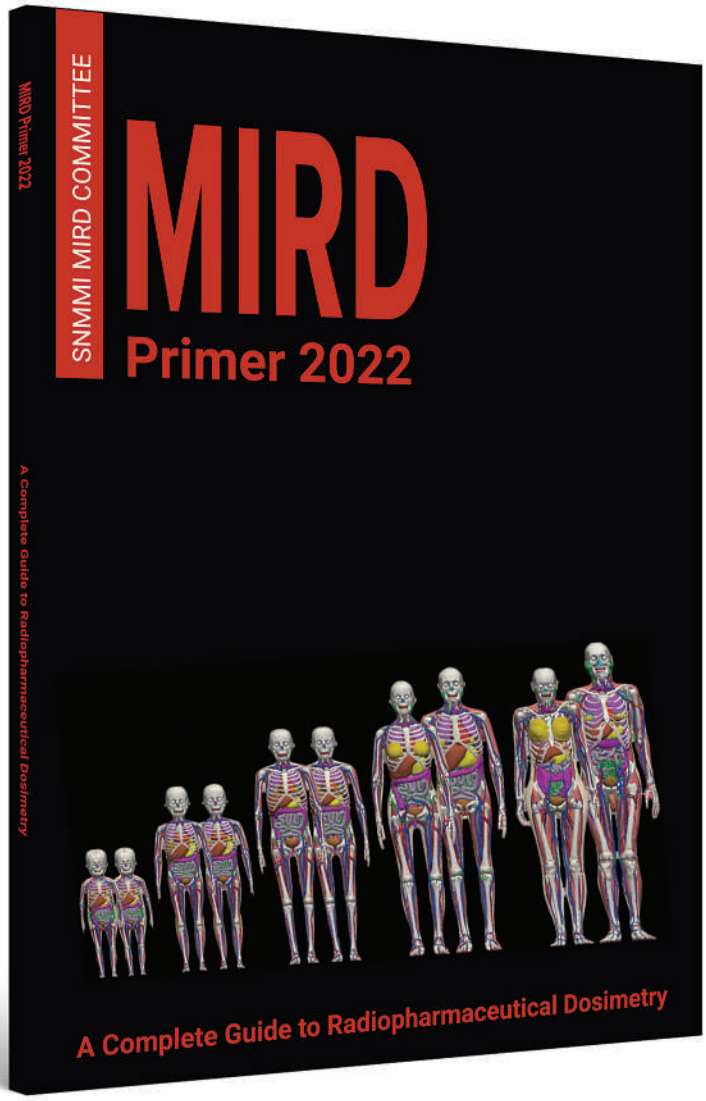

MIRD Primer 2022
A Complete Guide to Radiopharmaceutical Dosimetry

Richly illustrated and thoroughly referenced, the **MIRD Primer 2022** is a comprehensive, state-of-the-art guide to radiopharmaceutical dosimetry that reflects the dramatic evolution of the field of nuclear medicine, including molecular imaging and, increasingly, radiopharmaceutical therapy.

The MIRD Primer 2022 serves as

- a foundation for nuclear medicine and other medical professionals who require a working knowledge of internal radionuclide dosimetry and its radiobiological implications—without having to delve too deeply into the underlying mathematics.
- an authoritative reference on the latest, complete mathematical formulation of the MIRD schema for those seeking a more rigorous understanding of internal dosimetry.
- an invaluable teaching tool, with a large number and wide variety of clinically relevant calculational examples.

Order your copy today!

WWW.SNMMI.ORG/MIRD2022

SNMMI SOCIETY OF NUCLEAR MEDICINE & MOLECULAR IMAGING

2023 SNMMI Upcoming Webinars

Providing leading nuclear medicine and molecular imaging education is a critical part of our mission, and SNMMI's virtual curriculum gives you the flexibility to access this cutting-edge content where and when it works best for you. By connecting you with relevant topics and key expert speakers, SNMMI gives you the support needed to advance your career. ***Please note that all times listed are Eastern US Time***.

- **FAPI PET: Make It or Break It?**
  October 10 | 12:00-1:00 PM
- **The Role of [18F]FDG PET/CT in Multiple Myeloma**
  October 18 | 12:00-2:00 PM
- **Quick Tips for Planning & Execution of Radiopharmaceuticals**
  November 2 | 12:00-1:00 PM
- **Landscape of Molecular Imaging and Fluid Biomarkers**
  November 14 | 12:00-1:00 PM
- **PSMA PET**
  December 12 | 12:00-1:00 PM

SNMMI SOCIETY OF NUCLEAR MEDICINE & MOLECULAR IMAGING

Register today!
www.snmmi.org/webinars

SNMMI and IAC

Collaborate on New Program for Radiopharmaceutical Therapy

Radiopharmaceutical therapy is a powerful technique for treating cancer that is now being used to great benefit in patients with prostate and other cancers. It is essential that patients receiving radiopharmaceutical therapy be confident that their providers meet high standards of training and experience. The new SNMMI-IAC Radiopharmaceutical Therapy accreditation helps assure that sites delivering radiopharmaceutical therapy are qualified and experienced, have appropriate facilities and equipment, and can offer safe and reliable radiopharmaceutical therapy.

Richard L. Wahl, MD, PhD, FASE
SNMMI Immediate Past President,
Member of IAC Nuclear/PET Board of Directors

SNMMI is excited about this accreditation program because it builds upon both the SNMMI Radiopharmaceutical Therapy Centers of Excellence and the IAC nuclear medicine accreditation programs.

Munir Ghesani, MD, FACNM, FACR
SNMMI President

IAC and SNMMI have worked together for many years, as SNMMI is a founding sponsoring organization of the IAC Nuclear/PET accreditation program. The creation of the new Radiopharmaceutical Therapy accreditation offering is possible through our collaboration and leverages both organizations' strengths toward our aligned missions focused on quality and safe patient care. Through a multi-specialty approach, the SNMMI representatives along with our other sponsoring organizations, have contributed greatly to the development of standards for radiopharmaceutical therapy, ensuring that they are reflective of SNMMI guidelines and current best practices that lead to improved patient care.

Howard Lewin, MD, FACC, FASNC
President of the IAC Nuclear/PET Board of Directors

In partnership with the Society of Nuclear Medicine and Molecular Imaging (SNMMI), the IAC is proud to announce a new accreditation program for Radiopharmaceutical Therapy.

Radiopharmaceutical Therapy Accreditation Program

SNMMI SOCIETY OF NUCLEAR MEDICINE & MOLECULAR IMAGING | IAC INTERSOCIETAL ACCREDITATION COMMISSION

The new program offers facilities a mechanism for demonstrating their commitment to quality and patient safety in radiopharmaceutical therapy and will join the existing IAC accreditation areas:

Nuclear Cardiology, General Nuclear Medicine and **Positron Emission Tomography (PET)**.

Learn more today at intersocietal.org/nuclear.

IAC
Improving health care through accreditation®
intersocietal.org | 800.838.2110

IAC Offering 20% Reduction on Base Application Fees for 2023

To learn more or access our Online Fee Estimator, scan the QR code to the left or visit our website at ***intersocietal.org/iac/2023fees***.

10
23

The Journal of Nuclear Medicine

October 2023 ■ Vol. 64 ■ Pages 1505–1669